

Department of Civil and Environmental Engineering

University of Strathclyde

**A Suction – Based Breaching Model
for Flood Defence Embankments
Subjected to Overflow**

Thesis presented for the Degree of Doctor of Philosophy

By

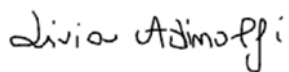
Livia Adinolfi

2022

Declaration of authenticity and author's right

This thesis is the result of the author's original research. It has been composed by the author and has not been previously submitted for examination which has led to the award of a degree.

The copyright of this thesis belongs to the author under the terms of the United Kingdom Copyright Acts as qualified by University of Strathclyde Regulation 3.50. Due acknowledgement must always be made of the use of any material contained in, or derived from, this thesis.

Signed: 

Date: 19/03/2022

Abstract

Historical and recent flood events demonstrated that, very often disastrous floods occurred due to the breaching of dams, dikes and levees resulting from the overflow induced by extreme weather conditions.

The breaching process of flood defence embankment is generally gradual and comprises a series of time-dependent mechanisms that may lead to the final catastrophic failure, when a gap or a proper channel develops across the embankment allowing the inundation of the protected areas.

The assessment of the performance of these geo-structures during extreme weather events is, therefore, essential for flood risk management and mitigation.

In the last decades, the understanding of breaching processes improved consistently thanks to an extraordinary research effort. Laboratory and in-situ tests provided an in-depth description of the fundamental physical mechanisms leading to breach initiation and growth.

In many instances, the final aim of these experimental investigation was the development of breaching models able to predict modes and times of embankment failures during overflow.

Despite the latest achievements, there is a general agreement that the prediction power of the numerical models currently available is still unsatisfactory such that the application in engineering practice is so far very limited.

In this work, a suction – based breaching model for flood defence embankment subjected to overflow was developed, starting from the observation that at the onset of overflow the soil constituting the embankment is usually in a partially saturated state.

Based on this fundamental statement a new conceptual framework to interpret the different macro-erosion failure mechanisms is presented. For the first

time, the focus is moved from soil erodibility and hydrodynamic forces on the coupled soil mechanics and hydraulic phenomena that can have a significant impact on breach formation during overflow.

The conceptual model is implemented adopting traditional finite element methods available to study typical soil mechanics problems.

Ultimately, a qualitative validation conducted against field experiments shows that the suction-based breaching model is a promising predictive tool capable of mimicking the large-scale erosion processes like mini-slopes failures evolving with time.

Acknowledgments

This research project was made possible thanks to the encouragement received, under both the scientific and personal points of view, by a multitude of people.

First of all, I would like to thank my Supervisor, Prof. A. Tarantino for his constant and patient guidance. I am deeply grateful for the fantastic opportunity he gave me of working with him and with his Research Group at University of Strathclyde, contributing to my professional and personal growth. I felt fortunate for the incredible experiences he exposed me throughout the PhD years, like the attendance to the 8th International Conference on Scour and Erosion; the Secondment with the MAGIC Project; the involvement in the TERRE Research Project; the collaboration with the Environment Agency. He brought his experience and he shared with generosity his profound knowledge of Soil Mechanics and his method of Scientific Study. His passion and his dedication to the Research were for me fundamental inspirations for the completion of this PhD.

Life is made of encounters and decisions, and the other essential person that I had the fortune to meet in my path is Prof. R. Vassallo, from University of Basilicata. Without him all these incredible and exciting years would have never happened. Since my Master Thesis he was an important presence in my life, first as Scientific and Technical Mentor and afterwards as a sincere friend. I will always be thankful for his substantial and material support to the development of this Research idea. He constantly gave me scientific and personal advice. His thoughts have always been for me a further light which guided me through this PhD. But, most importantly, he always motivated me and offered his help like friends do, with honesty and generosity. For this and for everything that will come next, an immense thanks.

When I decided to take on the PhD challenge, I was first of all enthusiastic, willing to learn and to improve, but at the same time I was conscious of all the difficulties and of my personal as well as professional limits. What I could

not have imagined when I left my small village in the South of Italy, was the Strathclyde family that I met once in Glasgow. It is a microcosm made of Professors, Researchers, other PhD Students, Administrative Staff and Laboratory Technicians always there to assist and most importantly to let you feel that you are not alone. In this context I had the luck to meet colleagues that soon became special friends. Most of them contributing effectively to the development of this Thesis.

At this regard I would like to thank Michela Martina who first helped me with the assembling of the preliminary experimental device, the Strathclyde Erosion Channel. She was for me one of the most inspiring persons I met when I moved to Glasgow. I admired her expertise as Geotechnical Researcher and she was another source of encouragement. Her strength and positivity were for me a light in the Geomechanics Laboratory as well as outside, in the real world. Since this experience she became another sister and now I could not imagine my life without her fundamental presence.

I would like to thank Anastasia Capotosto, who was helpful especially in the first phases of my Research project. I will be always grateful for the time she spent with me in the Laboratory and for sharing her experience as Researcher.

For the same reason I would like to thank Matteo Pedrotti, who revealed me the secret of “kaolin” sample preparation and for the incredible support he gave me afterwards with the numerical modelling. Another friend at work and outside the University.

A massive thanks to James Minto, the omnipresent person in Laboratory and in the Department. He also gave me plenty of suggestions for the initial experiments, but most importantly he introduced me to the fantastic world of Computation Fluid Dynamic and to OpenFoam. I will never forget the Saturdays and Sundays spent with me teaching me Linux, C++ and OpenFoam, one of the most fascinating and challenging aspect of this Research. His contribution added an enormous value to this Thesis and to my technical skills.

I would like to thank, Elena, Raniero and Emmanuel who were with me in the

Strathclyde “Erosion Team” under the guidance of Prof. A. Tarantino and Dr. Grainne El Mountassir. I was really excited for collaborating with you to the development of the Jet Erosion Test (JET), spending hours in brainstorming and physical work in the Laboratory. This experience inevitably turned out with the present of a good friendship.

To the rest of the Strathclyde family: Brunella, Alessia, Gea, Riccardo, Silvia, Sara, thank you for welcoming me in your family, thank you for all the laughs, the adventures and all the love shared during the Glasgow years which is continuing. To Carolina, thank you for being the best flatmate I could have ever desired. There are no words to describe how lucky I feel for having meet you.

I would like to thank my new mentors and colleagues in Rendel for the encouragement and understanding in this last period of writing up.

To my aunties Maria and Antonietta, to my grandmother Colomba and to the memory of my grandfather Donato, a special thank you. To the rest of my relatives in England and in Italy, to my friends, thank you for all your thoughts and for being close even at long distance.

To my sisters, Nadia and Arianna, thank you for the unlimited source of encouragements and love.

To my mother and to my father, Vincenza and Matteo, if I decided to go through this path, if I am what I am and for everything I have done so far in my life, I can only thank you.

Contents

Abstract.....	II
Acknowledgments.....	IV
List of Figures.....	XII
List of Tables	XXXI
Chapter 1. Introduction.....	1
1.1 PROBLEM DEFINITION AND RESEARCH QUESTIONS.....	3
1.2 STRUCTURE OF THIS THESIS.....	7
Chapter 2. Background	10
2.1 Hydraulics of Embankment Overflow.....	11
2.2 Observed Breaching Mechanisms in Coarse-Grained and Fine-Grained Embankments During Overflow	15
2.3 Soil Erodibility.....	23
2.3.1 Soil Erosion Tests	27
2.3.2 Erosion of coarse-grained soils.....	30
2.3.3 Erosion of fine-grained soils	32
2.4 Modelling of the Observed Breaching Processes.....	36
2.4.1 Conceptual Models for Headcut Erosion.....	42
2.4.2 The Last Generation of Physically-Based Breaching Models ..	56
2.5 Conclusions.....	71
Chapter 3. The Role of Suction in the Onset of Overflow Induced Flood Embankment Breaching.....	73
Abstract	73
3.1 Introduction.....	74

3.2	Towards a new conceptual model for breach formation.....	77
3.2.1	<i>Shear Strength of Unsaturated Soils</i>	80
3.2.2	<i>Stress State at the Embankment Toe</i>	81
3.3	Hydrodynamic Analysis of Embankment Overflow	83
3.3.1	<i>The interFoam solver of OpenFoam</i>	86
3.4	Soil Water Flow Analysis	89
3.5	Soil Slope Stability Analysis.....	92
3.6	Application to an ideal homogeneous embankment.....	98
3.6.1	<i>Hydrodynamic Model in OpenFOAM</i>	98
3.6.2	<i>Finite Element Model in PLAXIS 2D</i>	109
3.7	Results	120
3.7.1	<i>Hydrodynamic Forces</i>	120
3.7.2	<i>Water Flow Analysis in Plaxis 2D</i>	132
3.7.3	<i>Stability analysis in Plaxis 2D</i>	138
3.8	Conclusions.....	140

Chapter 4. Unsaturated Soil Mechanics Breaching Model:

	Development of the Numerical Approach	143
	Abstract	143
4.1	Introduction.....	143
4.2	Breaching models.....	151
4.3	The concept of Suction-Based Breaching Model.....	155
4.4	Definition of the failure criterion	161
4.5	The “Lego Strategy”: application of the failure criterion in PLAXIS 2D.....	167
4.5.1	<i>Algorithm to define a ‘failed’ soil element</i>	168
4.5.2	<i>Algorithm for the removal of the failed soil elements</i>	170
4.5.3	<i>Calibration and Validation of the Failure Criterion</i>	180

4.5.4 <i>Benchmarking ‘Lego’ failure criterion against Upper Bound mechanism</i>	185
4.6 Conclusions.....	188
Chapter 5. Unsaturated Soil Mechanics Breaching Model:	
Qualitative Validation	190
ABSTRACT.....	190
5.1 Introduction.....	190
5.2 IMPACT Project Tests	195
5.2.1 <i>Test #1: Homogeneous Clay embankment (Test 1-02) - Test Overview</i>	197
5.2.2 <i>Test #2: Homogeneous Gravel Embankment (Test 2C-02) – Test Overview</i>	201
5.2.3 <i>Test #3 and Test #4: Composite Structures</i>	205
5.2.4 <i>Summary of IMPACT field test inputs and recommendation</i> .	208
5.3 Implementation of the Suction-based Breaching Model with FEM..	209
5.3.1 <i>Embankment Geometry</i>	211
5.3.2 <i>Hydro-mechanical constitutive models</i>	215
5.3.3 <i>Material Properties of fine-grained soil</i>	218
5.3.4 <i>Material Properties of coarse-grained soil</i>	224
5.3.5 <i>Calculation phases: from construction to overflow</i>	230
5.4 Results	236
5.4.1 <i>Homogeneous Fine-Grained Embankment</i>	236
5.4.2 <i>Homogeneous Coarse-Grained Embankment</i>	277
5.5 Discussion.....	309
5.6 Conclusions.....	320
Chapter 6. Conclusion and recommendations	323
Definition of a new framework for embankment breaching by overflow:	
Research Questions #1- #3 - #4	324

PRELIMINARY PROOF OF CONCEPT: RESEARCH QUESTIONS #2	325
FORMULATION AND VALIDATION OF THE SUCTION-BASED BREACHING MODEL: RESEARCH QUESTIONS #5 AND #6	326
RECOMMENDATIONS AND FUTURE WORKS.....	330

References

**Appendix A. CFD Simulation of Turbulent Flow of Two Immiscible
Fluidsb**

A.1 Governing Equations of Fluid Flows.....	b
<i>A.1.1 Navier-Stokes Equations in the context of the Finite Volume Method.....</i>	<i>c</i>
A.2 Turbulence Modelling	g
<i>A.2.1 The k-ε model.....</i>	<i>l</i>
<i>A.2.2 Wall laws.....</i>	<i>n</i>
<i>A.2.3 Implications in turbulence modelling.....</i>	<i>p</i>
<i>A.2.4 The k-ω model</i>	<i>q</i>
<i>A.2.5 The SST k-ω model.....</i>	<i>r</i>
<i>A.2.6 Conclusion on turbulence modelling</i>	<i>r</i>
A.3 Finite Volume Method.....	s
<i>A.3.1 Spatial Discretization.....</i>	<i>s</i>
<i>A.3.2 Equation Discretization</i>	<i>u</i>
<i>A.3.3 Temporal Discretization.....</i>	<i>y</i>
<i>A.3.4 Boundary and Initial Conditions</i>	<i>z</i>
<i>A.3.5 Modelling Multiphase Flow</i>	<i>bb</i>
<i>A.3.6 Solution Procedure</i>	<i>gg</i>

Appendix B. Proof of Concept Via the Infinite Slope Case..... jj

B.1 Proof of concept: the infinite slope case	jj
<i>B.1.1 Water Flow Analysis</i>	<i>jj</i>

B.1.2 Factor of safety of an unsaturated infinite slope..... kk

B.2 Application to an ideal case.....ll

B.3 Results.....oo

B.4 Conclusionsrr

List of Figures

Figure 2-1: Plan view of overflow for a river flood-defence embankment after Michelazzo (Michelazzo, 2014)	12
Figure 2-2: Longitudinal section of a side-weir with no downstream flow (a) and with transition from supercritical flow to subcritical flow with formation of hydraulic jump (b) after Borghei et al. (Borghei, Jalili and Ghodsian, 1999)	13
Figure 2-3: Typical flow regimes during overflow of embankments and associated erosion zones after Powledge et al. (George R. Powledge et al., 1989)	14
Figure 2-4: Longitudinal profile along the breach channel centreline measured during overflow experiments on sands embankments (Coleman, Andrews and Webby, 2002).....	15
Figure 2-5: Typical breaching process of coarse-grained embankment by surface erosion due to overflow.....	16
Figure 2-6: Different phases of breach formation in sand-dikes observed by Visser (Visser, 1998)	17
Figure 2-7: Cross – sections for Stage (1), (2) and (3) when the length of the downstream slope L is within the limits of the adaptation length of the flow l_n and the adaptation length of the sediment transport l_a (Visser, 1998).....	18
Figure 2-8: Mechanism of sediment transport when (a) $L > l_a$ and when (b) $L \gg l_a$ (Visser, 1998).....	19
Figure 2-9: Different stages of breach formation observed during field-test experiments on fine-grained embankments. (a) formation of networks of rills and (b) evolution of the initial rills into a multi-stepped profiles in Stage I; (c) headcut backwards migration and transition to Stage II (d) headcut	

advancement to the crest and transition to Stage III; (e) crest lowering and transition to Stage III; (f) breach widening at Stage IV (G. J. Hanson, K. R. Cook and S. L. Hunt, 2005).....	21
Figure 2-10: Typical breaching process of fine-grained embankment by headcut erosion during overflow after (Hahn, Hanson and Cook, 2000)	22
Figure 2-11: Forces around clayey aggregates subjected to water flow after (Briaud, 2008).....	24
Figure 2-12: The linear constitutive law for erosion, usually derived from erosion tests	25
Figure 2-13: Classification of soil erodibility as function of critical shear stress and erodibility coefficient (Hanson and Simon, 2001)	26
Figure 2-14: Classification of soil erodibility proposed by Briaud (Briaud, 2008)	27
Figure 2-15: Differences in erosion rate index measured with HET and JET devices (Wahl, 2010)	28
Figure 2-16: Critical Shear-Stress obtained from HET and JET tests (Wahl, 2010)	29
Figure 2-17: Sliding mechanism for spherical particles and incipient motion conditions (a) and rolling mechanism (b) after (Briaud et al., 2001)	31
Figure 2-18: Modified Shields Diagram after (CIRIA, 2013).....	32
Figure 2-19: Geometric parameters of an idealised trapezoidal breach cross-section (a) and outflow hydrograph relating discharge and time during failure of Teton Dam on 5 th June 1976 (b). (Zhang et al., 2016)	37
Figure 2-20: A sketch of the condition corresponding to the transition from phase 2 to phase 3 after Temple and Hanson (Temple and Hanson, 1994).....	44

Figure 2-21: Headcut advancement model proposed by Hanson et al. (Hanson, Robinson and Cook, 2001).....	47
Figure 2-22: Erosion processes affecting headcut stability assuming an erodible bed: (1) shear erosion along headcut top surface: (2) erosion along headcut slope; (3) scour due to the impinging jet undermining the base of the headcut and (4) slope mass failure after (Zhu, 2006)	51
Figure 2-23: Scour hole due to impinging jet downstream of a headcut (Zhu, 2006)	52
Figure 2-24: Sketch of headcut failure (Zhu, 2006)	53
Figure 2-25: Forces acting on the soil block at failure (Zhu, 2006)	54
Figure 2-26: Division of the embankment in sections and definition of the initial notch profile after Morris (Morris, 2011).....	58
Figure 2-27: Screenshot from EMBREA Lite online guidance highlighting the inputs required for the initial notch and selection of erosion equations, from EMBREA for members HR Wallingford (dambreach.org)	59
Figure 2-28: Flow-chart describing the calculation sequence in HR BREACH and EMBREA after Morris (Morris, 2011).....	60
Figure 2-29: Breach channel growth: cross-section (a) and profile (b) after Morris (Morris, 2011)	61
Figure 2-30: Slope stability analysis performed in EMBREA (a) overturning, (b) shear after Mohamed et al. (Mohamed et al., 2002)	62
Figure 2-31: Side- view (a) and 3D view (b) of the breach channel for coarse-grained homogeneous embankment during overflow after Wu (Wu, 2016)	64
Figure 2-32: Side- view (a) and 3D view (b) of the breach channel for fine-grained homogeneous embankment during overflow after Wu (Wu, 2016)	65

Figure 2-33: Longitudinal section of breach in (a) intensive breaching period under critical flow conditions and (b) in general evolution period after Wu (Wu, 2016).....	66
Figure 2-34: Progressive surface erosion simulated in DLBreach, (a) cross-section and (b) profile, after Wu (Wu, 2016).....	68
Figure 2-35: Breach side slope stability modelled in DLBreach. according to a planar failure surface inclined by α to the horizontal after Wu (Wu, 2016)	69
Figure 2-36: Initial stage of headcut migration after Wu (Wu, 2016).....	70
Figure 3-1: Ground water flow process and propagation of the saturation front within an embankment during overflow. (a) Initial condition; (b) increase of river water level and infiltration from the upstream slope; (c) overflow when water levels exceed the embankment crest; (d) overflow progression and infiltration from the downstream slope as well as from the upstream side..	79
Figure 3-2: Representative stress states (a) near the crest (b) near the toe. Green lines are referring to the initial condition. Blue lines represent the overflow event.....	83
Figure 3-3 Water flow associated with the overflow with the increase of shear stresses downstream and flow velocity and shear stress profiles along the direction of flow in Section A-A	85
Figure 3-4: Solution procedure implemented in InterFoam after (Korchagova, 2017)	89
Figure 3-5: Forces acting in an infinite slope.....	93
Figure 3-6: Different contributions of (a) friction, apparent and effective cohesion on the total FoS of an infinite slope (b) FoS when cohesion is neglected.....	96

Figure 3-7: Cross-section of the ideal homogeneous embankment modelled	98
Figure 3-8: Block scheme of the procedure to set up the OpenFoam case ..	99
Figure 3-9: Computational domain implemented (a) view in the plane Y-X (b) three-dimensional view showing the mono-cell and the small thickness in the Z direction.....	101
Figure 3-10: Initialisation of the function alpha.water to set the initial water region up to 4m from the bottom boundary	102
Figure 3-11: Turbulence model specified to solve the RANS equations...	103
Figure 3-12: Assessment of k and ω values based on conversion with free stream velocity, turbulence intensity/level and turbulence length scale (https://www.cfd-online.com/Tools/turbulence.php)	107
Figure 3-13: Model extent and Finite Element Mesh	110
Figure 3-14: Soil water retention curve	113
Figure 3-15: Hydraulic Conductivity Function	113
Figure 3-16: Hydraulic Shear Stress Distribution from Open Foam and averaged over segments 1m long (a) and distributed load introduced in Plaxis 2D (b)	116
Figure 3-17: Hydraulic Boundary Conditions for the initial phase	117
Figure 3-18: Second calculation phase and hydraulic boundary conditions	117
Figure 3-19: River appears on the upstream side, followed by a consolidation phase	118
Figure 3-20: Hydraulic boundary conditions associated with an extreme weather event, leading to the increase of the water levels up to the crest level	

.....	119
Figure 3-21: Hydraulic boundary conditions which simulate the overflow event.....	120
Figure 3-22: Free surface elevations at (a) t = 8 sec; (b) t = 16 sec; (c) t =24 sec; (d) t = 32 sec; (e) t = 120 sec and (f) t = 180 sec, showing the steady state condition after t = 32 sec.....	122
Figure 3-23: Time sequence of the velocity vectors at: (a) 16 sec; (b) 24 sec; (c) 40 sec and (d) 180 sec.....	124
Figure 3-24: Wall Shear Stress and water velocity profiles in the X direction at: (a) the downstream toe; (b) middle of the slope and (c) downstream edge of the crest for t = 24, 44, 120 and 180 sec	125
Figure 3-25: Wall Shear Stress and water velocity profiles in the Y direction at: (a) the downstream toe; (b) middle of the slope and (c) downstream edge of the crest for t = 24, 44, 120 and 180 sec	126
Figure 3-26: Example of water velocity profile measured with the ADCP technique during the data (Stephen M. Westenbroek, 2006).....	128
Figure 3-27: Resultant of the shear stresses distribution along the downstream slope at different time instants.....	129
Figure 3-28: Shear stress distribution obtained performed with CHEN 3D (Briaud et al., 2008).....	130
Figure 3-29: Effective suction distribution at four different embankment locations: (a) crest, (b) at approximately one third of the downstream slope; (2) at approximately two third of the downstream slope; (3) near the downstream toe. The Time Step selected are the initial river level (brown line); 10 hours flood (blue line), 5 min overflow (dotted light blue line) and 15 min overflow (discontinues black line).....	133

Figure 3-30: Contour plot of the pore water pressure distribution at the end of the overflow phase	134
Figure 3-31: Selected time-step of Hydraulic conductivity at: (a) embankment crest; (b) one third of the downstream slope; (c) tow third of the downstream slope; (d) downstream toe	135
Figure 3-32: Water flow at selected time-steps from the increase water level phase: after (a) 5 hours; (b) 8 hours; (c) 10 hours and water level at the crest; (d) 15 minutes of overflow	137
Figure 3-33: Failure mechanisms for (a) overflow with hydraulic shear stresses; (b) overflow without hydraulic shear stresses	138
Figure 3-34: Factor of Safety resulting from the Safety analysis for the two scenarios analysed with and without hydraulic shear stresses	139
Figure 4-1: Examples of Breaches in riverine embankments. (a) Croston Breach Winter Floods 2015/2016, Lancashire (Simm et al., 2017); (b) Tetney Breach, Yorkshire, 5th December 2013 (Environment Agency, UK).....	144
Figure 4-2: Typical hydraulics of embankment overflow and associated erosion zones after (George R Powledge et al., 1989).....	145
Figure 4-3: Schematic layout of progressive surface erosion characteristic of the breaching process of coarse-grained embankment fills	147
Figure 4-4: Schematic layout of headcut erosion characteristic of the breaching process of fine-grained embankment fills.....	147
Figure 4-5: Classification of erosion processes based on grain size where uncertainties are emphasised with question marks after (Morris, 2011) ...	148
Figure 4-6: Images collected during one of the experiments conducted at the U.S. Geological Survey on large-scale embankment constructed with fine sand. (a) formation of the stepped profile and (b) migration of the steps	

upstream forming a single large headcut. White arrows indicate the base of the steps and headcut. After Walder et al. (Walder et al., 2015)..... 151

Figure 4-7: Typical loop with sub-models constituting physically-based breaching models 153

Figure 4-8: A sketch of the ground water flow process and propagation of the saturation front within an embankment during overflow. (a) initial condition; (b) increase of water levels and infiltration on the upstream slope; (c) overflow generating when water levels exceed the embankment crest with the advancement of the saturation front to the toe; (d) overflow progression and infiltration from the downstream slope as well as from the upstream side 156

Figure 4-9: Typical stress states (a) near the crest (b) near the toe. Green lines are referring to the initial condition. Blue lines represent the overflow event 159

Figure 4-10: Stress state in the Mohr plane for a point which violates the failure criterion (a) and stress-strain relationship, with green point representing the yielding condition and red point beyond the elastic strain threshold representing plastic shear strain 161

Figure 4-11: Deformation and sliding of a block by increasing the horizontal force, under constant vertical force. (0) Initial condition when nothing happens; (1) development of elastic deformation; (2) the applied force is equal to the material resistance and yielding is occurring; (3) the applied horizontal force increases, plastic deformation are accumulated and at a certain point the block slides. Green lines refer to the inherent resistance of the block. Red lines represent the applied horizontal force. The dotted line is the block in its original configuration..... 162

Figure 4-12: Plastic points represented as green dots and failure points in red, formed within the embankment as consequence of the infiltration processes associated to the overflow 163

Figure 4-13: Accumulation of plastic deformation leads to an increase of the number of failure points. A shear zone evolving in a continuous slip surface is identified, constituting the failure mechanism..... 164

Figure 4-14: The first small headcut in the process of headcut initiation observed at the toe of the embankment..... 165

Figure 4-15: Formation of the second headcut (a) and application of the failure criterion resulting in the new embankment configuration 166

Figure 4-16: A sketch of headcutting backwards migration process up to the condition of breach formation when the crest is reached..... 167

Figure 4-17: Geometry built in PLAXIS 2D, where the blue lines represent the triangular soil elements constituting the embankment body while the grey triangles are the finite element mesh automatically generated in the Mesh Mode 168

Figure 4-18: A sketch of the 15-node element constituting the finite element mesh. The black points represent the 15 nodes and the blue crosses the 12 Stress Points 168

Figure 4-19: Definition of a soil failed element based on the number of stress points in failure condition. Elastic stress points are represented by blue crosses, plastic points are green crosses and failure points are red crosses 170

Figure 4-20: Flowchart describing the algorithm which implements the failure criterion and the soil removal based on the failure surface found at the time-step of reference..... 171

Figure 4-21: A small portion of the embankment analysed (a) initial configuration corresponding to Step #0 in the flowchart; (b) subset of failed elements obtained with sub-routine “failed elements” at Step #1 172

Figure 4-22: Step #2 assuming that the first iteration of the loop starts from element El. 1 of the subset of the failed elements on the surface..... 172

Figure 4-23: In yellow are presented all the neighbour elements of El. 1, recognised with the sub-routine” neighbour element” at Step #3. Four scenarios are possible starting from El. 1.....	173
Figure 4-24: Scenario 1 leads to a potential failure surface as the neighbour element El. 2 has an edge on the surface	174
Figure 4-25: El. 3 is not on the surface and the process comes back at Step #3. The new set of elements of El. 3 is presented in orange	175
Figure 4-26: Sub-case 1 of scenario 2, which considers the path El. 1 + El. 3 + El. 7. The element considered is the yellow triangle while the orange triangles are the neighbour elements found.....	175
Figure 4-27: Two possible sub-cases after scenario 2. On the left it is shown a path that ends without arriving at Step #5. On the right the path followed exits on the surface, but the failure surface found is not concave	177
Figure 4-28: Scenario 4 can be further subdivided into two possible subcases: Scenario 4.1 and Scenario 4.2	178
Figure 4-29: In Scenario 4.1, the yellow triangles are the ones followed to arrive on element El. 40 on the surface, but the envelope identified is not included in the list of potential failure surfaces.....	179
Figure 4-30: Scenario 4.2 leading to Scenario 4.2.1 following the neighbour elements of El. 26. Among the different possibilities Scenario 4.2.1.2 is represented leading to El. 33 on the surface and the associated path is stored in the list of the potential failure surfaces	180
Figure 4-31: Slope geometry adopted for the calibration of the failure criterion	181
Figure 4-32: Example of DLO applied to the undrained stability of a footing after (LimiteState Ltd, 2016).....	181

Figure 4-33: Total Multiplier provided by the Safety Calculation in Plaxis 2D versus Calculation Step, with the corresponding friction angles	183
Figure 4-34: Plastic Point plots at calculation step 60.....	184
Figure 4-35: Failure mechanism identified at step 60 represented in terms of deviatoric strain	184
Figure 4-36: Failure mechanism in LimitState:GEO assuming friction angle equal to 16.50° and cohesion equal to 2.05 kPa corresponding to the strengths parameters at step 50 in PLAXIS	185
Figure 4-37: Comparisons between failure mechanisms provided by LimitState:GEO and the slip-surface identified with the failure criterion defined for the removal of soil elements. (a) slip surface based on 11 failure points per elements; (b) 8 failure points and (c) 3 failure points.....	187
Figure 5-1: IMPACT Field Test site location (Morris, 2009).....	196
Figure 5-2: Test1-02 of the IMPACT project (Hassan and Morris, 2008)....	197
Figure 5-3: Homogeneous fine-grained test embankment (Impact, Test1-02)	198
Figure 5-4: Grain size distribution of the embankment material for IMPACT Test1-02 (Morris, Hassan and Vaskinn, 2005).....	199
Figure 5-5: (a) Interface between embankment and rock at the left abutment as seen from the upstream edge; (b) view of the left abutment from downstream; (c) downstream face and left abutment during the test; (d) piping processes observed during the test at the left abutment (Morris, 2009)	201
Figure 5-6: Test2C-02 of the IMPACT project (Hassan and Morris, 2008)	202
Figure 5-7: IMPACT Test 2C-02 frozen embankment (Morris, 2009)	203

Figure 5-8: Headcutting observed in the coarse-grained embankment during Test2C-02 of the IMPACT project due to frozen conditions after (Morris, 2011)	204
Figure 5-9: Breach side after test completion with overhanging region. (Morris, 2009).....	204
Figure 5-10: Configuration adopted for the Field Test 1-03 (Hassan and Morris, 2008).....	205
Figure 5-11: Configuration adopted for the Field Test 2-03 (Hassan and Morris, 2008).....	207
Figure 5-12: Embankment geometry input in Plaxis 2D	211
Figure 5-13: Initial mesh considered to draw the triangular soil elements constituting the embankment.....	212
Figure 5-14: Embankment geometry composed of triangular soil elements	213
Figure 5-15: Triangular soil clusters drawn are represented in blue and the computational mesh elements in grey lines.....	214
Figure 5-16: Tests on samples compacted in laboratory after (D’Onza et al., 2016)	220
Figure 5-17: Failure surface resulting after a period of 30 minutes of overflow for the different values of stiffness considered (a) entire embankment; (b) zoom on the toe area.	222
Figure 5-18: SWRC introduced in Plaxis 2D to model the hydraulic behaviour of the silty clay constituting the embankment.....	223
Figure 5-19: Hydraulic conductivity function representative of the silty clay material.....	224

Figure 5-20: Compressibility of Jossigny 50 % +sand at the Proctor optimum upon wetting (Fleureau et al., 2002).....	226
Figure 5-21: Failure surfaces resulting after 30 minutes of overflow for the case of the coarse-grained embankment for different values of the Young Modulus (a) entire embankment; (b) zoom on the downstream slope	227
Figure 5-22: SWRC introduced in Plaxis 2D to model the hydraulic behaviour of the ideal sand constituting the embankment	229
Figure 5-23: Hydraulic conductivity function assumed for the coarse-grained material.....	230
Figure 5-24: Boundary conditions in the initial phase.....	232
Figure 5-25: Embankment placement in the second calculation phase.	233
Figure 5-26: Increase of water level on the upstream side simulating the presence of a river/water body.....	233
Figure 5-27: Extreme weather event leading to the progressive increase of the water level up to the embankment crest.....	234
Figure 5-28: Frist overflow phase simulated by imposing zero water pressure along the downstream slope, while the water head is kept constant on the upstream side.....	235
Figure 5-29: Overflow simulated (a) and field test (b) at the initial stage.	240
Figure 5-30: First signs of soil removal. Interpretation of the process observed	241
Figure 5-31: Pore water pressure distribution resulting from the first 10 minutes of the overflow phase. Suction is positive. Maximum Value is 62.06 kN/m ² (i.e. dark blue contour) and minimum is -130.4 kN/m ² (i.e. red contour)	243

Figure 5-32: Effective suction profiles at selected cross sections along the embankment downstream slope (a) profiles of relative shear along the same cross-sections (b) after 10 min of overflow 244

Figure 5-33: Selected points on the slope surface (a). Stress paths in p' - q plane for soil elements at toe area (b) and at the embankment crest (c) 245

Figure 5-34: Stress state of different soil elements during overflow presented in the p' - q plane. 247

Figure 5-35: Comparison between the simulated overflow and the interpreted profile assessed from the field test at a similar same stage of the breaching process..... 249

Figure 5-36: Pore water pressure distribution resulting after 70 minutes of the overflow phase. Suction is positive. Maximum Value is 57 kN/m^2 (i.e. dark blue contour) and minimum is -139 kN/m^2 (i.e. red contour)..... 250

Figure 5-37: Effective suction profiles at selected cross sections along the embankment downstream slope (a) profiles of relative shear along the same cross-sections (b) after 70 min of overflow 251

Figure 5-38: Selected points on the slope surface (a). Stress paths in p' - q plane for soil elements C, D and E (b) 252

Figure 5-39: Simulated failure surface (a), field test photos (b) and (c)... 254

Figure 5-40: Comparison between the simulated overflow (a) and the assessed embankment profile from the field test (b) 255

Figure 5-41: Pore water pressure distribution resulting after 170 minutes of the overflow phase. Suction is positive. Maximum Value is 54.4 kN/m^2 (i.e. dark blue contour) and minimum is -139 kN/m^2 (i.e. red contour) 256

Figure 5-42: Effective suction profiles at selected cross sections (a) profiles of relative shear along the same cross-sections (b) after 170 min of overflow

.....	257
Figure 5-43: Stress paths from 70 min to 170 min of overflow duration of points close to the surface (a) along cross – sections C (b), D and E (c)...	259
Figure 5-44: simulated failure surface (a) field test photos (b) and (c) at half-way of the total breaching process.....	261
Figure 5-45: Comparison between the simulated failure surface(a) and the field site test (b)	262
Figure 5-46: Pore water pressure distribution resulting after 280 minutes of the overflow phase. Suction is positive. Maximum Value is 51 kN/m ² (i.e. dark blue contour) and minimum is -139 kN/m ² (i.e. red contour)	264
Figure 5-47: Effective suction profiles at selected cross sections (a) profiles of relative shear along the same cross-sections (b) after 280 min of overflow	265
Figure 5-48: Selected points on the slope surface (a). Stress paths in p’-q plane for soil elements D and E (b).....	266
Figure 5-49: Calculated headcut (a) and field test photos (b) at the 80% of the overall embankment breaching.....	267
Figure 5-50: Comparison between the simulated failure surface (a) and the field site test (b)	269
Figure 5-51: Pore water pressure distribution resulting after 450 minutes of the overflow phase. Suction is positive. Maximum Value is 50 kN/m ² (i.e. dark blue contour) and minimum is -139 kN/m ² (i.e. red contour)	270
Figure 5-52: Effective suction profiles at selected cross sections (a) profiles of relative shear along the same cross-sections (b) after 450 min of overflow	271
Figure 5-53: Selected points on the slope surface (a). Stress paths in p’-q plane	

for soil elements D and E (b).....	272
Figure 5-54: Headcut breaks through the crest causing the opening of the breach formation. Predicted embankment profile (a) and photos from the large-scale test (b) and (c)	275
Figure 5-55: Pore water pressure distribution resulting after 550 minutes of the overflow phase. Suction is positive. Maximum Value is 48 kN/m ² (i.e. dark blue contour) and minimum is -139 kN/m ² (i.e. red contour)	276
Figure 5-56: Final catastrophic failure showing the open channel flow through the breach	277
Figure 5-57: Initial phase of breach formation for coarse-grained embankment (a) predicted profile after 10 minutes of overflow; (b) Field test #2 after 7 min of test run; (c) Field test #3 after 17 min from the start of overflow	280
Figure 5-58: Interpretation of the embankment profile after 17 minutes the overflow process of the Test #3.....	281
Figure 5-59: Pore water pressure distribution resulting after 10 minutes of the overflow phase. Suction is positive. Maximum Value is 55 kN/m ² (i.e. dark blue contour) and minimum is -134 kN/m ² (i.e. red contour).....	282
Figure 5-60: Effective suction profiles at selected cross sections along the embankment downstream slope (a) profiles of relative shear along the same cross-sections (b) after 10 min of overflow	283
Figure 5-61: Selected points on the slope surface (a). Stress paths in p'-q plane for soil elements A, B, C (b) D and E (b)	286
Figure 5-62: Breach formation of coarse-grained embankment (a) predicted profile after 25 minutes of overflow; (b) Field test #2 after 17 min of test run; (c) Field test #3 after 46 min from the start.....	288

Figure 5-63: Progressive surface erosion towards the embankment crest and formation of a single step at the toe area for the simulated embankment profile at the 44% of the total breach formation process.	289
Figure 5-64: Interpretation of the IMPACT Field Test #3 embankment profile at the 46 minutes after the beginning of overflow	290
Figure 5-65: Pore water pressure distribution resulting after 25 minutes of the overflow phase. Suction is positive. Maximum Value is 50 kN/m ² (i.e. dark blue contour) and minimum is -136 kN/m ² (i.e. red contour).....	291
Figure 5-66: Effective suction profiles at selected cross sections along the embankment downstream slope (a) profiles of relative shear along the same cross-sections (b)	292
Figure 5-67: Selected points along the slope (a). Stress paths in p'-q plane for the selected soil elements C, D, E (b)	294
Figure 5-68: Breach formation process of coarse-grained embankment (a) predicted profile after 45 minutes of overflow; (b) Field test #2 after 34 min of test run; (c) Field test #3 after 95 min from the start of overflow	297
Figure 5-69: Combination of progressive surface erosion and headcut resulting from the suction-based breaching model after 45min of overflow	297
Figure 5-70: Interpretation of the embankment profile observed during the Field Test #3 after 95 min of overflow	298
Figure 5-71: Pore water pressure distribution resulting after 45 minutes of the overflow phase. Suction is positive. Maximum Value is 45 kN/m ² (i.e. dark blue contour) and minimum is -138 kN/m ² (i.e. red contour)	299
Figure 5-72: Effective suction profiles at selected cross sections along the embankment downstream slope (a) profiles of relative shear along the same cross-sections (b)	300

Figure 5-73: Selected points along the slope (a). Stress paths in p'-q plane for the selected soil elements D, E (b).....	301
Figure 5-74: Breach formation in the coarse-grained embankment according to the suction-based model (a), IMPACT Field Test #2 and IMPACT Field Test #3.....	303
Figure 5-75: Breach Formation according to the suction-based breaching model after 57 min of overflow.....	304
Figure 5-76: IMPACT Field Test #2 breach formation and growth, highlighting the vertical sides of the breach profile and overhanging material at the crest level.	305
Figure 5-77: IMPACT field test #3 few minutes before breach formation (a) side view; (b) aerial view	307
Figure 5-78: Pore water pressure distribution at breach formation phase. Suction is positive. Maximum Value is 44 kN/m ² (i.e. dark blue contour) and minimum is -138 kN/m ² (i.e. red contour).....	308
Figure 5-79: Predicted embankment profiles for fine-grained (a) and coarse-grained (b) breach formation process.	310
Figure 5-80: Particle size distribution adopted in the IMPACT laboratory test series (Morris, Hassan and Vaskinn, 2007a).....	313
Figure 5-81: calculated profiles (a) IMPACT laboratory test (b).....	314
Figure 5-82: numerical results after 25 minutes of simulated overflow (a), (b) laboratory test after 15 seconds from the test start	315
Figure 5-83: breach development after 35 minutes of simulated overflow (a) IMPACT laboratory test (b)	316
Figure 5-84: breach formation in the numerical model (a), IMPACT laboratory test (b).....	317

Figure 5-85: Test embankment cross-section (a) and final test configuration
(b) (Zhu, 2006) 318

Figure 5-86: Comparison between simulated (a) embankment profile and (b)
laboratory experiment (Zhu, 2006) for homogeneous coarse-embankment
..... 319

List of Tables

Table 2-1: Historical overview of the main physically – based breaching models available in literature extracted from (Morris et al., 2009).....	39
Table 3-1: Fluid Properties for the embankment overflow problem	102
Table 3-2: Boundary conditions defined for the embankment overflow problem	105
Table 3-3: Soil properties assumed for the ideal silty-clay material	111
Table 3-4: Hydraulic model parameters implemented for the silty-clay adopted	112
Table 3-5: Calculation phases and type of analysis implemented in Plaxis 2D	115
Table 4-1: Soil parameters initially considered for the slope stability analysis in PLAXIS 2D	182
Table 5-1: List of the breaching tests undertaken during the IMPACT project (Morris, 2009).....	197
Table 5-2: Embankment geometry of the Test1-02 of the IMPACT project (Hassan and Morris, 2008).....	198
Table 5-3: Soil properties for Field Test #1 (Hassan and Morris, 2008)...	199
Table 5-4: Geometrical details for Test 2C - 02 of the IMPACT (Hassan and Morris, 2008).....	202
Table 5-5: Material Properties reported for the Test 2C-02 of the IMPACT project (Hassan and Morris, 2008)	202
Table 5-6: Geometrical details for Test 1-03 (Hassan and Morris, 2008) .	205

Table 5-7: Material Properties reported for the Moraine Core used in Test 1-03 (Hassan and Morris, 2008)	206
Table 5-8: Material Properties reported for the Rockfill used in Test 1-03 (Hassan and Morris, 2008)	206
Table 5-9: Test 2-03 geometry (Hassan and Morris, 2008)	207
Table 5-10: Details of the embankment geometry adopted	211
Table 5-11: Element sizes as generated by the triangulation procedure in PLAXIS 2D used to build the final embankment geometry	212
Table 5-12: Details of the final computational mesh.....	213
Table 5-13: Material properties for the Mohr-Coulomb model adopted for the silty-clay representative of the fine-grained homogeneous embankment..	219
Table 5-14: Hydraulic parameters adopted for the ideal silty clay material	223
Table 5-15: Mechanical Properties adopted in input to simulate the overflow of coarse-grained embankment.....	225
Table 5-16: Parameters of the van-Genuchten model characterising the ideal sand constituting the embankment.....	229
Table 5-17: Calculation phases implemented in PLAXIS 2D common to both fine-grained and coarse-grained embankments simulated with the suction-based breaching model.....	231

Chapter 1. Introduction

Earthen embankments are the most traditional and widespread infrastructure adopted to retain water, with the main functions of flood defence and control, irrigation, hydropower, and water supply. As such, these structures contributed significantly to the socio-economic development and prosperity of ancient and modern populations.

Nowadays, earthen embankments comprising dikes and levees are the primary asset of flood defence systems, with several hundreds of thousands of kilometres built along rivers and coastal lines all over the world. Flood defence embankments act as a barrier preventing the water flow towards the protected lands. However, the long list of historical and recent flood events has demonstrated the high vulnerability of this form of protection where the failure of earthen structures caused dramatic losses of lives, economic-environmental damages and disruptions to infrastructures and buildings. The impact of floods becomes much more catastrophic because of the breach of flood defence embankments. Therefore, the assessment of the performance of these geotechnical structures during extreme weather events is essential for flood risk management and mitigation.

The points of weakness of flood defence embankments and earthen dams are various and can be identified with their inherent heterogeneity (i.e. geometries/configurations/forms, filling materials, types of loads, riverine, estuarine or coastal environments, etc.) and erodible nature. Flood defence embankments are often ancient structures, built throughout centuries without precise design standards and construction criteria. Very often they have been subjected to a complicated series of historic events that might have required rebuilding, repairing, increasing the crest levels using different sources of material without necessarily matching the original conception of the structure. Traditionally, earthen embankments have been built with low-cost and locally won soils mainly consisting of fluvial deposits from historical floodplain excavated from ditches close to the embankment location or materials retrieved from river sediments. Therefore, most of these structures were built with fine silts and clayey materials rich in organic content. Sometimes a berm consisting of

cobbles and boulders was formed in front of the embankment toe to improve the erosion resistance in this zone. In many cases, the crest was raised with soils dredged from riverbeds. It is also important to mention that, in contrast with the most recent construction techniques aiming to produce an engineered fill through heavy compaction of soils laid in layers, old embankments have been built without these modern standard specifications. This implies that the heterogeneous superficial deposits used as source of filling materials also constitute the embankment foundations, governing groundwater flow, settlements and stability. In many cases no treatments were performed to improve mechanical properties. Consequently, flood defence embankments can be highly variable structures which tend to reflect the geological history, the environmental characteristics and the traditional construction techniques of the specific location in which they were raised.

Another key aspect to be considered is that flood defence embankments deteriorate over time mainly due to: (1) vegetation and tree roots responsible for the formation of macro-porosities; (2) animal activities resulting in burrows and holes; (3) desiccation cracks and fissures resulting from dry and wet cycles; (4) surface erosion and (5) human vandalism. All these factors can undermine the functionality of the structure and can contribute to poor performance particularly during extreme weather events.

Flood risk is rising worldwide as acknowledged by Governments, Operating Authorities, and scientific community, and perceived by the public. Heavy rainfalls and extreme storms are becoming more severe and more frequent due to climate change. Also, many climate change scenarios show that this trend is expected to worsen in the near future. On the other hand, the changes of rains patterns, dry and wet cycles can significantly impact the state and condition of the material constituting the embankments (i.e. desiccation cracks). The situation is further aggravated by the growth of the population and excessive urbanisation of floodplains. As a result, flood events are increasing in magnitude, frequency and destructive potential.

Due the key role played by earthen embankments in mitigating flood risk, one of the main urgencies is the improvement of the current level of knowledge and understanding of the behaviour of flood defence embankments under pre-flood

conditions and during extreme hydraulic loads. On one hand, this is key to the management, maintenance and remedial works of existing structures, as well as for the design requirements and construction techniques of new ones. On the other hand, this analysis is fundamental to develop tools and methods for predicting modes and times of failure for early warning systems and risk planning. This is the primary objective of breaching models.

1.1 Problem Definition and Research Questions

Flood defence embankments can fail due to different causes and mechanisms. However, the analysis of historical events, case studies and experimental investigation has highlighted that breaching induced by overtopping/overflow is the most common type of failure.

Overflow occurs when the water levels exceed the structure capacity and water flows along the embankment downstream slope inundating the protected areas. This situation triggers a series of time-dependent processes associated with the water overflowing. The resulting progressive removal of the embankment materials can lead to the formation of a gap which divides the structures in two distinctive segments and allows the uncontrolled passage of the flood water. This condition otherwise known as breach constitutes the final catastrophic failure.

Understanding these processes with the aim of breach prediction via numerical simulations requires the study of the multiple interactions between the structure, the water overflow and inflow, the response of the soil constituting the embankment and its foundation. In this context, a multidisciplinary approach must be adopted involving theories and methods of hydrology, hydraulic, hydrodynamic and soil mechanics.

In the last decades many research programmes and task committees have contributed to provide a description of the fundamental physical mechanisms leading to breach initiation and growth. The current interpretation is that breaching due to overflow is an external erosion problem driven by hydrodynamic shear forces developed at the water-soil interface. Erosion starts when shear forces, which are proportional to the increasing water velocities along the downstream slope, exceed a

characteristic soil resistance. Erosion then proceeds at a certain rate depending on the erodibility properties of the embankment material. This concept has been mathematically described by a linear constitutive law for erosion comprising two soil erodibility parameters, that are the critical shear stress and the erodibility coefficient. The need of determining the erosion resistance of soils has driven the development of an increasing number of experimental devices (EFA, HET, HET, RETA, etc.), which differ essentially for the flow conditions imposed to the soil sample (i.e. submerged vertical jet, rotating flow, flow parallel to the surface) and for the interpretation methods. However, currently, significant advancements in the field of soil erosion tests are still missing such that it is difficult to find laboratories that can perform the most common erosion tests mentioned. The difficulties in finding a satisfactory test setup have been experienced directly by the author of this work when dealing with a piston style device (i.e. Erosion Function Apparatus) and Jet Erosion Test (i.e. JET). This direct experience pointed out the need of sophisticated systems of measurement like particle image velocimetry (i.e. PIV) to characterise turbulent water flow and the need of a robust interpretative framework of the measurements undertaken. Most of the time the combinations of these requirements can be anti-economical and impractical, resulting in more approximate and less reliable solutions.

Experimental campaigns on field test embankments and more often at laboratory scale, have been reported in the literature. The most important outcome has been that failures are very sensitive to the material forming the embankment. Progressive-surface erosion and headcutting are the two main macro-erosion mechanisms characterising breaching failure of coarse-grained and fine-grained embankments respectively. These two modes of failure present significant differences especially at the beginning of overflow. Progressive-surface erosion is a quick process where the crest and the downstream slope are rapidly eroded layer-by-layer. Headcut erosion takes place through the formation of overfalls starting from the downstream toe that tend to merge in larger steps while migrating backwards to the crest. Headcut erosion is typically much slower than progressive-surface erosion. These two mechanisms dictate the timing of breach initiation and progression. Hence, in the context of breach modelling, it is essential to understand when, how and why headcut or progressive

surface erosion are expected.

For many years, research efforts have focussed on erodibility properties of soils, under the assumption that headcutting takes place in fine-grained soils because these materials are more erosion-resistant than coarse-grained materials. Because of this, fine-grained soils can sustain the formation of headcuts. However, many experimental investigations have revealed very complex dynamics, combining surface and head-cut mechanisms within the same breaching process. These observations suggest that such a schematic distinction between macro-erosion behaviours based on material erodibility categories tend to over-simplify the reality and that multiple factors may play a critical role.

Furthermore, it is important noticing that the description of soil erodibility through erosion law and erodibility parameters, widely accepted in the research community, is still far from being satisfactory. At present, both theoretical framework and experimental procedures need to be improved to reduce the uncertainties and contradictions highlighted in many comparative research works. To date, it is not possible to identify a reliable predictive tool that can provide a consistent characterisation of soil erodibility, especially for fine-grained soils where it appears that erodibility is influenced by physical, chemical, biological and mechanical properties of soil, pore and erosive fluids. In addition, there is an increasing recognition of the importance of climate-related processes, the so-called subaerial erosion, which have impacts on soil water content changes resulting in the softening and weathering of the embankment materials with time. It is not possible to model hydraulic erosion without considering these aspects. These two processes are mutually dependent.

The fact that headcut formation can also occur in coarse-grained materials under specific conditions indicate that the embankment state at the time of overflow must be taken into account. For example, headcutting was observed in one of the field tests conducted as part of the IMPACT Project where the contingent climate conditions induced the freezing of the gravelly soil constituting the test embankment. The formation of headcut has been explained as the consequence of the enhanced erosion resistance experienced by the frozen soil.

The overlapping erosion behaviours with a mix of headcut and surface erosion in

coarse-grained geomaterials have also been observed in laboratory experiments. The common aspect of these investigations was the measurement of negative pore-water pressures within the embankment body. This indicates, once again, that the state of the material and particularly its degree of saturation and its evolution in time during water overflow is an essential aspect of the embankment response to overflow.

These experiences have contributed to increase the awareness on the importance of the material conditions and states prior to the flood event. However, these aspects are almost always neglected or only partially included in the most recent physically-based breach models. This is due to the inherent complexity of the phenomena to be modelled but also to the relatively poor understanding of the mechanical and physical processes behind the concept of erodibility at different scales. In this respect, it is not surprising that, despite the great efforts and the large number of numerical methodologies proposed in the past decades, currently there are very few examples of reliable physically breaching models. Most importantly, although the latest achievement and continued improvements, the development of the predictive capabilities of these models has progressed very slowly as confirmed by the fact that there is a substantial lack of tools adopted in common engineering practice. Although physical features and different stages of progressive-surface erosion and headcutting have been extensively described with a satisfactory level of knowledge, there are still many questions that need to be answered to generate a new generation of more robust breaching models. Some of them constitute the core of this research study and are summarised below:

Research Question #1 *Why the breach onset occurs in such significantly different modes (i.e. progressive surface erosion and headcutting) if the same hydrodynamics loads are imposed at the beginning of overflow?*

Research Question #2 *Do the hydrodynamic shear stresses exerted by the water overflow represent the only possible triggering mechanism for soil mobilisation or are there other factors that can play a relevant role?*

Research Question #3 *What are the fundamental reasons behind the*

development of headcutting and/or progressive-surface erosion?

Research Question #4 *Why headcut forms always in fine-grained materials and very rarely in coarse-grained ones?*

Research Question #5 *Is it possible to contextualise embankment breaching due to overflow with an alternative approach to erosion models and erodibility parameters?*

Research Question #6: *What if large-scale erosion processes are modelled like mini-slopes stability problems progressing with time?*

Ultimately, the final objective of this work is to investigate the applicability of a novel alternative numerical methodology for breach modelling that can provide full or partial answers to the research questions identified.

1.2 Structure of this Thesis

The structure of this thesis reflects the approach adopted during the entire research work and the progressive steps undertaken to develop the core idea of the suction-based breaching model. The thesis is composed of five chapters and two appendices. Each chapter has been thought to be standing-alone and as such there are repetitions of concepts, texts and figures for which the author apologises. The content of each chapter is as follows:

Chapter 1 introduces the research work. The problem studied is briefly defined focussing on the current scientific needs and research questions.

Chapter 2 summarises the knowledge gained during the literature review covering the essential background elements for this work. An overview of the problem of the embankment overflow is presented. The overflow is described by considering both the hydraulic and hydrodynamic processes leading to the macro-erosion mechanisms observed during embankment breaching failures. These are outlined through the most relevant investigation campaigns conducted in the last decades.

Finally, an insight on the concepts and methods of soil erodibility is presented. The aim of this chapter is twofold. On one hand it provides the theoretical framework and the context of this research. On the other hand, it emphasises the gaps in the state-of-the-art and helps delineate the research questions introduced in Chapter 1.

Chapter 3 first introduces key observations reviewed from the literature instrumental to the core idea that inspires the new conceptual model for breach onset developed in this thesis. The various hydro-mechanical stages in which the embankment soils are subjected during a typical extreme weather event are qualitatively explored. The starting point of this analysis is the acknowledgement of the unsaturated state of the soils constituting the embankment, as this is the most frequent situation encountered in the real world and documented in various research and technical reports. The theoretical basis to study the embankment overflow in the context of unsaturated soil mechanics is then presented. This is the first step to introduce the role of suction as a possible alternative explanation of the observed breaching mechanisms. To provide a proof of concept of the suction-based breaching model, the stability of an ideal homogeneous embankment subjected to a flood-induced overflow is analysed with a finite element model (FEM) according to the strength reduction method. The effects of hydrodynamic forces and soil shear strength reduction on the onset of breaching are assessed by comparing the factor of safety with regards to the embankment stability calculated with and without the application of the hydraulic shear stresses along the downstream slope. The hydrodynamics forces developed at the interface water-soil are derived in a separate model based on the finite volume method (FVM) solution of the 3D Reynolds averaged Navier-Stokes equations. Research Questions #1, #2, #3, #4 are addressed. Research Question #2 dealing with the relative importance of the hydrodynamic forces is particularly challenged and a conclusion is advanced.

Chapter 4 deals predominantly with the Research Questions #5 and #6. The typical structure of the physically-based breaching models developed to date is first introduced. Afterwards, the new suction-based breaching model is laid down. The

failure criterion assumed has been formulated based on the concept of plastic and failure points and geometrical requirements. Operationally, this methodology has been implemented in Plaxis 2D according to an approach referred to as “Lego-strategy”. The algorithm behind the “Lego-strategy” has been detailed with various scenarios. This chapter ends with the calibration and validation of the failure criterion by benchmarking the failure surface derived from the proposed criterion with the failure surfaces obtained within the framework of Upper-Bound Limit Analysis (using LimitState) and resulting from the FEM Safety Calculation using Plaxis 2D.

Chapter 5 presents the implementation of the suction-based breaching model and its qualitative validation. Two ideal homogenous embankments are studied considering the cases of fine-grained and the coarse-grained materials respectively. The mechanisms of progressive-surface erosion and headcutting are simulated according to the suction-based breaching model developed in this study. The numerical results, in terms of embankment profiles and times of breaching failures are compared with the processes observed during the most important set of field tests conducted as part of the European IMPACT project.

Appendix A outlines the background for the development of the computational fluid dynamics model and the simulation with Open Foam conducted in Chapter 3.

Appendix B describes the proof of concept of the suction based breaching model applied to the case of the infinite slope adopting a simplified approach for the analysis of the ground water flow.

Chapter 2. Background

Flood earthen embankments may fail due to overflow/overtopping, piping, internal erosion, and foundation or structural instability. However, statistical analysis of historical earthen embankment failures indicates that overflow/overtopping is the main cause of breaching.

Overflow occurs when the level of the water body (i.e. river, reservoir, sea) exceeds the embankment crest and water flows towards the protected land with increasing velocity due to the relatively steep slopes characterising the downstream side of the embankment. Overflow is the result of the insufficient hydraulic capacity of the defence structure that is typically observed during extreme floods (Zhang *et al.*, 2016). This scenario is becoming very frequent and is expected to be more and more critical in the near future due to climate change and continuous urbanisation of flood prone areas. The former is responsible for the escalating number and severity of extreme weather events while the latter accounts for the growing exposure to damages of lands, properties and human activities. In this context, flood defence systems aim to reduce flood risk but the consequences induced by embankment breaching are much more catastrophic than natural floods (Michelazzo, 2014).

Earthen embankment breaching is a time-dependent failure mechanism associated with the interactions between water overflow, soil constituting the embankment and the structure itself. A series of physical processes can cause the formation of a hole or gap in the embankment allowing for the uncontrolled passage of flood water leading to final failure. The breaching process encompasses any phases of failure, from breach initiation and formation up to the condition in which the breach is fully developed, cutting the embankment in two distinctive segments (Morris *et al.*, 2009)

Factors like the type of structure and construction details, the hydraulic loading, the nature and properties of the material constituting the embankment are all key aspects affecting breach initiation and breach progression. Understanding and predicting breaching therefore require a multidisciplinary approach and the coupling of the hydrodynamic analysis of water flow and flow patterns over the embankment

with the study of soil response to various soil-water flow processes. In this respect, the study of the fundamental physical mechanisms responsible for breaching onset is essential to predict the overall failure process. However, little quantitative information is currently available about breach initiation (Mohamed *et al.*, 2002) and the vast majority of breaching predictive models developed so far tend to neglect this aspect assuming almost arbitrarily an initial breach location.

2.1 Hydraulics of Embankment Overflow

The current state of the art, based on analysis of case studies, laboratory and in-situ tests converge towards a common interpretation that identifies external erosion as the primary triggering mechanism for the onset of breach due to overflow. It is generally assumed that the water flowing along the downstream slope generates hydraulic shear stresses that induce the removal of soil particles once a critical soil resistance threshold is exceeded. This is the reason why embankment breaching by overflow is often referred to as overflow/overtopping erosion in the literature.

A comprehensive overview of the mechanics of overflow erosion is provided by Powledge *et al.* in two companion papers (Powledge *et al.*, 1989 I, II). Part I summarises the most important research studies on embankment overflow conducted predominantly in the UK and the USA during the 80s; while Part II presents theoretical aspects of the hydraulics of water flow over embankment and a review of the different behaviours observed during overflow.

The hydraulics of embankment overflow is described in the framework of the open channel or free-surface flow theories, with reference to broad-crested weirs. In analogy with this configuration, three typical flow regimes characterise the hydraulics processes of embankment overflow:

- (1) subcritical flow at the upstream edge of the embankment crest.
- (2) transition between subcritical and supercritical flow through critical condition between the middle crest and the downstream edge.
- (3) supercritical flow along the downstream slope, with high flow velocity due to the steep slope and decrease of water depth.

A hydraulic jump might develop at the downstream toe, due to the transition from supercritical to subcritical flow induced by the change of slope (i.e. steep to horizontal bed at the downstream toe and afterwards). The hydraulic jump is characterised by an abrupt increase of the water level associated with surface rollers and large energy dissipation (Chaudhry, 2008).

The formation and the characteristics of the hydraulic jump depend on the downstream boundary conditions and particularly on the presence of tailwater and its depth (Fritzi and Hager, 1998). It has to be considered that, when the overflow occurs the flood defence embankment (i.e. like levees and dikes along rivers) acts as a side weir, typically used in channel to divert the flow laterally. In fact the river flows parallel to the embankment as shown in the sketch below.

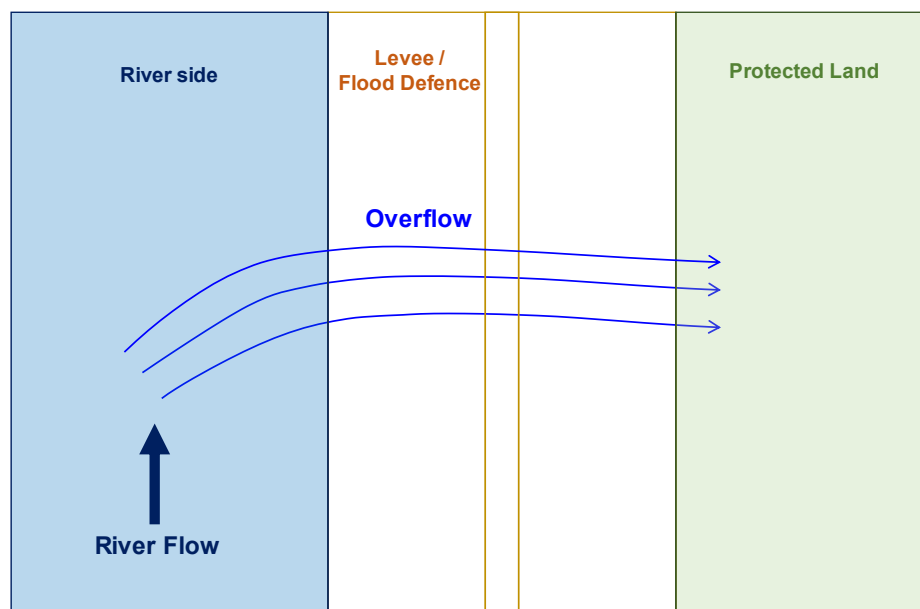
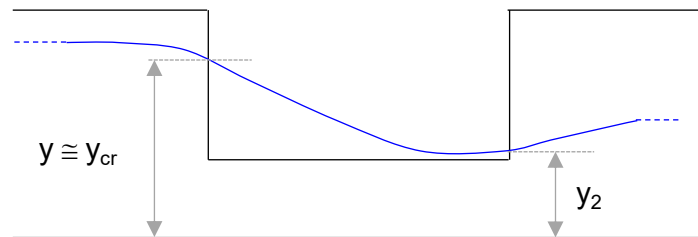


Figure 2-1: Plan view of overflow for a river flood-defence embankment after Michelazzo (Michelazzo, 2014)

In this configuration, as observed by Borghei et al. (Borghei, Jalili and Ghodsian, 1999), a hydraulic jump will occur within the downstream slope if the critical profile develops upstream and a subcritical flow (with depth greater than critical) is the downstream condition. Therefore, the formation of the hydraulic jump is dictated by the water depth at the downstream side. Because water is not flowing along the protected land prior to the overflow, no tailwater is expected and the increase of water

depth downstream will be gradual or with a weak undulating jump, characterised by little energy dissipation. Typically this has been observed for Froud Number between 1 and 1.7 (Chaudhry, 2008). The longitudinal section of a side weir in Figure 2-2 shows these two cases.

(a) Supercritical flow with no tailwater downstream



(b) Supercritical flow with subcritical downstream flow and formation of the hydraulic jump

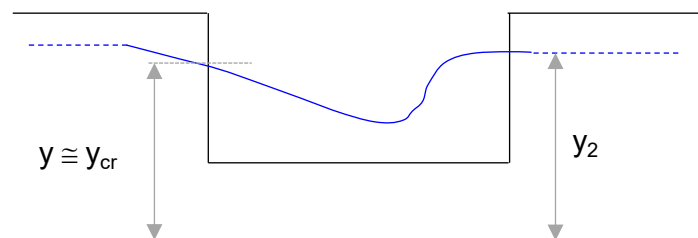


Figure 2-2: Longitudinal section of a side-weir with no downstream flow (a) and with transition from supercritical flow to subcritical flow with formation of hydraulic jump (b) after Borghei *et al.* (Borghei, Jalili and Ghodsian, 1999)

In addition, it is worth noticing that the overflow develops over a not-fixed surface, and the hydraulic jump is likely to be an unstable flow structure because of the deformation of the channel bed under the hydraulic stresses (Michelazzo, 2014).

The three flow regimes at the crest and along the downstream slope, are associated with corresponding erosion zones based on the relative energy of the sub-critical, critical, and super-critical flow respectively as shown in Figure 2-3.

In erosion zone 1 (sub-critical flow), the energy level and the energy slope are small and consequently the hydraulic forces developed are low and typically not sufficient to start the erosion process.

Erosion zone 2 corresponds to the transition from subcritical to supercritical flow

through the critical condition. The energy level is unchanged while the energy slope tends to increase, determining high hydraulic forces. However, these develop over a limited length and therefore little erosion occurs.

In erosion zone 3, flow accelerates significantly due to the steep slope inducing large hydraulic shear stresses with a high erosive potential. When these forces exceed the critical resistance of the material erosion processes are activated.

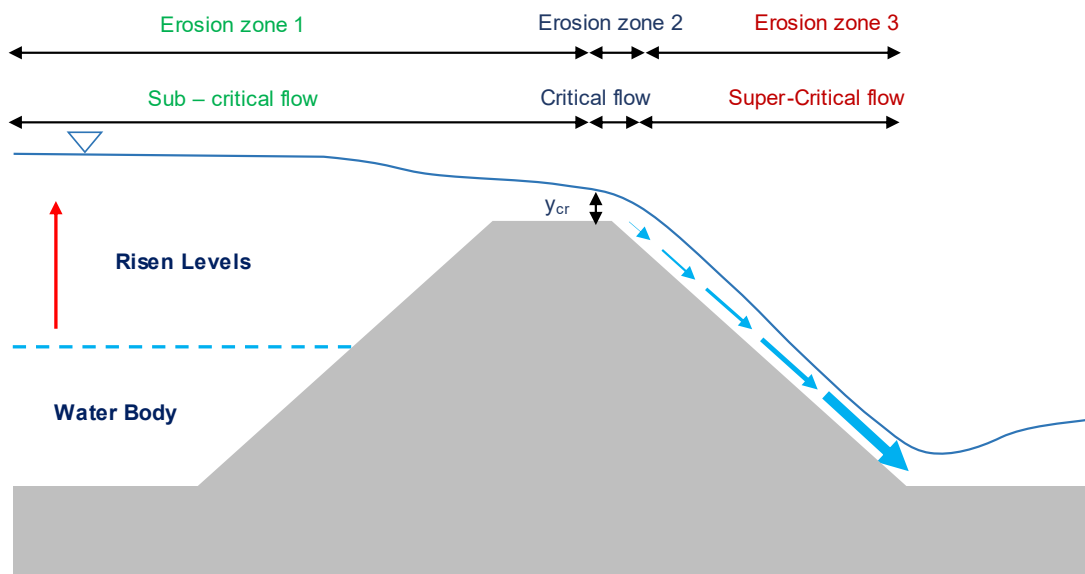


Figure 2-3: Typical flow regimes during overflow of embankments and associated erosion zones after Powledge *et al.* (George R. Powledge *et al.*, 1989)

Erosion can occur at any point of the slope, depending on local discontinuities and concentration of stresses, but very often the starting point is the toe where the water flow tends to dissipate its energy because of the increasing flow velocities. Initially a small overfall and a scour hole have been commonly observed. Their enlargement is directly related to the type of material constituting the embankment. Powledge *et al.* observed that overfalls are higher and more stable in fine-grained soils than in coarse-grained geo-materials (George R. Powledge *et al.*, 1989).

2.2 Observed Breaching Mechanisms in Coarse-Grained and Fine-Grained Embankments During Overflow

In the last decades, the role of the embankment materials in the process of breaching has been widely investigated. Large-scale physical tests (Hahn, Hanson and Cook, 2000; G. J. Hanson, K. R. Cook and S. L. Britton, 2003; Vaskinn, LØvoll and Höeg, 2003; G. J. Hanson, K. R. Cook and S. L. Hunt, 2005) and small-scale laboratory models (Visser, 1998; Coleman, Andrews and Webby, 2002; Zhu, 2006; Morris, Hassan and Vaskinn, 2007a; Schmocker and Hager, 2009; Luo *et al.*, 2014; Wei *et al.*, 2016; Zhao, 2016; Bereta *et al.*, 2020) showed that two main characteristic macro-erosion behaviours differentiate breach initiation and growth in coarse-grained and fine-grained embankments.

Coarse-grained fills tend to erode quickly according to a mechanism known as progressive surface erosion, where soil is removed layer by layer as consequence of tangential flow stresses. This mechanism has been observed for example by Coleman *et al.* in a series of laboratory experiments conducted in flume on small scale embankment models (approximately 0.3m high and with a crest 0.065m wide) constructed with medium and coarse sands (Coleman, Andrews and Webby, 2002). The longitudinal profiles of the breach channel centreline for medium-sand model measured during the test is shown in Figure 2-4.

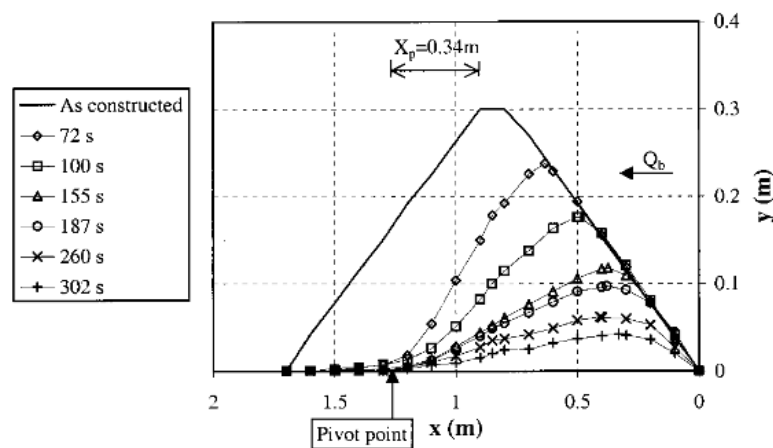


Figure 2-4: Longitudinal profile along the breach channel centreline measured during overflow experiments on sands embankments (Coleman, Andrews and Webby, 2002)

The downstream embankment face flattens progressively by rotating around a pivot-point usually located around the downstream toe (Coleman, Andrews and Webby, 2002; Volz, 2013). Once the breach channel is formed, lateral erosion occurs through the failure of relatively large volume of material collapsing into the centre of the channel and transported downstream.

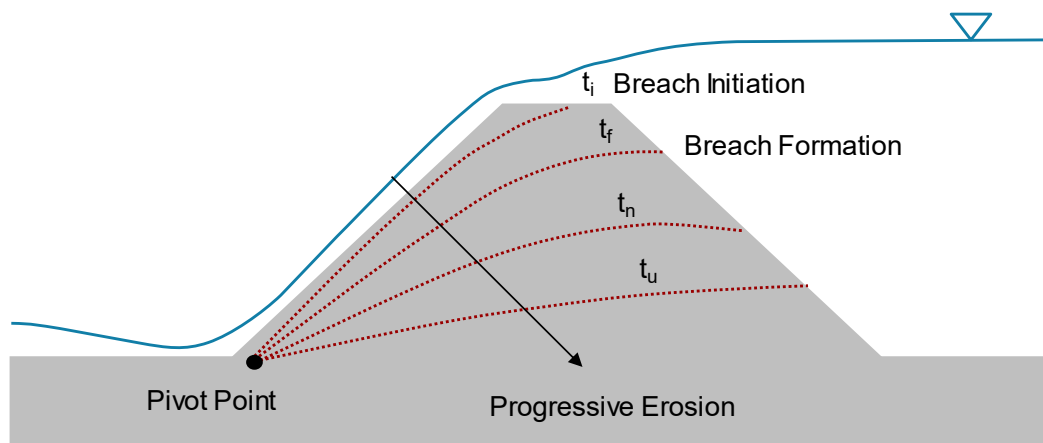


Figure 2-5: Typical breaching process of coarse-grained embankment by surface erosion due to overflow

This initial phase is schematically represented by the embankment profile t_i in Figure 2-5 and it is commonly identified as breach initiation. When the erosion front reaches the upstream edge, the embankment crest is extensively and rapidly eroded leading to the breach formation stage at t_f . At this point the discharge rapidly increases, the water flow becomes more turbulent and therefore more erosive, resulting in an acceleration of the breach growth. The breach channel starts to flatten due to the slope failure on the upstream slope. As erosion continues the embankment section is completely eroded towards the bed and the breach grows laterally. These phases are described by the embankment profiles t_n to t_u in Figure 2-5.

It is worth specifying that breach initiation is defined by Wahl (Wahl, 1998) as the time that spans from the first flow over the embankment initiating warning, evacuation, or heightened awareness of embankment failure, to the breach formation phase. The breach formation phase is the time that spans from the first lowering of the upstream embankment crest to the point at which the upstream face is eroded to near full depth of the embankment.

The erosion process might also affect the soil of the embankment foundation, depending on the material properties.

A different mechanism has been observed by Visser. Based on experimental studies on sand dikes Visser describes five stages of the breaching process of coarse-grained embankment: (1) steepening of the downstream slope up to the crest; (2) upstream erosion resulting in a reduction of the crest width; (3) crest completely eroded and therefore lowered; (4) critical flow condition established through the breach which continues to grow; (5) subcritical flow reached with continuous lateral erosion at a lower rate than stage (4) (Visser, 1998).

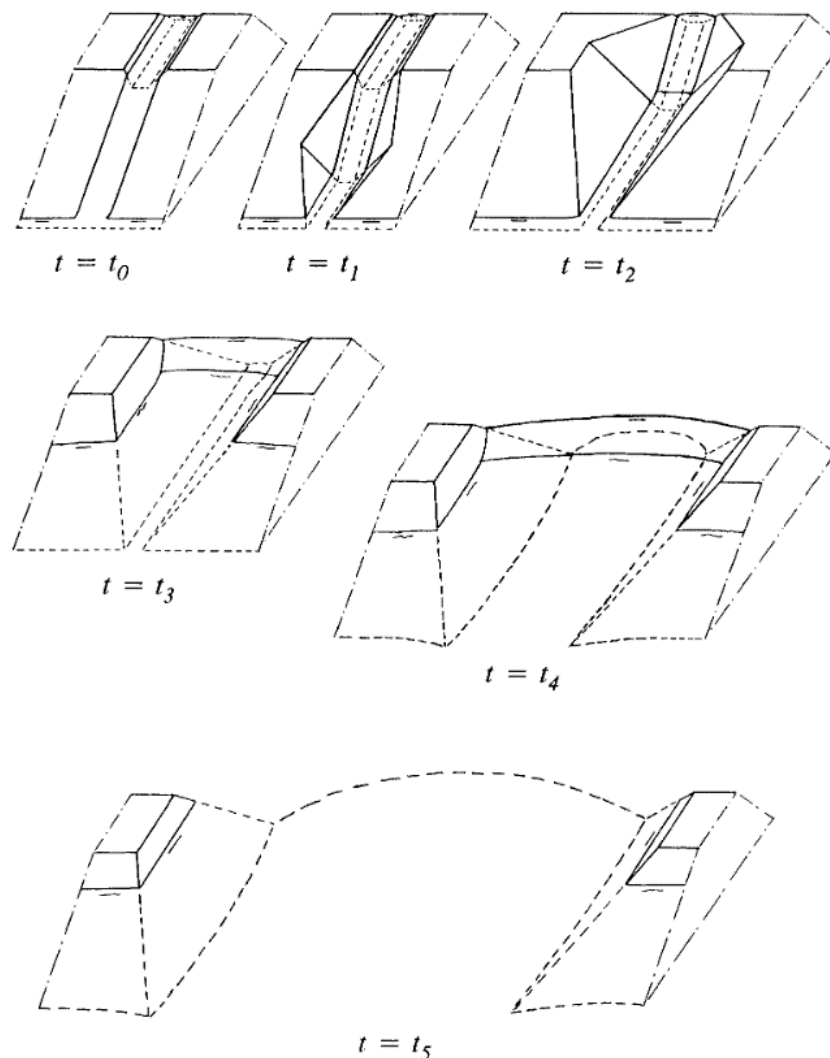


Figure 2-6: Different phases of breach formation in sand-dikes observed by Visser (Visser, 1998)

Stages (1) and (2) refers to breach initiation; stage (3) is the breach formation, and stages (4) and (5) describe the breach transverse growth. A sketch of these different stages is presented in Figure 2-6. The cross – section views, where the initial steepening of the downstream slope is more clearly observed is shown below.

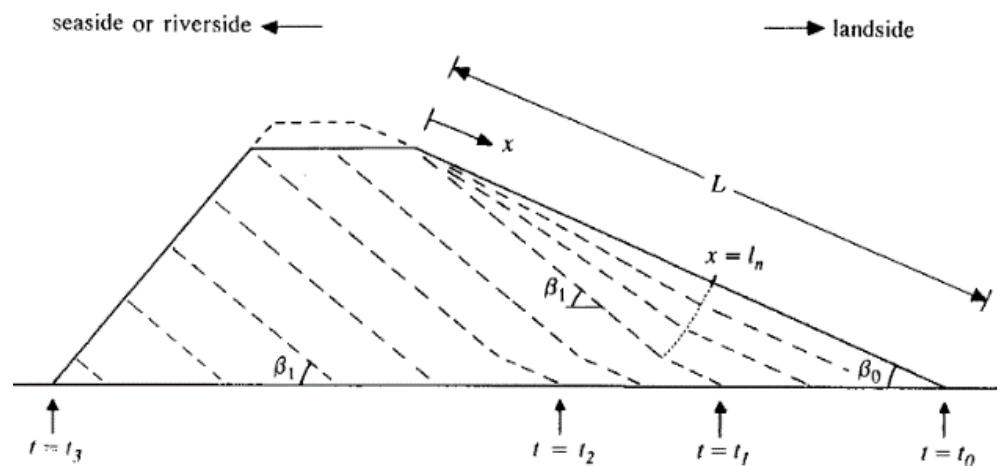


Figure 2-7: Cross – sections for Stage (1), (2) and (3) when the length of the downstream slope L is within the limits of the adaptation length of the flow l_n and the adaptation length of the sediment transport l_a (Visser, 1998)

In stage (2) the channel retrogrades at a constant angle β_1 causing a reduction of the crest width. Depending on the length of the slope L compared to the adaptation length of the suspended load transport l_a different situations might occur as shown in Figure 2-8a, b. If the $L > l_a$ the erosion for $x > l_a$ tends to stop. After some time a bar can form at $x \sim l_a$ and the supercritical flow can decelerate inducing more turbulence. This means that the sediment transport capacity increases and the process continue even for $x > l_a$. If the $L \gg l_a$ the erosion of the inner slope occurs with an initial lowering of the crown of the dike which results in an increase of the flow rate. This in turn induces the removal of the remaining sediments downstream and the process evolves as in Figure 2-7.

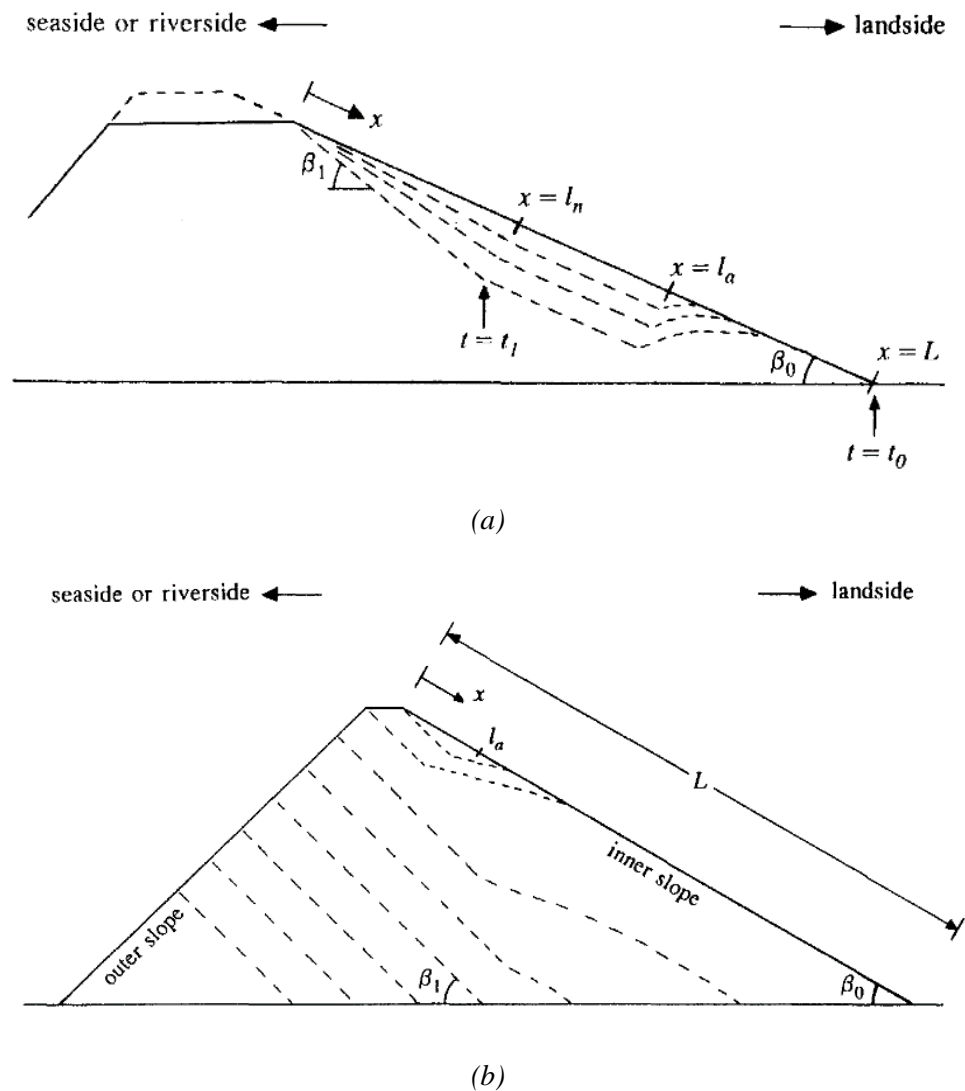


Figure 2-8: Mechanism of sediment transport when (a) $L > l_a$ and when (b) $L \gg l_a$ (Visser, 1998)

The primary erosion mechanism observed during the overflow of fine-grained embankments is known as headcutting. The headcut is defined as a vertical or nearly vertical drop of the channel bed elevation, which is typically observed during breaching of fine-grained embankments (Hahn, Hanson and Cook, 2000).

In analogy with the approach adopted by Visser, a four-stage description of the breach erosion process for fine-grained embankments has been proposed, based on observations of experimental studies conducted at the USDA-ARS Hydraulic Unit in Stillwater, Oklahoma. Seven overtopping tests were performed on 2.3m high and 1.5m

high embankment models, constructed with three different materials, ranging from silty sand to lean clay. The embankments were constructed in lifts with soil layers compacted using a self-propelled vibratory pad-foot roller. The overtopping was initiated by cutting a notch which lowered a section of the embankment crest.

Pictures of these experiments are shown in Figure 2-9. A sketch of the downstream profile evolution due to headcutting processes observed is presented in Figure 2-10. In more details, these tests showed that the initial sheet flow at the beginning of the overtopping induces the formation of a network of micro-rills along the downstream slope, which develops in one or more master rills (Figure 2-9a,b). The experiments indicated that one rill would dominate leading to the formation of the main headcut. In this phase, the downstream slope profile evolves into a series of cascading overfalls which tend to merge generating one single large headcut. While the overtopping continues, this single step was observed to migrate backwards, from the downstream toe to the embankment crest Figure 2-9c. The process described has been identified as the first stage of breaching by headcut erosion, which ends when headcut advancement reaches the crest (time step t_3 in Figure 2-10).

At this point, the breach is initiated, and lateral erosion is observed. The breach widening is classified as the second phase of the global process which lasts until the erosion front cuts through the upstream edge of the crest (Figure 2-9d,e and time step t_f in Figure 2-10). The third phase consists of crest lowering resulting in an important increase of the water flow and discharge into the breach channel. The third stage is considered finished when the erosion processes downstream are completed and further breach widening occurs leading to the fourth final stage with the full breach (Figure 2-9f and time step t_n in Figure 2-10).



Figure 2-9: Different stages of breach formation observed during field-test experiments on fine-grained embankments. (a) formation of networks of rills and (b) evolution of the initial rills into a multi-stepped profiles in Stage I; (c) headcut backwards migration and transition to Stage II (d) headcut advancement to the crest and transition to Stage III; (e) crest lowering and transition to Stage III; (f) breach widening at Stage IV (G. J. Hanson, K. R. Cook and S. L. Hunt, 2005)

In a similar way to the coarse-grained embankment, breach initiation occurs during the first and second stages, while the breach formation is related to third stage.

The mechanism of headcut formation is attributed to the shear failure of the soil around the overfalls initially formed. Because of the stepped and non – uniform profile, the water flow impinges on the downstream toe like a jet, inducing high erosive forces at the toe which are responsible for the headcut advancement.

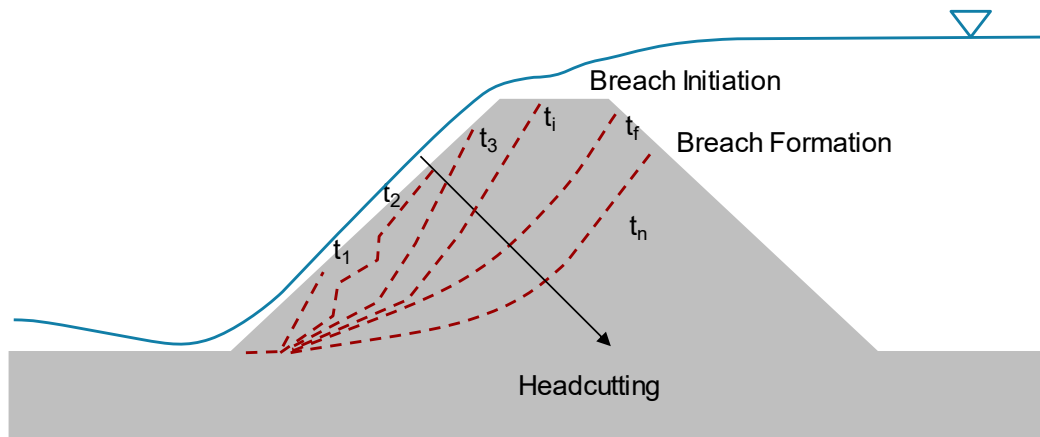


Figure 2-10: Typical breaching process of fine-grained embankment by headcut erosion during overflow after (Hahn, Hanson and Cook, 2000)

One of the most important conclusions of this series of tests is that the type of soil plays a key role in the overall breaching process. Breach initiation occurred more rapidly (16 minutes) for the embankment constructed with silty-sand (i.e. 70% sand, 25% silt, 5% clay) than the embankment with high clay content (164 minutes). For the three soils tested, a single headcut was identified at the end of the first stage. The measured headcut migration rate is higher for the silty-sand embankment (7.4 m/hr) and decreases as the clay content increases (0.68 m/hr and 0.14 m/hr). The tests on lean clay embankments terminated after 1200 minutes of overflow without any further erosion, such that stage 2 was not terminated. On the contrary, breach formation was observed after 51 minutes for the silt-sand and after 432 minutes for soil 2 (63% sand, 31% silt, 6% clay).

These experimental observations provide a comprehensive description of surface and headcut erosion mechanisms. However, it seems clear that these are typical macroscopic behaviours of coarse-grained and fine-grained geo-materials

respectively, there are still fundamental aspects which need to be further investigated.

Starting from the observation that the hydraulic and hydrodynamic mechanics of overflow is identical for the two types of material, with the highest hydraulic bed stresses occurring around the downstream toe, the first question is:

Why headcut erosion typically starts at the toe for fine-grained soils, but this is not observed in surface erosion of coarse-grained embankments?

This raises a second question, which is:

Why is there a substantial difference between these two modes of failures experimentally observed?

The current state of knowledge tends to ignore the first question and provides only a partial answer to the second one, considering soil erodibility as the main critical factor. In fact, (Morris, 2011) explains that headcut erosion is the predominant mechanism in fine-grained soils because these are less erodible than coarse-grained materials and therefore can sustain the formation of a stepped profile.

2.3 Soil Erodibility

Erodibility is considered an inherent soil characteristic describing the resistance of a soil subject to water flow. There is a common agreement within the research community about the use of erosion equations rather than equilibrium sediment transport equations, originally adopted for modelling erosion processes. The reason is that sediment transport equation refers to problems of river hydraulics and were derived upon steady state equilibrium conditions, which are very far from the dynamics and short-term characteristics of the water flow during embankment breaching (Samuels *et al.*, 2008; Morris, 2011; Michelazzo, 2014).

In light of this considerations, Briaud (Briaud *et al.*, 2008; Briaud, 2013) proposed a definition of soil erodibility as the relationship between the erosion rate experienced by the soil and the state of stresses associated with the flow at the soil-water interface. This is a constitutive law for erosion, known as erosion function, which can be expressed in the most complete and general form as:

$$\frac{\dot{\epsilon}}{v} = \alpha \left(\frac{\tau_w - \tau_c}{\rho v^2} \right)^m + \beta \left(\frac{\Delta\tau}{\rho v^2} \right)^n + \delta \left(\frac{\Delta\sigma}{\rho v^2} \right)^p \quad \text{Equation 2-1}$$

where $\dot{\epsilon}$ is the erosion rate (m/s) and v the water velocity (m/s), τ_w is the hydraulic shear stress (N/m²), τ_c (N/m²) is the threshold or critical shear stress below which no erosion occurs, $\Delta\tau$ (N/m²) is fluctuation of the shear stress due to turbulence of the water flow and $\Delta\sigma$ (N/m²) is the turbulent fluctuation of the net uplift normal stress, ρ is the mass density of water (kg/m³), α , β , δ , m , n , p , are all characteristic of the soil being eroded. This model considers the following processes which can occur when water flows over particles or particle aggregates: (1) drag forces and associated shear stresses develop τ_w at the interface between water and soil particles, (2) the normal stress on top of the soil particles decreases because of the water flow, and (3) the normal stresses and shear stresses applied at the boundaries fluctuate with time because of the turbulence. The combination of the mean value and the fluctuations around the mean of the drag force and uplift force can induce the entrainment and subsequent motion of the soil particles or aggregates thus generating erosion. For clayey materials the forces involved in the erosion process during water flow are shown in Figure 2-11, where V_x is the water velocity in the x direction and τ is the hydraulic shear stress that for Newtonian fluids is proportional to the velocity field through the fluid viscosity μ , f_{ai} and f_{ri} are attractive and repulsive interparticle forces, f_{ci} are contact inter-particle forces, u_w is the pore water pressure.

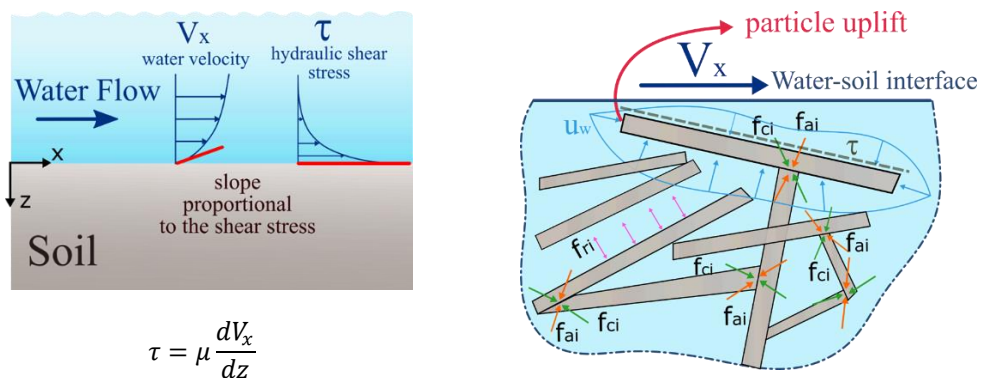


Figure 2-11: Forces around clayey aggregates subjected to water flow after (Briaud, 2008)

Despite the robust physical mechanisms underlying this model, the number and

nature of the parameters to be determined make its application impractical. This is the reason why Equation 2-1 is generally reduced to:

$$\dot{\varepsilon} = f(\tau_w) \tag{Equation 2-2}$$

which considers only the contribution of the hydraulic shear stress to the erosion rate.

This concept is not new in literature and similar models were proposed in the past, like the one from Duboys in 1897 (Knapen A. *et al.*, 2007). Currently, the most common erosion constitutive model adopted in literature and implemented in the new generation of breaching numerical models is the excess stress equation:

$$\dot{\varepsilon} = k_d(\tau_w - \tau_c) \tag{Equation 2-3}$$

where:

- $\dot{\varepsilon}$ is the erosion rate (m/s),
- k_d is the erodibility coefficient (cm³/N s),
- τ_w is the hydraulic shear stress (Pa),
- τ_c is the critical shear stress (Pa)

The linear constitutive law shown in Figure 2-12 describes the initiation of erosion expressed by the critical shear stress τ_c and the erosion kinetic, represented by the erodibility coefficient k_d .

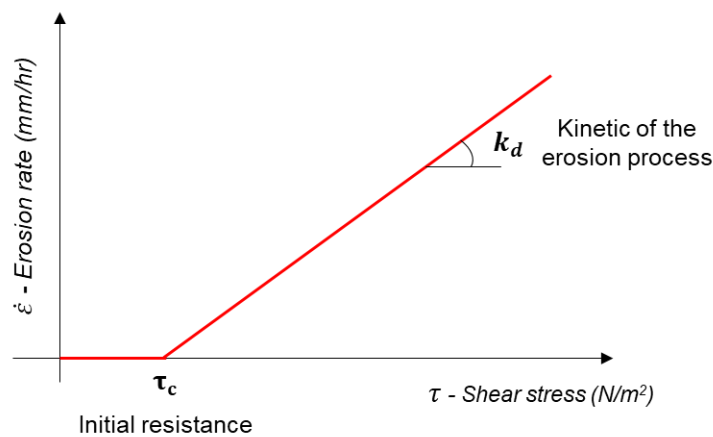


Figure 2-12: The linear constitutive law for erosion, usually derived from erosion tests

These two terms are known as erodibility parameters assumed to be characteristic of a

given soil. The critical shear stress τ_c is the threshold corresponding to the initiation of erosion, (i.e. the soil erodes when the shear stress exerted by the flow exceeds this critical value). Hence this parameter accounts for the soil resistance to initiation of erosion. The coefficient of erodibility k_d is an index of the amount of soil loss per unit time under a given shear stress once erosion is triggered. It indicates how quickly soil particles are eroded. This parameter has been observed to range from 0.001 to 1000 cm^3/Ns . Low values represent erosion resistant soils and high values are representative of more erodible soils.

Soil erodibility classifications are available in literature. Hanson and Simon (Hanson and Simon, 2001) proposed the chart shown below, based on results of critical shear stress and erodibility coefficient from 83 field jet erosion tests conducted in fine-grained streambeds.

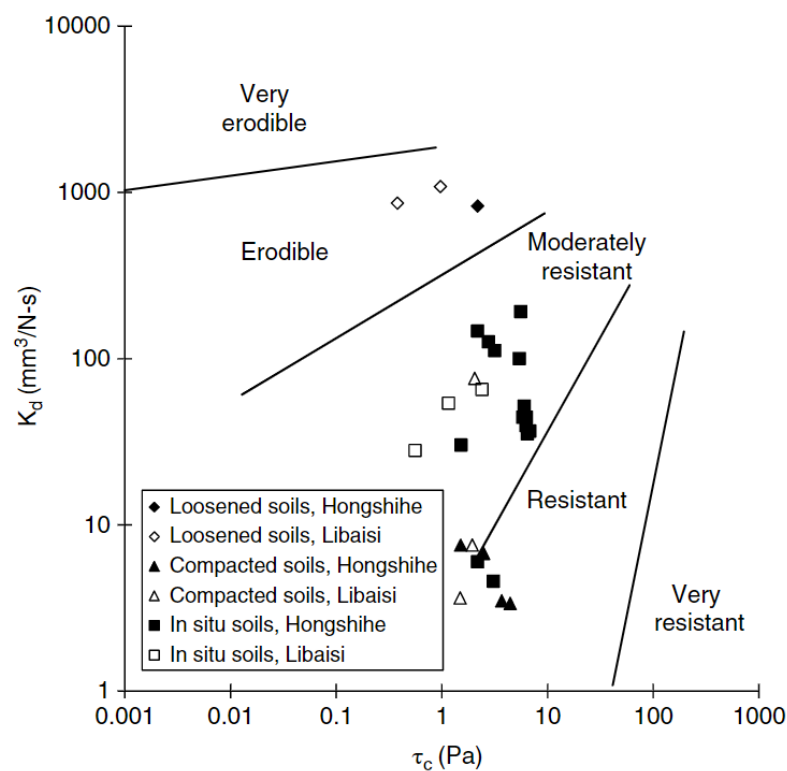


Figure 2-13: Classification of soil erodibility as function of critical shear stress and erodibility coefficient (Hanson and Simon, 2001)

Five categories were identified (very erodible, erodible, moderately resistant, resistant

and very resistant) with the critical shear stress varying over six orders of magnitude and four orders of magnitude for the erodibility coefficient. It is evident that the higher the critical shear stress and the lower the erodibility coefficient the more erosion resistant is the soil tests.

Another classification chart was proposed by Briaud (Briaud, 2008) where the erosion rate is plotted versus the hydraulic shear stress. Six categories were defined based on 15 years of erosion testing experience. In Figure 2-14 it is highlighted that soil compaction leads to an increase of the erosion resistance.

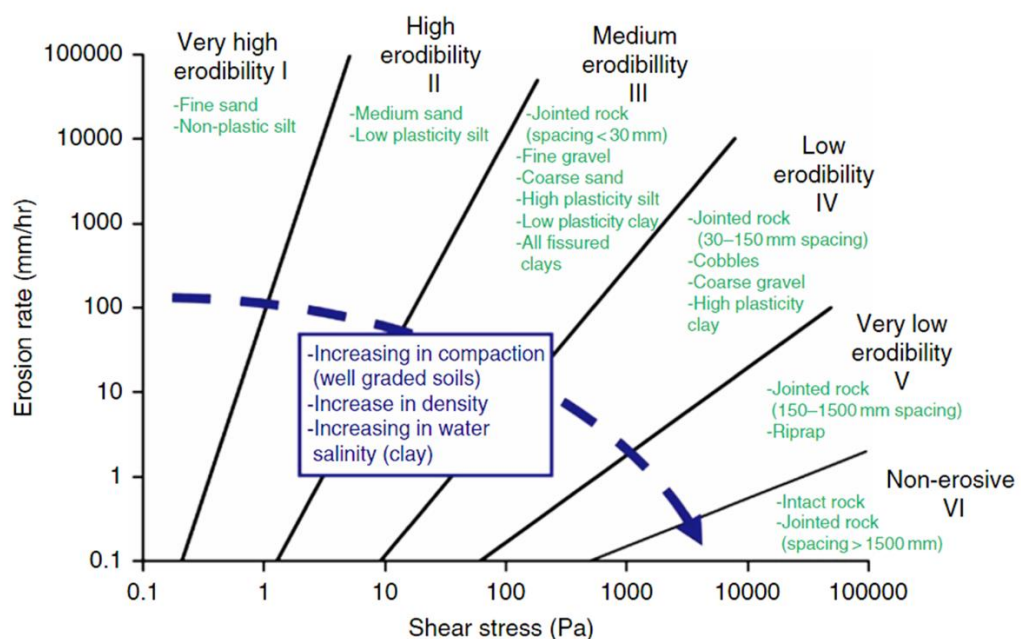


Figure 2-14: Classification of soil erodibility proposed by Briaud (Briaud, 2008)

2.3.1 Soil Erosion Tests

The two soil erodibility properties in Equation 2-3 should be determined experimentally (particularly for fine-grained materials) in laboratory and/or in-situ, in analogy with the common methodology adopted in geotechnical engineering problems.

In the last 25 years, many experimental devices have been proposed to determine the erodibility parameters. The Erosion Function Apparatus (EFA) developed by (Briaud *et al.*, 2001), the Hole Erosion Test (HET) developed by Wan and Fell (Fell *et al.*,

2003), the Jet Erosion Test (JET) developed by Hanson and Cook in laboratory and in situ (Hanson and Cook, 2004), the (RETA) Rotating Erosion Testing Apparatus (Bloomquist *et al.*, 2012) are just few examples of test procedures available to assess the erodibility parameters.

However, these approaches are not consistent, and it seems that different test methods conducted on similar materials tend to provide controversial results. Hence, erodibility parameters measured are dependent on the test method applied. Wahl (Wahl, 2010) compared the results of Hole Erosion (HET) and Jet Erosion (JET) tests on paired soil samples. It was found that JET tests provided a higher erosion rate and a lower critical shear stress than the HET. A similar trend was observed also in the experimental investigation conducted by Regazzoni *et al.* (Regazzoni and Marot, 2013) with the HET and JET. Tests results are reported in Figure 2-15 and Figure 2-16 respectively. In both plots, the abscissa indicates the soil sample tested and the corresponding USCS classification.

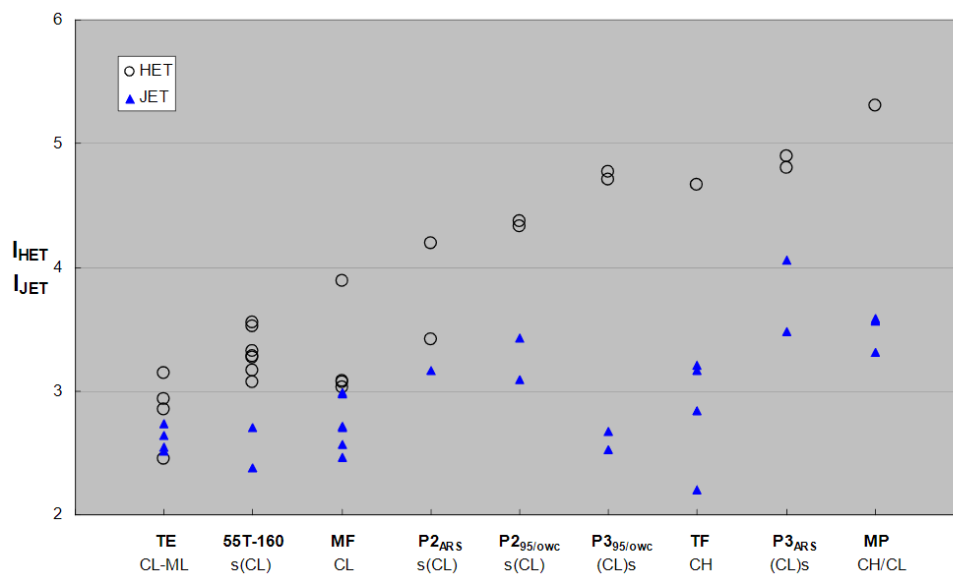


Figure 2-15: Differences in erosion rate index measured with HET and JET devices (Wahl, 2010)

The erosion rate index I as proposed by Wan and Fell (Wan and Fell, 2004) is defined as below:

$$I = -\log_{10} C_e \quad \text{Equation 2-4}$$

where C_e (kg/s/m²/Pa) is the coefficient of soil erosion that is related to the erodibility coefficient through the relationship $C_e = k_d \rho_d$ with ρ_d soil dry density (kg/m³).

Typical values of this index range between 1 and 6 with larger values indicating an increase of erosion resistance.

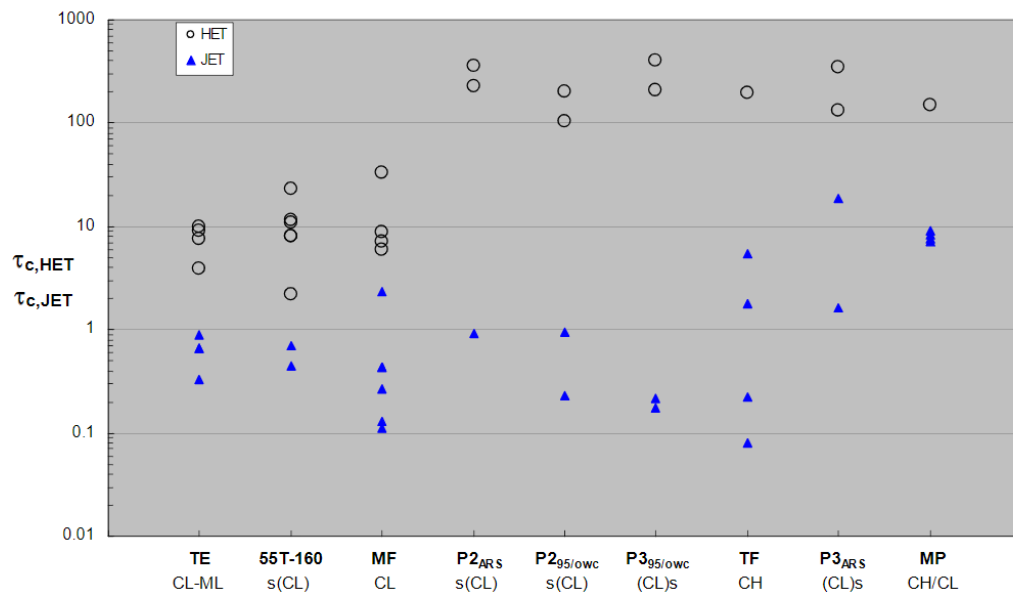


Figure 2-16: Critical Shear-Stress obtained from HET and JET tests (Wahl, 2010)

A comparison of EFA and JET (Bahri, Osouli and Stendback, 2016) confirms that there is a test influence on the erodibility parameters. Nevertheless, all these tests are considered nowadays as “standard” geotechnical tests.

The observed discrepancy can be attributed to the different hydraulic conditions imposed in these tests. For example, the JET is based on the action of a submerged water jet impinging the soil surface, while the HET and the EFA measures erosion rates caused by a water flow running parallel to the soil surface.

It is evident that there is a series of problems which the scientific community is still attempting to clarify. The main discussion is about: (1) the linearity of the erosion law; (2) the description of soil erodibility with more than two parameters; (3) the introduction of separate erosion models to interpret different hydraulic loads (i.e. water jet and longitudinal water flow) and (4) the review and improvement of the theoretical

framework behind the interpretation of the experimental measurements in erosion tests. In addition, further investigations are necessary to understand the relationship between erodibility, physical and state soil properties traditionally adopted in geotechnical engineering practice. According to Bonelli these are all open questions and needs of further research (Bonelli, 2019).

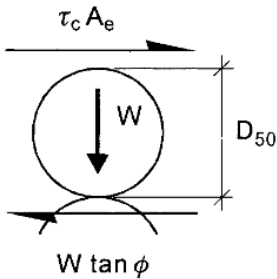
It is worth mentioning that the new generation of breaching models implement Equation 2-3 and the predictions of the macro-erosion behaviours of surface or headcut erosion are strongly dependent on the choice of the erodibility parameters. Hence, the enhancement of breaching models capabilities can be obtained if the accuracy of the erodibility characterisation of soil is effectively improved.

Besides laboratory and in situ tests (JET in situ and in-situ flume), the idea of deriving erodibility coefficient and critical shear stress through correlations with traditional engineering soil properties has been investigated by many researchers in the past decades. To introduce the most relevant governing factors a distinction between fundamental erosion mechanisms of coarse- and fine-grained materials is briefly presented in the following.

2.3.2 Erosion of coarse-grained soils

For coarse-grained soils such as sands and gravels, erosion occurs typically through a particle-by-particle process. The incipient motion of the particle is typically controlled by sliding and rolling mechanisms and can be expressed in terms of critical shear stress.

Assuming that the soil particles are spheres, sliding occurs when the tangential force due the water flow is equal to $\tau_c A_e$ (N) and it is greater than the friction resistance between the two particles $W \tan \phi$ (N) where in Equation 2-5 τ_c (N/m²) is the critical shear stress, A_e (m²) is the effective friction area of the water on the particle, W (N) is the submerged weight of the particle, ϕ (degrees) is the friction angle of the interface between the two particles. The neighbours spheres are subjected to the same forces and therefore will move in the same direction at the same rate without developing resisting forces.

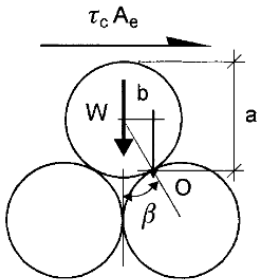


$$\tau_c A_e = W \tan \phi \quad \text{Equation 2-5}$$

$$\tau_c \propto \frac{\pi D_{50}^2}{4} = (\rho_s - \rho_w) g \frac{\pi D_{50}^3}{6} \tan \phi \quad \text{Equation 2-6}$$

$$\tau_c = \frac{2 (\rho_s - \rho_w) g \tan \phi}{3 \alpha} D_{50} \quad \text{Equation 2-7}$$

(a)



$$\tau_c A_e a = W b \quad \text{Equation 2-8}$$

$$\tau_c \propto \frac{\pi D_{50}^2}{4} \left(\frac{D_{50}}{2} + \frac{D_{50} \cos \beta}{2} \right) =$$

$$= (\rho_s - \rho_w) g \frac{\pi D_{50}^3}{6} \sin \beta \quad \text{Equation 2-9}$$

$$\tau_c = \frac{2 (\rho_s - \rho_w) g \sin \beta}{3 \alpha (1 + \cos \beta)} D_{50} \quad \text{Equation 2-10}$$

(b)

Figure 2-17: Sliding mechanism for spherical particles and incipient motion conditions (a) and rolling mechanism (b) after (Briaud et al., 2001)

Equation 2-6 develops further the expression for the effective area A_e and the submerged weight in Equation 2-5. The term α is the ratio of effective friction area over the maximum cross section of the spherical particle, D_{50} (mm) is the mean diameter, representative of the soil particle distribution, ρ_s and ρ_w (kg/m^3) are the mass density of soil and water respectively, g is the gravity acceleration (m/s^2). Equation 2-7 clarifies that the critical shear stress is essentially a function of the mean particle size D_{50} .

Similarly, for the rolling mechanism, the rotation equilibrium expressed in Equation 2-8 leads to a relation between τ_c and D_{50} in Equation 2-10. In this case the incipient motion is controlled also by the angle β indicative of the relative density (i.e. loose or dense arrangements).

Although the simplistic assumptions, the sketches and relationships in Figure 2-17 show that the main resistance to water flow of coarse-grained soils, depends on the immersed weight of the grain, grain density, shape and size. Nevertheless, as observed by Briaud (Briaud *et al.*, 2001), these expressions simplify the real mechanisms, hence experimental methods are always preferred. Generally, the mobility of coarse-grained materials (i.e. τ_c) can be assessed with the Shields chart (Shields, 1936). In his pioneering work, Shields conducted a series of flume experiments on sand beds subjected to water flows. The results of the experiments were plotted in a dimensionless chart known as Shields diagram. The Shields parameter is the ratio of the shear stress and the particle's submerged weight per unit of surface area at critical condition (i.e. initiation of motion) and therefore provides an indication of the critical shear stress. An example of the Shields chart is shown below.

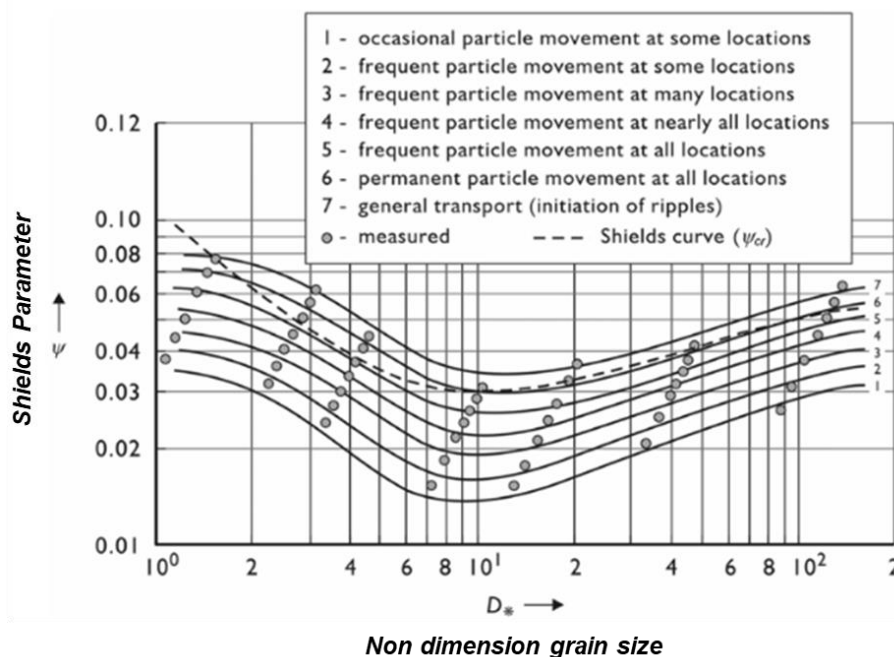


Figure 2-18: Modified Shields Diagram after (CIRIA, 2013)

2.3.3 Erosion of fine-grained soils

The erosion resistance of fine-grained soils is assumed to be predominantly governed by electrochemical inter-particle forces rather than the submerged weight of individual particles. A sketch of the forces involved has been presented in Figure 2-11.

In this case, erosion processes occur at the scale of aggregates or soil lumps rather than at the scale of single grain. Soil behaviour tends to evolve with time, depending on the series of past and recent events which might have impacts on the physical-chemical and biological interactions between soil, pore water and eroding fluid (Mehta *et al.*, 1989; Utley and Wynn, 2008). Because of all these factors, erosion in fine-grained materials is influenced by almost any soil property, this results in a complex problem with high spatial and temporal variability which is not fully understood (Knapen A. *et al.*, 2007).

Three main modes of erosion of fine grained-materials are reported in literature: (1) aggregate – by – aggregate, most commonly referred to as surface erosion; (2) mass erosion; and (3) re-entrainment of a stationary suspension (Mehta, 1986; Mehta *et al.*, 1989).

The first mode occurs when the hydrodynamic drag and lift forces are sufficiently high to break the inter-particle electrochemical bonds. Surface erosion can be associated with “peeling” or “pitting” of the surface depending on particle orientation within the aggregate. The first mechanism has been typically observed in face-to-face aggregates while stiff clay exhibits pitting surface where the removal of soil lumps leaves the soil surface with craters.

The aggregate breakdown mechanisms have been discussed by Le Bissonnais (Le Bissonnais, 1996). Depending on the causes, four types of aggregate breakdown have been suggested: (1) slaking due to the compression of entrapped air during wetting leads to the formation of micro-aggregates; (2) the internal pressure changes induced by differential swelling and shrinkage during wetting and drying tend to create microcracking of aggregates; (3) mechanical breakdown by raindrop impact induces a “splash effect” which is responsible for detachment and displacements of particles; (4) physico-chemical dispersion resulting from the reduction of the attractive forces between the particles in the aggregates during wetting.

Stability or dispersion depends on cation size and valence. Polyvalent cations cause flocculation (i.e. calcium and magnesium), on the contrary monovalent cations (i.e. sodium) cause dispersion. The most important soil properties which have been found to influence aggregate breakdown are: soil texture, clay mineralogy, organic

matter and cations concentration (Le Bissonnais, 1996; Utley and Wynn, 2008).

Mass erosion refers to the removal of relatively large blocks around weak planes below the surface. This typically occurs under severe flow conditions and determine much higher erosion rate than surface erosion.

The re-entrainment of fluid mud is not a fully understood phenomenon (Mehta *et al.*, 1989) and it seems to be related to wave-forms which tend to develop at the interface suspension/clear water.

The processes described above constitute what in literature is known as hydraulic erosion, because directly dependent on the water flow induced stresses. This is often considered different from subaerial erosion, which refers specifically to the weakening and weathering of soils associated with soil moisture conditions (Thorne, 1998; Julian and Torres, 2006). Subaerial erosion involves all those processes that can be related to climate conditions and atmospheric agents, operating independently from water flow and resulting in a reduction of the soil resistance. For this reason, subaerial erosion has been generally considered as “preparatory” rather than a proper erosive processes, in the sense that they contribute to increase susceptibility to hydraulic erosion (Utley and Wynn, 2008).

Wetting-drying as well as freeze-thaw repeated cycles are all considered subaerial erosion processes responsible of swelling and shrinkage respectively of soils, which can ultimately lead to the formation of cracking and fissures leading to a deterioration of the material, which then becomes more susceptible to erosion. A network of desiccation cracks in clay fill caused by tensile stresses associated to shrinkage and build-up of matric suction during period of drying have often been observed on the surface of flood defence embankments (Dyer, 2004; Dyer, Utili and Zielinski, 2007). These fissures can extend vertically up to 600mm below the surface and tend to terminate horizontally at depth such that the soil assumes a “ped fabric” where this two-dimensional system of cracks tend to isolate relatively large soil blocks. It is evident that desiccation cracks constitute plane of weakness, preferential path for water infiltration and additional source of high turbulence flow which accelerates mass erosion failures. At the same time, during wetting periods, the increase of water content is responsible for loosening of aggregates due to the reduction of magnitude of

interparticle bonds. Slaking occurs when an initially dry soil is subjected to a rapid wetting inducing the breakdown of aggregates (Thorne, 1998).

An interesting summary of several experiments conducted on undisturbed clay samples is reported in the work by (Gaskin *et al.*, 2003). These investigations were performed with different testing apparatus including flumes, rotating cylinder apparatus, drill-hole style and wave tank. The critical shear stresses were found to range between 0 and 450 kN/m² depending on the nature of the clay. Erosion typically initiated within cracks and continued as mass erosion with the removal of soil blocks or lumps. It was shown that these clays are very resistant to erosion when undisturbed and un-weathered, with erosion rates increasing significantly as soon as fissures appear. In the same work, the authors describe the experimental tests that they performed in flume and wave tank on undisturbed samples of the Champlain Sea clay from the banks of the St. Lawrence River between Montréal and Contrecoeur (Canada). They observed that the predominant erosion mode was mass erosion through removal of large soil blocks isolated by cracks and weak planes present in the natural structure of the clay. This process was similar in all the un-weathered samples at the in-situ water content. Also, the erosion was not significant until the water velocities reached 0.5 – 1.0 m/s. The analysis of samples initially dried and rapidly re-wetted showed that this sequence of events caused an increase of erosion rate by several order of magnitude. The presence of vegetation root in the soil sample was also investigated. It was observed that the root matrix slowed erosion rates.

These observations show clearly that erosion of fine-grained geomaterials is the result of a complex combination of physical-chemical and hydraulic phenomena and a sharp distinction between subaerial and hydraulic processes can be mistaken as these cannot be considered independently. The effects of soil weakening/weathering due to the temporal variability and dynamic of soil moisture content changes, imply that the erosion occurring during a particular water flow event, depends not only on the severity and duration of that event, but also on the soil state resulting from antecedent conditions (Wolam, 1959; Hooke, 1979; Thorne, 1998; Couper and Maddock, 2001).

Ultimately, many correlations between the erodibility parameters τ_c and k_d with fundamentals physical, chemical and mechanical soil properties (i.e. grain shape,

specific gravity, particle size distribution, Atterberg Limits, clay content, clay mineralogy, water content, organic matter, cation exchange capacity, pH, sodium adsorption ratio, void ratio, shear strength) have been proposed in literature and can be found for example in (Knapen A. *et al.*, 2007; Thoman and Niezgoda, 2008; Morris, 2011; Bonelli, 2013; Kimiaghalam, Clark and Ahmari, 2016; Shafii *et al.*, 2016; Zhang *et al.*, 2016).

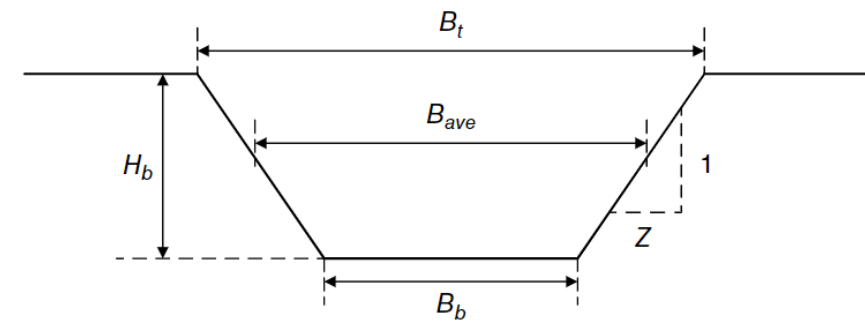
However, because of the multitude of factors influencing soil erodibility, where the soil state and environmental conditions need to be included, and given the large range of variability of the erosion parameters, it can be concluded that to date, a standardised method to predict soil erodibility with a satisfactory level of accuracy is still missing.

2.4 Modelling of the Observed Breaching Processes

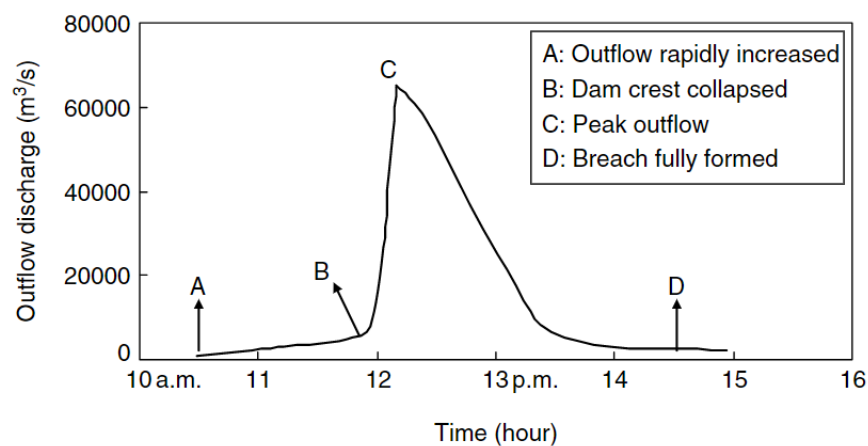
The simulation of the observed breaching processes is crucial for flood risk assessment, flood risk mitigation and emergency plan. Understanding the predominant erosion mechanism (i.e. headcutting or progressive surface erosion) can provide information on breach parameters including breach channel shape and size, breach formation time, peak discharge and the overall outflow hydrograph.

Geometric parameters including breach cross-section shape, breach depth, bottom, top and average width and side slopes are shown in Figure 2-19a. Hydrographic parameters forming the outflow hydrograph consisting of breach formation time and peak discharge are presented in Figure 2-19b.

Failure time is known as the period from the onset of breach to the ultimate stages of breach formation. In Figure 2-19b, the time of 10:30 a.m. is the breach initiation time (i.e. point A). From this moment onwards the volume of water realised through the breach channel is increasing and the erosion processes are accelerated until the collapse of the crest at 11:55 a.m. (i.e. point B). This is suddenly followed by the peak discharge that decreases while the breach is enlarging. In this case the failure time was approximately 4 hours.



(a)



(b)

Figure 2-19: Geometric parameters of an idealised trapezoidal breach cross-section (a) and outflow hydrograph relating discharge and time during failure of Teton Dam on 5th June 1976 (b). (Zhang et al., 2016)

The assessment of these breach parameters constitutes the aim of a breach model. In the past decades a consistent research effort has been dedicated to the development of methods for breach prediction ranging in accuracy and complexity. Different authors proposed different classification systems and the most accepted one is detailed by Morris et al. (Morris *et al.*, 2009) consisting of:

1. **Non – physically based or empirical models:** where discrete breach parameters like peak discharge or breach width are estimated through predictive equations derived from statistical analysis of past embankment failures. Despite the simplicity of these equations, there is a great level of

uncertainty affecting the results due to the dataset used to develop the equation and the associated constraints for the application to other cases. A list of equations can be found for example in Wahl (Wahl, 1998).

2. **Semi-physically based, analytical and parametric models:** to increase the level of accuracy while maintaining a relatively simple approach, methods incorporating physical processes but with simplified assumptions have been developed. The flow over the embankment is usually described with weir equations. The erosion rate for the breach growth or the final dimensions of the breach shape and time of breach formation are normally required in input. The approach of these model is to adjust the breach formation to fit this information. Hence the results are strongly related to the accuracy of the data provided by the user in input. An example is HEC-RAS (Hydrologic Engineering Centre's River Analysis System, developed by USACE - United States Army Corps of Engineers).
3. **Physically based models:** are the most complete methods aiming to simulate breach formation based on the hydraulic, hydrodynamics, erosion and instabilities processes observed during real failure and/or in experimental investigation. This means that computer programs are required to run complicated numerical models increasing the computation efforts. Many physically based models have been proposed over the last forty years ranging in complexity, assumptions, and methodology adopted. A historical overview of the numerical model development and a long list of available models (about 55 different breaching models) can be found in literature (Wahl, 1998; Morris and Hassan, 2002; Zhu, 2006; Morris, 2011). A more detailed description of the most recent and promising methods is provided by Zhong et al. (Zhong et al., 2016) and West et al. (West, Morris and Hassan, 2018).

An extract of the table published by Morris et al. (Morris *et al.*, 2009; Morris, 2011) based on the compilation of previous works from D'Eliso, 2007, Kahawita, 2007, Mohamed, 2002, Morris, 2009b, Zhu, 2006 is reported in the table below.

Table 2-1: Historical overview of the main physically – based breaching models available in literature extracted from (Morris et al., 2009)

Model	Breach Morphology	Flow Modelling	Erosion/Sediment Transport	Slope failure	Comments Limitations
CRISTOFANO (Cristofano, 1965)	Trapezoidal with constant bottom width.	Broad crested weir formula	Empirical formula developed by Cristofano	None	<ul style="list-style-type: none"> • Constant breach width and shape • No lateral erosion mechanism • No Slope Stability mechanism
PONCE-TSIVOGLOU (Ponce and Tsivoglou, 1981)	Constant Peak Flow Width	Full Hydrodynamic System	Meyer-Peter and Muller (1948) bed-load formula	None	<ul style="list-style-type: none"> • Initial breach geometry is to be specified in input • No slope stability model • No lateral erosion model
DAMBRK (Fread, 1984)	Rectangular, triangular, trapezoidal	Broad-crested weir flow	Linear predetermined erosion	None	<ul style="list-style-type: none"> • Final breach shape and final time of breach are required in input
NWS BREACH (Fread, 1988a)	Rectangular, trapezoidal	Broad-crested weir flow	Meyer-Peter and Muller modified by Smart	<ol style="list-style-type: none"> 1. Breach Side slope Stability 2. Top wedge failure 	<ul style="list-style-type: none"> • First model to include slope stability module, although inaccurate; • Uniform erosion of the breach; • Incompatible computation method for hydraulics and sediment;

Model	Breach Morphology	Flow Modelling	Erosion/Sediment Transport	Slope failure	Comments Limitations
BEED (Singh and Quiroga, 1987, Singh and Scarlatos, 1989)	Rectangular, trapezoidal	Broad-crested weir flow	Einstein – Brown (1950) Bed load formula	Breach side slope stability	<ul style="list-style-type: none"> • Similar approach to NWS BREACH model; • Uniform erosion of the breach; • Incompatible computation method for hydraulics and sediment; • Inaccurate slope stability analysis;
SITES (USDA – ARS, USA) (NRCS, 1997)	Three stages of failure including headcut formation	Spillway stage-discharge curve	Detachment model and energy dissipation equation	Spillway exit channel stability	<ul style="list-style-type: none"> • Incomplete modelling of embankment failure • Empirical coefficient to compute erosion
NCP – BREACH (Coleman and Andrews, 1998, Coleman et al., 2002)	Parabolic	Empirical formula	Empirical Formula	None	<ul style="list-style-type: none"> • Empirical expression based on small-scale models
BRES (Visser, 1998a,b)	Five stages of failure	Broad crested weir	Four sediment transport formula	None	<ul style="list-style-type: none"> • Use of sediment transport equations

HR BREACH (Hassan et al. 1999, Mohamed, 2002)	Effective shear stress equation; Exner equations and soil wasitng	Weir and 1D steady non uniform flow equation	Various sediment transport equations	Slope-Stability – Osman Core Stability	<ul style="list-style-type: none"> • Include option for uncertainties in material properties
SIMBA (Hanson et al., 2005c, Temple et al., 2005)	Rectangular, Trapezoidal	Broad crested weir	Parametric relations for headcut advance	Side slope erosion	<ul style="list-style-type: none"> • Developed on the basis of flume and larger scale experimental tests on headcut development
DamBreach (Wang and Bowles 2006a, b, c, d)	Undetermined	2D solution of St Venant equation	Sediment transport and erosion rate	None	<ul style="list-style-type: none"> • Non-cohesive;
DamBreach (Wang and Bowles 2007)	Undetermined	1D solution of St Venant equation	Sediment erosion rate formula	None	<ul style="list-style-type: none"> • Cohesive
BRES (Zhu, 2006)	Five stages of failure	Broad crested weir	Erosion rate for cohesive sediment with erodibility coefficient to be determined experimentally or empirically	None	<ul style="list-style-type: none"> • Developed from earlier 1998 model
HR BREACH Next Generation 2009 (Morris et al 2009)	Effective shear stress dependent	Variable weir and 1D steady non- uniform flow equation	Erosion equations: I Chen & Anderson II Hanson	Slope- Stability – Osman Core Stability	<ul style="list-style-type: none"> • Allows for multiple zones of variable erodibility soil

This historical excursus included only few examples of the great number of breaching models developed in the past. Despite the differences a common structure of physical – breach models can be identified. The main components are:

- 1. Hydraulic/Hydrodynamic sub-model:** for the calculation of the flow regimes (i.e. flow velocities and hydraulic shear stresses). The most common methods vary between the shallow water equations (1D and more recently 2D St Venant equations) and the simple crested-weir formula commonly used in open-channel problems.
- 2. Erosion sub-model:** interacts with the flow calculation to determine the volume of soil eroded over time. The oldest models adopted sediment transport equation from river hydraulics theories and only recent models started to implement the constitutive law for erosion (i.e. Equation 2-3).
- 3. Breach morphology sub-model:** the breach channel evolves based on the updates provided by the erosion processes simulated and many models predefine the shape of the breach cross-section that it is often an input to be specified by the user (i.e. parabolic, triangular, rectangular, trapezoidal)
- 4. Slope stability sub-model:** to simulate the instabilities of the breach channel slope. This is usually not present or simplified approaches are adopted.

2.4.1 Conceptual Models for Headcut Erosion

Table 2-1 includes breaching models like SITES (USD-ARS), SIMBA (Temple et al., 2005, Hanson et al. 2005b), BRES (Zhu, 2006) that simulate different stages of the breaching process governed by the headcutting erosion. These are based on different conceptual models of headcut formation and advancement. A common aspect is that the downstream profile is assumed to evolve into a single-step profile, thus neglecting the initial stages of headcut formation documented for example in Figure 2-9a, b. The differences are then related to the equations derived to study the single headcut failure, how overflow, erodibility and soil properties are considered.

The most common models implemented in the last generation of physically-based

breaching models to predict the headcutting mechanism, are discussed in the following.

2.4.1.1 SITES (1997) – Structure Site Analysis (Soil Conservation Centre and Agricultural Research Service)

SITES is a 2D model modelling the erosion processes in three phases. It is based on observation of laboratory and field investigations of vegetated spillways (Temple and Hanson, 1994). The three phases are: (1) failure of the cover vegetation, (2) headcut formation and (3) headcut advancement. Phases (1) and (2) are based on the calculation of the mass of soil removed over time (i.e. rate of soil detachment) according to Equation 2-3. In phase (1) the failure of the cover vegetation is calculated under the assumption that $\tau_w \gg \tau_c$ and the critical shear stress is zero.

The hydraulic shear stress τ_w in Pascal is given by:

$$\tau_w = \gamma_w d S (1 - C_F) \left(\frac{n_s}{n}\right)^2 \quad \text{Equation 2-11}$$

where γ_w is the unit weight of water, d is the flow depth, S is the slope energy line, C_F is a vegetal cover factor n_s is the soil grain roughness expressed in terms of Manning's coefficient and n is Munnings's n . The topsoil properties are represented by the Plasticity Index. The integration of Equation 2-11 over time until cover failure occurs gives:

$$\int_0^{t_f} \tau_w dt = 9PI + 50 \quad \text{Equation 2-12}$$

where t_f (in hours) is the time of vegetal cover failure and PI is the soil Plasticity Index. Equation 2-12 has been calibrated with data from field spillway experiments.

Once that the grass cover is detached, the process continues in phase (2) with the erosion of the material below the vegetation layer. The hydraulic shear stresses can be computed as:

$$\tau_w = \gamma_w (d + h) S \quad \text{Equation 2-13}$$

where d is the flow depth outside the concentrated flow area, h is the eroded depth in

the flow and stress concentration. Equation 2-13 is a special case of Equation 2-11 under the condition of phase (2) erosion. It is necessary at this point to be able to identify the critical shear stress and the erodibility coefficient of Equation 2-3. For fine-grained material experimental determination of the point of incipient motion requires either the application of subjective judgment or assumptions related to flow boundary interaction at low sediment transport rates. For coarse-grained material Shields' diagram is generally used as the basis for determining critical stress for incipient motion. An estimation of k_d proposed by these authors is based on the regression analysis of data from 10 documented studies on fine-grained materials and it is a function of clay content, dry unit weight and plasticity index. Alternatively, the coefficient may be determined from a direct measurement of soil erodibility using a JET test proposed by Hanson (Hanson, 1991).

Phase (2) erosion continues until the depth of erosion is sufficient to undermine the headcut formed and the headcut advancement begins. This occurs when erosion reaches a depth at which the flow plunges and impacts near the base of a vertical or near-vertical face accompanied with concentration of stress and flow energy dissipation at the base of the overfall. This condition can be approximated as the point at which the tailwater depth is equal to or less than critical depth.

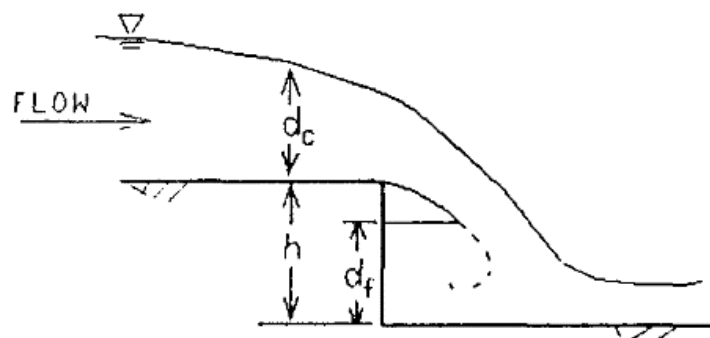


Figure 2-20: A sketch of the condition corresponding to the transition from phase 2 to phase 3 after Temple and Hanson (Temple and Hanson, 1994).

The headcut advancement is modelled using Equation 2-3 based on energy dissipation rate per unit width of headcut and a headcut erodibility index K_h that depends on the nature of the spillway materials.

$$\dot{E} = q \gamma_w H \quad \text{Equation 2-14}$$

where, \dot{E} is the energy dissipation rate, q is the unit discharge, γ_w is the unit weight of water and H is the change in energy line elevation through the headcut assumed equal to the height of the headcut. The headcut erodibility index K_h is computed as

$$K_h = M_s \left(\frac{RQD}{J_n} \right) J_s \frac{J_r}{J_a} \quad \text{Equation 2-15}$$

with M_s earth mass strength number, RQD rock quality designation, J_n joint set number, J_s relative ground structure number, J_r joint roughness number and J_a joint alteration number. The parameters can be assessed in the field. The mass strength number represents the strength of an intact representative sample of the material. The ratio $\frac{RQD}{J_n}$ represents the mean block or fragment size based on the relative spacing of joints within the mass. The ground structure number incorporates the effect of orientation of the material structure relative to the flow direction. The ratio $\frac{J_r}{J_a}$ represents the shearing strength of joints within the mass, or the shear strength of interparticle bonds.

There are two components in the headcut advance model. A threshold relation determines whether headcut advance occurs. An advance rate relation then determines the rate of headcut advance. Both the threshold and the rate are correlated with the headcut erodibility index. The threshold relation was calibrated against 46 data points for which headcut advance could be described qualitatively. The advance rate relation was correlated using data from 33 headcuts for which advance rates could be estimated. The headcut advance model was validated against 10 additional headcuts not included in the calibration analysis. In only three of these cases the results were heavily dependent on phase (3) erosion (headcut advancement). For two of these spillways constructed in weaker materials, the model predicted erosion consistent with that observed. For one spillway constructed in stronger materials, the model underpredicted the observed process. In this case, the authors had doubts about the determination of the headcut erodibility index for the eroded materials.

2.4.1.2 SIMBA (2005) – SIMplified Breaching Analysis

SIMBA is the evolution of SITES and it is considered a physically – based empirical model. SIMBA is the result of an intense research activity at the U.S. Department of Agriculture - ARS Hydraulic Engineering Research Unit, Stillwater, OK by Temple and Hanson. It was one of the three models evaluated as part of the review program promoted by the working group of the Dam Safety Interest Group (DSIG) of CEATI International (Morris *et al.*, 2012).

SIMBA was developed to analyse headcut erosion observed in large-scale laboratory tests on homogenous fine-grained embankment. The erosion algorithms and codes of SIMBA have been incorporated in WinDAM (i.e. Windows Dam Analysis Modules) a modular software (Temple *et al.*, 2006) under development at USDA (i.e. United States Department of Agriculture) for which several versions are currently available. Research is ongoing and new versions of WinDAM (i.e. WinDAM D and E) are planned to be released in the future.

The conceptual model for headcut erosion implemented in SIMBA and then in WinDAM is detailed in the following.

SIMBA is based on the assumptions that the headcut begins at the top of the downstream slope while the crest remains at its original level until the headcut reaches the upstream edge of the crest. Idealized three-dimensional shape and growth of breach are determined by coupling a headcut development and advance model with hydraulic calculations based on normal depth flow and unit flow rates. Flow rate is approximated by assuming hydrostatic pressure and an energy coefficient of unity at the point of hydraulic control. The erosion rate is a function of a soil detachment rate coefficient k_d and the excess stress applied ($\tau_w - \tau_c$) according to Equation 2-3.

Headcut migration is modelled using the deterministic approach developed by Hanson et al. (Hanson, Robinson and Cook, 2001). The rate of headcut migration is based on a 2D stability analysis according to the Culmann method. The forces considered are represented in the figure below.

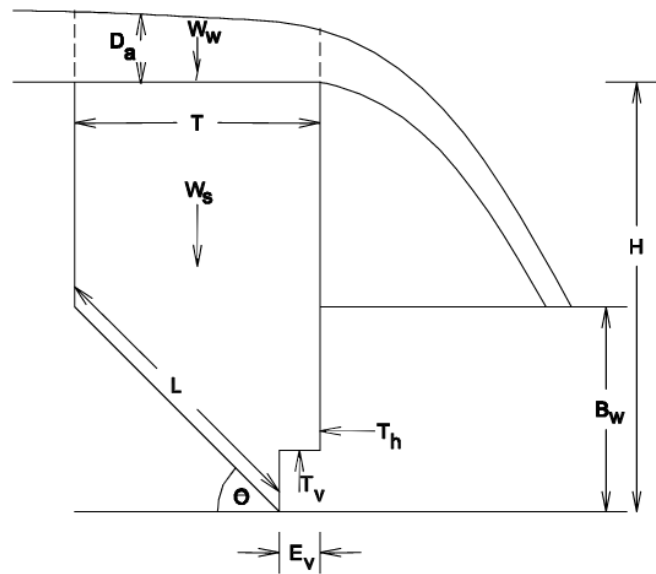


Figure 2-21: Headcut advancement model proposed by Hanson et al. (Hanson, Robinson and Cook, 2001)

The attacking forces are the weight of the soil W_s at failure and the weight of water W_w at the top of the overfall. Due to the continuous erosion and/or undercutting, the weight of the soil block changes in time. The resisting forces are associated with the vertical and horizontal backwater components T_v and T_h and the soil strength due to cohesion c and internal angle of friction φ .

At failure, the equilibrium of these forces gives:

$$(W_s + W_w - T_v - c L \sin \theta)[\tan(\theta - \varphi)] - T_h - c L \cos \theta = 0 \quad \text{Equation 2-16}$$

where L and θ are the length and the angle of the failure plane respectively.

In this model the shear failure is assumed to be the predominant mechanism and once it has happened, the headcut advances upstream at a distance T assumed equal to $H/2$, with H the height of the headcut. At this point, the failed soil block is deposited at the toe of the slope until the flow will remove it.

Further simplistic assumptions are that (1) the headcut is at its maximum height and migrates upstream at that height, (2) the soil blocks failed downstream have no impacts on the migration process, (3) the headcut stability can be described in terms of unconfined compressive strength.

The headcut advancement is considered as a cyclic process. When the headcut fails

another event starts until the stability is overcome again and another failure occurs. The rate of migration can be described as the distance of movement T divided by the time of each failure t_f according to Equation 2-17.

$$\frac{dX}{dt} = \frac{T}{t_f} \quad \text{Equation 2-17}$$

The time of failure t_f is related to the soil erodibility and depends on the rate of soil removed on the vertical face E_v inducing headcut instability.

$$t_f = \frac{E_v}{k_d(\tau_w - \tau_c)} \quad \text{Equation 2-18}$$

hence, Equation 2-17 can be written as:

$$\frac{dX}{dt} = \frac{Tk_d(\tau_w - \tau_c)}{E_v} \quad \text{Equation 2-19}$$

In Equation 2-16 the terms W_s , T_v and L depends on E_v .

In fact, the weight of the failing soil block is:

$$W_s = \gamma_s(T - E_v) \frac{2H - (T - E_v) \tan \theta}{2} + \gamma_s E_v H \quad \text{Equation 2-20}$$

with γ_s the soil unit weight.

The vertical component of the backwater force T_v is equal to:

$$T_v = \gamma_w B_w E_v \quad \text{Equation 2-21}$$

and the length L is:

$$L = \frac{X - E_v}{\cos \theta} \quad \text{Equation 2-22}$$

The other terms that are not dependent on E_v are W_w and T_h that can be written as:

$$W_w = \gamma_w D_a T \quad \text{Equation 2-23}$$

where D_a is the depth of water on the top of the headcut and:

$$T_h = \frac{1}{2} \gamma_w B_w^2 \quad \text{Equation 2-24}$$

The erosion that will cause failure can be determined by introducing Equation 2-20, 2-21, 2-22, 2-23 and 2-24 in Equation 2-3.

The authors considered undrained conditions assuming that the soil strength is provided by $c_u = q_u/2$ with q_u unconfined compressive strength.

Ultimately, erosion on the vertical face is estimated by solving the algebraic Equation 2-25.

$$a + b(E_v) + c(E_v)^2 = 0 \quad \text{Equation 2-25}$$

where a , b

$$a = \frac{\gamma_s}{2} \quad \text{Equation 2-26}$$

$$b = \gamma_w B_w - \frac{\gamma_s}{2} H - 2c_u \quad \text{Equation 2-27}$$

$$c = c_u H + \frac{\gamma_w}{2} B_w^2 - \frac{3}{8} \gamma_s H^2 - \frac{1}{2} \gamma_w D_a H \quad \text{Equation 2-28}$$

In SIMBA the process of breach development is modelled in four stages: (1) headcut development at the downstream head of the crest; (2) headcut advancement through the crest up the upstream edge; (3) lowering of the crest; (4) breach widening.

In stage (1) erosion of soil is estimated with Equation 2-3 driven by normal depth flow on the slope using Manning's formula.

Solution of Equation 2-25 comes into play to calculate the advancement rate during stage (2) starting when the eroded depth exceeds the critical flow depth. and during the breach formation stages. When phase (4) is reached the breach can only widen.

2.4.1.3 BRES – Breach Erosion in Sand-dikes -Visser (1998) and Zhu (2006)

BRES was initially developed by Visser (Visser, 1998) to model observed breaching processes of homogeneous coarse-grained embankment dam during overtopping. As presented in Figure 2-6, breach processes of coarse-grained embankment are divided in 5 stages. In stage 1 the downstream slope is steeping from an initial slope up to a critical condition. At this point stage 2 starts, and the discharge

flow continues to erode the downstream slope, which remains a constant value. Then, the crest moves toward the upstream until the end of this stage, when the crest is entirely moved by downstream erosion and disappears. In stage 3, erosion starts to deepen the breach bottom toward the base of the embankment at a constant slope angle. As the breach deepens, it widens at a constant slope angle. As the breach reaches the base of the embankment bottom, stage 3 ends. In stage 4 the breach continues to grow in both the vertical and horizontal directions and is controlled by the bottom erosion rate and side slope erosion rate. The side slope angles remain at the critical angle. As the discharge flow changes from critical to subcritical, stage 4 ends and stage 5 starts. In this stage, lateral erosion is the main erosion process. The breach continues to enlarge until the end of the breach.

The five-stage approach has been further extended by Zhu (Zhu, 2006) to model the observed breaching processes of fine-grained fills where headcut formation and migration are the dominant breaching mechanisms. In stage (I) an initial notch is assumed on the embankment crest where the soil is eroded under the hydraulic shear stress and a small-scale headcut may form along the downstream slope. The erosion at the toe is generally large than the erosion on the upper part. Due to this different erosion zones the downstream slope is steepening over time until a critical slope angle is reached and stage (II) starts. This is essentially the headcut formation. During stage (II) further erosion of the surface of the slope and the scour hole formed downstream due to the jet impingement leads to the first headcut failure and transition to stage (III). In stage (III) the same failure mechanisms are repeated cyclically of a weaker and thinner embankment. The breach enlarges rapidly, as well as the flow rate and accelerates the breach erosion process consequently. At the end of stage (III) the embankment body has been washed away and in stages (IV) and (V) erosion continues only laterally with side-slope instabilities. In this context

Zhu (Zhu, 2006) considers four different types of erosion that can occur once that the headcut is formed at stage (II). With reference to Figure 2-22, these are (1) flow shear erosion on the top surface of the headcut and (2) along the headcut slope due to the water shear stresses; (3) scour hole formed at the embankment foundation due to the impinging jet that tends to undermine the stability of the headcut by undercutting;

(4) slope mass occurs when the base of the headcut is eroded and the headcut becomes unstable under its weight and seepage forces. The process is cyclic meaning that after each slope mass failure the headcut migrates by the width of the soil block failed, a new impinging jet will start a new cycle of headcut erosion. Owing to the above-mentioned erosion, the width of the embankment crest decreases and the height of headcut reduces in time, accordingly the overtopping flow discharge increases.

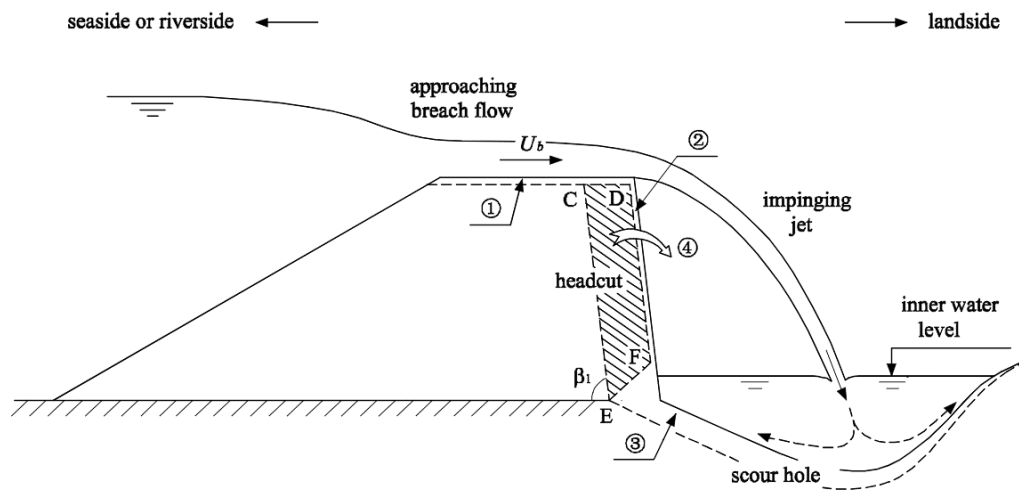


Figure 2-22: Erosion processes affecting headcut stability assuming an erodible bed: (1) shear erosion along headcut top surface; (2) erosion along headcut slope; (3) scour due to the impinging jet undermining the base of the headcut and (4) slope mass failure after (Zhu, 2006)

A mathematical model has been developed based on these four mechanisms. The shear erosion (1) and (2) is calculated through Equation 2-3, where the hydraulic shear stresses are calculated by:

$$\tau_w = \frac{1}{C^2} \rho g U^2 \quad \text{Equation 2-29}$$

where C is the Chezy coefficient, ρ is the water density, g is the gravity acceleration and U is the averaged flow velocity.

In Figure 2-23, U_0 is the jet velocity, T_0 is the jet width and χ is the jet entry angle. The potential core is defined as the region where the jet velocity U_0 is constant. The length and the height of the potential core are J_p and H_{pc} respectively, while J is the length of the jet from the entry point to the bed. H is the depth of the scour hole and

h_p is the depth of tailwater above the original foundation.

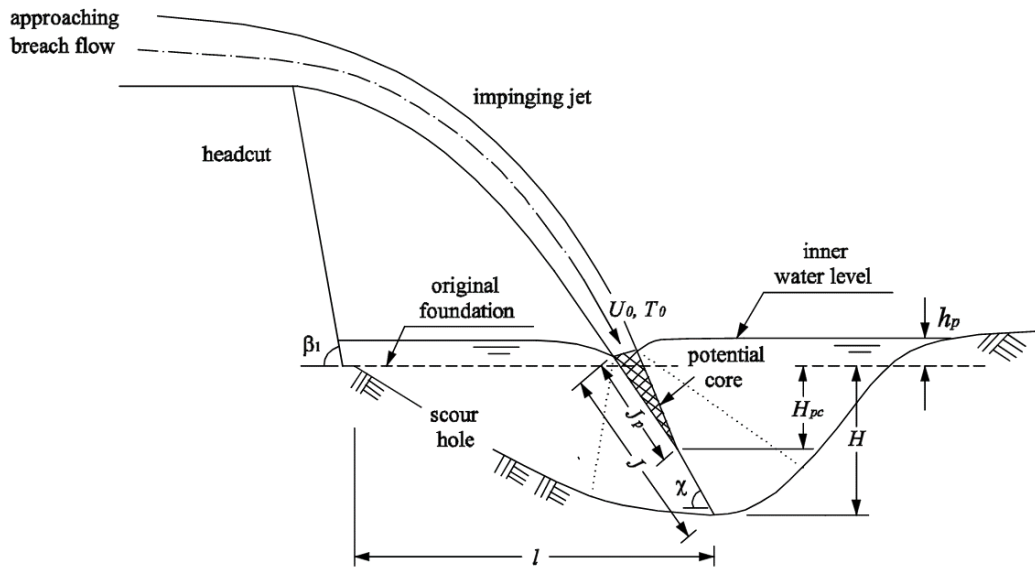


Figure 2-23: Scour hole due to impinging jet downstream of a headcut (Zhu, 2006)

The scour hole development represented in Figure 2-23 is calculated according to the analytical equation proposed by Stein et al. (Stein and Julien, 1993). In the potential core region (i.e. $J < J_p$) the maximum shear stress due to the jet is given by:

$$\tau_{w,j} = C_f \rho U_0^2 \quad \text{Equation 2-30}$$

And outside of the potential core (i.e. $J > J_p$) the shear stress is calculated as:

$$\tau_{w,j} = C_d^2 C_f \rho U_0^2 \frac{T_0}{J} \quad \text{Equation 2-31}$$

where C_f is a friction coefficient and C_d is a diffusion constant approximately equal to 2.60. The scour depth H is found as:

$$H = J \sin \chi - h_p \quad \text{Equation 2-32}$$

While the scour rate (length/time) can be calculated in the same manner as Equation 2-3:

$$\frac{dH}{dt} = \frac{k_{df}}{\rho_b} (C_f \rho U_0^2 - \tau_c)^s \quad \text{Equation 2-33}$$

valid for the potential core region and for $H > H_{pc}$ the same is instead:

$$\frac{dH}{dt} = \frac{k_{df}}{\rho_b} \left[\frac{C_f \rho U_0^2 (H_{pc} + h_p)}{H + h_p} - \tau_c \right]^\zeta \quad \text{Equation 2-34}$$

in which

$$H_{pc} = C_d^2 T_0 \sin \chi - h_p \quad \text{Equation 2-35}$$

k_{df} is the erodibility coefficient of the embankment foundation, τ_c is the critical shear stress and ζ is a constant to be determined experimentally. Stein et al. (Stein and Julien, 1993) found that $\zeta = 1.5$ for coarse-grained materials and $\zeta = 1.0$ for fine-grained soils.

In Figure 2-22 and Figure 2-23 the headcut tends to become unstable when the scour hole is undercutting through its base. For simplicity the surface of the headcut undercutting represented by the line EF in the figure below is simplified as a plane with a slope angle of 45 degrees to the horizontal. The slope of the upstream boundary of the scour hole m_f has often been found to range between 1.0 – 4.0 depending on soil properties and flow conditions (Stein and Julien, 1993)

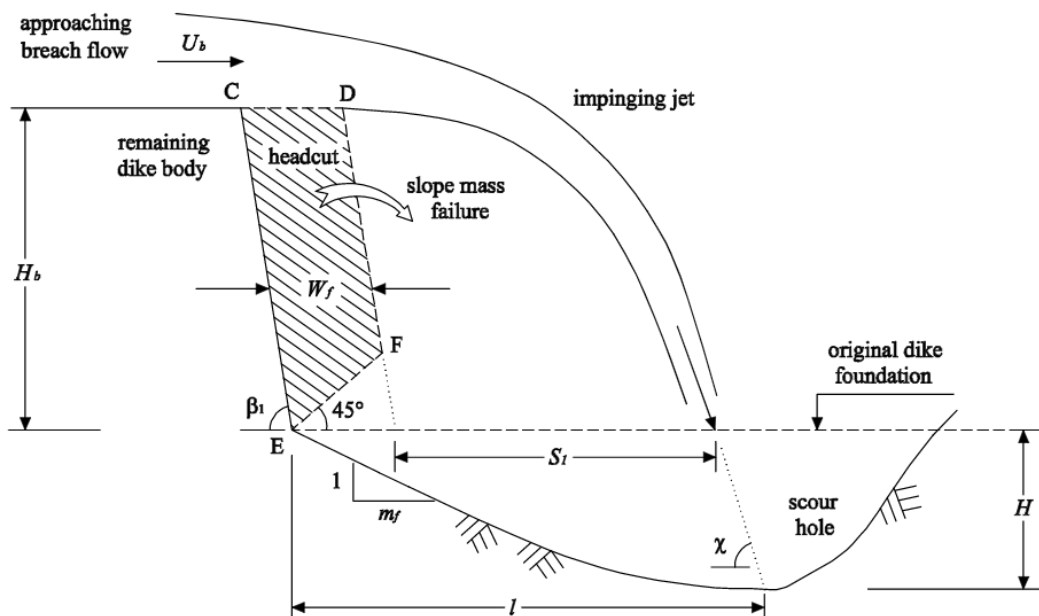


Figure 2-24: Sketch of headcut failure (Zhu, 2006)

It is assumed that the soil block CD₁FE fails due to overturn around the point E. The forces acting on the unstable block are represented below, where AB is the phreatic line dividing the block in two parts: CDBA with weight G_1 and ABFE with weight G_2

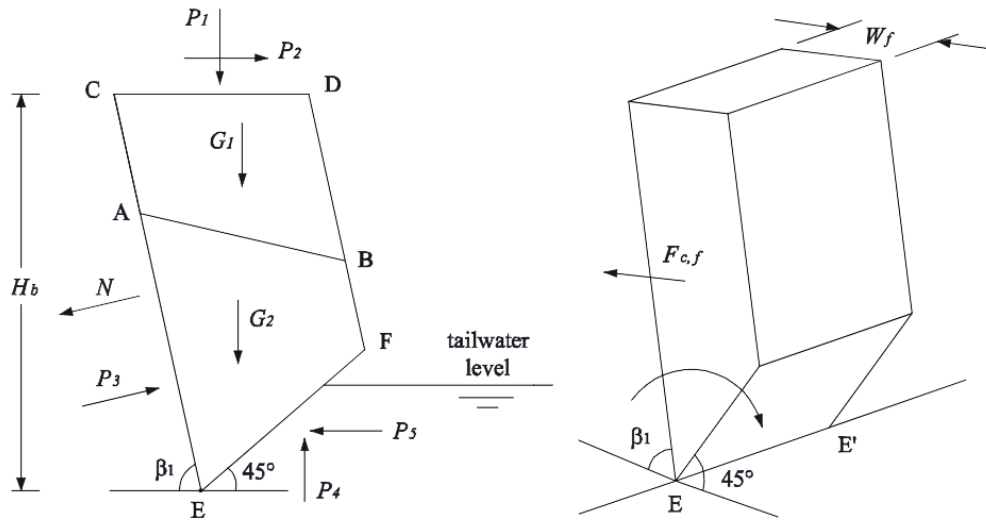


Figure 2-25: Forces acting on the soil block at failure (Zhu, 2006)

P_1 and P_2 are respectively the weight and shear force exerted by the water overflowing on the top of the block top; P_3 is the pore water pressure acting on the plane AE; P_4 and P_5 are respectively the vertical and horizontal forces due to the tailwater; N is the force between the failure block and the new headcut face; and $F_{c,f}$ is the force acting on the two lateral surfaces of the block. The forces imposed by the inner water are generally relatively small and therefore neglected here. The destabilising forces are P_1, P_2, P_3, G_1 and G_2 while the resisting forces are N, P_4, P_5 and $F_{c,f}$. The failure conditions are reached when the moments of the destabilising and resisting forces equal to zero:

$$P_1 d_{P1} + P_2 d_{P2} + P_3 d_{P3} - 2F_{c,f} d_{c,f} + G_1 d_{G1} + G_2 d_{G2} - N d_N = 0 \quad \text{Equation 2-36}$$

where $d_{P1}, d_{P2}, d_{P3}, d_{c,f}, d_{G1}, d_{G2}$ and d_N are the lever arms of the respective forces around the point E. Following the failure of the soil block, the headcut retreats by the

distance W_f (i.e. the width of the block) a new jet entry point is determined and therefore a new cycle is started leading to a new headcut failure.

2.4.1.4 Discussion

The main conceptual models developed in the past to describe and predict the physics of headcut erosion have been presented. However, to date there is not a common accepted approach.

SITES is based on several simplified assumptions of flow, erosion conditions and soil properties. It applies empirical correlations to estimate the headcut erodibility index determined by fitting procedures to field data collected at NRCS (i.e. National Resources Conservation Service) between 1983 and 1994 (Wahl, 1998). The conclusion was that more studies and research were needed to refine the analysis of the time of headcut formation (Temple and Hanson, 1994).

SIMBA is a research tool developed to replicate headcut erosion tests on homogeneous earth embankment constructed with fine-grained materials, therefore it is calibrated against specific datasets. SIMBA requires as input the soil unit weight, the undrained shear strength and the critical shear stress. One of the strongest hypotheses of the model is that SIMBA predicts headcut formation from the top of the slope (i.e. from the downstream edge of the crest), in contrast with the observed headcutting mechanisms where the onset is initially localised at the toe.

BRES applies a stress-based approach like SIMBA to compute headcut advancement incorporating the effects of the erodible foundation of the embankment. However, the equations adopted to determine the scour hole due to a water impinging jet are still under study. Uncertainties related to the velocity field at the entry point and the jet diffusion are not fully understood. In addition, BRES assumes for simplicity that the downstream profile during overflow evolves into a single – step headcut, and that the scour hole undermines the headcut along a plane inclined by 45 degrees to the horizontal, fact for which there are no evidence. The model has been calibrated with the data of four laboratory experiments. Based on the calibrated soil erodibility coefficient k_d for these four experiments, a relationship has been established between

k_d and the available soil properties. With this relationship, the model was validated against the other two laboratory experiments. Although the results between the model predictions and the measurements are in reasonable agreement, the importance of scale-effect should be recognised. At the same time, the model validation against a failure of a prototype dike in China in 1998 shows that the model underestimated the final breach width (Zhu, 2006).

In conclusion, in all the three models described, headcut is represented for simplicity as a vertical cut of the downstream slope, hence the initial phases where the profile is multi-stepped are systematically neglected. In addition, geometrical aspects like slope angle and maximum length of retreat are assumed as part of the conceptual model. It has been shown that both SIMBA and BRES consider headcut failure as a stability problem and that headcut migration occurs when destabilising forces equals stabilising components.

The overflow velocity and hence the hydraulic shear stresses are calculated with approximate empirical equations (i.e. Chezy equation, Manning's equation) valid under specific conditions.

Overall, it seems that there is a poor understanding of how headcut forms in the first instance and how the onset of headcut is related to erosion mechanism at particle or aggregate scale.

2.4.2 The Last Generation of Physically-Based Breaching Models

The last generation of physically based models is often the result of improvements of previous versions to overcome some of the key limitations identified.

For example, EMBREA developed at HR Wallingford UK supersedes HR BREACH (Samuels *et al.*, 2008; Morris, 2011) that was first introduced between 1998-2001 by Mohamed Hassan (Mohamed *et al.*, 2002). HR BREACH has been updated through the years and different versions were produced as part of tasks of European Union projects, like CADAM, IMPACT, FLOODsite, and FloodProBE (Morris, 2011; Wahl, 2017). These initiatives included many laboratory and large-scale breach tests, where the improvements in knowledge and understanding of the observed physical processes as well as key information were used to calibrate the model.

Other recent models are DLBreach (Wu, 2016) and the model developed by Volz et al. (Volz, 2013; Volz *et al.*, 2017) that present the novelty of modelling the groundwater flow within the embankment structure and considers the effect of suction-induced apparent cohesion (West, Morris and Hassan, 2018).

An overview of HR – BREACH/EMBREA and DLBreach capabilities and limitations is detailed in the following, as these are recognised as the most promising breaching models of the last 10 years.

2.4.2.1 HR – BREACH (Mohamed, 2002) evolved in EMBREA (HR Wallingford UK, 2012)

HR BREACH and EMBREA adopt principles of hydraulics, sediment transport, and soil mechanics. It predicts breach growth through embankment structures, providing breach characteristics such as size, shape and outflow hydrographs. Different breaching mechanisms can be analysed like: (1) overtopping failure of both coarse-grained and fine-grained homogeneous embankments, including headcut and side slope instability; (4) overtopping failure of composite embankments (i.e. core, embankment body and protective layers); (3) initial erosion of protective layers like grass or rock cover; (5) internal erosion leading to pipe formation through the embankment (Wahl, 2017). In the following only the overtopping of homogenous embankment is analysed. EMBREA introduced several improvements like the layered embankment option but the fundamental strategy of HR BREACH is hold.

The breach initiation and formation processes are modelled by dividing the embankment in sections, whose spacing must be specified in input (i.e. generally the spacing is assumed to be equal to the half of the breach width). In this way flow, erosion and slope stability equations are solved sections by sections.

Unlike SIMBA and BRES the breaching process is not discretised in a series of predefined stages. However, the users must specify in advance an initial notch through the embankment crest and along the downstream slope where the overflow runs, as shown in Figure 2-26. In addition, surface erosion or headcutting must be defined in the input, hence the user must assume the expected breaching processes. This decision is usually based on the analysis and judgment of the erodibility properties of the

embankment fill.

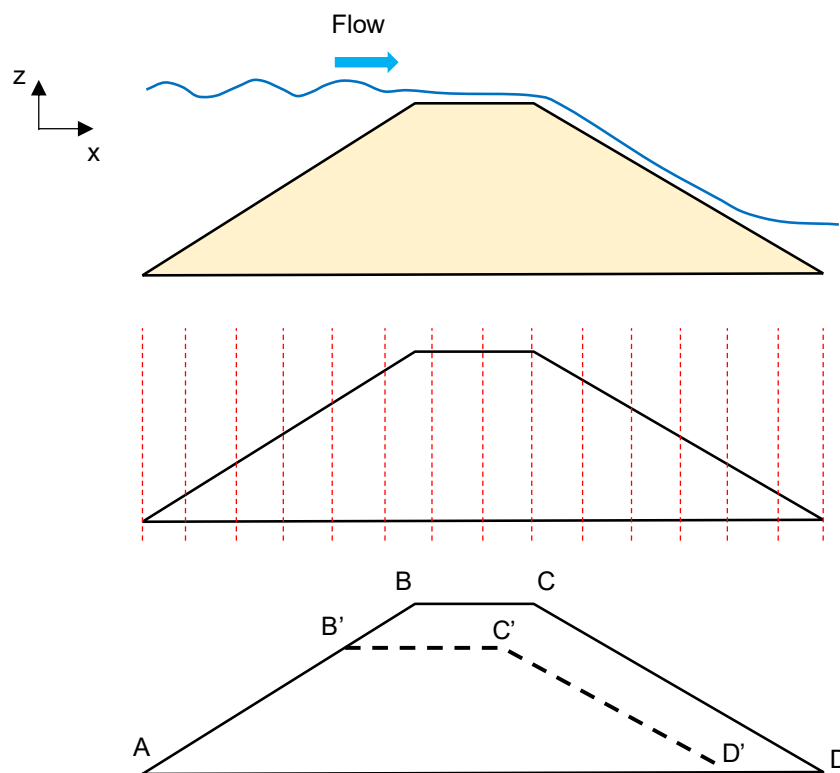


Figure 2-26: Division of the embankment in sections and definition of the initial notch profile after Morris (Morris, 2011)

The EMBREA online guidance, of which an extract is shown in Figure 2-27, explains that an “initiation channel constrains the initial breach flow and provides the focal point for breach simulation. In practical terms, this simulates a hole or dip in the embankment or dam crest that might arise for a number of reasons, resulting in the focus of overtopping flow, leading to breach. [...] When selecting initial breach channel depth and width, the user is recommended to use small values appropriate to the case being studied. If breach does not initiate, these values may be increased. The user should always consider the practical implications of having to increase the initiation channel to large dimensions in order to induce breach. Failure to breach an embankment or dam is a valid output from the EMBREA model.” (from [EMBREA for members | HR Wallingford \(dambreach.org\)](#)).

These can be considered as limitations of the model because the modes of failure and

breach onset (i.e. initial notch) should be results of the simulation rather than constraints to simplify hydraulic and macro-erosion behaviours.

For an overtopping failure, the required parameters include the initial breach depth and width, maximum allowed breach depth and width, initial breach side slope (currently only vertical side slopes are allowed - i.e. side slope = 0), initial reservoir level, and the equation to be used in the calculation of sediment transport during the breaching process.

The screenshot shows the 'Breach' tab selected in a navigation menu. Below the menu, a blue button labeled 'Overtopping' is highlighted. To the right, a form titled 'Overtopping properties' contains the following input fields:

- Sediment Transport Equation: A dropdown menu set to 'Original Hanson (Cohesive)'.
- Initial Breach Depth (m): A text input field containing '0'.
- Initial Breach Width (m): A text input field containing '0'.
- Initial Reservoir Level (mOD): A text input field containing '0'.
- Max. Breach Depth (m): A text input field containing '0'.
- Max. Breach Width (m): A text input field containing '0'.

Figure 2-27: Screenshot from EMBREA Lite online guidance highlighting the inputs required for the initial notch and selection of erosion equations, from [EMBREA for members / HR Wallingford \(dambreach.org\)](https://www.dambreach.org/)

The sequence of calculations in HR BREACH and EMBREA are described in the flow chart of Figure 2-28 after Morris (Morris, 2011).

First, the position of the critical flow section (i.e. section where the flow changes from sub to supercritical flow along the embankment crest) is assumed according to five methods. A detailed description of these approaches is out of the scope here but these can be found in Morris and on the EMBREA website guidance (Morris, 2011; EMBREA Lite - HR Wallingford, 2022). It is worth mentioning that the location of the critical section is important because flow profile upstream and downstream will be calculated from this section.

The second step is the calculation of the discharge through the breach. The model adopts a weir equation to calculate the discharge at the critical flow section where a discharge coefficient between 1.5 and 2.2 must be introduced. Flow approaches the embankment crest from the upstream slope within a channel that converges to the breach width at the upstream crest edge at any given time step with a recommended

angle of 30 degrees. A non – uniform flow equation is used to identify the free surface profile based on the use of the Manning’s equation for the friction slope.

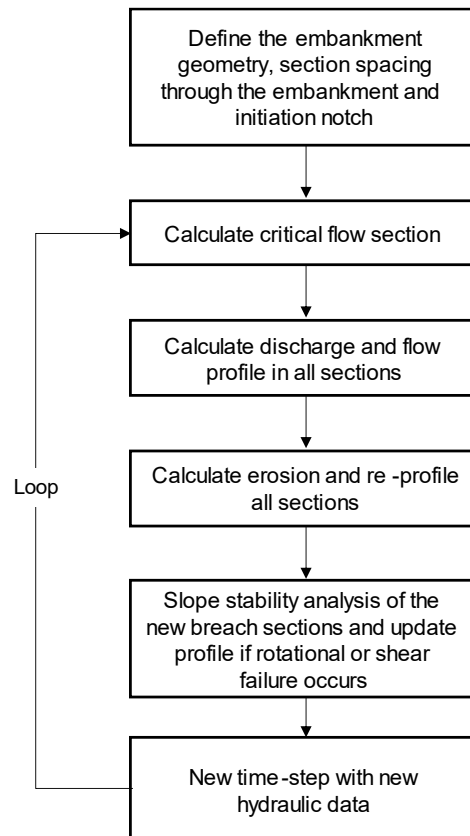


Figure 2-28: Flow-chart describing the calculation sequence in HR BREACH and EMBREA after Morris (Morris, 2011)

Once that the flow profile is known, the shear stress distribution around the flow section can be determined and in the third step the eroded material is calculated via sediment transport or erosion equations. EMBREA provides several options including a mixture of erosion equations, (i.e. Equation 2-3 style) and equilibrium transport equations i.e. Meyer-Peter-Müller, Yang (1979) and Bagnold-Visser (1997) for fine- and coarse-grained soils. The routing (i.e. the modelling of the transport of the material once eroded) is not considered. The EMBREA website guidance encourages the use of erosion equations rather than the equilibrium ones. Support is provided through the guidance to select the erodibility parameters required in input.

At this point, within each time step, the model defines a new breach section profile

and a new water level for the next time step, as A-1-3-B'-C'-4-2-D and A-1-3-B' in the below. It must be highlighted that the erosion rate is calculated sections by sections, but an average value is applied at each section to avoid large variations between adjacent sections. In addition, it is assumed that the maximum lateral erosion D_b is equal to the vertical erosion D_h . The top width is kept constant until slope instability occurs.

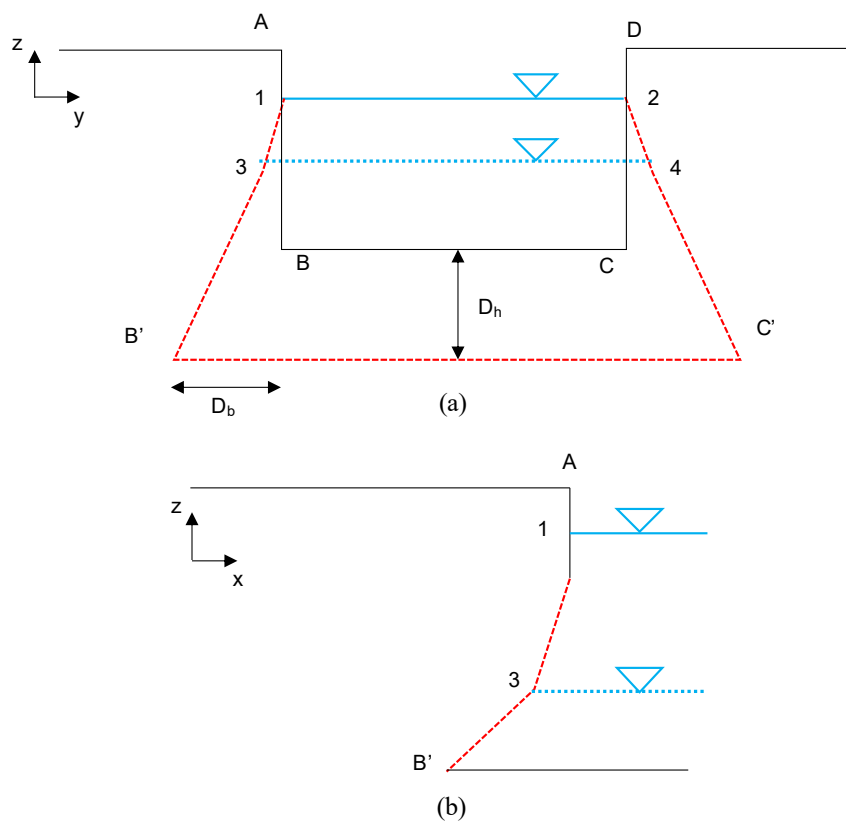


Figure 2-29: Breach channel growth: cross-section (a) and profile (b) after Morris (Morris, 2011)

By default EMBREA considers the stability of the breach sides for each individual cross section. This means that the analysis for the stability of each section is independent of those adjacent. The user can decide to model only sediment erosion and in this case the breach growth is only determined by sediment erosion, or if shear failure and/or tension failure should be included. In this latter case, breach growth is given by the eroded material and the instability of discrete overhanging soil blocks

occurring due to overturn and/or shear mechanisms as shown in Figure 2-30a, b.

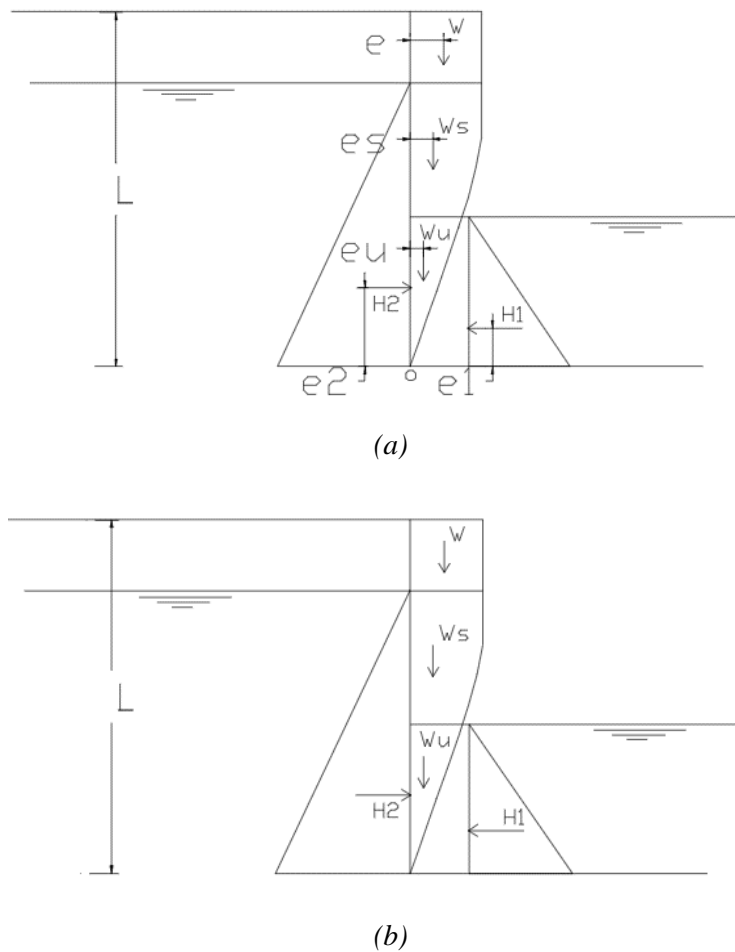


Figure 2-30: Slope stability analysis performed in EMBREA (a) overturning, (b) shear after Mohamed et al. (Mohamed et al., 2002)

In the slope stability analysis, suction is neglected above the water table and the soil is considered dry. Also, change of the water level during failure are assumed to be slow and therefore these are neglected.

The loop in Figure 2-29 is repeated until the final failure.

In conclusion, EMBREA has been identified by the DISG (Dame Safety Interest Group) as one of the most promising breach models that can be potentially adopted in industry practice in future. The model has been validated against four historical cases, seven field cases and eighteen laboratory tests, showing positive results.

Among the main advantages it should be mentioned: (1) the possibility of simulating

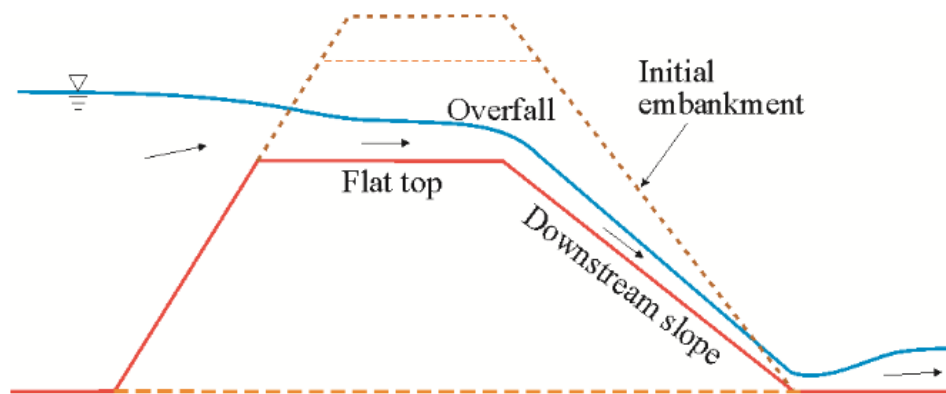
different types of failure (i.e. overtopping and piping due to internal erosion); (2) for the overtopping case, both surface erosion and headcutting can be selected; (3) complex geometries ranging from homogenous to zoned and layered (i.e. heterogenous) embankment can be implemented; (4) breach growth is estimated considering both erosion and slope stability processes.

On the other hand, the most important drawbacks are: (1) assumption of the mode of failure that must be pre-defined in input (i.e. surface erosion or headcutting) while it should be an output of the simulation; (2) assumption of the initial breach geometry where the dimensions of the initial notch must be given in input (i.e. initial breach depth and initial breach width) as well as the maximum allowed depth and width; (3) simplified simulation of the overflow with 1D weir equations and calculation of the hydraulic shear stress with the Manning's equation; (4) when the headcut mechanism is simulated, the initial location of the headcut (i.e. crest, toe or crest and toe) must be specified in input while it should be an output of the simulation; (5) the headcut migration is computed adopting both the SIMBA (i.e. shear stress based) and the SITES (i.e. energy dissipation based) methods. Therefore, in practice, when dealing with headcutting, EMBREA reduces to SIMBA and/or SITES reflecting the limitations of both (Risher and Gibson, 2016). The EMBREA guidance recommends using the maximum results of both calculations (EMBREA Lite - HR Wallingford, 2022).

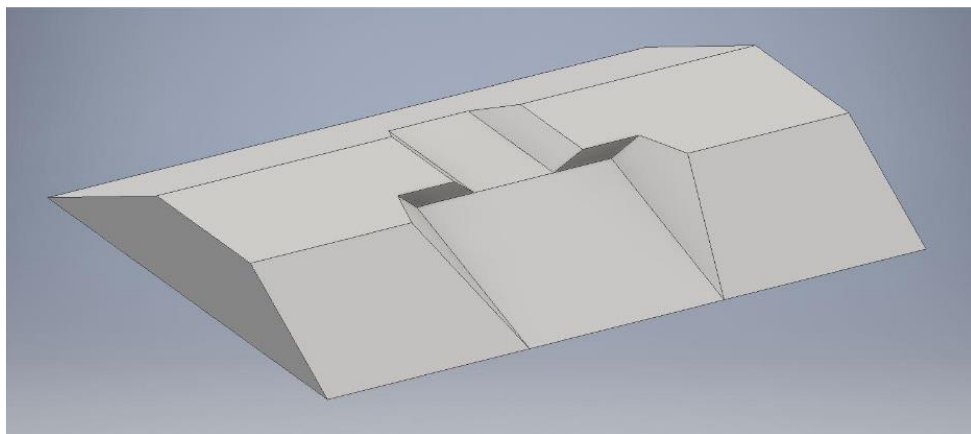
2.4.2.2 *DLBreach* (Wu, 2016)

The first version of DLBreach (i.e. Dam and Levee Breach) was developed by Wu in 2013, while the newest release (Wu, 2016) was revised to consider both on-direction and two-direction breach for the coastal and estuarine levees (i.e. upstream and downstream). The proposed model aims to simulate the breach formation in coarse- and fine-grained materials of homogeneous and composite structures triggered by external erosion associated with overflow or through internal erosion leading to piping failure. In the following only the one-direction breach is presented for homogeneous embankment.

For coarse-grained material during overflow the breach forms through the progressive surface erosion. An initial breach with a trapezoidal cross-section is assumed as in Figure 2-31a, b.



(a)



(b)

Figure 2-31: Side-view (a) and 3D view (b) of the breach channel for coarse-grained homogeneous embankment during overflow after Wu (Wu, 2016)

For fine-grained embankment where breach formation is supposed to occur via headcutting the idealised geometry considered in DLBreach is shown in Figure 2-32a, b.

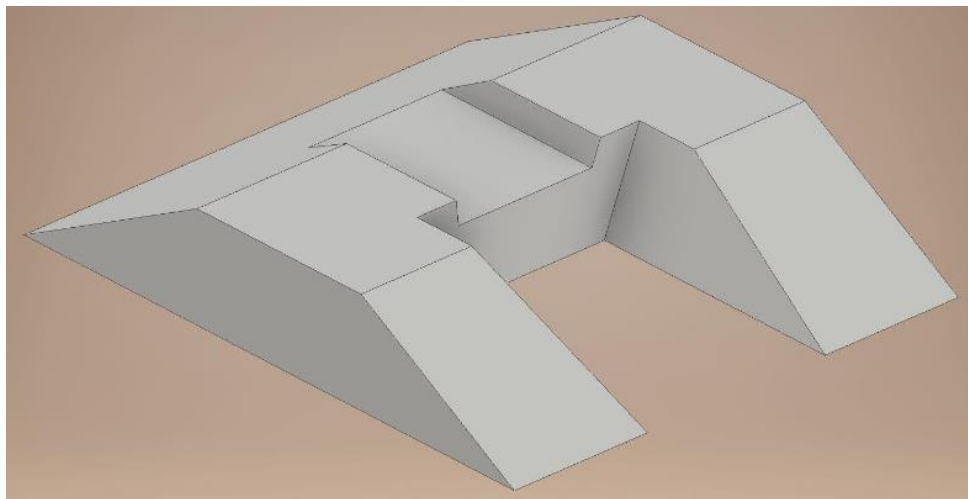
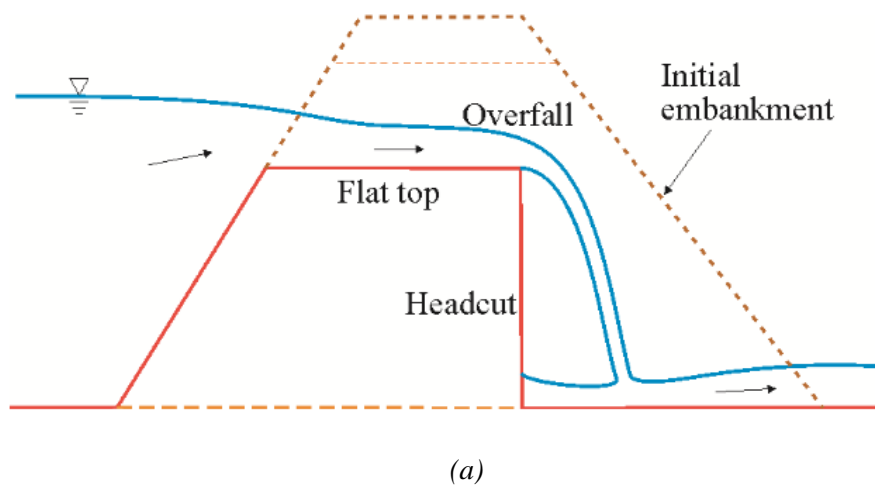


Figure 2-32: Side-view (a) and 3D view (b) of the breach channel for fine-grained homogeneous embankment during overflow after Wu (Wu, 2016)

In DLBreach, the headcut is assumed to start at the downstream toe and migrates upstream gradually. The cross-sections of breach flat top and the section downstream of the headcut are approximated as trapezoidal, and undergo downcutting and widening.

It is worth emphasising that DLBreach assumes a trapezoidal cross-section of the initial breach channel for both progressive surface erosion and headcutting.

The flow is simulated with a broad-crested weir equation in the intensive

breaching period, when the flow conditions on the flat top of the breach are considered to be the critical; and the Keulegan equation during the evolution period, when the flow maybe sub-critical. The latter is a simplified non-uniform flow with local head loss where an additional term to consider the wind action is added. The differences between the conditions are presented in the figure below.

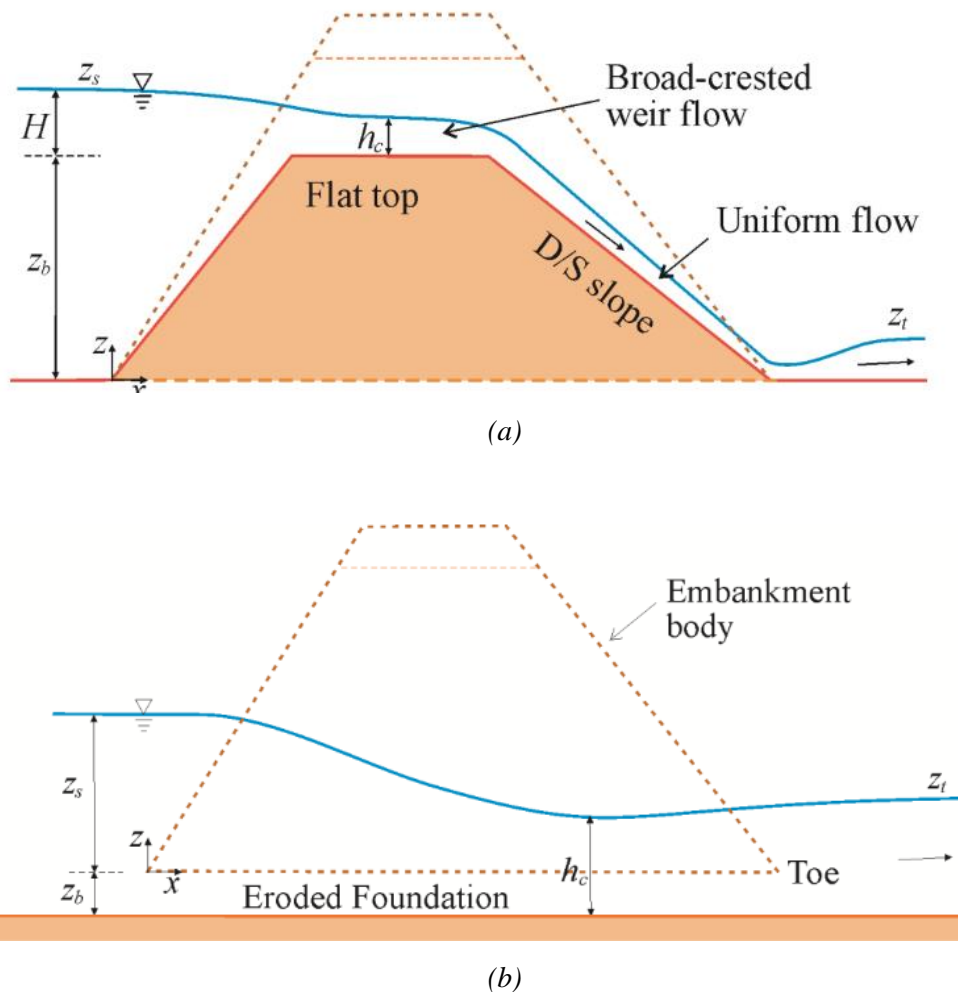


Figure 2-33: Longitudinal section of breach in (a) intensive breaching period under critical flow conditions and (b) in general evolution period after Wu (Wu, 2016)

The user must specify the intensive breaching period through three options: (1) intensive breaching period is equal to the simulation period; (2) the intensive breaching period occurs until the erosion reaches the embankment base or when the upstream

and downstream water levels are higher than the breach bottom elevation; (3) the difference between the upstream and downstream water levels is less than 30% of the upstream elevation above the breach bottom DLBreach offers the possibility of considering the effects of waves in coastal environments to derive a net- wave overtopping discharge. The relative equations can be found in Wu (Wu, 2016).

On the downstream slope, uniform flow conditions are assumed and the Manning's equation is implemented. The aim once again is to map the flow profile and the flow depth to derive the relative hydraulic shear stresses. The sediment transport capacity to compute erosion in coarse-grained soils is determined with a combination of the suspended-load formula of Zhang (1961) and the bed-load formula of Wu et al. (2000) considering the effect of steep slope (Wu 2007).

For fine-grained materials the erosion rate is calculated with Equation 2-3, where the erodibility parameters should be derived experimentally via Jet Erosion Test (Hanson and Cook, 2004), Erosion Function Apparatus (Briaud *et al.*, 2001) open channel flume in laboratory and other devices. In absence of tests data the critical shear stress is calculated using the Shields diagram as suggested in SITES. Because cohesive sediment transports and erodes in flocs, Wu suggested the representative cohesive sediment size to be 0.03 mm in DLBreach. Thus, the critical shear stress is about 0.15 Pa according to the Shields Diagram. This value is a lower bound of cohesive soils in practice. SITES suggestion for the erodibility coefficient an empirical relationship with the clay content and soil unit weight. Wu (Wu, 2016) observed that the values obtained in this way for the erodibility coefficient are too small, probably because this relationship was derived in a low-shear stress regime typical of surface erosion, while when the headcut develops the breach flow is stronger corresponding to higher shear stresses. Among the two parameters, the erodibility coefficient is the most important because it is found to significantly govern the erosion rate.

The sediment transport equations and the shear-stress based equation for coarse- and fine-grained soils respectively provide the volume of soil loss used to determine breach morphology at each time-step. In the progressive surface erosion mode, the sediment on the side walls above the water surface will fall into the breach channel by sliding in the case of non-cohesive sediment and by mass failure in the case of cohesive

sediment. In this latter failure should be analysed in terms of slope stability which is affected by soil as cohesion and friction angle. However, DLBreach assumes the failure block to be gradually released to the channel bottom like for non-cohesive sediment by particle sliding. At the downstream slope, the profile rotates about the toe, therefore here the erosion thickness is zero while it increases along the slope in the upstream direction. The above processes as modelled in DLBreach are shown in figure.

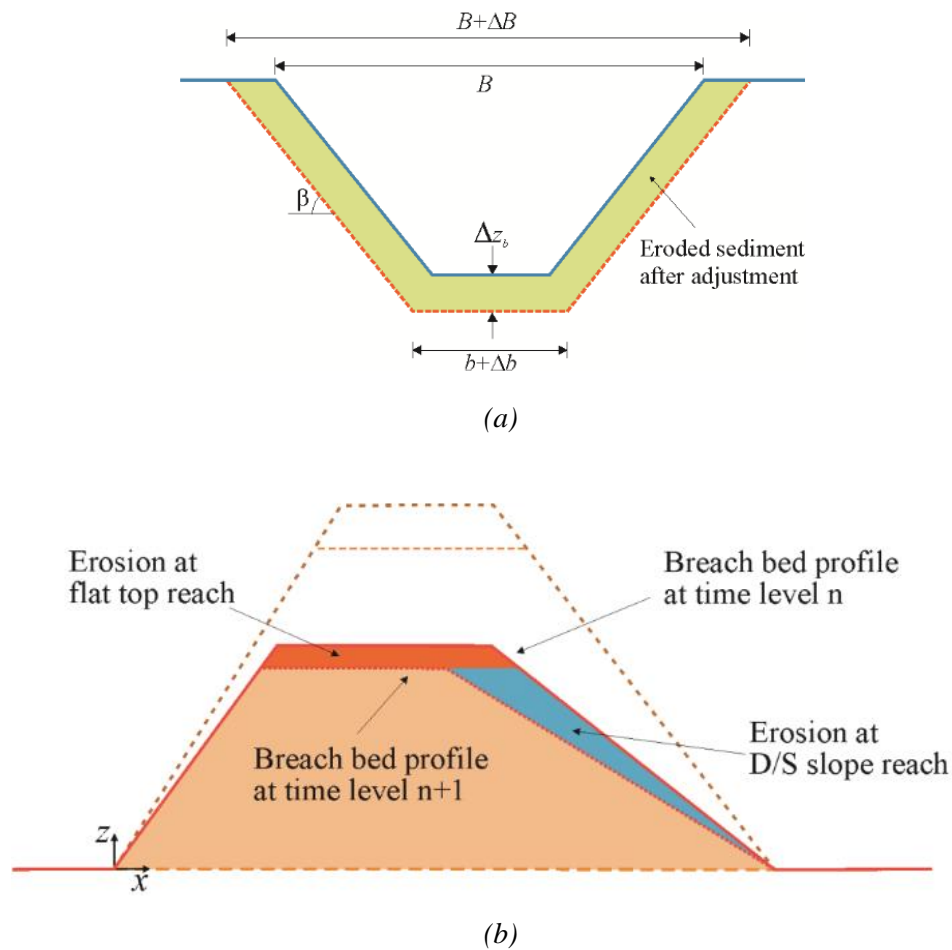


Figure 2-34: Progressive surface erosion simulated in DLBreach, (a) cross-section and (b) profile, after Wu (Wu, 2016)

In the following time-steps the breach cross-section and the longitudinal section evolve while the crest is progressively lowered.

The stability of the breach side slope is analysed in DLBreach according to a

simple planar failure mechanism as the one shown below.

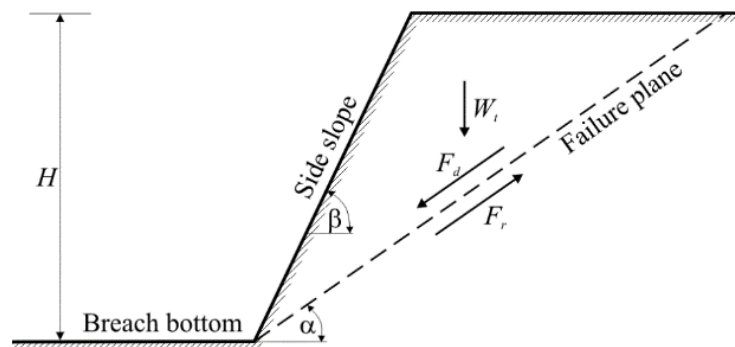


Figure 2-35: Breach side slope stability modelled in DLBreach, according to a planar failure surface inclined by α to the horizontal after Wu (Wu, 2016)

At each time-step the slope angle β in Figure 2-35 is calculated by solving the stability problem. If the β value changes between the previous and current time steps, mass failure has occurred. Initially the breach side slope is assumed to be vertical due to the shallow depth of the initial breach channel. When the breach bed is eroded, the breach side walls lose stability and mass failure occurs. This leads to reduction of the side slope. As the breach continues deepening, it widens and its side walls fail again. When the erosion reaches to the non-erodible foundation, only lateral widening continues.

In the case of headcutting mechanism DLBreach implements three energy-based headcut migration models: (1) the equation introduced in SITES program discussed in 2.4.1.1; (2) and (3) two equations proposed by Temple in 1992 and 2005 after Wu (Wu, 2016). The default option is the (2). In all these formulations, the rate of headcut migration is related to the headcut height, the unit discharge and a material-dependent coefficient (i.e. headcut erodibility index in SITES). When the headcut migration rate is calculated before the headcut has reached the crest a correction factor is applied to the full embankment height H (see Figure 2-36), to consider the fact that in this condition headcut migration is faster.

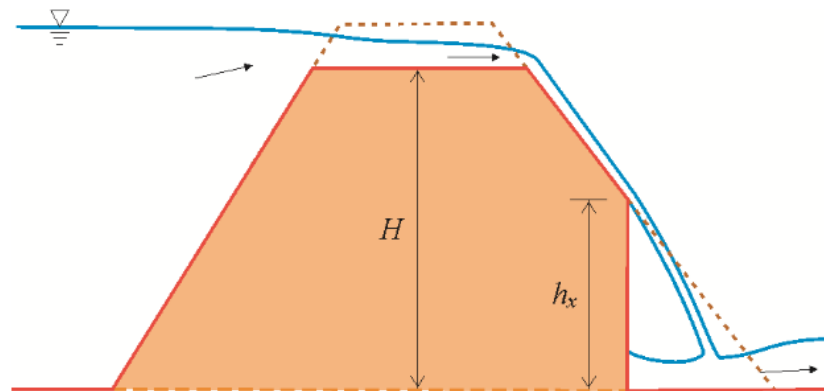


Figure 2-36: Initial stage of headcut migration after Wu (Wu, 2016)

Like EMBREA, DLBreach presents advantages and disadvantages. The most important innovation is that DLBreach allows to model breach in both-directions and considers the effect of waves. This is particularly useful in coastal environments during storm surge. Like EMBREA external and internal erosion can be simulated and homogeneous as well as zoned embankment can be studied. Another common aspect between the two models is the use of 1D broad – crested weir and Manning’s equations to compute discharge and hydraulic shear stress respectively. In DLBreach, erosion of fine-grained materials is addressed with the common shear stress equation as well as EMBREA, while a different approach is introduced for granular soils. In both model the failure mode must be known in advance as the user must specify if failure occurs via progressive surface erosion or headcutting. Again, because the transitions between these two typical behaviours is not fully understood and the coexistence of both mechanisms has normally been observed experimentally, a breach model should be capable to predict the occurrence of progressive surface erosion and/or headcutting through the simulation of the physical processes involved, materials properties and conditions. In both models, overflow is triggered by cutting an initial breach channel whose dimension must be specified by the user, therefore an initial breach geometry must be pre-determined. Unlike EMBREA, the stability analysis of the breach side slope is less sophisticated. The main drawback of both models consists of the modelling of headcut erosion. EMBREA and DLBreach incorporates methods previously developed in SITES and SIMBA thus reflecting the relative limitations

discussed.

2.5 Conclusions

Despite the progresses achieved, there is a general agreement that the prediction power of the breaching models currently available is still unsatisfactory, such that application in engineering practice is so far very limited.

Morris (Morris et al., 2009; Morris, Kortenhaus and Visser, 2009; Morris, 2011) identifies a number of reasons why the developments in breaching modelling are progressing slowly. The importance of embankment material types, properties and conditions at the onset of overflow has been often neglected, whilst experimental evidence show that these aspects govern the modes of failure observed. For fine-grained filling materials, the research conducted at the USDA-ARS shows that soil erodibility can vary by several order of magnitude as compaction water content and compaction efforts change (Hanson and Hunt, 2007). Given the importance of the construction material in breaching processes, the second issue is related to the use of erosion laws and the relative parameters to incorporate these aspects in the numerical models. In essence, a breach model should mimic erosion and slope instability phenomena hence principles of soil mechanics and adequate constitutive laws must be applied to represent soil behaviours.

A third issue is related to the effect of embankment size on the occurrence of progressive surface erosion or headcutting. This aspect is still to be clarified by future research. A further question is the model calibration and validation problem. Usually, models are built based on data sets from laboratory experiments and rarely from field tests. These models may perform well for that particular dataset, but they might fail for other cases. Finally, the model validation against data from case studies is likely to be affected by the uncertainty of associated with the hydraulic and mechanical characterisation of the embankment and its foundation.

It is intuitive that embankment breaching should be modelled by adopting a multidisciplinary approach, where hydrodynamics and geotechnical processes are equally coupled. However, the review of the state-of-the-art reveals that so far the

problem has been studied almost exclusively within the framework of classical hydrodynamics. Soil behaviour is described adopting concepts and principles of river hydraulics, such as sediment transport equation for coarse grained materials and erosion law for fine-grained materials (i.e. Equation 2-3). Ideally, the erodibility parameters of fine-grained materials must be assessed experimentally.

A long series of devices have been developed such as Jet Erosion Test JET, (Hanson and Cook, 2004); Hole Erosion Test, HET (Benahmed and Bonelli, 2012; Bonelli et al., 2006; Fell et al., 2003); Erosion Function Apparatus, EFA (Briaud et al., 2001). However, there are still significant uncertainties in terms of test methods of soil erodibility (Mitchell and Brown, 2018).

Wahl (Wahl, 2010), for example, compared the results of JETs and HETs tests conducted on same soil samples. The difference of erodibility parameters found was about 2-3 order of magnitude among these two tests. Currently, experimental apparatus and data interpretation procedures are under investigation (Bonelli, 2019) and a well-consolidated practice is not yet established. This is crucial in the context of breaching models as the modes of failure driven by surface progressive erosion and/or headcutting depend quantitatively on the erodibility parameters adopted in input.

The persisting doubts on soil erosion behaviours, the problems encountered to derive representative erosion constitutive models and relative parameters, along with the needs to consider the presence of an unsaturated zone and the effects of the infiltration as emphasised by experimental observation, suggest that the processes observed during embankment breaching might be explained from an unsaturated soil mechanics perspective.

The following questions arise:

1. Is it possible to “replace” the erodibility parameters with more familiar soil models commonly adopted in geotechnical problems?
2. What if the “erosion” is treated as a “mini-slope” stability? In other words, can the breaching process be simulated as a slope stability problem at a mini scale?

To answer these two problems, a new model concept aiming at simulating the breaching of embankments during overflow is proposed in this work.

Chapter 3. The Role of Suction in the Onset of Overflow Induced Flood Embankment Breaching

Abstract

A suction-based conceptual breaching model is presented for the first time as a possible alternative interpretation of the macro-erosion mechanisms typically observed during the overflow breaching of flood defence embankments. The model is developed within the theoretical framework of unsaturated soil mechanics, based on the observation that the occurrence of a regime of negative pore-water pressures (i.e. suction) is the most likely situation encountered at the onset of the overflow. Under unsaturated conditions the embankment material is characterised by higher shear strength and stiffness due to suction, which acts as a natural “soil reinforcement”. When the soil starts to saturate because of the transient infiltration processes occurring from both the upstream slope and the overflowed downstream slope, the resulting loss of suction is responsible for a progressive reduction of the soil shear strength.

The conceptual model discussed in this chapter first illustrates qualitatively the hydro-mechanical processes involved at the onset of overflow breaching of earthen embankments. These are used to explain the headcutting in fine-grained and the progressive-surface erosion in coarse-grained soils. Although there is an increasing awareness of the importance of the embankment material conditions in the processes of breach initiation and formation, currently, the common approach adopted in breaching models still considers hydrodynamic forces developed at the interface water-soil during overflow and soil erodibility as the main triggering factors for breaching.

To investigate the relative importance of hydrodynamic shear stresses and loss of soil strength due to the decrease of suction, a comparative analysis is conducted. The

stability of an ideal homogenous silty-clay embankment is studied in a Finite Element Model (FEM) with the strength-reduction method, for two scenarios. One considers the overflow condition only simulated by imposing zero pore-water pressure on the downstream slope and the second case considers, in addition, a distribution of hydrodynamic shear stresses applied along the downstream slope of the embankment during the overflow. The hydraulic shear stresses have been determined with the computational fluid dynamic open-source software Open Foam.

3.1 Introduction

The breaching of flood defence embankments during overflow has been modelled as an erosion problem of the downstream slope. The water flow resulting from the crest overtopping is assumed to trigger erosive processes when the hydraulic shear stresses developed at the water-soil interface exceed the critical shear stress value characteristic of the embankment material. Based on considerations of hydraulic and hydrodynamics features of open channel flows, it is understood that the highest erosion potential is developed around the toe area due to the increasing flow velocities along the slope and intense turbulences created by the sharp change in slope at the toe (George R. Powledge *et al.*, 1989; Gilbert and Miller, 1991; Wahl, 1997; M. Morris, Dyer and Smith, 2007; Chaudhry, 2008; Hughes and Nadal, 2009; Hughes *et al.*, 2011; Hughes, Shaw and Howard, 2012).

For many years the research effort has been focussed on the study of soil erodibility and on the hydraulics/hydrodynamics of embankment overflow, as these were considered the main factors governing the breaching process. Experimental investigations conducted via laboratory models (Visser, 1998; Coleman, Andrews and Webby, 2002; Zhu, 2006; Morris, Hassan and Vaskinn, 2007b; Schmocker and Hager, 2009; Wei *et al.*, 2016; Asghari Tabrizi *et al.*, 2017; Zhao, Peeters and Visser, 2019) and field tests (G. J. Hanson, K. R. Cook and S. L. Britton, 2003; Vaskinn, LØvoll and Höeg, 2003; G. J. Hanson, K. R. Cook and S. L. Hunt, 2005; Hunt *et al.*, 2005; Hassan and Morris, 2008; Morris, 2009) have revealed that progressive surface erosion and headcutting are the two fundamental macro-erosion mechanisms involved in breach

initiation and formation.

Progressive surface erosion is typically observed during overflow of coarse-grained embankments. In this case, the embankment material is removed layer-by-layer like an exfoliation process. The downstream face tends to flatten progressively starting from the crest and rotating around a pivot-point usually located at the downstream toe (Coleman et al. 2002; Volz 2013). The failure advances rapidly because the embankment crest is eroded since the beginning of the overflow, implying a fast lowering of the crest levels and allowing for a significant increase of the water flow through the breach channel formed. When the downstream face reaches a minimum slope, erosion tends to continue laterally resulting in the breach widening.

Headcutting has been identified as the critical erosion behaviour of fine-grained embankment fills. In the initial phase of overflow, small steps tend to form predominantly at the toe area. As erosion progresses, these steps tend to merge into few large headcuts, while propagating backwards from the toe to the crest. These headcuts are vertical or sub-vertical in the downstream slope. Generally, one single large headcut is formed during the backward migration phase which eventually cuts the upstream edge of the embankment crest resulting in an increase of the flow rate.

Headcut erosion is a much slower process than surface erosion because for long time local failures are concentrated at the bottom of the embankment while the crest is unaffected. This means that the water flow remains under control until the headcut recedes back to the crest. On the contrary, progressive surface erosion starts at the crest and simultaneously along the downstream slope such that the increase of the flow rate and the failure are very fast. The differences between these two behaviours are significant from a qualitative and quantitative point of view. The most critical aspect is the time of breach initiation which is usually much shorter for coarse-grained embankment. Therefore, it is essential to be able to predict when, how and why surface erosion is expected rather than headcutting.

The occurrence of these two modes of failure has been related to the erodibility characteristics of coarse-grained and fine-grained soils. Morris (Morris, 2011) explains that headcutting tends to occur in fine-grained geomaterials because these are more erosion-resistant than coarse-grained soils and therefore can sustain the formation of a

stepped-profile.

However, most recent experimental investigations indicate that the distinction of macro-erosion behaviours based purely on material nature tends to over-simplify the real physical processes involved in embankment breaching. Other factors such as material state and embankment conditions are essential aspects that can significantly influence the modes of breaching failure.

For example, headcut formation was unexpectedly observed during the test conducted on a gravelly embankment as part of the IMPACT project (Vaskinn, LØvoll and Höeg, 2003; Hassan and Morris, 2008; Morris, 2009). The authors explained that the most superficial layers of the embankment test froze due to the extremely low temperature prior and during the test. This resulted in an improvement of the erosion resistance attributed to the peculiar frozen condition. More complex dynamics combining progressive surface erosion and headcutting have been observed also in other experimental studies. It is shown that headcutting occurs in coarse-grained soils under certain conditions assumed to enhance the material mechanical behaviour such as compaction efforts and the existence of negative pore water pressures (Al-Riffai *et al.*, 2009; Pickert, Weitbrecht and Bieberstein, 2011; Mizutani *et al.*, 2013; Al-Riffai, 2014; Walder, 2015).

It appears that erosion mechanisms triggered by overflow are not dependent exclusively on soil erodibility properties and hydrodynamic stresses induced by the overflow. The complex interactions between soil behaviour, water flow, embankment structure and climate-atmospheric agents should be considered together to provide a comprehensive description of the multiple time-dependent physical processes involved in the breach initiation and progression. Despite the latest achievements, the occurrence of headcutting or progressive surface erosion and the coexistence of these mechanisms during the same flood event, are still not fully understood. In addition, it is recognised that there are still many uncertainties on soil erodibility parameters and modelling although the ‘erosion’ approach continues to be implemented into predictive tool for breaching. Other geotechnical processes, like the response of soil to water infiltration and the variability in time and space of soil conditions are instead systematically neglected or oversimplified.

Overall, there seems to be a relatively poor understanding of the mechanical and physical processes behind the concept of erodibility and breach formation. The headcutting observed when initial negative pore-water pressures exist, independently of the erodibility characteristic of the material being either sand or clay, suggests that partial saturation and suction may play a key role in the response of the embankment to overflow.

This chapter discusses the role played by suction and water content that undergo variations during the overflow process. The main hypothesis is that ‘erosion’ is associated with a loss of shear strength of the embankment material due to the decrease of suction and the increase of the degree of saturation following inward infiltration from the overflowed slope. This can provide an explanation of why headcutting starts at the toe and why progressive surface erosion is instead noticed at the crest.

Starting from the observation that the hydrodynamics stresses at the onset are the same for coarse-grained and fine-grained embankments, this preliminary study presents an analysis to investigate whether the dominant triggering factor for breach onset is associated with hydrodynamic loading or loss of soil resistance due to suction reduction. The analysis of soil behaviour is conducted in the context of the unsaturated soil mechanics without any reference to empirical erosion constitutive laws. The analysis is limited here to the onset of the erosion process, i.e. when a first soil layer is removed once the overflow takes place.

3.2 Towards a new conceptual model for breach formation

The fundamental idea inspiring this conceptual model is based on the observation that the soil forming the embankment is usually in an unsaturated state at the onset of overflow. In normal working conditions and for most of their design life, flood defence embankments are exposed to low hydraulic heads with water tables located predominantly at foundation level (Dyer, 2004; Dyer, Utili and Zielinski, 2007; el Mountassir *et al.*, 2011; CIRIA, 2013). Therefore, negative pore water pressures develop within the embankment material. Pore-water pressures become even more negative due to evaporation and transpiration occurring at the embankment slope

surface.

The situation changes drastically during extreme weather events when the rapid increase of water levels on the upstream side leads to the overtopping of the embankment crest. Water flowing over the downstream slope creates a quasi-zero water-pressure on the boundary generating high hydraulic gradients responsible for transient water inflow resulting in variations of the state of stress of the embankment material. This water flow process is controlled by the hydraulic conductivity and water retention behaviour of the unsaturated soils, which are governed by suction and degree of saturation.

A qualitative analysis of the ground water flow processes during a flood event is illustrated in. Under pre-flood conditions (Figure 3-1a), water levels are well below the crest and the unsaturated zone above the phreatic surface extends to almost the entire embankment body. During extreme events, the water levels increase rapidly and can reach the embankment crest in a few hours. The risen water level produces an increase of the total stress on the waterside embankment slope and generates a ground water flow from the upstream slope towards the embankment body and foundation. Figure 3-1b,c shows the advancement of the saturation front fuelled by the high river water level, hence the partially saturated zone starts reducing at a rate that depends on soil hydraulic characteristics.

However, at the onset of overflow a large portion of the embankment is still in an unsaturated state. From this point onwards the overflow is established, and flood water starts to penetrate along the downstream slope, driving a second infiltration process in a sub-orthogonal direction to the slope, as shown in Figure 3-1d. As the overflow proceeds there is a continuous inward infiltration, which causes a progressive increase of the degree of saturation and a reduction of suction in the most superficial layers of the downstream slope.

In essence, the soil constituting the embankment experiences two main infiltration processes, a first one from the upstream side due to the increase of water levels and the second one, along the downstream slope due to the overflow. Both processes cause the advancement of the saturation front within the inner part of the embankment and hence a reduction of the partially saturated zone.

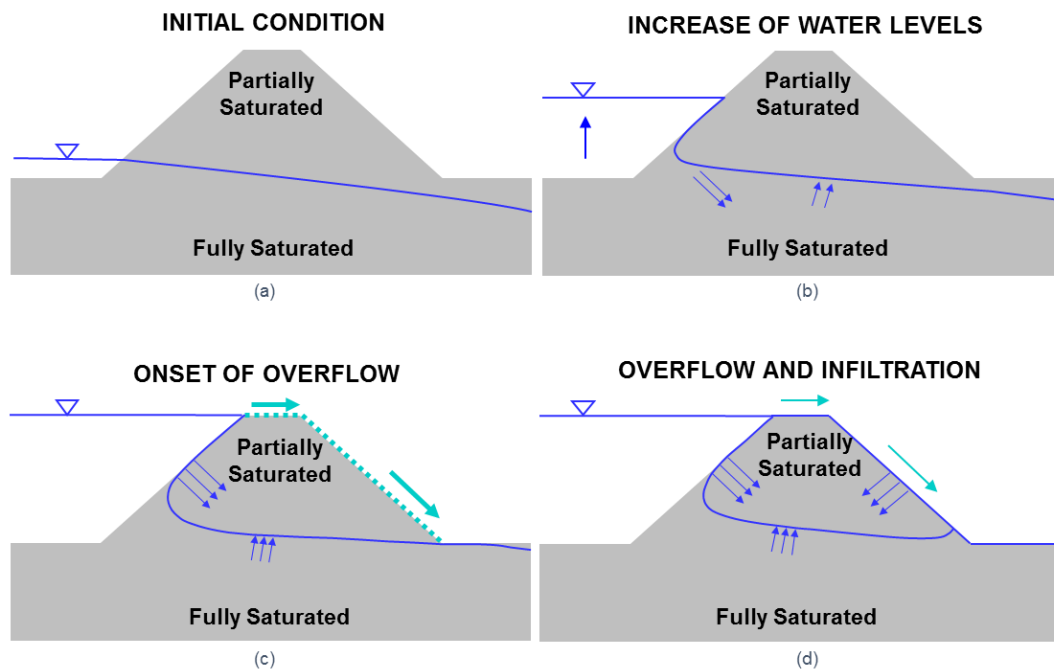


Figure 3-1: Ground water flow process and propagation of the saturation front within an embankment during overflow. (a) Initial condition; (b) increase of river water level and infiltration from the upstream slope; (c) overflow when water levels exceed the embankment crest; (d) overflow progression and infiltration from the downstream slope as well as from the upstream side.

The importance of studying the response of embankment material to water infiltration is related to the cognition that geomaterials in the unsaturated zone are characterised by higher resistance and stiffness than the same soil in a fully saturated state (Tarantino and di Donna, 2019). If suction is held for a long period, failure processes are in principle delayed because of this natural soil “reinforcement”. However, when pore water pressures increase as consequence of infiltration (from negative towards zero or positive values), the embankment material experiences a loss of that additional strength given by suction and becomes more prone to fail. The quantitative prediction of this phenomenon requires the study of a hydro-mechanical problem to enable determination of the changes of soil shear strength during overflow.

3.2.1 Shear Strength of Unsaturated Soils

The effects of suction and unsaturated conditions on soil shear strength have been the focus of numerous investigations in the past years. Several shear strength criteria are available in the literature, which can be subdivided in two broad categories depending on the stress variables considered. In one approach two independent state variables (i.e. net stress and matric suction) are introduced and the effects of partial saturation on shear resistance are purely related to suction.

In this work, the shear strength unsaturated soil behaviour is studied by considering the Bishop's effective stress σ'' (Bishop and Blight, 1963):

$$\sigma'' = \sigma - u_a + \chi (u_a - u_w) \quad \text{Equation 3-1}$$

where σ is the total stress, u_a is the pore-air pressure (and $\sigma - u_a$ is the total net stress), u_w is the pore-water pressure and χ is a soil parameter expressed considered in function of the degree of saturation $\chi = f(S_r)$. If the atmospheric pressure is assumed as reference, Equation 3-1 becomes:

$$\sigma'' = \sigma + \chi s \quad \text{Equation 3-2}$$

where $s = -u_w$ indicates the matric suction.

For dry or fully saturated soil the Bishop's parameter is $\chi = 0$ or $\chi = 1$ respectively and the Bishop's effective stress reduces to the Terzaghi's effective stress formulated for a two-phase material (i.e. solid particle and single pore fluid).

The Mohr-Coulomb failure criterion expressed in terms of Bishop's effective stress accounts for the independent contribution of suction and degree of saturation to the ultimate shear strength of unsaturated soils. Different formulations have been proposed depending on the meaning attributed to the Bishop's parameter χ (Sheng, Zhou and Fredlund, 2011). Despite the criticisms highlighted by several authors and the advancement achieved in the last decades (Vanapalli *et al.*, 1996; Tarantino and Tombolato, 2005; Tarantino, 2007; Tarantino and El Mountassir, 2013), the most popular approach considers $\chi = S_r$ which provides the following ultimate shear strength for partially saturated soils (Öberg and Sällfors, 1997):

$$\tau = c' + \sigma'' \tan \varphi' \Rightarrow$$

$$\Rightarrow c' + (\sigma + S_r s) \tan \varphi'$$

Equation 3-3

where c' is the effective cohesion, σ'' (kN/m²) is the Bishop's effective stress, σ (kN/m²) is the total stress, s is suction (kN/m²), S_r is the degree of saturation and φ' is the 'saturated' angle of shearing resistance. Equation 3-3 can be better expressed as:

$$\tau = c' + \sigma \tan \varphi' + S_r s \tan \varphi'$$

Equation 3-4

It is worth noticing that this approach implies a coupling between shear strength and water retention behaviour of the unsaturated soil through the relationship between matric suction and degree of saturation (i.e. the soil water retention function).

The term $S_r s \tan \varphi'$ in Equation 3-4 represents the additional component of the shear strength due to suction and it is often referred to as apparent cohesion (Tarantino and di Donna, 2019). This contribution is "weighed" by degree of saturation $S_r < 1$, meaning that for the same suction, different degrees of saturation provide different values of the ultimate shear strength.

Apparent cohesion is fleeting in the sense that it disappears once suction drops to zero. However, the soil constituting the embankment can take advantage of this additional strength for long time, as the unsaturated state tends to persist and evolves according to the water infiltration process governed by the soil hydraulic conductivity and water retention capacity.

3.2.2 Stress State at the Embankment Toe

The comparison between the different positions that the phreatic surface takes in the phases preceding the overflow (Figure 3-1a,b,c) and after the overflow (Figure 3-1d), shows clearly that the most vulnerable embankment part is the toe. There are two reasons for this: (1) Under pre-flood river conditions, the embankment toe is characterised by the lowest suction, since this is the unsaturated zone closest to the phreatic surface; (2) the toe is the point in which the saturation fronts from the upstream side and from the downstream surface, are likely to meet first, causing the saturation of soil and a faster reduction of the shear strength due to the loss of the

apparent cohesion. The embankment material at downstream toe is weaker than soils in regions faraway and therefore it is more prone to fail.

This concept is represented in Figure 3-2. In the Mohr plane a typical stress state near the toe and another one near the crest are shown for the initial condition (green circle) and for the overflow phase (blue dotted circle). The change of effective stress due to the overflow is more significant at the toe and it could lead to a stress state that lies on the failure envelope (Figure 3-2b). This loss of strength of the embankment material can be considered one of the primary reasons why the breach initiation is observed initially at the toe for the headcutting erosion mode. Fine-grained materials characterised by a low hydraulic conductivity tend to hold suction for a relatively long period due to the slow changes in pore water pressures caused by the transient water flow. This is particularly true towards the crest where the initial suction is much greater than the toe and the state of effective stress tends to be like Figure 3-2a while overflow is progressing.

On the contrary, coarse-grained geomaterials are much more permeable and tends to saturate quickly. Because the water flow process is rapid, apparent cohesion is erased almost simultaneously at both crest and toe, resulting in a different mode of failure such as the one referred to as ‘progressive surface erosion’.

To conclude, the qualitative analysis of the geotechnical mechanisms occurring during overflow shows that the infiltration processes and the associated change of the soil shear strength due to variation of suction and degree of saturation can lead to local instabilities and hence failure of small portion of embankment. At the same time, breaching models developed so far assume that the hydrodynamic forces are the predominant trigger of erosion/instability neglecting the phenomenon of shear strength reduction described above. However, the hydrodynamics of embankment overflow is an invariant for the types of embankment materials and hence the onset of breach should exhibit similar features for both fine-grained and coarse-grained soils. Instead, different modes of breaching are observed suggesting that shear strength loss induced by water infiltration suction plays a key role in initiation and progression of breaching.

To prove this concept, the stability of an ideal homogeneous embankment subjected to a flood event is analysed with a finite element model (FEM). The effects

of hydrodynamic forces and soil shear strength reduction on the onset of breaching are assessed by comparing the factor of safety with regards to the embankment stability calculated with and without the application of the hydraulic shear stresses along the downstream slope. The hydrodynamics forces developed at the interface water-soil are derived in a separate model based on the finite volume method (FVM) solution of the 3D Reynolds averaged Navier-Stokes equations.

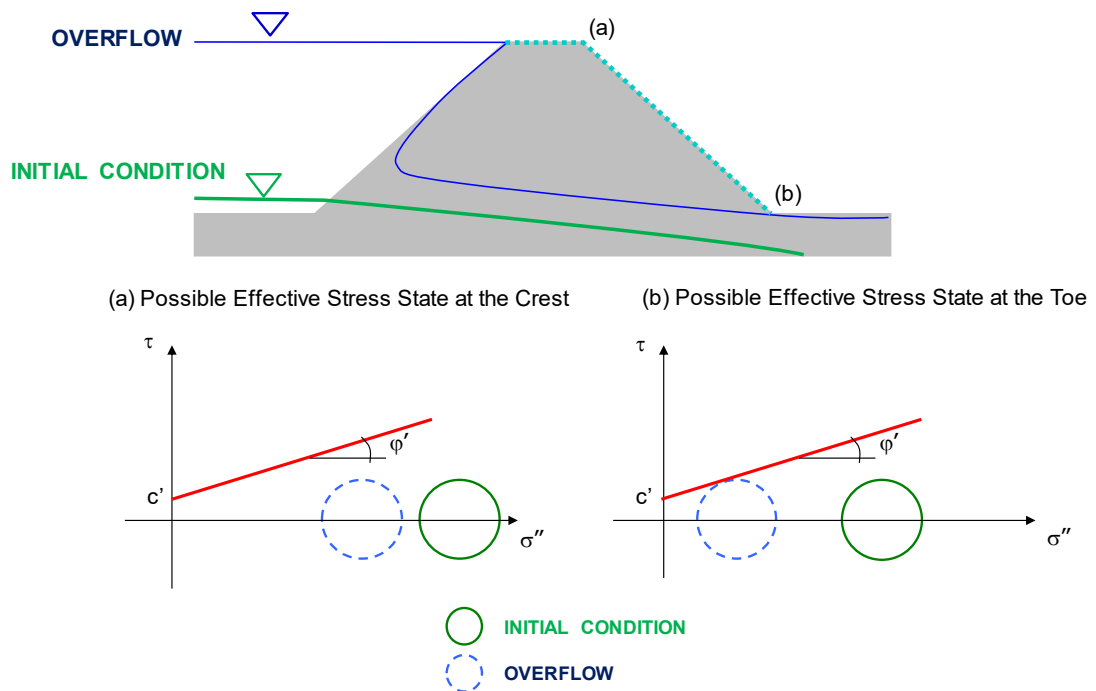


Figure 3-2: Representative stress states (a) near the crest (b) near the toe. Green lines are referring to the initial condition. Blue lines represent the overflow event

3.3 Hydrodynamic Analysis of Embankment Overflow

The embankment overflow problem resembles the situation of an open-channel flow over a broad-crested weir. This falls within the category of rapidly varied flow, where the flow depth tends to decrease downstream as the flow regime becomes supercritical. The decrease of water depths in the direction of flow results in an increase of flow velocity and shear stresses. When the water flow reaches the toe of the embankment the slope changes from steep to mild inducing possible formation of hydraulic jump, great turbulences, and energy dissipation. As discussed in 2.1 the hydraulic jump tends

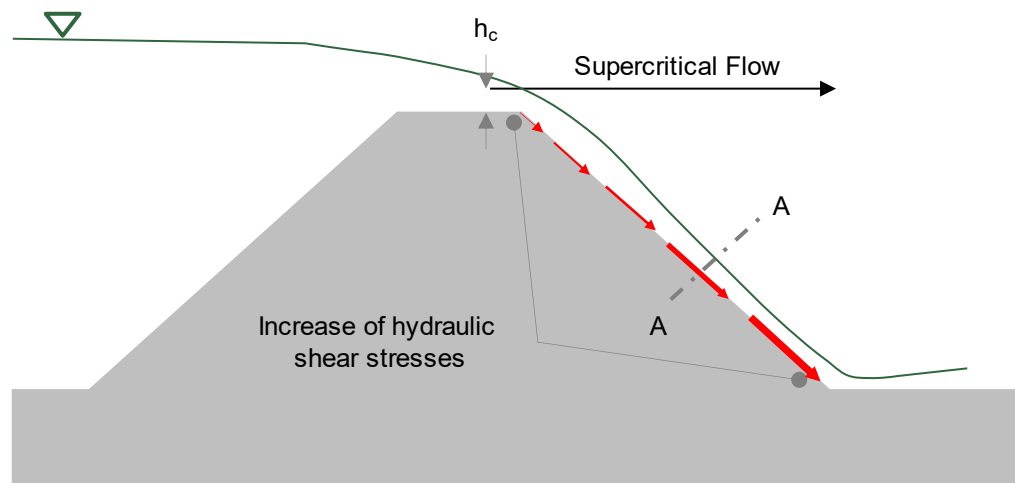
to form when the downstream flow is subcritical, implying an abrupt increase of the water depth. Because tailwater is not present at the downstream toe it is assumed that no hydraulic jump will form and the transition from supercritical flow at downstream to a is gradual with a little increase of the water levels.

This mechanics is qualitatively represented in Figure 3-3 in terms of water velocity profile and associated shear stress in the direction of flow. The shear stresses are proportional to the slope of flow velocity through the fluid viscosity μ , according to the Newtonian fluid constitutive model.

It is worth noticing that rapidly varied flows are characterised by significant vertical acceleration and the assumption of parallel streamlines which allows assuming a hydrostatic pressure distribution over the water depth becomes invalid. This means that the shallow-water theory adopted for gradually varied flow is not applicable and the study of the water flow requires a two-dimensional or three-dimensional analysis (Chaudhry, 2008).

However, most of the breaching models available in literature describe the hydrodynamic of overflow with reference to broad-crested weir equations or implementing shallow-water equations. In the first case, the discharge is empirically related to the flow depth over the weir. Once that discharge and flow depth are known, empirical relations like Manning's or Chezy's equations are generally adopted to calculate the shear stresses (Gilbert and Miller, 1991).

The second approach is based on simplified Reynolds averaged Navier-Stokes equations derived from the hypotheses that flow velocity is constant in normal direction and that pressure distribution is hydrostatic. Conservation of mass and momentum provide a set of two partial differential equations (i.e. shallow water equations) which can be numerically solved to assess the flow velocity field. The shear stresses are determined again with reference to empirical friction formulae (Delestre *et al.*, 2017).



SECTION A - A

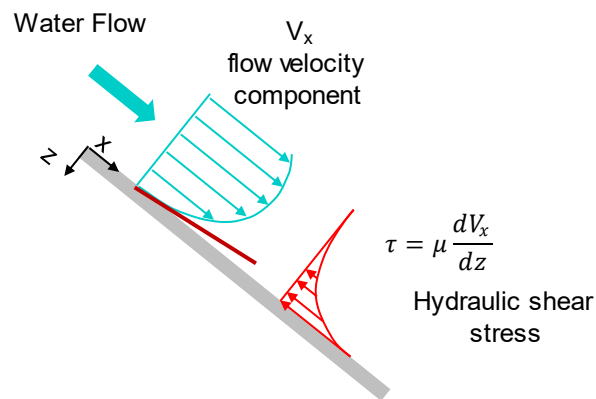


Figure 3-3 Water flow associated with the overflow with the increase of shear stresses downstream and flow velocity and shear stress profiles along the direction of flow in Section A-A

In this study, the calculation of the hydraulic shear stress is performed with the aid of computational fluid dynamics (CFD). This comprises a set of methodologies developed to analyse multiple fluid flow problems by means of computer simulations. CFD codes are built around the numerical algorithms implemented and typically consist of: (1) a pre-processor; (2) a solver and (3) a post-processor. The pre-processor deals with the definition of the inputs to be provided to the CFD program, such as geometry, mesh, boundary conditions and fluid properties. The solver implements the numerical technique which transforms the governing partial differential equations in a system of algebraic equations solved by an iterative method. The numerical technique

most adopted in CFD is the Finite Volume Method (FVM) because it mirrors the physics of the conservation principles underlying the fluid flow problems. Essentially the FVM transforms the partial differential equations representing conservation laws over differential volumes into discrete algebraic equations over finite volumes. In this way the FVM reproduces the concept of control volume (i.e. Eulerian formulation) where the integration of the conservation equations is performed. The volume integrals are expressed as the averaged value over the cells, while the surface integrals are replaced with the summation over all the bounding faces of the control volume (Moukalled, Mangani and Darwish, 2016). Finally, the post-processor is a software which enables to visualise the results.

Among the different CFD tools available, OpenFOAM (Open-source Field Operation and Manipulation) has been selected to solve the overflow problem over the embankment. This is modelled as a solid-fixed boundary.

OpenFOAM is a set of pre-compiled C++ libraries that take advantage of this object-oriented coding language to write a variety of executables. These are divided in: (1) utilities for the pre- and post-processing tasks and (2) solvers, designed for specific continuum mechanics problems, including compressible and incompressible fluid flow, multiphase flow, and free surface flow, considering various turbulence modelling techniques (Weller *et al.*, 1998; Moukalled, Mangani and Darwish, 2016; Greenshields, 2021).

3.3.1 The interFoam solver of OpenFoam

In the context of CFD, the embankment overflow is a multiphase flow problem that requires the assessment of the free-surface. The OpenFoam solver for this case is the interFoam solver specific for two (i.e. air and water in this case) incompressible, isothermal immiscible fluids. The Volume of Fluid Method (VOF) phase-fraction based is implemented in interFoam to predict the free-surface. The mathematical formulation of the Navier-Stokes equations, the turbulence modelling, the discretization according to the finite volume method (FVM) and the application of the VOF in interFoam are described in Appendix A. The essential concepts and equations are summarised below:

$$\nabla \cdot \mathbf{u} = 0 \quad \text{Continuity Equation}$$

$$\frac{\partial(\rho\mathbf{u})}{\partial t} + \nabla \cdot (\rho\mathbf{u}\mathbf{u}) = -\nabla p + \nabla \cdot \boldsymbol{\tau} + \rho\mathbf{g} + F \quad \text{Navier-Stokes Equations}$$

where ρ is the fluid density, $\mathbf{u} = (\mathbf{u}, \mathbf{v}, \mathbf{w})$ is the three-dimensional velocity field, (therefore $\rho\mathbf{u}$ is the momentum per unit volume), p is the pressure, $\boldsymbol{\tau}$ is the viscous stress tensor, \mathbf{g} is the gravitational acceleration assuming that the only external body force acting on the fluid is gravity; F is an internal force associated with the surface tension generated at the interface separating the two fluids. The viscous stress tensor $\boldsymbol{\tau}$ for a Newtonian fluid is defined as:

$$\nabla \cdot \boldsymbol{\tau} = \nabla \cdot (\mu\nabla\mathbf{u}) + (\nabla\mathbf{u}) \cdot \nabla\mu \quad \text{Viscous Stress Tensor}$$

where μ is the fluid dynamic viscosity.

The volume of fluid method (VOF) is based on the volume fraction α , a scalar indicator function, ranging between zero and one. A value of zero indicates the presence of one fluid and a value of unity indicates the presence of the second fluid only. On a computational mesh, volume fraction values between these two limits capture the interface and the values itself indicates the relative proportions occupying the cell volume.

$$\alpha(x, y, z, t) = \begin{cases} 1 & \text{for } (x, y, z, t) \text{ occupied by fluid 1} \\ (0,1) & \text{for } (x, y, z, t) \text{ at the interface} \\ 0 & \text{for } (x, y, z, t) \text{ occupied by fluid 2} \end{cases}$$

Therefore, an additional transport equation for the function α is introduced in the set of equations to address the interface problem:

$$\frac{\partial\alpha}{\partial t} + \nabla \cdot (\alpha\bar{\mathbf{u}}) + \nabla \cdot [\mathbf{u}_r\alpha(1 - \alpha)] = 0 \quad \text{Transport equation for } \alpha$$

where $\bar{\mathbf{u}} = \alpha\mathbf{u}_1 + (1 - \alpha)\mathbf{u}_2$ is a mixture velocity and $\mathbf{u}_r = \mathbf{u}_1 - \mathbf{u}_2$ is the vector of relative velocity between the two fluids.

The surface tension force is modelled in interFoam as an approximation of the gradient of the volume fraction α :

$$F = \sigma\kappa \frac{\rho}{0.5(\rho_1 + \rho_2)} \nabla\alpha \approx \sigma\kappa\nabla\alpha \quad \text{Surface Tension}$$

where κ is the curvature and σ is the surface tension coefficient (defined as the amount of work necessary to create a unit area of free-surface).

OpenFoam uses a modified form of the pressure p^* (p_rgh in OpenFoam), which removes the hydrostatic pressure $\rho\mathbf{g} \cdot \mathbf{x}$ from the pressure p , i.e. $p^* = p - \rho(\mathbf{g} \cdot \mathbf{x})$ and therefore $\nabla p^* = \nabla p - \rho\mathbf{g} - \mathbf{g} \cdot \mathbf{x}\nabla\rho$

The final form of the momentum equation to be solved is therefore:

$$\begin{aligned} \frac{\partial(\rho\mathbf{u})}{\partial t} + \nabla \cdot (\rho\mathbf{u}\mathbf{u}) - \nabla \cdot (\mu\nabla\mathbf{u}) \\ = -\nabla p^* + (\nabla\mathbf{u}) \cdot \nabla\mu - \mathbf{g} \cdot \mathbf{x}\nabla\rho + \sigma\kappa\nabla\alpha \end{aligned} \quad \begin{array}{l} \text{Navier-Stokes} \\ \text{Equations} \end{array}$$

This form of the Navier-Stokes equations, the continuity equation, the transport equation for α are solved together with the constitutive relations for density and dynamic viscosity:

$$\rho = \alpha\rho_1 + (1 - \alpha)\rho_2,$$

$$\mu = \alpha\mu_1 + (1 - \alpha)\mu_2$$

where $\rho_1, \rho_2, \mu_1, \mu_2$ are the density and dynamic viscosity of the two fluids respectively. Additional two transport equations are considered for the turbulence modelling according to the RANS (Reynolds Averaged Navier-Stokes) methodology. The *SST k- ω* model is adopted in this study as it has been proven to be a good compromise between the $k - \varepsilon$ model and the $k - \omega$ model. The first allows obtaining accurate solution of fully turbulent flows and the second provides better results when the fluid motion interacts with a solid surface (Versteeg and Malalasekera, 2007). This latter problem is the focus of the CFD simulation for the embankment overflow with the final aim of calculating the wall shear stress along the embankment slope.

The problem definition is completed with the initial conditions and different types of boundary conditions defining the values of the variables or their gradients at the inlet, outlet and walls (i.e. solid faces). The solution procedure is outlined in the block diagram:

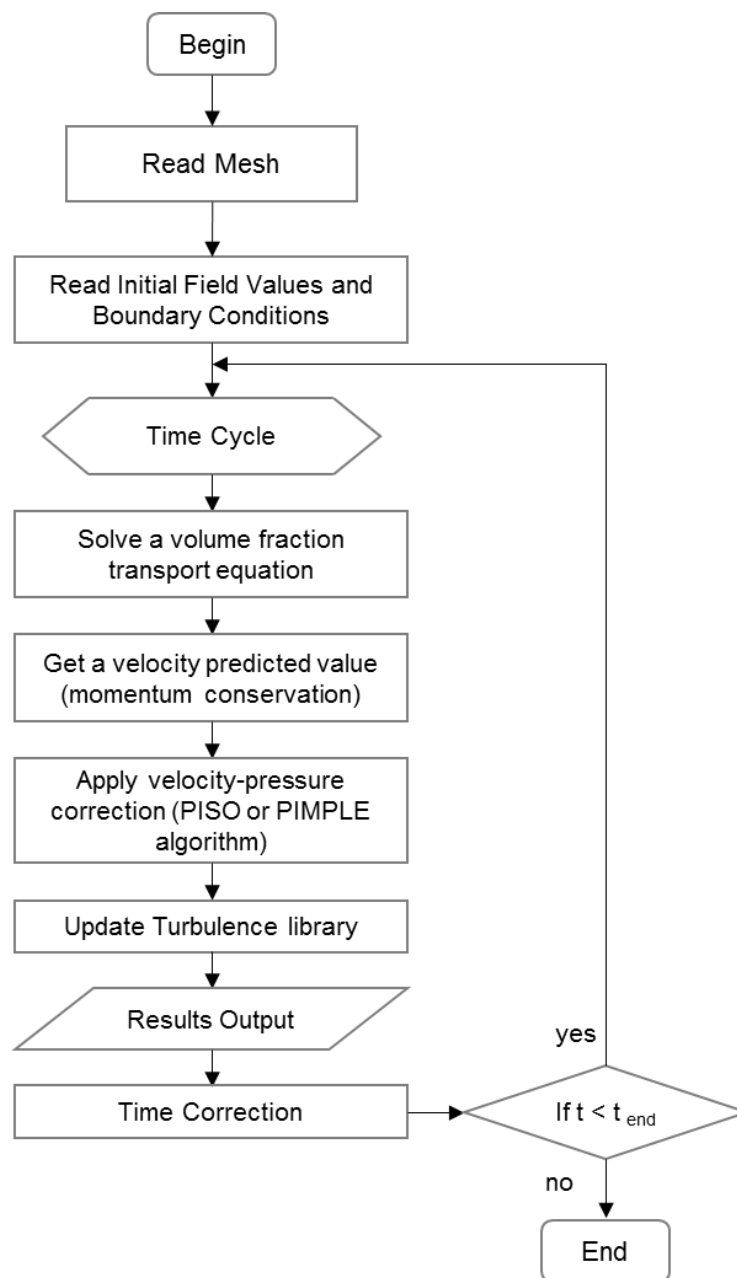


Figure 3-4: Solution procedure implemented in InterFoam after (Korchagova, 2017)

3.4 Soil Water Flow Analysis

A typical flood event scenario leading to the embankment overflow is shown Figure 3-1. The sketch describes qualitatively the two transient water flow processes that can be triggered under extreme weather conditions. Water flow from the upstream side due to the rapid increase of the water level behind the structure. The resulting high

hydraulic gradients drive a water movement from the upstream slope towards the embankment body. Afterwards, once that the overflow is established, a thin layer of water is formed on the surface and flood water starts to permeate inward along the downstream slope. This generates a second transient water flow due to the differences in pore-water pressures between the surface, subjected to quasi-zero pressure, and the inner zones of the slope. When these two water flows occur, pore water pressures vary in space and time. This implies that the soil constituting the embankment is subjected to changes in the effective stress states and, consequently, the soil skeleton deforms affecting the water storage capacity. To capture these processes a fully-coupled ground water and deformation analysis should be performed by solving simultaneously continuity and momentum balance equations (Tarantino and di Donna, 2019).

For a two-dimensional water flow in X and Y direction, assuming isothermal conditions, incompressible water and solid grains, the continuity equation can be written as:

$$\frac{\partial v_x}{\partial x} + \frac{\partial v_y}{\partial y} = - \left(n \frac{\partial S_r}{\partial t} + S_r \frac{\partial n}{\partial t} \right) \quad \text{Equation 3-5}$$

where v_x and v_y (m s^{-1}) are the flow velocities in X and Y directions respectively, n is soil porosity, S_r is the degree of saturation and t (s) is time.

The flow of water through the soil is described using the Darcy's law:

$$v_x = -k_x \frac{\partial h}{\partial x} \quad \text{Equation 3-6}$$

$$v_y = -k_y \frac{\partial h}{\partial y} \quad \text{Equation 3-7}$$

where k_x and k_y (m s^{-1}) are the soil hydraulic conductivities in X and Y, $h = y + \frac{u_w}{\gamma_w}$ is the hydraulic head, with y (m) elevation of the element considered, u_w (N m^{-2}) is the water pressure and γ_w (N m^{-3}) the unit weight of water.

By substituting Equation 3-6 and Equation 3-7 into Equation 3-5 the following equation is obtained:

$$\frac{\partial}{\partial x} \left[k_x \frac{\partial h}{\partial x} \right] + \frac{\partial}{\partial y} \left[k_y \frac{\partial h}{\partial y} \right] = n \frac{\partial S_r}{\partial t} + S_r \frac{\partial n}{\partial t} \quad \text{Equation 3-8}$$

Equation 3-8 is a form of the Richards' equation which describes ground water flow in saturated as well as unsaturated soils.

For the case under study, the most likely condition of the embankment material at the onset of overflow is the unsaturated state. This means that the degree of saturation S_r and the hydraulic conductivity k in Equation 3-19 are both function of suction via the water retention behaviour of the soil constituting the embankment. In the unsaturated state, changes in porosity associated with changes in pore-water pressure are relatively small and the term $S_r \frac{\partial n}{\partial t}$ is negligible compared to the variation associated with the term $n \frac{\partial S_r}{\partial t}$. In other words, water volume variation is only associated with changes of the degree of saturation S_r . Under this assumption along with the assumption of isotropic material ($k_x = k_y = k$), the water flow equation can be written as:

$$\begin{aligned} \frac{\partial}{\partial x} \left[k(u_w) \frac{\partial}{\partial x} \left(\frac{u_w}{\gamma_w} + y \right) \right] + \frac{\partial}{\partial y} \left[k(u_w) \frac{\partial}{\partial y} \left(\frac{u_w}{\gamma_w} + y \right) \right] \\ = n \frac{\partial S_r(u_w)}{\partial u_w} \frac{\partial u_w}{\partial t} \end{aligned} \quad \text{Equation 3-9}$$

The assumption of negligible changes in porosity also uncouples the hydraulic problem from the mechanical one, i.e. solving the water flow equation does not require the simultaneous solution of the stress balance equation.

The solution of the water flow equation provides the pore-water pressure distribution in space and time. Because hydraulic conductivity and degree of saturation depend on the unknown pore-water pressure, Equation 3-9 is highly non-linear such that it can be solved analytically only for specific forms of hydraulic conductivity and water retention functions. Most commonly the solution of the water flow equation is achieved with numerical methods. Its integration is possible once that initial and boundary conditions for the problem of interest are specified and once that the hydraulic behaviour of the unsaturated soil is characterised.

This is defined by two characteristic functions: (1) the Soil Water Retention Curve (SWRC) describes how the degree of saturation varies with suction, indicating the different states of saturation (i.e. saturated, quasi-saturated, partially saturated and residual) which the soil can experience in different range of suctions and (2) the Hydraulic Conductivity Function (HFC) states the concept that water movements within the soil skeleton depend on its saturation state. Pore-water can move more easily if there is a certain continuity in the water phase, while, on the contrary, when the pore space is mainly occupied by air, water movement is obstructed like if the pore size is reduced, and the soil results therefore less permeable. In this sense, the hydraulic conductivity is typically presented as a function of the degree of saturation, where the saturated hydraulic conductivity is scaled by relative hydraulic conductivity k_r , which is a function of the degree of saturation $k = k_{sat} \cdot k_{rel}(S_r)$.

In this work, the ground water flow processes associated with the embankment overflow are solved with a finite element approach implemented in the software Plaxis 2D v.2018.01 ('Plaxis 2018, Users Manual', 2018).

3.5 Soil Slope Stability Analysis

This study aims to investigate the stability of flood defence embankments under the effects of two possible mechanisms occurring during overflow, which are responsible for a drop of the Factor of Safety (i.e. FoS) with respect to the condition prior to the flood. The reduction of the FoS, defined as the ratio between the forces resisting movement and by the forces driving movement, is due to an increase of the destabilising forces and/or a decrease of material shear strength.

For the case of flood embankments subjected to overflow, the focus is on: (1) the destabilising effect associated with the hydraulic shear stresses developed at the interface water-soil during overflow; and (2) the reduction in shear strength of the embankment material due to the progressive loss of suction resulting from the water flow processes described in Figure 3-1. To demonstrate the relative importance of these two sources of instability, the FoS is calculated with and without the application of the hydraulic shear stresses estimated with the hydrodynamic analysis. The

reduction of soil shear strength material is characterised by Equation 3-4, i.e. soil shear strength is a function of the soil mechanical properties (effective friction angle and effective cohesion), total normal stress, and suction and degree of saturation, which vary in space and time as the water flow progresses.

Let us imagine that the downstream slope behaves like an infinite slope (approximation valid for the most superficial layers), and let us consider the equilibrium of a slice.

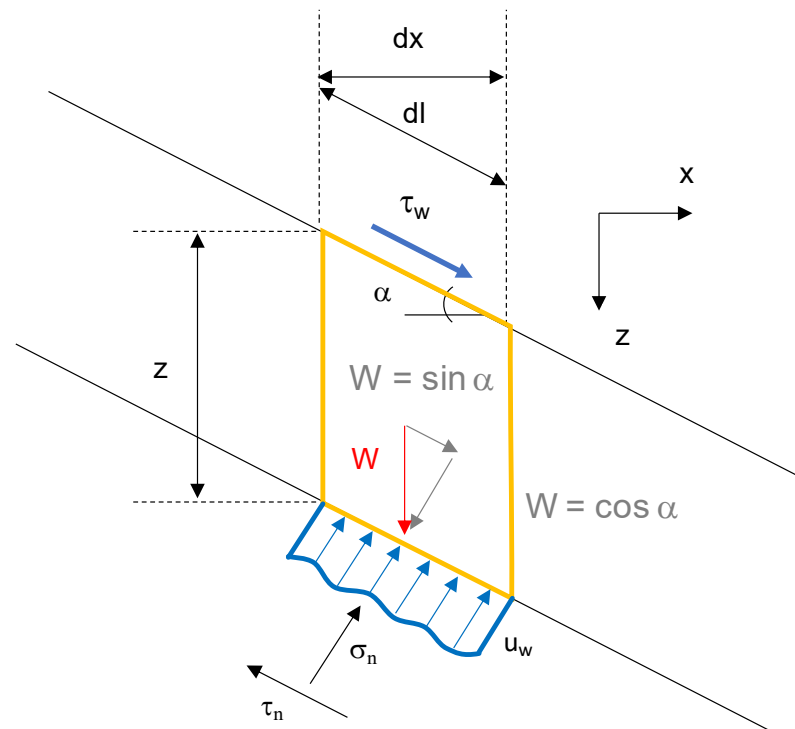


Figure 3-5: Forces acting in an infinite slope

The FoS for the case of Figure 3-5 is given by:

$$FS = \frac{\tau_{lim}}{\tau} = \frac{c' + \sigma \tan \varphi' + (-u_w) S_r \tan \varphi'}{\tau} \quad \text{Equation 3-10}$$

$$FS = \frac{z \gamma' \cos \alpha^2 \tan \varphi'}{\tau_w + z \cdot \gamma' \sin \alpha \cos \alpha} + \frac{c' + (-u_w) S_r \tan \varphi'}{\tau_w + z \gamma' \sin \alpha \cos \alpha} \quad \text{Equation 3-11}$$

where γ' (kNm^{-3}) is the submerged unit weight of the soil, z is the vertical coordinate (m), φ' is the soil friction angle (rad), c' is the effective cohesion (kNm^{-2}), u_w is the

pore-water pressure (kNm^{-2}), S_r is the degree of saturation (-), τ_w is the hydraulic shear stress (kNm^{-2}) associated with the hydrodynamic flow and α (rad) is the inclination of the infinite slope to the horizontal. The case of the infinite slope has been first studied with a simplified analytical approach, described in Appendix B. The most important outcome is that the crest is characterised by the highest FoS because the initial value of suction is 60 kNm^{-2} , while the hydraulic shear stress derived from the CFD analysis is 0.125 kNm^{-2} . This is considerably lower than soil strength, also enhanced by the contribution of apparent cohesion. After 5 hours of infiltration due to overflow, suction is imposed to be zero on the surface, but it is 8 kNm^{-2} at shallow depth (i.e. 3cm below surface level) increasing downwards. Therefore no soil movement is triggered. This is because the infiltration process is governed by the hydraulic conductivity that on turns depends on suction. At the crest, the hydraulic conductivity is lower than the toe and the most superficial layers of the infinite slope remain stable because apparent cohesion persists throughout the overflow durations considered (i.e. 1 hour, 5 and 24 hours). In other words, the upper and middle zones of the downstream slope are stable because even few centimetres below the surface, the order of magnitude of apparent cohesion is one time bigger than the order of magnitude of the hydrodynamic shear stresses, preventing the formation of shallow failure surfaces.

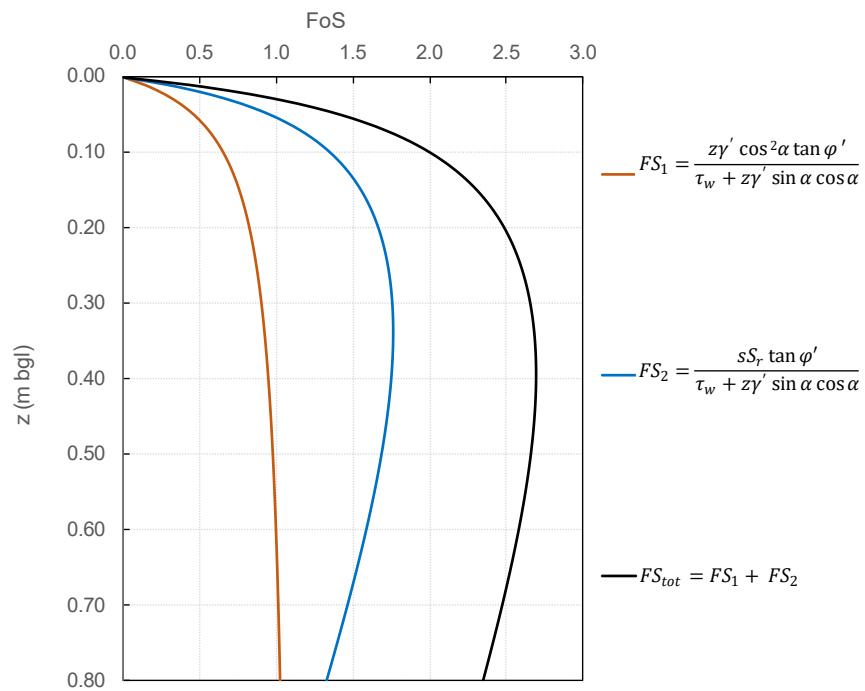
At the toe, in pre-flood conditions the value of suction is 20 kNm^{-2} , that is lower than the initial value present at the crest, but anyway higher than the hydrodynamic shear stress (i.e. 0.2 kNm^{-2}). However, in the toe area the material is more permeable, due to the suction dependence of the hydraulic conductivity. After an assumed overflow of 5 hours, suction on the surface is zero and it is almost zero in the soil layer just below the surface. In fact, at 3cm from the top level, it is found a value of suction of 0.07 kNm^{-2} . This is lower than the 0.2 kNm^{-2} stress induced by the overflow. The toe is therefore unstable because of the very rapid drop of suction. The exercise in Appendix B. shows that the first 4 cm of the slope are “washed away” (i.e. $\text{FoS} = 0.72$).

It is worth specifying that this simplified assessment has been conducted with an ideal material assuming an effective cohesion equal to zero. It is evident that for fine-grained material even a small effective cohesion can considerably improve the stability at shallow depth. For the case analysed in Appendix B. the toe area would have been

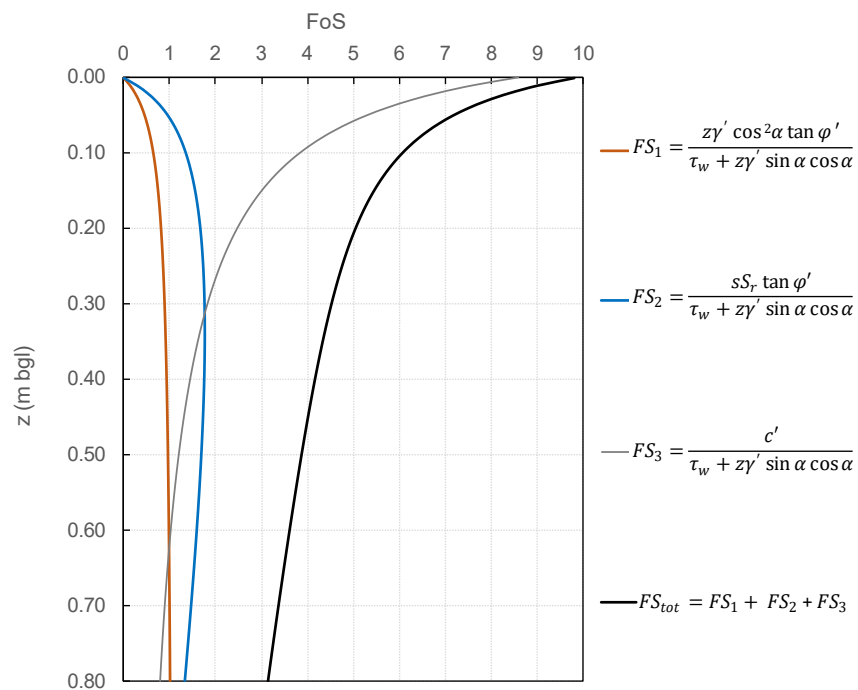
stable with a minimum effective cohesion of 0.2 kNm^{-2} equal to the hydraulic shear stress calculated in the CFD model.

Even if the infinite slope is an ideal and simplistic example, it provides some preliminary general indications on the role of hydrodynamic forces and their interactions with different types of soil. Besides, the analogy with the infinite slope idealisation can explain the progressive surface erosion observed in coarse-grained geomaterials and why this is unlikely to occur in fine-grained ones. In more details, it has been shown that permeable soils without effective cohesion, like coarse-grained ones, can fail at shallow depth (i.e. first 2 cm below ground surface in Figure 3-6b) because the hydrodynamic shear stresses associated with the overflow present values that are on the same order of magnitude of the soil strength. In the infinite slope case, the resulting shallow failure mechanisms are associated with the formation of superficial slipping planes, that are analogues to the exfoliation or the layer-by-layer soil removal, typically described in progressive surface erosion. On the contrary, shallow failure mechanisms are not predicted in the case of fine-grained geomaterials. During an overflow event, because of their characteristic low permeability, fine-grained materials can benefit of the natural reinforcement given by the apparent cohesion for relatively long periods, particularly at the crest. On the other hand, superficial instabilities are unlikely to occur even when suction drops to zero, like the toe area. Typical values of effective cohesion of fine-grains soils will be still higher than the hydrodynamic shear stress, preventing the formation of superficial modes of failure. In addition, the impacts of the effective cohesion on the stability of the infinite slope, are significant on the surface while tend to be attenuated with depth as shown in Figure 3-6b. The effects of apparent cohesion and the friction term are instead increasing with depth.

It can be concluded that thanks to the contribution of effective cohesion, the stability of the most superficial layers is not undermined by the overflow. Failures tend to occur with deeper mechanisms involving larger soil volumes, like in the headcutting affecting soil blocks.



(a)



(b)

Figure 3-6: Different contributions of (a) friction, apparent and effective cohesion on the total FoS of an infinite slope (b) FoS when cohesion is neglected.

In this chapter, the embankment stability problem is analysed with a finite element approach with the aid of the software Plaxis 2D ('Plaxis 2018, Users Manual', 2018). The method implemented calculates the changes of effective stress by solving a fully coupled flow-deformation analysis. The effects of partial saturation are included in the soil shear strength criterion.

In Plaxis 2D, an indication of the FoS is obtained by performing a "Safety" calculation based on the strength reduction method, also known as "phi-ci reduction". This technique consists in reducing progressively the mechanical soil strength properties in small increments until failure occurs. The total multiplier $\sum M_{sf}$ provides the soil strength parameters at a given time-step:

$$\sum M_{sf} = \frac{\tan\phi_{initial}}{\tan\phi_{reduced}} = \frac{c'_{initial}}{c'_{reduced}} = \frac{c_{u,initial}}{c_{u,reduced}} \quad \text{Equation 3-12}$$

The safety analysis starts with a $\sum M_{sf} = 1$ and in the following time-steps it increases as the material strength parameters are reduced. The failure occurs when a fully developed mechanism can be identified in the displacements or deviatoric strain contours plot and the associated $\sum M_{sf}$ provides the FoS.

3.6 Application to an ideal homogeneous embankment

To demonstrate the role of suction in the breaching mechanisms of flood defence embankment during overflow an ideal homogeneous embankment is studied under the hydrodynamic and hydro-mechanical point of view. The geometry is shown in Figure 3-7. The height is 6m, the crest is 2m wide, the inward and outward slope angle is 23° .

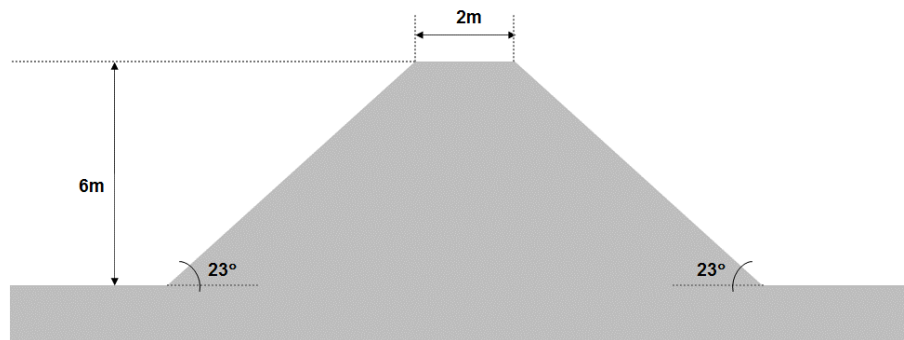


Figure 3-7: Cross-section of the ideal homogeneous embankment modelled

3.6.1 Hydrodynamic Model in OpenFOAM

The starting point adopted to set up the OpenFoam case is the Spillway Tutorial (Olsen, 2012, 2015). The methodology and the structure of the OpenFoam case are outlined in the block scheme in Figure 3-8.

The first step is to generate the computational mesh. In this case the blockMesh utility of OpenFoam has been adopted that reads the blockMesh dictionary stored in the System directory and writes out the mesh data in terms of points, faces, cells and boundaries. In the second step, the phase fraction α_{water} is specified in the setFieldsDict stored in the System directory by running the utility setFields. This is required to assign the initial water regions to specific cells behind the embankment. The most important aspect in this case is the calculation of the shear stress and therefore the post-process object function wallShearStress must be included in the controlDict dictionary.

The material properties and the turbulence type model are specified in files stored in the Constant directory. Ultimately, the initial and boundary conditions for each vector and scalar field, are provided in the 0 directory, which represents the time zero of the simulation.

After the launch of the interFoam solver, other directories are created at the specified time-step. These directories are named after the corresponding time-step and contain the database of the flow solution visualised in Paraview.

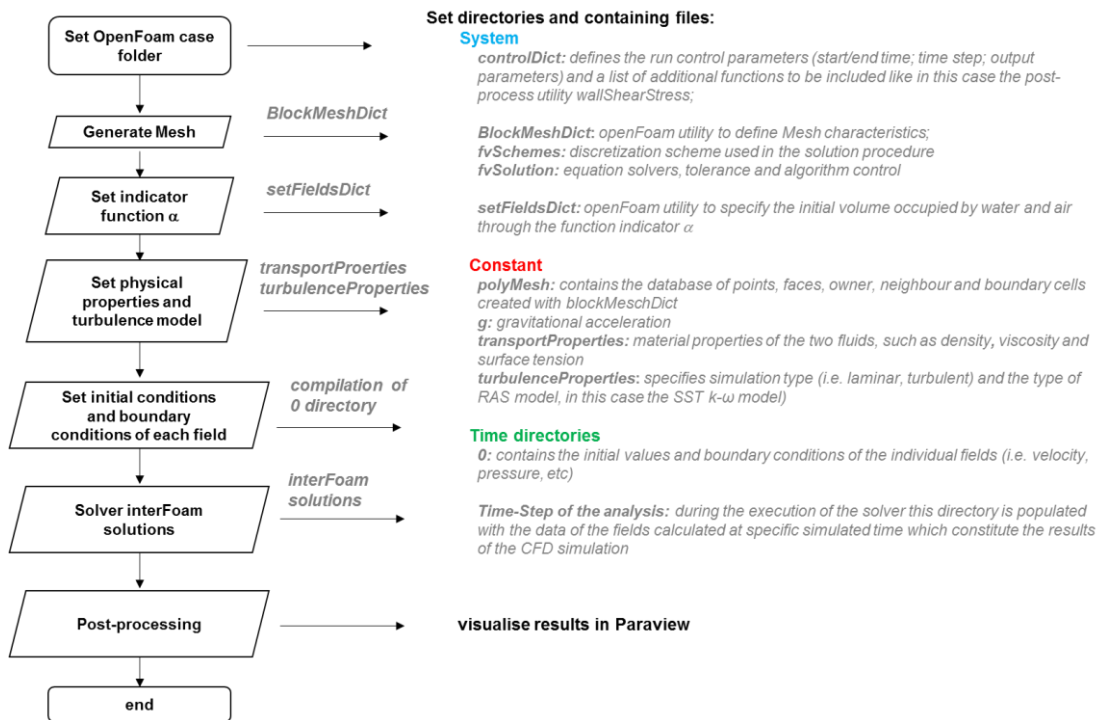


Figure 3-8: Block scheme of the procedure to set up the OpenFoam case

3.6.1.1 Computational Mesh

The blockMeshDict is compiled such that the flow domain is divided into 8 hexahedral blocks identified by 8 vertices each (i.e. points with coordinates x, y, z). The blocks contain 75 and 30 cells in the in X and Y directions respectively, while 1 cell is considered along Z. Strictly speaking the geometry is three-dimensional but a very small thickness is assigned along Z. In this way the problem can be approximated to a two-dimensional configuration as it is shown in Figure 3-9b.

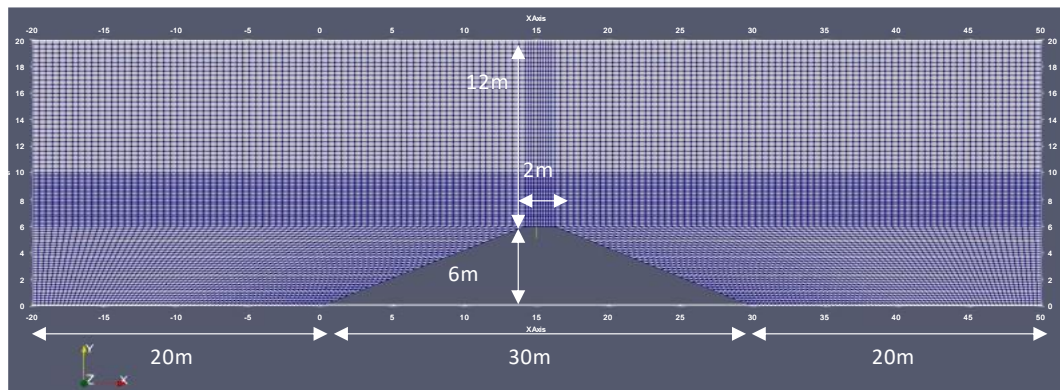
The computational domain extends laterally 20m from the two embankment toes and 12m above the crest as can be seen in Figure 3-9a. A more refined discretisation is adopted around the embankment slopes and above the crest, which are the regions of interest for the calculation of the wall shear stress and the water-air interface. Here the block cell size is 0.26m in X, 0.27m in Y and 1m in Z directions, while it is 0.45m

in X, 0.33m in Y and 1m in Z directions towards the boundaries. In total there are 28762 points, 14100 cells, 56680 faces of which 27920 are internal faces.

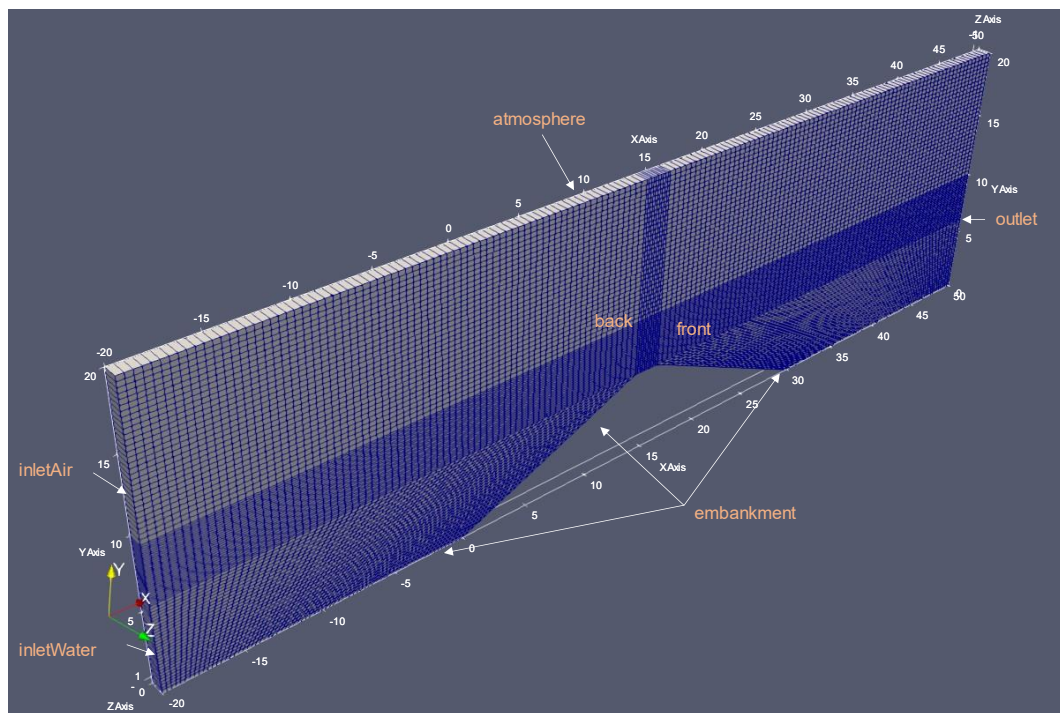
Another essential aspect of the mesh description is the boundary of the flow domain, which must be provided in the list named “boundary” of the blockMeshDict dictionary. Every boundary is broken into patches re-named with an appropriate keyword. A patch is identified by a list of faces and it is characterised by its type, which can be either geometrical constraints (i.e. wall, empty, wedge, etc.) associated with that region or a generic type “patch” where no geometrical or topological information are required, but some boundary conditions must be specified.

In this application, the left boundary is split into two patches: *inletWater* (from 0 to 6m in height) and *inletAir* (from 6m to 20m in height) described by the generic type “patch”. The right hand-side is named *outlet* (from 0 to 20m) and the top boundary *atmosphere*; the generic type “patch” is assigned to both boundaries. The bottom boundaries are named *embankment* and the patch type is “wall” to represent the solid boundaries. The two patches *front* and *back* are planes with normal in the Z direction for which the solution is not required (i.e. the analysis is two-dimensional in X and Y), therefore these regions are defined as an “empty” patch. The boundaries described are shown in Figure 3-9b.

The meshing process is completed by setting the initial water regions for which the scalar indicator function “alpha.water” is equal to one. In this case an initial water level of 4m is assumed as starting point of the simulation as shown in Figure 3-10. In order to run the setFields utility a file “alpha.water.orig” must be present in the 0 directory which specifies the boundary condition for the field alpha.water. After running the utility setFields an alpha.water file is generated in the 0 directory which contains the list of the cells where alpha.water is one and the list where alpha.water is 0.



(a)



(b)

Figure 3-9: Computational domain implemented (a) view in the plane Y-X (b) three-dimensional view showing the mono-cell and the small thickness in the Z direction.

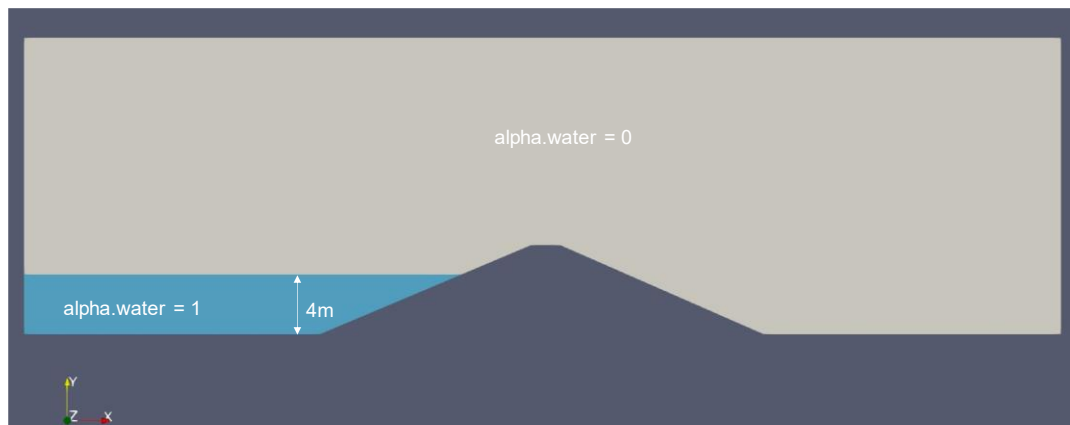


Figure 3-10: Initialisation of the function *alpha.water* to set the initial water region up to 4m from the bottom boundary

3.6.1.2 Material Properties

Material properties specified in the “transportProperties” file are density (ρ), kinematic viscosity (ν) for water and air and the surface tension coefficient (σ). The values adopted in this simulation are presented in the table below.

Table 3-1: Fluid Properties for the embankment overflow problem

Water Properties	Unit	Symbol	Value
Density	Kg m^{-3}	ρ	1.0×10^3
Kinematic viscosity	$\text{m}^2 \text{s}^{-1}$	ν	1.0×10^{-6}
Air Properties	Unit	Symbol	Value
Density	Kg m^{-3}	ρ	1.0
Kinematic viscosity	$\text{m}^2 \text{s}^{-1}$	ν	1.48×10^{-5}
Properties of both phases	Unit	Symbol	Value
Surface Tension	N m^{-1}	σ	0.07

The gravitational acceleration \mathbf{g} is uniform across the domain and acts in the Y direction, therefore the file \mathbf{g} is set equal to the vector (0 -9.81 0) m s⁻². Ultimately the file “turbulenceProperties” is specified as shown in Figure 3-11.

```

FoamFile
{
  version      2.0;
  format       ascii;
  class        dictionary;
  location     "constant";
  object       turbulenceProperties;
}
// *****

simulationType RAS;

RAS
{
  RASModel      kOmegaSST;

  turbulence     on;

  printCoeffs   on;
}

// *****

```

Figure 3-11: Turbulence model specified to solve the RANS equations

In this simulation the RAS or RANS method is adopted, for which additional equations must be included to predict the Reynolds Shear Stresses resulting from turbulence effects. Different types of models are available in CFD, based on the form and number of the additional transport equations introduced. For the embankment overflow problem, the “*Shear Stress Transport (SST) $k-\omega$* ” model (i.e. komegaSST in the figure above) is chosen, because it constitutes a good compromise between the solution of fully turbulent flow (i.e. high Reynolds number) and “near walls” flow (i.e. low Reynolds number). More details about the mathematical aspects of turbulent fluid flow problems and the different types of solution methods available in CFD are presented in Appendix A.2 Turbulence Modelling. Here it is also discussed why the SST $k-\omega$ model has been chosen among the possible options.

3.6.1.3 Boundary and Initial Conditions

The mathematical definition of the transient fluid flow problem for the embankment overflow is completed with the specification of the initial and boundary conditions assigned to each patch in Figure 3-9b and for all the flow variables. A general overview

of boundary conditions and the typical approaches applied in CFD practice are provided in Appendix A.3.4 Boundary and Initial Conditions, while the table **Error! Reference source not found.** summarises the prescribed boundary conditions for the problem studied.

It is worth clarifying that the two fundamental categories of boundary conditions are “fixedValue”, which is a Dirichlet condition specifying a value of the variable ϕ on the boundary; and “fixedGradient” which is a von Neumann condition as it prescribes the normal gradient $\frac{\partial \phi}{\partial n}$ of the variable at the boundary. A particular case of “fixedGradient” is “zeroGradient”, which defines a normal gradient equal to zero. More complex boundary conditions have been implemented in OpenFoam starting from these two basic ones. A description of the boundary conditions and values adopted to study the embankment overflow is provided for the six boundaries in the following **Error! Reference source not found.**

Inlet: inletAir and inletWater

At the inlet all the flow variables must be specified with a “fixedValue” (Versteeg and Malalasekera, 2007) condition. In the case studied, the fluid flow is driven initially by the water velocity vector with a magnitude of 1 ms^{-1} in the X direction and then, after the overflow occurs, by gravity along the downstream side towards the outlet boundary. In this way, the fluid flow is continuously fuelled by the water velocity distribution specified at the inletWater patch until the simulation is terminated. The prescribed magnitude of 1 ms^{-1} has been selected based on typical ranges of order of magnitudes of mean flow velocity found in literature for similar works. For example, to estimate the velocities and shear stresses associated with the overflow of the levee system in New Orleans during Hurricane Katrina, (Briaud *et al.*, 2008) considered a CFD simulation adopting an inflow velocity of 3 ms^{-1} . In the study of the velocity distribution in a natural river section during high floods, (Moramarco, Saltalippi and Singh, 2011) considered 6 velocity measurements undertaken in the period 1984-1997 at Pontelagoscuo hydrometric site on Po river in northern Italy. The measured mean flow velocity at the gauge river station varied in the range $0.5 - 2 \text{ ms}^{-1}$.

Table 3-2: Boundary conditions defined for the embankment overflow problem

Patch	Variables				
	Alpha.water	U [ms ⁻¹]	p_rgh [kg m ⁻¹ s ⁻²]	k [m ² s ⁻²]	omega [s ⁻¹]
inletAir	fixedValue uniform 0	fixedValue uniform (0 0 0)	fixedFluxPressure uniform 0	fixedValue uniform 0.0037	fixedValue uniform 0.12
inletWater	fixedValue uniform 1	fixedValue uniform (1 0 0)	fixedFluxPressure uniform 0	fixedValue uniform 0.0037	fixedValue uniform 0.12
Atmosphere	inletOutlet uniform 0	pressureInletOutletVelocity uniform (0 0 0)	totalPressure uniform 0	inletOutlet uniform 0.0037	inletOutlet uniform 0.12
Embankment	zeroGradient	noSlip	fixedFluxPressure uniform 0	KqRWallFunction uniform 0.0037	omegaWallFunction uniform 0.12
Outlet	zeroGradient	zeroGradient	fixedFluxPressure uniform 0	zeroGradient	zeroGradient
Front and Back	empty	empty	empty	empty	empty

In an interesting study on the importance of flow velocity for the extent of flood damages recorded in the South-East of Germany during the severe flood in August 2002 (Kreibich *et al.*, 2009), typical mean flow velocity considered were in the range of $0 - 3 \text{ ms}^{-1}$.

For the scalar function “alpha.water” a uniform fixed value of 0 and 1 is assigned at the inletAir and inletWater, implying the presence of 100% of air (i.e. alpha.water is zero) or water (i.e. alpha.water is one) respectively.

At both inletAir and inletWater the pressure is unknown. A boundary value is extrapolated from the internal cells of the flow domain. Ubbink (Ubbink, 1997) suggests to apply a zeroGradient boundary for the pressure at the inlet. In this case the “fixedFluxPressure” boundary condition implemented in OpenFoam is adopted according to the example “damBreak” presented in the OpenFoam manual (Greenshields, 2021). This boundary condition is recommended for pressure in situation where “zeroGradient” should be applied but the solution equations include gravity and surface tension terms. This condition adjusts the pressure gradient such that the flux on the boundary is that specified by the velocity boundary condition.

Ideally, the boundary values at the inlet for the turbulent kinetic energy k and the turbulence frequency $\omega = \frac{\varepsilon}{k}$ should be provided with measurements. In reality, these data are usually not available and it is common practice to estimate the turbulence properties at the inlet with approximate equations. In this case, the online CFD tool (<https://www.cfd-online.com/Tools/turbulence.php>) shown in Figure 3-12 is considered, where the conversion with the turbulence intensity T_u , the length-scale T_{uL} and the freestream velocity U_∞ .

A turbulence intensity (defined as $T_u = \frac{\sqrt{k \frac{2}{3}}}{U}$) equal to 5 % has been considered, assuming that the case under study falls under the “medium-turbulence case” where turbulence intensity is typically between 1% and 5%. The length-scale T_{uL} refers to the size of the large eddies in a turbulent flow and the value equal to 0.5 m adopted is based on the size of the discretised grid. The values obtained in this way are comparable with the values presented in the “Spillway Tutorial” (i.e. $k = 0.000216$

m^2s^{-2} and $\omega = 0.147 \text{ s}^{-1}$).

Turbulence Properties, Conversions & Boundary Estimations			
Properties			
Freestream velocity	U_∞	<input type="text" value="1"/>	[m/s]
Turbulence kinetic energy	k	<input type="text" value="0.003750000000000000"/>	[J/kg] = [m ² / s ²]
Turbulence dissipation	ϵ	<input type="text" value="0.00004133513940946"/>	[J/kg/s] = [m ² / s ³]
Specific turbulence dissipation	ω	<input type="text" value="0.1224744871391589"/>	[1/s]
Turbulence intensity/level	Tu	<input type="text" value="5"/>	[%]
Turbulence length scale	Tu_L	<input type="text" value="0.5"/>	[m]
Kinematic viscosity	ν	<input type="text" value="1.5e-05"/>	[m ² /s] (Air: 1.5e-05, Water: 1E-06 at room temp & pressure)
Conversions			
<input type="radio"/> ω from k and ϵ using $\beta^* = C_\mu = 0.09$, see the definition of ω for formula used <input type="radio"/> ϵ from k and ω using $\beta = C_\mu = 0.09$, see the definition of ω for formula used <input checked="" type="radio"/> Turbulence variables (k, ϵ , ω) from turbulence intensity (Tu), length-scale (Tu_L) and freestream velocity (U_∞) <input type="radio"/> Turbulence variables (k, ϵ , ω) from turbulence intensity (Tu), eddy viscosity ratio (μ_t/μ), freestream velocity (U_∞) and kinematic viscosity (ν) <input type="radio"/> Turbulence intensity (Tu) from turbulence kinetic energy (k) and freestream velocity (U_∞) <input type="radio"/> Turbulence length scale (Tu_L) from turbulence kinetic energy (k) and dissipation (ϵ) <input type="radio"/> Turbulence length scale (Tu_L) from turbulence kinetic energy (k) and specific dissipation (ω) <input type="radio"/> Turbulence eddy viscosity ratio (μ_t/μ) from turbulence kinetic energy (k) and dissipation (ϵ) <input type="radio"/> Turbulence eddy viscosity ratio (μ_t/μ) from turbulence kinetic energy (k) and specific dissipation (ω)			

Figure 3-12: Assessment of k and ω values based on conversion with free stream velocity, turbulence intensity/level and turbulence length scale (<https://www.cfd-online.com/Tools/turbulence.php>)

Atmosphere

This is the top boundary of the flow domain free to the atmosphere and therefore both inflow and outflow are allowed based on the internal flow. For this reason derived types of boundary conditions are adopted.

For alpha.water, k and ω the “inletOutlet” condition switches between “zeroGradient” when the fluid flows out from the patch faces (i.e. outlet) and becomes a “fixedValue” type when the fluid flows into the region (i.e “inlet). This means that the zeroGradient condition at the atmosphere boundary is well posed in case of outflow; however, when there is an inflow, the phase fraction assumes a fixed value of zero and the cells are completely filled by air (i.e. 100% air). Similarly, the fixed values valid at the inlet are considered for k and ω .

For pressure and velocity vector the combination of totalPressure and “pressureInletOutletVelocity” is commonly adopted when an inflow might occur, but the inlet flow velocity is unknown. This is implemented for example at the atmosphere

boundary in the damBreak tutorial.

The “pressureInletOutletVelocity” condition on velocity specifies zeroGradient in an outflow situation, but for inflow the normal velocity is allowed to find its own value.

The totalPressure condition on pressure is a fixedValue type calculated from specified total pressure p_0 and local velocity U when the flow is inward; while it is equal to p_0 in an outflow situation.

Embankment

The keyword embankment indicates all the bottom boundaries of the flow domain corresponding to rigid surfaces, commonly known as “walls”. For the velocity the “noSlip” condition means that at the embankment, the velocity components in X, Y and Z directions are zero. For the pressure the “fixedFluxPressure” condition is applied as for the inlet.

For the turbulent kinetic energy k and the turbulence frequency ω , wall functions are adopted on solid surfaces to account for the behaviour of the fluid flow in the near-wall regions, where the velocity gradients are steeper than the fully developed flow. Because of this proximity to the walls, the mesh resolution should be adequately fine to capture the steep velocity profile. To avoid the need of reducing the cells size on solid surface which results in an increase of the computational efforts, the wall function approach is introduced. These are empirical functions representing the velocity profile at certain distances from the wall (i.e the viscous sub-layer, the buffer layer and the log-law as shown in Figure A - 2). These have been obtained by fitting experimental measurements of flow velocities close to the wall and DNS simulation. These are particularly important for the calculation of the wall shear stresses and the velocity profile in the near-wall region is addressed in more details in Appendix A.2.2

Wall laws

In OpenFoam, the “KqRWallFunction” is the only one providing the zeroGradient condition. On the contrary, the omegaWallFunction is a special wall function that can switch between viscous and logarithmic region according to the position of y^+ (dimensionless distance from the wall). At the intersection of the viscous sublayer and log-law region, values are calculated through blending the viscous and log-law

sublayer values. A comprehensive mathematical description of wall function boundary conditions implemented in OpenFoam has been provided by Liu (Liu, 2017)

Outlet or open boundary

The outlet boundary has been located 20m from the embankment downstream toe where a fully developed state is established and there are small variations in the flow direction. For this reason, it is sufficient to set the gradients of all variables equal to zero except for the pressure, where the fixedFluxPressure condition is applied.

Front and Back

Finally, on the Front and Back planes of the 2D problem the “empty” type is selected for all variables because no solution is expected along the Z direction.

3.6.2 Finite Element Model in PLAXIS 2D

The 6m high ideal embankment shown in Figure 3-7 has been analysed in the finite element software Plaxis 2D assuming a homogeneous material for both the embankment body and the foundation soil. This situation often occurs in real case scenarios. Flood embankments have been raised, upgraded, and repaired over years with techniques that typically involve local sources for the excavation of filling materials. Because of the natural environment, these locally won materials consisted of fluvial deposits from old floodplain typically composed of silt and clay (Dyer, 2004; M. Morris, Dyer and Smith, 2007).

A possible sequence of events has been implemented starting from an initial condition where only the original foundation material was present, to the embankment construction, followed by a consolidation phase assuming an initial elevation of the river water surface at the embankment upstream side. The flood event has been simulated by rising the water levels according to a time-dependent function which ultimately leads to the final calculation phase represented by the overflow event. Two models have been run. One considers the overflow with the simultaneous application of a distributed load tangential to the downstream slope, with a magnitude given by the hydraulic shear stresses calculated in the hydrodynamic model. In the second

model, only the effects of the overflow have been analysed. In both cases, the overflow calculation was followed by the assessment of the evolution of FoS associated with the overflow.

The model set up with the canonical procedural steps is presented in detail in the following sections. It consists of (1) creation of the computational mesh; (2) description of the material properties and constitutive laws adopted to capture the hydro-mechanical soil behaviour; and (3) the definition of initial and boundary conditions.

3.6.2.1 Computational Mesh

The model extent and the finite element mesh are shown in the figure below.

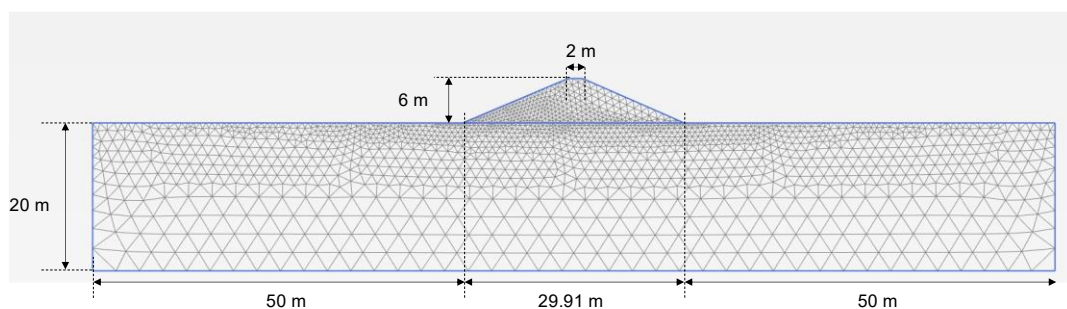


Figure 3-13: Model extent and Finite Element Mesh

The domain is discretized in 3313 triangular elements adopting the 15-Node configuration. The average element size is 1.15 m and a local refinement has been applied within the embankment body and along the slopes.

3.6.2.2 Mechanical and Hydraulic Soil Properties

The elastic-perfectly plastic model with Mohr-Coulomb failure criterion and the van Genuchten equation have been selected to model shear strength and water retention behaviour respectively. Drained conditions have been considered for all the calculation phases, therefore effective stresses soil parameters have been introduced. The mechanical soil properties required for the Mohr-Coulomb constitutive model in Plaxis 2D are presented in Table 3-3.

Table 3-3: Soil properties assumed for the ideal silty-clay material

<i>Mechanical Properties (Elastic-Perfectly Plastic Model)</i>		
Soil Property	Symbol and Unit	Value
Young Modulus	E' [kNm ⁻²]	10000
Poisson's ratio	ν' [-]	0.33
Effective Cohesion	c' [kNm ⁻²]	3
Effective friction angle	ϕ' [°]	24.0
Dilatancy Angle	ψ' [°]	0.0

A saturated unit weight of 19.5 kNm⁻³ and a dry unit weight of 16 kNm⁻³ have also been considered. The van Genuchten function is implemented in Plaxis 2D with the equation below (Galavi, 2010; Brinkgreve *et al.*, 2018):

$$S(\psi) = S_{res} + (S_0 - S_{res})[1 + (g_a |\psi|)^{g_n}]^{g_c} \quad \text{Equation 3-13}$$

where:

- S_{res} is residual degree of saturation related to the water that remains in soil even at high suctions;
- S_0 is the degree of saturation at zero suction.
- $\psi = -\frac{u_w}{\gamma_w}$ [m] is the suction head, where u_w is the pore-water pressure and γ_w is the water unit weight.
- g_a is related to the air entry value (AEV). Its dimension is [1/m].
- g_n accounts for the rate of water extraction from the soil when the air entry value is overcome.
- g_c controls the position of the inflection point. It is assumed that:

$$g_c = \frac{1 - g_n}{g_n} \quad \text{Equation 3-14}$$

The relative hydraulic conductivity is function of the effective degree of saturation is given by Equation 3-15.

$$k_{rel}(S) = S_e^{g_c} \left[1 - \left(1 - S_e^{\left(\frac{g_n}{g_n - 1} \right)} \right)^{\frac{g_n - 1}{g_n}} \right]^2 \quad \text{Equation 3-15}$$

where:

$$S_e = \frac{S - S_{res}}{S_0 - S_{res}} \quad \text{Equation 3-16}$$

is the effective degree of saturation.

The parameters required in input in Equation 3-13 adopted for the ideal silty - clay considered in this exercise are shown in Table 3-4. The soil water retention curve is also presented in Figure 3-14.

Table 3-4: Hydraulic model parameters implemented for the silty-clay adopted

<i>Hydraulic Parameters of the van Genuchten water retention curve</i>			
Soil Property	Symbol and Unit	Value	
Residual degree of saturation	S_{res} [-]	0.04	
Saturated degree of saturation	S_{sat} [-]	1	
Air Entry Value related	g_a [1/m]	0.098	
Water extraction related	g_n [-]	2.0	
	$g_c = \frac{1 - g_n}{g_n}$	g_c [-]	-0.5

Assuming a saturated hydraulic conductivity of 10^{-7} m/s representative for an ideal silty - clay and according to Equation 3-15, the hydraulic conductivity function is shown in Figure 3-15.

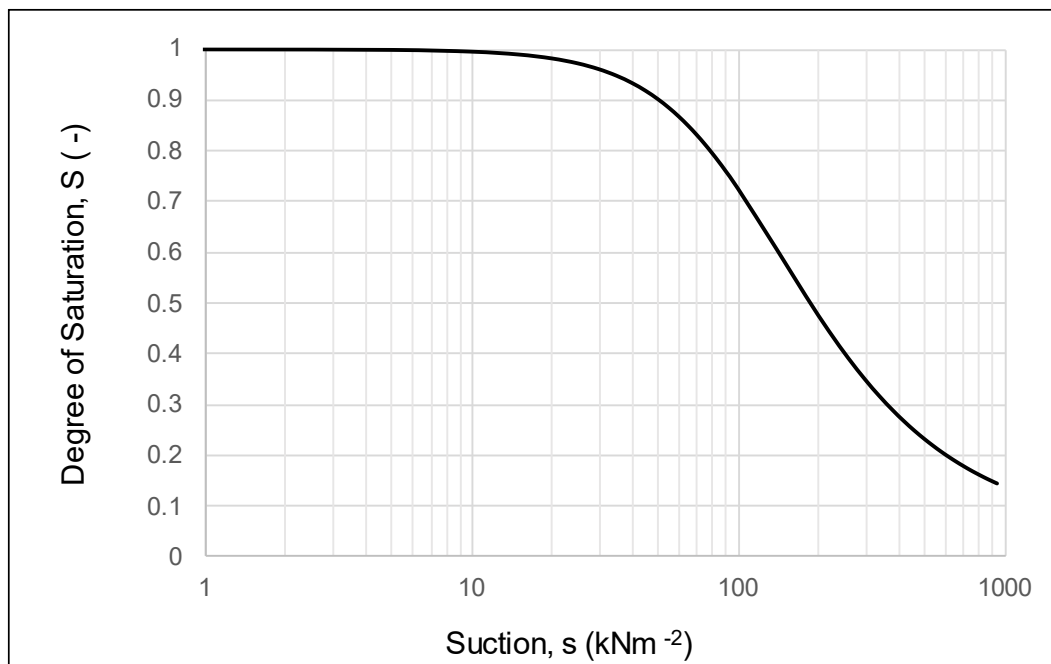


Figure 3-14: Soil water retention curve

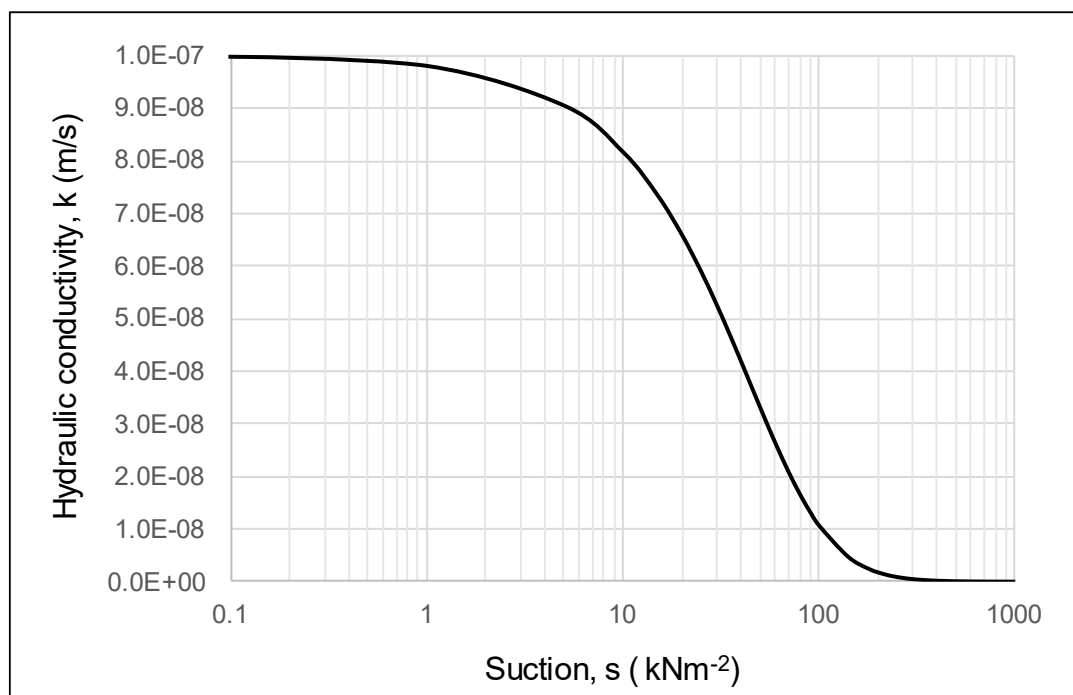


Figure 3-15: Hydraulic Conductivity Function

A more detailed discussion of the hydro-mechanical properties assumed for this silty-clay material will be provided later in the context of another application described in Chapter 5. However, it is worth specifying that both, mechanical and hydraulic parameters, will affect the results of the stability analysis. Obviously, a delay in the failure processes will be observed for higher values of effective cohesion and friction angle. Similarly, soils that tend to stay unsaturated for a longer period and with a low hydraulic conductivity, will tend to hold suction, contributing to stabilise the slope during the overflow. This means that the plateau and the suction air entry value of the soil water retention curve, play an important role, as well as the saturated hydraulic conductivity. In the van Genuchten model implemented in Plaxis, high values of the parameter g_a are associated with low air entry suction (i.e. AEV) and small plateau in the SWRC. The parameter g_n is a function of the rate of water extraction from the soil once the AEV has been exceeded. High values of g_n are associated with gentler slope of the SWRC and smaller plateau in the low suctions range. The overflow is a wetting process and therefore the hysteresis of the soil water retention behaviour should be considered.

In absence of experimental soil characterisation, a sensitivity analysis of these parameters should be conducted, to have a better appreciation of the effects on the embankment stability during overflow.

3.6.2.3 Model Phases and Boundary Conditions

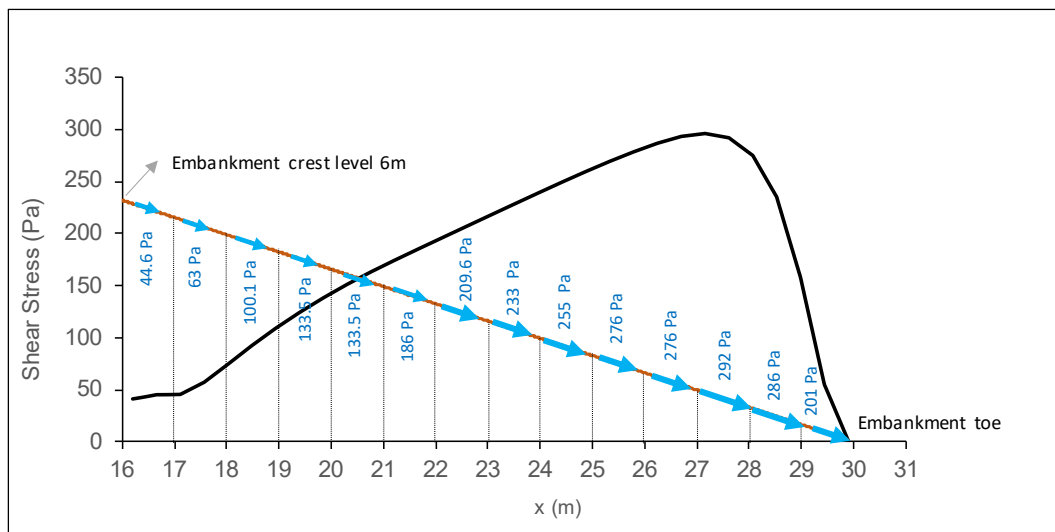
The model consists of seven calculation phases that simulate the sequence of events prior to the overflow scenario. The overflow phase is followed by a safety analysis to determine the global factor of safety. Two distinctive models have been run, with and without the hydraulic shear stresses resulting from the CFD model. A summary of the calculations performed is provided in Table 3-5 below.

In Plaxis 2D the distributed load in plain-strain geometry is provided in kN/m/m and to represent the shear stress distribution, the downstream slope has been divided in strips 1m long. The average shear stresses over each segment have been calculated as shown in Figure 3-16a and the components in the X and Y direction have been

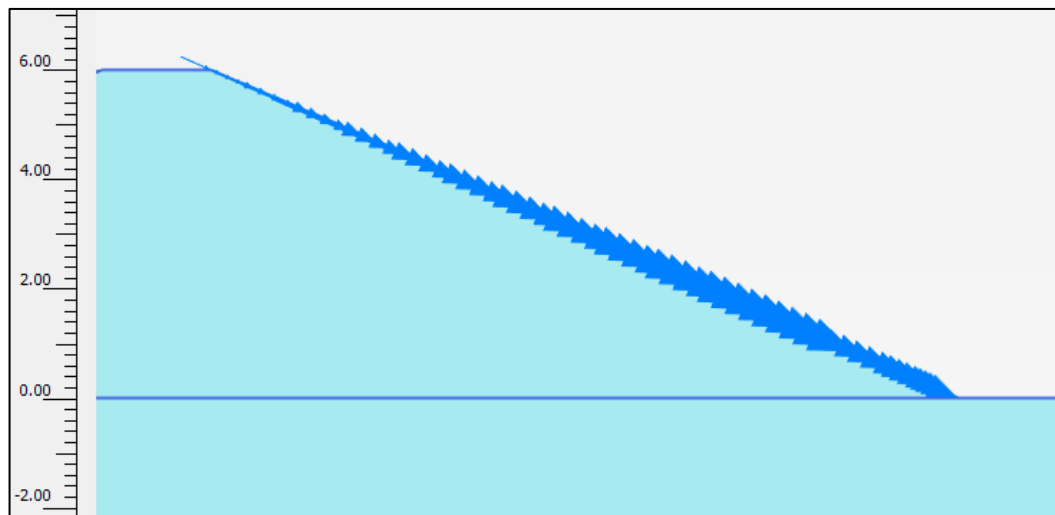
introduced in Plaxis 2D as per Figure 3-16b.

Table 3-5: Calculation phases and type of analysis implemented in Plaxis 2D

No.	Phase	Type of Calculation
1	Initial Phase	Gravity Loading: plastic calculation which establishes the initial stress field before the embankment placement. An initial groundwater table is assumed.
2	Embankment placement	Plastic deformation analysis simulating the embankment construction.
3	River water level	Fully coupled flow-deformation analysis which simulates the presence of a river on the left side of the embankment constructed in the previous phase.
4	Consolidation	A consolidation process is likely to occur during the embankment life. It is assumed that no additional loads are applied during this phase and that the target Degree of Consolidation is 90%.
5	Extreme weather event	Fully coupled flow-deformation analysis where a time-dependent boundary condition applied on the river side and along the embankment upstream slope, produces the increase of the water levels up to the crest. The duration of this event is assumed to be 10 hours.
6	Overflow	Fully coupled flow-deformation analysis where the water pressure on the downstream slope is zero (i.e. hydraulic head equal to the elevation). This phase is supposed to last 15 min.
7	Stability	Safety calculation according to the phi-ci reduction method to estimate the global factor of safety associated with the overflow.



(a)



(b)

Figure 3-16: Hydraulic Shear Stress Distribution from Open Foam and averaged over segments 1m long (a) and distributed load introduced in Plaxis 2D (b)

Initial Phase

The initial conditions and the initial stress field are set for the foundation soil when the embankment is not present yet. The groundwater table is obtained by imposing a constant hydraulic head of 0 m on the left boundary and a constant hydraulic head of -1.5 m on the right side as shown in Figure 3-17 (the datum is set at the ground surface).

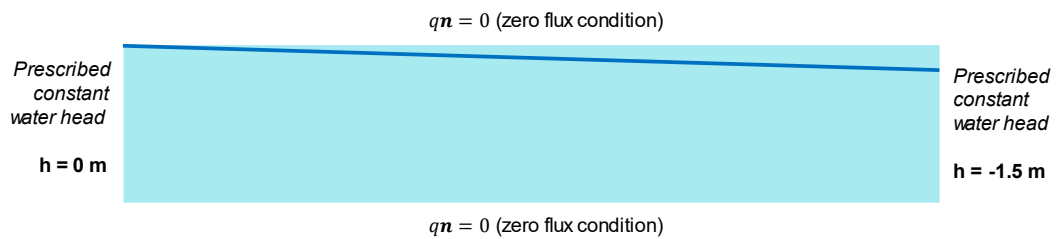


Figure 3-17: Hydraulic Boundary Conditions for the initial phase

Embankment Placement

When the embankment is placed with a plastic analysis (Figure 3-18), it is supposed that the initial groundwater table remains unchanged. Therefore, hydraulic boundary conditions are applied in a similar way of the Initial Phase.

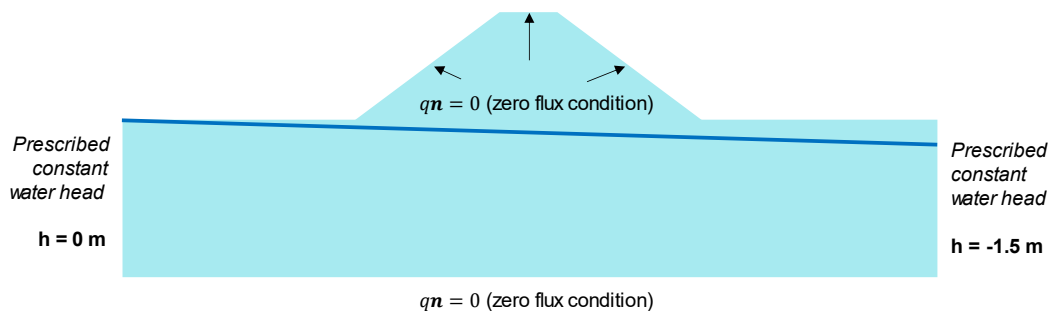


Figure 3-18: Second calculation phase and hydraulic boundary conditions

River water level and Consolidation analysis

In the third phase, the water levels on the left side of the model domain are increased over time to simulate the rise of the water level to the prior-to-flood value. The increase of the water level is imposed with a time-dependent boundary condition, specified by a function of time. It is assumed that over a period of one year (i.e. 31536000 s) an increment of water head Δh of 0.625 m is reached. A fully coupled flow-deformation analysis is performed.

This phase is then followed by a fully coupled flow-deformation analysis (i.e. the fourth phase in the sequence) where the prior-to-flood value is maintained constant over time.

The prescribed water head imposed on the downstream side will influence the

position of the water level at the toe. Obviously, if the water level is initially high, the toe area will be saturated prior to the overflow. In this ideal model, it is realistically assumed that at this stage the water table is still deep enough to leave the toe area in a partial or quasi – saturated state. It is also worth noticing that there are situations, for example in earthen dams, where a certain tailwater level can be present downstream of the structure, implying that at the downstream toe a hydraulic jump might form. This should be simulated in the CFD model. This particular situation has not been investigated in this work.

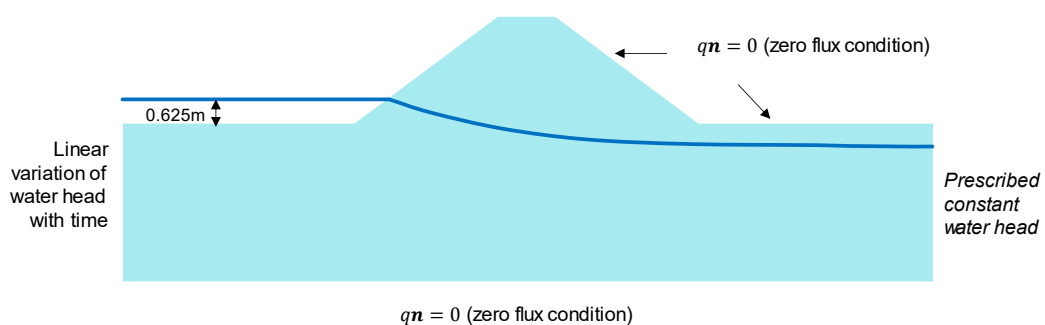


Figure 3-19: River appears on the upstream side, followed by a consolidation phase

Rising of water levels during an extreme weather event

In this phase again a fully coupled flow-deformation calculation is performed to model an extreme weather event, which causes the increase of the water level on the upstream side. It is supposed that in 10 hours an increment of water level of $\Delta h = 5.375$ m is achieved. The function $h = f(t)$ is again linear.

It is worth noticing that the rate at which the water level increases on the upstream side, will affect the first infiltration process, therefore the pore water pressures and the degree of saturation at the onset of overflow, depend on the duration of the filling phase. If the filling phase is long, the embankment material will have enough time to become saturated (depending also on the soil water retention behaviour); consequently the saturated area within the embankment will be more extended. The initial value of suction will be lower than a case of short filling periods.

All these aspects govern the onset of failure and the locations of the first instabilities. It is evident that the time required to reach the full capacity of the water

body is an important parameter of the model, that ultimately influences mode and time of breaching processes.

In theory, the duration of what here is defined filling phase, can be assessed - for a particular site - by performing hydrologic studies, with the statistical analysis of past flood events within the catchment and through the assessment of hydrometric data for a given water body. In this ideal case, the time of the filling phase has been arbitrarily assumed based on typical durations occurred during severe floods, ranging between few hours to days. However, it can be observed that due to these time-scales, less important differences are expected for a fine-grained material, for which the saturation process is in general slow and the effects of 10 hours or 48 hours durations, will produce similar results in terms of pressure distribution and degree of saturation, especially because of typically low hydraulic conductivities.

On the contrary, coarse-grained soils will be more sensitive to this parameter and a delay of 24 hours can result in a big difference in the saturated region accompanied by a decrease of the initial suction value. Therefore, when a sand embankment is under study, in absence of real data, a sensitivity analysis should be performed to explore multiple scenarios.

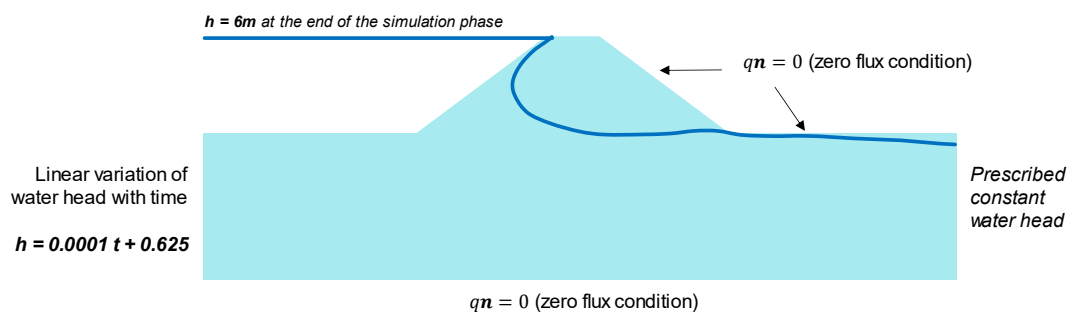


Figure 3-20: Hydraulic boundary conditions associated with an extreme weather event, leading to the increase of the water levels up to the crest level

Overflow and Safety

Starting from the filling phase, the overflow is simulated considering the hydraulic boundary conditions represented in Figure 3-21. A fully coupled flow deformation analysis is performed over a time-step of 900 seconds at the end of which the stability of the embankment is assessed. The global FoS is calculated immediately after the

overflow phase in a Safety calculation phase. If the FoS remains greater than 1, a further time step of 900 seconds is considered, and the stability assessed again at the end of this time step. The iteration is ended when the FoS of the slope becomes lower than unity. The time-step adopted for the overflow is decided arbitrarily. However, for the aim of this stability analysis the particular value of the time-step adopted has a secondary importance and will not affect the final result.

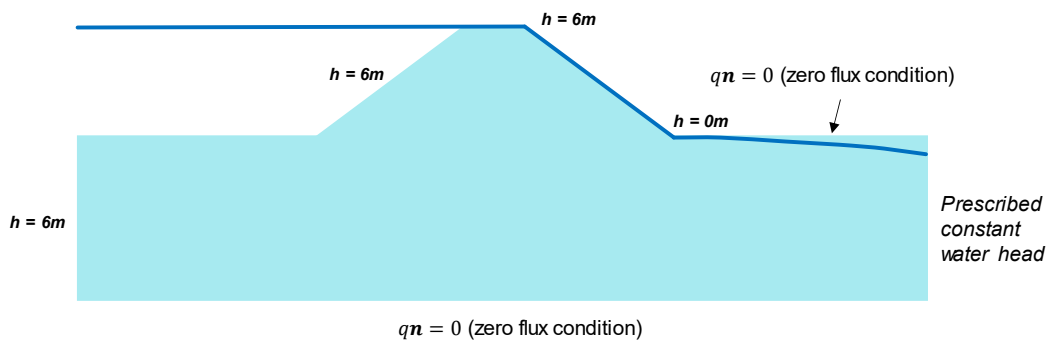


Figure 3-21: Hydraulic boundary conditions which simulate the overflow event.

3.7 Results

3.7.1 Hydrodynamic Forces

The water velocity of 1 m s^{-1} imposed at the water-inlet boundary along the X direction in the CFD model causes the overflow. However, it is worth specifying that the overflow is a consequence of the water flowing in the orthogonal direction to the ideal cross-section considered. Due to the increase of the discharge in the water body during the flood event, this flow results in the lateral growth of the water levels behind the embankment, which is simulated in the model with a continuous water velocity in the longitudinal direction X.

The duration of the overflow simulated is 180 seconds with a time-step of 10^{-4} seconds, but the hydrodynamic steady state condition (i.e. hydrodynamic flow variables become constant with time) is reached after 40 seconds from the start.

Figure 3-22 shows the evolution of the free surface elevation (corresponding to the phase fraction equal to 0.5) at selected time - steps. At the downstream end of the crest, water depth is 0.47 m at $t = 16$ sec; 0.86 m at $t = 24$ sec; 1.08 m at $t = 32$ sec;

and starting from $t = 48$ sec the water elevation is 1.20 m above the crest and remains constant until the end of the simulation.

After 16 sec from the start, the overflow is triggered along the downstream slope and a thin layer of water is formed. In the middle section, at 23 m from the upstream toe, water depth varies from 0.25 m at $t = 24$ sec up to 0.5 m at $t = 40$ sec and until the end of the overflow. As expected, the water depth is considerably shallow along the downstream slope compared to the crest, due to the rapid acceleration of the water flow driven by gravity.

At the downstream toe, because of the transition in the bed, the water flow decelerates, and the free surface is slightly higher than over the slope. At this location the simulated water depth varies from 0.36 m at $t = 24$ sec up to 0.6 m when the steady state condition is established.

Figure 3-23 shows the velocity vectors distribution over the entire computational domain at four different time-steps of the overflow process. The white contour indicates the free-surface elevation, corresponding to the phase fraction “alpha.water” equal to 0.5. The maximum flow velocity of approximately 20 m s^{-1} is reached in the air phase when water starts to overflow along the downstream slope (Figure 3-23a). The high velocity value observed is associated with strong turbulent structures as shown by the vortices identified in the velocity arrows plot at the downstream side. This wind created at the head of the water-front impinging the slope is due to the large pressure difference between the upstream (high pressure zone) and downstream side (low pressure). The water-air interactions are clearly visible in the vector plots in Figure 3-23b and the light blue and green arrows, corresponding to the velocity range of $5\text{-}6 \text{ m s}^{-1}$, indicate these intense exchanges between water and air. This effect tends to attenuate as the overflow progresses like in Figure 3-23c,d, showing that the air-entrainment process and flow condition become constant at steady state.

The maximum flow velocity of approximately 20 m s^{-1} is reached in the air phase when water starts to overflow along the downstream slope (Figure 3-23a). The high velocity value observed is associated with strong turbulent structures as shown by the vortices identified in the velocity arrows plot at the downstream side. This wind created at the head of the water-front impinging the slope is due to the large pressure

difference between the upstream (high pressure zone) and downstream side (low pressure). The water-air interactions are clearly visible in the vector plots in Figure 3-23b and the light blue and green arrows, corresponding to the velocity range of $5\text{--}6\text{ m s}^{-1}$, indicate these intense exchanges between water and air. This effect tends to attenuate as the overflow progresses like in Figure 3-23c,d, showing that the air-entrainment process and flow condition become constant at steady state.

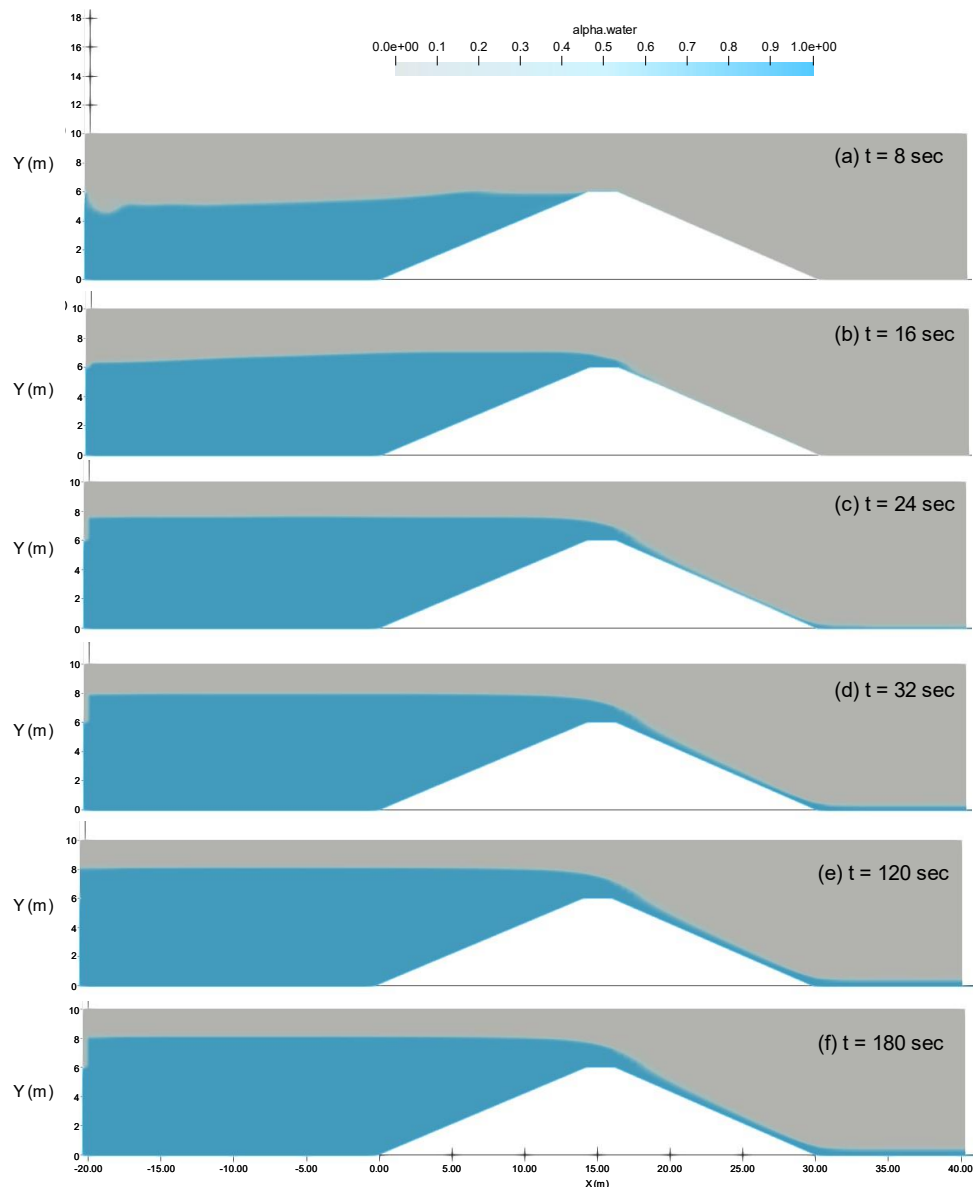
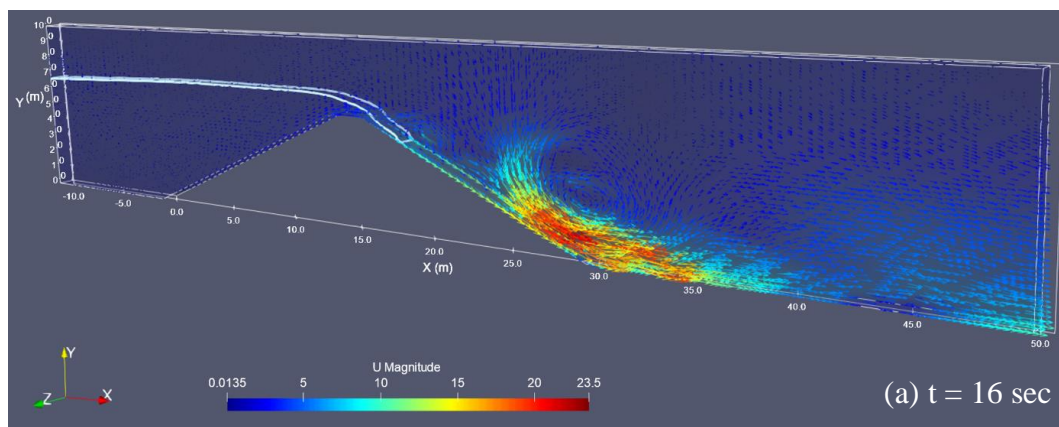


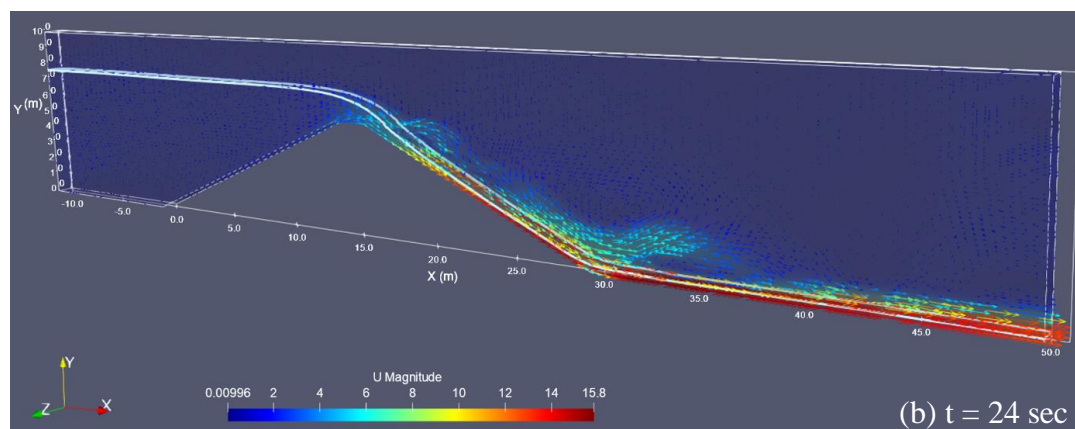
Figure 3-22: Free surface elevations at (a) $t = 8$ sec; (b) $t = 16$ sec; (c) $t = 24$ sec; (d) $t = 32$ sec; (e) $t = 120$ sec and (f) $t = 180$ sec, showing the steady state condition after $t = 32$ sec

When the overflow is fully established (Figure 3-23b,c), the maximum velocity oscillates between 15 - 15.8 m s⁻¹ at 24 and 40 seconds respectively (Figure 3-23 – b and Figure 3-23 - c). At 180 seconds the maximum flow velocity is 14.8 m s⁻¹. The fact that after 40 seconds the peak velocity varies in the range 15-14.8 m s⁻¹ means, once again, that the water flow reaches the steady state condition.

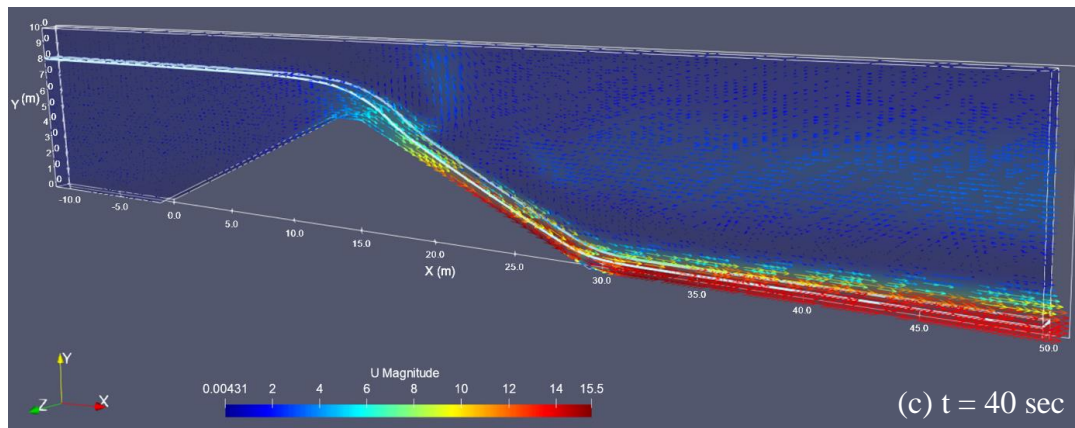
It is worth highlighting that the maximum velocity is higher at 24 seconds than the final time, because the water depth is still shallow and the flow continues to accelerate compared to the last phase. As expected, it is noted that the velocity peak develops around the middle section of the slope down to the toe area and continues along the horizontal surface towards the outlet boundary.



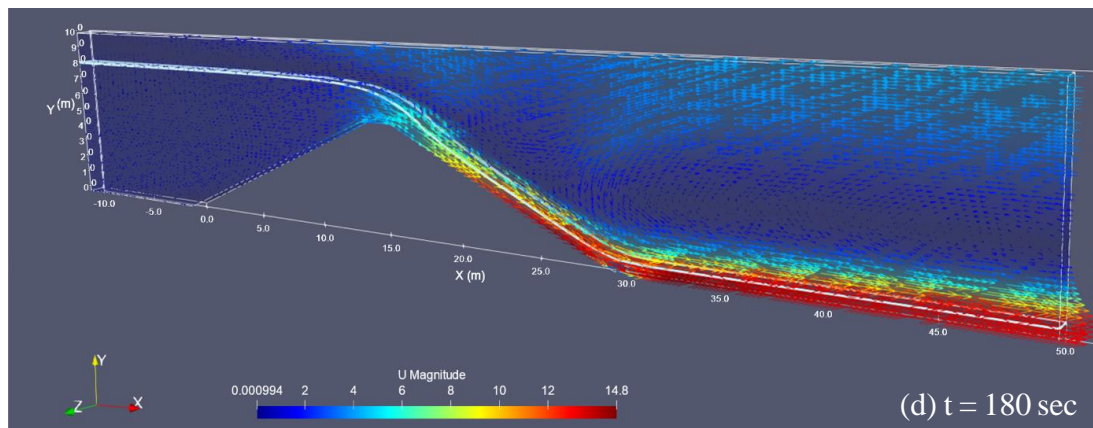
(a)



(b)



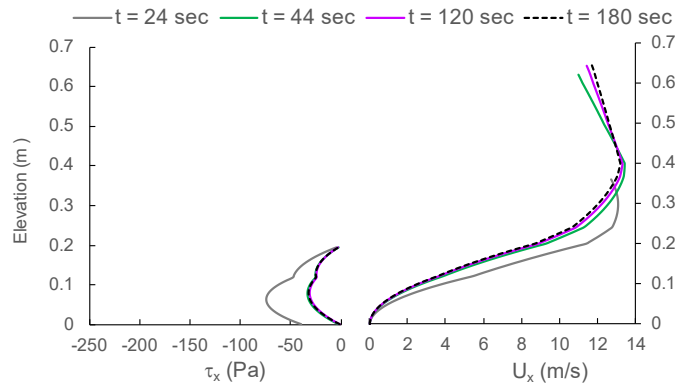
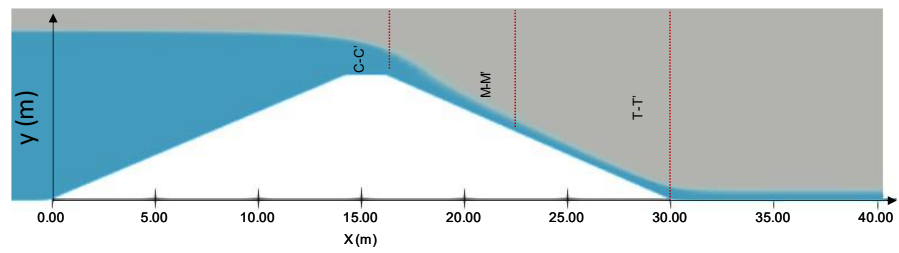
(c)



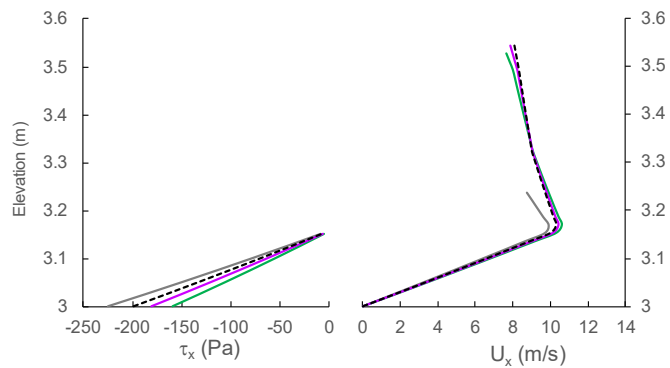
(d)

Figure 3-23: Time sequence of the velocity vectors at: (a) 16 sec; (b) 24 sec; (c) 40 sec and (d) 180 sec

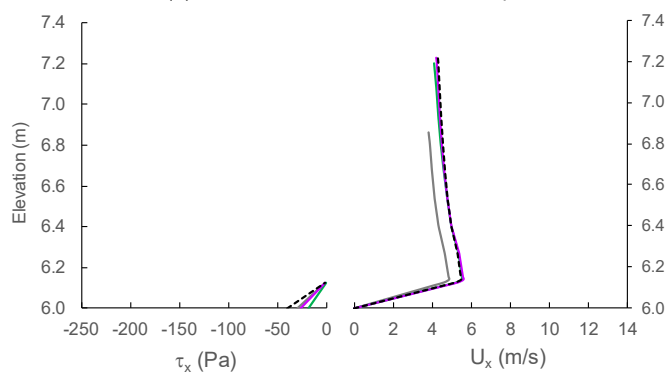
The velocity profiles in the X and Y directions and the relative wall shear stresses are shown in Figure 3-24 and Figure 3-25 respectively. Cross-sections at the downstream toe, at the middle of the slope and at the downstream edge of the embankment crest are presented for the selected times: 24, 44, 120 and 180 seconds respectively.



(a) Cross Section T -T': downstream toe

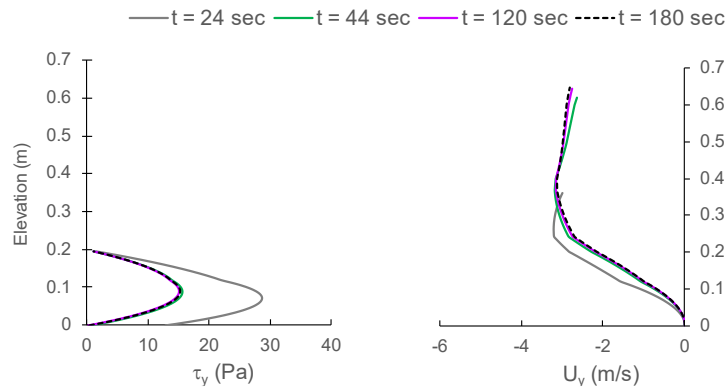
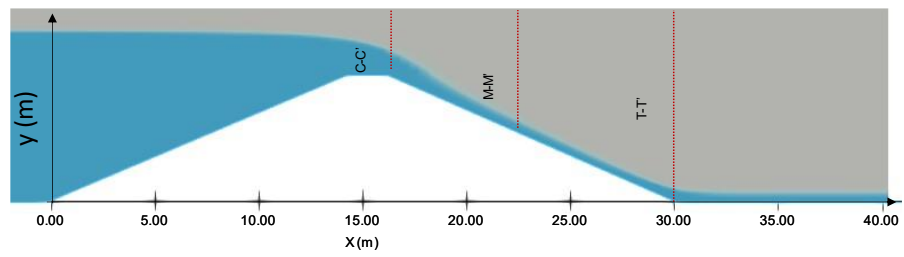


(b) Cross Section M - M': middle slope

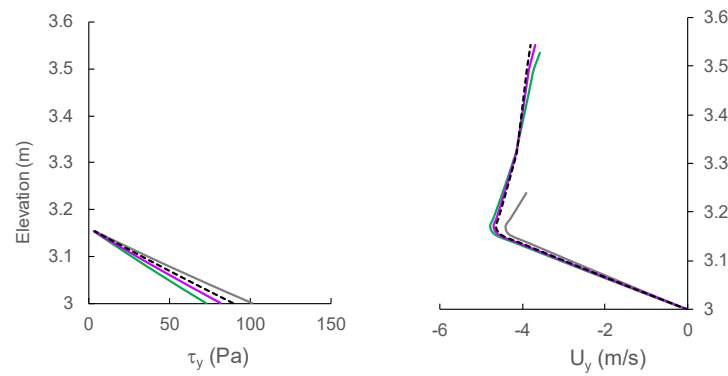


(c) Cross Section C - C': downstream crest

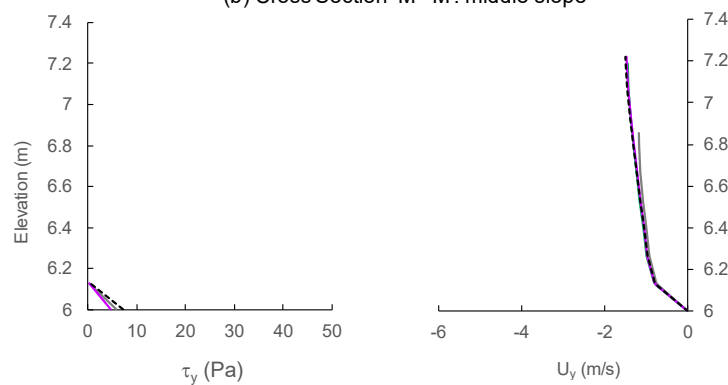
Figure 3-24: Wall Shear Stress and water velocity profiles in the X direction at: (a) the downstream toe; (b) middle of the slope and (c) downstream edge of the crest for $t = 24, 44, 120$ and 180 sec



(a) Cross Section T - T': downstream toe



(b) Cross Section M - M': middle slope



(c) Cross Section C - C': downstream crest

Figure 3-25: Wall Shear Stress and water velocity profiles in the Y direction at: (a) the downstream toe; (b) middle of the slope and (c) downstream edge of the crest for $t = 24, 44, 120$ and 180 sec

These profiles have been drawn over the water depth by considering the velocity and shear stress values when the alpha.water function varies in the range 0.5 – 1.

Figure 3-24 confirms some aspects of the water flow process discussed earlier, like the end of the transient phase around approximately 40 seconds of the simulated overflow. The predominant velocity component is U_x for which the peak velocity is observed at the downstream toe, while the lowest value occurs at the embankment crest. However, the contribution of U_y to the water flow, in the transversal direction, is not negligible and this is the reason why the resultant of the velocity vector has been considered in Figure 3-23. Under steady state conditions, the greatest water elevations are at the crest (i.e. 1.20 m) and at the lowest are at the downstream toe (i.e. 0.6 m) as shown already in Figure 3-22.

Most importantly, the velocity and the shear stresses profiles in Figure 3-24 and Figure 3-25 provide a good picture of the water flow near the embankment slope and prove that the simulation is in line with qualitative theoretical considerations. As expected, water velocity is zero at the embankment bed due to the no-slip boundary condition. The water velocity profile is characterised by significant gradients near the embankment surface and up to the peak value. This is not reached at the water surface elevation but at a certain water depth due to the water-air interactions at the free surface. Similar velocity profiles have been reported by the USGS as part of a data-collection and data-analysis program on the Lower Fox River in north-eastern Wisconsin (Stephen M. Westenbroek, 2006). The water velocity profiles were measured adopting a pulse-to-pulse coherent acoustic Doppler current meter (ADCP) attached to a boat with an adjustable rod. The method is based on the measurements of the Doppler shift of acoustic signals that are reflected by suspended matter within the water column. An example of the velocity profile measured during this investigation campaign is shown Figure 3-26 below. The author specifies that this profile is strongly affected by the presence of wind flowing in the opposite direction to the river flow. This situation presents some analogies with the overflow case, where the importance of the water-air interactions has been discussed.

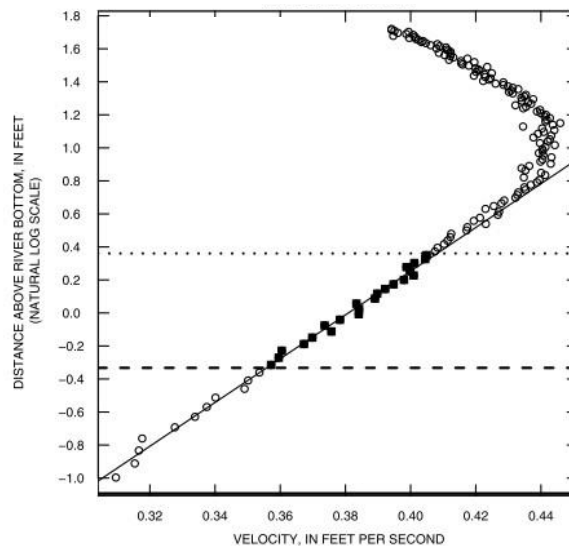


Figure 3-26: Example of water velocity profile measured with the ADCP technique during the data (Stephen M. Westenbroek, 2006)

The wall shear stresses have been calculated with post-processing utility of OpenFoam “wallShearStress” which calculates $\tau = \mathbf{R} \cdot \mathbf{n}$ (in $\text{m}^2 \text{s}^{-2}$), where \mathbf{R} is the shear-stress symmetric tensor retrieved from the turbulent model according to Equation A - 35 and \mathbf{n} is the normal vector to the patch. The results in Pa obtained by multiplying the Open Foam output by the water density show that τ_x is negative while τ_y is positive. This trend follows the analytical framework, for which the shear stresses are opposite to the water velocity vector. It is also important to highlight that the highest shear stresses have been calculated at the cross-section located at the middle of the downstream slope, where the velocity gradients are significantly higher whereas, as expected, the lowest values have been obtained at the embankment crest.

To consider the effects in the longitudinal and transverse directions, the resultant wall shear stress has been calculated. Figure 3-27 shows the shear stress distribution along the downstream slope at different time-steps. At the steady state, the peak is approximately 300 Pa and takes place just before the embankment toe, while the average value along the slope is 180 Pa.

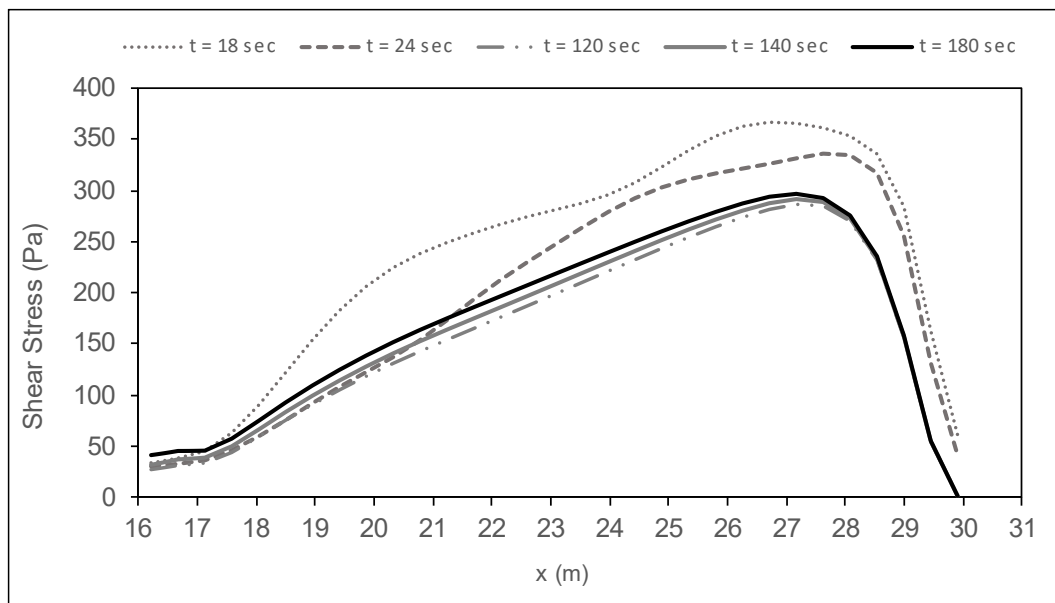


Figure 3-27: Resultant of the shear stresses distribution along the downstream slope at different time instants

The most appropriate approach to validate the numerical model is the direct measurements of water velocity and bed shear stresses with laboratory and field tests on real-scale flood defence embankments. This would require important resources, sophisticated instruments, safety issues and time. Furthermore, the problem of the validation of the hydraulic shear stress is out of the scope of the present work. Nevertheless, an assessment of the validity of the numerical results obtained is still necessary. Therefore, the validation of this numerical model has been conducted with reference to data found in literature on similar problems. The order of magnitude of the peak shear stress has been compared with values published by (Briaud *et al.*, 2008) as part of the work undertaken to study the embankments breaching failures by overtopping in New Orleans, occurred during Hurricane Katrina (2005). A CFD simulation was conducted with the program CHEN 3D to calculate the velocity fields and the bed shear stresses. The overtopping was simulated in a similar way to the present work, by adopting the RANS approach and an interface-capturing method for the air-water interface. On the other hand, the differences in terms of model set up should also be considered in this comparison. Particularly, the simulation conducted by Briaud *et al.* considered a landward side slope of 11.3° , and the overtopping was

triggered with an inlet water velocity in the longitudinal direction of 3 m s^{-1} , starting from an initial water elevation of 1 m above the embankment crest. On the contrary, in this study a steeper angle of 23° has been adopted.

In the initial condition of this simulation water elevation is 2 m below the embankment crest and an initial inlet velocity of 1 m s^{-1} . Figure 3-28 shows the shear stress distribution over the downstream slope at different instants (Briaud *et al.*, 2008). The steady state condition occurs after 3.19 seconds, and the peak shear stress is approximately 60 Pa in the toe area. This is an order of magnitude lower than the value obtained in the numerical simulation presented in this work. However, this is due to the fact that the embankment geometry adopted is not the same.

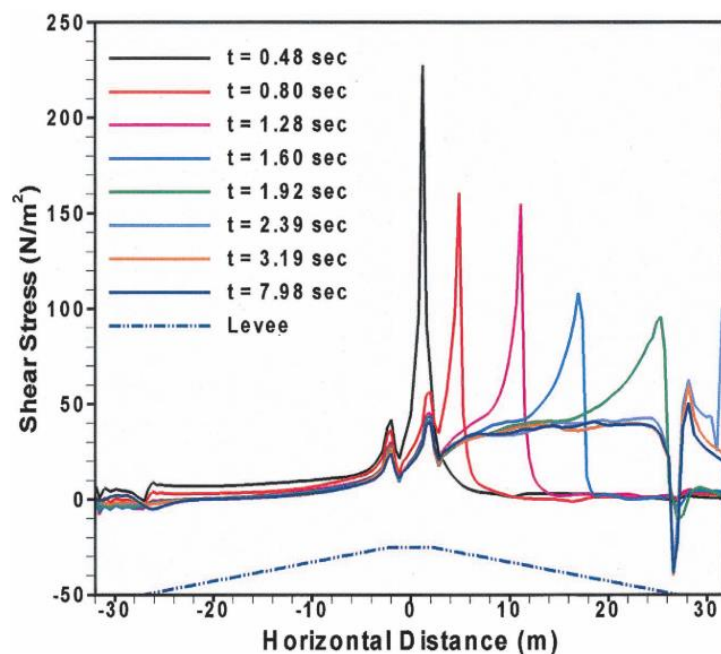


Figure 3-28: Shear stress distribution obtained performed with CHEN 3D (Briaud *et al.*, 2008)

To further validate the numerical result, an estimate of the shear stress has been derived with the following equation:

$$\tau = \gamma_w h S_f \quad \text{Equation 3-17}$$

where γ_w is the water unit weight (i.e. 10 kN m^{-3}), h (m) is the water depth perpendicular to the slope and S_f is the friction slope, with $S_f = \sin \alpha$ where α is the

slope angle of the landward side. The well-known empirical relation can be adopted to calculate the water discharge over a broad-crested weir (Chaudhry, 2008; Hughes, Shaw and Howard, 2012):

$$q = 0.5443 \sqrt{g} h_1^{3/2} \quad \text{Equation 3-18}$$

where q is the discharge per unit length ($\text{m}^3 \text{s}^{-1}$ per m), g is the gravitational acceleration (9.81 m s^{-2}), h_1 is the upstream water elevation. Ultimately, the mass continuity is applied:

$$h = \frac{q}{v} \quad \text{Equation 3-19}$$

In this way h over the slope is known and Equation 3-17 provides the bed shear stress. In this case the simulation shows that at the steady state condition $h_1 = 0.9\text{m}$ (corresponding to $\alpha.\text{water} = 1$, which means that only the water phase occupies the computational cells) therefore considering Equation 3-18:

$$q = 0.5443 \sqrt{g} h_1^{3/2} = 0.5443 \sqrt{9.81} 0.9^{3/2} = 1.45 \quad \text{m}^3 \text{s}^{-1} \text{ per m}$$

From Equation 3-19

$$h = \frac{q}{v} = \frac{1.45}{14} = 0.10 \text{ m}$$

And from Equation 3-17:

$$\tau = \gamma_w h S_f = 10 \cdot 0.1 \sin(23^\circ) = 0.40 \text{ kN m}^{-2} = 400 \text{ Pa}$$

which is of the same order of magnitude of the value obtained in the CFD simulation. This procedure is presented (Hughes, Shaw and Howard, 2012) in the Report for the experimental tests on small-scale earthen embankment as part of the Southeast Region Research Initiative (SERRI) program in Tennessee. Ultimately, the shear stress distribution at 180 seconds resulting from the hydrodynamic analysis has been adopted to investigate the embankment stability.

3.7.2 Water Flow Analysis in Plaxis 2D

The distributions with depth of effective suction (i.e. the product suction times degree of saturation) are shown in Figure 3-29 for different calculation stages: at the initial river level (brown line); at 10 hours from the start of the flood event when the water level in the river reaches the embankment crest (blue line); after 5 and 15 minutes from the start of the overflow (dotted light blue line and point-dotted black line, respectively). The contour plot of the pore water pressure distribution extracted from Plaxis 2D at the end of the overflow phase is presented in Figure 3-30. The convention adopted in Plaxis is that negative values indicate positive pore-water pressure, hence positive values are for suctions. It can be immediately observed that the toe area is in fully saturated conditions after 15 minutes of overflow, however at the embankment crest there still a suction of approximately 60 kNm^{-2} .

Four locations along the embankment crest and downstream slope have been selected to analyse how the degree of saturation and suction values vary within the embankment body. Prior to the overflow event, the pore-water pressure is characterised by a quasi-hydrostatic distribution as indicated by the initial river level and the 10-hour flood curves.

The cross-section A-A* passing through the centre of the embankment crest, is characterised by the highest suction values at the highest elevation. Suction decreases with depth as the embankment material goes from a quasi-saturated state to full saturation achieved below the embankment foundation level (Figure 3-29a). Suction values on the surface become lower and lower while moving towards the downstream toe. It is worth noticing that cross-section D-D* shows the same suction distribution for the 10-hour flood and for all the overflow time-steps analysed. In fact, when the overflow occurs this part of the embankment is already in a fully saturated state (Figure 3-29d). On the contrary, the intermediate locations along the downstream slope, show a progressive reduction of suction with depth, from the start to the end of overflow. It is worth observing that this decrease of suction from the surface downwards is more gradual for cross-sections B-B* and C-C* than cross-section A-A*. For this latter, in fact, suction varies from 2.7 kN/m^2 on the surface (as consequence of the overflow) to

57 kN/m² at a depth of 24 cm below the embankment surface. This means that suction gradients on the crest are higher than elsewhere.

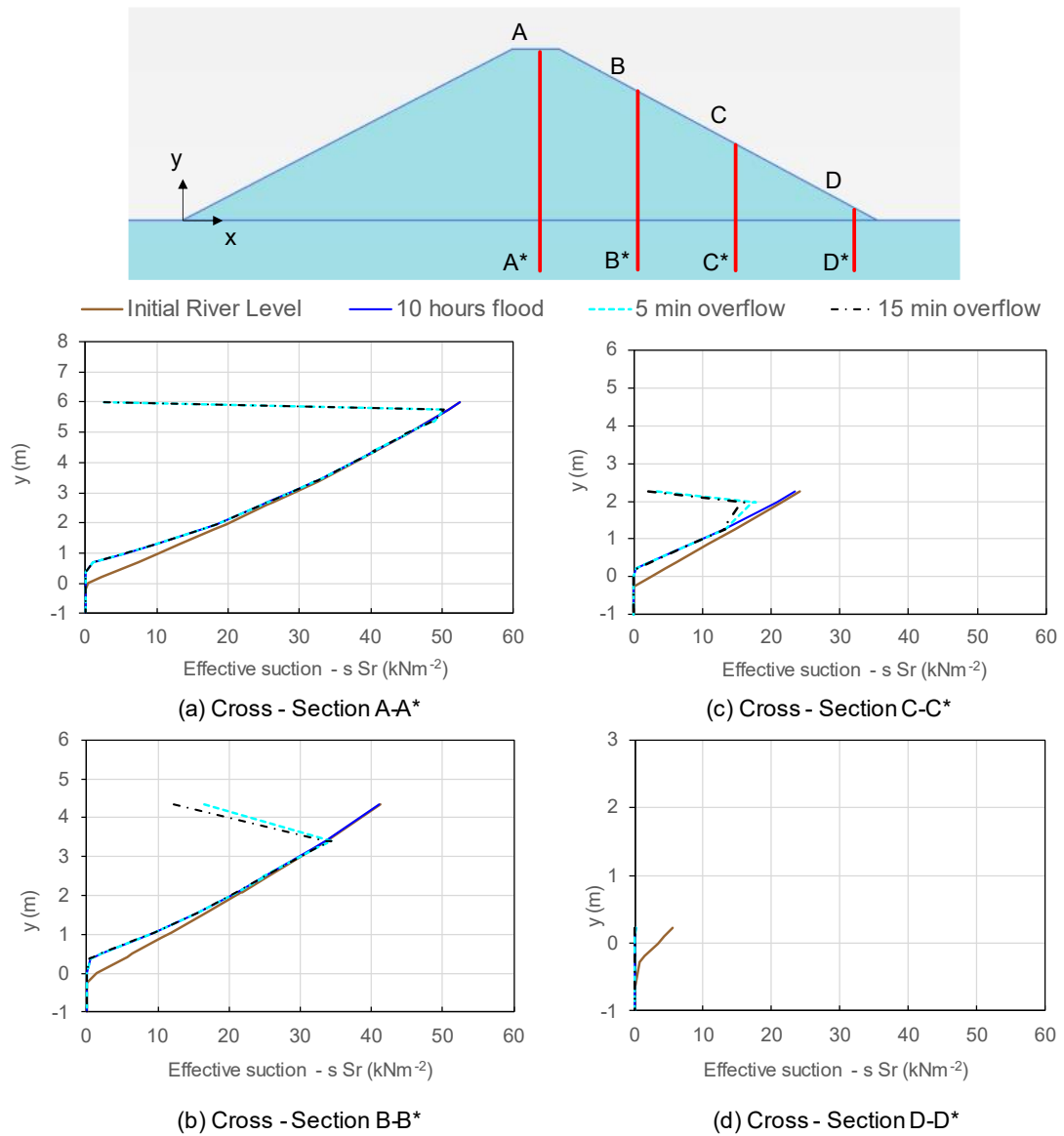


Figure 3-29: Effective suction distribution at four different embankment locations: (a) crest, (b) at approximately one third of the downstream slope; (2) at approximately two third of the downstream slope; (3) near the downstream toe. The Time Step selected are the initial river level (brown line); 10 hours flood (blue line), 5 min overflow (dotted light blue line) and 15 min overflow (discontinues black line)

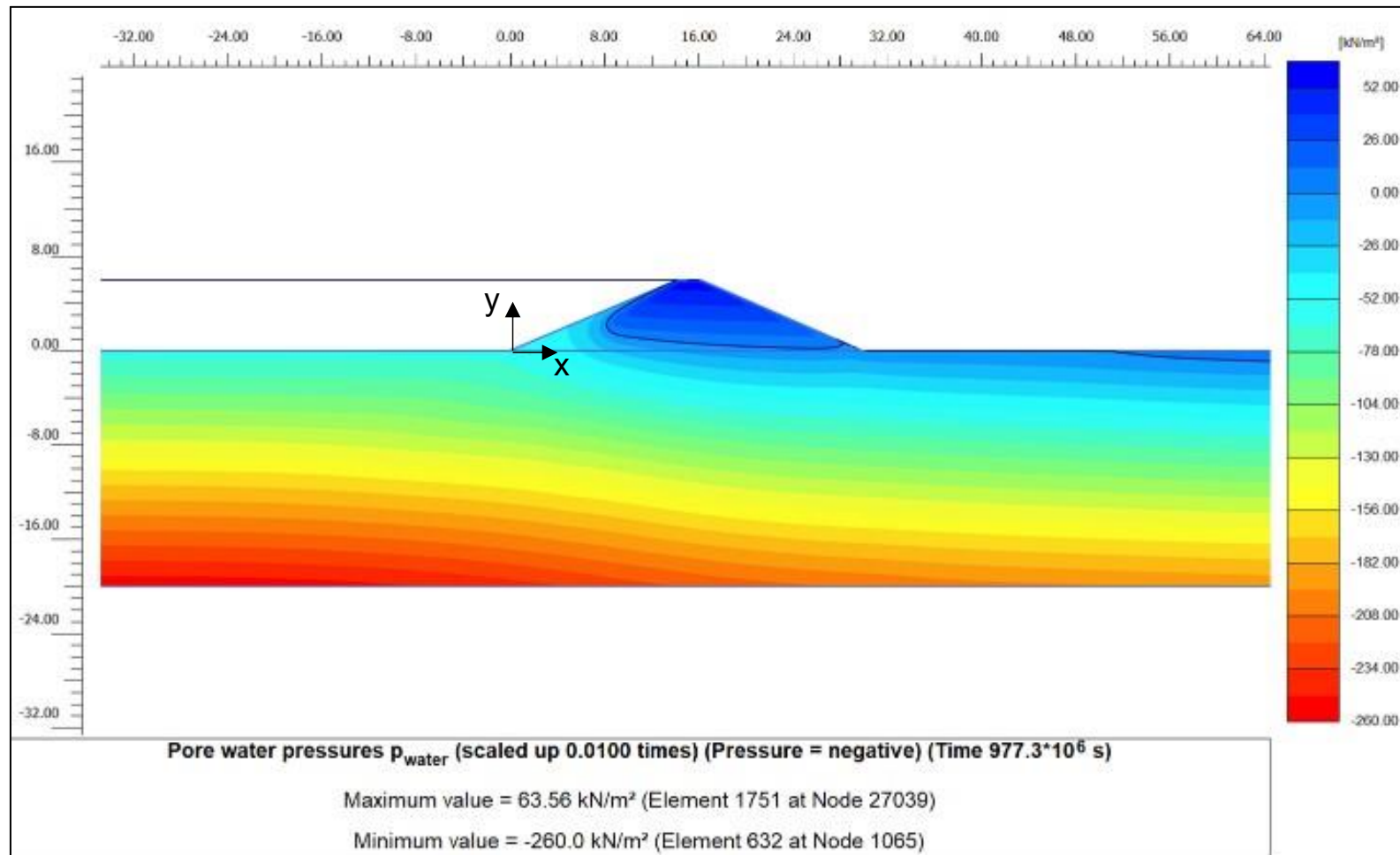


Figure 3-30: Contour plot of the pore water pressure distribution at the end of the overflow phase

It is also interesting to point out that the differences between suction distribution for the two overflow times considered are negligible for the cross-section at the crest and at the toe. In the first case, this is because the time of infiltration considered is not sufficient to determine tangible changes. In fact, the hydraulic conductivity in this range of suctions is still considerably low. At the toe, instead, the saturated conditions are established already from the beginning of the extreme weather event. For completeness, the variation of the hydraulic conductivity with depth for the four cross-sections is shown in Figure 3-31.

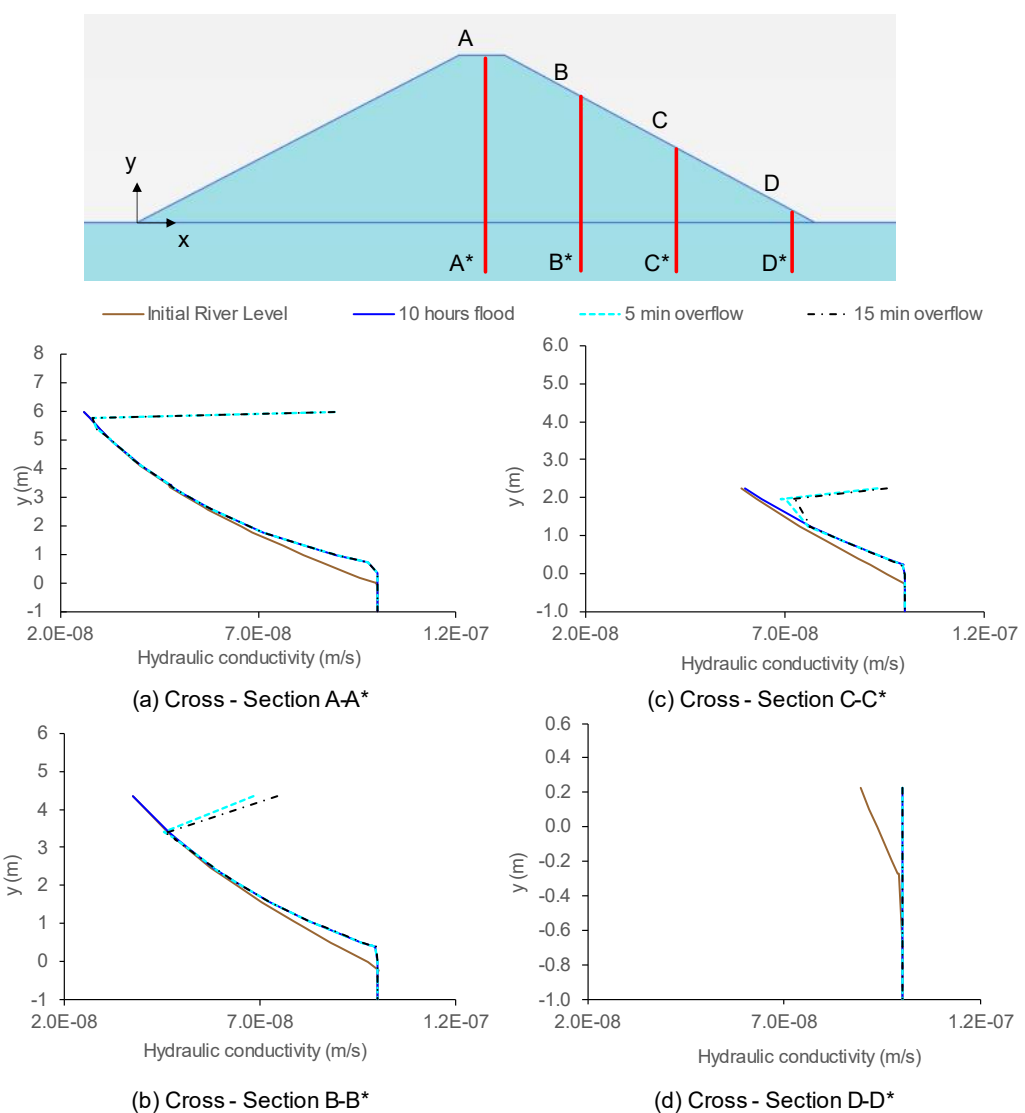
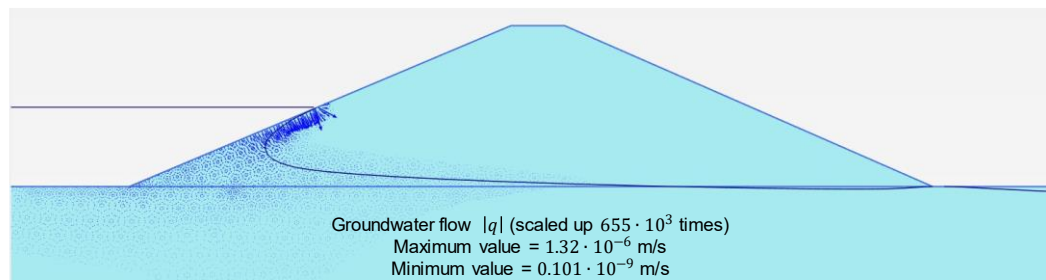


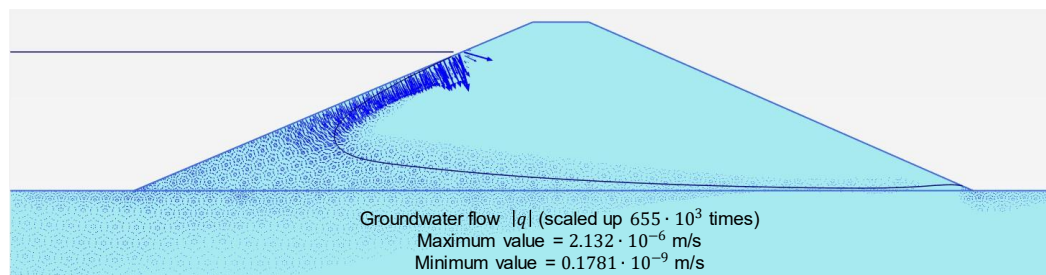
Figure 3-31: Selected time-step of Hydraulic conductivity at: (a) embankment crest; (b) one third of the downstream slope; (c) tow third of the downstream slope; (d) downstream toe

Again, these plots confirm that the effects of the infiltration processes are less important at the embankment crest, which remains in a quasi-saturated state for the entire duration of the overflow.

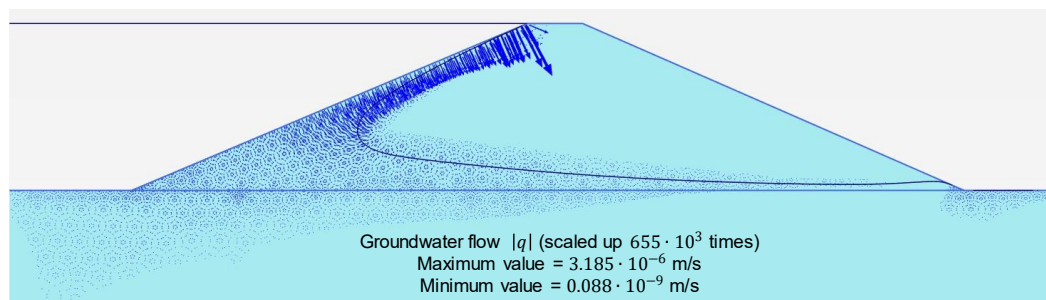
Figure 3-32 shows the progressive increase of the water levels imposed by the time-dependent boundary condition on the upstream side. The blue line indicates the position of the phreatic surface and therefore the advancement of the saturation front within the embankment body. Figure 3-32d refers to the final step of the overflow phase, with groundwater flow occurring from the downstream slope in a sub-orthogonal direction towards the inner part of the structure. It is worth noticing again that the downstream toe is saturated since the early stage of the flood event simulated.



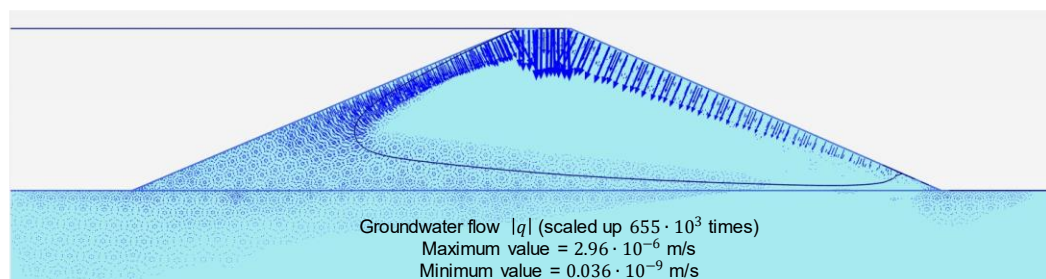
(a) Increase water level stage (5 hours filling phase)



(b) Increase water level stage (8 hours filling)



(c) Increase water level (10 hours filling)

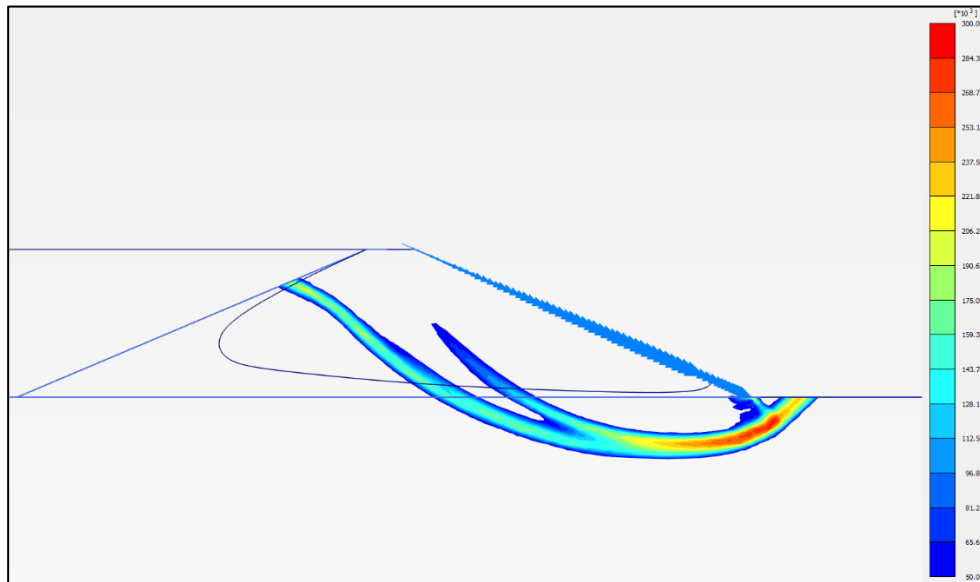


(d) Overflow (15 minutes)

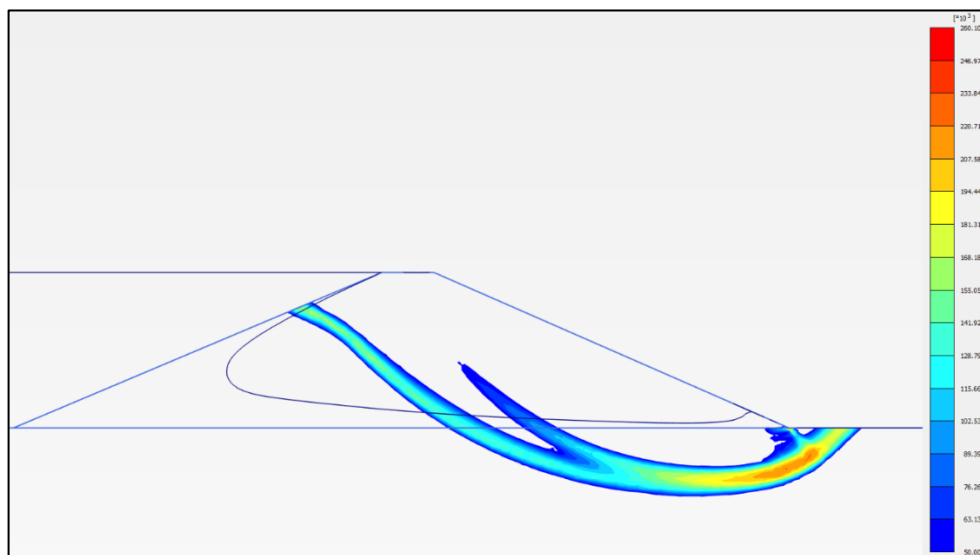
Figure 3-32: Water flow at selected time-steps from the increase water level phase: after (a) 5 hours; (b) 8 hours; (c) 10 hours and water level at the crest; (d) 15 minutes of overflow

3.7.3 Stability analysis in Plaxis 2D

The global factor of safety (FoS) of the overflow phase is plotted for the two scenarios studied.



(a) Phase deviatoric strain for the overflow with hydraulic shear stress (max $292.7 \cdot 10^3$ – min $0.0104 \cdot 10^{-3}$)



(b) Phase deviatoric strain for the overflow without hydraulic shear stress (max $260.1 \cdot 10^3$ – min $0.012 \cdot 10^{-3}$)

Figure 3-33: Failure mechanisms for (a) overflow with hydraulic shear stresses; (b) overflow without hydraulic shear stresses

It is worth highlighting that the resulting shear band associated with the FoS is qualitatively the same for the two overflow cases as it can be observed in Figure 3-33.

The main difference is that the maximum deviatoric strain is slightly higher in Figure 3-33a than Figure 3-33b because of the presence of additional applied tangential forces along the slope. At the same time, this difference is negligible because the failure mechanism is fully developed in both cases with the highest strain concentrated at the downstream toe.

A negligible difference is also shown in terms of values of the FoS as it can be easily observed in Figure 3-34.

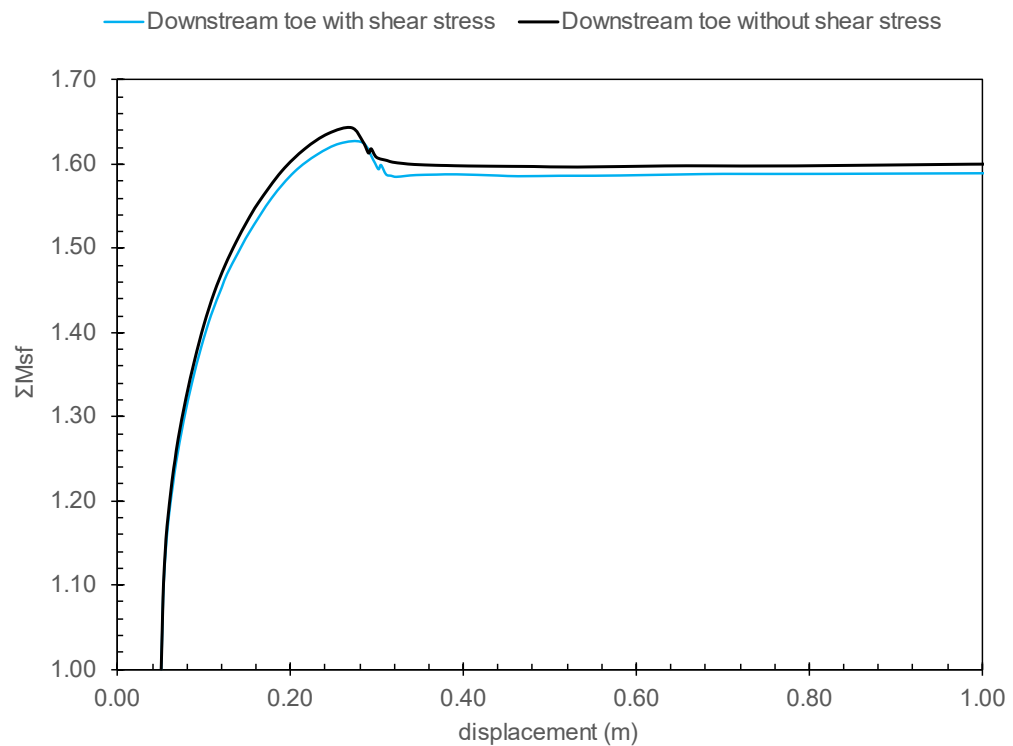


Figure 3-34: Factor of Safety resulting from the Safety analysis for the two scenarios analysed with and without hydraulic shear stresses

The overflow without shear stress presents a FoS of 1.60, while the application of the hydraulic shear stresses produces a FoS of 1.59.

3.8 Conclusions

A new conceptual model to interpret the onset of overflow-induced breaching has been introduced for the first time, within the theoretical framework of unsaturated soil mechanics. The qualitative analysis of the responses of fine- and coarse-grained soils to multiple transient water flow processes, led to the conclusion that breach initiation mechanisms can be associated with a loss of shear strength due to the decrease of suction and the increase of saturation, as a result of the advancing of two water fronts: one from upstream side and one from the overflowed downstream slope. In this way, the new conceptual model provides an alternative explanation to soil erodibility and hydrodynamic effects, traditionally invoked to model embankment breaching mechanisms.

To prove the new model concept, the dominant triggering factors for breach onset have been investigated. The focus was on two fundamental aspects: (1) the destabilising effects associated with the hydrodynamic shear stresses; (2) the reduction in shear strength of the embankment material due to the progressive loss of suction during flood conditions. To understand the relative importance of these two sources of instability, the Factor of Safety (FoS) and the associated failure mechanisms have been assessed for an ideal homogeneous embankment, with and without the application of the hydrodynamic shear stresses along the downstream slope.

The hydrodynamic shear stresses were calculated with the Computational Fluid Dynamic (CFD) software Open Foam, adopting the *SST* $k - \omega$ turbulence model. As expected, at steady state, the lowest shear stresses were found at the embankment crest, while the peak shear stresses occurred at the embankment toe area. It was shown that the order of magnitude of hydrodynamic shear stresses is ~ 300 Pa and these values were in good agreement with: (1) similar studies published in literature, (2) approximate hand-calculations and (3) analytical predictions.

The same embankment geometry was modelled in the FEM software Plaxis 2D to analyse the onset of instability. Seven calculation phases have been considered to simulate a typical sequence of events prior to the overflow scenario. The impacts of model parameters, like the initial position of the water table and the time assumed to

fill the water body behind the embankment have been discussed. It was concluded that particularly for fine-grained materials, these aspects are less important for the time-scales of the processes studied. However, sensitivity analysis is recommended, especially when coarse-grained materials are considered.

A safety analysis according to the strength reduction method was conducted at the end of the overflow phase to determine the global factor of safety and the relative failure surface. Two distinctive models have been run, with and without the application of hydraulic shear stresses calculated with the CFD model.

The FEM results of the transient water flow process confirmed the qualitative predictions of the conceptual model. The crest was characterised by the highest suction values. For the type of material considered, an ideal silty clay, the embankment crest remained in a quasi-saturated state during the whole simulation. On the other hand, the toe was found already in fully saturated conditions at the onset of overflow. Along the downstream slope, a progressive reduction of suction with depth is simulated while the overflow takes place. The decrease of suction from the surface downwards is more gradual in the middle zone of the downstream slope than the crest. Overall, the effects of the infiltration processes were less critical at the embankment crest level than the middle and toe areas.

The global stability analysis reveals that the failure mechanisms and the associated Factors of Safety are found to be practically equal for the overflow with and without the hydrodynamic tangential stresses. A fully developed failure mechanism with the highest deviatoric strain concentrated at the downstream toe is observed in both cases. The negligible effects of the hydrodynamic tangential stresses on the overall embankment stability are due to the order of magnitude of these stresses (i.e. 0.1 – 0.3 kN/m²) being very low compared to the applied loading typically encountered in geotechnical engineering problems. However, hydraulic shear stresses can play a more significant role at shallow depth, where due to the overflow, suction drops to zero and the effective stress are low. It was shown that this situation is particularly critical for coarse-grained material, where effective cohesion is absent. In fine-grained materials, instead, the stabilisation provided by the effective cohesion implies that when a failure mechanism occurs, this will involve larger volume of soil rather than shallow layers,

like in the headcutting process.

In conclusion, this comparative study provided a partial answer to *Research Question #2: is the hydrodynamic shear stress exerted by the water flow the only possible triggering mechanism for soil mobilisation or are there other factors that can play a role?* It was demonstrated that, at the onset of overflow, the global stability of the downstream slope is not affected by the water entrainment forces developed at the soil-water interface. Hence, the fundamental conclusion is that at the onset of overflow hydrodynamic effects can be neglected in first instance in the analysis of breaching initiation processes, at embankment scale.

Chapter 4. Unsaturated Soil Mechanics

Breaching Model: Development of the Numerical Approach

Abstract

Overflow-induced breaching is a major mechanism of failure of flood defence embankments. Two distinct macro-erosion processes are generally associated with coarse- and fine-grained geomaterials that are, respectively, surface erosion and headcutting. However, most recent investigations emphasize unexpected and mixed behaviours observed experimentally, where the formation and propagation of an headcut tends to occur also in coarse-grained embankments. The assumption made in this work is that, regardless the nature of the embankment material, the onset of failure can be associated with a loss of shear strength of the constituting soil due to the decrease of suction and the increase of the degree of saturation as a result of the advancing of two water fronts, one from upstream side and one from the overflowed downstream slope. This chapter presents the numerical implementation of the new suction-based breaching model.

4.1 Introduction

Flood earthen embankments are water retaining structures constructed along rivers and coastal lines with the primary function of protecting human lives and activities against the threats of floods. These constitute the principal infrastructure of a flood defence system with several hundreds of thousands of kilometres all over the world (CIRIA, 2013). There is a long list of historical and recent events revealing the vulnerability of this form of protection. Hurricane Katrina in U.S. (2005), Cyclone Cynthia in Western Europe (2010), the North Sea tidal surge (2013) in UK and Netherlands, are just a few examples of disastrous floods, whose impacts were significantly aggravated by the

breaching of the flood defence embankments.

Unlike non-erodible structures that tend to break almost instantaneously, the breaching process of earthen embankment is generally gradual and comprises a series of time-dependent mechanisms leading to breach initiation and formation. Breach growth may result in the final catastrophic failure, when a gap or a proper channel develops across the embankment allowing the inundation of the protected areas (Figure 4-1).



Figure 4-1: Examples of Breaches in riverine embankments. (a) Croston Breach Winter Floods 2015/2016, Lancashire (Simm et al., 2017); (b) Tetney Breach, Yorkshire, 5th December 2013 (Environment Agency, UK)

The crucial role played by earthen embankments in the struggle against floods, the increasing risks posed by more severe flood conditions due to climate change and urbanisation and a general lack of knowledge of the physical processes involved, are all urgencies that have attracted the attention of Operating Authorities and scientific community and are currently considered critical priorities. In addition, understanding the performance of flood defence embankments, particularly during extreme weather events, can help identify the most effective improvement works and maintenance strategies to retrofit existing structures and design more resistant new ones (Mark Morris, Dyer and Smith, 2007).

The first and most immediate source of information to study embankment performance is the analysis of case studies and post-failure investigations. The main triggering mechanisms identified for breach initiation are surface erosion of the

landward slope due to overtopping/overflow, internal erosion associated to seepage flow and piping, and structural failures due to slope instabilities or foundation issues. Although these processes may act simultaneously, external erosion induced by overflow has been recognised as the most frequent cause of embankment breaching (Costa, 1985; Foster, Fell and Spannagle, 2000). This applies for levees as well as for dams.

Powledge et al., (Powledge et al., 1989) summarised the most important research in UK and USA conducted during the 80s. The three hydrodynamic flow regimes typically occurring during embankment overflow are associated with erosion zones based on the relative energy of the sub-critical, critical and super-critical flows respectively (Figure 4-2). According to this approach, the most serious condition is related to the third zone along the downstream slope, where flow becomes supercritical and exerts the highest dragging forces. When these forces exceed the critical resistance of the material, erosion processes are activated.

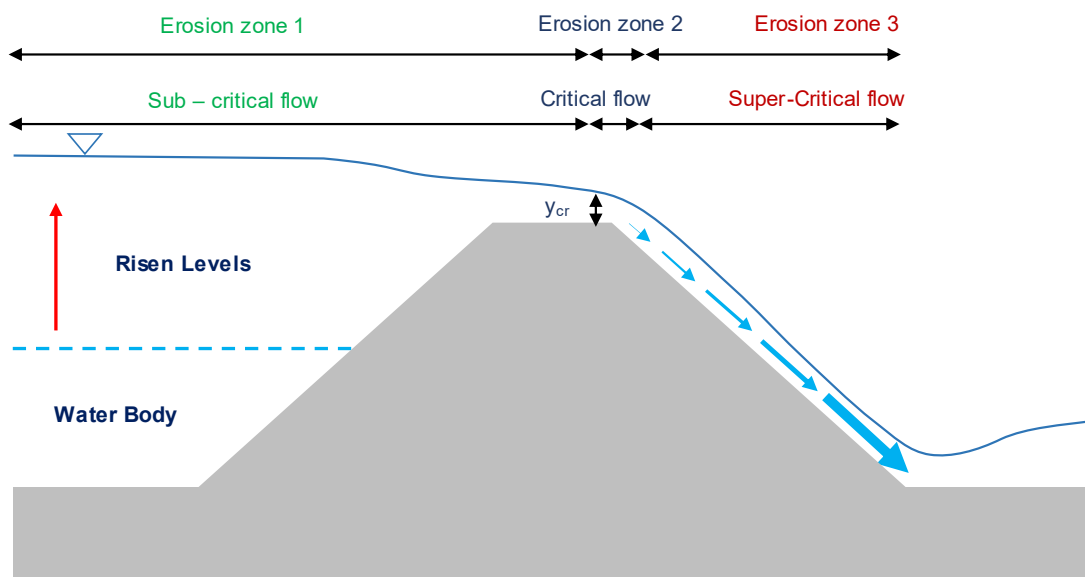


Figure 4-2: Typical hydraulics of embankment overflow and associated erosion zones after (George R Powledge et al., 1989)

Erosion can occur at any point of the slope, depending on local discontinuities and concentration of stresses, but very often the starting point is the toe where the water flow tends to dissipate its energy because of the sharp change of slope. Initially a small

overflow and a scour hole have been commonly observed. Their enlargement is directly related to the type of material forming the embankment. The authors observed that in fine-grained soils overfalls are higher and more stable than in coarse-grained geomaterials.

Most recently, significant progresses have been achieved thanks to experimental campaigns conducted as part of research programmes in Europe and USA. CADAM (Concerted action on dambreak modelling, 1998-2000), IMPACT (Investigation of Extreme Flood Processes & Uncertainty, 2001-2005), FLOODSite (2004-2009), FloodProBe (2009-2013) are the most important projects supported by the European Commission, with specific tasks dedicated to the analysis of the breaching initiation process. In the same years, in U.S. the USDA - ARS, (Agricultural Research Service, Stillwater, Oklahoma), Bureau of Reclamation - Dam Safety Office, U.S. Geological Survey and other operating organisations promoted studies in this field.

This research highlighted that the most important factors influencing the breaching processes are the type of embankment structures (i.e. homogeneous, composite, presence of additional structures), the hydraulic loads (i.e. reservoir, fluvial or costal/estuarine embankments), the construction materials (i.e. fine-grained fill, coarse-grained fill or rock-fill) and their relative conditions (i.e. soil compaction and water content).

These experiments suggest that two main erosion mechanisms are associated with breach formation in fine-grained and coarse-grained embankment fills respectively (ASCE/EWRI Task Committee on Dam/Levee Breaching, 2011). Progressive surface erosion is typically observed in coarse-grained materials (i.e. sand and gravel), which are commonly recognised as highly erodible. The failure mechanism consists in the removal of soil, layer by layer, from the downstream face and from the crest. The eroded surface progressively retreats towards the inner part of the structure, flattening the slope and lowering the crest (Figure 4-3).

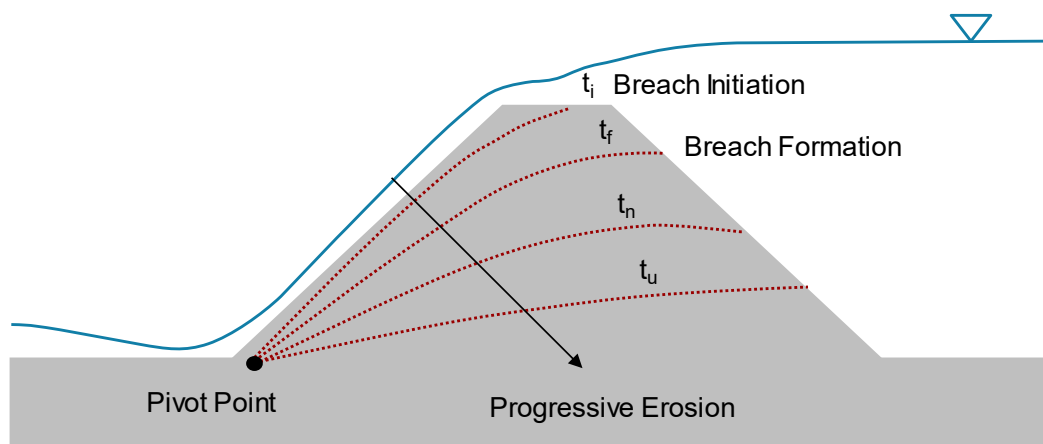


Figure 4-3: Schematic layout of progressive surface erosion characteristic of the breaching process of coarse-grained embankment fills

The overall failure process is very rapid as the upstream crest is often affected since the early stage of erosion, thus increasing the water flow through the breach formed (Morris *et al.*, 2009; ASCE/EWRI Task Committee on Dam/Levee Breaching, 2011; Zhu *et al.*, 2011; Volz, 2013; Zhang *et al.*, 2016).

The predominant erosion mechanism observed during overflow of embankment constructed with fine-grained soils is known as headcut erosion. Hanson *et al.*, (G. J. Hanson, K. R. Cook and S. L. Britton, 2003) define the headcut as a vertical or sub-vertical drop of the bed channel. Figure 4-4 below shows a the headcutting erosion process. This consists in the formation of a stepped, non-uniform profile of the landward slope.

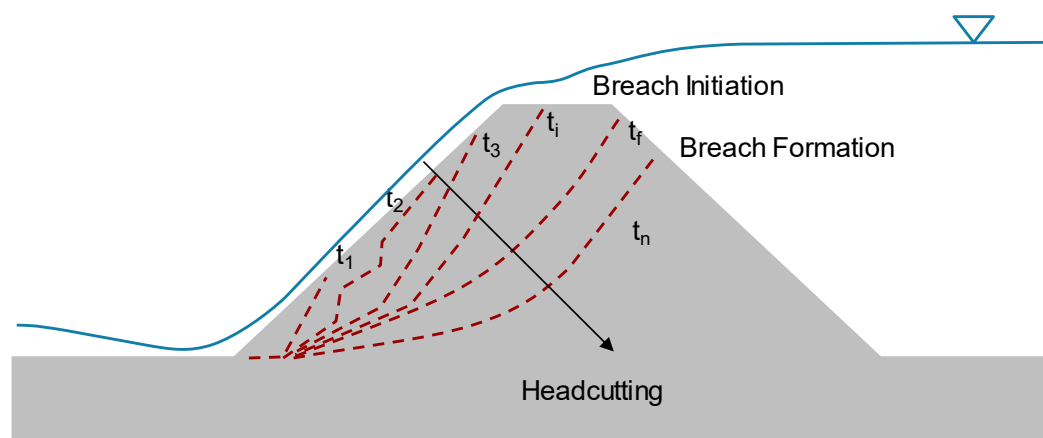


Figure 4-4: Schematic layout of headcut erosion characteristic of the breaching process of fine-grained embankment fills

Initially, small steps (i.e. headcuts) are observed at the downstream toe (Wahl, 1998; Morris, 2009; Zhang *et al.*, 2016). These tend to merge into several or even a single larger headcut that progressively propagates backwards, undercutting the slope. The critical condition occurs when the headcut propagation arrives at the crest, resulting in its lowering and hence in an increase of the discharge. This stage is known as breach formation. At this point, headcut and surface erosion tend to assume the same characteristics resulting in breach widening and growth, up to the final failure. It is worth noticing that the two erosion mechanisms directly affect the time of breach formation. It is recognized that fine-grained geomaterials are typically less erodible than coarse-grained fills and consequently the process of headcutting is much slower than progressive surface erosion (Morris *et al.*, 2009).

The occurrence of these two different modes of failure has been explained with reference to the strength and erodibility properties exhibited by coarse-grained and fine-grained materials (Figure 4-5).

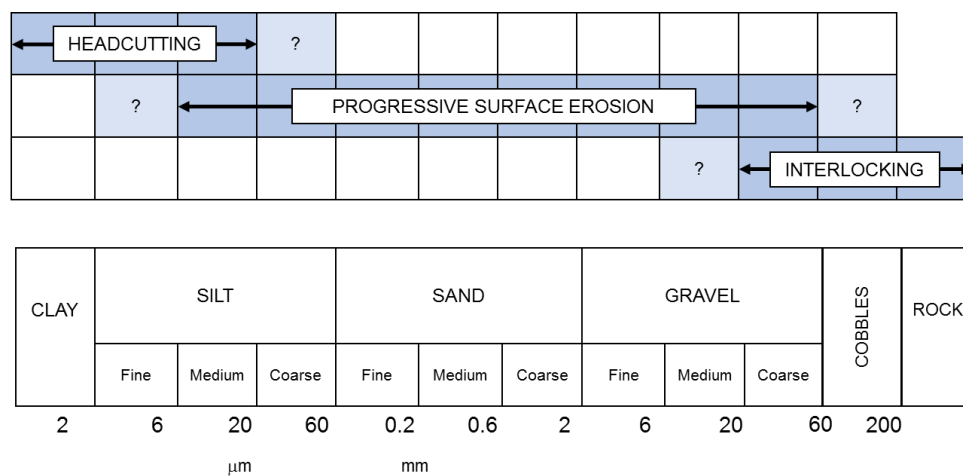


Figure 4-5: Classification of erosion processes based on grain size where uncertainties are emphasised with question marks after (Morris, 2011)

However, a more complex dynamics combining surface and headcut mechanisms has been observed and regions of overlapping behaviours still need to be understood (Hanson *et al.*, 2011; Morris, 2011; Zhu *et al.*, 2011; Mizutani *et al.*, 2013; Wei *et al.*, 2016). These aspects are the core of current research (Mitchell and Brown, 2018; West, Morris and Hassan, 2018). Based on recent experimental studies mainly at laboratory

scale, it appears that headcut erosion also occurs in coarse-grained embankments when the material properties are enhanced through compaction and when negative pore-water pressures exist.

An extensive experimental programme was conducted at the Hydraulic Laboratory of the University of Ottawa to investigate the behaviour of unsaturated soils and their influence on breaching processes (Al-Riffai *et al.*, 2009; Al-Riffai and Nistor, 2010, 2013; Al-Riffai, 2014). Small- and large-scale homogeneous coarse-grained embankment models were constructed by compacting sand in successive layers. Different compaction efforts were considered within the compaction test series. In parallel, another test series was performed with and without the installation of a toe-drain. During the tests, water surface level and pore-water pressures were measured.

The most important results of these tests revealed that compaction efforts had the effect to increase the erosion resistance of the material. Side-slope failures of the breach channel were less frequent for higher compaction and when the drainage system was present. The lag-time (i.e. time between the start of the overflow and the peak discharge through the breach) resulted longer for the tests with the toe-drain and for the denser soil, compared to models without seepage control and with low compacted filling. The presence of a drainage system creates a larger unsaturated zone and the time delay observed in the breach formation is due to the infiltration process resulting in the saturation of the soil on the downstream side, while in tests without drainage the saturation is more rapid. In conclusion, these series of experiments showed that the physical processes associated to embankment overflow should be analysed considering the influence of fundamental geotechnical aspects such as degree of saturation and density. Unsaturation and compaction had both the effect to delay the breach formation.

Pickert *et al.*, (Pickert, Weitbrecht and Bieberstein, 2011) performed a series of small-scale overflow tests on homogenous embankments constructed with coarse, medium and fine sands on fixed bed. The embankments tested were equipped with instrumentation to measure water levels, breach discharge, erosion rate, breach side slope and pore-water pressures. One of the key results was that breaching evolved more rapidly for the coarse sand and the process was characterised by a constant

erosion rate. On the contrary, erosion in fine sands was found to be unsteady and influenced by apparent cohesion. Vertical and overhanging breach side slopes were also noticed. In general, different erosion behaviours were observed as result of the presence of an unsaturated zone. The authors concluded that a general classification of the breach profile is difficult because of the influence of the suction-induced apparent cohesion and various erosive behaviours.

The U.S. Geological Survey conducted three experimental campaigns between 2010-2013 to investigate the overflow failure of 13 large-scale dams built with compacted sand. During the construction of the embankment, piezometers and tensiometers were placed in different zones at various heights. Particle image velocimetry (PIV) was used to determine the water-surface velocity. Photogrammetric analysis was used to define the water surface elevation and the evolution of the embankment profile. A stepped longitudinal profile was observed (Figure 4-6a). The upstream migration of the steps evolved in the formation of a headcut (Figure 4-6b), which eventually merged with the embankment crest.

Local failure of soil blocks formed a nearly vertical profile of the breach banks. This was attributed to the effect of suction-induced apparent cohesion. The groundwater flow analysis calibrated against the pore-water pressures measured was performed for two of the thirteen experiments. Difference in the progression of the breach were related to differences in the suction profiles. The banks of the breach channel were more stable at greater heights for the experiment with the highest suctions (Walder, 2015).

This review of the most important experimental studies of the past two decades shows that a substantial improvement of knowledge and understanding of the physical mechanisms responsible for breach onset and progression has been achieved. This can be considered as the first step for the development of the last generation of simulation tools able to predict modes and times of failure, providing key information for flood risk assessment, flood forecasting and early warning system. All these researches emphasize that breach initiation and formation is a multi-disciplinary and multivariable problem which depends on the mutual interactions between water flow, soil and structure (ASCE/EWRI Task Committee on Dam/Levee Breaching, 2011).

Hence, predictive models should consider a reasonable number of these variables and processes to simulate the different physical aspects of embankment breaching, the various types of materials and structures that might be encountered. In particular, the role of suction and partial saturation of the embankment in the initiation and progress of erosion eventually leading to breaching does not appear to have been investigated in a consistent and robust fashion.

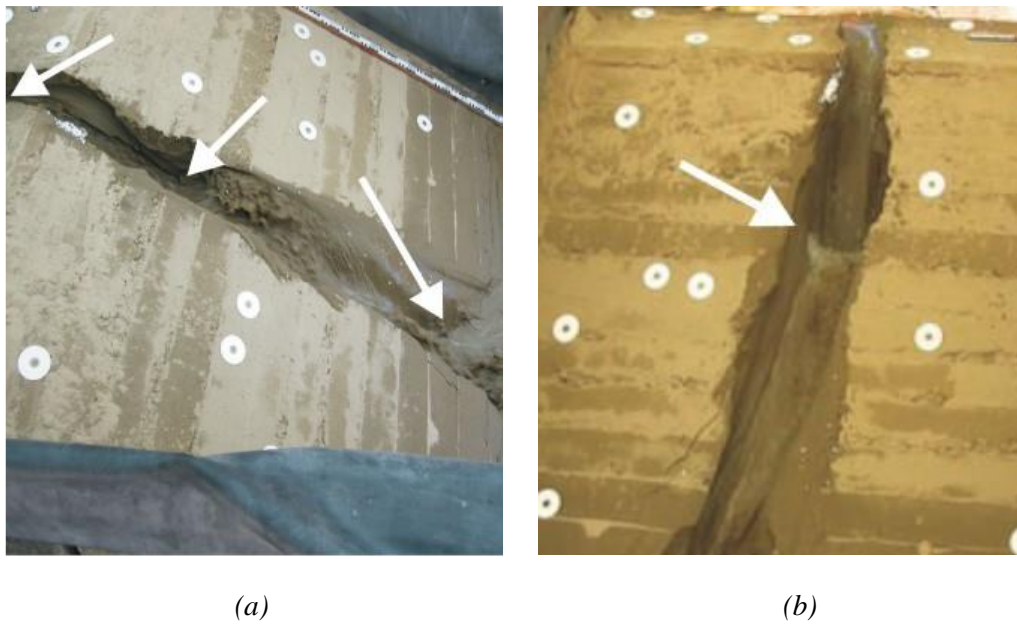


Figure 4-6: Images collected during one of the experiments conducted at the U.S. Geological Survey on large-scale embankment constructed with fine sand. (a) formation of the stepped profile and (b) migration of the steps upstream forming a single large headcut. White arrows indicate the base of the steps and headcut. After Walder et al. (Walder et al., 2015)

4.2 Breaching models

The focus of a breach model is the prediction of the processes and breach characteristics (i.e. shape, size, formation time), the routing of the upstream inflows and the outflow hydrograph. In this analysis the first task is known to be the most uncertain of all the problems related to flood forecasting (Wahl, 1998; Mohamed *et al.*, 2002; Zhu, Visser and Vrijling, 2004; ASCE/EWRI Task Committee on Dam/Levee Breaching, 2011).

Different authors proposed different classification systems. In paragraph 2.4 the

classification introduced by Morris et al. (Morris *et al.*, 2009) has been presented while here it is made reference to the one proposed by Wahl (Wahl, 1998) where four categories are identified: (1) comparative analysis, when breach parameters are estimated based on similarities with failed dams for which an extensive documentation can be used for comparisons; (2) non-physically based methods, adopt predictive equations statistically derived through the regression analysis of data collected from historical failures, (3) semi-physical based models, introduce some of the physical processes of breaching but with strong simplified assumptions; (4) physically based models, that are typically numerical methods applying principles of hydraulics, erosion and soil mechanics to simulate the fundamental mechanisms observed during breach formation and progression.

In any case, the last category adopts the most rigorous approach, aiming to provide a complete and accurate prediction of embankment breaching, required moreover for area and situation where flood risk is particularly serious and/or there are no or little data of historical failures.

Many physically based models have been proposed over the last forty years ranging in complexity, assumptions, and methodology adopted. A historical overview of the numerical model development and a long list of available models (about 55 different breaching models) can be found in (Wahl, 1998; Morris and Hassan, 2002; Zhu, 2006; Morris, 2011). An extract of these models with the main characteristics has been provided in Table 2-1 at paragraph 2.4. A more detailed description of the most recent and promising methods is provided by Zhong et al. (Zhong *et al.*, 2016) and West et al. (West, Morris and Hassan, 2018).

Despite the substantial differences existing between the various breaching models proposed, a common approach can be identified.

In general, a physically based model comprises: (1) a hydraulic/hydrodynamic sub-model to simulate the water flow processes (i.e. overflow and/or overtopping and/or piping) which calculates the discharge through the breach, the water velocity field and hence the hydraulic shear stresses exerted at the interface water - soil; (2) a sediment transport/erosion sub-model, which defines the soil erosion rate and the volume of material removed under the stresses calculated in the hydraulic model; (3)

a slope stability sub-model can be present to analyse the conditions of the breach side-slopes; (4) a breach morphology model updates the breach cross-section, reflecting the material removed due to erosion and slope instabilities.

These sub-models are typically organized in a loop as shown in Figure 4-7, such that at each time-step the breach shape (i.e. breach morphology) is obtained as result of the erosion and slope instabilities processes due to the water flow induced by overflow/overtopping or piping. When a cycle is completed, the following starts with the calculation of the water flow in the new breach configuration and the various sub-models are repeated.

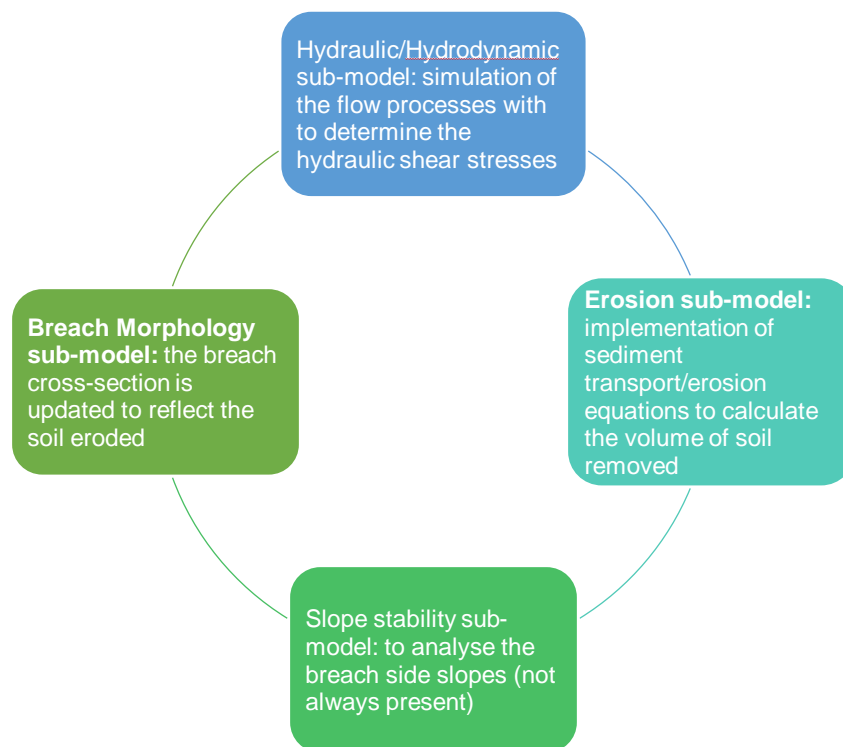


Figure 4-7: Typical loop with sub-models constituting physically-based breaching models

The oldest models (Cristofano, 1965; BRDAM, 1967; Lou, 1981; DAMBRK, 1984; BEED, 1985, NWS Breach, 1988; DEICH_N1 and DEICH_N2, 1998; BRES, 1998; BRES, 2006; HR Breach, 2002; WinDAM/SIMBA, 2005) were based on simplified assumptions like the use of the broad crested weir formula or the 1D Saint Venant equations to model the hydraulic processes. This approach tends to simplify the mathematical aspects and is based on the hypothesis of small channel bed slope

and steady-state flow resistance laws for the derivation of bed shear stresses (i.e. Manning Equation), which are quite far from reality (i.e. steep embankment slope and transient flow conditions). Significant limitations are related to the assumption of the breach shape, which is normally pre-defined in input (i.e. rectangular, trapezoidal or parabolic) rather than an output of the model. Also, erosion of the breach is simulated as a uniform process, which is deeply unrealistic as different zones erode at different erosion rates. A very critical aspect is the choice of the sediment transport/erosion equation to be implemented. This is traditionally a field of river hydraulics and the various studies conducted allowed to derive sediment transport equations for steady-state sub-critical flow and for specific sediment types and sizes. On the contrary, during the overflow of embankments different materials may be involved and the flow is typically unsteady. Hence the application of sediment transport equations leads to unrealistic erosion sub-model. Ultimately, the assessment of the stability of the breach side-slope and other soil mechanics aspects are normally neglected or over-simplified (Mohamed *et al.*, 2002). All these assumptions had the advantage to set up very simple physically based models, but the processes simulated are very far from reality.

The last generation of physically based models produced is often the result of improvements of previous versions to overcome some of the key limitations identified. For example, EMBREA developed at HR Wallingford UK is the revised version of HR BREACH (Samuels *et al.*, 2008; Morris, 2011). EMBREA can model overtopping and internal erosion failures for homogeneous, composite and layered embankments. It is possible to distinguish between coarse-grained and fine-grained geo-materials and it can simulate surface and head-cut erosion. It incorporates slope stability analysis of the lateral slope of the breach. Finally, breach growth (i.e. morphology of the breach channel) is not imposed.

Other recent models are DLBreach (Wu, 2016) and the model developed by Volz *et al.* (Volz, 2013; Volz *et al.*, 2017) that present the novelty of modelling the groundwater flow within the embankment structure and considers the effect of suction-induced apparent cohesion (West, Morris and Hassan, 2018). An overview of the two most important physically based breaching model was presented in paragraph 2.4.2. A critical analysis on the state-of-the art and the research questions inspiring this work

can be found in section 2.5.2.4.2

4.3 The concept of Suction-Based Breaching Model

The core idea of the suction-based breaching model takes inspiration from the observation that flood defence embankments remain in an unsaturated state for most of their time. Prior to the flood, these structures are exposed to low hydraulic heads imposed by the levels in the water body. During extreme weather events, this condition changes and the structure is subjected to a drastic increase of the hydraulic heads with a transient ground water flow developing within the embankment and its foundation (Dyer, 2004; Dyer, Utili and Zielinski, 2007; Mark Morris, Dyer and Smith, 2007). The change of the pore-water pressure regime due to this infiltration process depends on soil condition and properties, particularly on degree of saturation and hydraulic conductivity.

These processes have never been considered in a coherent fashion and modelling has mainly focused on surface water flow associated with the overflow (i.e. hydraulic shear stress) and erodibility properties, rather than the analysis of soil strength due to the change of pore-water pressures. Nevertheless, experimental evidence suggests that progressive surface erosion and headcutting leading to breach formation, are strongly dependent on these fundamental geotechnical processes.

This suction based breaching model introduces an alternative interpretation and a new method to simulate the physical mechanisms observed during overflow within the context of unsaturated soil mechanics. The starting point of this method is the analysis of the ground water flow within the embankment body as illustrated in Figure 4-8.

The prior-to-flood condition is represented in Figure 4-8a, when the water levels in the river are not critical and the unsaturated zone is quite extended. During extreme events, the levels in the water body increase rapidly and can reach the embankment crest in a few hours. The rise of water level generates a ground water flow from the upstream slope towards the embankment body and foundation.

Figure 4-8b,c shows the advancement of the saturation front fuelled by this high water level, hence the partially saturated zone starts reducing at a rate that depends on

soil characteristics. However, at the onset of overflow a large portion of the embankment is still in an unsaturated state. From this point onwards the overflow establishes, and flood water starts to flow along the downstream slope and drives a second infiltration process in a sub-orthogonal direction to the slope, as shown in Figure 4-8d. While the overflow proceeds there is a continuous inward infiltration, which causes a progressive increase of the degree of saturation and a reduction of suction, in the most superficial layers of the downstream slope.

Under overflow conditions, the embankment experiences two main infiltration processes, the first one from the upstream side due to the increase of water levels and the second one from the downstream slope due to the overflow. Both processes cause the advancement of the saturation front within the inner part of the embankment and a reduction of the partially saturated zone.

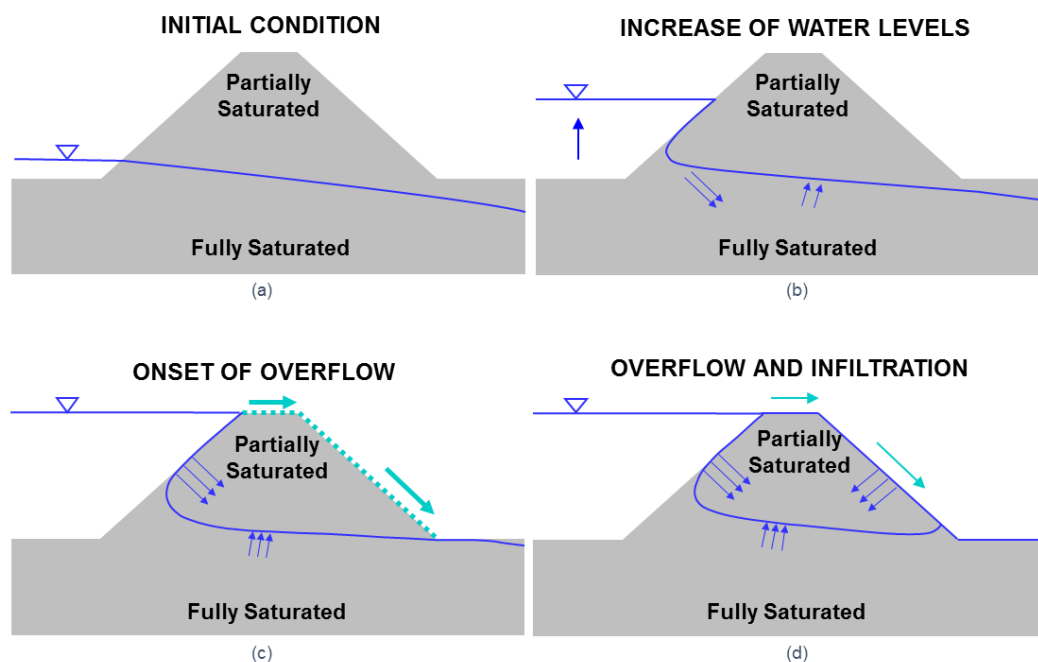


Figure 4-8: A sketch of the ground water flow process and propagation of the saturation front within an embankment during overflow. (a) initial condition; (b) increase of water levels and infiltration on the upstream slope; (c) overflow generating when water levels exceed the embankment crest with the advancement of the saturation front to the toe; (d) overflow progression and infiltration from the downstream slope as well as from the upstream side

The shear strength and stiffness of unsaturated soils are higher than saturated

condition (Tarantino and di Donna, 2019). Negative pore-water pressures (i.e. suction) and degree of saturation govern soil behaviour.

The simplest approach to consider the independent contribution of suction and degree of saturation to the ultimate shear strength of unsaturated soil is by extending the Mohr-Coulomb failure criterion (Equation 4-1) within the framework of Bishop's effective stress (Sheng, Zhou and Fredlund, 2011). For saturated soils:

$$\tau = c' + \sigma' \tan \varphi' = c' + (\sigma - u_w) \tan \varphi' \quad \text{Equation 4-1}$$

where τ is the soil shear strength (kN/m²), c' is soil cohesion (kN/m²), σ is the total stress (kN/m²), u_w the pore water pressure (kN/m²) and φ' is the soil friction angle (°).

For unsaturated soils, the effective stress proposed by Bishop (Equation 4-2) are defined as function of the net stress and matric suction (Murray and Sivakumar, 2010):

$$\sigma'' = \bar{\sigma} + \chi s \quad \text{Equation 4-2}$$

where $\bar{\sigma} = \sigma - u_a$ is the net stress, with σ is the total stress, u_a is the pressure of the air-phase, $s = (u_a - u_w)$ is the matric suction and χ is a parameter generally assumed to be a function of degree of saturation S_r . χ is therefore 0 for dry material and it is equal to unity for saturated soil.

If Bishop's effective stress is incorporated in the Mohr-Coulomb failure criterion, assuming the atmospheric pressure as the zero-reference level, and considering that commonly χ is supposed to be equal to the degree of saturation S_r (Nuth and Laloui, 2006), an equation for the ultimate shear strength of unsaturated soil is found as:

$$\tau = c' + \sigma'' \tan \varphi' = c' + (\sigma + S_r s) \tan \varphi' \quad \text{Equation 4-3}$$

which can be better expressed as:

$$\tau = c' + \sigma \tan \varphi' + S_r s \tan \varphi' \quad \text{Equation 4-4}$$

The term $S_r s \tan \varphi'$ represents the additional component of the shear strength due to suction and it is often referred as apparent cohesion (Tarantino and di Donna, 2019). It is worth noticing that this contribution is "weighed" by the degree of saturation $S_r < 1$, meaning that for the same suction, different degrees of saturation provide different values of the ultimate shear strength (Tarantino and El Mountassir, 2013).

Apparent cohesion is fleeting, in the sense that it disappears once suction drops to zero. However, the soil constituting the embankment can take advantage of this additional shear strength for long time, as the unsaturated state tends to persist and evolves according to the water infiltration process governed by the hydraulic conductivity of the material.

In this scenario, the most vulnerable part of the embankment is the toe, being the point in which the two saturation fronts (i.e. the one coming from upstream and the other one from the downstream surface) are likely to meet first. Therefore, around the downstream toe, the embankment material is close to a saturated state and to the condition of zero suction. In other terms, the soil at the toe experiences a faster reduction of the shear strength due to the loss of the apparent cohesion and, for this reason, is more prone to fail than soil in regions faraway.

This concept is represented in Figure 4-9 showing the stress state near the toe and another one near the crest for the initial condition (green circle) and for the overflow phase (blue dotted circle). The change of effective stress due to the overflow is more significant at the toe and it could lead to a stress state that lies on the failure envelope (Figure 4-9b). This loss of strength or softening of the embankment material can be considered as another possible reason to explain why the breach initiation is observed initially at the toe, especially for the headcutting erosion mode.

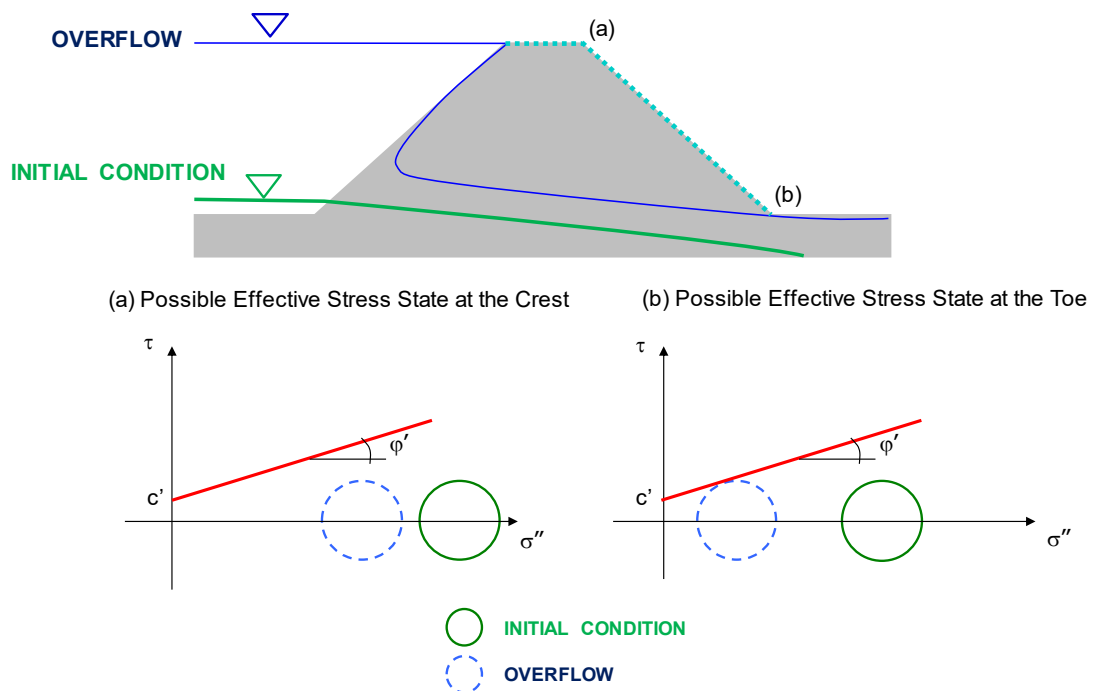


Figure 4-9: Typical stress states (a) near the crest (b) near the toe. Green lines are referring to the initial condition. Blue lines represent the overflow event

The qualitative analysis of the main geotechnical mechanisms occurring during overflow shows that the infiltration processes and the associated change of the soil shear strength due to change of suction and degree of saturation, can lead to local instabilities and hence failure of small portion of embankment. At the same time, breaching models developed so far, assume that the hydrodynamic forces are the predominant destabilising source which can cause the removal of soil particles, neglecting the soil shear strength reduction phenomenon. The hydrodynamics of embankment overflow is an invariant for the types of embankment materials and hence the same failure mode should be observed for fine-grained and coarse-grained soil. Indeed, experience proves that different physical mechanisms arise.

The role played by the embankment material is considered via adopting erosion laws and erodibility parameters for which important uncertainties still exist (i.e. conflicting results, low erosion rate compared to physical processes at embankment scale). Based on these issues, the suction based breaching model characterise soil properties adopting theories and principles of classical soil mechanics without introducing any empirical erosion law or transport sediment equation.

Because the hydraulic shear stresses developed on the downstream slope are typically in the order of magnitude of $0.1\text{-}0.5 \text{ kNm}^{-2}$, especially in the early stage of overflow, it is assumed that these can be neglected in first instance. Indeed, in Chapter 3 it was shown that hydraulic forces acting along the downstream surface, had very little impact on the global stability of the embankment during overflow. However, at very shallow depth, where the stress levels are low, the destabilising effects of the hydrodynamic shear stresses can become more relevant. Here, these forces can be responsible for the formation of superficial failure mechanisms. This situation tends to occur in coarse-grained materials because few centimetres below the slope surface, apparent cohesion is significantly reduced, if not erased. Besides, soil strengths are on the same order of magnitude of the hydraulic forces because of the low stresses. This can explain why coarse-grained embankments experience the observed exfoliation process, where soil is progressively washed away due to the formation of shallow failure planes. On the contrary, fine-grained materials can benefit of apparent cohesion also at very shallow depth and even when it becomes zero (for example on the surface), these materials still possess effective cohesion. Typically, effective cohesion is one or two order of magnitude bigger than the hydrodynamic stresses. Thanks to the resisting contribution of effective cohesion, shallow failure mechanisms are prevented, hence the headcutting backwards processes observed experimentally. In other words, the different responses of fine-grained and coarse-grained geomaterials to overflow forces and infiltration, can be explained in the context of the different hydro-mechanical behaviours of the two broad categories of soils.

The fundamental concept of the suction based breaching model is that, the failure mechanisms leading to embankment breaching (i.e. progressive surface erosion and headcutting), can be both simulated as a series of mini-slope stability problems at the centimetre scale, which gradual develops in breach formation. This requires the definition of a failure criterion able to capture the physics of the mechanisms observed.

4.4 Definition of the failure criterion

The failure criterion defined incorporates stress-strain and geometrical considerations. According to the elastic-perfectly plastic soil model, when the state of stress at any point is equal to the material resistance τ_{lim} , this point enters the range of plastic behaviour. At the same time, the mobilisation of the shearing resistance is a necessary condition for the formation of a failure mechanism, but it is not yet sufficient. A kinematics will form once that the plastic region is large enough to generate a continuous surface, along which the soil mass starts moving relative to the intact part. In Figure 4-10a the point on the Mohr-Coulomb failure envelope represents the necessary condition. At this stage, the sufficient condition occurs when shear strains overcome the strain corresponding to the threshold of the elastic behaviour and plastic shear strains γ_p develop, as shown by the red point in Figure 4-10b.

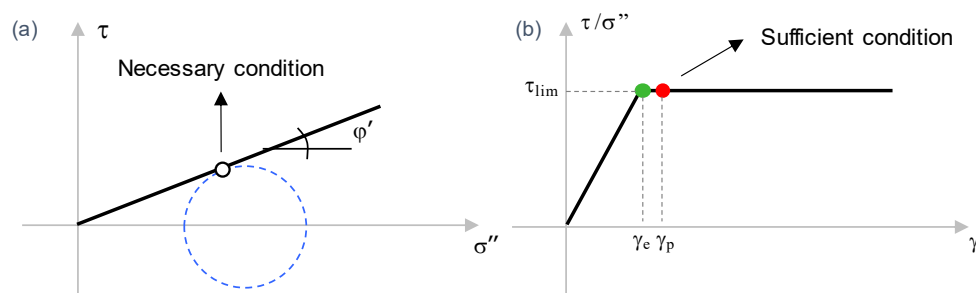


Figure 4-10: Stress state in the Mohr plane for a point which violates the failure criterion (a) and stress-strain relationship, with green point representing the yielding condition and red point beyond the elastic strain threshold representing plastic shear strain

To explain this concept more clearly, let us consider a block on a horizontal plane subjected to a system of constant vertical force and a horizontal force that is progressively increased. For small values, the block experiences purely elastic deformation as shown in Figure 4-11.

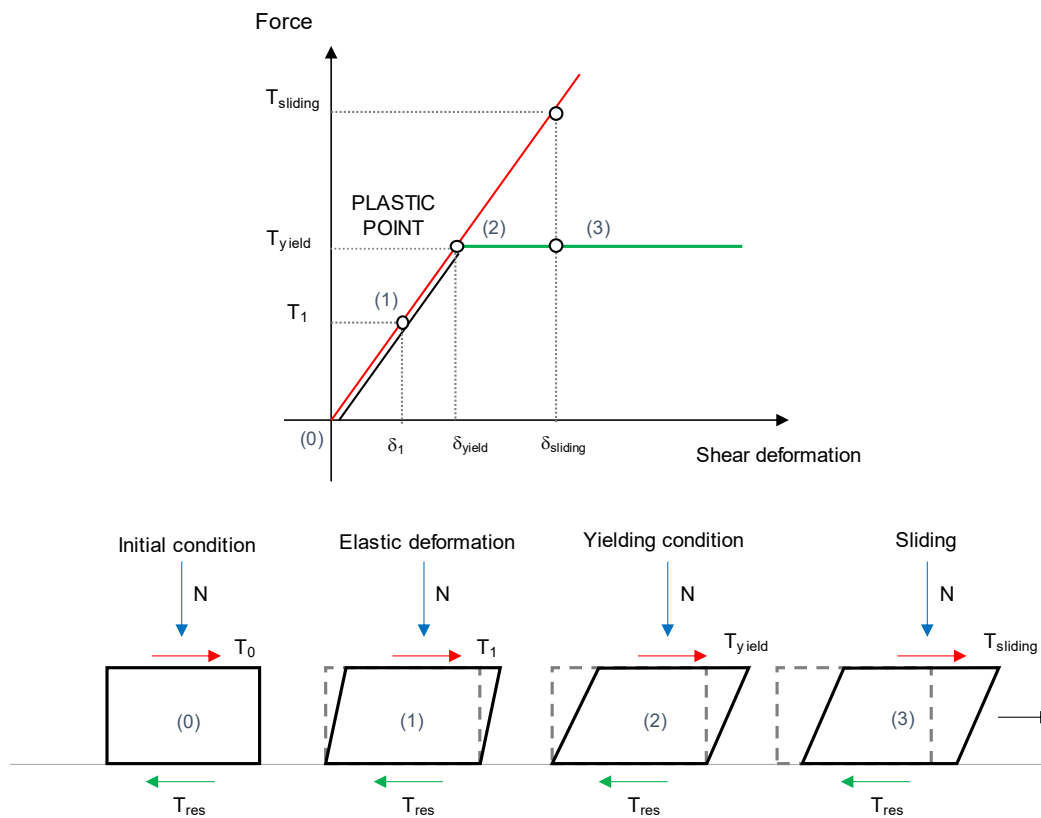


Figure 4-11: Deformation and sliding of a block by increasing the horizontal force, under constant vertical force. (0) Initial condition when nothing happens; (1) development of elastic deformation; (2) the applied force is equal to the material resistance and yielding is occurring; (3) the applied horizontal force increases, plastic deformation are accumulated and at a certain point the block slides. Green lines refer to the inherent resistance of the block. Red lines represent the applied horizontal force. The dotted line is the block in its original configuration

Similarly, the movement of a soil mass occurs when the destabilising forces reach the material resistance (i.e. necessary condition), plastic deformations start to develop (i.e. sufficient condition) and increase up to a point in which a continuous shear band is formed and a portion of soil starts to move.

This general concept is applied to the case of embankment overflow, with particular reference to the headcutting failure mechanism. The change of pore-water pressure induced by the infiltration processes illustrated earlier, produces a variation of the state of effective stress. As shown in Figure 4-9 it is possible that in many points of the soil, the state of stress becomes tangent to the Mohr-Coulomb failure envelope so that plastic points appear and start to spread particularly around the toe area and in

the most superficial layer of the downstream slope. An example of this situation is presented **Error! Reference source not found.**

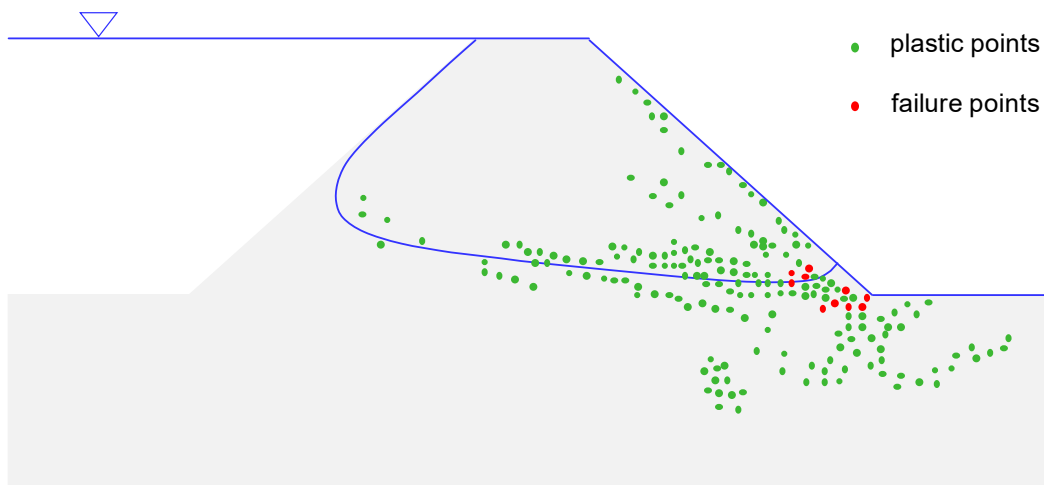


Figure 4-12: Plastic points represented as green dots and failure points in red, formed within the embankment as consequence of the infiltration processes associated to the overflow

Plastic points for which the shear strain is greater than the elastic threshold (i.e. $\gamma > \gamma_e$) as the red points in Figure 4-10b, are defined here as ‘failure’ points (the red dots in Figure 4-12).

As the overflow proceeds, points plastically stressed spread in an adequately extended region where shear strains increase indefinitely beyond the elastic threshold. In this area, the accumulation of large plastic deformation results in the development of a shear zone and eventually a local slip surface form. At this stage, a failure mechanism is defined when it is possible to find a continuous path connecting the most external failure points, following a concave pattern with an entry and exit point on the ground surface as shown in Figure 4-13.

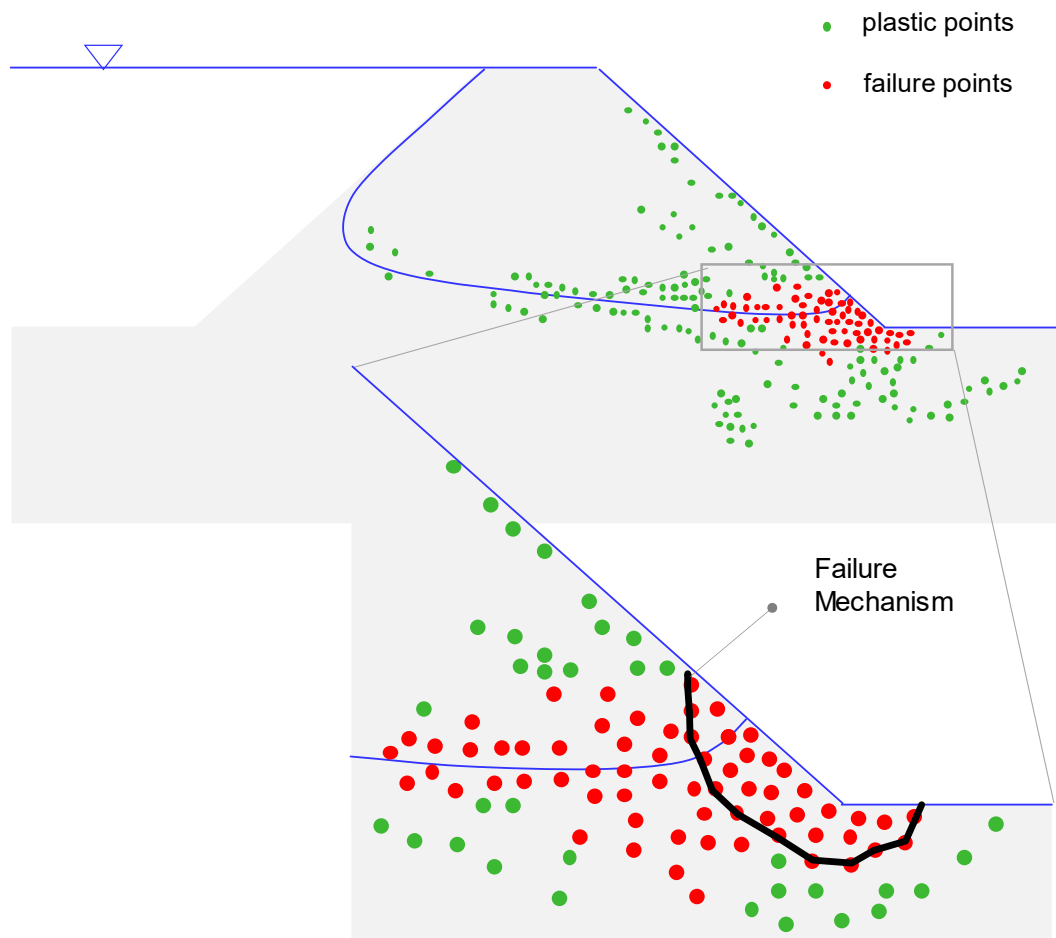


Figure 4-13: Accumulation of plastic deformation leads to an increase of the number of failure points. A shear zone evolving in a continuous slip surface is identified, constituting the failure mechanism

The failure criterion adopted in this work is summarised as follows:

- Formation of ‘plastic’ points which are points where the state of stress lies on the failure envelope and shear strains are no greater than the elastic shear threshold;
- Formation of ‘failure’ points: which are points where the state of stress lies on the failure envelope and shear strains are greater than the elastic shear threshold;
- Formation of a slip surface which interpolates the most external failure points, starting and ending on the ground surface by following a concave path;

Having defined the failure mechanism to be implemented, at the heart of the suction based breaching model is the strategy of removing the unstable soil blocks delimited by the failure surface identified. Figure 4-14 shows the first headcut formation. The blue lines are the phreatic surfaces, and the arrows refer to the continuous water infiltration due to the overflow established in the new configuration, following the removal of soil blocks.

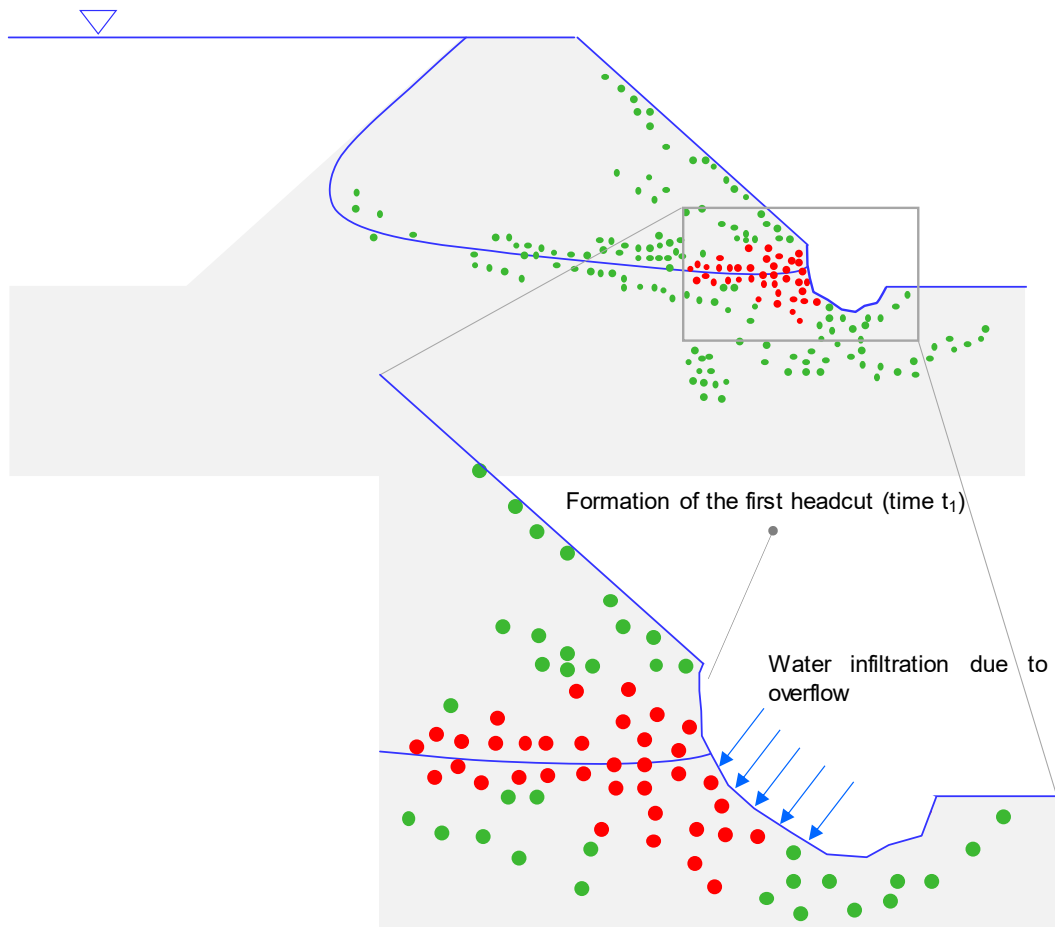


Figure 4-14: The first small headcut in the process of headcut initiation observed at the toe of the embankment

After a certain time-interval, a new plastic region will develop with failure points spreading over a larger area. The failure criterion is applied again (Figure 4-15a) and other soil elements are removed, resulting in the new embankment profile of Figure 4-15b.

These sketches illustrate the headcut initiation and propagation in a fine-grained

material. It is worth noticing that no assumption has been made about where the first ‘erosion’ should occur and the headcut initiation at the toe of the embankment is a result of the simulation. It is anticipated that the same ‘stability’ criterion applied to a coarse-grained embankment should return the progressive surface erosion, i.e. the second mode of failure typically observed in coarse-grained embankment.

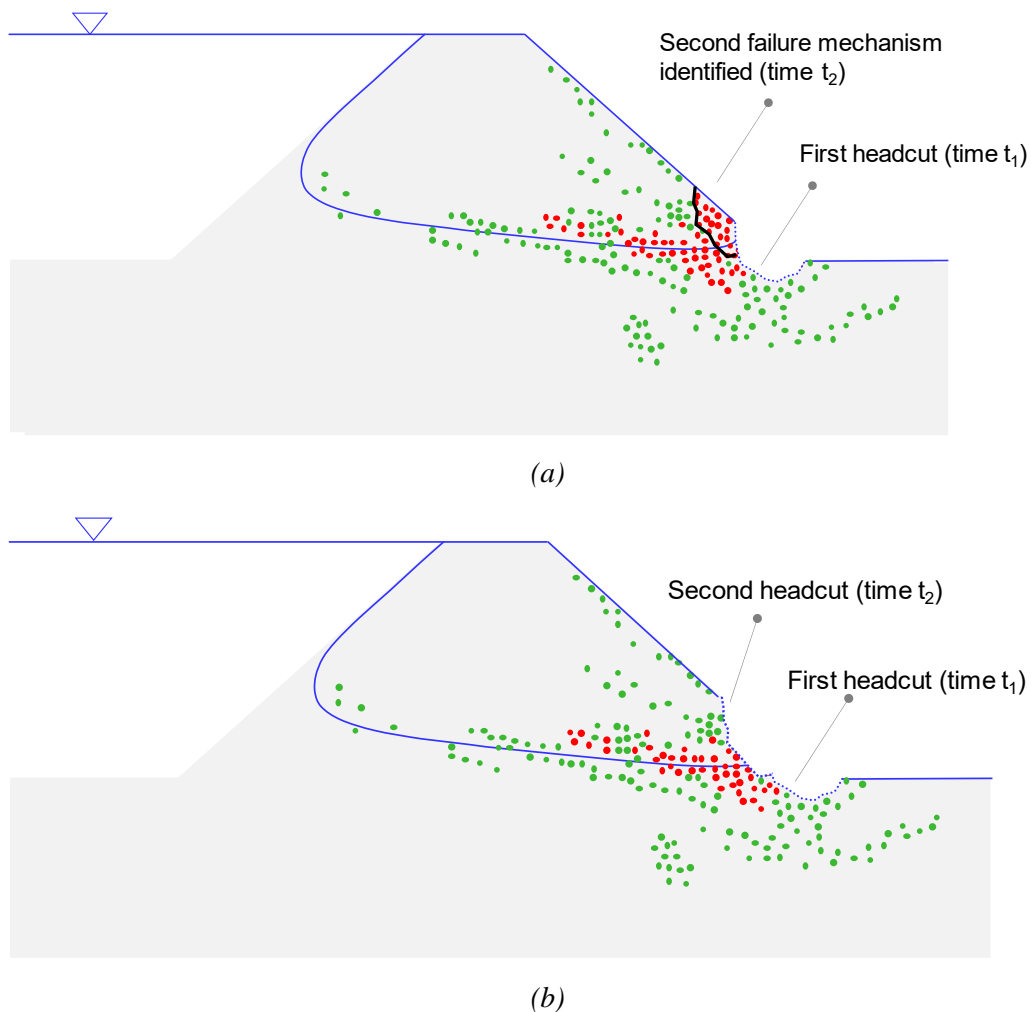


Figure 4-15: Formation of the second headcut (a) and application of the failure criterion resulting in the new embankment configuration

In summary, the headcut backwards migration is simulated by removing soil blocks, step- by-step, as a result of a chain of mini slope instabilities. Breach formation occurs when the headcut recedes backwards and intersects the embankment crest at the time step t_f in Figure 4-16. After this stage, the failure process is speed up because

the discharge through the breach increases and can lead to the final catastrophic failure.

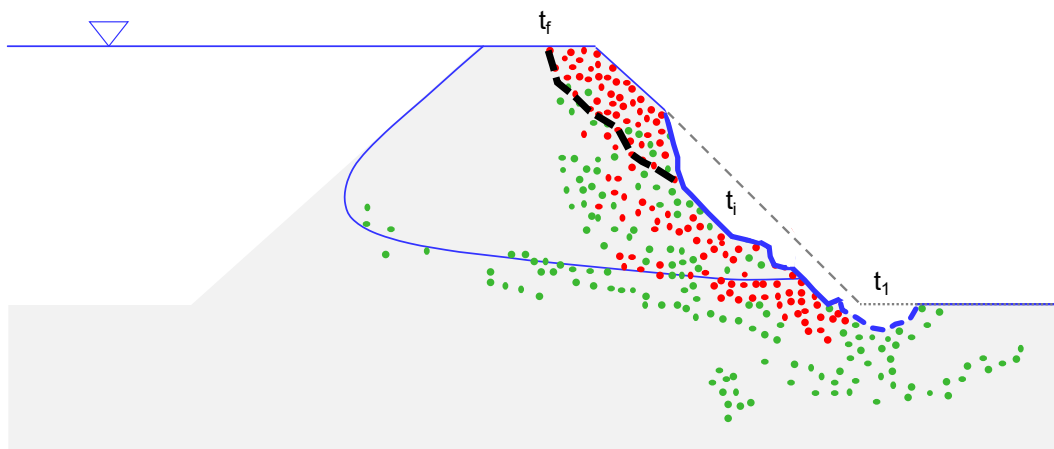


Figure 4-16: A sketch of headcutting backwards migration process up to the condition of breach formation when the crest is reached

4.5 The “Lego Strategy”: application of the failure criterion in PLAXIS 2D

The procedure introduced in general terms in the previous paragraph has been implemented in the geotechnical software PLAXIS 2D (‘Plaxis 2018, Users Manual’, 2018). The advantage of using PLAXIS 2D is that it allows easy generation of complex geometry with the aid of customized macros. The calculations can be performed in staged construction mode, which gives the possibility to activate/deactivate geometrical entities, loads, soil properties and flow conditions, without affecting the results of the previous phases. All these features have been useful to implement the suction-based breaching model strategy. It is worth specifying that the method proposed uses existing tools routinely applied by practitioners.

The geometry of the embankment has been built with a macro that automatically draws a series of soil triangular elements, represented with the blue lines in Figure 4-17. The finite element mesh is automatically generated in PLAXIS 2D based on a robust triangulation procedure that can be constrained by the user to refine the element distribution. In this case the mesh parameters are chosen such that the soil blocks constituting the embankment and the mesh elements coincide.

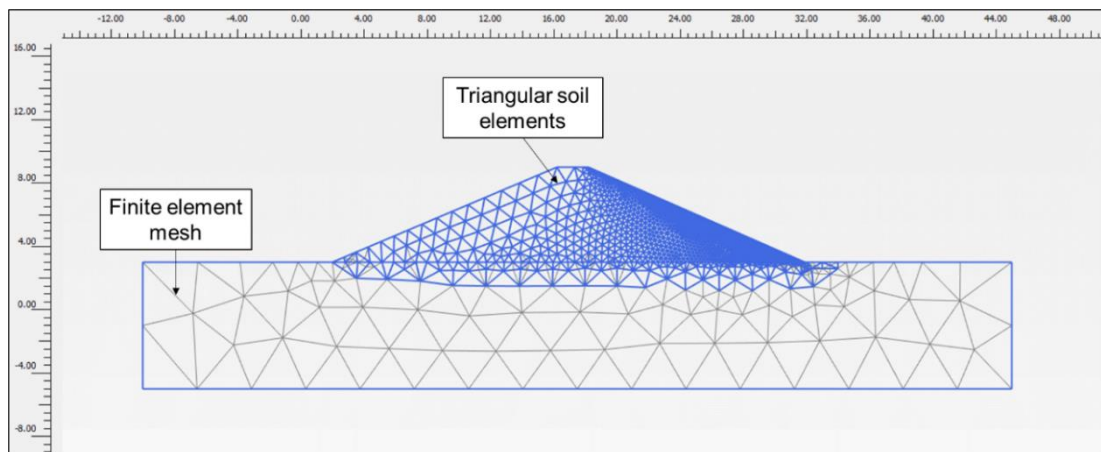


Figure 4-17: Geometry built in PLAXIS 2D, where the blue lines represent the triangular soil elements constituting the embankment body while the grey triangles are the finite element mesh automatically generated in the Mesh Mode

The 15-Node element was selected since it provides a finer distribution of nodes and therefore more accurate results than the 6-Node option. The configuration of the 15-Node element is given in Figure 4-18, where the black points represent the 15 nodes and the blue crosses refer to the 12 Gauss Points or Stress Points for the numerical integration.

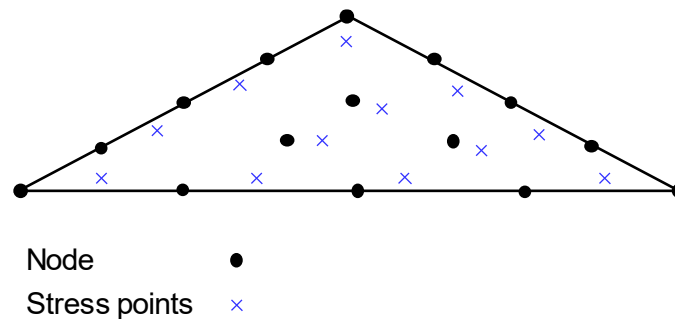


Figure 4-18: A sketch of the 15-node element constituting the finite element mesh. The black points represent the 15 nodes and the blue crosses the 12 Stress Points

4.5.1 Algorithm to define a ‘failed’ soil element

The total number of stress points that are in a plastic state (i.e. points for which the state of stress lies on the Mohr-Coulomb failure envelope) is provided in output in a plastic point plot for a generic overflow calculation phase. The results in terms of plastic points, effective mean stresses p' and shear strains γ of the phase analysed are

extracted from the Plaxis 2D Output program and examined in an Excel Spreadsheet.

The elastic threshold for the shear strain is simply calculated with the Hooke's law:

$$\begin{bmatrix} p' \\ q \end{bmatrix} = \begin{bmatrix} K & 0 \\ 0 & 3G \end{bmatrix} \begin{bmatrix} \varepsilon_v \\ \varepsilon_q \end{bmatrix} \Rightarrow \varepsilon_q = \frac{q}{3G} \quad \text{Equation 4-5}$$

where, p' is the mean effective stress, q is the deviatoric stress, ε_v is the volumetric strain, ε_q is the deviatoric strain, $K = \frac{E'}{3(1-2\nu')}$ is the bulk modulus and $G = \frac{E'}{2(1+\nu')}$ is the shear modulus, with E' and ν' Young Modulus and Poisson's ratio respectively.

At failure:

$$q = Mp' \quad \text{Equation 4-6}$$

$$M = \frac{6 \sin\phi'}{3 - \sin\phi'} \quad \text{Equation 4-7}$$

where ϕ' is the friction angle of the embankment soil.

Therefore, the elastic shear strain is given by:

$$\varepsilon_q = \gamma_e = \frac{Mp'}{3G} \quad \text{Equation 4-8}$$

For all the plastic points found, it is checked whether the shear strain for the overflow phase considered is greater than the elastic threshold calculated with Equation 4-8. In this case a failure point is formed. If this is the case, the 'plastic' point acquires the status of a 'failure' point.

A triangular soil element is considered 'failed' when at least 8 points of the 12 Gauss Points are in failure condition (i.e. plastic points with plastic shear strain exceeding the threshold given by Equation 4-8). The number of 'failure' points required to turn an element into a 'failure' element (8 out of 12) is somehow arbitrary. It is based on the observation that an element cannot be considered failed if only one of a few stress points are under failure condition. At the same time, it is excessively restrictive to consider an element failed when all the 12 stress points become 'failure' points. Therefore, it is assumed that at least 8 of the 12 stress points, corresponding to the 66% of the total number of integration points, must be at failure for defining an

impending failed element as shown in Figure 4-19.

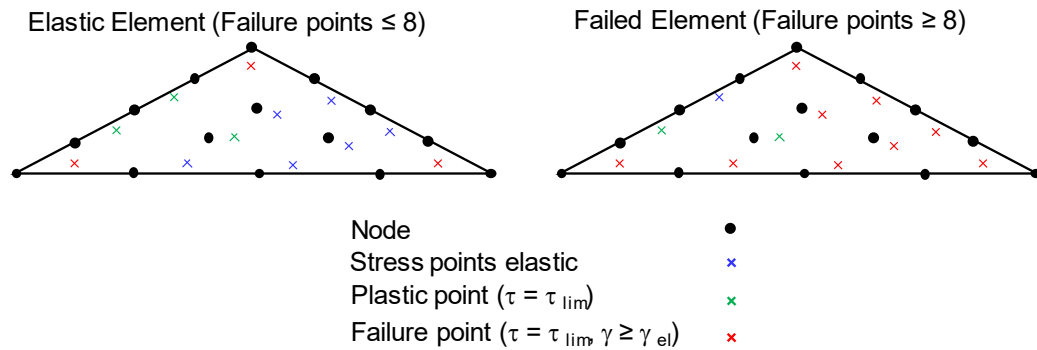
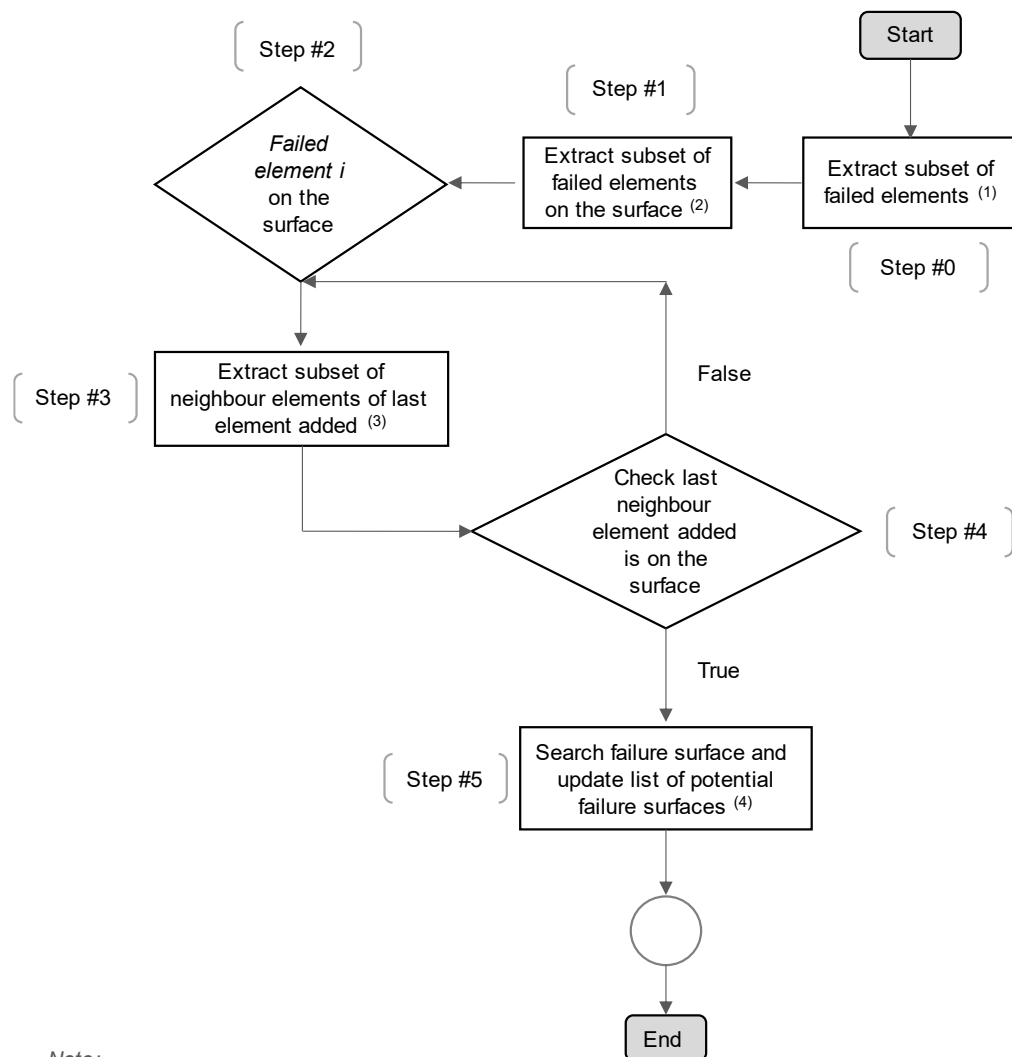


Figure 4-19: Definition of a soil failed element based on the number of stress points in failure condition. Elastic stress points are represented by blue crosses, plastic points are green crosses and failure points are red crosses

The criterion based on at least 8 failure points for a single triangular element required to generate a ‘failure’ element has been then calibrated/validated in Section 4.5.4.

4.5.2 Algorithm for the removal of the failed soil elements

The failure criterion has been implemented through the algorithm described in the flowchart below.



Note:

- (1) Sub-routine "failed elements"
- (2) Sub-routine "elements on surface"
- (3) Sub-routine "neighbour element"
- (4) Sub-routine "failure surface"

Figure 4-20: Flowchart describing the algorithm which implements the failure criterion and the soil removal based on the failure surface found at the time-step of reference

This algorithm is a loop composed of several blocks which re-call subroutines defined separately from the main body. The flowchart is further explained with sketches representing the sequence of steps in parenthesis in Figure 4-20, corresponding to the various tasks addressed.

The initial configuration at Step #0 is presented in relation to a small part of the embankment along the downstream slope. This is the starting point from which the

sub-routine “failed elements” extract the subset of all the soil elements in failure conditions. These are represented in pink in the Figure 4-21b.

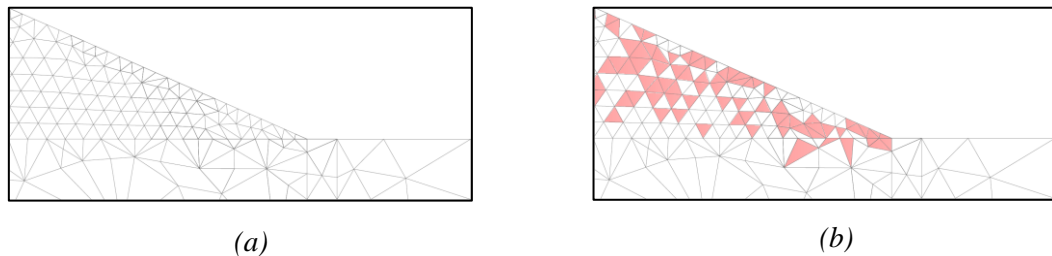


Figure 4-21: A small portion of the embankment analysed (a) initial configuration corresponding to Step #0 in the flowchart; (b) subset of failed elements obtained with sub-routine “failed elements” at Step #1

The second task is to search, among the list of the failed elements, those that are on the surface and the subroutine “elements on surface” will extract this subset. At this point Step #2 is carried out considering a generic failed element previously identified. Let us imagine that El.1 represented in red in Figure 4-22 has been selected.

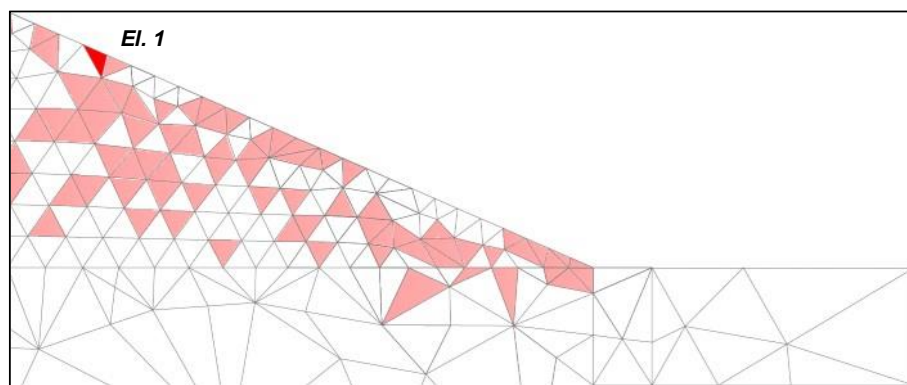


Figure 4-22: Step #2 assuming that the first iteration of the loop starts from element El. 1 of the subset of the failed elements on the surface

If the element considered is not on the surface, the loop is not executed, and the algorithm ends. If the element is on the surface, as is the case here, the first iteration is started, and the sub-routine “neighbour elements” will extract all the elements with at least one node in common with El.1. This is Step #3 of the flowchart which is shown in Figure 4-23 where the yellow triangles (i.e. El. 2, El. 3, El. 4, and El. 5) are the surrounding elements of El. 1. At this point, depending on the first element selected

after El. 1, four different scenarios are possible and are analysed separately within the first loop. In turn, each scenario will have a series of sub-cases depending on the neighbour elements found.

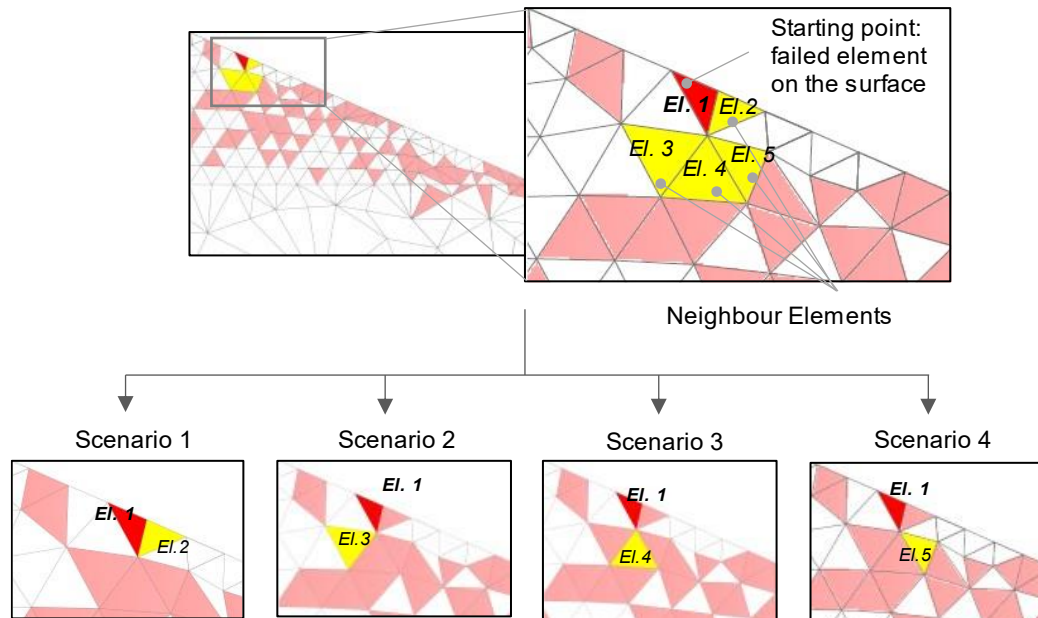
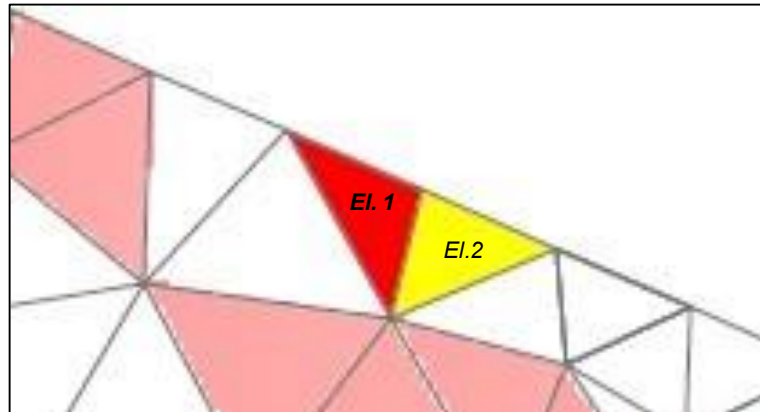


Figure 4-23: In yellow are presented all the neighbour elements of El. 1, recognised with the sub-routine "neighbour element" at Step #3. Four scenarios are possible starting from El. 1

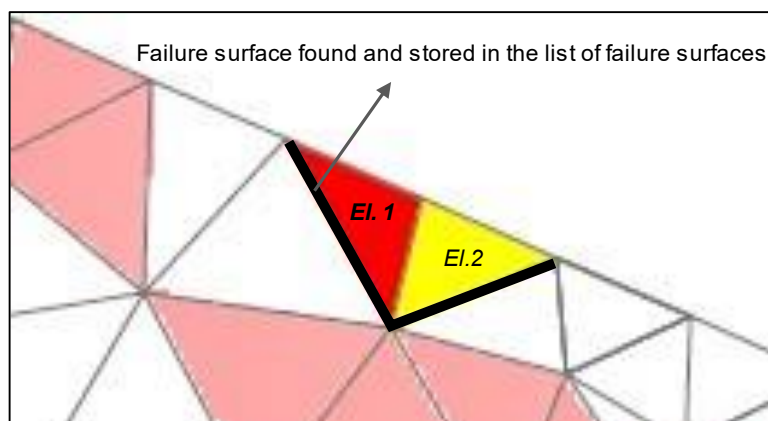
Scenario 1 considers El. 2 and at Step #4 it is checked that the neighbour element selected is on the surface. If this is true than the sub-routine "failure surface" will look for a possible envelope of the contours of the failed elements thus defining a potential failure surface. This case is shown in Figure 4-24 and because it is completed, the loop ends here. The failure surface found is not the final one, as this will be compared with the potential envelopes found in the other sub-cases. The failure surface chosen at the end of this process is the largest one.

The remaining three scenarios on the contrary will not pass this check as the corresponding neighbour elements are not on the surface therefore, the loop comes back and will look for the neighbour elements of the last added.

Scenario 1: Neighbour element El. 2 found



Step #4: it is checked that El. 2 is on the surface. If this is true the subroutine failure surface will find a potential failure surface.



Step #5: A potential failure surface is found as the path is concave. This will be stored in the subset of potential failure surfaces. In fact, the loop will analyse all the possible cases until the largest potential failure surface is identified. However, scenario 1 stops here and the algorithm proceeds with other cases.

Figure 4-24: Scenario 1 leads to a potential failure surface as the neighbour element El. 2 has an edge on the surface

Let us consider scenario 2 and scenario 4 separately.

If scenario 2 is considered, the neighbour element El. 3 is not on the surface. The condition at Step #4 is not satisfied therefore the process starts again looking for the neighbour element of last added, which is El. 3. At this stage in the flowchart, Step #3

will be repeated, and new sub-cases will be derived as shown **Error! Reference source not found.** In Figure 4-25 the orange triangles are all the possible neighbour elements of El. 3.

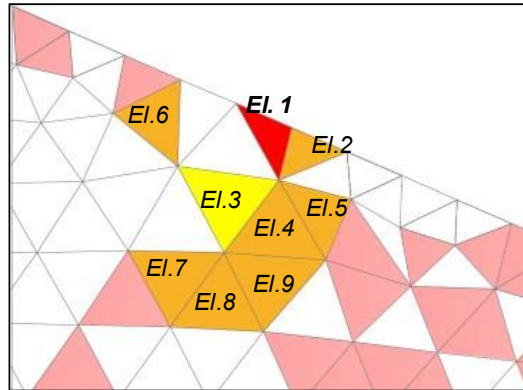


Figure 4-25: El. 3 is not on the surface and the process comes back at Step #3. The new set of elements of El. 3 is presented in orange

Among the different possible sub-cases that could be followed let us consider the path El. 1 + El. 3 + El. 7 as represented with the black arrows in figure **Error! Reference source not found.**

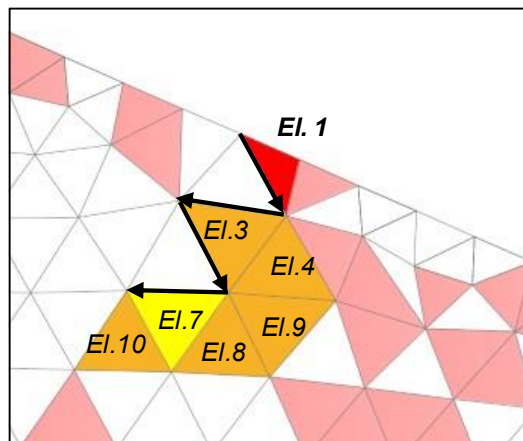


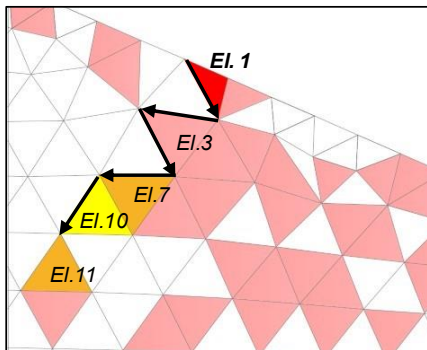
Figure 4-26: Sub-case 1 of scenario 2, which considers the path El. 1 + El. 3 + El. 7. The element considered is the yellow triangle while the orange triangles are the neighbour elements found

Again, at Step #4 it is checked that the last element added (i.e. El. 7) is on the surface. Since this condition is not satisfied the algorithm will go back and will check for the neighbour elements of El. 7. At this point, depending on which of the orange

triangles are selected there are other subcases.

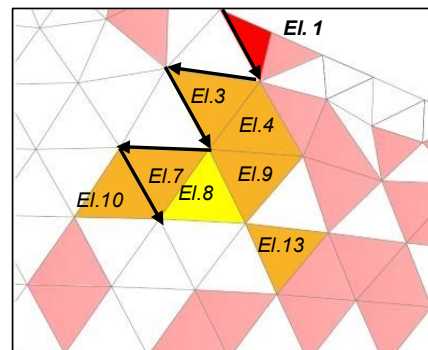
Let us imagine following two possible paths separately: El. 1 + El. 3 + El. 7 + El. 10, renamed Scenario 2.1.1. and El. 1 + El. 3 + El. 7 + El. 8 called Scenario 2.1.2.

Scenario 2.1.1



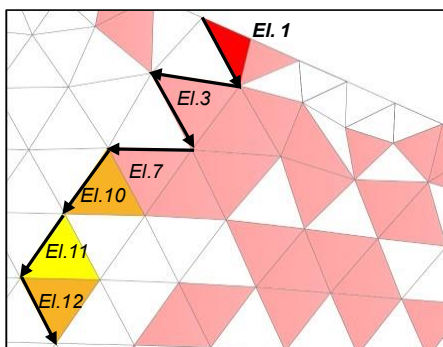
Step #4: it is checked that El. 10 is on the surface. This condition is false and Step #3 is repeated, and neighbour element of El. 10 are found.

Scenario 2.1.2



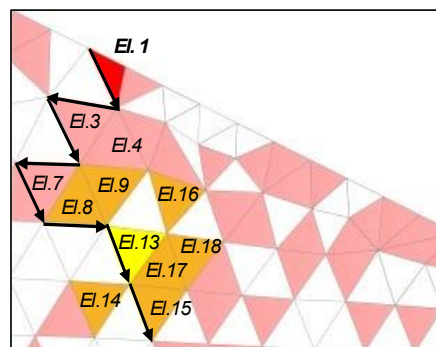
Step #4: it is checked that El. 8 is on the surface. This condition is false and Step #3 is repeated, and neighbour elements of El. 8 are found.

Scenario 2.1.1.1



The path El.1 + El.3 + El.7 + El.10 + El.11 + El.12 stops because El. 12 is isolated from other failed elements. For this subcase it is not possible to determine a potential failure surface and the algorithm ends.

Scenario 2.1.2.1

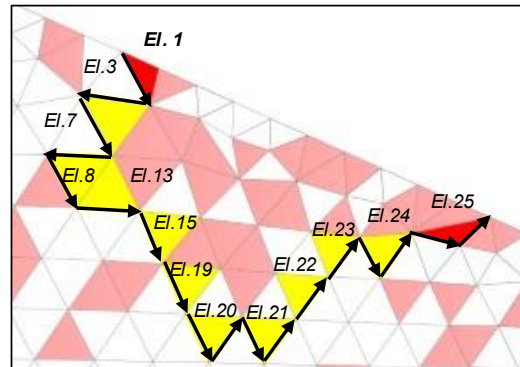


Step #4: it is checked that El. 13 is on the surface. This condition is false and Step #3 is repeated, and neighbour elements of El. 13 are found.

Scenario 2.1.1.1

ENDS at Step #4

Scenario 2.1.2.1.2



Let suppose that from El. 13, the path followed is the one reported with the yellow elements. When El. 25 is reached this is on the surface. The loop stops here and the subroutine failure surface will search for a potential surface. However, in this case this is not found, as the path of successive neighbour element is not concave, so the algorithm stops and ends

Figure 4-27: Two possible sub-cases after scenario 2. On the left it is shown a path that ends without arriving at Step #5. On the right the path followed exits on the surface, but the failure surface found is not concave

As represented in Figure 4-27, Scenario 2.1.1.1 on the left will not reach Step #5 of the flowchart as the last element added is not on the surface and there are no other neighbour elements, therefore the process ends. On the contrary, the path followed in Scenario 2.1.2.1.2. will found an exit element on the surface which is El. 25. At the same time once that the process is at Step #5, the subroutine “failure surface” is not able to find a potential failure envelope, because the contours of the yellow and red elements is not concave.

Now, let us move to Scenario 4. The neighbour element El. 5 is not on the surface, therefore the algorithm is not able to proceed at Step #5 and comes back to Step #3, where neighbour elements of El. 5 are found. These are the orange triangles in Figure 4-28. Among the different possibilities two options are selected.

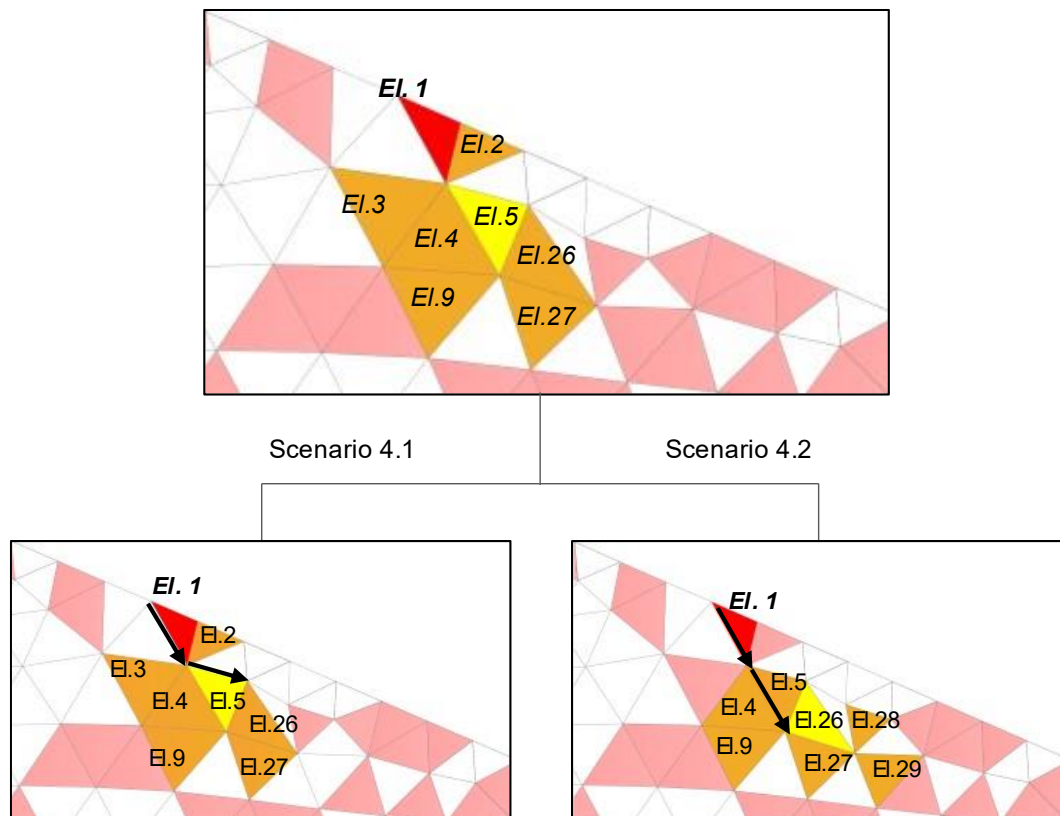
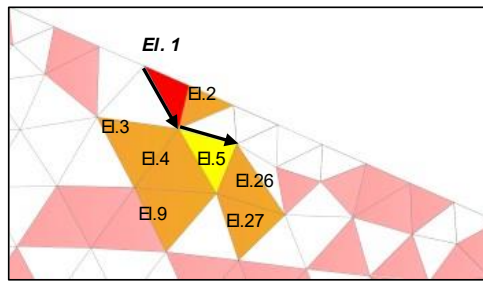


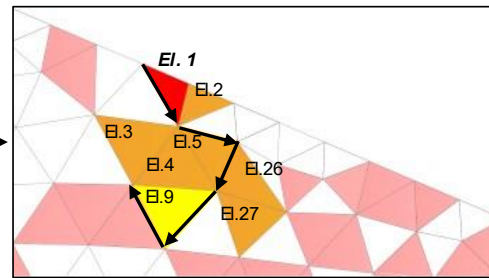
Figure 4-28: Scenario 4 can be further subdivided into two possible subcases: Scenario 4.1 and Scenario 4.2

Following Scenario 4.1, if El. 9 is selected, the algorithm can find a failure element on the surface according to the path outlined in Figure 4-29. However, this is not considered as a potential failure surface, because the envelope is again not concave and therefore it is not meeting the geometrical requirements imposed by the failure criterion.

Scenario 4.1



Looking for neighbours of El.5 and found El.9



Failure El. 40 on the surface is found. This failure envelope is discarded because it is not compatible with the geometrical requirements of the failure criterion assumed

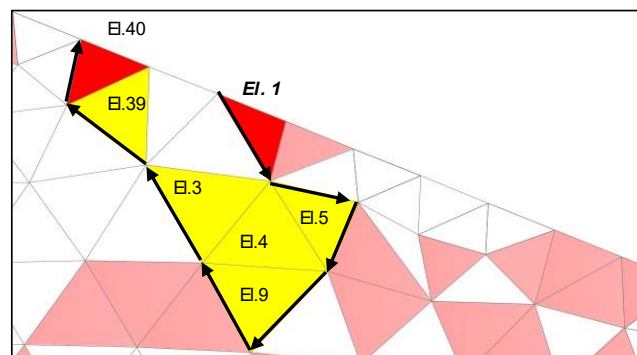


Figure 4-29: In Scenario 4.1, the yellow triangles are the ones followed to arrive on element El. 40 on the surface, but the envelope identified is not included in the list of potential failure surfaces

If Scenario 4.2 is considered in Figure 4-30, among the different possibilities there is Scenario 4.2.1.2 which represents a potential failure surface because it is a concave path linking failed elements with an entry and an exit element on the slope surface. This is therefore stored in the list of all the failure surface identified at this stage. The algorithm stops and ends.

Once that all the possible paths have been explored, the longest failure surface is selected, and the failed elements enveloped will be removed. For the cases analysed in this example, scenario 4.2.1.2 provides the final failure surface to be adopted for the iteration considered.

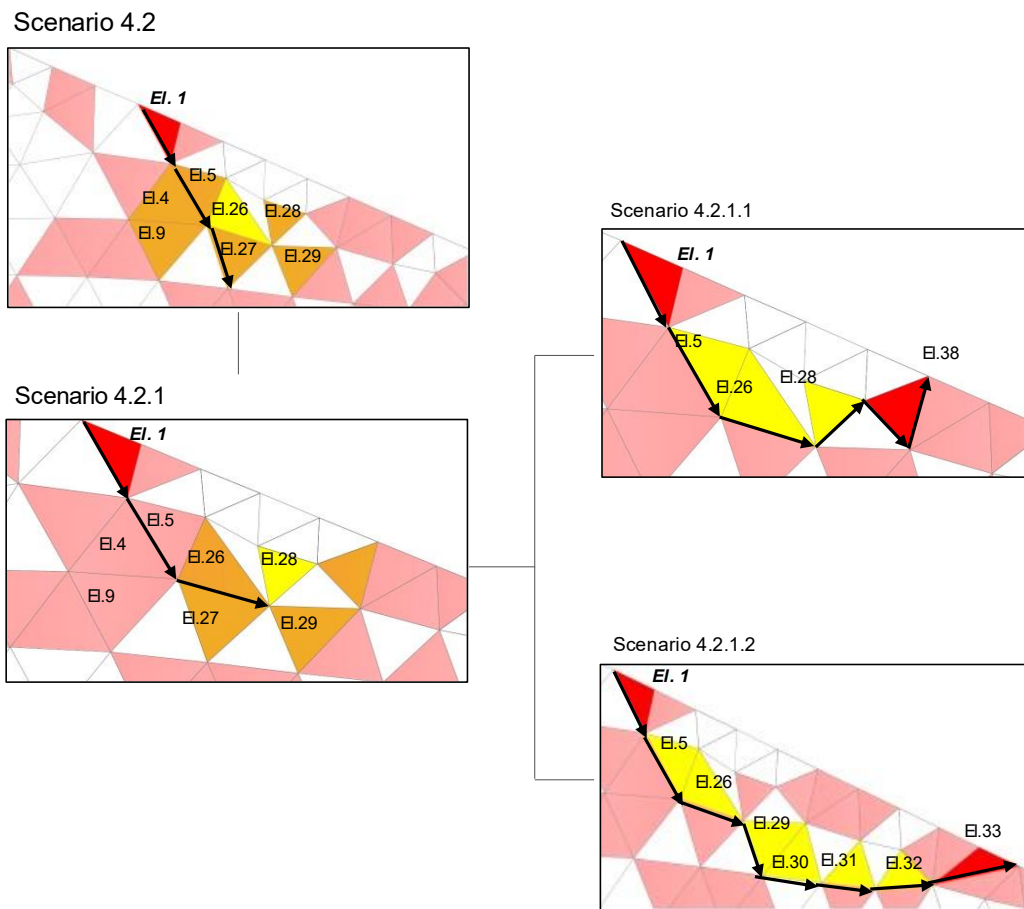


Figure 4-30: Scenario 4.2 leading to Scenario 4.2.1 following the neighbour elements of El. 26. Among the different possibilities Scenario 4.2.1.2 is represented leading to El. 33 on the surface and the associated path is stored in the list of the potential failure surfaces

4.5.3 Calibration and Validation of the Failure Criterion

The calibration of the failure criterion is based on the analogy between the failure surface obtained within the framework of Upper Bound Limit Analysis and that resulting from the FEM Safety Calculation with Plaxis 2D. In this last case, the output is analysed as described in the previous paragraph and the failure surface is found by applying the criterion defined. The minimum of 8 failure points corresponds to the condition for which the two different approaches provide the best fit.

For simplicity and without losing in generality, this analysis has been conducted on an ideal slope in dry condition represented in Figure 4-31.

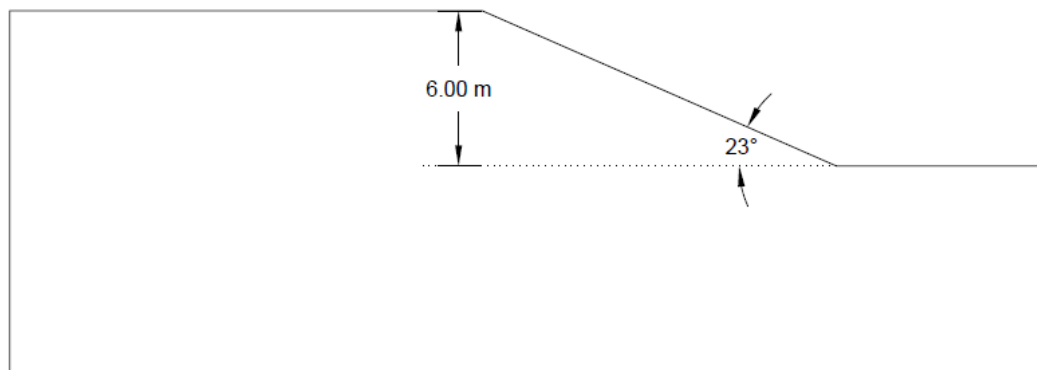


Figure 4-31: Slope geometry adopted for the calibration of the failure criterion

The Upper Bound Limit Analysis approach has been selected because provides a rigorous solution for the slope stability problem (and for many other geotechnical application), based on the two theorems of plasticity. More specifically, the software Limit State:GEO (LimiteState Ltd, 2016) has been used. The solution consists in an adequacy factor applied to loads or material strengths along with the associated failure mechanism, composed of soil blocks which are reciprocally sliding or rotating. Limit State:GEO applies the Upper Bound Theorem of Plasticity and it is based on the computational Limit Analysis technique of Discontinuity Layout Optimization (DLO) (Smith and Gilbert, 2007). This is a rigorous mathematical optimization procedure which allows to find the most critical set of slip-lines at the ultimate state, among all the possible layouts formed by joining the nodes used to discretize the problem under examination.

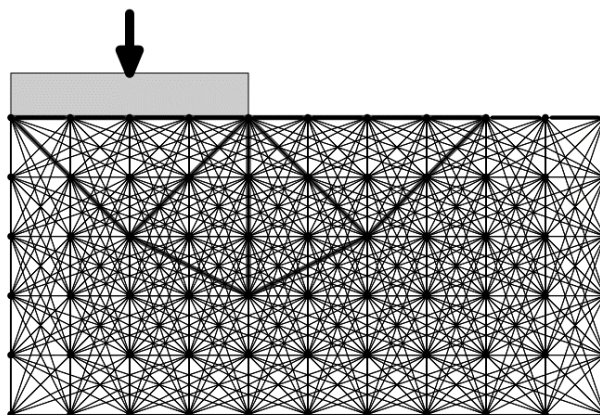


Figure 4-32: Example of DLO applied to the undrained stability of a footing after (LimiteState Ltd, 2016).

The failure mechanism is characterised by a collapse load factor which is an upper bound of the true collapse load.

The other method applied is the FEM with PLAXIS 2D. The Safety Calculation performed in PLAXIS, adopts the strength reduction method. The shear strength parameters ϕ' and c' are progressively reduced until the failure of the structure is reached. The total multiplier ΣM_{sf} initially equal to unity, provides the ratio between the input strength parameters and the reduced ones at each step of the analysis. In other terms ΣM_{sf} at failure is the factor of safety. The solution is thus expressed with a factor of safety and with a fully developed failure mechanism, characterised by a constant value of ΣM_{sf} while the deformation grows indefinitely. This is typically visualised with a shear band in the deviatoric strain plot.

4.5.3.1 Slope stability analysis with Plaxis 2D and LimitState:GEO

The stability of the slope in Figure 4-31 has been assessed in PLAXIS 2D adopting the Mohr-Coulomb soil model which corresponds to the well-known elastic perfectly plastic model. The input parameters considered are reported in Table 4-1. It is worth specifying that this exercise refers to a purely ideal slope.

Table 4-1: Soil parameters initially considered for the slope stability analysis in PLAXIS 2D

Unit weight, γ (kN/m³)	15
Young Modulus, E (kN/m²)	5000
Poisson's ratio	0.378
Cohesion, c' (kN/m²)	4
Friction angle, ϕ' (°)	30
Dilatancy angel, ψ (°)	0

The soil model implemented in LimitState:GEO is the rigid perfectly plastic model which requires in input only cohesion and friction angle. To compare the failure

mechanisms provided by the two software, a series of models are performed in LimitState:Geo adopting as input strength parameters those corresponding to different values of the total multiplier ΣM_{sf} in Plaxis. In other words, the total multiplier ΣM_{sf} in Plaxis, is analysed for each calculation step.

$$\Sigma M_{sf} = \frac{\tan \varphi'_{input}}{\tan \varphi'_{reduced}} = \frac{c'_{input}}{c'_{reduced}} \quad \text{Equation 4-9}$$

Based on Equation 4-9, friction angle φ ($^{\circ}$) and cohesion c (kN/m^2) are determined at each step. Figure 4-33 shows the plot of the total multiplier for the different steps of the safety calculation in Plaxis. It is worth noticing that after step 35, the total multiplier is constant and equal to 1.94. This represents the factor of safety of the slope with strength parameters adopted in input. The corresponding friction angle is also shown in the figure. The slope analysed is therefore considered at failure (i.e. Factor of Safety equal to unity) for a friction angle of 16.45° and a cohesion equal to 2.04 kN/m^2 . The ‘reduced’ cohesion and friction angle constitute the input for the Limit Analysis calculation.

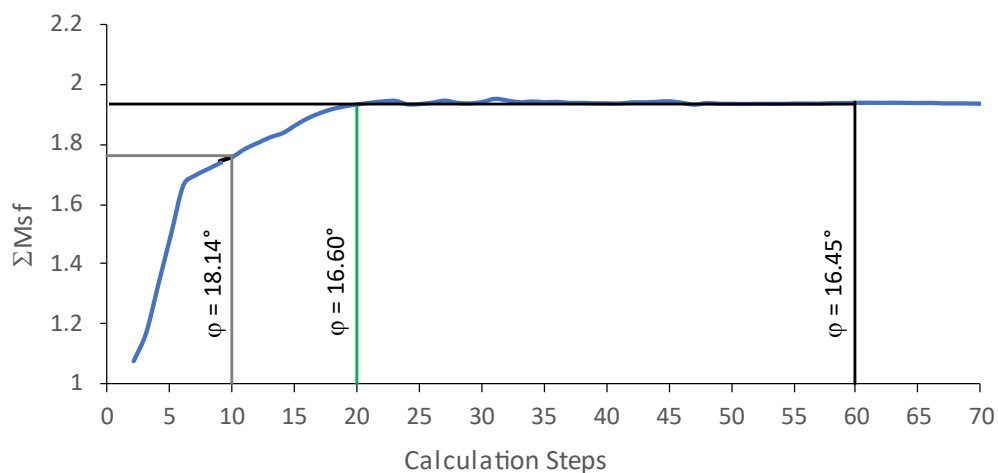


Figure 4-33: Total Multiplier provided by the Safety Calculation in Plaxis 2D versus Calculation Step, with the corresponding friction angles

The plot of plastic points and deviatoric strain at step 60, corresponding to the failure condition, are reported in Figure 4-34. Figure 4-35 shows the shear band formed that generates the slip-surface determining the movement of the unstable soil mass.

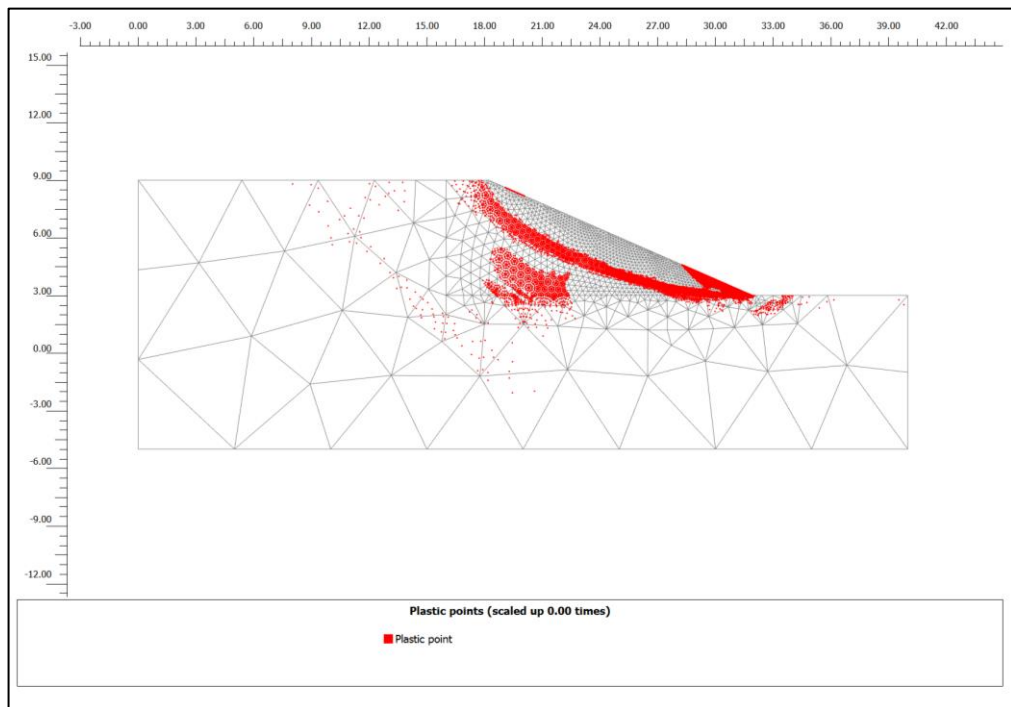


Figure 4-34: Plastic Point plots at calculation step 60

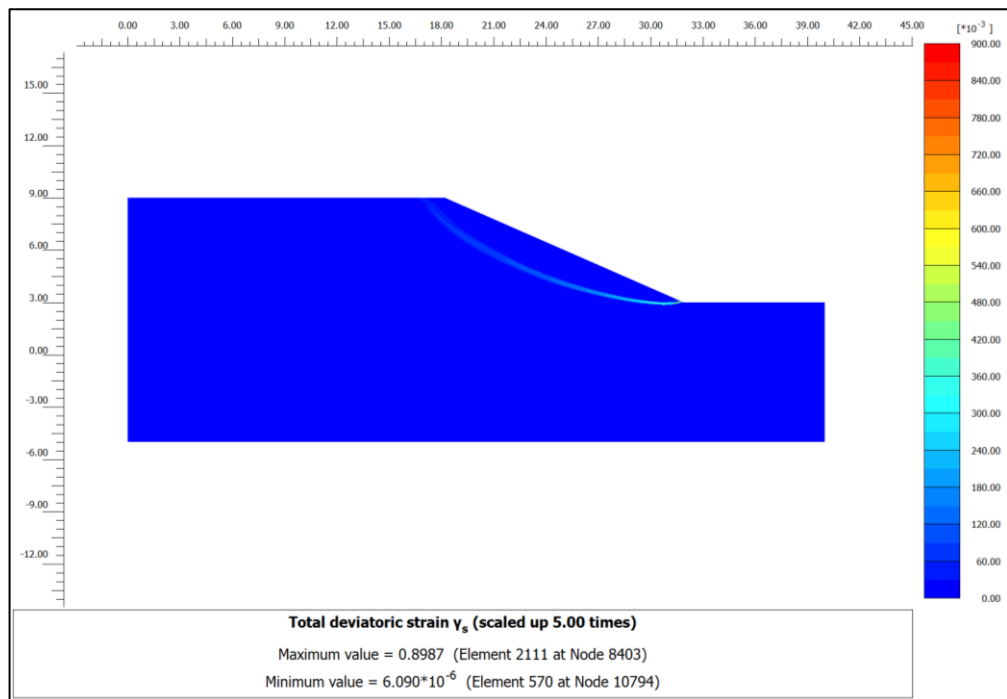


Figure 4-35: Failure mechanism identified at step 60 represented in terms of deviatoric strain

The analysis in LimitState:GEO was carried out by inputting a friction angle equal

to 16.50° and a cohesion equal to 2.05 kN/m^2 , that is the reduced strength parameters that generated failure in PLAXIS. Figure 4-36 shows the failure mechanism returned by LimitState:GEO that compares favourably with shear band returned by Plaxis (Figure 4-35). The Factor of Safety in LimitState:GEO was also found almost equal to unity (1.05).

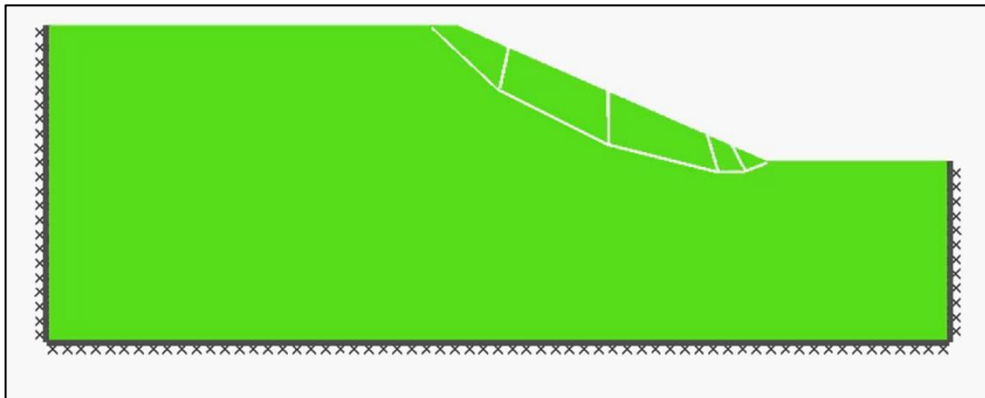


Figure 4-36: Failure mechanism in LimitState:GEO assuming friction angle equal to 16.50° and cohesion equal to 2.05 kPa corresponding to the strengths parameters at step 50 in PLAXIS

4.5.4 Benchmarking ‘Lego’ failure criterion against Upper Bound mechanism

A key aspect of the numerical implementation of the ‘Lego’ approach is the criterion used to turn an element into a ‘failure’ element by identifying a threshold for the minimum number of failure points within an element (stress points where the elastic limit is exceeded). The criterion of 8 failure points out of 12 was tested by comparing the failure surface derived from the Lego approach and the failure surface returned by LimitState:GEO. Once the failure elements are identified, these elements are then connected to define the slip surface as illustrated above.

Figure 4-37 shows the comparison between the failure mechanism resulting from the Upper Bound Theorem obtained with LimitState:Geo (Figure 4-36) and the slip surface derived with the application of the proposed failure criterion. Three cases are considered. In Figure 4-37a the minimum number of failure points required to identify the failure’ element is 11, i.e. any soil elements containing 11 or more failure points

becomes a failed element to be included in the failure mechanism. Figure 4-37b shows the failure mechanism obtained when the minimum number of failure points was set to 8 and finally Figure 4-37c reports the case of 3 failure points.

It can be easily noted that the application of the failure criterion with 11 failure points, results in a slip surface which is considerably different from the one derived with the Limit Analysis solution. This is because the assumption adopted is very restrictive and the continuity of the failed elements comprised in the formation of the failure surface is interrupted. The procedure introduced can find a slip surface around the toe area, but it is clearly not representative of the failure condition for the slope analysed.

On the contrary, the slip surface associated to 3 failure points per soil element is closer to the failure mechanism than the previous case, but it tends to involve a greater soil volume than the limit analysis solution, both at the crest and at the toe regions. This can lead to an overestimation of the number of soil elements to be considered at failure.

The failure surface identified with 8 failure points per soil element provides the best fit with the Limit Analysis mechanism. It can therefore be concluded that this constitutes a more realistic option for the definition of failed elements.

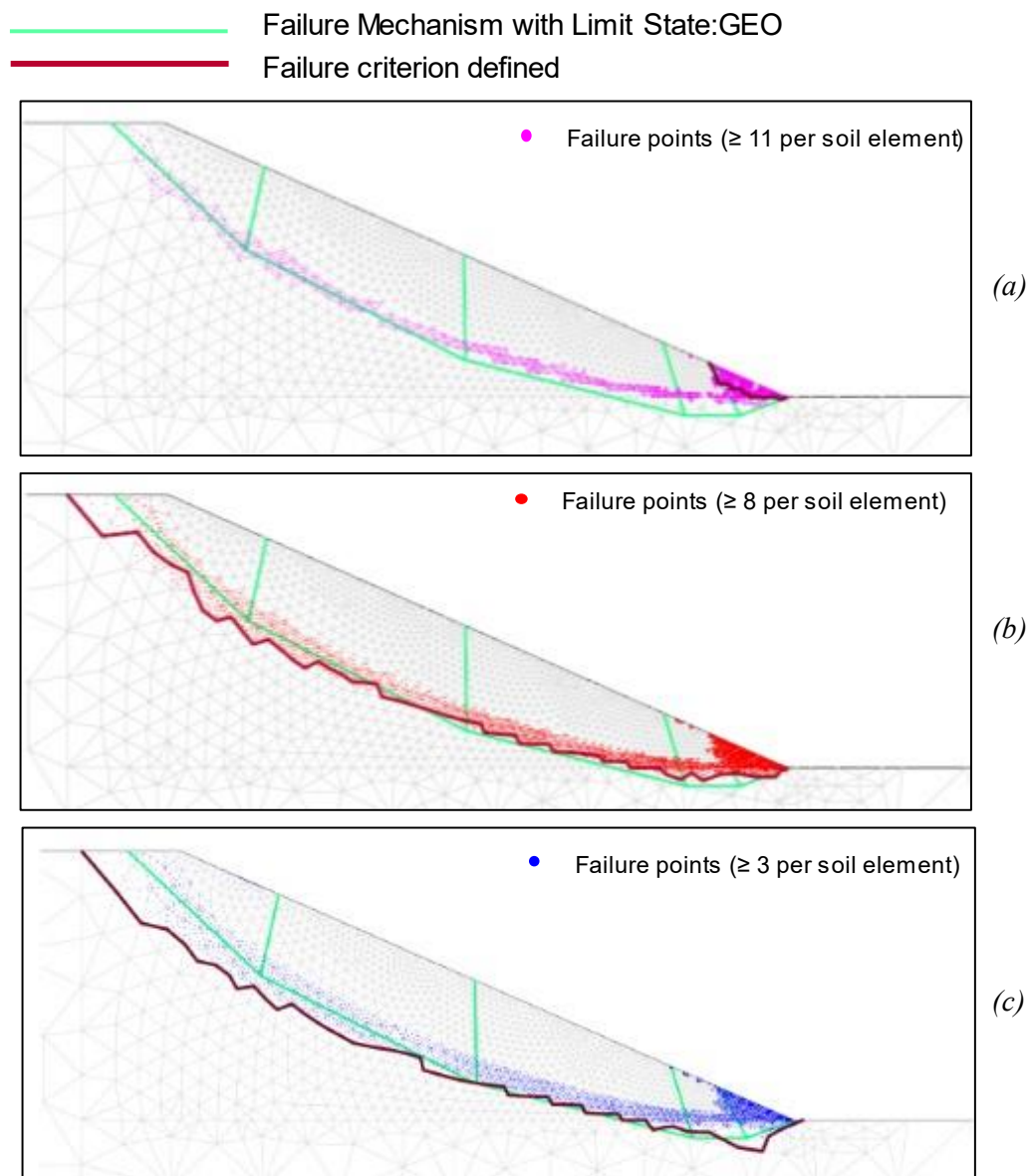


Figure 4-37: Comparisons between failure mechanisms provided by LimitState:GEO and the slip-surface identified with the failure criterion defined for the removal of soil elements. (a) slip surface based on 11 failure points per elements; (b) 8 failure points and (c) 3 failure points

It should be noted that mesh coarseness and element size are also parameters of this model, as they will affect shape and length of the failure surface. Indeed, if the mesh elements are relatively large, plastic points will be spread over a relatively big area. The resulting failure surface is likely to be quite extended and characterised by many angularities. On the contrary, if very tiny mesh elements are adopted, plastic

points will be concentrated over a small zone and the failure surface is likely to be less long and smoother than large mesh. A sensitivity analysis has not been conducted to explore the effects of different element size and mesh coarseness. Nevertheless, the accuracy of this approach is still valid, due to a very fine mesh in the region of interest. In addition, the size of the mesh element is comparable with the size of soil blocks/aggregates being removed as seen in experimental observation.

4.6 Conclusions

The heart of the suction-based breaching model is that the ‘erosion’ process (either progressive surface erosion or headcutting) can be simulated as a series of mini-slope stability problems triggered by the loss of suction, which gradually develops into breach formation. The practical application requires a criterion able to define, when and how the soil blocks constituting the embankment can be removed, thus simulating the progressive failure processes.

The analogy with the sliding of a block along a surface under the effect of an increasing horizontal force, has been used to explain the meaning of plastic and failure point in the framework of the elastic-perfectly plastic soil model. It was assumed that the movement of a soil mass can occur under two conditions:

1. The formation of a ‘plastic point’ (i.e. necessary condition) when the state of stress is equal to the material resistance. In the ‘sliding block’ example this corresponds to the stage in which the block is prone to slide in a plastic manner.
2. The formation of a ‘failure point’ (i.e. sufficient condition) due to the accumulation of deformation beyond the elastic threshold. In the example adopted, this happens when the block is irreversibly distorted and any increment of the force, no matter how small is, produces the sliding of the block.

As the overflow proceeds, due to the change of the pore-water pressures associated with transient water flows, failure points will spread in an adequately extended region, where the accumulation of large plastic deformation results in the formation of a shear zone and eventually a local slip surface will develop alongside

with the movement of small portions of the embankment material. In this approach, hydraulic shear stresses acting on the slope surface are not considered because, typically, their order of magnitude is lower than fine-grained material strengths and apparent cohesion. Nevertheless, superficial failure surface may form in coarse-grained material because non-cohesive.

The concept that failure occurs when a ‘stream’ of failure points develop was incorporated into a ‘Lego strategy’. In Plaxis 2D the embankment is constructed via triangular elements. A soil triangular element becomes a ‘failure element’ when at least 8 of its 12 stress points are ‘failure points’ (i.e. plastic points where the shear strain is greater than the elastic threshold). Once that ‘failed’ elements are found at given time step, an algorithm is operated for the removal of soil elements that concur to identify a concave failure surface.

This Lego strategy including the criterion consisting of a minimum of 8 of 12 failure points required to turn an element into a failure element was then benchmarked satisfactorily against the results from Upper Bound Limit Analysis (LimitState:GEO) and the FEM analysis (Plaxis).

The most important result is that the new numerical approach presented is based exclusively on existing and well-established soil mechanics theories and tools, without introducing concepts of soil erodibility and empirical erosion functions. This specifically addresses Research Question #5 (is it possible to contextualise embankment breaching due to overflow with an alternative approach to erosion models and erodibility parameters?) and Research Question #6 (What if large-scale erosion processes are modelled like mini-slopes stability problems progressing with time?).

Chapter 5. Unsaturated Soil Mechanics

Breaching Model: Qualitative Validation

Abstract

The suction-based breaching model applies the fundamental idea that the embankment breaching due to overflow can be predicted with a sequence of local slope stability failures at the mini-scale. The instabilities are induced by the progressive loss of shear strength associated with the decrease of suction resulting from the advancement of the water fronts from the upstream side and the overflowed downstream slope. The rate of the inward water flow and, hence, the loss of shear strength is controlled by the hydraulic properties of the embankment material.

The numerical methodology implemented uses Plaxis 2D to study the transient water flow and characterises the state of stress and strain during the overflow. Based on this solution an algorithm to define failed soil elements and slip surface is implemented allowing the progressive removal of the unstable soil mass. The iteration of this procedure over time results in the evolution of the embankment profile up to breach formation. This Chapter presents the qualitative validation of the new suction-based reaching model conducted against photos and observations attained from the IMPACT field tests.

5.1 Introduction

The validation of numerical breaching models is a longstanding problem. Since 2004 the importance of model validation was recognised by the Working Group on Embankment Dam Erosion and Breach Modelling organised by the Dam Safety Interest Group (DISG) of CEATI International. The first task addressed by this collaborative research project was the collection of data from real-word case studies

and from laboratory experiments to produce data-sets useful for future model validations (Wahl *et al.*, 2008). This initial review was further extended with a list of more than 726 laboratory breaching tests conducted on small-scale models and reported by the ASCE/EWRI-Task Committee (ASCE/EWRI Task Committee on Dam/Levee Breaching, 2011). These experimental campaigns were mainly performed on homogeneous coarse-grained prototypes ranging from 0.15 m to 1 m in height.

In the last decade, the increasing understanding of the key factors governing the process of breaching initiation and growth pushed new series of laboratory experiments taking advantage of the latest technologies to improve the quality of the measured data. The focus was on the erosion processes observed in different types of materials (i.e. fine- and coarse-grained) and their state (i.e. mainly compaction and water content) (Hanson and Hunt, 2007; Elkholy *et al.*, 2015; Feliciano Cestero, Imran and Chaudhry, 2015; Wei *et al.*, 2016). Various embankment structures have been tested in an attempt to cover a wide range of cases that might be encountered in real applications (i.e. zoned and layered structures). The influence of scale effects was also investigated by several researchers (Schmocker and Hager, 2009; Zhao, Visser and Peeters, 2014). Measurements of pore water pressures were introduced in many experimental set-up to study the effects of the infiltration processes within the embankment material during overflow (Pickert, Weitbrecht and Bieberstein, 2011; Walder *et al.*, 2015; Volz *et al.*, 2017) as well as the influence of toe-drains (Al-Riffai *et al.*, 2009).

The intensified experimental effort was essential for improving knowledge and understanding of the multiple triggering mechanisms of breach in flood defence embankments during overflow. On the other hand, the simulation capabilities improved very slowly and, even if numerous methods were produced through the years, currently there are very few examples of models available to engineering practice (Morris, 2011; Zhenzhen, 2015).

Mitchell *et al.*, (Mitchell and Brown, 2018) in their “Report on EURCOLD workshop on overflow of dams and levees” pointed out that the uncertainties characterising soil erodibility tests in terms of procedures and standards are still critical. This is inevitably reflected in the advancement of modelling capabilities,

which are strongly dependent on soil erosion parameters. Despite the latest achievements, it seems that “the overall progress is by a series of small steps, and this is likely to be true for future progress, such that it may be a decade or more before simple, reliable analytical methods of breach production are available for all types of dam and failure modes”.

The reasons of this slow progress can be associated with the inherent complexity of the phenomena to be modelled and the inter-disciplinary approach required to combine hydrodynamic, hydraulic and geotechnical problems within a common framework. To some extent, this is also due to misconceptions arising when key processes must be recognised and simulated and when model validation is performed. In this regard, Morris (Morris, 2011) presented an interesting analysis where he identified several factors that contributed to the slow progress in the development of more accurate breaching models. He highlighted that breaching models were initially calibrated against data from experiments in laboratory flumes conducted mainly on coarse-grained small-scale embankments. It is therefore evident that these models could only be applied to limited cases and for the particular conditions tested in the experiments. Common practice for the implementation of numerical models is still direct calibration against laboratory datasets rather than assuming theoretical analysis as starting point. This means that a calibrated model can inexorably simulate well the tests material and conditions, but it is likely to fail when applied to more generic configurations. In addition, model validation has often been conducted using the same experimental set up adopted for the initial calibration, hence calibration and validation might be carried out on material in a similar state, thus neglecting the assessment of this critical factors in breaching onset and progression (Morris, 2011). It is also worth specifying that the quality of the experimental data available in literature is quite poor with a general lack of many important details on material properties and state.

Another relevant problem when using laboratory experimental results for model validation, is that these are intrinsically affected by scale effects. If flow conditions can be adapted, this is not equally applicable to material strengths, embankment construction process and modes. Although the quality of laboratory data measured can be very high, as laboratory experiments are conducted under well-controlled

conditions with the aid of the most modern instrumentations and technologies, there are no doubts that the associated scale effects remain one of the biggest challenges when validation has to be performed.

On the other hand, the use of data from full-scale case studies to validate breaching models poses other challenges. Very little information is normally available about the embankments that are therefore characterised with an extremely high level of uncertainties in terms of history, construction details and material properties (Wahl *et al.*, 2008; ASCE/EWRI Task Committee on Dam/Levee Breaching, 2011).

Nonetheless, field tests are currently the most meaningful and valuable reference for model validation, as these allow for comparisons against full-scale conditions that realistically reproduce the physical processes of embankment breaching due to overflow (Volz, 2013). However, it is important to stress that field-tests results are suitable only for qualitative model validation, since detailed measured data are generally not available. Indeed, the installation of instruments and accurate measurements are more complicated than laboratory experiments. In addition to these drawbacks, it must be recognised that planning and running field-tests is logistically more complex, economically expensive and time demanding. These are all issues that explain why there are only two significant test programs available in the literature conducted under relatively controlled conditions and providing substantial information and observations to be used for comparisons with numerical results. In Europe, the most accredited tests were conducted within the IMPACT project. In the U.S., the studies carried out by the Agricultural Research Service (ARS) in 2005, constitute a milestone in the context of documented full-scale tests. These full-scale tests were therefore used for qualitative assessment of the proposed suction-based breaching model.

For the IMPACT full scale embankment experiments, a large set of images have been made available mainly in the review produced as part of the FloodSite EU funded project (Vaskinn *et al.*, 2004; Hassan and Morris, 2008; Morris, 2009). These images will be used to show that the two distinct behaviours of progressive surface erosion and headcut erosion observed in coarse-grained and fine-grained embankments respectively can be captured by the suction-based breaching model.

The point will be made that these two erosion mechanisms arise from differences in the unsaturated hydraulic conductivity rather than erodibility characteristics. Coarse-grained geomaterials are much more permeable than fine-grained soils. They tend to saturate rapidly, losing the additional component of the shear strength provided by suction more quickly than in fine-grained geomaterials. This occurs on the downstream slope during overflow within the first soil layers, giving the typical exfoliation or progressive surface erosion mechanism. In fine-grained soils, the hydraulic conductivity is lower due to the small pores size. On the downstream slope, the soil layers exposed to infiltration by overflow remain unsaturated for longer, while the area most likely to saturate first is the toe. The loss of the suction-induced apparent cohesion occurs at the downstream toe earlier than in the most superficial layers close to the crest and leads to the formation of small steps that retrogressively undercut the embankment producing the typical headcut erosion observed.

In this way, the suction-based breaching model simulates the erosion processes without implementing any erosion model. The erodibility parameters required as an input in the erosion laws or sediment transport equations, which are fundamental part of traditional physically based breaching models, are not required within this framework. As such, the model is not affected by those uncertainties related to the definition of an erosion law and furthermore to the assessment of erodibility parameters via soil erosion tests. Indeed, the suction-based breaching model incorporates soil properties with clear geotechnical meaning.

The second fundamental innovation introduced by the suction-based breaching model is that hydrodynamic tangential forces are not considered a major triggering mechanism. Although it is acknowledged that hydrodynamic tangential forces may play a fundamental role in the overall breaching process, it can be observed that, flow velocities and turbulence are still very low at the onset of overflow. It would then seem reasonable to neglect in first instance the hydrodynamic tangential forces and simulate the breaching processes via existing geotechnical software.

In this application, the suction-based model is implemented in PLAXIS 2D to simulate a fully coupled hydro-mechanical problem in unsaturated soil. The performance of the suction-based model is validated qualitatively against the images

from the IMPACT field-tests.

5.2 IMPACT Project Tests

IMPACT (<http://www.impact-project.net/>) was an EU funded research project conducted between 2001 – 2004 under the Fifth Framework Programme (1998-2009). The main credit of this research was the extensive programme of field and laboratory tests undertaken to collect reliable data, comprising detailed photographic records, assessment of breach growth rates, flow, water levels and control of soil parameters.

Specifically, five field tests on homogeneous and composite embankments were undertaken to investigate failure by overtopping and piping in different materials at a remote site in Norway. In the same period a series of 22 laboratory tests were undertaken at a scale 1:10 (Morris, Hassan and Vaskinn, 2007b) of the test embankment at HR Wallingford Laboratory (UK).

The Norwegian SWECO conducted the field testing in Norway in conjunction with a supporting Norwegian national research programme on dam safety. A range of additional Norwegian partners operated on this project; Norconsult was responsible for the field test construction, implementation and data collection and processing. The considerable amount of data was further reviewed and analysed in more detailed during the European Commission project FLOODSite between 2004-2009. At present, these data are still the reference for understanding of failure processes and widely used for breaching model validation.

It should be highlighted that the review conducted during the FLOODSite project lead by HR Wallingford (UK) revealed significant inconsistencies and discrepancies between the proposed and as built condition of the field tests data. These differences were mainly found in relation to embankment geometry and soil properties. Hence, the two Reports produced as part of the FLOODSite Project: T06 – 08 – 11 (Morris, 2009) and T04 – 08 – 04 (Hassan and Morris, 2008) have been considered as main reference documents.

The test site was located downstream of the Tustervassdammen Dam that impounds the large Røssvatn reservoir, in Nordland County, near the town of Mo i

Rana (Figure 5-1). This location allowed to control the inflow to the reservoir behind the test embankments by regulating one or more of the Røssvassdammen spillway gates. A volume of approximately 70.000 m³ of water was retained behind a 6m high test embankment and used to create a breach (Morris, 2009).

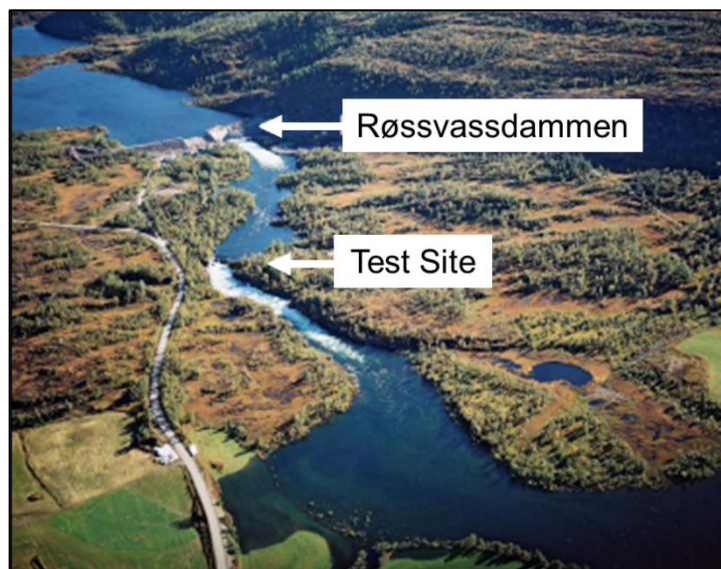


Figure 5-1: IMPACT Field Test site location (Morris, 2009)

The five large-scale tests undertaken between 2002 and 2003 are summarised in Table 5-1. As it will be clear afterwards, the information provided, especially with regards to soil properties, are not sufficient to build mechanical and hydraulic soil models necessary to undertake a fully coupled flow deformation analysis for unsaturated soil. Hence, the details of the field tests presented in the following have been adopted to probe only qualitatively the suction-based breaching model.

Table 5-1: List of the breaching tests undertaken during the IMPACT project (Morris, 2009)

No	Reference	Height	Description	Failure
1	Test1-02	6m	Homogeneous fine-grained	Overtopping
2	Test2C-02	5m	Homogeneous coarse-grained	Overtopping
3	Test1-03	6m	Composite (gravel with moraine core)	Overtopping
4	Test2-03	6m	Composite (gravel with moraine core)	Piping/Overtopping
5	Test3-03	4.5m	Homogeneous (moraine)	Piping

5.2.1 Test #1: Homogeneous Clay embankment (Test 1-02) - Test Overview

The test embankment was constructed during the period 14 August to 10 September 2002. The test configuration is shown in Figure 5-2 and an image of the intact embankment before the test is reported in Figure 5-3.

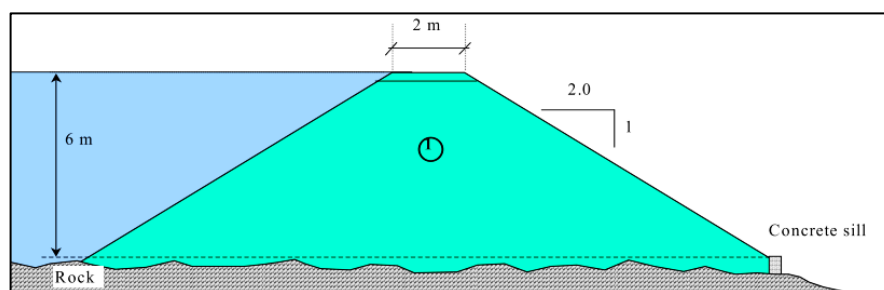


Figure 5-2: Test1-02 of the IMPACT project (Hassan and Morris, 2008)

Some details of the embankment geometry are presented in Table 5-2.

Table 5-2: Embankment geometry of the Test1-02 of the IMPACT project (Hassan and Morris, 2008)

Height (m)	Upstream slope	Downstream slope
5.9	1:2.4	1:2.25



Figure 5-3: Homogeneous fine-grained test embankment (Impact, Test1-02)

The material used is classified as “lean clay” characterised by 15% of sand, 60% of silt and 25% of clay, as can be seen from the grain size distribution in Figure 5-4 (Morris, Hassan and Vaskinn, 2005).

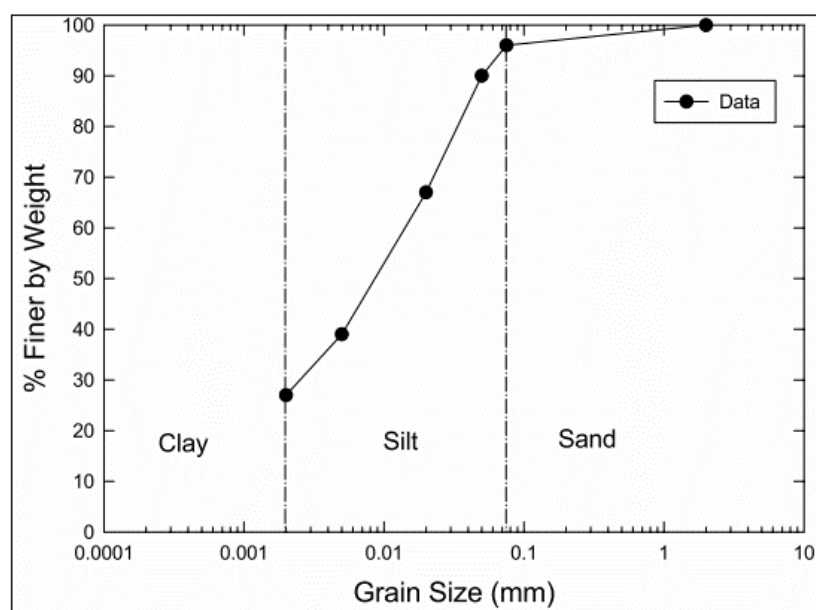


Figure 5-4: Grain size distribution of the embankment material for IMPACT Test1-02 (Morris, Hassan and Vaskinn, 2005)

Soil properties as reviewed during the FLOODSite project, are summarised in the table below.

Table 5-3: Soil properties for Field Test #1 (Hassan and Morris, 2008)

<i>Soil Properties (Field Test #1 – Test 1-02)</i>	
Moisture Content	30
D50 (mm)	0.007
Porosity	0.46
Friction Angle	22.9°
Cohesion(kN/m ²)	4.9
Specific weight dry (kN/m ³)	14.8

The original specification to build the test embankment was to compact the material in 0.15 m layers. However, due to the high-water content of the clay deposit and the wet conditions, it was decided to increase the thickness of the layers to 0.4 m

and to reduce the compaction pressure to accelerate the construction phases when the embankment was almost 2 m high from foundation level. This means that the embankment constructed comprised two zones characterised by different soil properties, resulting in significant consequences on breaching initiation time.

In addition, other issues arose during the tests. The upstream water level oscillated periodically trying to keep the hydraulic load constant. Cracks and fissures were present in the embankment prior to the overtopping tests and seepage occurred on the left abutment at the interface earth-rock. Although the main failure mechanism still consisted of headcutting, the seepage process in this area nearly induced a piping failure (Morris, 2009) as shown in Figure 5-5.

These aspects must be considered when model validation is performed. For example, when the HR BREACH was assessed against this field test data, soil erodibility parameters were increased significantly to achieve a satisfactory simulation. This was necessary to reflect the uncertainties on the construction and material properties characterising this field test (Morris, 2011).

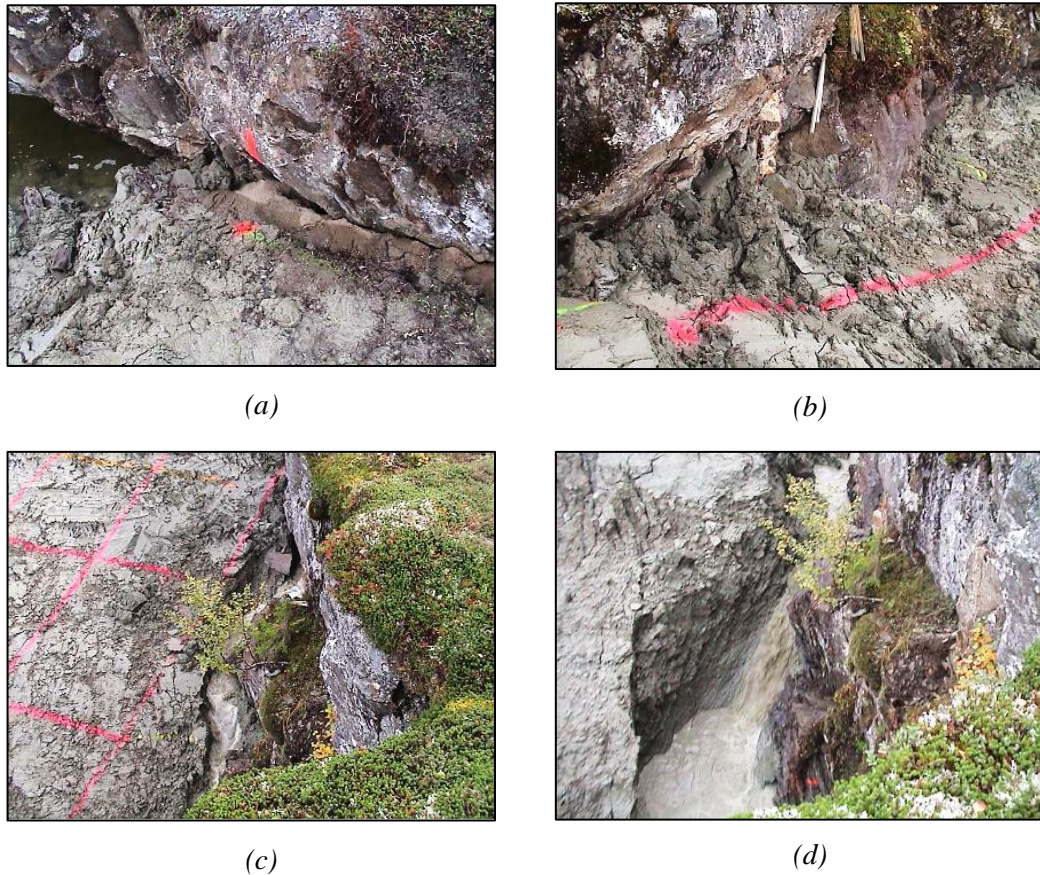


Figure 5-5: (a) Interface between embankment and rock at the left abutment as seen from the upstream edge; (b) view of the left abutment from downstream; (c) downstream face and left abutment during the test; (d) piping processes observed during the test at the left abutment (Morris, 2009)

5.2.2 Test #2: Homogeneous Gravel Embankment (Test 2C-02) – Test Overview

The second test of the IMPACT project was conducted on an embankment built mainly with coarse-grained materials with less than 5% fines. It is an overtopping test aiming at observing the failure mechanisms leading to breach formation in homogeneous coarse-grained embankments. The test configuration as presented in the FLOODSite T04-08-04 Report (Hassan and Morris, 2008) is shown in Figure 5-6 and geometrical details reported in Table 5-4.

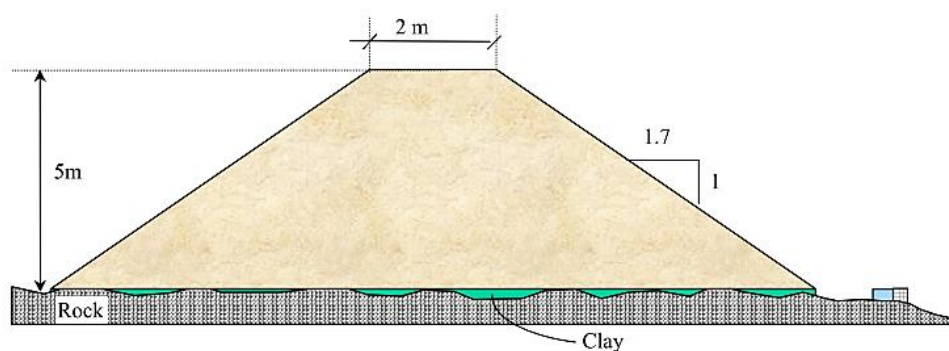


Figure 5-6: Test2C-02 of the IMPACT project (Hassan and Morris, 2008)

Table 5-4: Geometrical details for Test 2C - 02 of the IMPACT (Hassan and Morris, 2008)

Height (m)	Upstream slope	Downstream slope
5.0	1:1.9	1:1.6

Available soil properties as reviewed during the FLOODSite project are summarised in Table 5-5.

Table 5-5: Material Properties reported for the Test 2C-02 of the IMPACT project (Hassan and Morris, 2008)

Soil Properties (Field Test #2 – Test 2C-02)	
Moisture Content	7
D50 (mm)	4.75
Porosity	0.22
Friction Angle	42°
Cohesion(kN/m ²)	0.9
Specific weight dry (kN/m ³)	21.2

The embankment was constructed using vibratory rolling compaction in 0.5 m layers and the test was undertaken on the 16th October 2002, when in Norway the very

low temperatures caused the freezing of the upstream reservoir as well as the superficial layers of the downstream slope of the embankment (Figure 5-7).



Figure 5-7: IMPACT Test 2C-02 frozen embankment (Morris, 2009)

It is evident that the “frozen” condition considerably affected the test procedure and the results observed. First the crest material had to be defrosted. This was achieved by blocking water with a plank placed in the initial notch cut in the embankment crest to initiate the overtopping. Afterwards, when the water levels raised sufficiently to melt the ice formed, the sandbags were removed, and the test started. But the most important features of this test are the failure mechanisms observed due to the frozen conditions. In spite of the common assumption that the predominant process leading to breach in coarse-grained geomaterial is progressive surface erosion, breach failure was led purely by headcutting as shown in the figure below.



Figure 5-8: Headcutting observed in the coarse-grained embankment during Test2C-02 of the IMPACT project due to frozen conditions after (Morris, 2011)

When the breach formed and after test completion, the faces of the breach remained almost vertical with overhanging pieces as can be seen in Figure 5-9.



Figure 5-9: Breach side after test completion with overhanging region. (Morris, 2009)

This unexpected behaviour for coarse-grained geomaterial clearly reflects the particular “freezing” condition when the test was run. Hence, this proves once again the importance of soil conditions and states during overflow.

Under the point of view of model validation, even at a qualitative level, this field test presents important uncertainties which make it unrepresentative for the study of

the failure mechanism by progressive surface erosion.

5.2.3 Test #3 and Test #4: Composite Structures

The tests conducted on composite structures have been considered as source of comparison for progressive surface erosion, which was poorly documented in Field Test #2.

Test 1-03 – Test Overview

The third test was conducted in August 2003 to increase the understanding of the breach formation processes in composite embankments due to overflow.

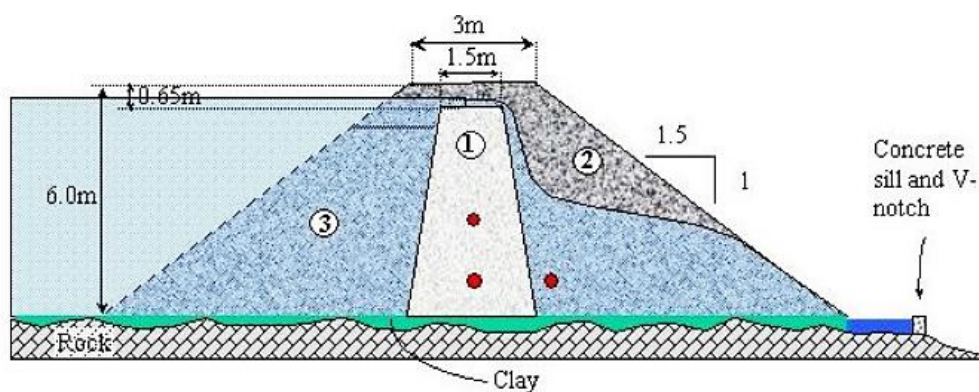


Figure 5-10: Configuration adopted for the Field Test 1-03 (Hassan and Morris, 2008)

Details about the geometry are reported in the above figure and in Table 5-6. The structure is composed of a moraine core while rock fill was used in the upstream and downstream areas.

Table 5-6: Geometrical details for Test 1-03 (Hassan and Morris, 2008)

Height (m)	Upstream slope	Downstream slope	Core Slopes
5.9	1:1.55	1:1.55	4:1

As in the previous tests, several discrepancies were found in the data provided. The recommended values for material properties are summarised in Table 5-7 and

Table 5-8. The central moraine core was compacted with vibratory roller in 0.5m layers. The rockfill material was also compacted with vibratory roller in layer 1m thick.

Table 5-7: Material Properties reported for the Moraine Core used in Test 1-03 (Hassan and Morris, 2008)

<i>Moraine Core Properties (Field Test #3 – Test 1-03)</i>	
<i>Moisture Content</i>	<i>0.06</i>
<i>D50 (mm)</i>	<i>7</i>
<i>Porosity</i>	<i>0.244</i>
<i>Friction Angle</i>	<i>45.6°</i>
<i>Cohesion(kN/m²)</i>	<i>20</i>
<i>Specific weight dry (kN/m³)</i>	<i>20.6</i>

Table 5-8: Material Properties reported for the Rockfill used in Test 1-03 (Hassan and Morris, 2008)

<i>Rockfill Core Properties (Field Test #3 – Test 1-03)</i>	
<i>Moisture Content</i>	<i>0.02</i>
<i>D₅₀ (mm)</i>	<i>85</i>
<i>Porosity</i>	<i>0.235</i>
<i>Friction Angle</i>	<i>42°</i>

Headcutting and progressive surface erosion were both observed, however the headcut formed never reached the upstream crest and surface erosion appeared to be the dominant mechanism for breach initiation.

Test 2-03 – Test Overview

The fourth test was undertaken on a composite structure like the previous one, with a central moraine core and rockfill material on the upstream and downstream shoulders. However, because the purpose was to investigate the mechanisms of failure due to piping the structure was perforated at the bottom and a pipe was installed with a valve at the downstream end to control the flow. Two triggering options were considered. In Option #1 the pipe was filled and surrounded by sand for a certain extent, while in Option #2 the sand fill was extended up to the top. This is shown in Figure 5-11.

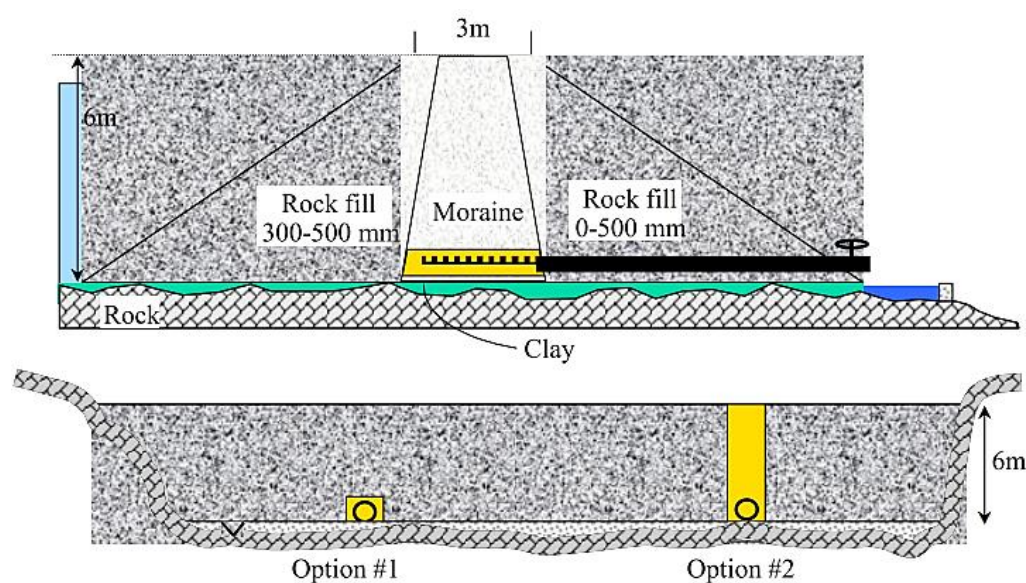


Figure 5-11: Configuration adopted for the Field Test 2-03 (Hassan and Morris, 2008)

Some details of the embankment geometry are also presented below.

Table 5-9: Test 2-03 geometry (Hassan and Morris, 2008)

Height (m)	Upstream slope	Downstream slope	Core Slopes
6.0	1:56	1:1.48	4:1

The same material properties (Table 5-7 and Table 5-8) and construction methods for Test 1-03 were used for this test. This was run in September 2003 and although the

purpose was to investigate failure induced by piping processes, overtopping was allowed by creating a depression on the embankment crest. This was thought to be necessary because both Option #1 and #2 appeared to be unsuccessful as breaching did not occur. However, the researchers found that Option #1 worked and ultimately it would have led to breach formation if the test was run for longer (Morris, 2009)³. Hence what is documented in this test, is a failure by overtopping. In contrast with the other tests, where headcut erosion was prevailing in this case breach initiation and progression were distinctly dominated by mechanisms of surface erosion and therefore are used as main source of comparison for the qualitative validation.

5.2.4 Summary of IMPACT field test inputs and recommendation

This brief overview of the IMPACT field tests allowed to derive the following considerations:

1. The discrepancies between the proposed and as built test conditions in relation to geometries and material properties were significant. The review conducted during the FLOODSite project provided recommended values. Nevertheless, the data provided especially with regards to material properties and conditions are only partial and not sufficient for the estimation of the soil parameters required to model the hydro-mechanical behaviour of the embankment material with the suction-based breaching model.
2. The issues characterising Test #1, especially the different compaction efforts used to build the embankment, the presence of cracks and the seepage observed on the left abutment, had significant impacts on the time-related processes and failure. These effects can be hardly quantified but, at the same time cannot be neglected when model validation is performed.
3. Test #2 cannot be considered representative of the typical behaviour expected for coarse-grained homogeneous embankment during overflow. In this case, the extremely low temperatures caused the freezing of the most superficial layers of soil constituting the embankment with significant implications on the breaching processes. Headcutting was observed to be the predominant failure mechanism leading to breach onset, in contrast with the results obtained in Series 1 of

laboratory experiments conducted on a scaled embankment of the Field Test #2 (Morris, Hassan and Vaskinn, 2007a). This latter, indeed, showed that breach occurred mainly by progressive surface erosion. This progressive failure mechanism is commonly considered to be the typical process characterising the behaviour of coarse-grained geomaterials during overflow, as documented by many previous studies.

Based on these issues and given the unquantifiable uncertainties affecting the input data provided, it was concluded that the direct simulation of the field tests would have been inevitably misleading and not very relevant.

As a result, the implementation of the suction-based breaching model was conducted with reference to a generic embankment configuration likely to be encountered in real cases. The embankment materials were selected considering an ideal silty-clay and an ideal sand. The field tests data were used for qualitative comparison.

5.3 Implementation of the Suction-based Breaching Model with FEM

The theory behind the suction-based breaching model was presented in Chapter 3 and Chapter 4, along with the definition and calibration of the failure criterion formulated to assess the stability of the embankment materials and ultimately to remove the failed soil mass.

Here, the focus is on the implementation of the numerical model and its application to simulate the overflow of two ideal embankments constructed with fine-grained and coarse-grained geomaterials, respectively.

In this application, the methodology is implemented in PLAXIS 2D. This is a two-dimensional finite element program that allows solving multiple geotechnical and soil-structure interaction problems. The main reason why PLAXIS 2D has been selected among the others, is because it works in calculation phases that simulate a specific problem according to the project sequence. These phases can be for example the application of loads, excavations, construction of new elements, the introduction of a

consolidation period (Brinkgreve, Kumarswamy and Swolfs, 2017). In other words, it is possible to define many phases where geometries, loads, boundary conditions and material properties can be changed, activated, or deactivated within the same project without affecting the previous calculation phases.

For the suction-based breaching model, this means that soil elements forming the embankment can be deactivated in each calculation phase (without changing the results of the previous phases) to simulate the removal of the instable soil elements identified with the methodology presented in Chapter 4. The sequence of calculation phases where soil clusters are progressively deactivated, and boundary conditions adapted is designed to simulate the time-dependant processes leading to breach formation. This methodology can be performed provided that the whole embankment is subdivided in soil elements. For this purpose, the overall implementation of the suction-based breaching model in PLAXIS 2D is broken down into the following steps:

1. Definition of the 2D geometry of the embankment.
2. Mesh Generation to obtain nodes coordinates of the soil triangular elements which constituted the clusters for the embankment discretization.
3. Definition of the final configuration in triangular soil blocks resulting from the first mesh generation conducted at “step 2”.
4. Final Mesh Generation for the finite element calculation.
5. Definition of material properties according to the mechanical and hydraulic models available in PLAXIS 2D.
6. Definition of the Calculation Phases and relative Boundary Conditions.
7. Analysis of the results in the post-processor program of PLAXIS 2D of the last overflow calculation phase and application of the suction-based breaching model failure criterion.
8. Iteration of step 6 and step 7 up to breach formation.

These are presented in detail in the following paragraphs.

5.3.1 Embankment Geometry

The embankment geometry implemented in PLAXIS 2D is shown in Figure 5-12 and in the table below.

Table 5-10: Details of the embankment geometry adopted

Embankment Height (m)	Upstream slope	Downstream slope	Crest width (m)
6.0	23°	24°	2.0

This is based on the information provided by the first IMPACT field test, but it can be considered representative of real flood embankments.

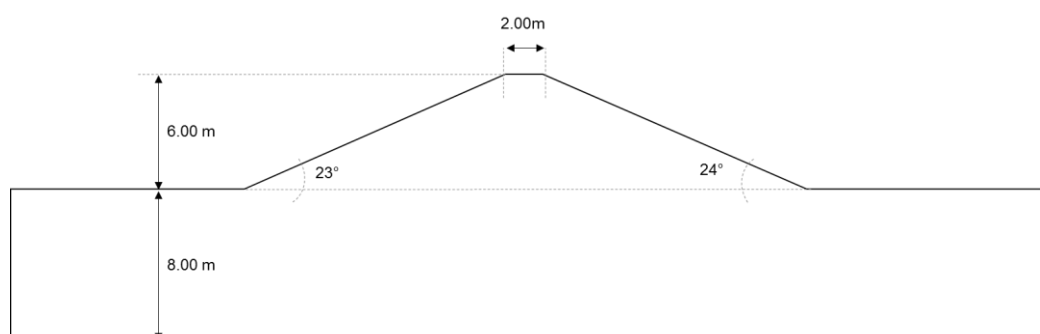


Figure 5-12: Embankment geometry input in Plaxis 2D

This initial geometry has been discretised in mini triangular soil blocks obtained with the triangulation procedure used in PLAXIS 2D to automatically generate the finite element mesh. This is what here is referred as “LEGO” strategy.

In PLAXIS 2D, 6-node or 15-node triangular elements are available. The first is associated to a second order of interpolation for displacements and three Gauss points for the numerical integration. On the contrary, the 15-node configuration is based on a fourth order interpolations for displacements and twelve Gauss points. To generate the mesh used to draw the final embankment geometry, the 6-node triangle option is selected, because the mesh is not for computational purposes and therefore, accuracy is not a requirement. The main mesh characteristics are presented in Table 5-11.

Table 5-11: Element sizes as generated by the triangulation procedure in PLAXIS 2D used to build the final embankment geometry

Model	Plane strain
Elements	<i>6-Node</i>
Nr of soil elements	<i>2478</i>
Nr of Nodes	<i>5111</i>
Average element size	<i>0.537 m</i>
Maximum element size	<i>3.209 m</i>
Minimum element size	<i>0.0736m</i>

Figure 5-13 shows the mesh representation and it is worth noting that different degrees of coarseness are used.

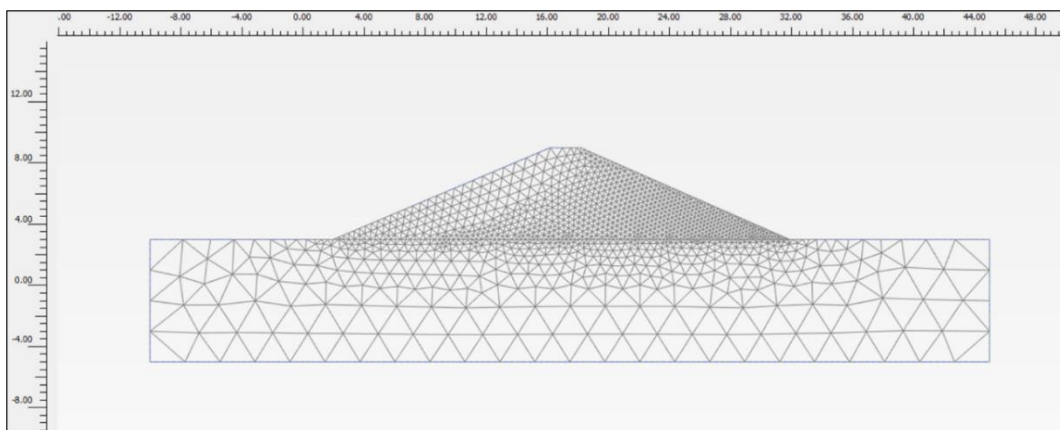


Figure 5-13: Initial mesh considered to draw the triangular soil elements constituting the embankment

The finite elements are smaller along the downstream slope and in the toe area compared with the upstream slope and the lower part of the embankment. This is because the downstream slope and toe are the focus of this study where a better quality and numerical accuracy is required.

The element sizes l_e in PLAXIS are defined based on the geometry domain dimension and on the parameter r_e (relative element size factor) depending on the

coarseness level. In this case $r_e = 0.67$ corresponding to the “fine” level of coarseness. A local refinement is performed on the downstream slope to a coarseness factor of 0.2, on the crest and upstream slope this is set up to 0.6.

At this stage, no calculations are performed, and the output are the nodes coordinates of triangles generated within the triangulation procedure. These have been input into a macro that selects the vertices of the mesh triangles and automatically draws the geometry in PLAXIS 2D. The final geometry of the embankment constructed as whole of triangular soil elements is shown in Figure 5-14.

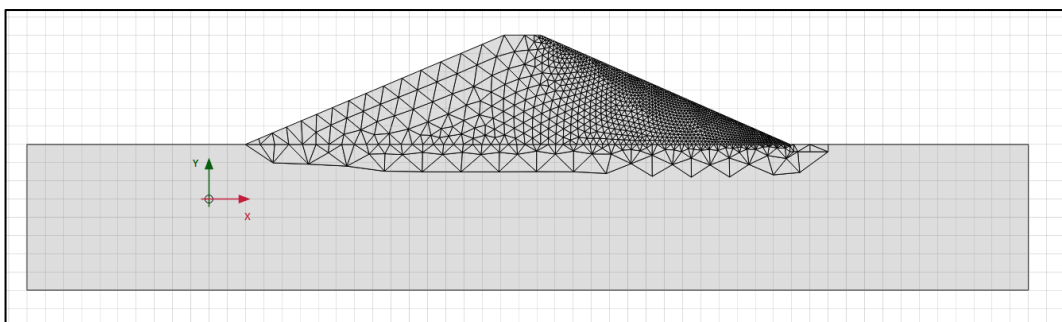


Figure 5-14: Embankment geometry composed of triangular soil elements

The details of the final mesh can be found in Table 5-12.

Table 5-12: Details of the final computational mesh

Model	Plane strain
Elements	<i>15-Node</i>
Nr of soil elements	<i>2732</i>
Nr of Nodes	<i>22253</i>
Average element size	<i>0.392 m</i>
Maximum element size	<i>5.274 m</i>
Minimum element size	<i>0.034 m</i>

The final finite element mesh for numerical calculation purposes is shown in

Figure 5-15. In this way the soil triangle elements constituting the embankment body (blue lines) and the computational mesh triangles (grey lines) tend to coincide in the area of interest.

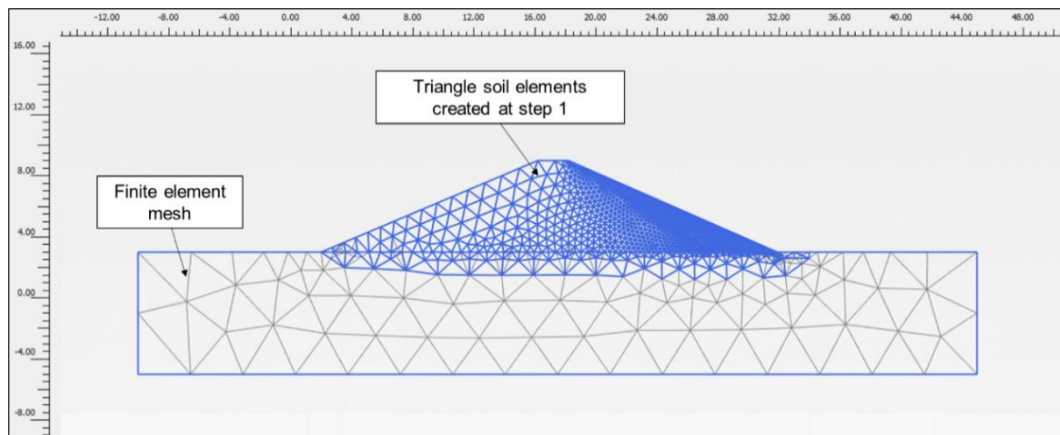


Figure 5-15: Triangular soil clusters drawn are represented in blue and the computational mesh elements in grey lines

Because of the failure criterion and based on the algorithm applied for the removal of the failed soil elements as described in paragraph 4.5, it is evident that the simulated failure processes, both in terms of shape and time evolution, are affected by the size of the mesh elements and mesh coarseness. If the mesh elements are large, the failure surface enveloping the failed elements will be bigger and deeper than a failure surface developed with smaller soil clusters. The failure mechanism will affect a larger area and the progressive failure will be accelerated because the propagation will require less time-intervals and a shorter overflow duration to arrive at the crest, than a model with small elements. The size of the element and the mesh refinement will also affect the shape of the failure surface. Very small and very fine mesh will result in a smoother slip line where the angularity of the triangular elements is less noticeable than big and coarse mesh. In addition, the number of failure points formed in a soil region will vary with the size of the element of the mesh. For a very fine mesh, the numerical solution is more accurate and more failure points will form in a localised area. This will induce the formation of more failed elements, compared to the case of a coarse mesh. The effects of the element size and mesh coarseness have not been investigated in this work and a sensitivity analysis should be performed to understand the influence of these

factors on the modes and times of breach formation. However, the adopted mesh is reasonably fine, especially along the toe of the downstream slope that is anticipated to be the most vulnerable area. The mesh refinement is considered to be sufficient to avoid mesh dependence effects on the numerical results.

5.3.2 Hydro-mechanical constitutive models

The suction-based breaching model analyses the change of pore-water pressures and soil deformation due to the multiple water flow processes prior and during the overflow phases. To model this problem, a fully coupled hydro-mechanical calculation is conducted. One of the essential ingredients of the hydro-mechanical problem formulation, is the choice of the constitutive laws describing the hydraulic and mechanical behaviour. In this application the Mohr-Coulomb model and the Van Genuchten equation as implemented in Plaxis 2D, have been considered to model the mechanical and hydraulic behaviour, respectively.

The Mohr-Coulomb soil model in Plaxis 2D is the linear elastic perfectly plastic model, defined in terms of the following effective stress σ'_{ij} :

$$\sigma'_{ij} = \sigma_{ij} - S \cdot u_w \cdot I \quad \text{Equation 5-1}$$

where σ_{ij} is the total stress, u_w is the pore-water pressure, and S is the degree of saturation, and I is the identity matrix. It is adopted assuming drained conditions for all the calculation phases. This model requires five input parameters in terms of “effective stress” analysis:

- E' : Young's Module (kN/m²)
- ν' : Poisson's ratio (–)
- c' : cohesion (kN/m²)
- ϕ' : friction angle (°)
- ψ : dilatancy angle (°)

The linear elastic perfectly plastic model with Mohr-Coulomb failure criterion implies a strong simplification of soil behaviour but introduces a relatively low number of soil parameters. For example, it is well-known that experimental stress-strain curves

are non-linear even at low stress level and are depending on the stress path followed, if it is the primary loading, unloading or re-loading condition.

The choice of the Young's modulus is therefore not a trivial task and requires some preliminary considerations based on the stress values anticipated for the problem studied. In addition, because the analysis is hydro-mechanically coupled, equilibrium, congruence and continuity equations are concurrently solved. The variation of water volume depends on both degree of saturation and soil porosity, which in turn depend on the time variation of suction and total stress as a result, soil stiffness play an important role for both the deformation and flow processes. It is expected that the stiffer the soil the more rapid is propagation of pore water pressure imposed at the surface.

For to the hydraulic model, the soil water retention curve was defined according to the Van Genuchten equation (Equation 5-2).

$$S(\psi) = S_{res} + (S_{sat} - S_{res})[1 + (g_a|\psi|)^{g_n}]^{g_c} \quad \text{Equation 5-2}$$

where:

- S_{res} is residual saturation related to the water that remains in soil even at high suction head.
- S_{sat} is the saturation at zero suction.
- $\psi = \frac{p_w}{\gamma_w}$ [L], is the pore-water pressure head, where p_w is pore-water pressure and γ_w is the water unit weight.
- g_a is related to the air entry value (AEV). Its dimension is [1/L].
- g_n accounts for the rate of water extraction from the soil when the air entry value is overcome.
- g_c controls the asymmetry of the curve with respect to its inflection point. In Plaxis 2D it is assumed that:

$$g_c = \frac{1 - g_n}{g_n} \quad \text{Equation 5-3}$$

This last assumption allows to convert Equation 5-2 into a two-parameter equation (Mualem), such that only the soil-dependent parameters g_a and g_n must be entered in

input.

According to Mualem - Van Genuchten model, the relative permeability is function of the effective degree of saturation as described by Equation 5-4:

$$k_{rel}(S) = S_e^{g_c} \left[1 - \left(1 - S_e^{\left(\frac{g_n}{g_n-1} \right)} \right)^{\frac{g_n-1}{g_n}} \right]^2 \quad \text{Equation 5-4}$$

where S_e is the effective degree of saturation.

$$S_e = \frac{S - S_{res}}{(S_{sat} - S_{res})} \quad \text{Equation 5-5}$$

Finally, the hydraulic conductivity k is given by

$$k(S) = k_{sat} \cdot k_{rel}(S) \quad \text{Equation 5-6}$$

where k_{sat} is the saturated hydraulic conductivity.

In summary, to describe the soil water retention behaviour in Plaxis 2D, S_{sat} , S_{res} , the parameters g_a , g_n and the saturated hydraulic conductivity k_{sat} are required as input values. A full detailed description about the implementation of these models in Plaxis 2D can be found in the Plaxis Reference and Material Manuals ('Plaxis 2018, Users Manual', 2018).

The following two paragraphs outline the parameters considered in the numerical simulation. Clearly, the choice of parameters such as the effective cohesion and the peak friction angle, will influence the development of plastic points and therefore the formation of failure surfaces according to the criterion adopted.

At the same time, the SWRC and particularly the air entry value, in addition to the hydraulic conductivity function, will govern the multiple water flow processes from the pre-flood conditions to the overflow. It is evident that the effects of overflow in terms of loss of suction, will be accelerated if the material presents a low air entry value and a high hydraulic conductivity. This will result ultimately in a more rapid failure, characterised by superficial instabilities. On the contrary, materials with high air entry suction and low permeability, will arrive at the overflow starting from a more

favourable initial condition. This is because during the rise of the water levels, the water infiltration from the upstream slope will be very gradual and a large part of the embankment materials will have relatively high suction values. Afterwards, during the overflow, flood water will penetrate very slowly at the surface due to the low permeability associated with high suction. This means that the most superficial layers will be stable, depending also on the strength parameters. In this case, failure surface will form at greater depth, involving an extended portion of the slope, where it is more likely that the embankment material has lost suction due to saturation. It is also worth mentioning that this is a wetting process and when the hydraulic properties of the materials are selected, the hysteresis of the water retention behaviour must be considered.

A sensitivity analysis where cohesion, friction angle, SWRC and hydraulic conductivity are changed to understand the impacts on the numerical results, has not been performed. However, realistic assumptions have been conducted to represent typical behaviour of an ideal silty-clay and an ideal sand. In more details, the soil water retention curves for both materials have been derived based on available database in Plaxis 2D and particle size distribution considerations. The Mohr-Coulomb strength parameters assumed are in agreement with literature values for these materials.

5.3.3 Material Properties of fine-grained soil

Mechanical Properties of fine-grained soil

To study the breaching processes in a homogenous fine-grained embankment an ideal silty clay is considered. The material properties input in Plaxis 2D are summarised in Table 5-13. It is worth mentioning that a small value of effective cohesion has been considered because, especially at the onset of overflow, the attention of this analysis is on the most superficial layers of the downstream slope. This means that the stress levels are very low and a Mohr-circle representative of the state of stress of a soil element near the surface, will be close to the origin of the axis of the Mohr-Coulomb plane. For this range of stress, it is well known that the Mohr-Coulomb failure criterion is not a straight line but typically presents a curvature towards the origin. Hence the

assumption of a low intercept value.

Table 5-13: Material properties for the Mohr-Coulomb model adopted for the silty-clay representative of the fine-grained homogeneous embankment

Material Properties (Homogeneous fine-grained embankment)		
Unit weight (unsaturated)	γ_{unsat} [kN/m ³]	15.0
Unit weight (saturated)	γ_{sat} [kN/m ³]	19.5
Young Modulus	E' [kN/m ²]	10000
Poisson's ratio	ν' [-]	0.33
Effective Cohesion	c' [kN/m ²]	0.5
Effective friction angle	ϕ' [°]	24.0
Dilatancy Angle	ψ' [°]	0.0

The Young Modulus has been selected with reference to an experimental program conducted on a clayey silt from a flood defence embankment of the Po river (D'Onza *et al.*, 2016). The main aim of this investigation was the study of the influence of the compaction procedure on the soil water retention behaviour. Each sample was loaded to different net stress (i.e. $\sigma - u_a$, which are respectively the total stress and the air pressure), prior to conduct the test by applying a dry-wetting cycle in a Wissa oedometer apparatus, with changes of suction at 5, 10, 20, 50, 100, 200, 300, 400, 600 and 850 kN/m². All tests were terminated with a wetting path from the maximum suction level to the minimum of 5 kN/m². This is the situation occurring during the overflow process, where the most superficial layers of the soil constituting the embankment are subjected to a water flow which imposes a reduction of suction from the initial value to zero.

Figure 5-16 shows the variations of void ratio with suction for one of the samples compacted in the laboratory and loaded at the different net stresses (i.e. 50, 200 and 500 kN/m²).

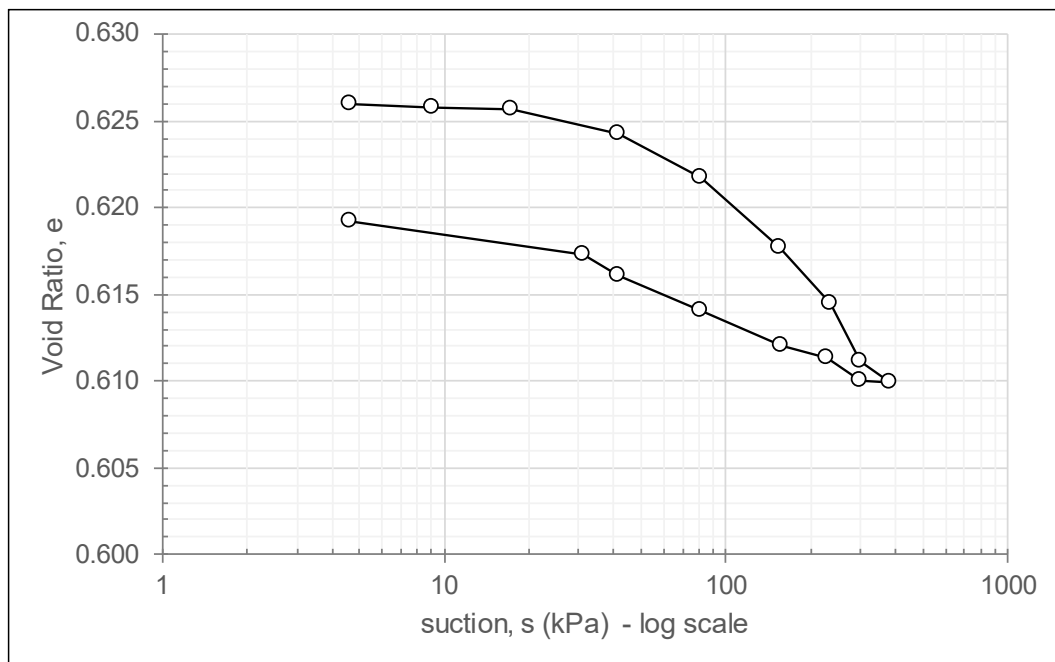


Figure 5-16: Tests on samples compacted in laboratory after (D'Onza et al., 2016)

With reference to the test conducted at net stress 50 kN/m^2 and considering the suction interval between $5\text{-}60 \text{ kN/m}^2$, which is expected for the case studied at the onset of overflow, (i.e. initial value of suction 60 kN/m^2 which tends to zero when water flow is imposed). Assuming that the bulk modulus K is given by :

$$K = \frac{\Delta s}{\Delta \varepsilon_v} \quad \text{Equation 5-7}$$

with

$$\Delta \varepsilon_v = \frac{\Delta e}{1 + e_0} \quad \text{Equation 5-8}$$

and specifically:

$$\Delta \varepsilon_v = \frac{0.620 - 0.615}{1 + 0.615} = 0.0031$$

we have:

$$K = \frac{55}{0.0031} \approx 17800 \text{ kN/m}^2$$

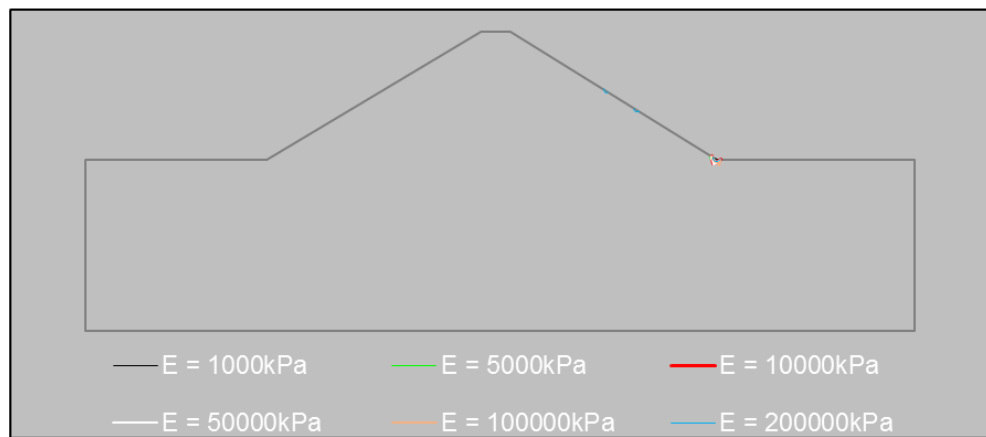
Given that:

$$E = 3K(1 - 2\nu) \qquad \text{Equation 5-9}$$

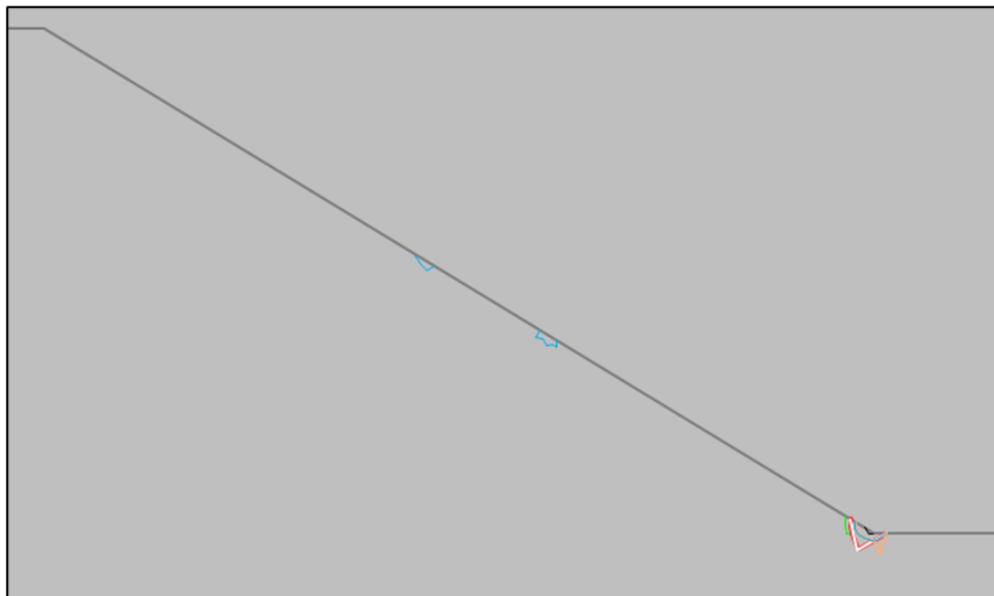
and assuming $\nu = 0.33$, we can finally derive an order of magnitude of the Young modulus of the ideal silty-clay:

$$E \approx 18120 \text{ kN/m}^2$$

To understand the impact of the value of the Young modulus E adopted, a sensitivity analysis was conducted considering the following values: 1000, 5000, 10000, 50000, 100000 and 200000 kN/m^2 . A first overflow phase corresponding to a period of half an hour has been performed and the results, in terms of plastic points and deformations, have been analysed according to the failure criterion presented in Chapter 4. The failure surfaces at the onset of instability resulting for each value of stiffness considered are shown in the figure below. It can be observed that, after 30 minutes of overflow, the failure conditions are concentrated at the toe area of the embankment for all the cases analysed regardless of the value of E . In addition, it seems that the Young modulus influence is negligible as the failure surfaces determined are nearly the same for all the values of E . This means that regardless of the stiffness selected, the same number of soil elements underlain by the failure surface will be removed within the Lego strategy.



(a)



(b)

Figure 5-17: Failure surface resulting after a period of 30 minutes of overflow for the different values of stiffness considered (a) entire embankment; (b) zoom on the toe area.

Hydraulic Properties of fine-grained soil

The SWRC assumed to be representative of the hydraulic behaviour of the silty clay constituting the embankment according to the van Genuchten equation is shown in Figure 5-18.

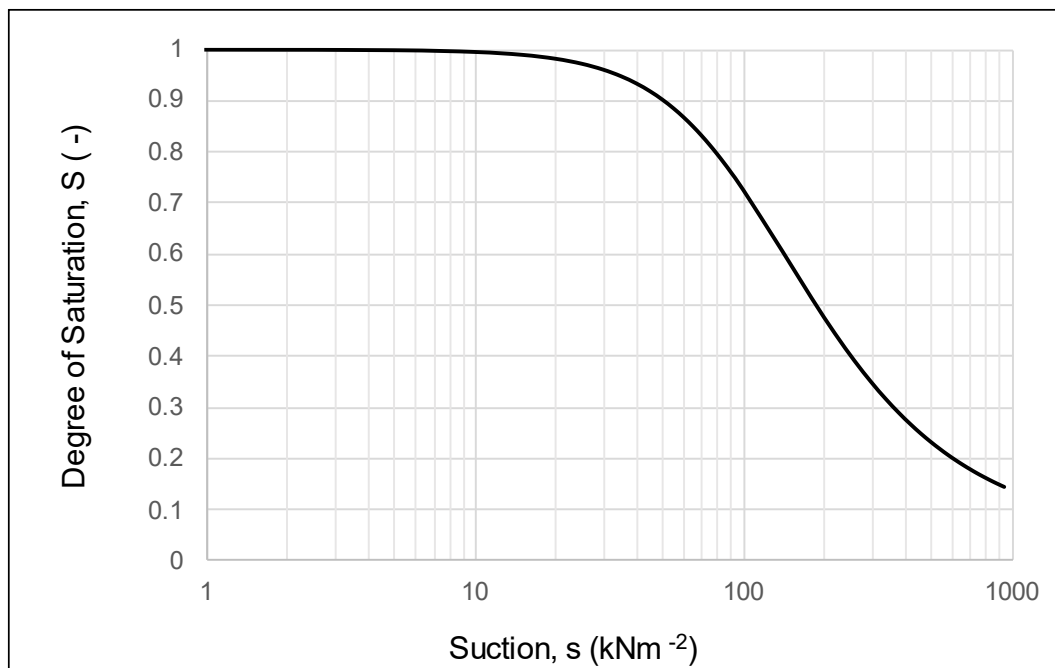


Figure 5-18: SWRC introduced in Plaxis 2D to model the hydraulic behaviour of the silty clay constituting the embankment

The parameters in Equation 5-2 are presented in the table below.

Table 5-14: Hydraulic parameters adopted for the ideal silty clay material

S_{res}	[-]	0.04
S_{sat}	[-]	1
g_a	[1/m]	0.098
g_n	[-]	2.0
g_l	[-]	-0.5

Assuming a saturated hydraulic conductivity of 10^{-7} m/s and following from Equation 5-4, the hydraulic conductivity function of the silty clay is given in Figure 5-19.

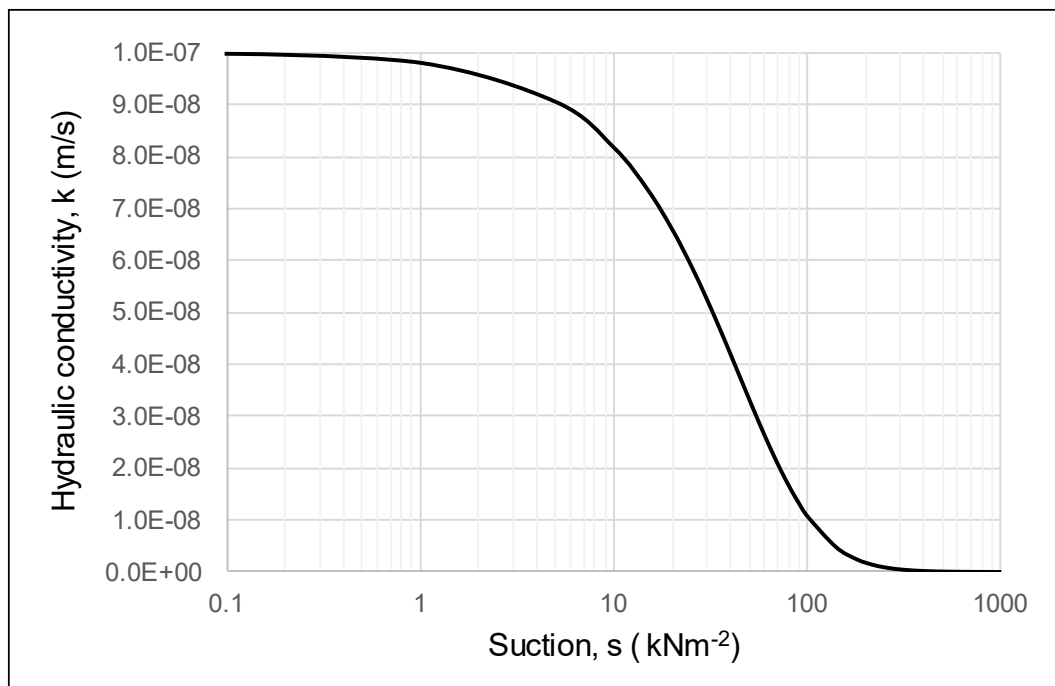


Figure 5-19: Hydraulic conductivity function representative of the silty clay material

5.3.4 Material Properties of coarse-grained soil

Mechanical Properties adopted for the coarse-grained soil

The overflow processes of an embankment built with coarse-grained material, has been studied with reference to an ideal sand. The mechanical properties adopted to implement the Mohr-Coulomb model in Plaxis 2D, are shown in Table 5-15.

Table 5-15: Mechanical Properties adopted in input to simulate the overflow of coarse-grained embankment

Material Properties (Homogeneous coarse-grained embankment)		
Unit weight (unsaturated)	γ_{unsat} [kN/m ³]	17.0
Unit weight (saturated)	γ_{sat} [kN/m ³]	20.0
Young Modulus	E' [kN/m ²]	50000
Poisson's ratio	ν' [-]	0.33
Effective Cohesion	c' [kN/m ²]	0.0
Effective friction angle	ϕ' [°]	35.0
Dilatancy Angle	ψ' [°]	35.0

As for the previous case, to get an order of magnitude of the Young modulus, experimental data were first analysed. The results presented by Fleureau et al., (Fleureau *et al.*, 2002) have been considered. The focus of this study was to investigate the behaviour of compacted soils on drying and wetting paths, for which consolidation tests on natural, artificial soils and on mixtures of clay and sand were performed. Additional data from literature were also considered.

The figure below shows the compressibility curve on wetting path of a sample compacted to the Proctor optimum. The soil selected consists of the mixture Jossigny 50% + sand.

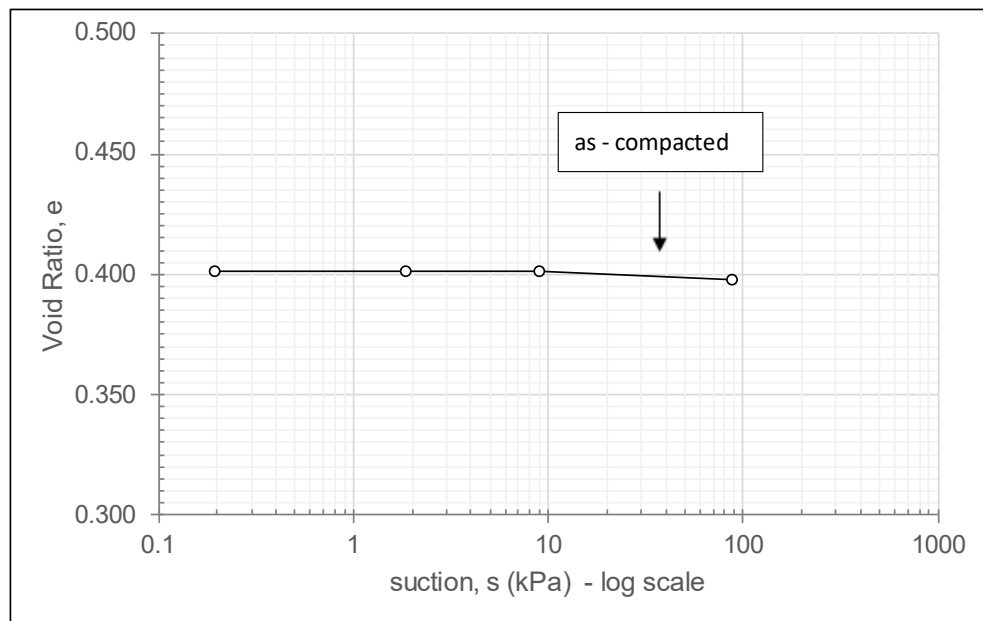


Figure 5-20: Compressibility of Jossigny 50 % + sand at the Proctor optimum upon wetting (Fleureau et al., 2002)

Based on Equation 5-7 to Equation 5-9 it is found that:

$$\Delta\varepsilon_v = \frac{0.4015 - 0.399}{1 + 0.4015} = 0.00178$$

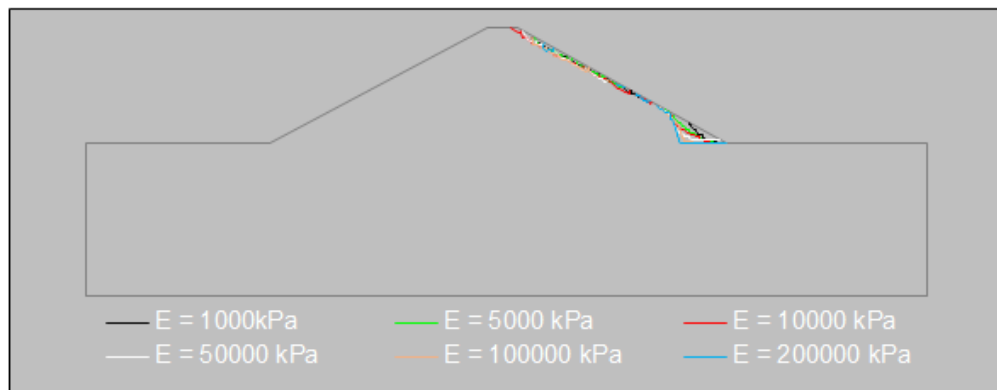
consequently:

$$K = \frac{60}{0.00178} \approx 33636 \text{ kN/m}^2$$

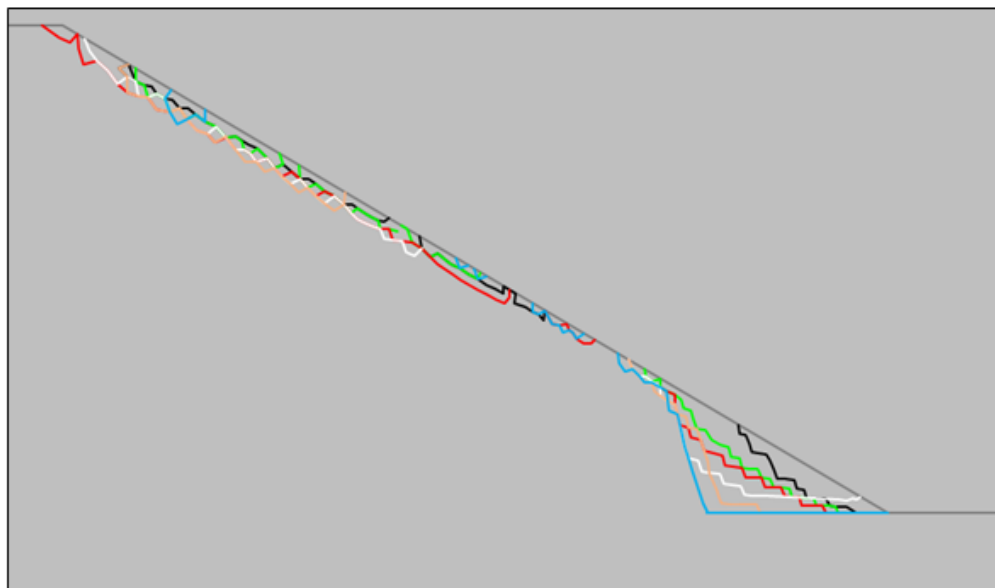
assuming $\nu = 0.33$ provides:

$$E \approx 34310 \text{ kN/m}^2$$

This value is assumed as order of magnitude for the ideal sand considered in this study. To understand the impact of this choice on the application of the failure criterion and hence on the removal of the soil elements, a sensitivity analysis has been conducted. As for the previous case, the values considered are: 1000, 5000, 10000, 50000, 100000 and 200000 kN/m². Similarly, to the fine-grained case an overflow process of 30 minutes has been simulated for each stiffness value. The numerical results were analysed to determine the corresponding failure surfaces. These are shown in figure below.



(a)



(b)

Figure 5-21: Failure surfaces resulting after 30 minutes of overflow for the case of the coarse-grained embankment for different values of the Young Modulus (a) entire embankment; (b) zoom on the downstream slope

Substantial differences can be observed compared to Figure 5-17 for the case of fine-grained soil. In this case, the influence of the Young Modulus on the definition of the failure surface is more evident than for the fine-grained soil. It seems that the failure surface and hence the number of soil elements removed, tend to increase as the stiffness increases. This is consistent with what can be anticipated theoretically. The dissipation of the excess pore water pressure is proportional to the Young modulus and therefore it is faster for stiffer materials. This means that the drop of suction from the initial value pre-overflow, towards zero suction imposed by the water flow, occurs

more rapidly for the material with high Young Modulus. Consequently, the additional component of soil shear strength due to suction disappears very quickly for the stiffer soils than for the more deformable ones. This is the reason why, for the same overflow duration, the stiff soil presents a deeper failure surface which involves a larger number of soil elements than for the soil characterised by lower values of the Young Modulus. However, it seems that there is an upper threshold after which this effect becomes less significant. It can be recognised that for the highest values of E considered (i.e. $E = 50000, 100000, 200000 \text{ kN/m}^2$) the failure surfaces are more similar leading to the removal of approximately the same amount of soil elements.

In addition, this analysis allows to draw a preliminary consideration. The comparison of Figure 5-17 and Figure 5-21 shows that during an identical overflow event, the behaviour of the two materials is considerably different. The embankment built with silty clay starts to fail in a small portion of the toe area involving very few soil elements, leading to the formation of the first headcut. On the contrary, the embankment in coarse-grained material presents a more widespread instability which affects the superficial layers of the downstream slope and a large part of the soil around the embankment toe. This behaviour can be explained in the framework of both progressive surface and headcut erosion. These aspects will be studied in more details in the following sections.

Hydraulic Properties adopted for the coarse-grained soil

The hydraulic behaviour of the ideal sand is modelled with the SWRC shown
Error! Reference source not found..

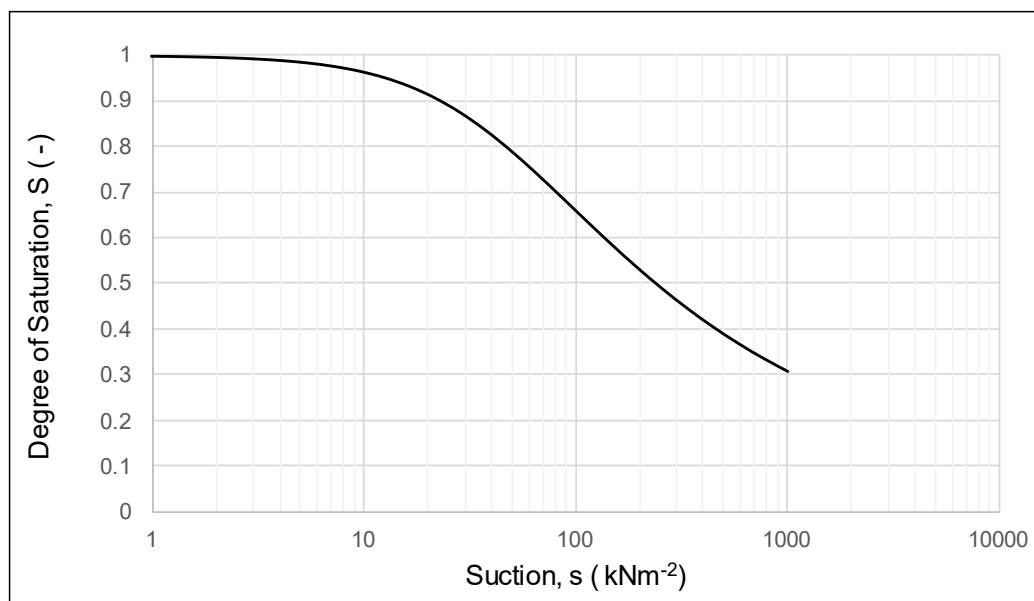


Figure 5-22: SWRC introduced in Plaxis 2D to model the hydraulic behaviour of the ideal sand constituting the embankment

The parameters of the van-Genuchten equation are presented in Table 5-16.

Table 5-16: Parameters of the van-Genuchten model characterising the ideal sand constituting the embankment

S_{res}	$[-]$	0.0446
S_{sat}	$[-]$	1
g_a	$[1/m]$	0.25
g_n	$[-]$	1.4
g_l	$[-]$	-0.28

The saturated hydraulic conductivity assumed is 10^{-5} m/s and the hydraulic conductivity function implemented is reported in Figure 5-23.

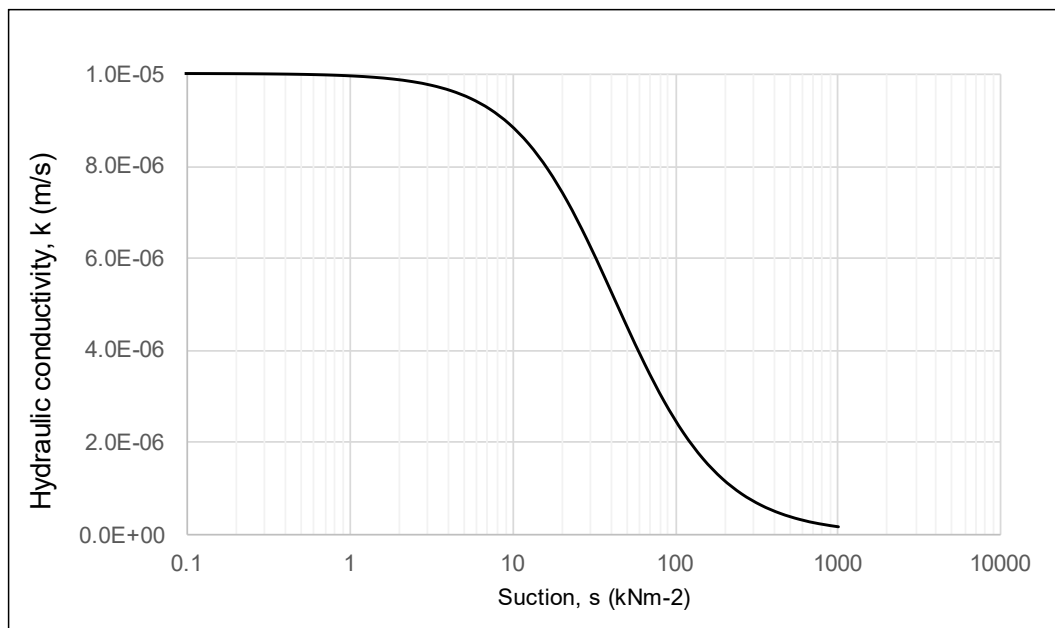


Figure 5-23: Hydraulic conductivity function assumed for the coarse-grained material

5.3.5 Calculation phases: from construction to overflow

The failure induced by overflow is simulated with a series of calculation phases that aim to reproduce the history of the embankment construction up to the overflow event.

These phases allow establishing the state of stress and strain of the embankment material at the onset of overflow.

Table 5-17: Calculation phases implemented in PLAXIS 2D common to both fine-grained and coarse-grained embankments simulated with the suction-based breaching model

#	Phase	Type of Calculation	Pore Pressure Calculation
1	Initial Phase	Gravity Loading: establishes the initial condition before the embankment construction	Steady-state groundwater flow
2	Embankment Placement	Consolidation in “Staged Construction” Mode. It means that the change of the geometry (i.e., embankment construction), stress state, weight, strength, and stiffness occur simultaneously with the consolidation process. A time interval of one year has been input.	Consolidation
3	Increase water level to baseline value	Fully coupled flow-deformation analysis calculating simultaneously deformation and pore water pressure.	Fully coupled flow-deformation analysis depending on time-dependant changes of the hydraulic boundary conditions.
4	Filling up to the crest	Fully coupled flow-deformation analysis simulating the extreme weather event by increasing the water level in the river until the crest of the embankment is reached before the overflow.	Fully coupled flow-deformation analysis based on time-dependant changes of the hydraulic boundary conditions.
5	Overflow 1	Fully coupled flow-deformation simulating the overflow after the water level has reached the embankment crest. When the water level in the river reaches the crest, the overflow is initiated, and a thin film of water starts to form along the downstream slope of the embankment. This situation is represented by imposing zero water pressure on the downstream slope (via setting the water head equal to the elevation). On the upstream side, the water head is kept constant and equal to the elevation of the crest. A fully coupled flow-deformation analysis is performed for a duration of 10 minutes.	Fully coupled flow-deformation analysis based on time-dependant changes of the hydraulic boundary conditions.
n	Overflows n	Fully coupled flow-deformation following the application of the failure criterion which leads to the removal of soil elements up to the stage of breach formation.	...

Initial phase

This calculation phase refers to the condition in which the embankment is not existing yet. Let us imagine that the groundwater table is characterised by the gradient shown below due to the difference in the water head between the left- and right-hand side of the model. This is reproduced by assigning two different water heads. Seepage boundary condition is assumed on the surface, while the bottom is considered as an impermeable boundary.

A seepage boundary conditions in PLAXIS 2D assigns a groundwater head equal to the elevation head if pore-water pressure at the boundary is non-negative and zero flux if pore-water pressure at the boundary is negative.

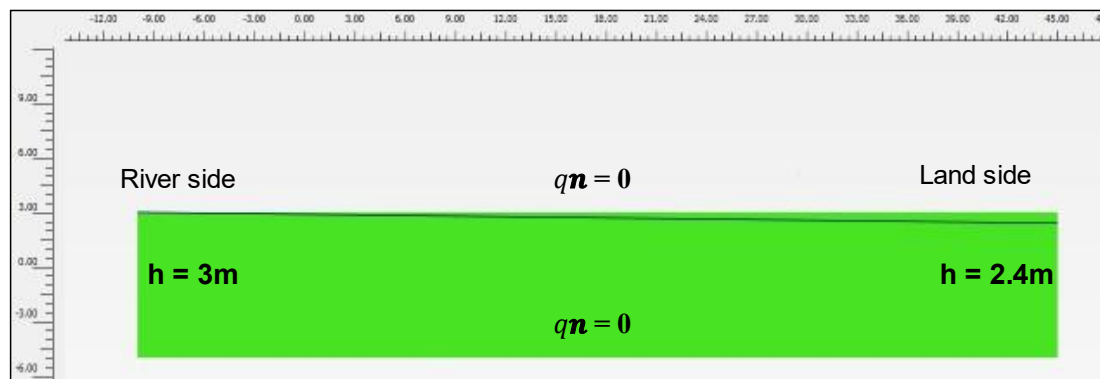


Figure 5-24: Boundary conditions in the initial phase

Embankment Placement

In the second phase the embankment is put in place and the associated consolidation process is assumed to be completed.

The hydraulic boundary conditions adopted are presented in the figure below. The water table of the initial phase is unchanged. Also in this case, a seepage boundary condition is assigned on the horizontal top boundary. No flow is assumed at the bottom boundary.

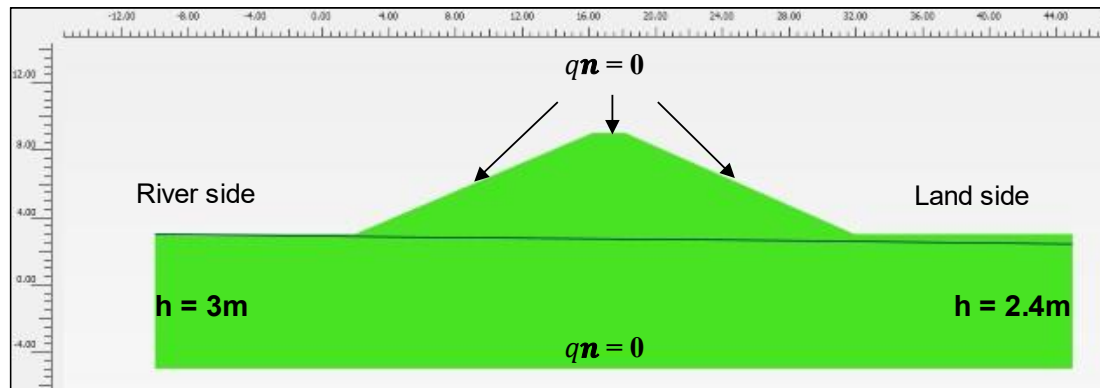


Figure 5-25: Embankment placement in the second calculation phase.

Increase of the water level to baseline value

Following the embankment placement, the presence of a water body on the left-hand side of the domain is simulated by increasing the water level with a time-dependant boundary condition. This is a function of the water head with time a water level of 0.625m above the ground surface is established at the final step as shown in Figure 5-26.

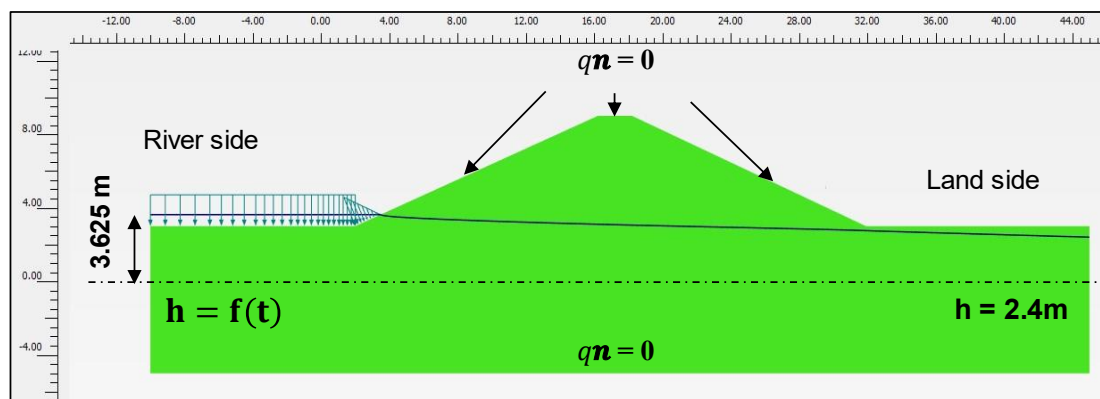


Figure 5-26: Increase of water level on the upstream side simulating the presence of a river/water body.

The conditions on the other boundaries are unchanged compared to the previous phase. The resulting phreatic surface table is higher because of the increase of the water head on the left portion of the model.

Filling phase

This stage reproduces an extreme weather event responsible for the increase of the water levels in the water body up to the embankment crest. This phase is therefore the prelude of the overflow phase.

The increase of water levels is simulated again with a time-dependent boundary conditions where the water head varies with time on the river-side. The hydrologic analysis required to derive the inflow hydrograph was out of the scope for this exercise, therefore the water level was assumed to reach the embankment crest in 10 hours. It was already discussed in paragraph 3.6.2.3 of Chapter 3 that, the time required to increase the water level up to the embankment crest is crucial for the numerical analysis. Indeed, a longer period will allow time to saturate the embankment material and will lead to lower suction values at the onset of overflow, than a faster increase. As such this is a parameter of the model that must be calibrated. However, depending on weather conditions, the time of filling can vary between few hours and days if not weeks. The assumed duration has been derived based on documented events in UK, like the catastrophic flood that affected the Humber-Estuary region in 2013 (Environment Agency, 2014). Nevertheless, a more detailed study should be conducted if real cases are to be modelled.

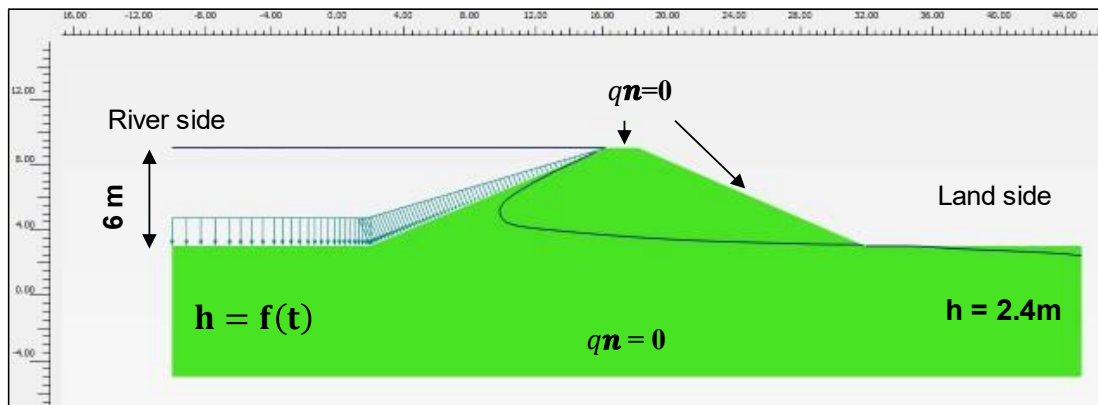


Figure 5-27: Extreme weather event leading to the progressive increase of the water level up to the embankment crest

As can be seen from Figure 5-27 an increase of the water levels on the upstream slope causes the increase of the phreatic surface on the downstream side and

particularly at the toe of the embankment. The embankment crest and the downstream slope are still treated as seepage boundary.

First Overflow Phase

The overflow condition is simulated with a prescribed water head equal to the elevation of the nodes (i.e. corresponding to the application of zero pressure) on the downstream slope. On the upstream slope the presence of the water body is again reproduced with a prescribed water head that is kept fixed at the embankment crest height for the entire duration of the overflow.

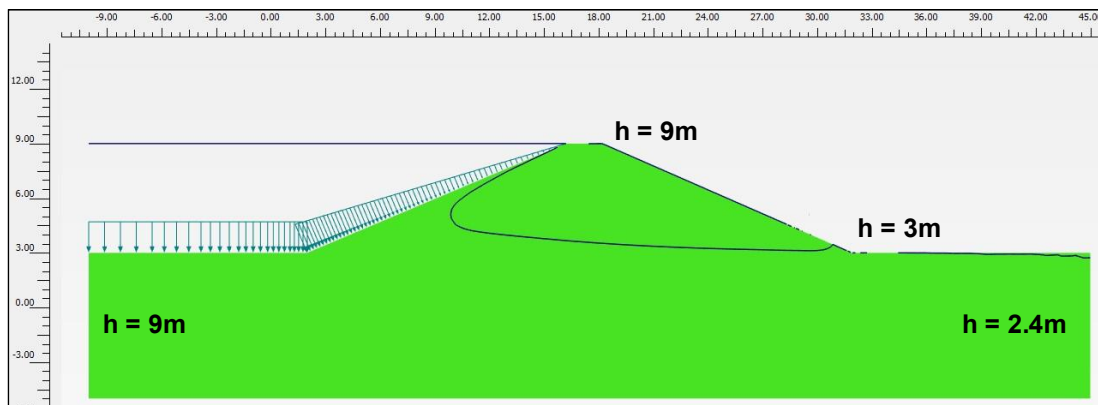


Figure 5-28: Frist overflow phase simulated by imposing zero water pressure along the downstream slope, while the water head is kept constant on the upstream side.

N - Overflow Phases

When the simulation stops, assuming an initial overflow duration of 10 minutes, the results are analysed in terms of plastic points and shear strain. The failure criterion described in Chapter 4 is applied to check if a failure surface is formed. In this case, a second overflow phase is defined in which the soil elements underlain by the failure envelope are deactivated. Boundary conditions are assigned on the new embankment configuration, to ensure that the resulting contours on the downstream slope are always at “zero pressure”. No changes are applied to the upstream side, the crest, and the bottom line of the model.

The number of overflow phases depends on the failure mechanisms developed. These might directly affect the crest, leading to a rapid breach formation or, in other

cases, the failure front might propagate backwards more slowly, reaching the crest after many overflow steps. The model terminates when breach formation occurs, which is the situation where the embankment crest starts to fail.

5.4 Results

The breach formation predicted with the suction-based breaching model is presented by showing the evolution of the embankment profile at different time intervals throughout the entire overflow process. In this way, the progressive mini-failure mechanisms and the retrogressive propagation of failure can be captured. The embankment profiles calculated for each overflow phase are then qualitatively compared with images from the IMPACT field tests by selecting the time corresponding to similar stage of the breach formation process.

Pore-water pressure distributions, effective suction and relative shear stress profiles (i.e the ratio between the mobilised shear strength and the maximum shear stress) at selected cross-sections along the downstream slope, and finally the state of stress in the $p' - q$ plane, are also shown for the same time-steps of the failure process.

5.4.1 Homogeneous Fine-Grained Embankment

The information available from the IMPACT Field Test #1 consists of the inflow and outflow hydrographs and the water level data. However, these have not been considered because the aim here is to predict the fundamental failure mechanisms due to the inward soil water flow rather than the tangential stresses generated by the water flowing over the downstream embankment slope. It is worth mentioning that the paper “Breach formation: Field test and laboratory experiments” (Morris, Hassan and Vaskinn, 2007a) presents, among the data collected, the pore water pressures within the embankment and the breach development using movement sensors. These data are not published in both the IMPACT (Vaskinn, Løvoll and Höeg, 2003; Morris, 2005) and in the FLOODSite reports (Hassan and Morris, 2008; Morris, 2009) and therefore could not be consulted.

Ideally, the measured embankment topographic profile would have been the most

suitable information for this comparison. In its absence, pictures available from the FLOODSite report “Breach Initiation & Growth: Physical Processes” (Morris, 2009) have been used to assess the different phases of breach development. Also, the authors highlighted that the clocks of the different cameras installed, were not set to a common datum making it difficult to synchronise the images from different standpoints. To avoid misleading conclusions the images from the “roving camera” have been discarded from this analysis, as it was explicitly warned to not use them for time-related considerations.

The following figures show the embankment profile simulated and the images from the field test at the same relative time. The total duration of the overflow simulated is 573 min, corresponding to the time of simulated breach formation.

The field test is documented up to the condition where an open channel is formed through the embankment with the breach totally open. The field test duration deducted by the times reported in the pictures is about 164 min. However, for the purpose of this comparison a duration of 107 min has been considered corresponding to the point in which the failure front cuts the embankment crest leading to breach formation.

The discrepancies between the time of breach formation simulated and the field experiment, can be due to multiple reasons. First, it is worth considering that the simulation is conducted along a cross-section of the embankment, therefore 3D effects that can accelerate breaching processes laterally are implicitly neglected. Furthermore, as mentioned in paragraph 5.2.1, there were several issues during the field tests. The formation of cracks was observed. These are points of weakness and at the same time constitute preferential paths for water infiltration, causing a rapid saturation and consequently a quick loss of shear strength of the embankment material.

Seepage leading to the initiation of a piping failure was noted at the left abutment as shown in Figure 5-5d, that certainly contributed to speed up the breach formation, although not through overflow. This process is not considered in the simulation.

Water levels were held for a long period to keep a constant hydraulic head on the crest and this might have impacts on the advancement of the saturation front within the embankment material prior to the overflow. Because of this hold period in the experiment, a more rapid reduction of suction compared to the simulation could have

occurred. It is worth remembering that, the time required to increase the water levels up to the structure capacity, is a parameter of the model, because it affects the initial pore water pressure distribution. In this case, this has been assumed.

Finally, the water flow processes simulated and the experiment are very much affected by the soil hydraulic conductivity. If the hydraulic conductivity assumed in the simulation and the one of the materials in the experiment are considerably different, then the differences in time can be easily explained. Factors like formation of cracks and presence of vegetation in the field experiment can also influence soil permeability, particularly on the most superficial layers, where the onset of failure occurs. These aspects have not been considered in the simulation. Ultimately, because of all the above-mentioned variables, the simulated and real times are indicated for completeness but are not comparable.

Stage 1 – Onset of failure

The onset of the ‘erosion’ process is analysed first. As observed from Figure 5-29a, the failure points are concentrated at the embankment toe, leading to the first mini-failure and soil removal. The isolated failure points in the middle of the downstream slope are shown for completeness but they are not yet forming a failure mechanism. The failure surface developed after 10 minutes of simulated overflow involves an area of 0.069 m², while its length is 0.75 m.

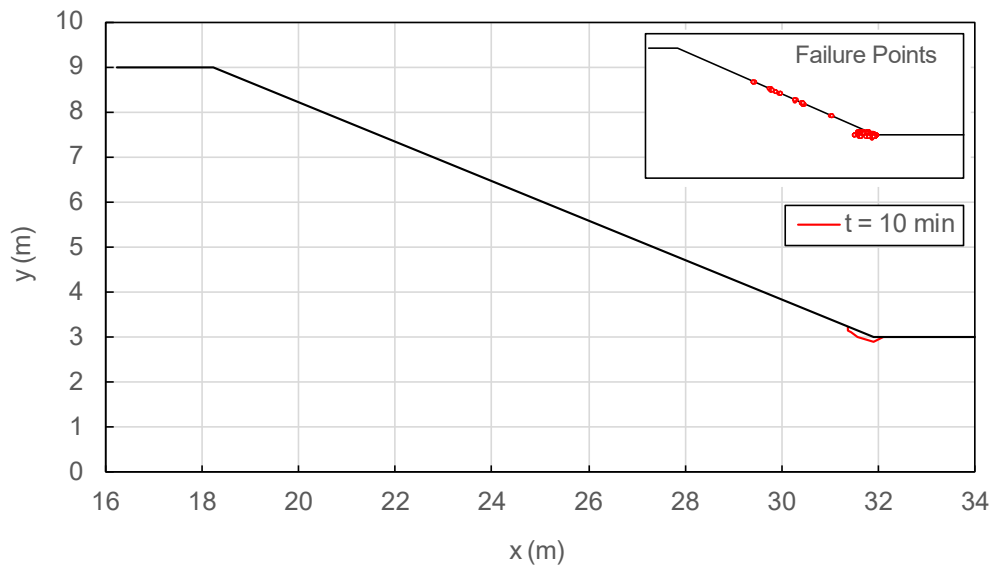
The simulated failure surface seems to capture the erosion process observed in the field at the beginning of the test (Figure 5-29b). This initial stage is commonly described by the authors as “surface erosion” because of the very shallow flow which causes the removal of weak soil spots from the most superficial layers of the downstream slope.

In Figure 5-30, the grid 1 x 2 m painted on the slope surface allows to draw some quantitative considerations. The water flow seems to be more turbid at approximately 0.3 m above the toe and this has been interpreted as first signs of soil removal. This seems to match the first failure surface of the simulated process, which cuts the slope at 0.2 m above the toe.

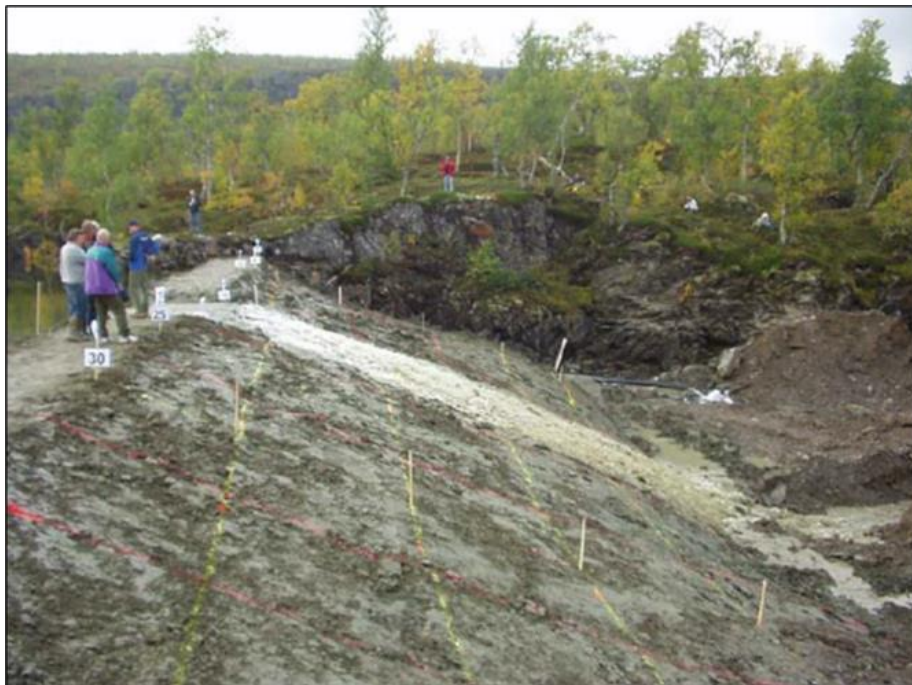
The contour plot of the pore water pressures after 10 minutes of overflow is shown

in Figure 5-31, where positive values indicate suction. It can be observed that the highest values of circa 60 kN/m^2 , are found at the embankment downstream crest (i.e. dark blue contours). Then, suction decreases along the slope and finally drops to zero at the toe (i.e. light blue contours) that is in fully saturated conditions. It is also clear that under the effect of the overflow, soil layers up to a depth of 20cm on average, are characterised by very low values of suction. Afterwards, suction tends to increase moving down towards the embankment body and finally pore water pressures in compression develop below the phreatic surface, corresponding approximately with the embankment foundation level (i.e. 3m elevation circa).

This trend can be better observed in Figure 5-32a, where the profiles of effective suction are plotted at selected cross-sections along the downstream slope. The light blue lines refer to the 10 minutes overflow phase, while the magenta lines indicate the corresponding distributions developed at the end of the filling (i.e. previous calculation phase). At the end of this first overflow simulation, the embankment material at the toe area has lost all the apparent cohesion, that was already very low at the end of the filling phase. The cross-section A-A* presents in fact effective suction equal to zero everywhere.

10 minutes of simulated overflow

(a)

Field Test #1 - 11:23 (5 min from the test start) – view from mid and upstream right bank

(b)

Figure 5-29: Overflow simulated (a) and field test (b) at the initial stage

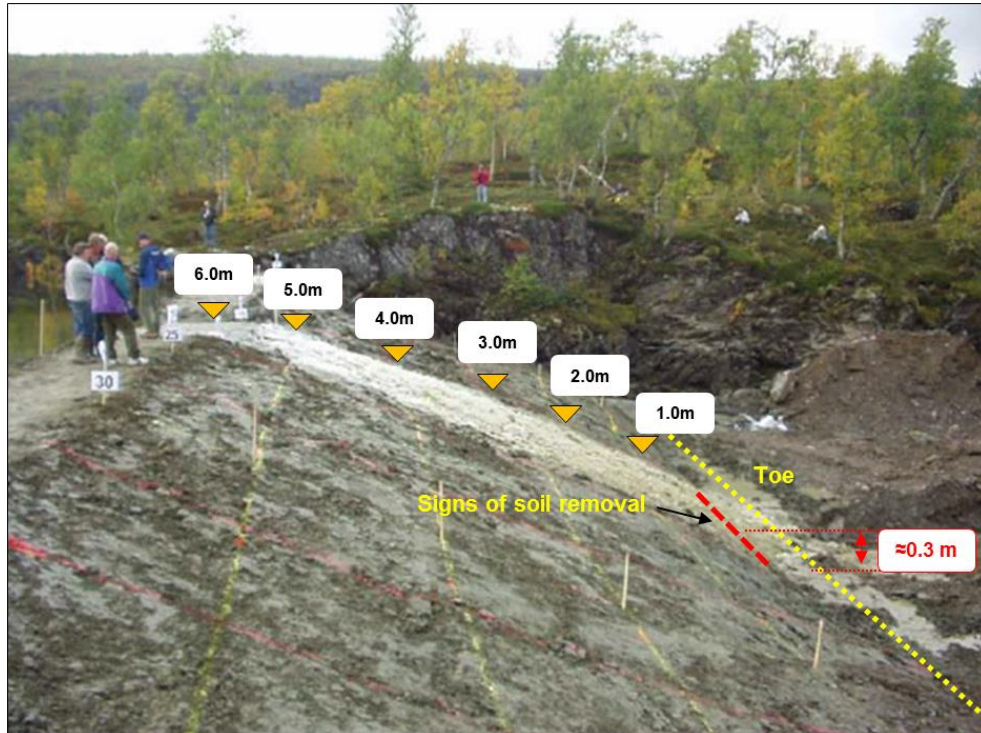


Figure 5-30: First signs of soil removal. Interpretation of the process observed

For all the cross-sections analysed it is evident that in the overflow scenario effective suction, s_r (kN/m^2), decreases on the surface compared to the previous filling phase, due to the water infiltration imposed by the zero-pressure condition on the slope surface. However, the change of pore water pressures is significant only at the top, while the differences with the filling suction values disappear with depth, and the two profiles (i.e. light blue and magenta lines in the figure) overlap. This is obvious because, thanks to the low permeability of the embankment material, the overflow water moves very slowly and is not yet able to penetrate the most internal soil elements. Below 20cm circa from the slope surface, suction values are practically unaffected.

In addition, it should be noted that the reduction of suction from filling to overflow phase, occurs more rapidly at the toe, like in cross-sections A-A* and B-B*. At these locations suctions were initially low, ranging from 4-8 kN/m^2 . Due to the suction dependence of the hydraulic conductivity, the embankment material is more permeable at the toe, therefore the infiltration here proceeds more rapidly than at the top. Based on the hydraulic conductivity function presented in Figure 5-19, in the range of

suctions at the toe, soil permeability is about 10^{-7} m/s while it is 5×10^{-8} m/s towards the crest. This is also the reason why in the cross-sections close to the crest, like D-D* and E-E*, effective suction returns more rapidly from the surface value to the previous filling value. This can be observed on the top profiles, characterised by steeper slope than the lower cross-sections. In other words, suction gradients are very big at the crest rather than at the toe. At the crest, only a very superficial portion of the embankment material is exposed to a small loss of apparent cohesion.

It is worth mentioning that the presence of the hydraulic shear stress at the interface soil-overflow could have been responsible for shallow instabilities. However, based on the order of magnitude of 0.2-0.3 kN/m² presented in Chapter 3, these destabilising effects would have been significant going down from section B-B*, where apparent cohesion at the top is 0.07 kN/m². Furthermore, even for the very small effective cohesion of 0.5 kN/m² considered for this silty-clay, the hydrodynamic forces would have not been sufficiently big to trigger soil movements anywhere along the slope surface. In practice, the fact that hydrodynamic shear stresses are not included in the calculation is not considered to have significant impacts on the local instabilities of the silty-clay embankment.

Figure 5-32b shows the profiles of relative shear stresses τ_{rel} , for the selected cross-sections. This output from Plaxis is defined as the ratio between the maximum shear stress τ_{max} and the mobilised shear strength τ_{mob} .

The first term is the shear stress corresponding to the case in which the Mohr's circle is expanded, maintaining the same centre, to become tangent to the Mohr-Coulomb failure envelope.

The τ_{mob} is instead the radius of the Mohr's circle of the stress point analysed.

Because of this definition, $\tau_{rel} = 1$ indicates that the stress point lies on the failure envelope ('Plaxis 2018, Users Manual', 2018).

It is interesting to note that τ_{rel} profiles mirror the effective suction trends. Soil elements on surface, for which suction is zero or very low, present $\tau_{rel} = 1$ indicating that the stress point is a plastic point. At the depth of maximum suction τ_{rel} reduces to 0.5 returning to the pre-flood values.

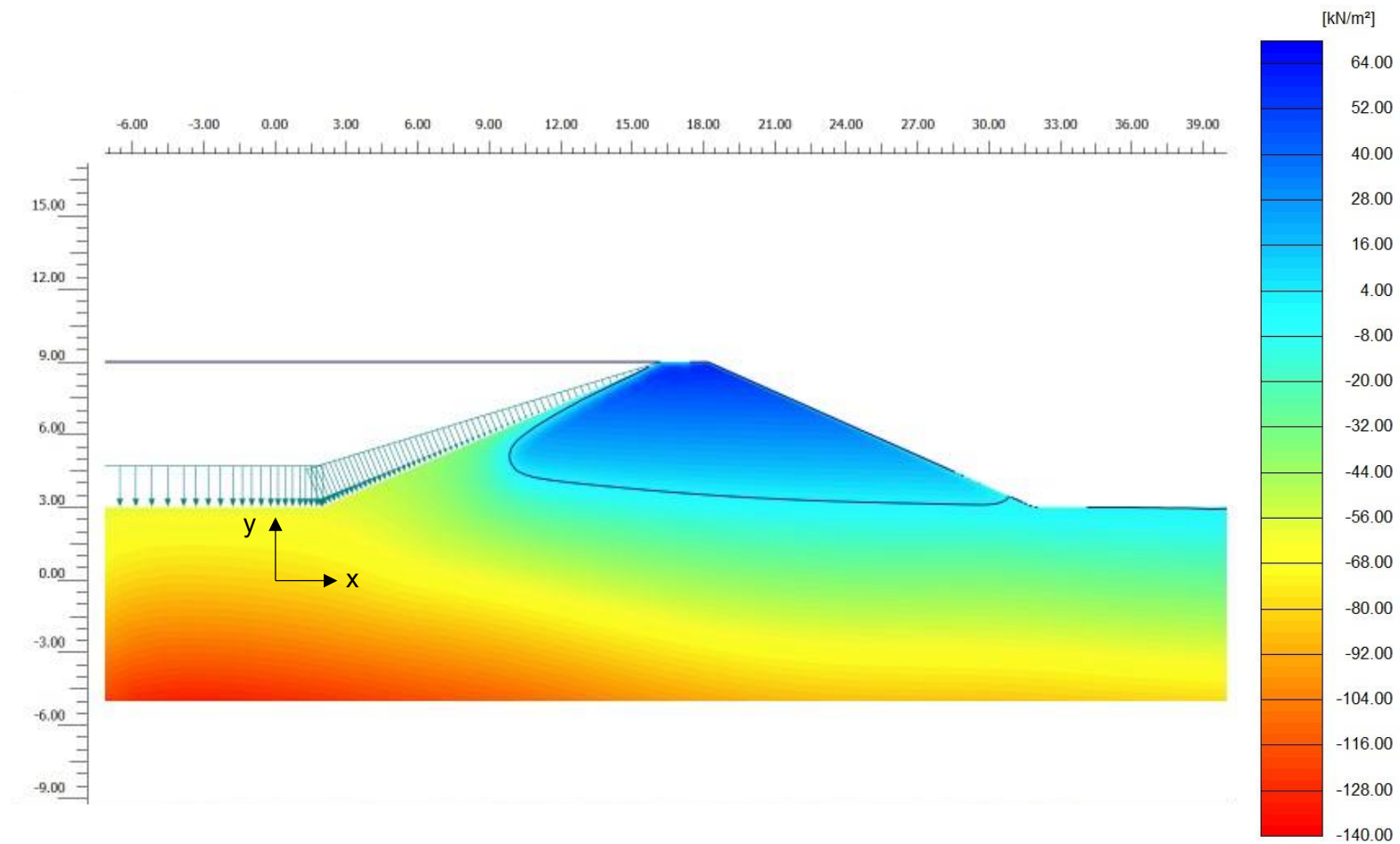
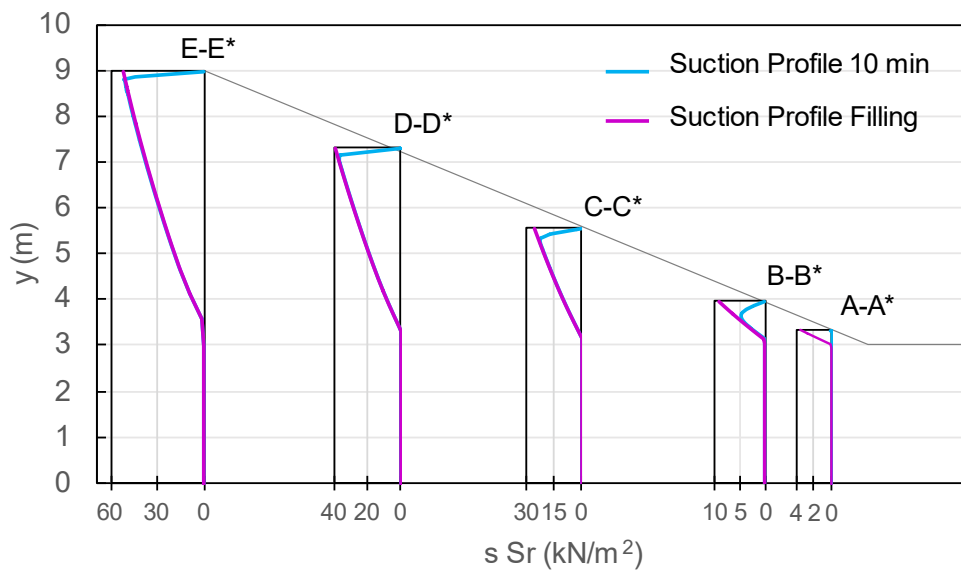
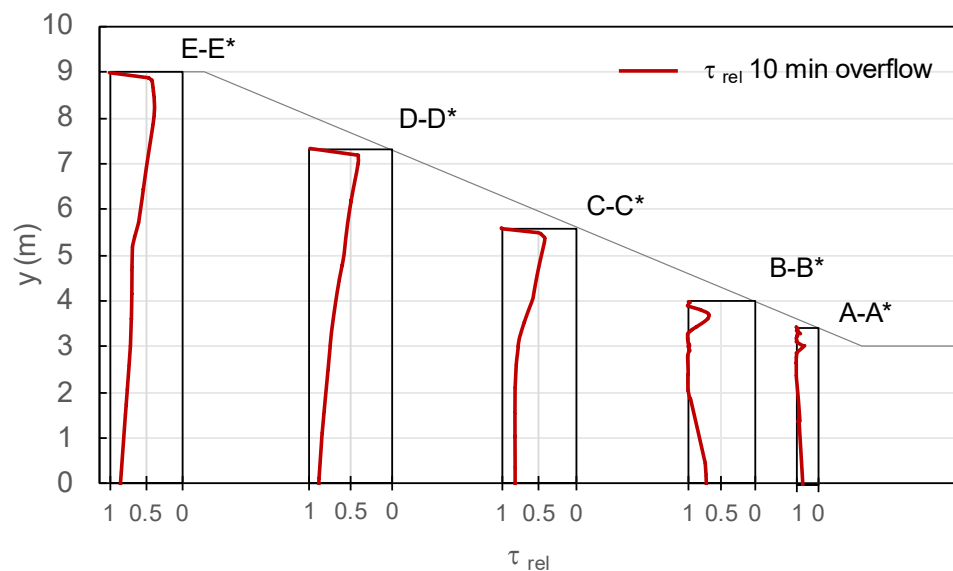


Figure 5-31: Pore water pressure distribution resulting from the first 10 minutes of the overflow phase. Suction is positive. Maximum Value is 62.06 kN/m^2 (i.e. dark blue contour) and minimum is -130.4 kN/m^2 (i.e. red contour)



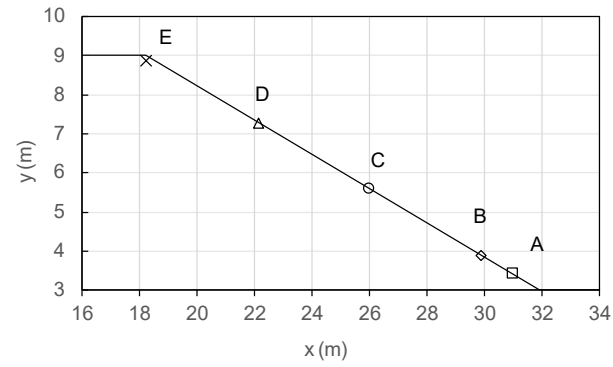
(a)



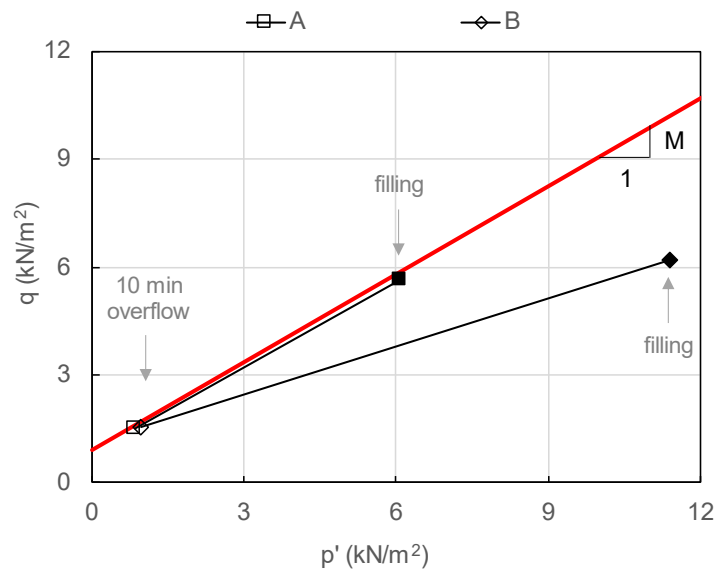
(b)

Figure 5-32: Effective suction profiles at selected cross sections along the embankment downstream slope (a) profiles of relative shear along the same cross-sections (b) after 10 min of overflow

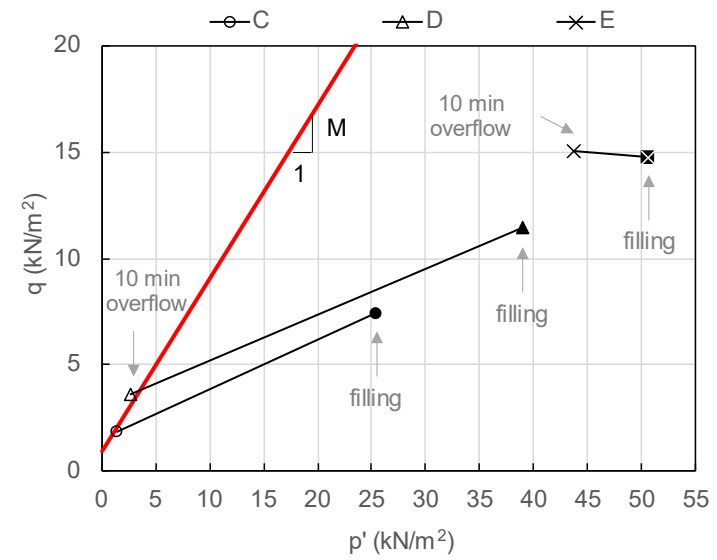
Afterwards τ_{rel} starts to increase again while going closer to the phreatic surface and below it, but is never equal to 1. It is worth clarifying that because of the definition of the failure criterion adopted in the suction - based breaching model, the fact that $\tau_{rel} = 1$ on the surface is not necessarily implying the formation of failure surface.



(a)



(b)



(c)

Figure 5-33: Selected points on the slope surface (a). Stress paths in p' - q plane for soil elements at toe area (b) and at the embankment crest (c)

Figure 5-33 shows the state of stress in the $p' - q$ plane for selected points on the slope surface. The black data points are representative of the state of stress at the end of the filling phase. In more details, Figure 5-33b refers to the soil elements on the slope surface at the toe. Because these elements lie on the surface (Figure 5-33a) and because the contribution of suction in this area is minimum, the effective stresses are low, especially if compared with the points located in the upper part of the embankment, where suction is significantly higher.

It is interesting to note that the state of stress of soil element A, is in practice on the failure envelope (i.e. red line in Figure 5-33b) since the filling phase. On the contrary, point B with 10 kN/m^2 of effective suction at the end of filling, is sufficiently far from the failure line. Due to the overflow the mean effective stress p' and the deviatoric stress q , drop significantly towards the origin and both elements A and B move on the failure envelope (i.e. becoming plastic points).

In Figure 5-33c, the initial state of effective stress of elements C, D and E, is relatively high, thanks to effective suction respectively of 26, 40 and 60 kN/m^2 . These soil elements are still relatively safe. However, during the overflow, elements C and D experience a sudden reduction of the state of stress caused by the loss of apparent cohesion and become plastic points. Element E, located 11cm below the crest, is subjected to a small reduction of the mean effective stress, with q almost constant. s_r is decreased from 52 kN/m^2 to 43 kN/m^2 and this element is still far from the plastic condition.

The stress paths from the filling to the overflow phase corroborate the idea that failure mechanisms occur first at the toe, where the initial apparent cohesion is low and a short overflow duration is sufficient to create a plastic region. In this case, plastic points will involve also soil elements below the surface level, because effective suction is zero due to the proximity with the phreatic surface. Hence, at these locations, a consistent number of plastic points is developed and shear strains will increase, leading to the formation of relatively shallow slip surfaces.

This concept is better expressed with reference to the figure below. The grey, blue and black datapoints represent the state of stress of soil elements B, C and D on the surface, already seen in Figure 5-33a, b, c. The white-filled points express the state of stress at 30cm below the surface, where apparent cohesion is maximum along the vertical.

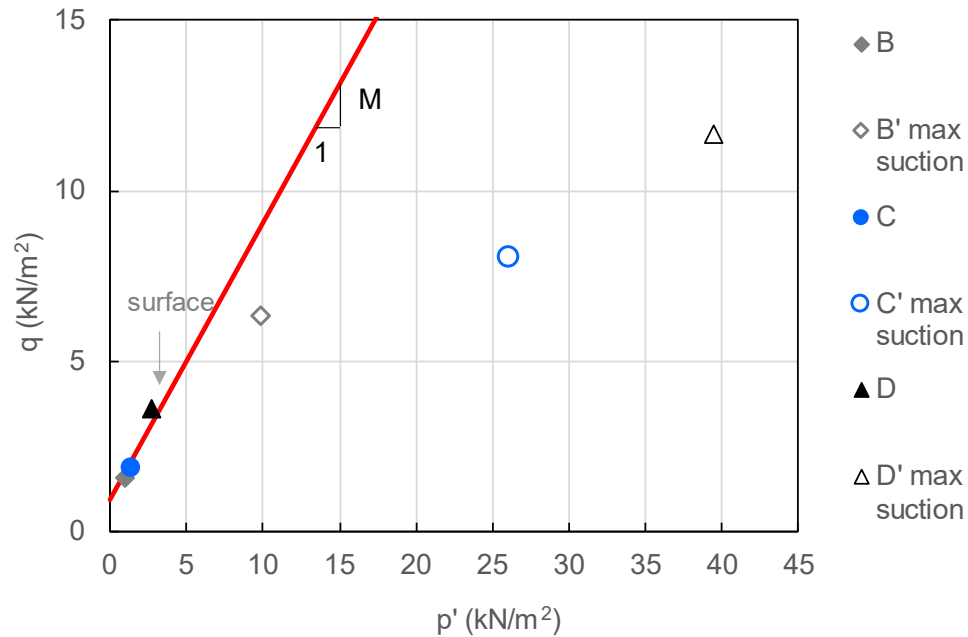


Figure 5-34: Stress state of different soil elements during overflow presented in the p' - q plane.

These points are quite far from the failure envelope and it is unlikely that failure mechanism will occur. This is also clear from the τ_{rel} plots of Figure 5-32b.

Stage 2 – Small Headcut Formed

A more detailed image with a better photography angle is available after 10 minutes from the beginning of the field test. The same stage is reached after 70 minutes in the simulation.

Figure 5-35b shows that in the field test a well-defined step is formed just below the second painted horizontal line, at a height of 2.0 m circa above the toe level. An interpretation of the embankment profile along the centreline is given by the red dotted line in Figure 5-35b. Some soil elements were also removed laterally, as indicated by the blue circle.

It appears that the failure mechanism identified by the suction-based breaching model tends to reproduce adequately the field observation. The failure surface exits on the downstream slope at 1.70m above the toe level, which is in good agreement with position of the failure surface inferred from the field test. The simulated failure surface extends towards the inner part of the embankment body, resulting in a deeper cut than

what can be understood from the field images, due to the presence of the overflowing water. It appears that the real embankment is undercut more superficially than the simulated profile. This can be reflected also in the time-difference observed between the test and the simulation. It is evident that it is required more time to form a deeper step undercutting the slope than a more superficial one, as it appears in the experiment.

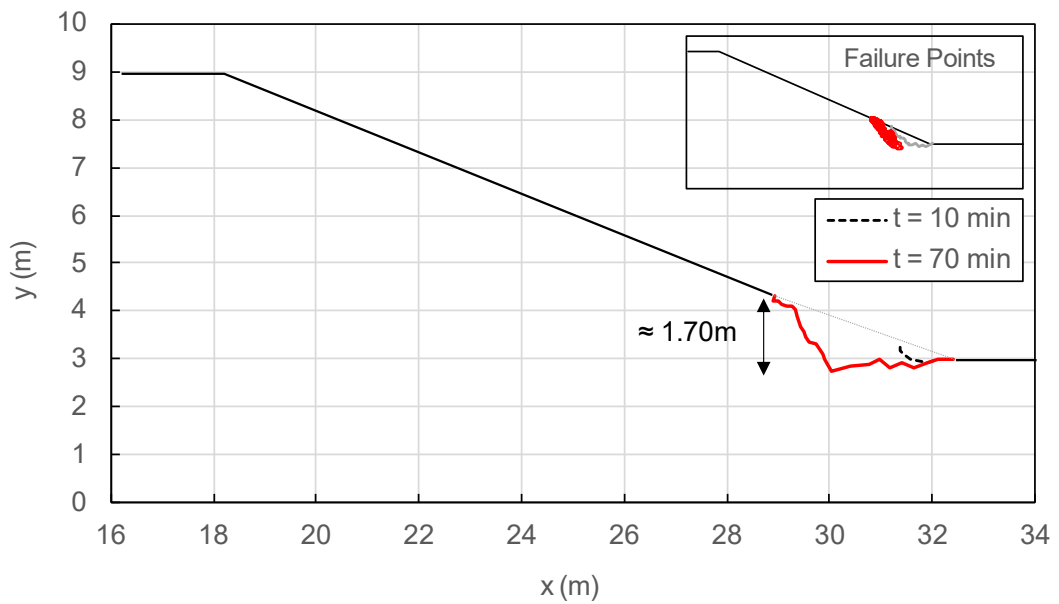
The pore water pressure distribution on the damaged embankment after 70 minutes of overflow is presented in Figure 5-36. This contour plot shows that the longer infiltration period resulted in a further reduction of suction, with the light blue contours extend at greater depths than in the previous calculation phases.

This trend is better observed in Figure 5-37a where the effective suction profiles are plotted for different cross-sections. The comparisons with the previous overflow phase profiles, indicated by the magenta lines, confirm that effective suction is almost zero on the surface and tends to merge at depth with the previous 10 minutes overflow profiles. However, due to the advancement of water infiltration, the increase of suction downwards along the vertical, is slower and the maximum values of the former simulated phase are not recovered. For example in section C-C* the maximum suction is 19 kN/m^2 achieved 0.5m below the surface, while, during the 10 minutes overflow phase, for the same cross-section the maximum value was 23 kN/m^2 almost equal to the filling phase recovered at 27cm below the slope surface. This effect seems to be more important for section C-C* and D-D* rather than for the section E-E* at the crest. Here suction gradients are still high, as it can be observed by the steep slope of the suction profile.

As discussed for the 10 minutes overflow case, the trends of the relative shear stress indicate that for depths at which suction is maximum, the soil elements are far from the plastic state.

Figure 5-38b shows the stress paths of soil elements C, D and E from the 10 minutes overflow to the 70 minutes duration. These elements are located 10 cm below the slope surface. In all the three cases presented, p' and q tend to decrease as the overflow duration increases. The reduction of apparent cohesion leads to stress states that are closer to the failure envelope.

70 minutes of simulated overflow



(a)

Field Test - 11:34 min (10 min from the test start) – view from mid and upstream right bank



(b)

Figure 5-35: Comparison between the simulated overflow and the interpreted profile assessed from the field test at a similar same stage of the breaching process

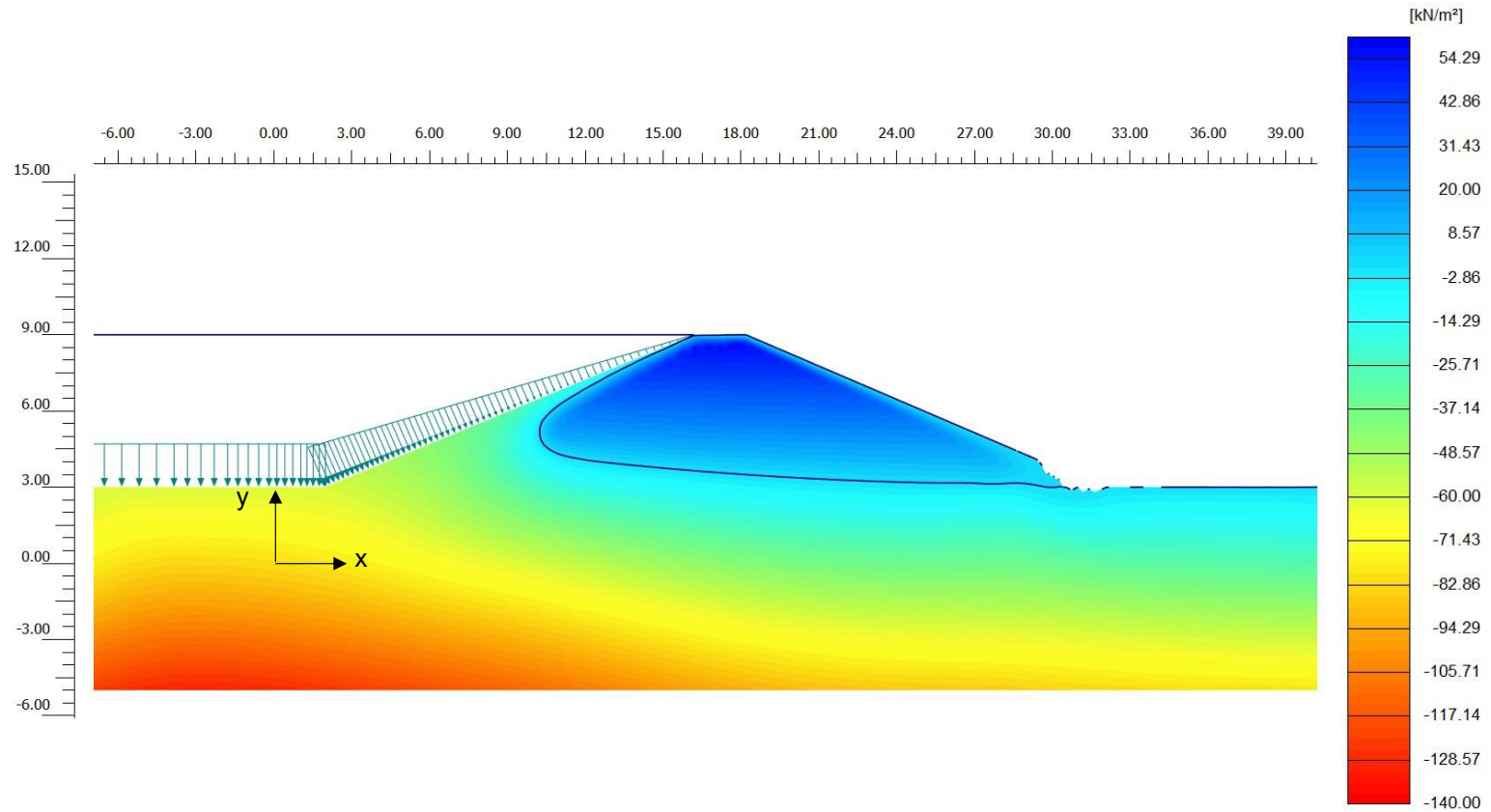
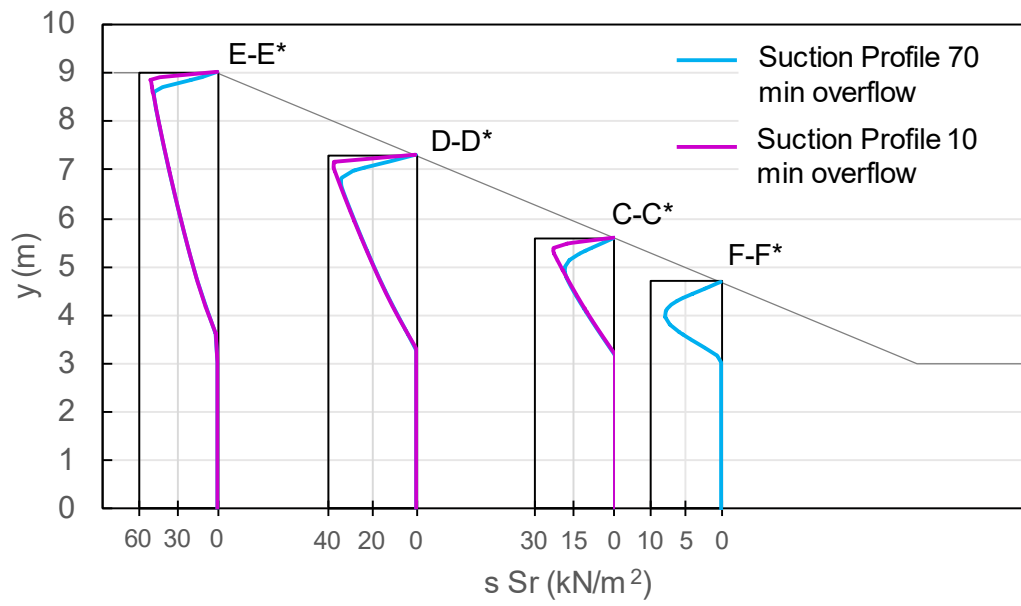
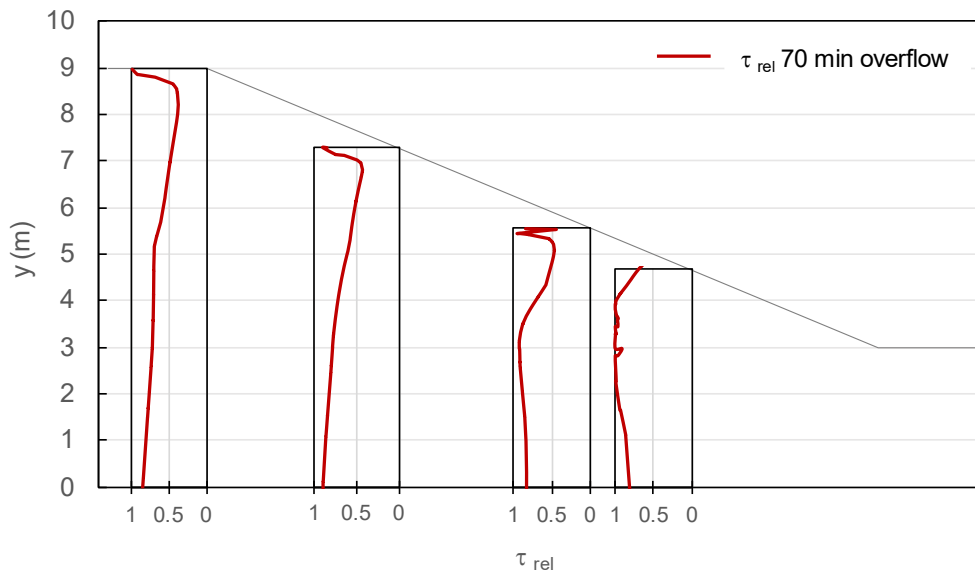


Figure 5-36: Pore water pressure distribution resulting after 70 minutes of the overflow phase. Suction is positive. Maximum Value is 57 kN/m² (i.e. dark blue contour) and minimum is -139 kN/m² (i.e. red contour)



(a)



(b)

Figure 5-37: Effective suction profiles at selected cross sections along the embankment downstream slope (a) profiles of relative shear along the same cross-sections (b) after 70 min of overflow

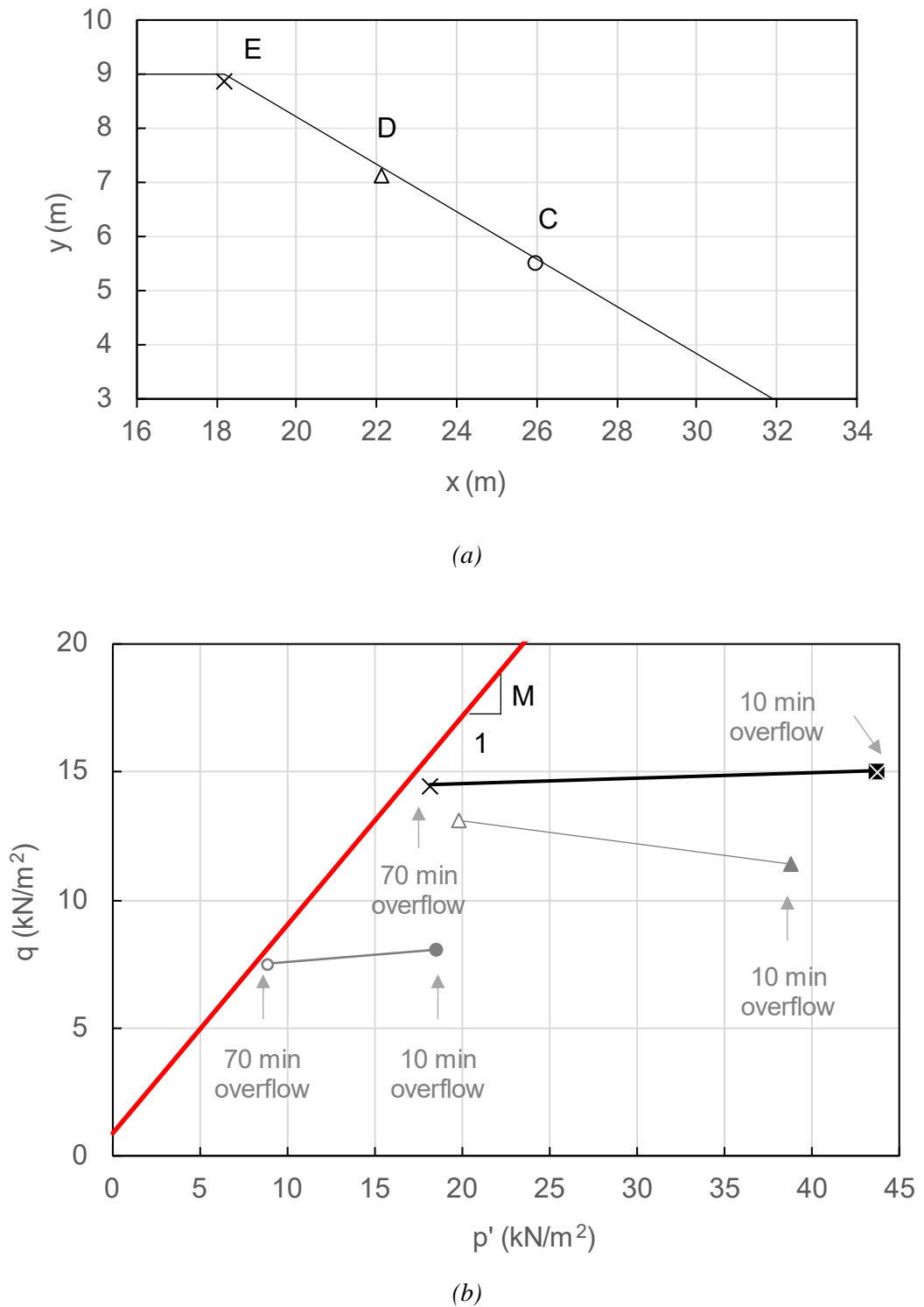
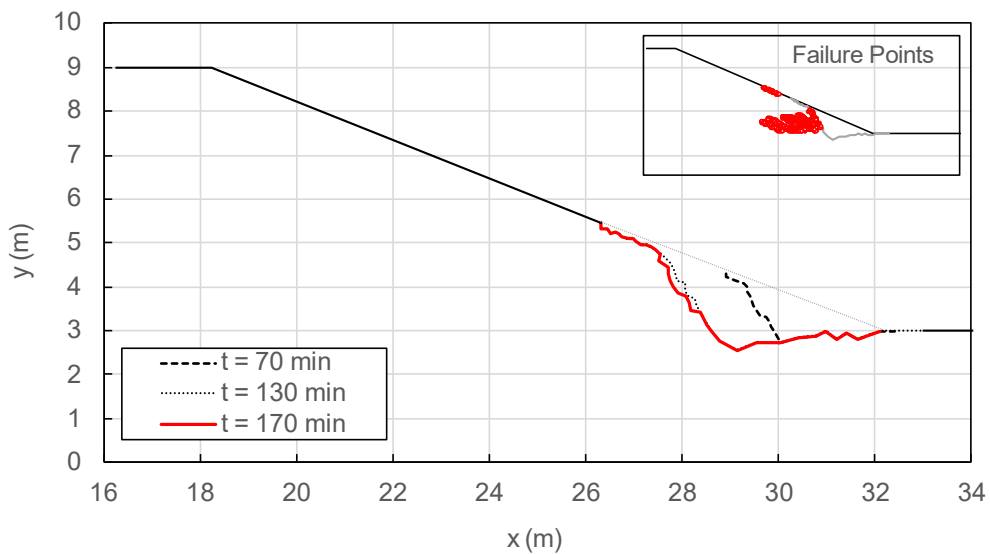


Figure 5-38: Selected points on the slope surface (a). Stress paths in p' - q plane for soil elements C, D and E (b)

Stage 3 – Headcut formation

Headcut formation occurred at 11:53 min in the field test as documented by the IMPACT researchers when the breaching process is estimated to be around the 30% of the total duration. The same stage is achieved after 170 minutes of simulated overflow.

Figure 5-39 shows the relative comparison. The difference between the previous stage 2 and the current one (stage 3) is substantial, with the simulated headcut having moved towards the crest of about 1.15 m. The centreline profile in the field test (Figure 5-39b,c) shows that the simulated and real failure mechanisms tend to be very similar, indicating the progressive propagation of the failure front along the vertical and horizontal directions.

170 minutes of simulated overflow

(a)

Field Test – 11:53 (35 minutes from the test start) view from mid and upstream right bank – (described as Headcut forming at toe)



(b)

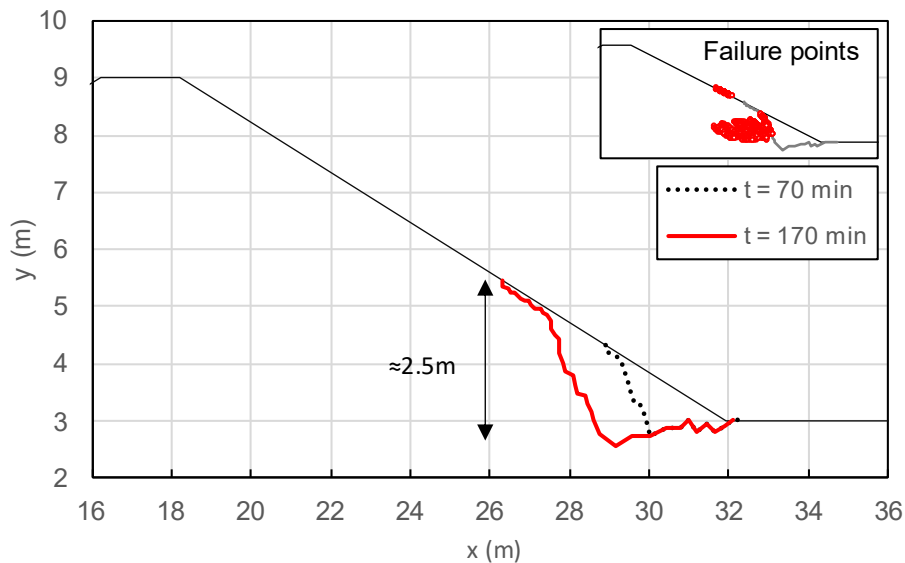
Field Test – 11:55 (37 minutes from the test start) view from downstream left bank (described as initial stages of headcut formation – erosion at weak point near toe of slope)



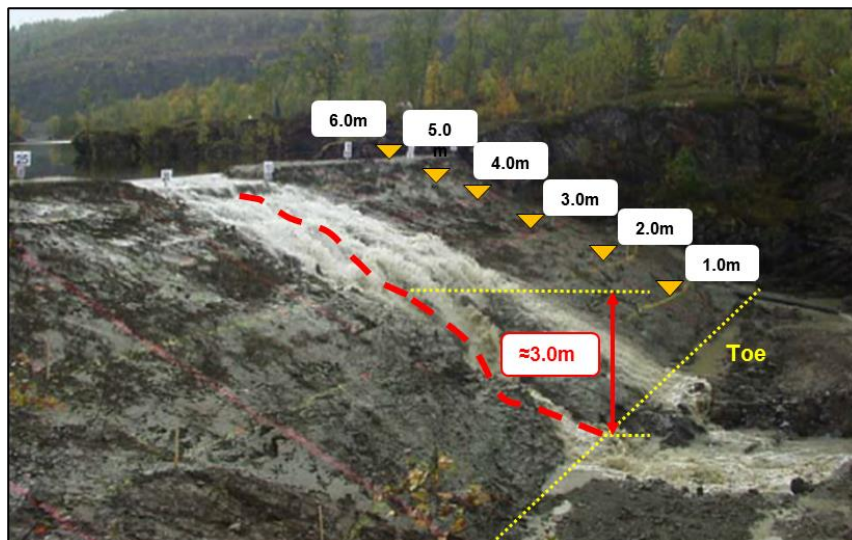
(c)

Figure 5-39: Simulated failure surface (a), field test photos (b) and (c)

The comparison presented in Figure 5-40 shows that the simulated profile and the one interpreted based on field observation tend to cut the slope approximately at the same height, between 2.5-3.0 m above the toe level. From the field image, it appears that a significant part of the embankment material has been removed. However, it is still very difficult to assess how deep the headcut is extending towards the internal portion of the structure.



(a)



(b)

Figure 5-40: Comparison between the simulated overflow (a) and the assessed embankment profile from the field test (b)

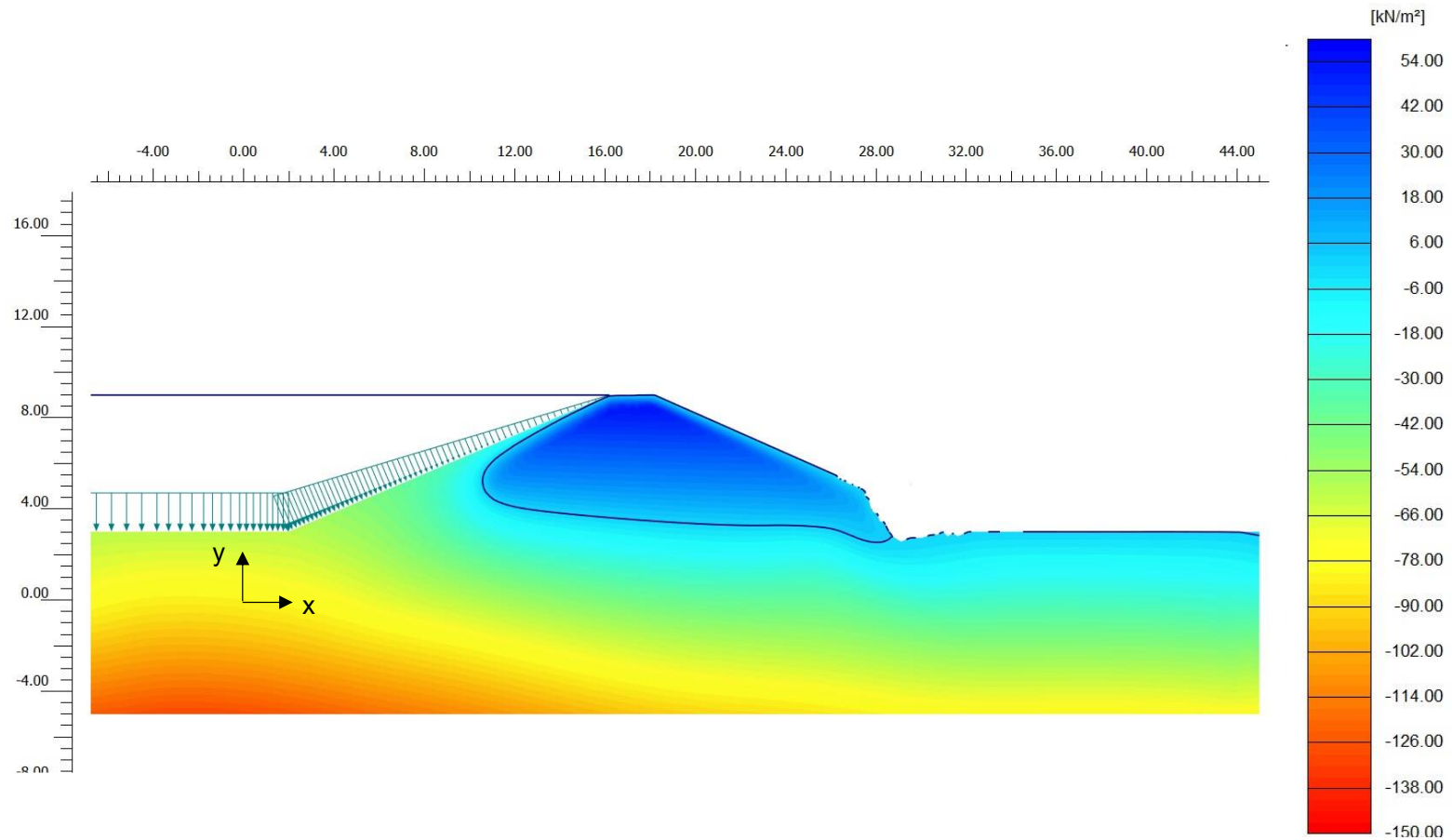
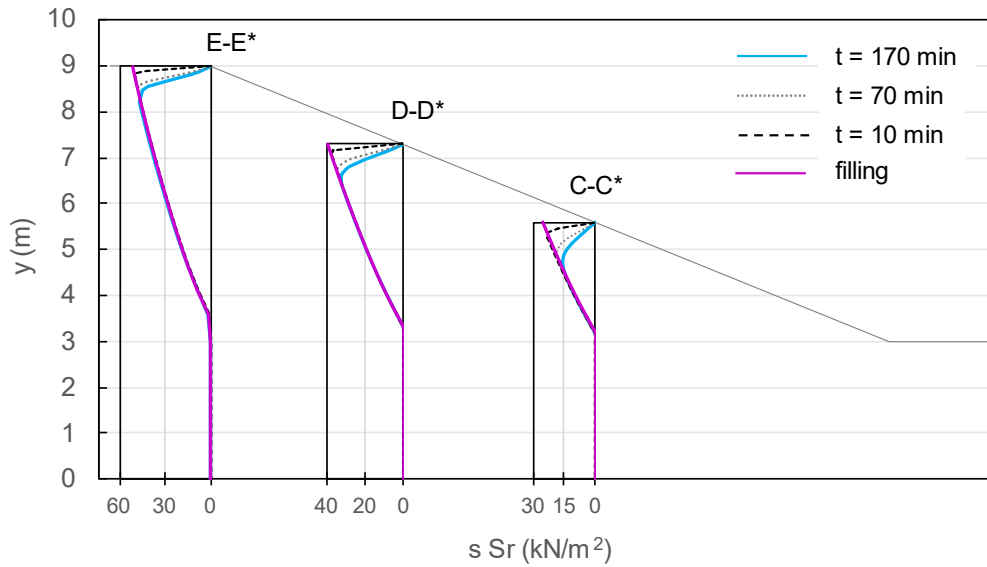
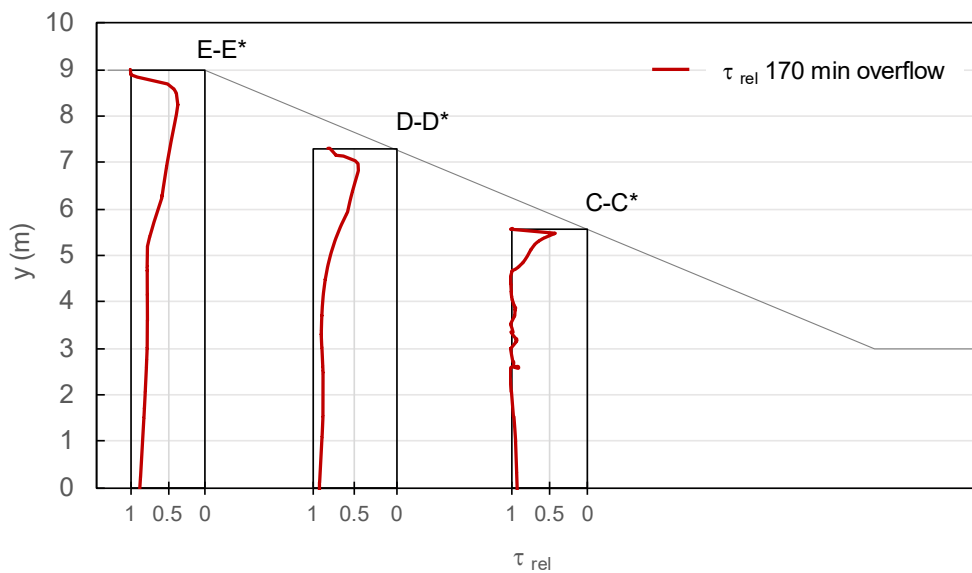


Figure 5-41: Pore water pressure distribution resulting after 170 minutes of the overflow phase. Suction is positive. Maximum Value is 54.4 kN/m^2 (i.e. dark blue contour) and minimum is -139 kN/m^2 (i.e. red contour)

The pore water pressure distribution in Figure 5-41 shows that the infiltration continues to saturate the superficial layer of the damaged embankment where suction ranges between 0-6 kN/m². In the inner part of the embankment and towards the crest suction is still about 50 kN/m².



(a)



(b)

Figure 5-42: Effective suction profiles at selected cross sections (a) profiles of relative shear along the same cross-sections (b) after 170 min of overflow

Effective suction plotted for three cross-sections in the intact portion of the structure are presented in Figure 5-42a. The previous time-steps are also shown to track the progression of water infiltration during overflow along the downstream slope. As already discussed, effective suctions decrease rapidly in the lower areas with a significant drop in section C-C* after 170 minutes of overflow. On the contrary, at the embankment crest the effects of infiltration are delayed. It can be easily observed how the blue line, representative of the 170 min duration, is very close to the dotted black and grey lines obtained after 70 and 10 minutes of overflow, respectively.

The relative shear stress plots in Figure 5-42b confirm that the mobilised shear stress tends to the maximum values at the surface, but when suction starts to increase again the states of stresses is far from the failure envelope.

The stress paths from 70 minutes to 170 minutes of overflow in Figure 5-43a, b show that soil element C located on the surface experiences a reduction of the mean effective stress that can be attributed to the decrease of suction resulting from the continuous infiltration. The change of effective stress brings this point to become tangent to the failure envelope. In fact, as can be observed from the stress point configuration in the top corner of Figure 5-39a, at this location plastic points were formed. However, they were not sufficient to develop a failure mechanism in the sense of the criterion applied with the suction-based breaching model.

Elements D and E located respectively at 17 cm and 31 cm below the slope surface, are subjected to a reduction of the mean effective stress as can be seen in Figure 5-43b. As a result the state of stress moves towards the failure envelope but still significantly far.

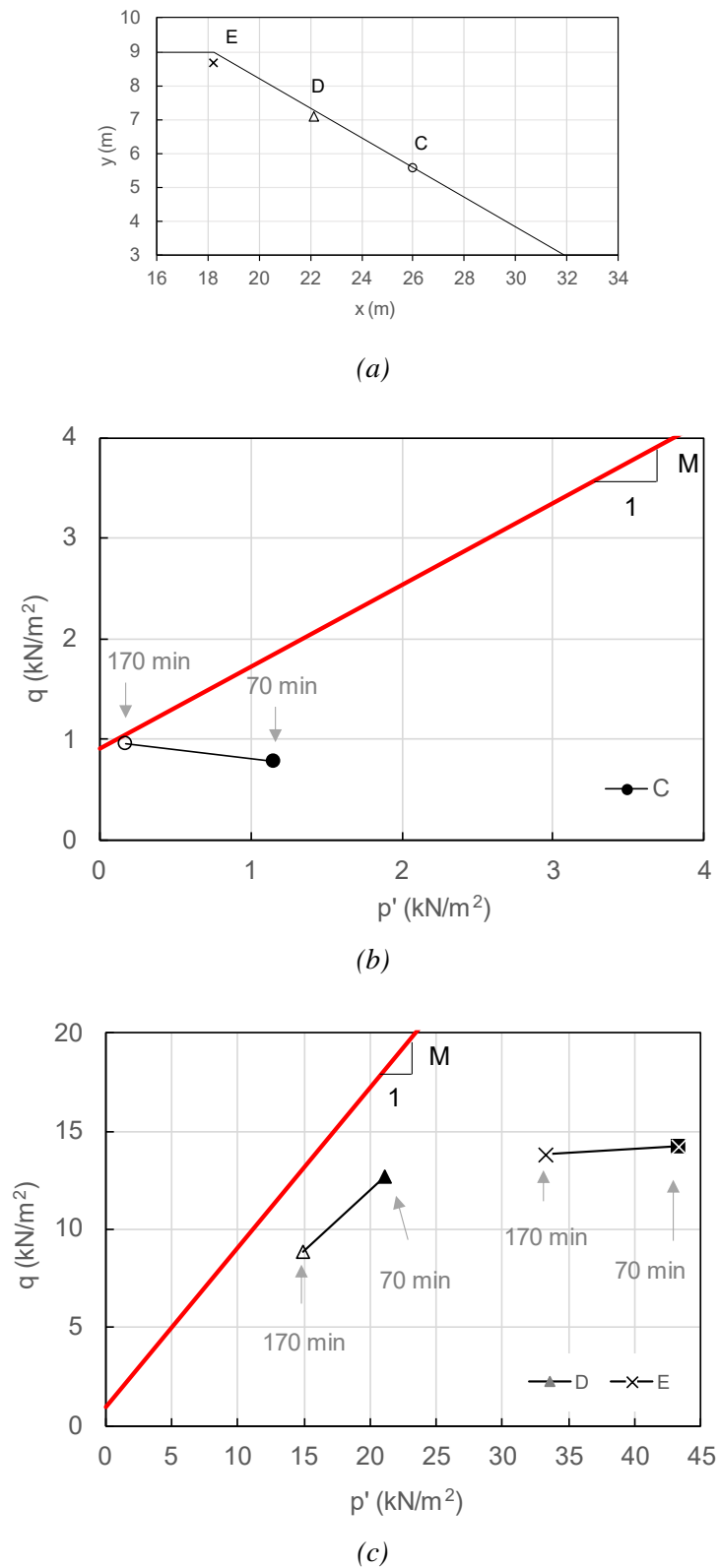


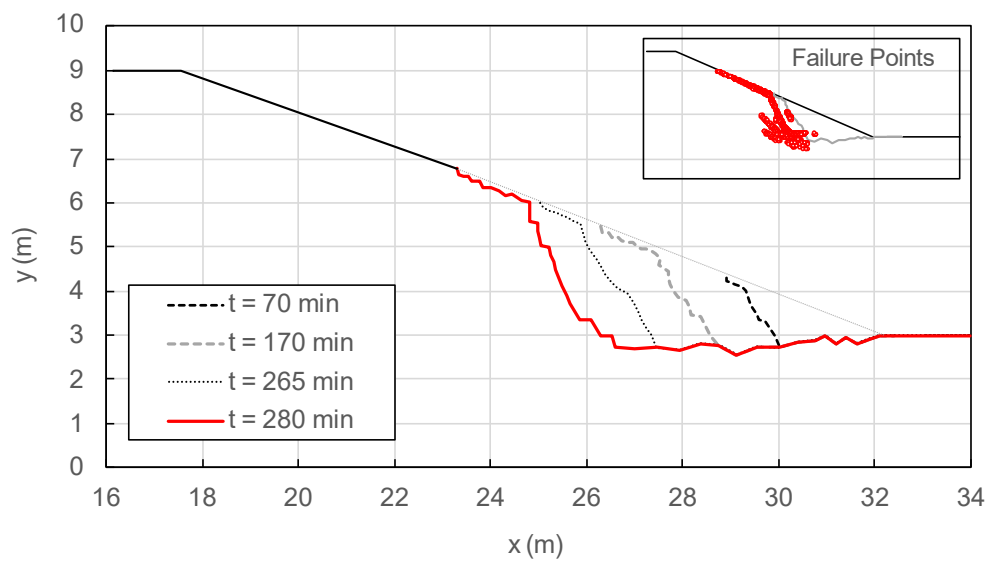
Figure 5-43: Stress paths from 70 min to 170 min of overflow duration of points close to the surface (a) along cross – sections C (b), D and E (c)

Stage 4 – Headcut advancement

Figure 5-44 shows the simulated and real embankment profile at the 50% of the total breach formation process. Figure 5-44b is described by the authors as “headcut progression” and the formation of a second step is observed. This photography angle also offers a view of the headcut width showing that it is almost in line with the initiation notch.

Figure 5-44c shows that the headcut profile is propagating backwards with sides that are almost vertical. Soil removal is involving also superficial layers near the crest. A more detailed comparison for this phase is presented in Figure 5-45. The simulated failure surface starts at the toe and exits on the slope at approximately 3.7 m, causing the removal of a large portion of the embankment.

280 minutes of simulated overflow



(a)

Field Test – 12:11 (53 minutes form the test start) view from mid and upstream right bank – (described as Headcut progression)



(b)

Field test – 12:15 (57 minutes from the test start) view from downstream left bank (described as enlargement of headcut near toe)

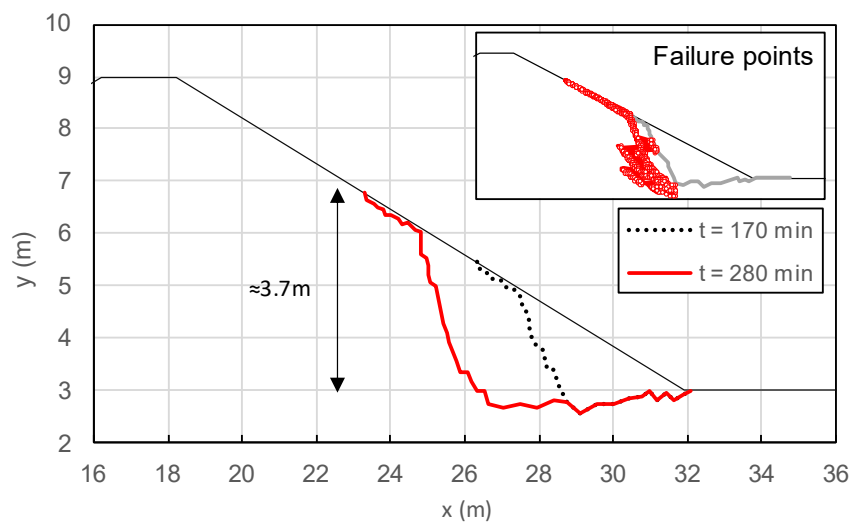


(c)

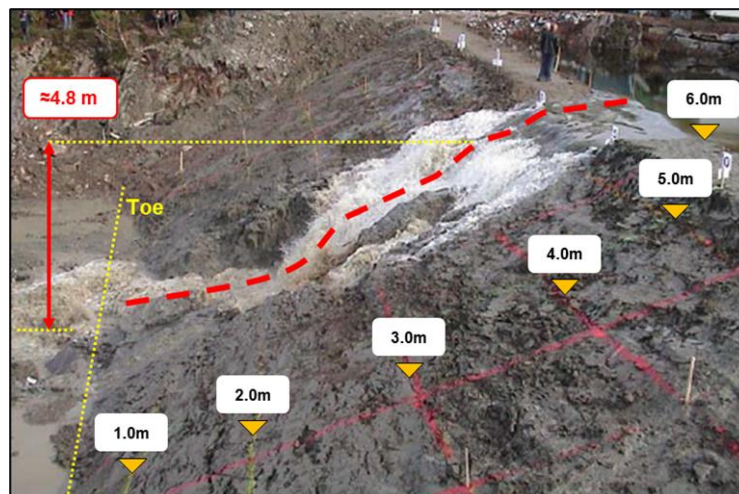
Figure 5-44: simulated failure surface (a) field test photos (b) and (c) at half-way of the total breaching process.

The interpretation of the field image is given again by the red dotted line in Figure 5-45b. As previously noted, the presence of the water and the photography angle re only allow for an approximate assessment of the headcut shape. However, it appears quite clearly that, while the headcut is propagating backwards, it is also extending towards the inner part of the structure. Two more superficial steps are formed towards the crest, cutting the slope at about 4.8 m from the toe level.

The failure front simulated progresses more slowly than the field test, here the headcut advances almost 1 m more towards the crest. However, the experimental failure mechanism and the simulated one still appears to be in good qualitative agreement.



(a)



(b)

Figure 5-45: Comparison between the simulated failure surface(a) and the field site test (b)

The pore water pressure distribution resulting from 280 minutes of overflow with the headcut already developed in Figure 5-46 shows how the dark blue portion representative of the high suction levels is significantly reduced. The damaged part and the intact superficial layers are almost towards the zero-pore water pressure as can be observed following the light blue contours.

Because the upper part of section C-C* has been washed away, effective suction profiles have been plotted only verticals D-D* and E-E*, that are still intact. As can be seen in Figure 5-47a the differences in terms of effective suction from the 170 minutes overflow phase are not significant.

The relative shear stress profiles confirm the trend already discussed in the previous phases.

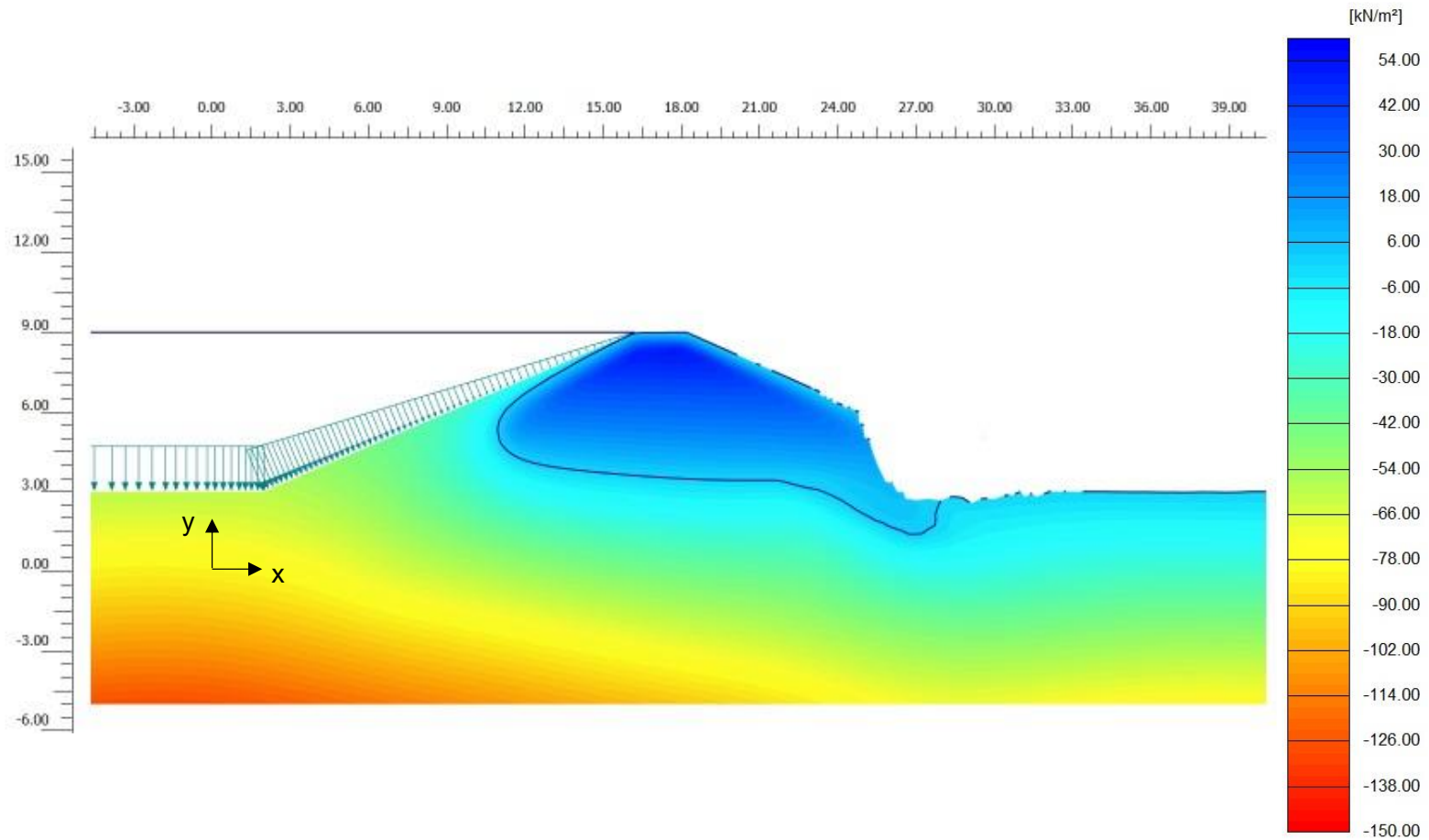
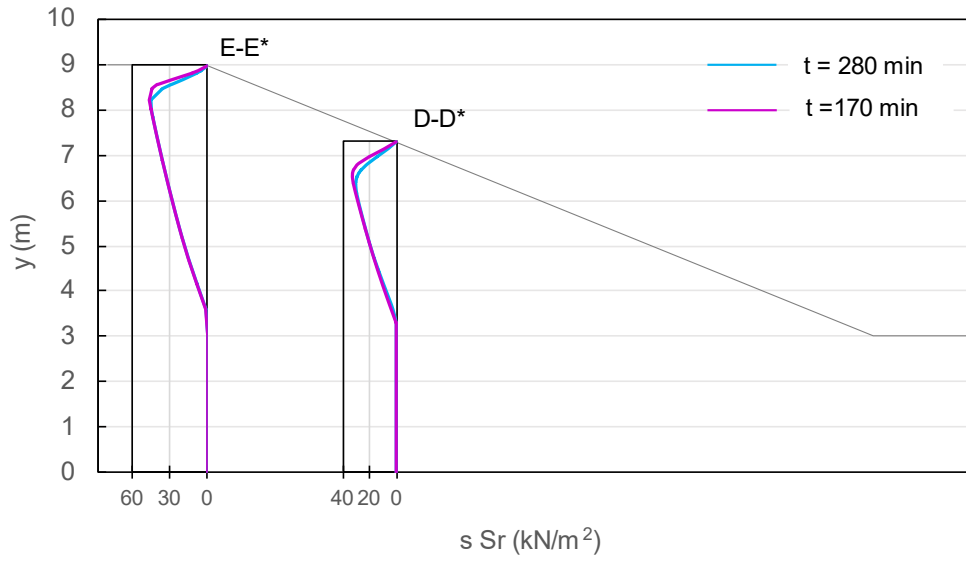
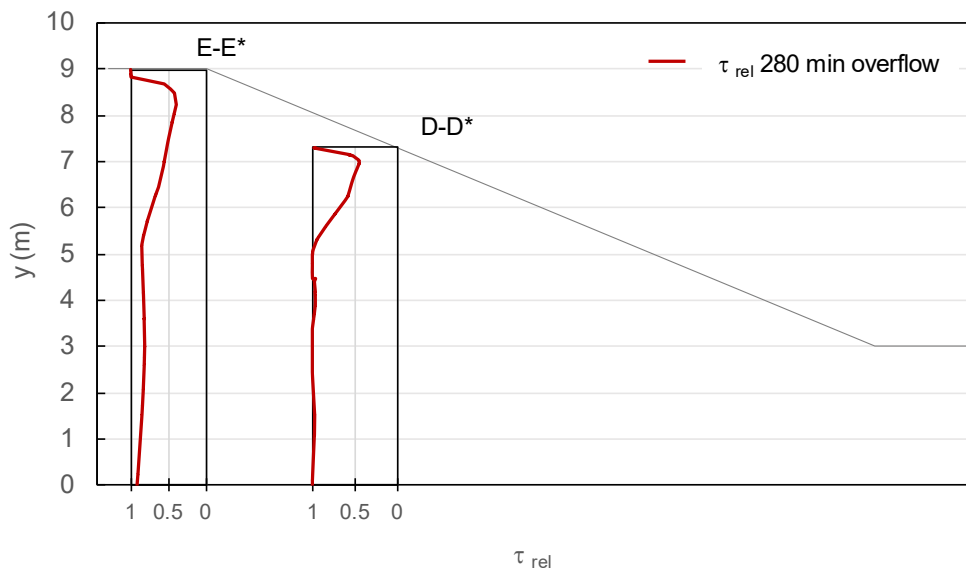


Figure 5-46: Pore water pressure distribution resulting after 280 minutes of the overflow phase. Suction is positive. Maximum Value is 51 kN/m^2 (i.e. dark blue contour) and minimum is -139 kN/m^2 (i.e. red contour)



(a)



(b)

Figure 5-47: Effective suction profiles at selected cross sections (a) profiles of relative shear along the same cross-sections (b) after 280 min of overflow

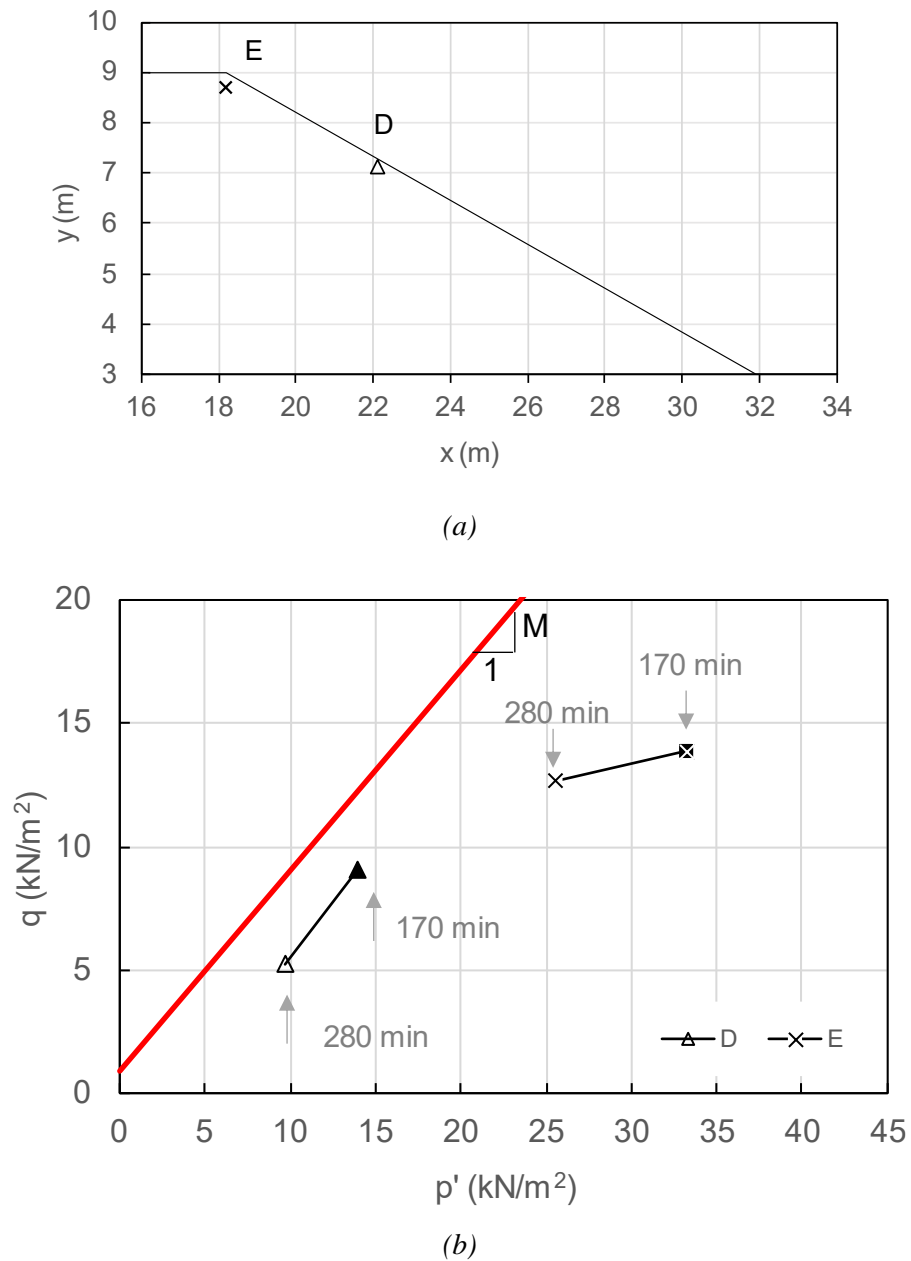


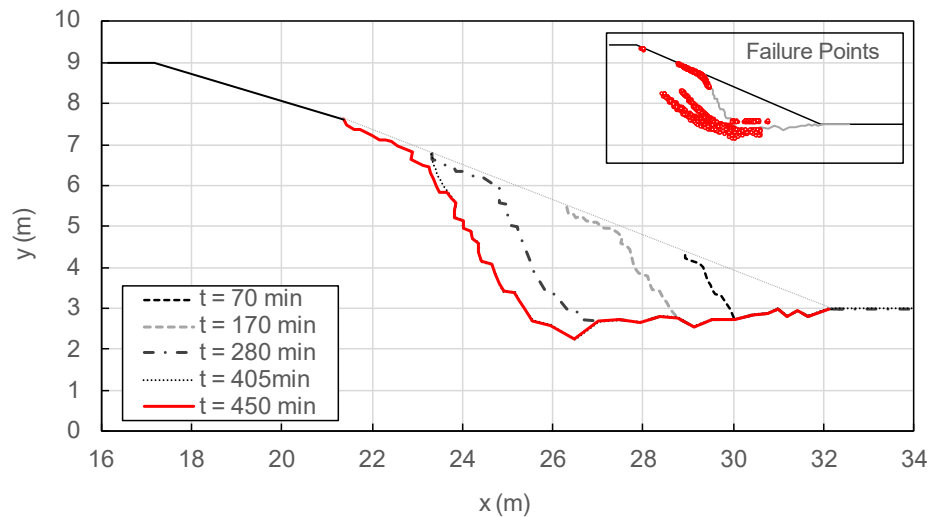
Figure 5-48: Selected points on the slope surface (a). Stress paths in p' - q plane for soil elements D and E (b)

Also for this overflow duration, it can be observed in the figure above, that the two soil elements D and E located 15cm below the surface, are subjected to a reduction of the state of stress moving towards the failure condition.

Stage 5 – Formation of a single large headcut

When the headcut reaches the 80% of the total breaching process a single large step is formed. This is presented in Figure 5-49 and Figure 5-50.

450 minutes of simulated overflow



(a)

Field Test – 12:41 (81 minutes form the test start) view from mid and upstream right bank – (described as Headcut progression)



(b)

Figure 5-49: Calculated headcut (a) and field test photos (b) at the 80% of the overall embankment breaching

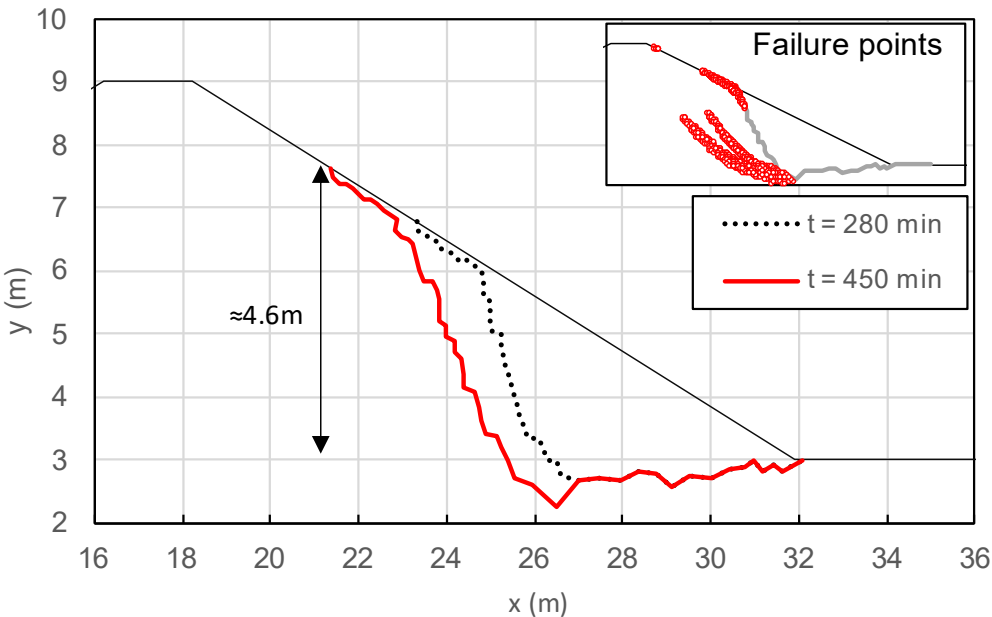
The single large step observed on site involves a significant portion of the embankment material, cutting the slope approximately 5.5 m above the toe level. It can also be assessed that the headcut breaks inside the embankment body for at least the five sixth (i.e. about 11.7m) with the breach sides almost vertical. The shape of the simulated profile is very similar to the observed one; it is 1 m shorter than the profile observed in the field test suggesting that the numerical simulation tends slightly to underestimate the headcut migration rate compared to the large-scale experiment.

Pore-water pressure distribution after 450 minutes of overflow is shown in Figure 5-51. The maximum suction value of 50 kN/m² is close to the previous phase analysed and overall there are no important differences between the two time-interval. However, it must be observed that because of the saturation of the most superficial soil layers upstream of section D-D* at approximately 22m along the embankment cross-section, shallow failure mechanisms are occurring leading to the removal of soil elements just below the slope surface. This is easily noted by the development of failure points shown in the right corner of Figure 5-49a.

In Figure 5-52, because section D-D* has been washed away, cross-section G-G* has been considered, located approximately 1m upstream from D-D*.

Suction profiles at section E-E* are plotted for the filling, 280 min and 450 minutes of overflow. It is evident that from the start of the overflow event, suction values are reduced and tend to become zero on the surface. However, 1 m below the crest level the suction values of the filling phase are recovered, and the strength of the soil at this location is similar to the initial condition. The profile of the relative shear strength in Figure 5-52b confirms that on the surface, the state of stress is close to the failure envelope, but as soon as suction is increased, a significant amount of strength is achieved until the phreatic line is met at greater depth.

Suction profiles between two consecutive overflow phases (i.e. 280 and 450 minutes) are almost identical, showing that the infiltration process is overall slow due to the hydraulic properties considered for the ideal silty – clay.



(a)



(b)

Figure 5-50: Comparison between the simulated failure surface (a) and the field site test (b)

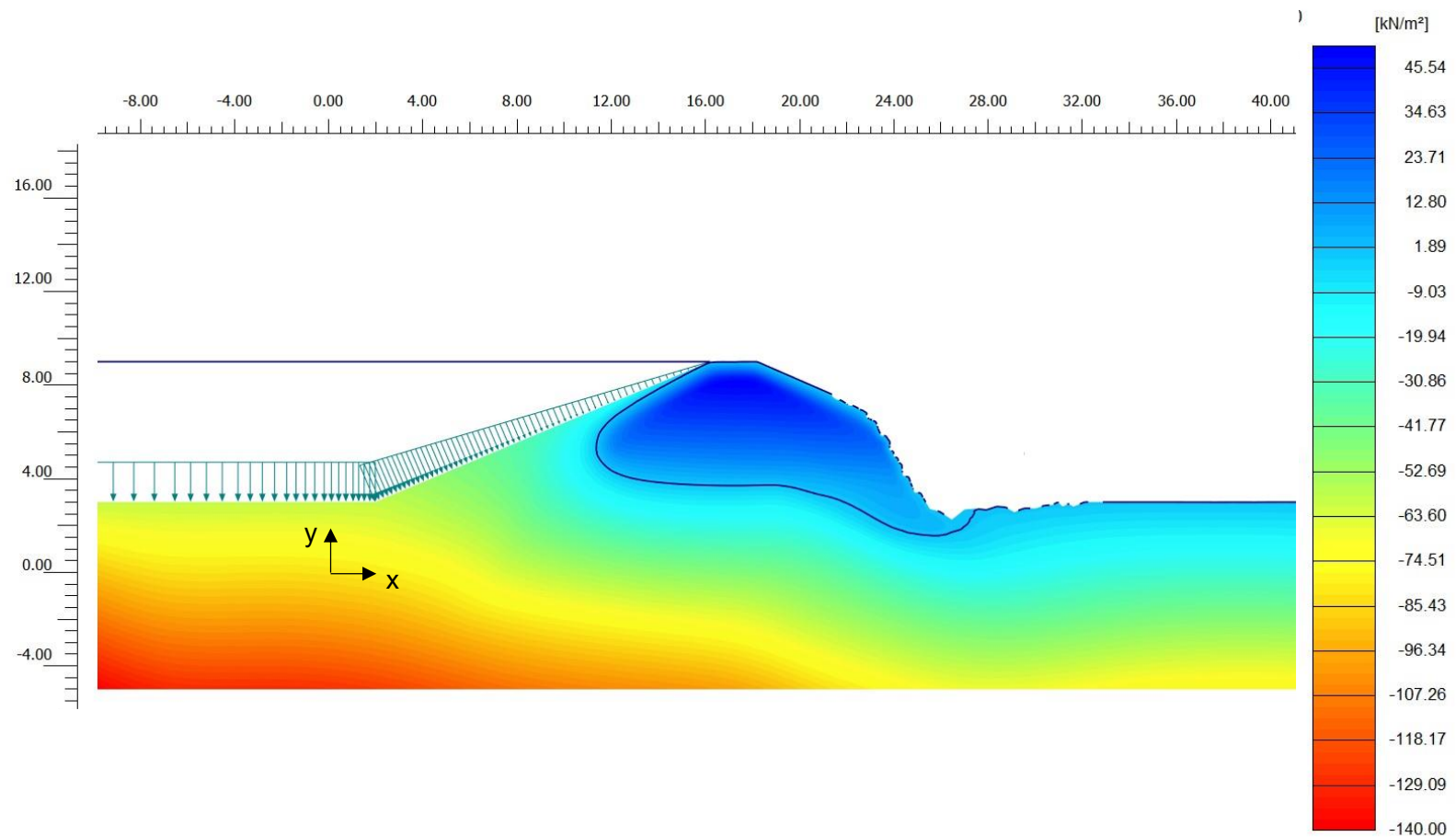
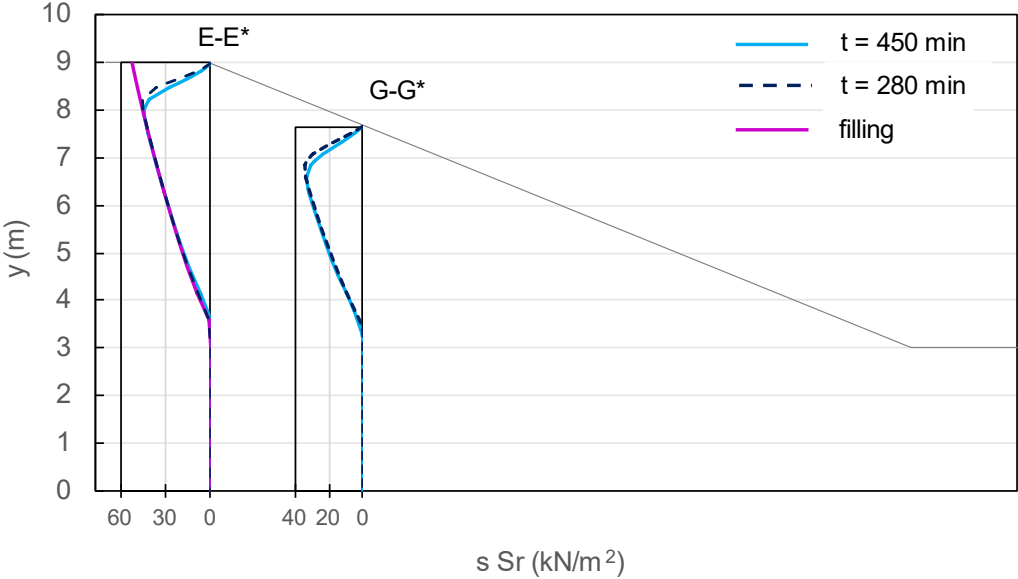
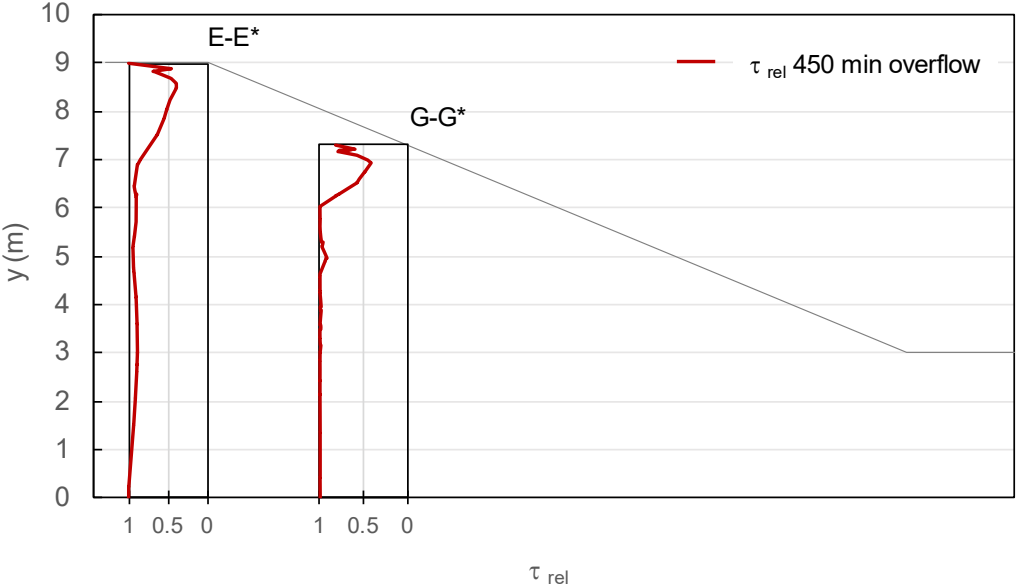


Figure 5-51: Pore water pressure distribution resulting after 450 minutes of the overflow phase. Suction is positive. Maximum Value is 50 kN/m^2 (i.e. dark blue contour) and minimum is -139 kN/m^2 (i.e. red contour)



(a)



(b)

Figure 5-52: Effective suction profiles at selected cross sections (a) profiles of relative shear along the same cross-sections (b) after 450 min of overflow

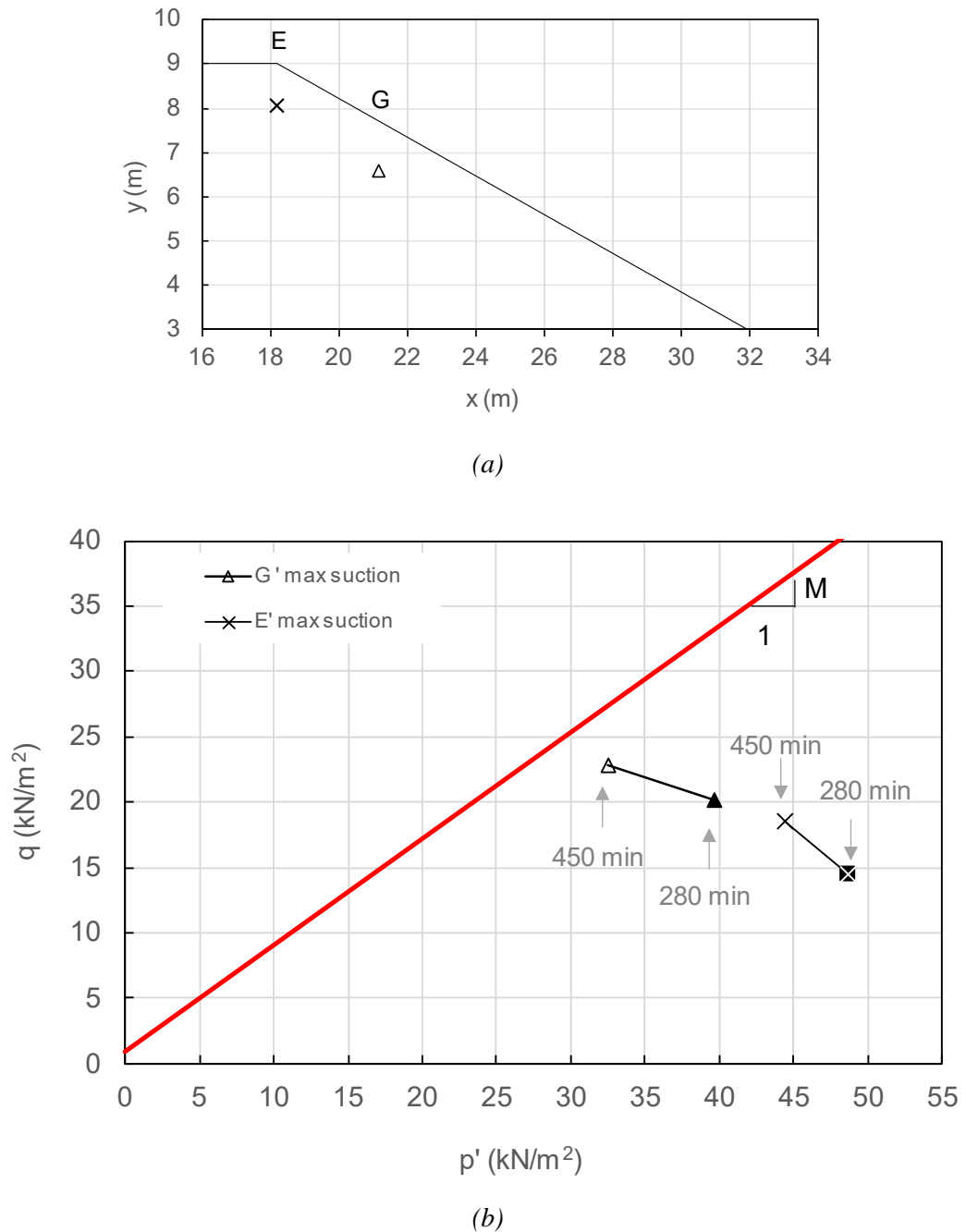


Figure 5-53: Selected points on the slope surface (a). Stress paths in p' - q plane for soil elements D and E (b)

The stress path of a soil element located at the depth of highest suction along the vertical through G-G*, is presented in Figure 5-53b for the current and the previous time-steps. Again, the state of stress evolves towards the failure envelope as consequence of the wetting process associated with the overflow. In essence, due to

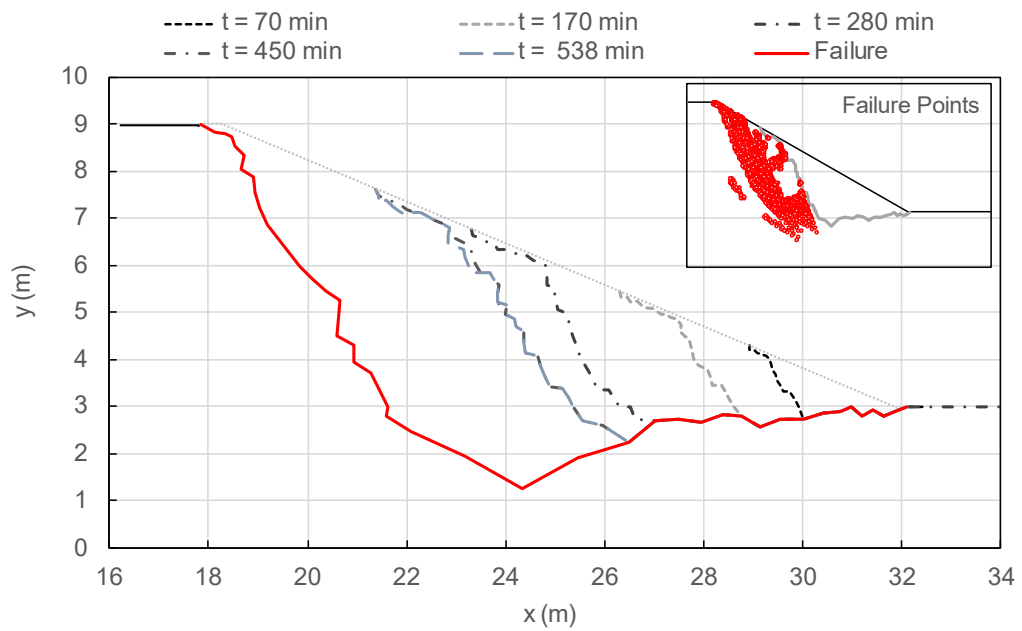
the suction reduction between the 280 min and the 450 min overflow, the mean effective stress decreases and the deviatoric stress increases and the soil element moves to a more critical condition.

Similarly, for a soil element below the crest level along the vertical E-E* it can be observed that the state of stress after 450 minutes of overflow become closer the red line in Figure 5-53b.

Stage 6 – Breach formation

Finally, the single step headcut breaks through the embankment crest leading to breach formation. This occurs after 550 min of simulated overflow and after 107 minutes of the field test. Figure 5-54b,c shows clearly that when the headcut breaks through the crest, the downstream slope has been completely removed and the breach is formed. This is therefore considered the ultimate phase of the progressive headcut migration. When the failure front cuts through the crest, there is a rapid increase of the water flow which falls almost vertically through the breach just formed. The high turbulence and the vortex action of the water flow associated with the formation of the breach tend to accelerate the failure process of the crest and the upstream slope, which consequently recedes backwards causing a sudden drop of the upstream water levels.

It can be observed in Figure 5-55 that, the suction values are still quite high at the crest (i.e. around 48 kN/m²), however on the downstream side the embankment is seriously damaged compromising the overall stability of the structure. Therefore this condition is considered as the final failure.

550 minutes of simulated overflow

(a)

Field test – 13:03 (105 minutes of simulated overflow) view from downstream left bank

(b)

Field Test – 13:05 (105 minutes of simulated overflow) view from downstream left bank



(c)

Figure 5-54: Headcut breaks through the crest causing the opening of the breach formation. Predicted embankment profile (a) and photos from the large-scale test (b) and (c)

The final catastrophic failure shown in Figure 5-56 occurs after 40 min from the onset of breach formation when also the upstream flow has been washed away and an open channel flow is established through the breach. It is worth highlighting that soil removal is still occurring at the side of the breach, as indicated by the yellow circles above. This can be easily understood because of the higher water turbidity at the sides compared to the centre of the breach.

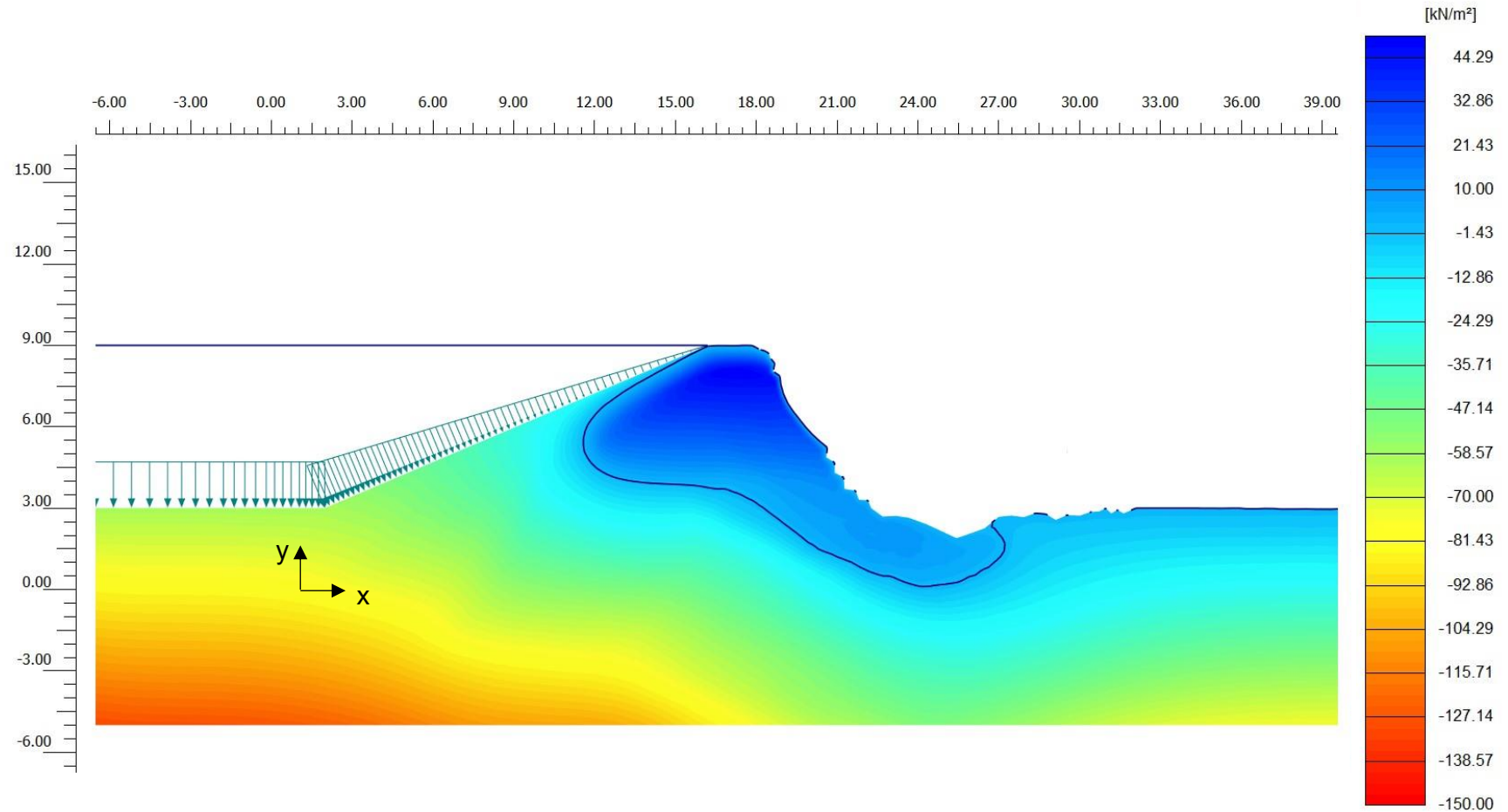


Figure 5-55: Pore water pressure distribution resulting after 550 minutes of the overflow phase. Suction is positive. Maximum Value is 48 kN/m^2 (i.e. dark blue contour) and minimum is -139 kN/m^2 (i.e. red contour)



Figure 5-56: Final catastrophic failure showing the open channel flow through the breach

5.4.2 Homogeneous Coarse-Grained Embankment

The numerical results for the coarse-grained homogeneous embankment are compared with images available from the second IMPACT field test. This test was undertaken in October 2002 on a homogeneous embankment built with coarse-grained material. However, the extremely low temperatures caused the freezing of the soil constituting the embankment. This exceptional condition significantly affected the material behaviour and hence the failure mechanisms observed. As it will be shown in the following, the breach formation occurred essentially through headcut erosion, which was not expected for this type of material. In addition, water level was raised to defrost the superficial layers and a plank was put across the notch to prevent the overflow. The notch area was flooded and the ice thickness on the crest was periodically assessed by digging a spade. It is evident that the differences between the field test and the simulation are multiple and because of these issues, the third IMPACT field test is presented for a better comparison. However, it must be said that this refers to the failure by overtopping of a composite embankment built with rock-fill on the shoulders and with a central moraine core. Time discrepancies between test and simulation can be therefore associated with the issues above mentioned.

IMPACT laboratory tests and results from other research programmes have also been included below for discussion, since Field Test #3 with the IMPACT project

cannot be considered strictly representative of the case analysed.

As for the previous case analysed, breach formation occurs when the failure front cuts through the crest, and this has been considered as the embankment failure condition. According to this reference the total time interval of simulated overflow is 56 min while breach growth continues up to 142 min. The total duration of the field test has been read from the times on the test pictures and it is 40 min for Field Test #2 and 95 min for Field Test #3. The final catastrophic failure occurred after 59 min for Field Test #2 and after 117 min for Field Test #3.

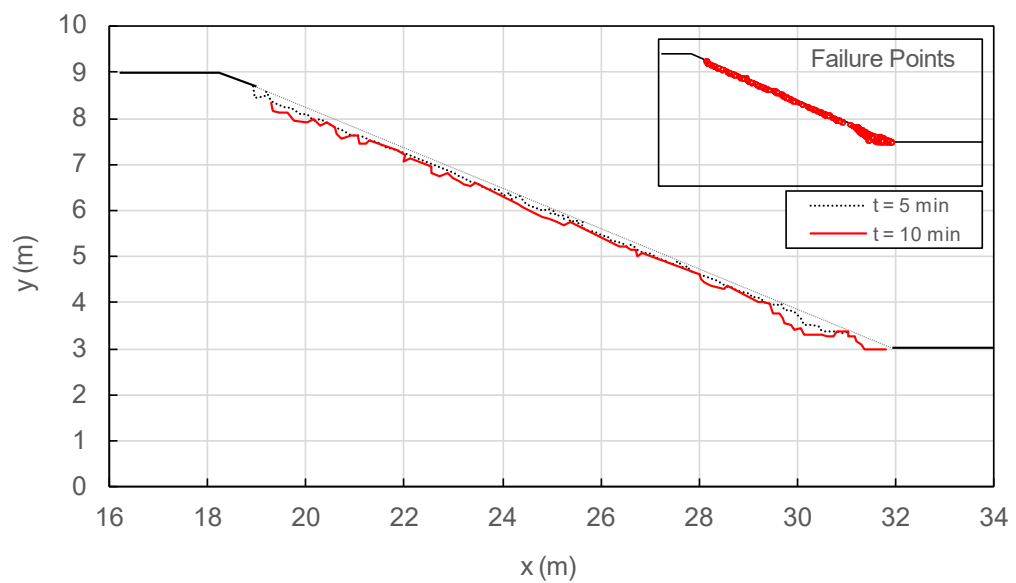
Stage 1 – Onset of Failure

Figure 5-57 refers to the initial phases of overflow showing the predicted embankment profile (Figure 5-57a) and images from the Field Test #2 (Figure 5-57b) and Field Test #3 (Figure 5-57c) after 7 and 17 minutes respectively from the starting time of overflow.

The simulated embankment profile after 10 min of overflow shows the typical features of what is defined in the literature as “progressive surface erosion”. The failure mechanism represented by the red line in Figure 5-57a induces the removal of the most superficial soil layers of the downstream face (approximately 0.2 m in depth), with an ‘eroded’ slope almost parallel to the intact one. In this case, the propagation of the failure front tends to create a gully along the downstream slope which becomes steeper as overflow progresses, receding towards the crest. This mechanism is described by (Visser, 1998) for the development of breach models of sand dike. However, the simulated failure mechanism presents the formation of two small steps around the toe area, reminding of the headcut formation process. This is not surprising, as the mixture of surface erosion and headcutting has been commonly observed during various IMPACT field tests. This fact highlights that, in reality, these two mechanisms tend to co-exist during the same breach formation process and that the definition of a sharp boundary can be mistaken. A breach model should therefore be able to capture the predominant mechanism responsible for the breaching onset. In this context, the suction-based breaching model is promising since it can effectively represent the main physical processes observed, without any additional inputs or constraints on erosion

behaviour and breach geometry.

10 minutes of simulated overflow



(a)

Field test #2 – 11:50 – (7 minutes from the test start) – Headcut Development (view from downstream right bank)



(b)

Field test #3 – 12:17 – (17 minutes from the test start) – Surface erosion and removal of superficial layers (view from immediately downstream right bank)



(c)

Figure 5-57: Initial phase of breach formation for coarse-grained embankment (a) predicted profile after 10 minutes of overflow; (b) Field test #2 after 7 min of test run; (c) Field test #3 after 17 min from the start of overflow

Figure 5-57b is shown for completeness, but the quality of this photo compromises any attempts of providing an interpretation of the embankment centreline profile, although the authors identified this stage as “headcut development”. A better understanding of the embankment behaviour can be achieved with the analysis of the last image taken from the IMPACT Field Test #3 in Figure 5-57c . The rockfill constituting the embankment shoulders creates a very rough surface and therefore the initial overflow tends to penetrate through the natural channels formed between the larger particles while dragging the fine contents downstream. This leads to the formation of a gully which in turn determines an increase of the flow energy enabling the removal of large soil particles. Figure 5-58 shows the embankment centreline profile.



Figure 5-58: Interpretation of the embankment profile after 17 minutes the overflow process of the Test #3

The pore water pressure distribution in Figure 5-59 shows that, after 10 minutes of overflow, the toe area is below the phreatic surface and pore water pressure are in compression (i.e. negative values because of the convention adopted). If this distribution is compared with Figure 5-31, it can be observed that, as for the silty-clay, suction is high at the crest, however in Figure 5-59, zero suction is observed not only on the surface but also at depth, for a thickness of approximately 11cm. This is not surprising and it is due to the different hydraulic behaviour of the ideal materials considered. The sand embankment is characterised by a lower air entry value and a higher hydraulic conductivity than the silty-clay. This means that the sand embankment tends to saturate rapidly and the infiltration is governed by a hydraulic conductivity that is close to the saturated value; and anyway few orders of magnitude greater than the relative permeability of the silty-clay. Overall the water flow in the sand embankment is faster and this explains why the superficial soil layers present pore-water pressure in compression, for the same overflow duration of the silty-clay.

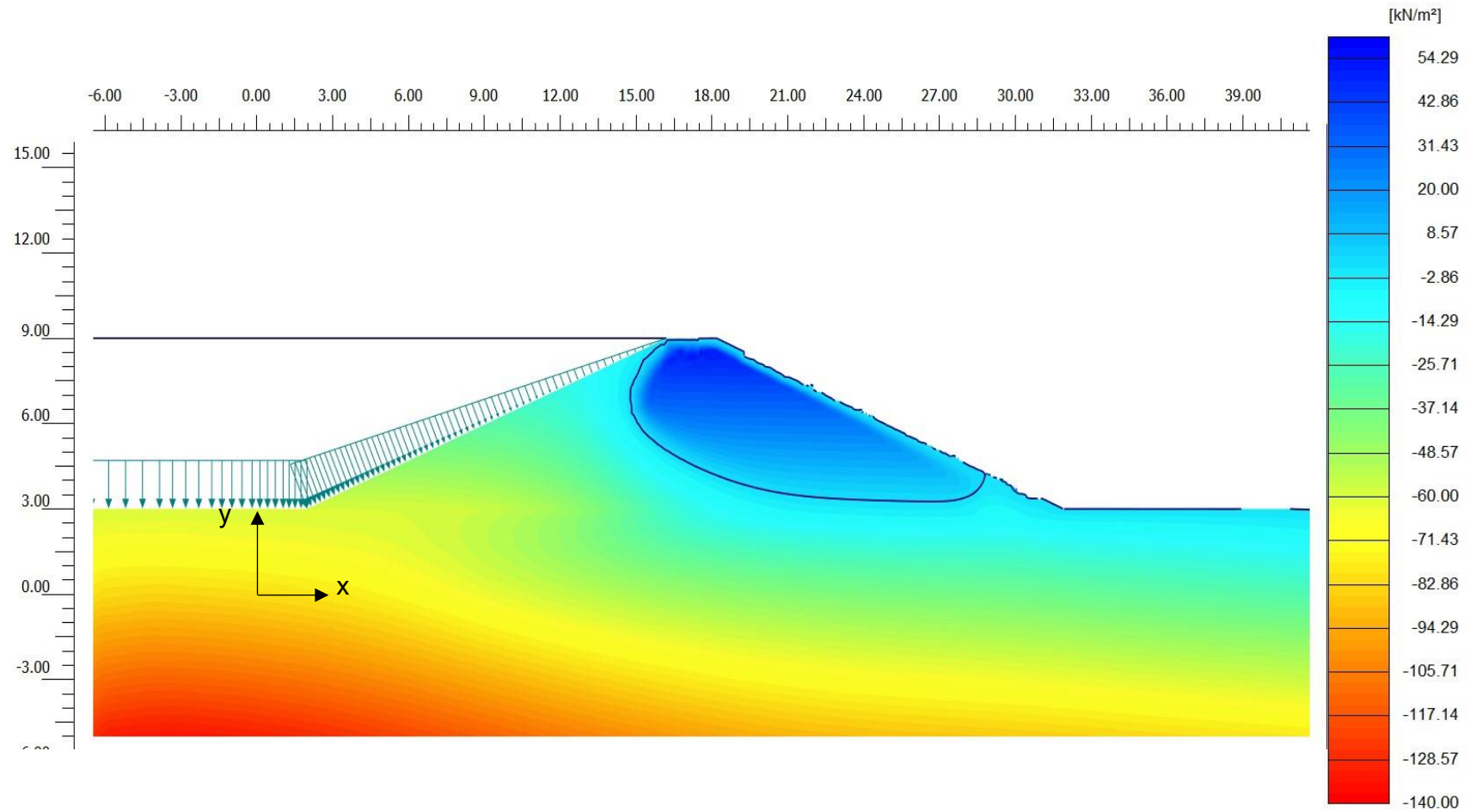
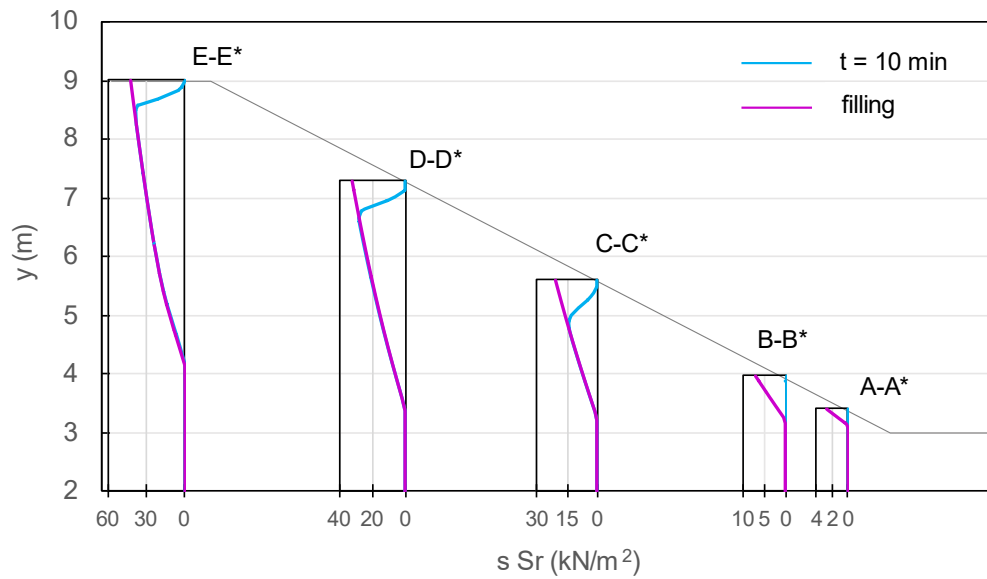
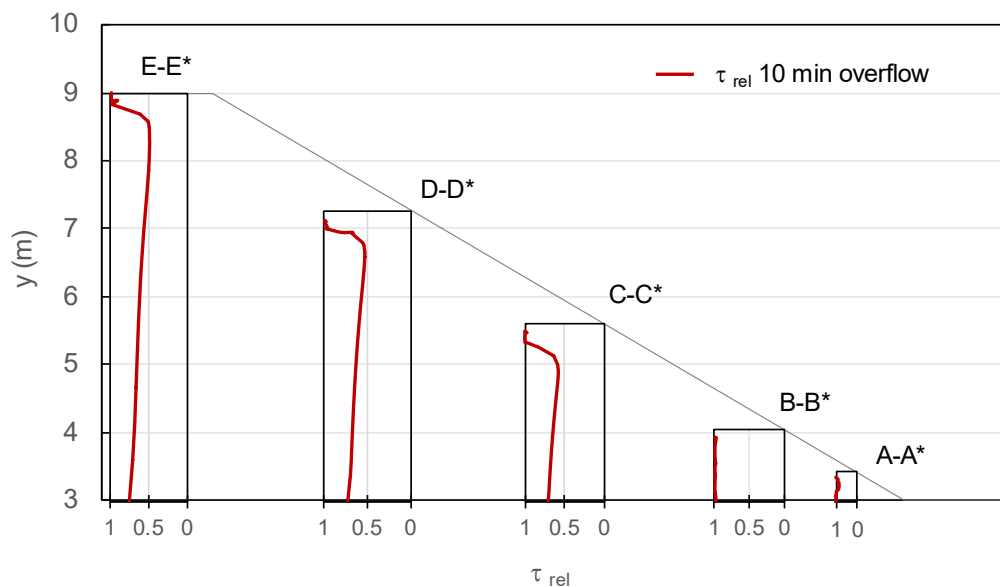


Figure 5-59: Pore water pressure distribution resulting after 10 minutes of the overflow phase. Suction is positive. Maximum Value is 55 kN/m^2 (i.e. dark blue contour) and minimum is -134 kN/m^2 (i.e. red contour)



(a)



(b)

Figure 5-60: Effective suction profiles at selected cross sections along the embankment downstream slope (a) profiles of relative shear along the same cross-sections (b) after 10 min of overflow

The fact that at the end of the first overflow phase, suction is zero on the surface and at shallow depth can be better observed above, in Figure 5-60a. The pressure profile at the end of filling is also presented to monitor the change of the pore-water pressure regime induced by the overflow. It can be seen that, suction was already low

in section A-A* and B-B*. The overflow caused suction to be zero everywhere along these sections. Along the vertical C-C*, suction goes from 21 kN/m² on the surface at the end of filling to zero during the first overflow, up to a depth 11cm. Then it tends to increase and returns to the pre-overflow values of about 14 kN/m² at 85cm below the surface. The same trend is observed also for section D-D* and E-E* but, the initial suction values are higher and are recovered at 45cm and 42cm below ground level respectively.

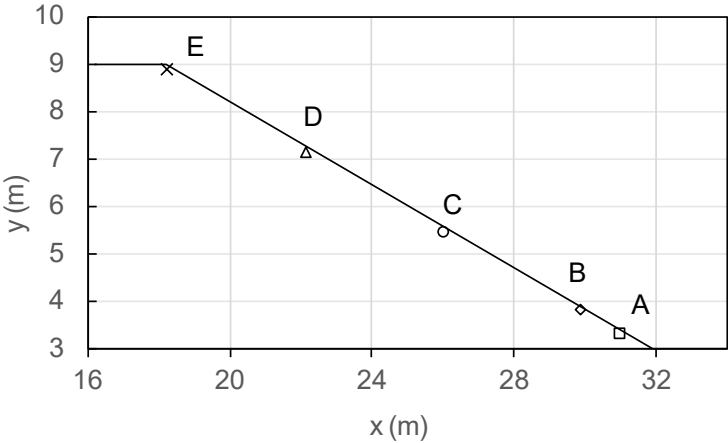
These same observations were reported for the silty-clay profiles in Figure 5-32a, meaning that qualitatively the processes are similar, but suction values and saturated regions are significantly different for the same overflow duration. In other words, the dominant factor is the different response of the two materials to the water flow that is then reflected in the different failure mechanisms observed and simulated.

The relative shear stress τ_{rel} in Figure 5-60b agrees with what has already been discussed for the silty-clay case. It is equal to one on the surface and until suction is zero. Then it tends to decrease with depth and it is the lowest at the depth of maximum suction. Below this point suction decreases again and the relative shear stress tends again to become equal to one. However, section B-B* and A-A*, fully saturated, are characterised by $\tau_{rel} = 1$, constant with depth.

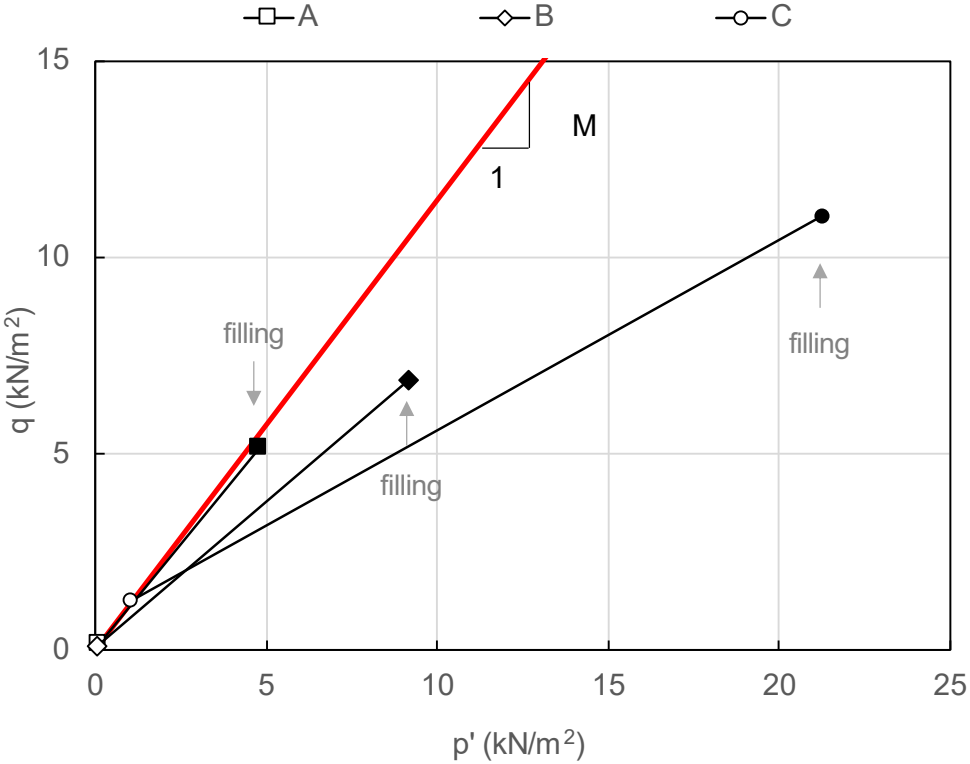
The mechanical and hydraulic aspects of this model can be better analysed by showing the stress-paths of several points close to the surface. The mean effective stress and the deviatoric stress are shown in Figure 5-61, at the end of filling and after 10 minutes of overflow for the same soil elements.

Due to the wetting process the soil elements close to the surface experience a drastic reduction of the mean effective stress and the state of stress drops towards the origin of the p' - q plot, lying on the failure envelope. This occurs for all the elements analysed, however, it is worth observing that initially, points A and B, located at the toe presented the most critical condition. Again, these results are qualitatively similar to the silty-clay case previously presented. This means that, also in this case, the toe is the area more prone to fail. However, the most important difference, here, is that at the end of overflow, the state of stress of points A, B, C and D is in practice the same and this might explain why a uniform failure mechanism involving the superficial soil layers has been identified. In fact, failure points cover almost uniformly the slope

surface as shown in the right corner of Figure 5-57a.



(a)



(b)

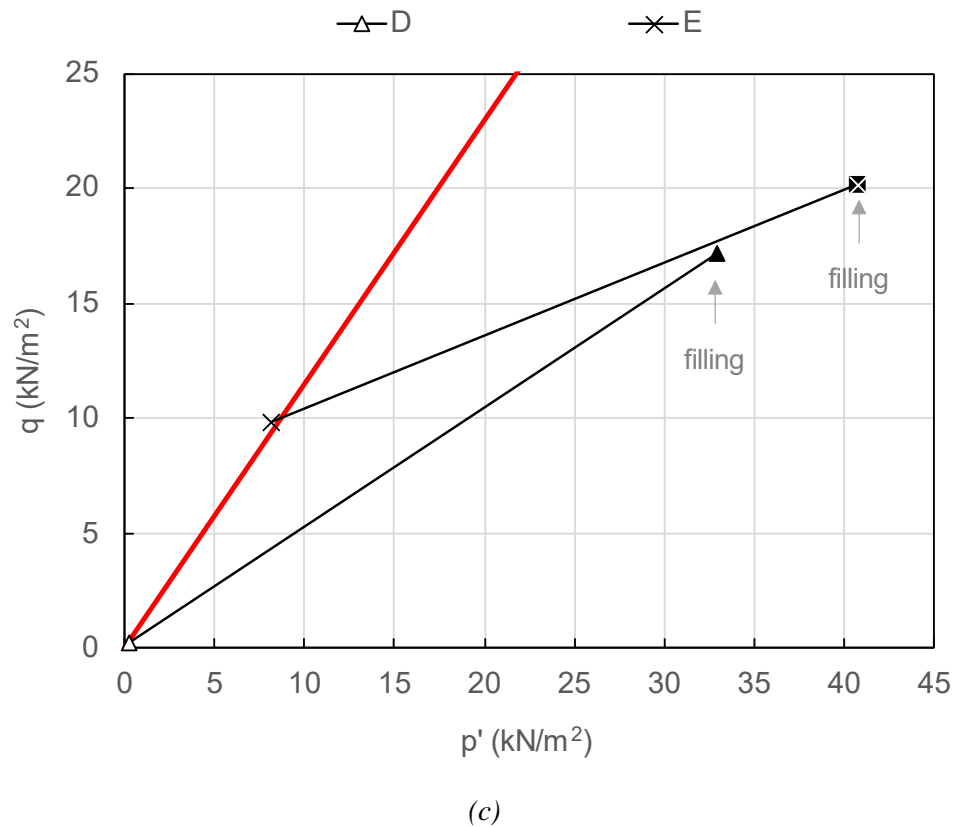
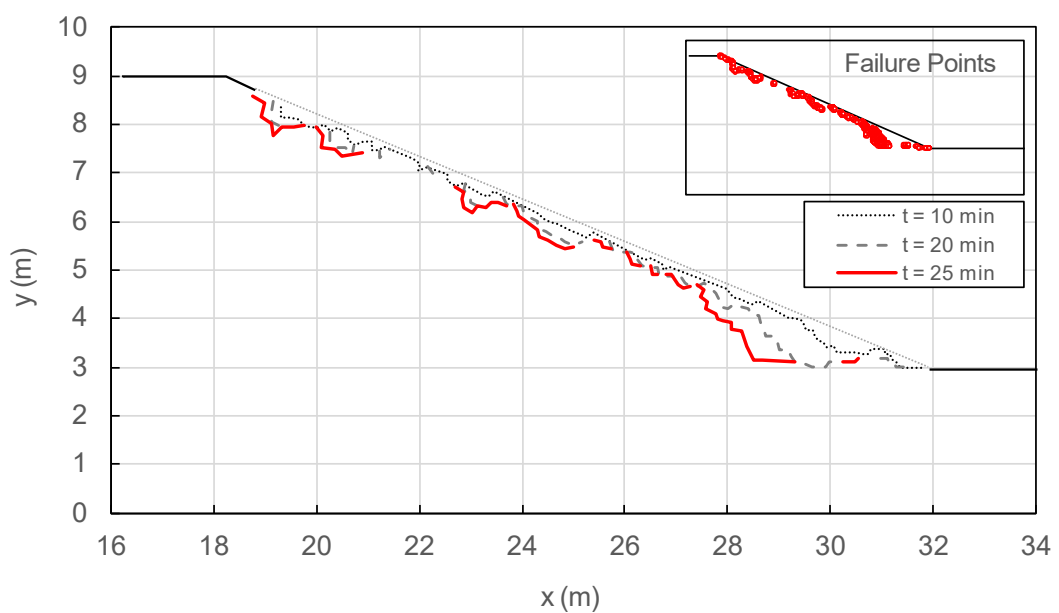


Figure 5-61: Selected points on the slope surface (a). Stress paths in p' - q plane for soil elements A, B, C (b) D and E (b)

It is also worth highlighting that, even in absence of hydraulic shear stresses on the slope surface, the suction based breaching model is still able to differentiate between progressive surface erosion and headcutting. As discussed previously, hydrodynamic forces for coarse – grained materials are more relevant because there is no effective cohesion. However, the results demonstrate that the qualitative behaviour is captured.

Stage 2 – Surface erosion

After 25 min of overflow the predicted profile in Figure 5-62a shows that the surface erosion is progressing, with additional superficial soil layers removed, especially in the middle of the downstream slope. Here, the downstream face recedes parallel to the initial slope up to 0.3 m depth. In the toe area, the initial small steps merged into one single step approximately 1.9 m in height. The simulated failure process seems to assume the typical features of the headcutting process. This phase therefore confirms that the simulation tends to predict a combined failure mechanism, with surface erosion at the top and headcutting at the toe, present simultaneously. This is shown also by the blue line in Figure 5-63.

25 minutes overflow

Field test #2 – 12:00 – 17 min from the test start – Two step Headcut (view from downstream right bank)



(b)

Field test #3 – 12:46 – 46 min from the test start – Surface erosion (view from immediately downstream right bank)



(c)

Figure 5-62: Breach formation of coarse-grained embankment (a) predicted profile after 25 minutes of overflow; (b) Field test #2 after 17 min of test run; (c) Field test #3 after 46 min from the start

The image from the Field Test #2 in Figure 5-63b is described in the FLOODSite report as two steps headcut formation. However, this cannot be clearly observed. An excerpt from the Field Test #3 reported in Figure 5-64 is more useful for the comparison. This shows that the embankment profile is characterised by a stepped shape, due to surface erosion focussed on the large discontinuity present on the surface and an initial headcut at the toe area which extends up to approximately 2.0 m above the toe level. These fields observations are in good qualitative agreement with the simulation.

Figure 5-65 shows the contour plot of the pore-water pressures after 25 minutes of overflow on the damaged embankment. It can be clearly observed that there is still a portion of the embankment material at the crest, with relatively high suction values. Along the slope, instead, water pressure is in compression as shown by the light blue contours. The fact that effective suction is zero superficially, can be better noted in the cross-section plots in Figure 5-66a. Results of the previous calculation phases are presented for comparisons.

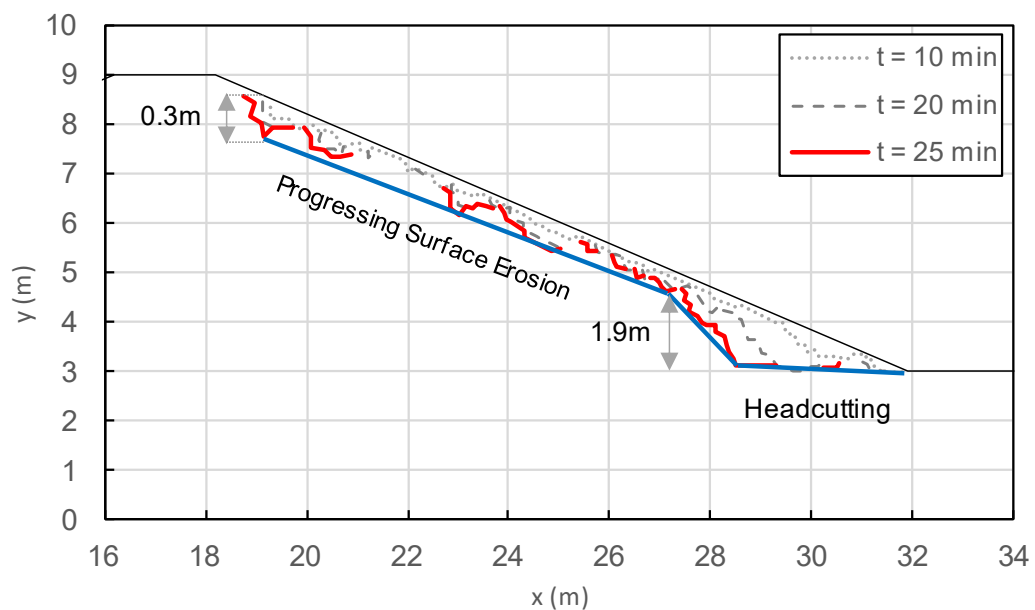


Figure 5-63: Progressive surface erosion towards the embankment crest and formation of a single step at the toe area for the simulated embankment profile at the 44% of the total breach formation process.



Figure 5-64: Interpretation of the IMPACT Field Test #3 embankment profile at the 46 minutes after the beginning of overflow

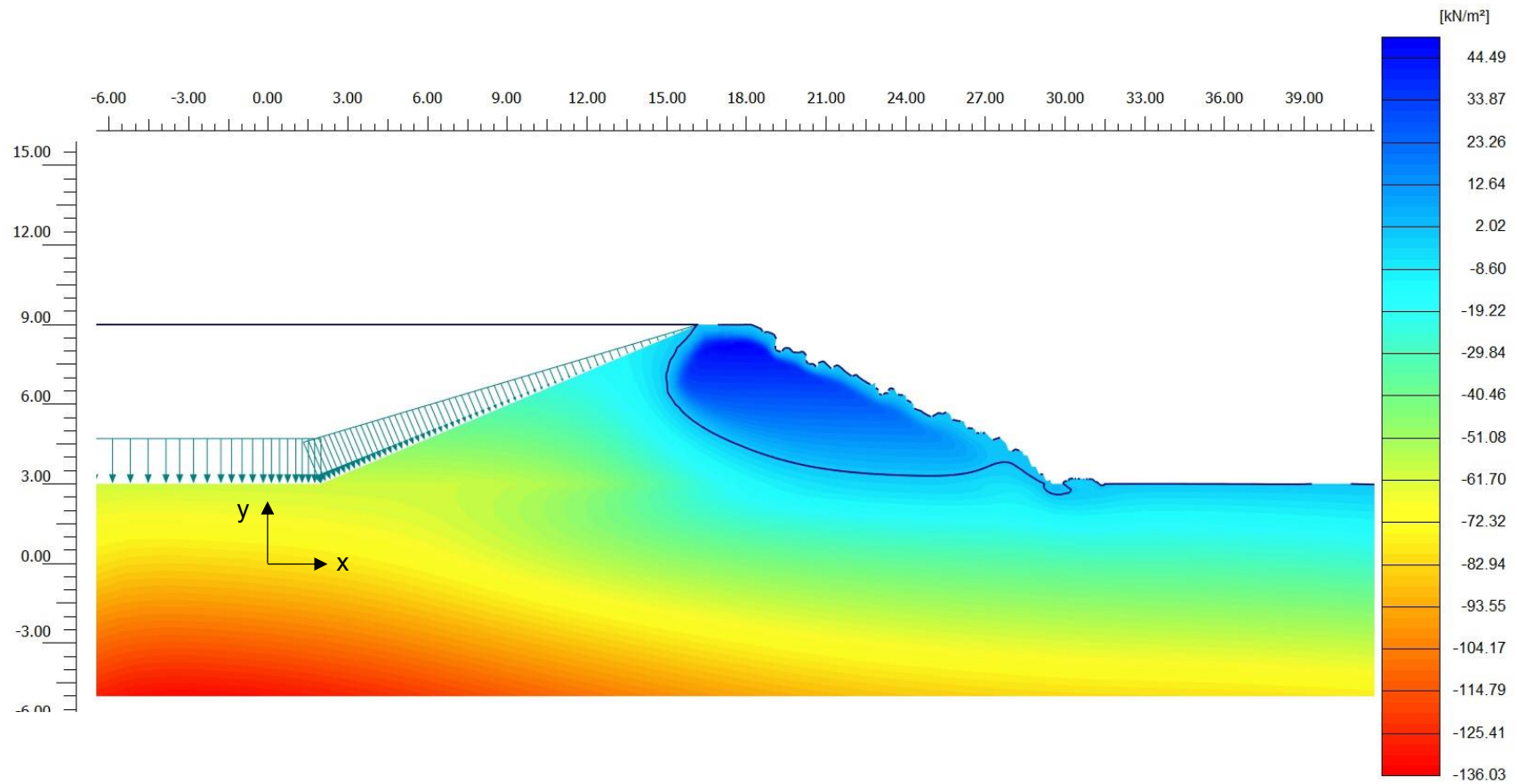
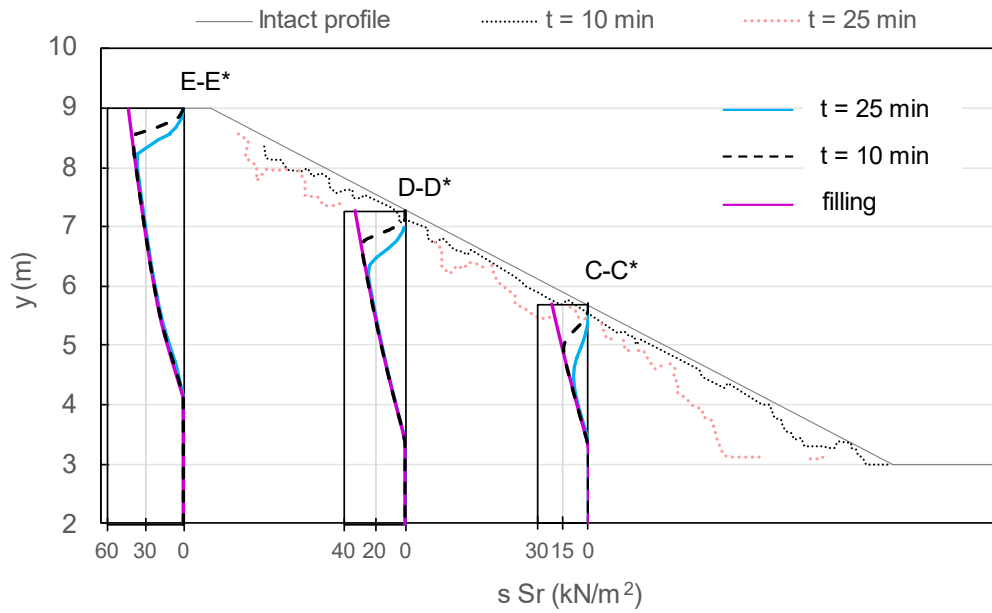
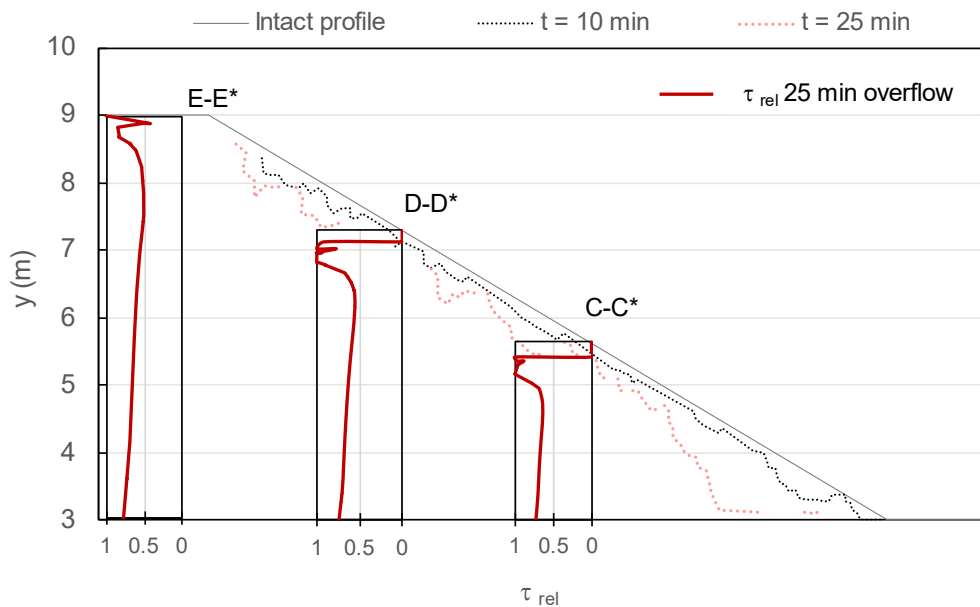


Figure 5-65: Pore water pressure distribution resulting after 25 minutes of the overflow phase. Suction is positive. Maximum Value is 50 kN/m^2 (i.e. dark blue contour) and minimum is -136 kN/m^2 (i.e. red contour)



(a)



(b)

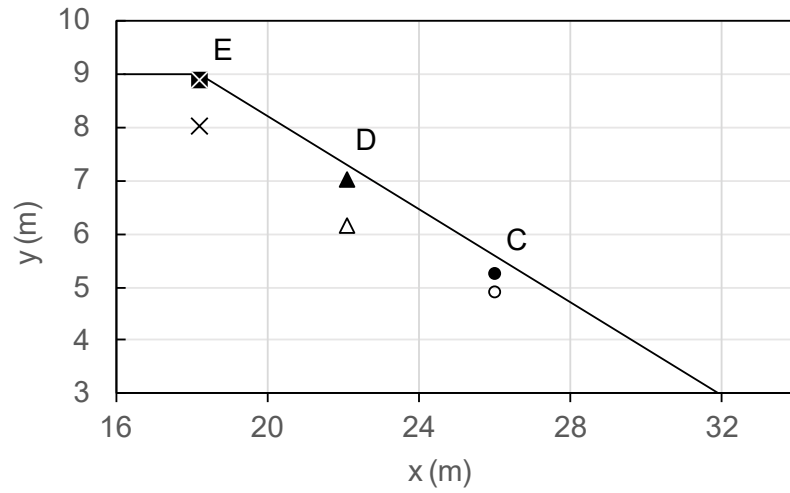
Figure 5-66: Effective suction profiles at selected cross sections along the embankment downstream slope (a) profiles of relative shear along the same cross-sections (b)

It should be noted that due to the type of failure by exfoliation, soil layers are removed on the surface and the comparisons with previous time-steps at the same depth can be mistaken. Indeed, as the overflow progresses, soil elements are washed

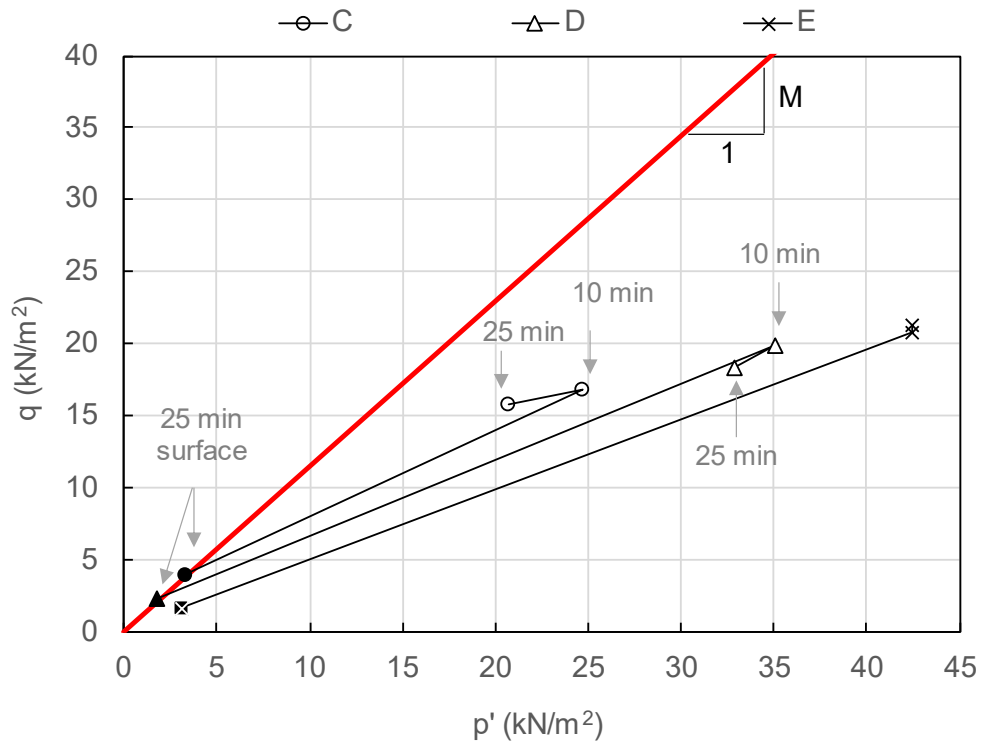
away and suction can be zero, not just because of the water flow advancing but essentially because soil elements are removed. For the same reason, the states of stress are lower than before (i.e. less soil above a given depth across two consecutive phases). As such, in Figure 5-66a,b cross section A-A* and B-B* are not considered anymore, while cross-section C-C*, D-D* and E-E* present the same geometry in the phases considered. It can therefore be concluded that, as the overflow advances, effective suction is significantly reduced, especially in cross-section C-C*. Here, the pre-flood effective suction is recovered at greater depths below the surface, as the time-step of the analysis increases. This qualitative trend occurs also for section D-D* and E-E*, but the effective suction here is higher and, moving towards the crest, effective suction profiles present greater gradients between the surface and the depth of maximum values.

The relative shear stress profiles are reported in Figure 5-66b for completeness. These confirm the trends already discussed.

The changes of stress states from 10 minutes to 25 minutes of overflow are shown in Figure 5-67b. The soil elements in Figure 5-67a have been selected close to the surface and at the depth corresponding to the maximum effective suction in the relative cross-section profile. In this way elements C, are at depths of 34cm and 67cm below the surface; elements D are 27cm and 113cm below ground and elements E are at 11 cm and 96cm, respectively. The most interesting observation is that, at the depth of maximum effective suction, there is a change of the effective stresses from the 10 minutes to the 25 minutes overflow, but this is smaller as the points are closer to the crest. At the crest (i.e. point E) this difference is almost negligible. This means that the effects of the infiltration and therefore the loss of strength, are more important towards the toe than at the crest, exactly like the silty-clay case. On the surface, instead, the state of stress is almost the same for all the points and tangent to the failure envelope. Points on the surface are less strong and more prone to fail, leading to the failure mechanisms simulated and observed on site. The main difference with the silty-clay case is related to the time-dependence of these processes and the initial suction values. Qualitatively the trends are similar, but in the silty-clay there is a delay due to initial higher suction regimes and slower response to the overflow advancement than in the sand embankment.



(a)



(b)

Figure 5-67: Selected points along the slope (a). Stress paths in p' - q plane for the selected soil elements C, D, E (b)

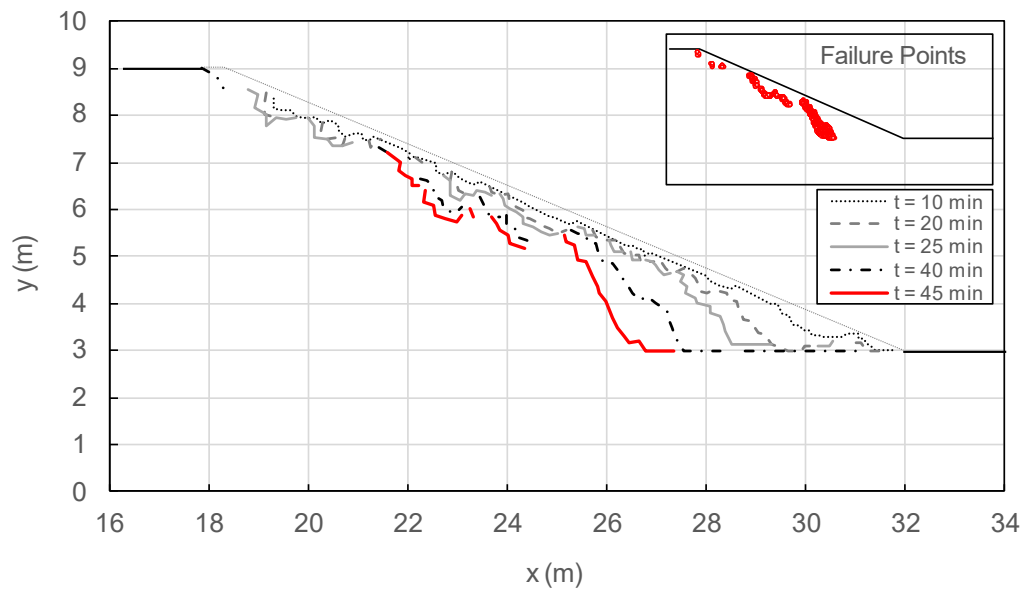
Stage 3 – Advancement of progressive surface erosion and headcut

Figure 5-68a presents the results of the predicted embankment profile after 45 min of overflow. At this stage, the process of breach formation has reached the 80% of its development. Figure 5-68b,c reports the corresponding images observed during IMPACT Field Test #2 and IMPACT Field Test #3 respectively.

The simulated profile at this stage of the breach formation process confirms the behaviour observed in the previous time-steps. The failure front advances backwards to the crest because of the combination of two mechanisms. Progressive surface erosion with soil elements removed layer by layer affects the upper portion of the downstream slope. This results in a centreline profile which has now become steeper than the initial slope. The maximum thickness of soil layers removed is approximately 1.1 m. On the contrary, at the bottom of the downstream slope, the single step previously formed continues to undercut the embankment reaching a height of 2.3 m as can be seen in Figure 5-69. For the Field Test #2 the authors identified this stage as “headcut progression”, although it is still difficult to assess from the image. Field Test #3 is again more useful for interpreting the processes observed.

The embankment centreline profile observed in the field test is drawn in Figure 5-70. The dotted red line allows inferring that there are strong similarities with the embankment profile simulated, in particular the presence of a large step formed at the toe area with height of 3.0 m approximately. At the same time, the upper portion of the downstream slope around the crest area appears to be relatively smooth as consequence of soil being removed layer by layer.

The pore water pressure distribution after 45 minutes overflow is shown in Figure 5-71. It can be observed that water pressure is in compression along the damaged embankment, including the area at the toe where soil has been removed (i.e. between 32 and 26.8m in the horizontal direction).

45 minutes overflow

(a)

**Field test #2 – 12:17 – 34 minutes from the test start – Headcut Progression
(view from downstream right bank)**

(b)

Field test #3 – 13:35 – 95 minutes from the test start – Headcut formation (view from immediately downstream right bank)



(c)

Figure 5-68: Breach formation process of coarse-grained embankment (a) predicted profile after 45 minutes of overflow; (b) Field test #2 after 34 min of test run; (c) Field test #3 after 95 min from the start of overflow

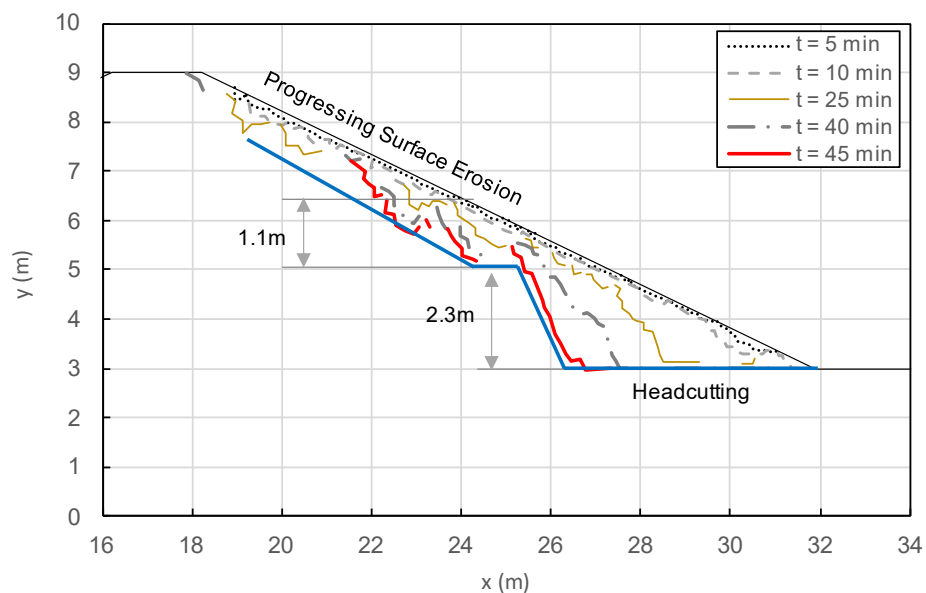


Figure 5-69: Combination of progressive surface erosion and headcut resulting from the suction-based breaching model after 45min of overflow



Figure 5-70: Interpretation of the embankment profile observed during the Field Test #3 after 95 min of overflow

In Figure 5-72, suction profiles and relative shear stress cross sections are shown for completeness. The same qualitative analysis discussed previously applies.

Similarly, the stress paths for soil elements located along the verticals D and E in Figure 5-73a,b agree with the trend already explained in the previous calculation phases. When the overflow duration increases from 25 to 45 minutes, soil elements are subjected to a decrease of the stress levels associated with the loss of suction and migrate towards the failure envelope.

It is worth specifying that the lower stresses for soil element E, are due to the fact that this point is located 51 cm below the surface, while point D is at 77cm below ground level.

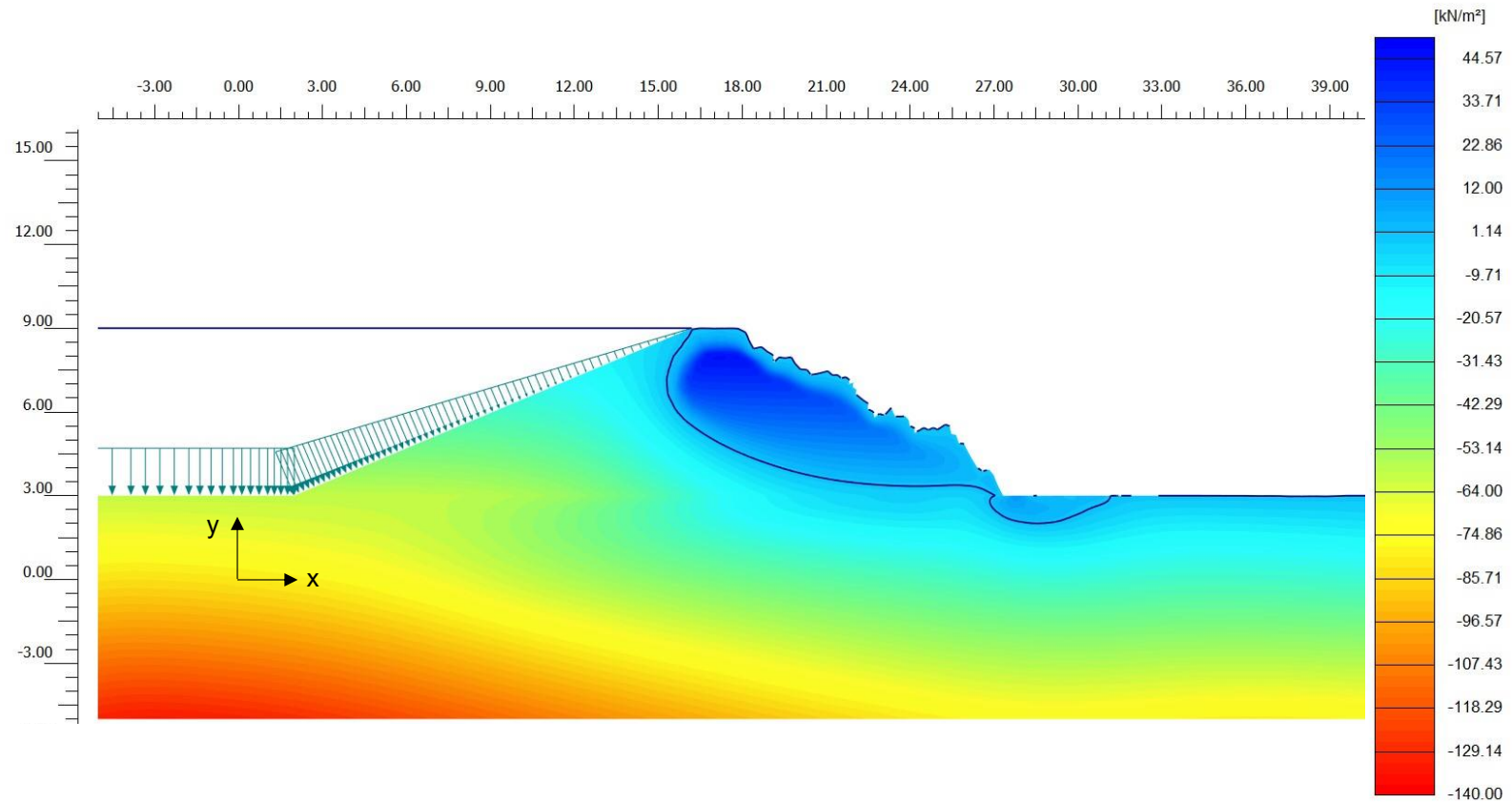
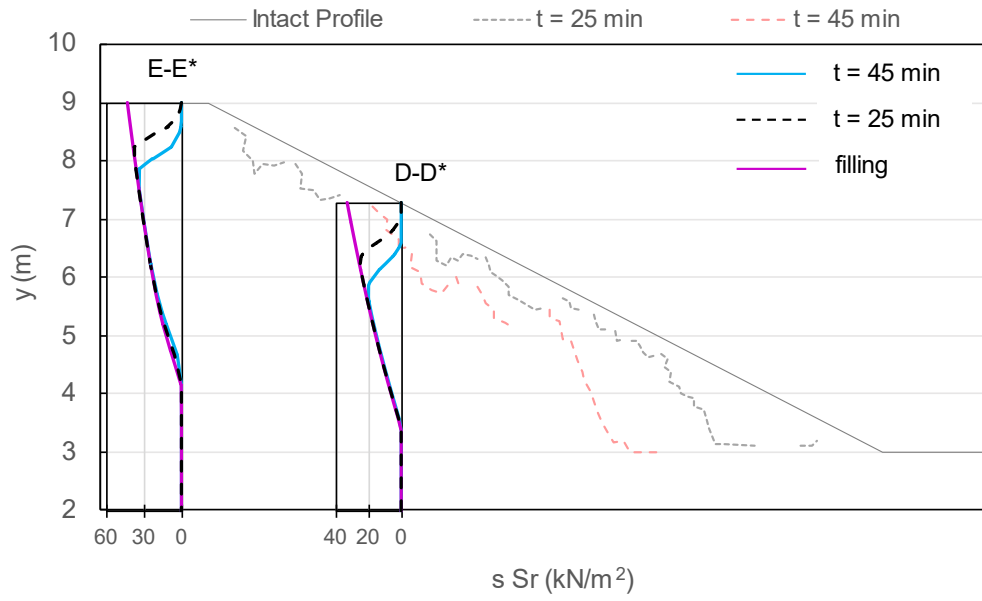
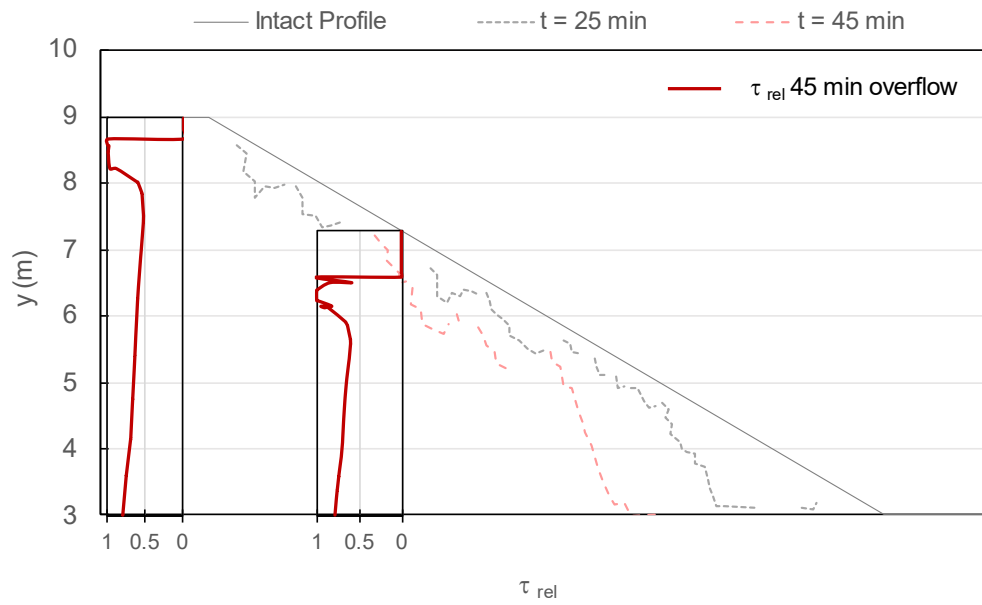


Figure 5-71: Pore water pressure distribution resulting after 45 minutes of the overflow phase. Suction is positive. Maximum Value is 45 kN/m^2 (i.e. dark blue contour) and minimum is -138 kN/m^2 (i.e. red contour)

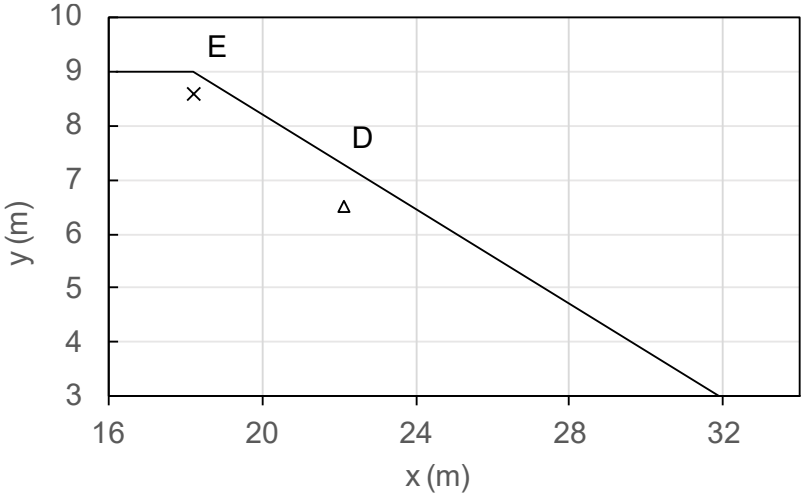


(a)

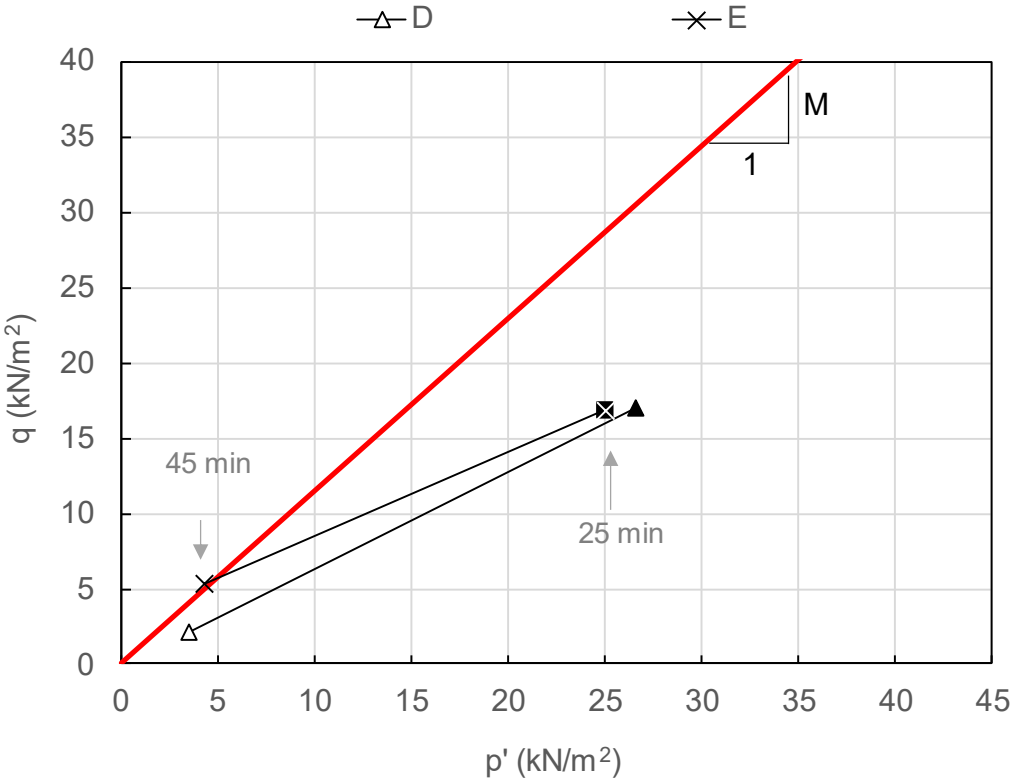


(b)

Figure 5-72: Effective suction profiles at selected cross sections along the embankment downstream slope (a) profiles of relative shear along the same cross-sections (b)



(a)

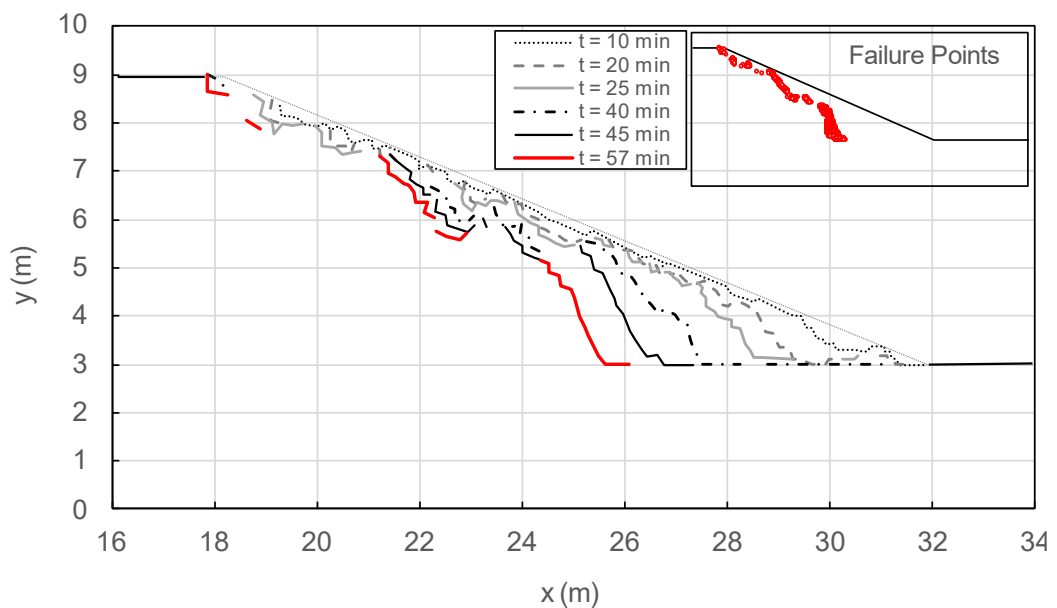


(b)

Figure 5-73: Selected points along the slope (a). Stress paths in p' - q plane for the selected soil elements D, E (b)

Stage 4 – Breach Formation

Eventually, the failure front cuts through the crest leading to breach formation considered as the final step of the breaching model. These are shown in Figure 5-74. It can be concluded from Figure 5-74a that, even if the two mechanisms of surface erosion and headcutting are co-existing during the entire duration of the overflow simulated, breach formation is predominantly caused by surface erosion. Indeed, the failure front propagation towards the crest is due to the continuous removal of soil layers from the downstream surface until it breaks through the crest. Meanwhile, the headcut remains confined around the toe area. This is not fully developed along the overall embankment height; therefore, it can be considered as a secondary process that is not directly responsible for breach formation.

57 minutes overflow

(a)

Field test #2 – 12:23 – 40 minutes from the test start – Breach Formation Progression (view from downstream right bank)



(b)

Field test #3 – 13:58 – 117 minutes from the test start – Erosion through upstream face (view from immediately downstream right bank)



(c)

Figure 5-74: Breach formation in the coarse-grained embankment according to the suction-based model (a), IMPACT Field Test #2 and IMPACT Field Test #3.

This process is better highlighted in Figure 5-75 where the combination of surface

erosion and headcutting can be more clearly visualised.

IMPACT Field Test #2 shows breach formation mainly via headcut mechanism as inferred by the authors. It must be said that, even if the process is dominated by headcutting in this case, it is much faster than what is typically observed in fine-grained materials.

Indeed, the embankment behaviour is dictated by the frozen conditions of the soil, rather than its nature. Breach formation occurs rapidly as consequence of a single headcut developed along the full embankment height and propagating backwards in a ‘rigid’ manner. This is not generally observed in coarse-grained soils, where the headcut process tends to evolve gradually elongating the duration of breach formation and growth.

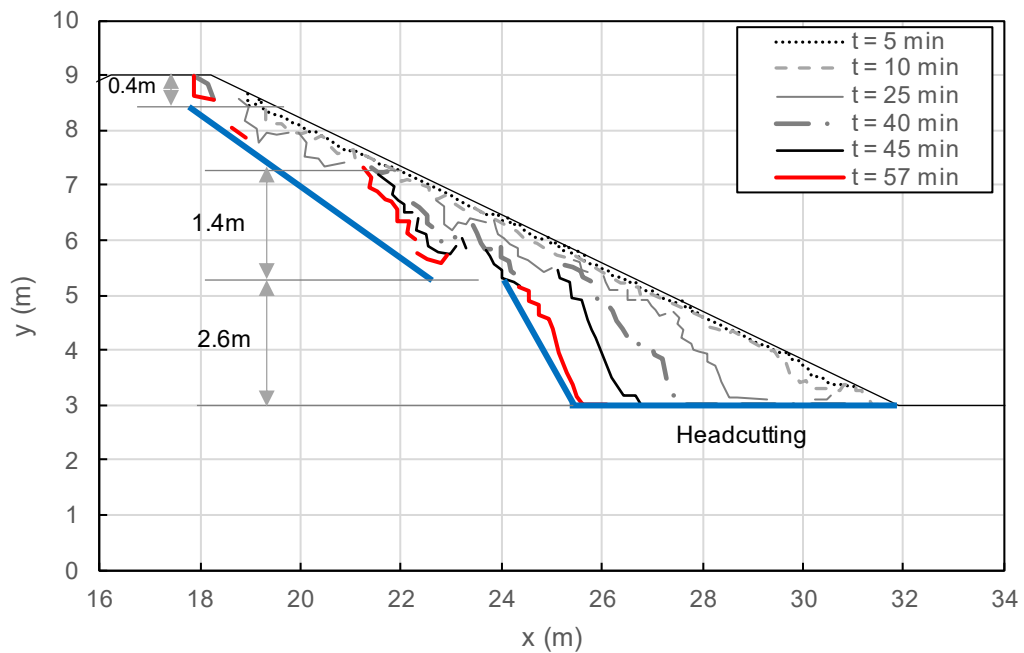


Figure 5-75: Breach Formation according to the suction-based breaching model after 57 min of overflow.

These observations are also confirmed by the Figure 5-76. Here, the vertical sides of the breach profile and the presence of overhanging material at the crest demonstrate the exceptional characteristic of this test due to the extreme weather condition. In a normal situation, the same coarse-grained material would have not been able to sustain those vertical cuts. Also, these aspects are very rarely observed in coarse-grained

embankment. This is the reason why the field test #3 is considered more representative of the behaviour of coarse-grained soil than field test #2.



Figure 5-76: IMPACT Field Test #2 breach formation and growth, highlighting the vertical sides of the breach profile and overhanging material at the crest level.

Figure 5-74c, related to field test #3 shows the moment in which the failure front reaches the embankment crest, although the leading mechanism for breach formation is not very clear from this photography angle. A better understanding of the physical processes involved prior to breach formation is given by the excerpts reported in Figure 5-77. These capture the embankment profile, few minutes before breach formation. The side and aerial views are both presented. This figure allows for an interesting observation. The embankment profile is essentially characterised by two zones, bounded by the line representing the top of the headcut. This can be recognised also in the aerial view as the boundary between clean water and a more turbid area towards the toe due to the sediment entrainment.

These images outline that the headcut is not developed for the entire height of the embankment and that the soil removed in the upper part of the slope seems to be

affected by surface erosion processes.

The field tests #3 seems to agree with the results of the suction-based breaching model applied to a coarse-grained embankment. However, it must be said that there are time-scale discrepancies. The breaching is triggered much more rapidly in the model than in the experiment and the difference is about 60 min. The reasons are multiple and substantial. It must be considered that the simulation assumes a hypothetical material which is not the same as the field experiment. Factors such as effects of compaction during construction are also complicated to assess and consequently modelled. Another crucial difference is that the experiment is conducted with reference to a composite embankment characterised by the presence of a moraine core which is most likely the main reason of the delay observed in the breach formation.



(a)



(b)

Figure 5-77: IMPACT field test #3 few minutes before breach formation (a) side view; (b) aerial view

The pore water pressure distribution at breach formation looks like the 45 minutes overflow plot. The results are reported for completeness in Figure 5-78.

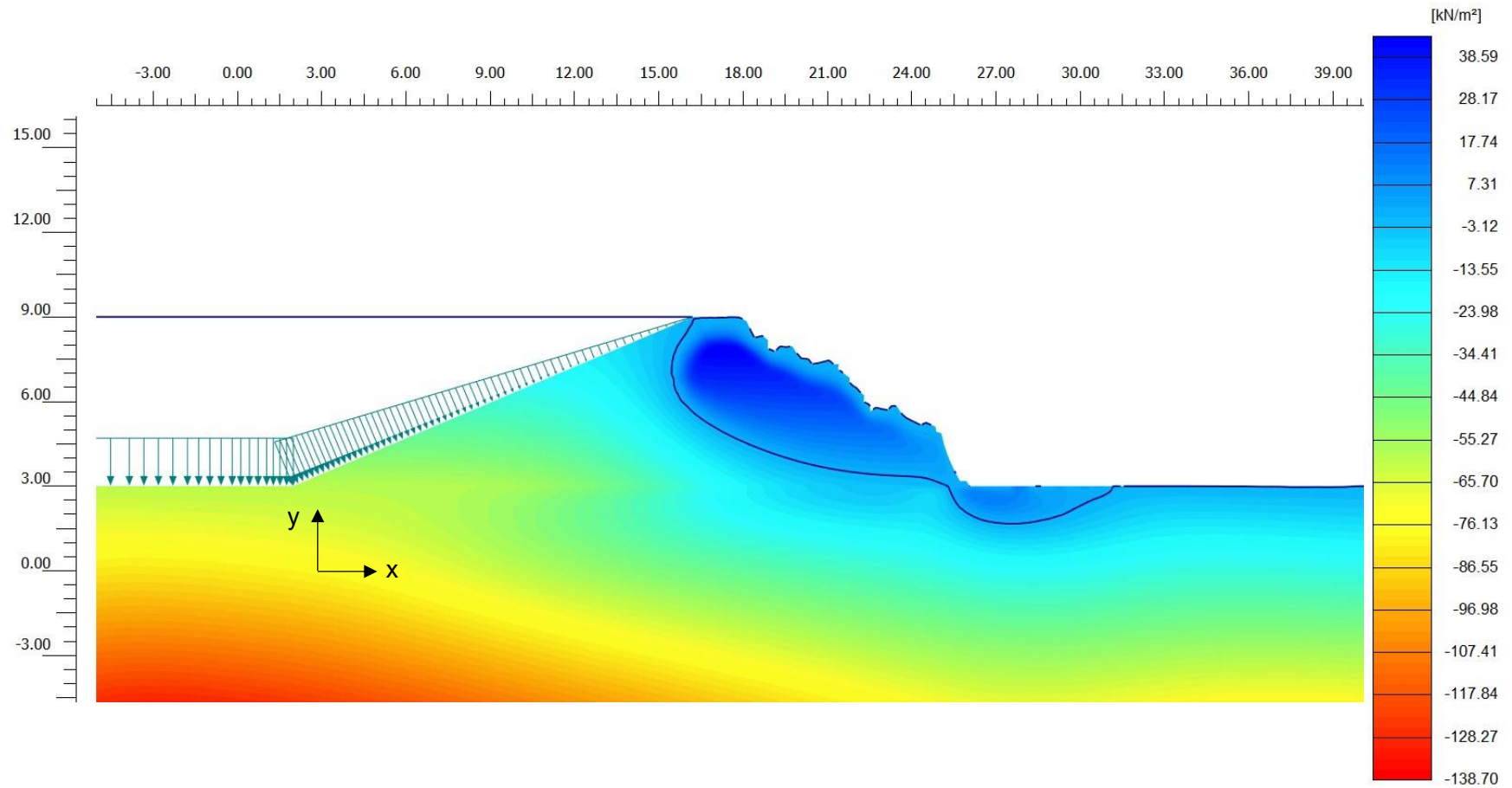


Figure 5-78: Pore water pressure distribution at breach formation phase. Suction is positive. Maximum Value is 44 kN/m^2 (i.e. dark blue contour) and minimum is -138 kN/m^2 (i.e. red contour)

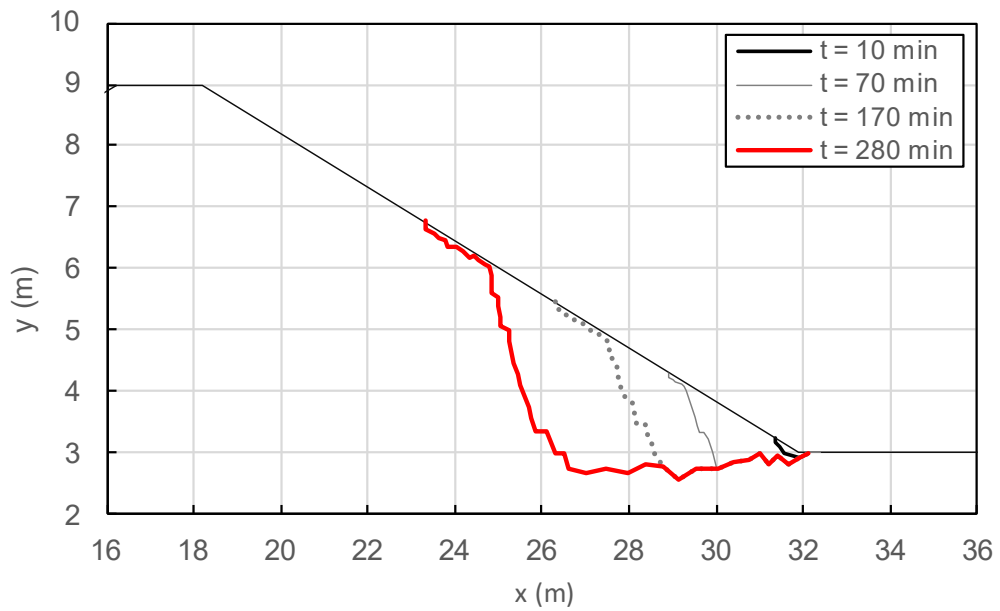
5.5 Discussion

The performance of the suction-based breaching model was assessed against its capability of reproducing qualitatively the response to overflow observed in fine-grained and coarse-grained embankments. The first aspect to emphasise is that the methodology implemented can effectively reproduce the failure mechanisms typically observed during overflow. The model can capture the main features of the hydro-mechanical behaviour of both embankments filling materials as visualised by the simulated profiles during the breach formation process. Figure 5-79 provides an example of the simulated cross-sections for the fine-grained and coarse-grained embankments, at a similar stage of breach formation. (West, Morris and Hassan, 2018)

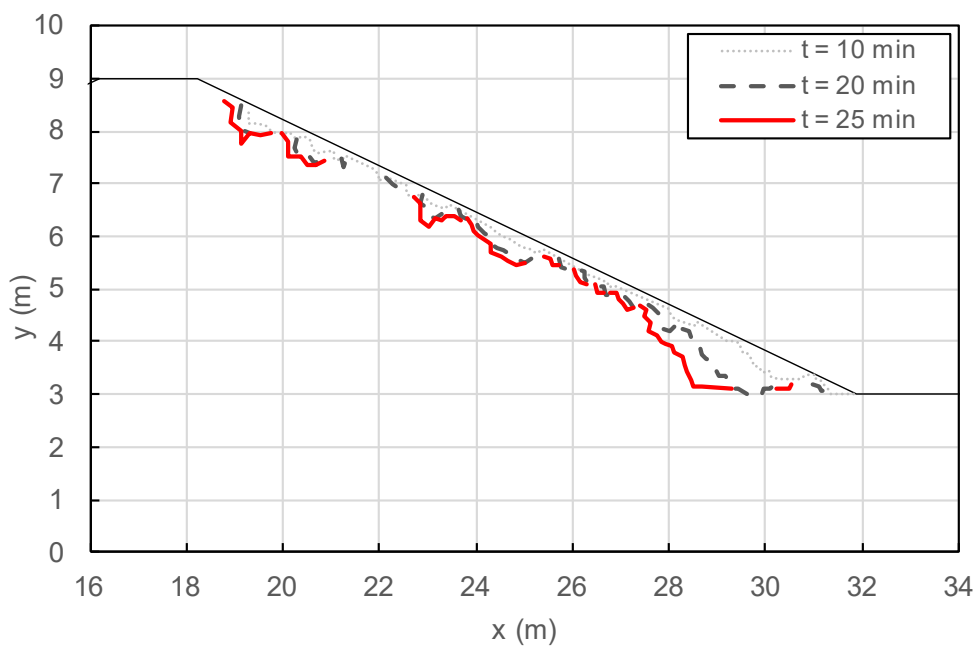
Besides the shape and geometry of the embankment centreline cross-section, another fundamental aspect is that the model can predict differences expected in terms of timing of breach formation for the two materials. The breaching process develops much more quickly in the coarse-grained model (i.e. 54 min) than in the fine-grained one (i.e. 573 min). This trend is well documented in literature and it is in line with observation from several experimental investigations (George R. Powledge *et al.*, 1989; Morris, Hassan and Vaskinn, 2007a; Morris, 2009; ASCE/EWRI Task Committee on Dam/Levee Breaching, 2011; Pickert, Weitbrecht and Bieberstein, 2011; CIRIA, 2013; Mizutani *et al.*, 2013; Zhang *et al.*, 2016). These studies pointed out two fundamental conclusions:

1. breaching of fine-grained embankments occurs generally more gradually than coarse-grained ones.
2. the diversity in the observed breaching times has been commonly interpreted as a consequence of the higher erosion-resistance characterising fine-grained soils (G. J. Hanson, K. R. Cook and S. L. Hunt, 2005; Morris, 2011; Bonelli, 2013).

These first considerations can be further developed with the comparative analysis between the results from the simulations and the IMPACT experimental data. Even if qualitative, this validation allows highlighting strengths and limitations of the suction-based breaching model.

Fine-grained embankment profile at the 50% of the breaching process

(a)

Coarse-grained embankment profile at the 44% of the breaching process

(b)

Figure 5-79: Predicted embankment profiles for fine-grained (a) and coarse-grained (b) breach formation process.

The simulated embankment profiles agree with the experimental observations. This is particularly true at the beginning of the overflow process, where it has been proven that geometry and size of the simulated profiles are very close to the field test interpretations (Figure 5-35 and Figure 5-40).

On the other hand, for the fine-grained embankment, it appears that the model tends to underestimate the propagation of the failure front. As show in Figure 5-50, the simulated headcut height is approximately 1 m lower that the experimental one. The fact that the suction-based breaching model performs better at the onset of overflow rather than at later stages, is not surprising and could have been anticipated. One of the strong assumptions adopted in this calculation is the absence of hydrodynamic forces associated to the overflow. This can be considered valid at the begging of the overflow, when the downstream slope is almost intact and the flow velocity, vortex and turbulence actions are yet low. Hydrodynamic effects are likely becoming more relevant as the downstream slope evolves into a more irregular, discontinuous, and steeper profile than the initial configuration. Under these conditions, flow velocities and turbulences are considerably higher, likely causing an increase of the “erosive” power exerted by the water overflowing. The coupling between hydrodynamic and geotechnical models is not performed in this work, hence this can be considered a limitation of the suction-based breaching model at this stage of development. However, this allowed limiting the complexity of the model, which is already quite high.

Another reason for the delay of the predicted failure compared to the field test can be attributed to the fact that in the IMPACT tests the overflow is initiated by cutting a notch in the crest. This means that the crest is lowered (by about 0.3 m) and a weakness is purposely created in the downstream profile. The presence of the notch has not been considered in the simulation.

Furthermore, it must be recalled that there the material properties considered in the simulation may not be representative of those of the real embankment, due to the scarcity of information concerning the geotechnical characterisation of the material used in the experiments. The time-related aspects of the breach formation process are strongly dependent on the hydraulic properties of the soil constituting the embankment and particularly they are governed by the hydraulic conductivity. This information,

which is essential for the implementation of the suction-based breaching model is not provided by the IMPACT dataset. Indeed, the hydraulic conductivity has been assumed based on typical values for fine-grained and coarse-grained soils. In addition, it must be considered that construction modes and particularly compaction efforts and water content adopted to build up the embankment can significantly affect properties and behaviour of the embankment materials. In engineering practice, degree of compaction and water content are design inputs to be specified for the embankment construction. These are initially assessed from laboratory tests, but obviously the final real-scale product might be different from the design values specified. Consequently, the soil properties provided in the IMPACT dataset reflect the construction techniques adopted to build the embankment test. These aspects can be hardly controlled in field and in the numerical simulation, but ultimately define the effective soil behaviour and the physic of breach formation. These are again major reasons for which the comparison between numerical simulation and field observation can be carried out only at a qualitative level.

For the coarse-grained case, the numerical model presents both progressive erosion and headcut failure modes. However, as expected, the predominant mechanism leading to breach formation occurs with mini failures at surface level, which tend to deepen the downstream slope almost at a constant angle, until the failure front reaches and lowers the crest determining the breach opening. Again, this result fits the experimental data especially from the IMPACT Field Test #3. As stressed by the IMPACT researchers, this was a particular case where a combination of surface and headcut erosion was detected. However, breach onset occurred by surface erosion as the headcut developed only partially.

This result is particularly interesting as it shows that the suction-based breaching model can predict the combination of both processes without pre-defining in advance the failure mechanisms expected. On the contrary, the vast majority of the physically-based models available require specifying the breach development as input of the calculation on the basis of engineering judgement and soil properties (West, Morris and Hassan, 2018).

It is worth stressing, once again, that the Impact Field Test #3, refers to a composite embankment configuration, with a central moraine core and rockfill

materials at both upstream and downstream slopes. As a result, the comparison with the numerical simulation is not ideal. Field Test #2 is also not considered representative because of the extreme weather condition that compromised the test results, although providing other unexpected information. For this reason, additional laboratory experiments are also presented in the following to further develop this discussion on the behaviour of homogenous coarse-grained embankment.

As part of the IMPACT project, three series of laboratory tests were undertaken in parallel to the field tests at HR Wallingford (UK) laboratory. The main aim was to reproduce the field tests and a scale factor of 1:10 was adopted between field and laboratory tests, resulting in 0.5-0.6 m high and 4 m wide test embankment.

The first series investigated the overtopping failure of embankments built from coarse-grained material. This test series was correlated with Field Test #2. A mixture of 4 different sands was used for the laboratory test embankment. The particle size distributions are shown below by the brown, black and green lines.

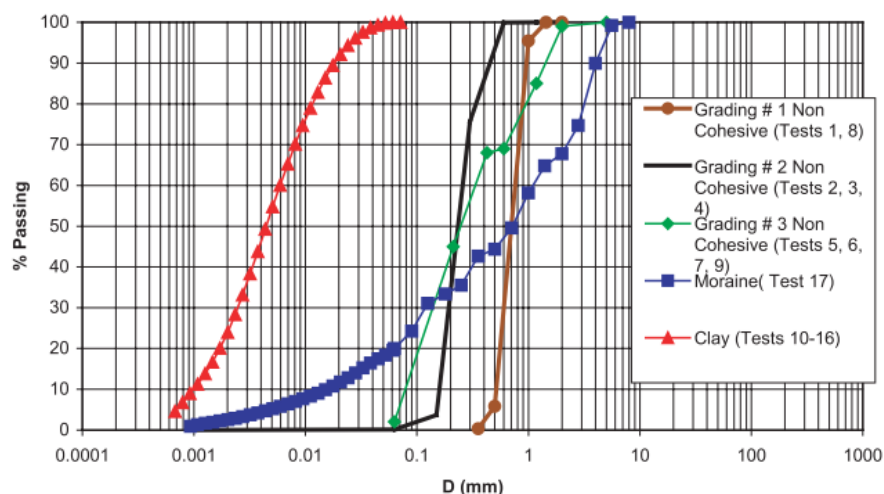
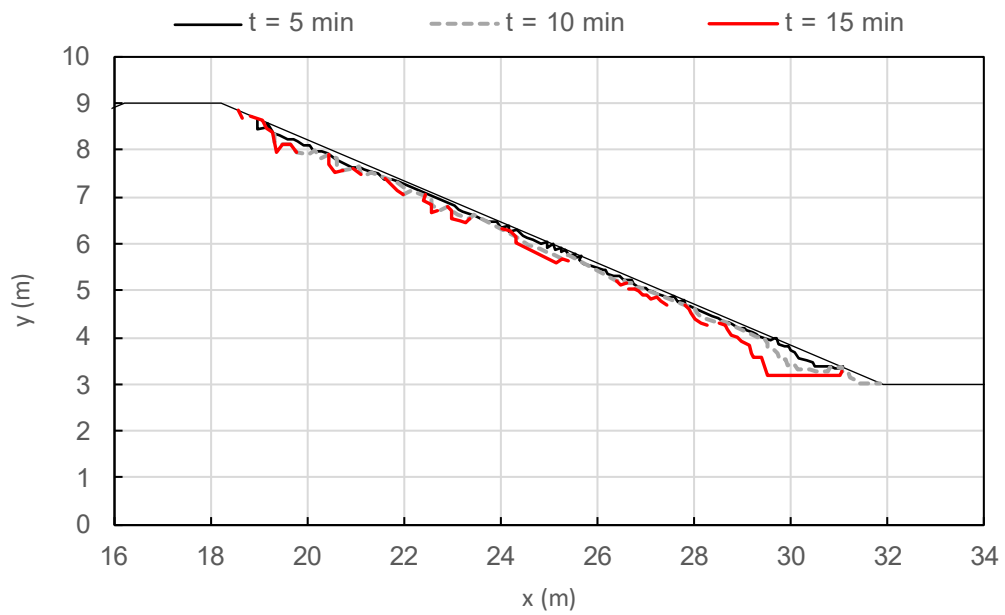


Figure 5-80: Particle size distribution adopted in the IMPACT laboratory test series (Morris, Hassan and Vaskinn, 2007a).

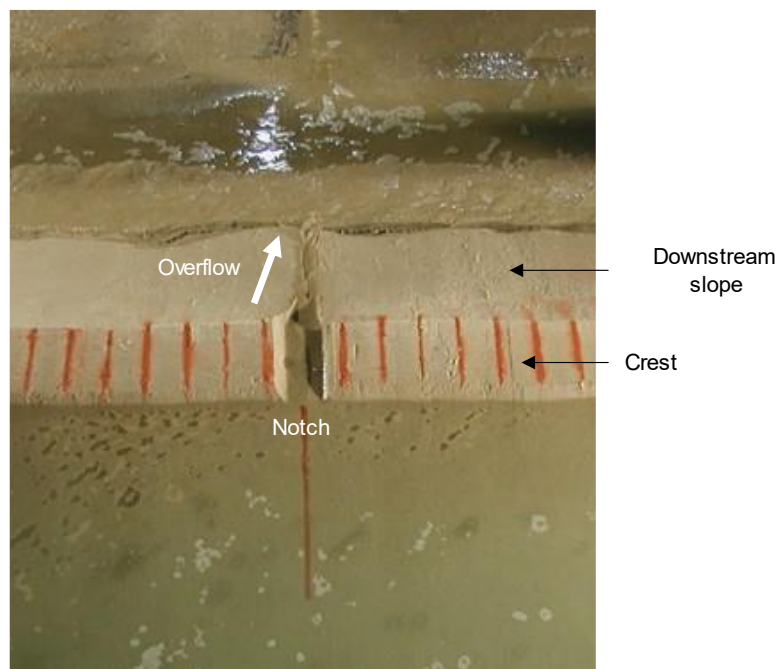
Images from the Test #3 are compared with the numerical results. Obviously, the laboratory test embankment failed very quickly in about 3.8 minutes, therefore these comparisons have to be considered qualitatively.

In the initial overflow phases the test profile consists of a narrow and superficial incision in the downstream slope with almost vertical sides. This gully tends to become

larger towards the toe area as shown in Figure 5-81b.



(a)

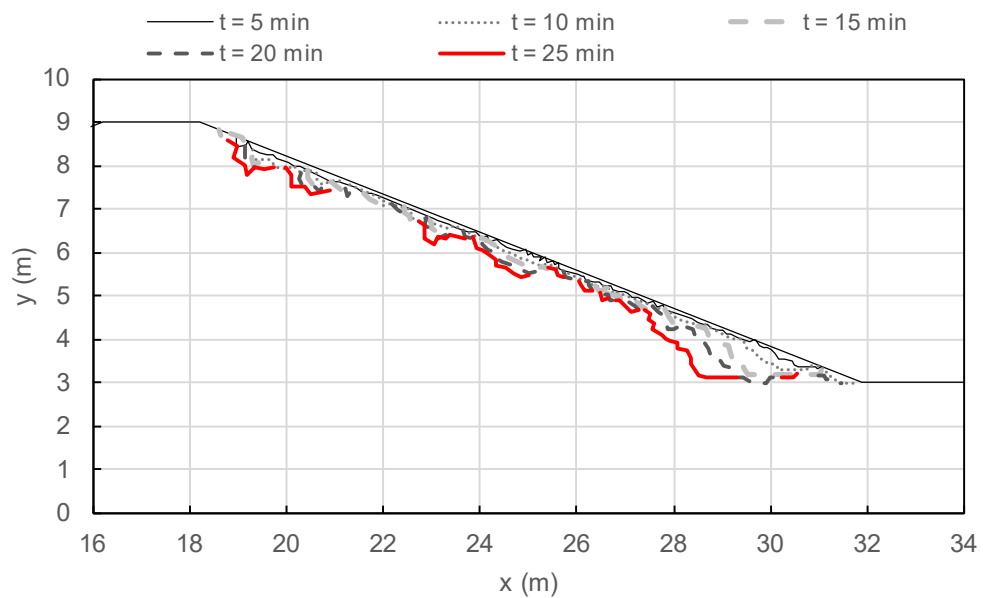


(b)

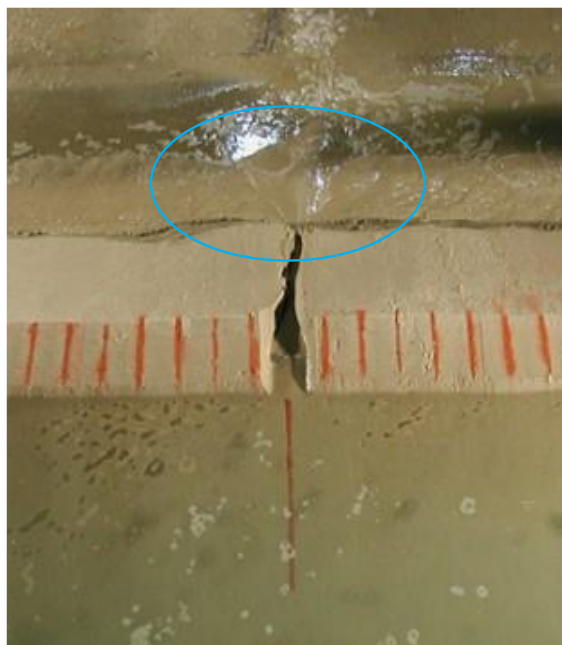
Figure 5-81: calculated profiles (a) IMPACT laboratory test (b)

The corresponding predicted cross-section represented by the red line in Figure 5-81a seems to reproduce the shape of the test profile in the upper and middle portions, while the step formed at the toe seems to be not present in the laboratory test.

The figures below show the process after 25 minutes from the start of the simulated overflow, where the initial gully incised by the water stream in the test embankment has now become deeper. The width seems unchanged, and the sides of the channel are kept vertical.



(a)

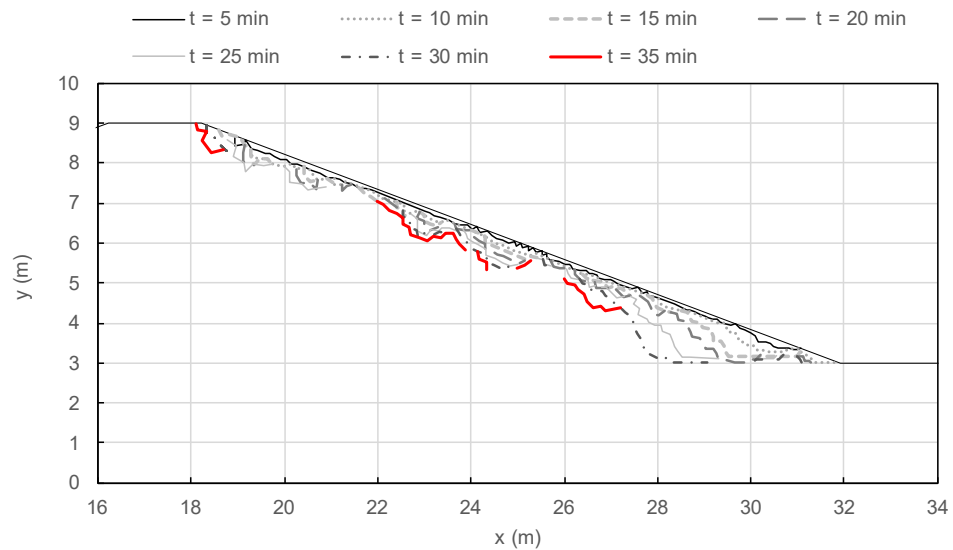


(b)

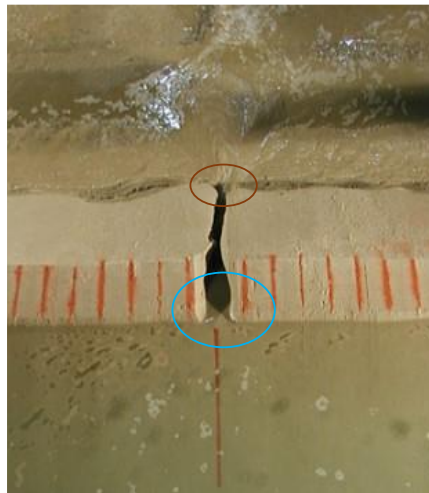
Figure 5-82: numerical results after 25 minutes of simulated overflow (a), (b) laboratory test after 15 seconds from the test start

The formation of small turbulence and the water currents at the exit of the downstream toe can be noted, while nothing is occurring in terms of soil removals. Again, the numerical model seems to predict correctly the mechanisms occurring near the crest, while it diverges at the toe.

The figure below shows the same aspects already mentioned, although it seems that more soils has been removed at the toe which presents a rounded profile.



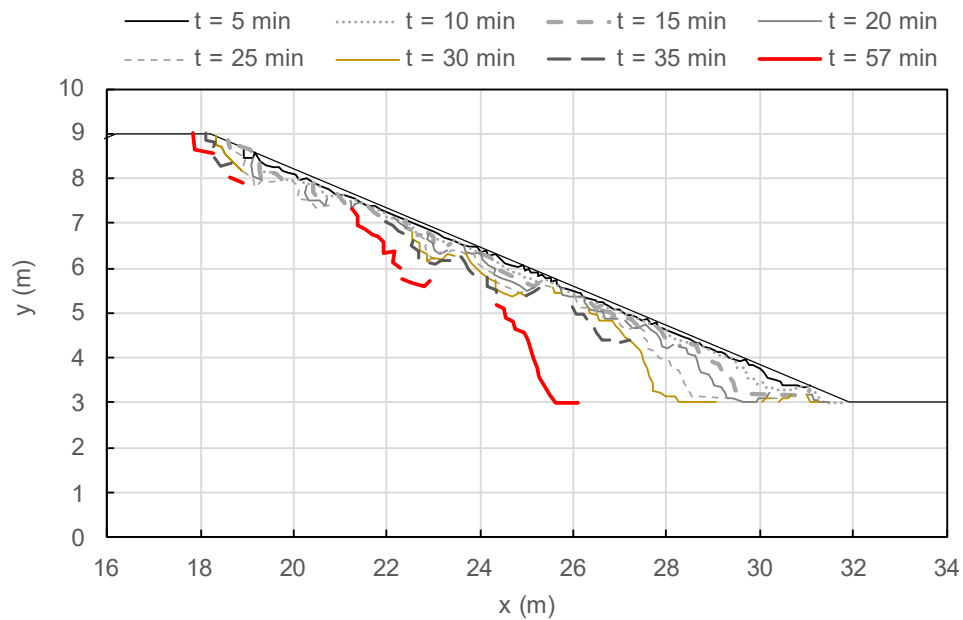
(a)



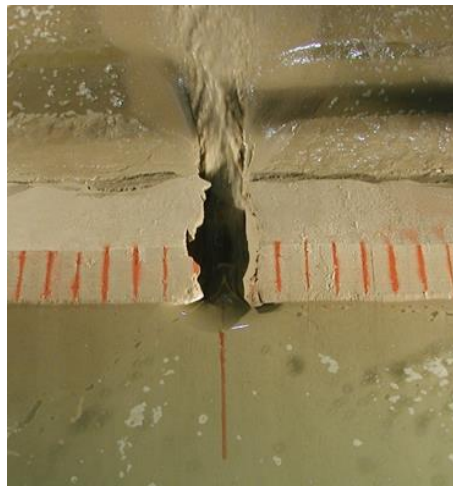
(b)

Figure 5-83: breach development after 35 minutes of simulated overflow (a) IMPACT laboratory test (b)

In addition, the simulated profile is about to cut the embankment crest and a similar condition seems to occur in the laboratory test as indicated by the water streamlines converging at the right side of the notch. Ultimately, the failure front breaks through the crest as reported in Figure 5-84.



(a)



(b)

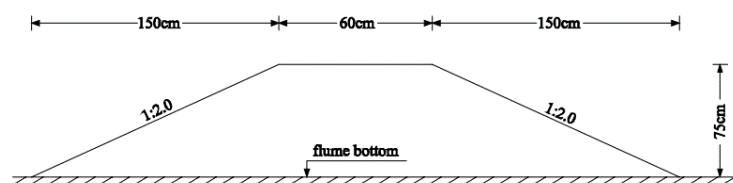
Figure 5-84: breach formation in the numerical model (a), IMPACT laboratory test (b)

A significant widening of the breach channel is occurring in the laboratory test, with frequent and rapid collapses of the lateral banks, while the overflowing water

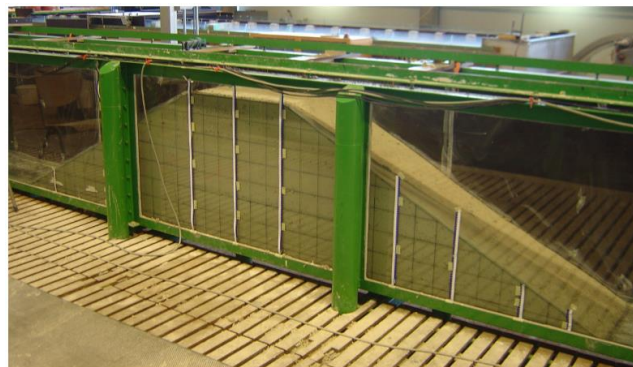
become more turbid with increasing flow velocity. Obviously, these 3D processes are not captured by the numerical model.

To finalise this discussion, results from laboratory tests performed in two straight flumes at Delft University of Technology are also presented (Zhu, 2006). The tested embankments were constructed with two types of soil material, one is pure sand, and the other are four mixtures of sand-silt-clay. For this comparison, the sand case is only considered.

The embankment geometry and a picture of the embankment constructed are shown respectively in Figure 5-85a, b.



(a)



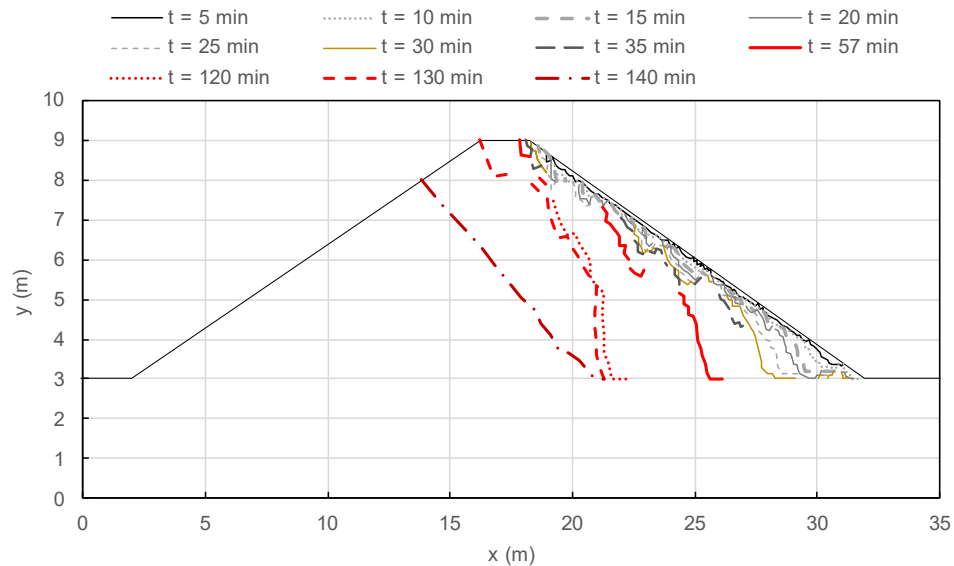
(b)

Figure 5-85: Test embankment cross-section (a) and final test configuration (b) (Zhu, 2006)

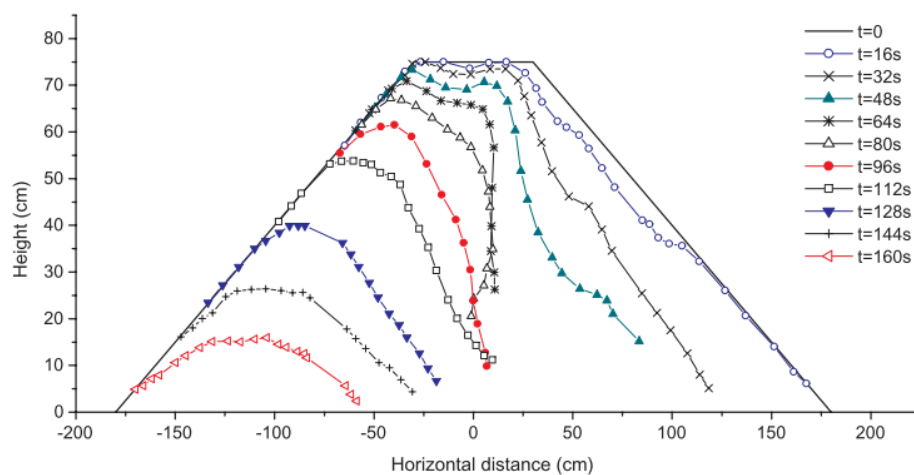
The test results confirmed that breach formation occurred more quickly in the sand case. Here, erosion was first observed to occur at the upper half of the downstream slope of the dike. Differently from the IMPACT laboratory test, headcut formation was also noted, although the backward migration of the failure front was mainly due to the surface erosion.

The figure **Error! Reference source not found.** shows the simulated profile and the laboratory test cross sections at different times of the overflow process. In this case

the simulation has been extended for a longer period after the breach formation when the failure front reaches the upstream slope. The laboratory test shows all the phases of breaching up to the point in which the test embankment fails completely.



(a)



(b)

Figure 5-86: Comparison between simulated (a) embankment profile and (b) laboratory experiment (Zhu, 2006) for homogeneous coarse-embankment

Notwithstanding the obvious differences between simulation and laboratory tests related to geometry and material properties, it can be observed that experiment and calculation provide very similar results, and this is particularly true as the breaching

process progresses.

A combination of progressive surface erosion and headcutting are both present, demonstrating once again that it is not possible to define a clear boundary between these two characteristic behaviours. In this regard, one of the main strengths of the suction-based breaching model is the capability of freely predicting the failure mechanism occurring during overflow without specifying it a priori.

5.6 Conclusions

This Chapter presented the validation of the suction-based breaching model against real scale experiments.

Although field tests on full scale embankments are the most meaningful and valuable reference for model validation, uncertainties related to ‘as built’ geometries and material properties, as well as a general lack of measured data, are all limiting factors precluding the use of field experiences for accurate quantitative assessments. As such, the capabilities of the innovative suction-based breaching model were assessed only from a qualitative standpoint.

The field tests performed as part of the European Project IMPACT were selected and an extensive overview was provided based on several published reports. The suction-based breaching model has been implemented to simulate a possible overflow scenario for two ideal homogenous embankments constructed with hypothetical ‘silty-clay’ and ‘sand’, respectively. Geometries and material properties of the IMPACT field tests have been adopted as indicative guidance for the model inputs.

The evolution of the embankment profiles resulting from the application of the numerical methodology has been compared with observations and representative images selected from three IMPACT field tests. Since the total overflow period simulated differed from the field test duration, the comparison has been conducted considering relative times, in terms of percentages of the total breach formation time.

The overall conclusion is that the simulated embankment profiles mimic satisfactorily the experimental observations in both cases. Despite the limitations of this assessment where aspects like the penetration of failure front towards the inner part of the structure and time-effects could not be adequately investigated, it was

demonstrated that the suction-based breaching model is able to reproduce the headcutting processes and progressive surface erosion mechanisms observed in the field.

It was also shown how the model can predict the expected differences in terms of timing of breach formation. In fact, the simulated time of failure for the ideal ‘silty-clay’ (i.e. 573 min) was one order of magnitude higher than the ‘sand’ (i.e. 57 min) embankment, in line with the trends typically observed experimentally.

Another key conclusion is that the suction-based breaching model simulated a mixed behaviour where progressive surface erosion and headcutting mechanisms occurred for the coarse-grained embankment. However, soil losses by exfoliation were still dominant on the overall failure process.

The coexistence of different erosion failure modes was observed in many experimental investigations, demonstrating that a sharp distinction of the failure processes based on material categories can be mistaken. At the same time, this aspect is not captured by the most physically-based models currently available. The type of erosion behaviour (headcutting or progressive surface erosion) is assumed a priori by these models rather than being an output of the simulation. On the contrary, the new proposed model predicts modes and times of failure ‘spontaneously’ from the numerical solution and without any constraint to the set of input information.

The different mode of erosion is here associated with different hydro-mechanical responses of the two categories of filling materials modelled. The hydraulic conductivity of the unsaturated soils is the most important soil property influencing the response of fine-grained and coarse-grained geomaterials to overflow. This concept and the different saturated states of various portions of the embankment during the flood event have been used to interpret headcut formation and progressive surface erosion without invoking any concept of soil erodibility.

The suction-based breaching model appears to perform better at the onset of overflow when the hydrodynamic forces are still relatively low and therefore negligible. The field tests, instead, indicate that when the downstream slope becomes steeper and the breach channel grows laterally, the discharge increases, more intense turbulent flow structures and vortices characterise the water flow, resulting in an acceleration of the failure processes. These 3D effects and the increasing destructive

power of the flood water endorsed by the presence of sediments and soil particles have not been modelled but are likely playing a key role in the late formation of the breach. These are the major limitations of the current version of the numerical method proposed.

Ultimately, the qualitative validation has demonstrated that the innovative numerical methodology developed is a promising tool for embankment breaching predictions. The Research Questions #5 and #6 have been addressed showing that it was possible to simulate overflow breaching as a chain of local and progressive mini-slope stability processes with an alternative approach to soil erosion methods. The model potential can be further improved with a 3D analysis and by coupling fluid dynamics modelling of the water overflow.

Chapter 6. Conclusion and recommendations

The objectives of this research work stemmed from the gaps in the state-of-the-art identified during the literature review that led to the following research questions:

Research Question #1: *Why the breach onset occurs in such significantly different modes (i.e. progressive surface erosion and headcutting) if the same hydraulic loads are imposed at the beginning of overflow?*

Research Question #2: *Do the hydrodynamic shear stresses exerted by the water overflow represent the only possible triggering mechanism for soil mobilisation or are there other factors that can play a relevant role?*

Research Question #3: *What are the fundamental reasons behind the development of headcutting and/or progressive-surface erosion?*

Research Question #4: *Why headcut forms in fine-grained materials but not in coarse-grained ones?*

Research Question #5: *Is it possible to interpret and model embankment breaching due to overflow with an approach alternative to erosion models and erodibility parameters?*

Research Question #6: *What if large-scale erosion processes are modelled like mini-slopes stability problems progressing with time?*

These questions were addressed as a whole by developing an innovative numerical methodology that, unlike the traditional physically - based breaching models, moves the focus on the coupled soil mechanics and hydraulic phenomena that can have a significant impact on the time-dependent processes leading to breach formation during overflow. In this way, the new approach attempts to overcome those uncertainties and discrepancies related to soil erodibility concepts and erosion modelling, which have been considered responsible for the slow progresses of classic numerical methods for breach prediction.

Definition of a new framework for embankment breaching by overflow: Research Questions #1- #3 - #4

First, a new conceptual model was developed, starting from the fundamental physical mechanisms observed during field-tests, laboratory experiments and case studies published in literature. The focus was on the most recent investigations that demonstrated indirectly the role of partial saturation.

At the onset of overflow, the soil constituting the embankment is usually in an unsaturated state. Suction and degree of saturation govern soil behaviour and it is well known that shear strength and stiffness of the soil in unsaturated states are higher than saturated conditions.

During extreme weather events various transient infiltration processes are triggered within the embankment body. Water levels increase in a few hours and the saturation front advances from the upstream side in the first instance, and from the downstream slope when the overflow is established. The soil starts to saturate and gradually loses the natural reinforcement provided by suction. The qualitative analysis of the transient water flow and the resulting state of effective stress led to the conclusion that the most vulnerable region is the toe, because here the soil tends to saturate since the early stage of the flood event. The hypothesis made was that this loss of strength of the embankment material can be considered one of the primary reasons of breach initiation at the toe.

It was highlighted the role played by the hydraulic conductivity on the development of the different ‘erosion’ behaviours of fine- and coarse-grained geomaterials. Fine-grained soils are characterised by low hydraulic conductivity and tend to hold suction for a relatively long period due to the slow changes in pore water pressures caused by the transient water flow. This is particularly true towards the crest where the initial suction is much greater than the toe and the state of effective stress is far from failure conditions. On the contrary, coarse-grained materials are much more permeable and tends to saturate more rapidly. Because the water flow process is faster, suction-induced loss of shear strength occurs almost simultaneously at both the crest and toe, resulting in a different mode of failure referred to as ‘progressive surface erosion’ in the literature.

This provides answers to Research Questions #1, #3 and #4 solely from a soil mechanics standpoint and an alternative interpretation to the occurrence of headcutting and progressive-surface erosion mode of breaching due to soil erodibility. The soil at the toe is more prone to failure because the loss of strength associated with the progressive decrease of suction, occurs more rapidly in this region rather than the crest. This is true for all the types of filling materials, but distinctive failure mechanisms are observed as result of the differences in hydraulic conductivity that soils typically present in relation to pore size and degree of saturation. This key conclusion has triggered Research Question #2.

Preliminary Proof of Concept: Research Questions #2

Having defined the framework of the suction-based breaching model, the next step was the numerical proof-of-concept this core idea. The conceptual model stands back from the commonly accepted interpretation that failure processes (i.e. headcutting and progressive-surface erosion) depend on the differences in soil erodibility of the fine-grained and coarse-grained materials and that these processes are triggered by the high erosive potential of the overflow at the embankment toe, due to the increasing flow velocity along the downstream slope. It has been assumed that these tangential hydrodynamic stresses should be of the same order of magnitude for both fine-grained and coarse-grained, at least in the initial phases of overflow.

To prove the relative importance between hydrodynamics forces and progressive loss of suction, the global stability of an ideal embankment during overflow was studied in Plaxis 2D. The factors of safety (FoS) were calculated with and without hydraulic shear stresses estimated with the computational fluid dynamic software Open Foam and applied in Plaxis 2D. The Plaxis model simulated a typical flood scenario from the increase of the water levels on the upstream slope to the overflow event on the landward side. The material considered was an ideal silty - clay. A Mohr-Coulomb constitutive model was adopted to characterise the mechanical behaviour and the van Genuchten equation was selected to describe the soil water retention properties.

The key results are:

1. The bed shear stresses calculated by solving the 3D Navier Stokes Reynolds Averaged (RANS) Equation (with the SST $k-\omega$ turbulence model) in Open Foam, were found to be in the order of magnitude of 0.3 kN/m^2 . These were validated with literature data and approximate hand calculations. The shear stresses numerically calculated were used as input loads applied along the downstream slope in Plaxis. It was observed that these values were very low compared to the typical loads encountered in geotechnical problems.
2. The global FoS and the associated failure surfaces for the two scenarios (i.e. with and without shear loads) were practically equal, demonstrating that, at least at the onset of the ‘erosion’ process, the hydraulic shear stresses associated with the entrainment forces developed at the interface water-soil, are not important destabilising factor for the global stability of the embankment.

This important conclusion provides the response to Research Question #2 and it was the starting point for further development of the numerical methodology.

On the other hand, the role of hydrodynamic forces at shallow depth and the impacts on local and superficial instabilities has been discussed. It was concluded that, because of the typical order of magnitude of these stresses compared to the effective cohesion of fine-grained soils, it is unlikely that failure at shallow depth will be triggered. Coarse-grained materials, for which effective cohesion is zero, are instead subjected to exfoliation processes at surface level, as it has been observed experimentally.

Formulation and validation of the suction-based breaching model: Research Questions #5 and #6

The heart of the new suction based breaching model is the idea that the ‘erosion mechanisms’ leading to embankment breaching (i.e. progressive surface erosion and headcutting) can be simulated as a series of mini-slope stability problems at the centimetre scale, which progressively evolve into breach formation. The hydro-mechanical behaviour of the soils forming the embankment is modelled within the common framework of unsaturated soil mechanics, without introducing erodibility

properties and erosion constitutive laws. Hydrodynamic shear stresses have not been considered in light of the results in the previous numerical analyses.

To implement this idea a failure criterion incorporating geometrical requirements and stress – strain considerations in the context of an elastic-perfectly plastic soil behaviour has been formulated. Such criterion identifies the most critical failure surface for a given time-interval of overflow.

The approach of removing unstable soil blocks delimited by the slip surface has been introduced for the first time. The potential of this idea was shown by reproducing the headcut backwards migration through the progressive removal of mini-soil blocks for different time-steps of overflow, as a sequence of local instabilities.

The procedure described in general terms has been implemented in Plaxis 2D. In the “Lego Strategy” presented, the embankment model was constructed with triangular soil elements associated with the finite element computational mesh. The algorithms for the definition of the failed soil elements and for the application of the failure criterion in Plaxis, have been discussed in detail.

A key aspect of the Lego Strategy is the calibration of the failure criterion that consists in identifying ‘failed’ elements and then removing the ‘failed’ elements that form a concave failure surface. This has been achieved by comparing the slip surfaces determined with the criterion defined against the results of the rigorous Upper Bound Limit Analysis, for the general case of a dry slope. The software Limit State: Geo based on the Upper Bound Theorem of Plasticity and on the discontinuity layout optimisation (DLO) technique was used.

The key conclusion was that triangular soil blocks can operationally be considered unstable and hence removable from the embankment body when at least 8 out of 12 stress points are ‘failure’ points (i.e. point on the Mohr-Coulomb failure envelope in a state of plastic shear strain). The condition of a minimum of 8 ‘failure’ stress points in a triangular mesh element returned the best match between the proposed approach and the Limit Analysis solution.

Finally, the model performance was assessed through a qualitative validation. The suction – based breaching model was implemented in Plaxis 2D to simulate the breaching of two homogeneous embankments, constructed with an ideal silty – clay

and an ideal sand. The progressive evolution of the embankment profiles up to the breach formation stage (i.e. the failure front reaches the embankment crest) were compared with photos and observations from three field tests conducted as part of the IMPACT project. Because of the particular frozen condition, Field Test 2# (i.e. gravelly embankment) was considered to be not fully representative of the behaviour of a coarse-grained embankment. Therefore, evidence from Field Test #3 on a composite geo-structure and laboratory experiments were additionally used to assess the capabilities of the suction-based model. The main conclusions were:

1. The simulated embankment profiles agree qualitatively with the experimental observations for both fine-grained and coarse-grained geomaterials. The simulated backward migration of the failure front was found to be in good agreement with the experimental evidence. However, it should be noted that the overflowing water covered the base of the slope in the field experiments making the penetration of the failure front difficult to observe from the photos.
2. For the coarse-grained case, the predicted time of breach formation was 57 min while it was 50 min and 95 min in Field Test #2 and Field Test #3, respectively.
3. For the ideal silty - clay the simulation overestimated the time of breach formation for the headcutting mechanism. In fact, the model predicted 573 min, against the 107 min of the field test. Several reasons were considered to explain this discrepancy:

3.1. A notch was cut through the embankment crest to initiate the overflow during the experiment. This was not considered in the simulation. The presence of the notch could have reduced the time of failure because it lowered the embankment by 0.3m affecting the rate at which the failure front arrived at the crest.

3.2. Differences are expected between the hydraulic conductivity of the material forming the test embankment and the one used in the numerical simulation, which was based on educated guess due to lack of information from the IMPACT project reports.

3.3. The suction-based breaching model is not yet coupled with hydrodynamics calculations that, although negligible at the onset, may become important when the embankment profile presents more complex configurations. In this case, intense turbulent flow structures and vortices have been observed on site resulting in an acceleration of the failure processes. These effects have not been considered.

3.4. Instability processes responsible for the lateral growth of the breach have not been simulated because the model is two-dimensional. However, the three-dimensional effects are not negligible once that the breach channel is formed at the later stage of the breaching process.

For these reasons, the comparison between numerical simulation and field observations should be carried out only qualitatively

4. The suction-based breaching model effectively reproduced the modes of failure observed in the real case scenarios. The new approach predicted the combined headcutting/surface erosion mechanism for the coarse-grained embankment, which has been observed repeatedly in laboratory and field experiments. The model appears to capture well the fundamental features that differentiate the hydro-mechanical behaviour of both fine- and coarse-grained materials. More specifically:

4.2. The simulated downstream slope profiles reflected the characteristic aspects of headcutting and surface erosion in terms of shapes and sizes.

4.3. The time of breach formation predicted was found to be considerably higher for the silty-clay than for the sandy embankment. This trend is in agreement with both laboratory and in situ experimental results.

5. The major strength of the suction-based methodology is that, unlike traditional methods, breach formation is predicted without pre-defining the erosion mechanisms either headcutting or surface erosion. Breach profiles, modes and times of failure are the result of the modelling of hydro-mechanical coupled

processes in the framework of unsaturated soil mechanics.

6. Due to his inherent flexibility, the suction – based breaching models can be easily applied to a variety of realistic scenarios, including heterogenous and more complex structures. Composite embankments as well as additional elements like flood walls on the crest, surface revetment along the slope, toe drains and so on, can be modelled and analysed in Plaxis 2D. Furthermore, layered embankments and more complex stratigraphy can be represented.

Most importantly, the role of vegetation that is capturing the attention of many researcher and Assets Managers like the Environment Agency, can be also incorporated. It is well known, in fact, that certain species of plants can improve the erosion resistance of the most superficial soil layers, under both hydraulic and mechanical perspectives. Hydraulically, because vegetation tends to hold suction in the surrounding soil, simply because of the water required for their life. Mechanically, through the complex system of roots that can absorb stresses and prevent shallow soil movements. Nevertheless, not all plant species are beneficial. For example, shrubs or trees characterised by large roots will be very dangerous during extreme weather events. It has been observed, indeed, that when this type of vegetation is removed by strong atmospheric agents, the large roots transported will leave big voids or spaces in the embankment structure. These, therefore, constitute weak planes in the soil matrix and preferential paths for water infiltration. The suction based breaching model, can incorporate the effects of vegetation for example by adjusting the soil hydraulic conductivity functions to reflect the high permeability conditions.

In conclusion, the suction-based breaching model was proven to be a promising predictive tool for embankment breaching due to overflow. For the first time the large-scale erosion processes were simulated as mini-slopes failures evolving with time.

Recommendations and future works

The strongest limitation of the suction – based methodology developed is that the external water flow was never modelled. It was demonstrated that this is acceptable at

the onset of overflow for the global downstream slope stability. However, for coarse-grained materials and when the embankment profile evolves towards stepped configurations or steeper slopes, the turbulences created by the water overflow and the associated hydrodynamic forces may become significant and accelerate the breaching processes.

The next step would be an appropriate investigation of these aspects with a computational fluid dynamic analysis of the water flow (for example in Open Foam) for progressive embankment configurations at given time-steps of overflow.

In this way the coupling of geotechnical and hydrodynamics models could be achieved, providing a more realistic multidisciplinary approach for embankment breaching during overflow.

In addition, the assessment of the performance of the suction based breaching model can be improved as follows:

- Sensitivity analysis on mesh coarseness and element size
- Hydrologic models for the assessment of the time of filling phase
- Calibration of soil water retention curve and hydraulic conductivity function adopted in the numerical simulation against properties of ‘real’ filling materials constituting the embankment
- More robust and consistent quantitative validation with real scale overflow experiments
- Extension to more complex structures like composite embankments

To complete these tasks a comprehensive experimental programme should be undertaken on real scale geo-structures with an in-depth hydro-mechanical characterisation of the embankment materials; field or mock-up laboratory tests should be accompanied by measurements of pore water pressures and volumetric water content within the embankment and near-bed flow fields; and measurement of the embankment morphology evolution during the overflow.

References

Al-Riffai, M. *et al.* (2009) 'Influence of compaction and toe-drains on the formation of breach channels of overtopped earth embankments: An experimental study', in *33rd IAHR World Congress*. Vancouver.

Al-Riffai, M. (2014) *Experimental Study of Breach Mechanics in Overtopped Noncohesive Earthen Embankments*. PhD Thesis. PhD Thesis. University of Ottawa, Canada.

Al-Riffai, M. and Nistor, I. (2010) 'Impact and analysis of geotechnical processes on earthfill dam breaching', *Natural Hazards*, 55(1), pp. 15–27. Available at: <https://doi.org/10.1007/s11069-010-9586-6>.

Al-Riffai, M. and Nistor, I. (2013) 'Influence of Seepage on the Erodibility of Overtopped Noncohesive Embankments', in *21st Canadian Hydrotechnical Conference*. Alberta. Available at: <https://doi.org/10.13140/2.1.3402.9441>.

ASCE/EWRI Task Committee on Dam/Levee Breaching (2011) 'Earthen Embankment Breaching', *Journal of Hydraulic Engineering*, 137(12), pp. 1549–1564. Available at: [https://doi.org/10.1061/\(ASCE\)HY.1943-7900.0000498](https://doi.org/10.1061/(ASCE)HY.1943-7900.0000498).

Ashgari Tabrizi, A. *et al.* (2017) 'Effects of compaction on embankment breach due to overtopping', *Journal of Hydraulic Research*, 55(2), pp. 236–247. Available at: <https://doi.org/10.1080/00221686.2016.1238014>.

Bahri, P.S., Osouli, A. and Stendback, E. (2016) 'Prediction of scour in overtopped floodwalls using JET and EFA', in *ICSE 2016 (8th International Conference on Scour and Erosion)*. Oxford, pp. 687–694.

Bereta, G. *et al.* (2020) 'Experimental study of cohesive embankment dam breach formation due to overtopping', *Periodica Polytechnica Civil Engineering*, 64(1), pp. 198–211. Available at: <https://doi.org/10.3311/PPci.14565>.

Bishop, A.W. and Blight, G.E. (1963) 'Some aspects of effective stress in saturated and partly saturated soils', *Geotechnique*, 13(3), pp. 177–197. Available at: <https://doi.org/10.1680/geot.1963.13.3.177>.

le Bissonnais, Y. (1996) 'Aggregate stability and assessment of soil crustability and erodibility: I. Theory and methodology', *European Journal of Soil Science*, 47, pp. 425–437.

Bloomquist, D. *et al.* (2012) 'The rotating erosion testing apparatus (RETA): A laboratory device for measuring erosion rates versus shear stresses of rock and cohesive materials', *Geotechnical Testing Journal*, 35(4), pp. 1–8. Available at: <https://doi.org/10.1520/GTJ104221>.

Bonelli, S. (2013) *Erosion of Geomaterials*. Available at: <https://doi.org/10.1002/9781118561737>.

Bonelli, S. (2019) 'The Hole Erosion Test. State of the Art, State of Practise and Open Questions'. EWG-IE 27th Annual Meeting European Working Group on Internal Erosion in Embankment Dam, Levees and their Foundations, p. 14.

Borghesi, S.M., Jalili, M.R. and Ghodsian, M. (1999) 'Discharge Coefficient for Sharp-Crested Side Weir in Subcritical Flow', *Journal of Hydraulic Engineering*, 125(10), pp. 1051–1056. Available at: [https://doi.org/10.1061/\(asce\)0733-9429\(1999\)125:10\(1051\)](https://doi.org/10.1061/(asce)0733-9429(1999)125:10(1051)).

Briaud, J. (2008) 'Case histories in soil and rock erosion: woodrow wilson bridge, Brazos River Meander, Normandy Cliffs, and New Orleans Levees', *Journal of Geotechnical and Geoenvironmental ...*, 134(October), pp. 1425–1447. Available at: [https://doi.org/10.1061/\(ASCE\)1090-0241\(2008\)134:10\(1425\)](https://doi.org/10.1061/(ASCE)1090-0241(2008)134:10(1425)).

Briaud, J.L. *et al.* (2001) 'Erosion Function Apparatus for Scour Rate Predictions', *Journal of Geotechnical and Geoenvironmental Engineering*, 127(2), pp. 105–113. Available at: [https://doi.org/10.1061/\(ASCE\)1090-0241\(2001\)127:2\(105\)](https://doi.org/10.1061/(ASCE)1090-0241(2001)127:2(105)).

Briaud, J.-L. *et al.* (2008) 'Levee Erosion by Overtopping in New Orleans during the Katrina Hurricane', *Journal of Geotechnical and Geoenvironmental Engineering*, 134(5), pp. 618–632. Available at: [https://doi.org/10.1061/\(ASCE\)1090-0241\(2008\)134:5\(618\)](https://doi.org/10.1061/(ASCE)1090-0241(2008)134:5(618)).

Briaud, J.-L. (2013) 'Erosion of Soils and Scour Problems', in Inc. John Wiley & Sons (ed.) *Geotechnical Engineering*. Hoboken, NJ, USA: John Wiley & Sons, Inc., pp. 823–871. Available at: <https://doi.org/10.1002/9781118686195.ch23>.

Brinkgreve, R.B.J. *et al.* (2018) 'Material Models Manual', *Plaxis Build 9462* [Preprint]. Delft: Plaxis bv.

Brinkgreve, R.B.J., Kumarswamy, S. and Swolfs, W.M. (2017) 'Plaxis 2D Reference Manual', *Plaxis bv* [Preprint]. Delft, The Netherlands: Plaxis bv.

Chaudhry, M.H. (2008) *Open-Channel Flow*. Second Edi. Edited by Springer. Boston, MA: Springer US. Available at: <https://doi.org/10.1007/978-0-387-68648-6>.

CIRIA (2013) *The International Levee Handbook. CIRIA C731*. London: CIRIA.

Coleman, S.E., Andrews, D.P. and Webby, M.G. (2002) 'Overtopping Breaching of Noncohesive Homogeneous Embankments', *Journal of Hydraulic Engineering*, 128(9), pp. 829–838. Available at: [https://doi.org/10.1061/\(asce\)0733-9429\(2002\)128:9\(829\)](https://doi.org/10.1061/(asce)0733-9429(2002)128:9(829)).

Costa, J.E. (1985) *Floods from dam failures. Open-File Report 85-560*. Denver, Colorado.

Couper, P.R. and Maddock, I.P. (2001) 'Subaerial river bank erosion processes and their interaction with other bank erosion mechanisms on the River Arrow, Warwickshire, UK', *Earth Surface Processes and Landforms*, 26(6), pp. 631–646. Available at: <https://doi.org/10.1002/esp.212>.

Delestre, O. *et al.* (2017) 'FullSWOF: Full Shallow-Water equations for Overland Flow', *The Journal of Open Source Software*, 2(20), p. 448. Available at: <https://doi.org/10.21105/joss.00448>.

D'Onza, F. *et al.* (2016) 'Effect of in situ and laboratory compaction on the retention behaviour of a clayey soil', in P. Delage *et al.* (eds) *E3S Web of Conferences*. Paris, p. 11003. Available at: <https://doi.org/10.1051/e3sconf/20160911003>.

Dyer, M. (2004) 'Performance of flood embankments in England and Wales', *Water Management*, 157(4), pp. 177–186. Available at: <https://doi.org/10.1680/wama.157.4.177.56738>.

Dyer, M., Utili, S. and Zielinski, M. (2007) *The Influence of Dessication Fine Fissuring on the Stability of Flood Embankments*.

Elkholy, M. *et al.* (2015) 'Effect of soil composition on piping erosion of earthen levees', *Journal of Hydraulic Research*, 1686(November), pp. 1–10. Available at: <https://doi.org/10.1080/00221686.2015.1026951>.

EMBREA Lite - HR Wallingford (2022) *EMBREA Lite*. Available at: <https://www.dambreach.org/tools/members/embrea-members#> (Accessed: 23 October 2022).

Environment Agency (2014) *Humber defence condition and fragility An investigation into the performance of the Humber flood embankments*.

Feliciano Cestero, J.A., Imran, J. and Chaudhry, M.H. (2015) 'Experimental Investigation of the Effects of Soil Properties on Levee Breach by Overtopping', *Journal of Hydraulic Engineering*, 141(4), p. 04014085. Available at: [https://doi.org/10.1061/\(ASCE\)HY.1943-7900.0000964](https://doi.org/10.1061/(ASCE)HY.1943-7900.0000964).

Fell, R. *et al.* (2003) 'Time for Development of Internal Erosion and Piping in Embankment Dams', *Journal of Geotechnical and Geoenvironmental Engineering*, 129(4), pp. 307–314. Available at: [https://doi.org/10.1061/\(ASCE\)1090-0241\(2003\)129:4\(307\)](https://doi.org/10.1061/(ASCE)1090-0241(2003)129:4(307)).

Fleureau, J.M. *et al.* (2002) 'Aspects of the behaviour of compacted clayey soils on drying and wetting paths', *Canadian Geotechnical Journal*, 39(6), pp. 1341–1357. Available at: <https://doi.org/10.1139/t02-100>.

Foster, M., Fell, R. and Spannagle, M. (2000) 'The statistics of embankment dam failures and accidents', *Canadian Geotechnical Journal*, 37(5), pp. 1000–1024. Available at: <https://doi.org/10.1139/t00-030>.

Fritzi, H.M. and Hager, W.H. (1998) 'HYDRAULICS OF EMBANKMENT WEIRS By Hermann M. Fritzi and Willi H. Hager,z Fellow, ASCE', *Manager*, 124(September), pp. 963–971.

G. J. Hanson, K. R. Cook and S. L. Britton (2003) 'Observed Erosion Processes During Embankment Overtopping Tests', in *2003 ASAE Annual International Meeting. Las Vegas, Nevada, USA 27- 30 July 2003*. St. Joseph, MI: American Society of Agricultural and Biological Engineers, p. Paper Number: 032066. Available at: <https://doi.org/10.13031/2013.13767>.

G. J. Hanson, K. R. Cook and S. L. Hunt (2005) 'Physical modeling of overtopping erosion and breach formation of cohesive embankments', *Transactions of the American Society of Agricultural Engineers*, 48(5), pp. 1783–1794. Available at: <https://doi.org/10.13031/2013.20012>.

Galavi, V. (2010) *Groundwater flow, fully coupled flow deformation and undrained analyses in PLAXIS 2D and 3D, Plaxis Internal Research Report*. Delft, The Netherlands.

Gaskin, S.J. *et al.* (2003) 'Erosion of undisturbed clay samples from the banks of

the St. Lawrence River’, *Canadian Journal of Civil Engineering*, 30(3), pp. 585–595.
Available at: <https://doi.org/10.1139/103-008>.

Gilbert, P.A. and Miller, P.S. (1991) *A Study of Embankment Performance During Overtopping, Technical Report GL-91-23*. Vicksburg, Mississippi.

Greenshields, C.J. (2021) *OpenFOAM, User Guide version 9*.

Hahn, W., Hanson, G.J. and Cook, K.R. (2000) ‘Breach Morphology Observations of Embankment Overtopping Tests’, in *Proc. Joint Conference of Water Resources Eng., Planning, and Management*. Reston, VA: American Society of Civil Engineers, pp. 1–10. Available at: [https://doi.org/10.1061/40517\(2000\)411](https://doi.org/10.1061/40517(2000)411).

Hanson, G.J. (1991) ‘Development of a Jet Index To Characterize Erosion Resistance of Soils in Earthen Spillways’, *Transactions of the ASAE*, 34(5), pp. 2015–2020. Available at: <https://doi.org/10.13031/2013.31831>.

Hanson, G.J. *et al.* (2011) ‘Development and Characterization of Soil Material Parameters for Embankment Breach’, *Applied Engineering in Agriculture*, 27(4), pp. 587–596.

Hanson, G.J. and Cook, K.R. (2004) ‘Apparatus, Test procedures, and Analytical Methods to Measure Soil Erodibility In Situ’, *Applied Engineering in Agriculture*, 20(4), pp. 455–462.

Hanson, G.J. and Hunt, S.L. (2007) ‘Lessons learned using laboratory JET method to measure soil erodibility of compacted soils’, *Applied Engineering in Agriculture*, 23(3), pp. 305–312.

Hanson, G.J., Robinson, K.M. and Cook, K.R. (2001) ‘Prediction of Headcut Migration Using a Deterministic Approach’, *Transaction of ASAE*, 44(3), pp. 525–531.

Hanson, G.J. and Simon, A. (2001) ‘Erodibility of cohesive streambeds in the loess area of the midwestern USA’, *HYDROLOGICAL PROCESSES Hydrol. Process*, 15, pp. 23–38.

Hassan, M. and Morris, M.W. (2008) *IMPACT Project Field Tests Data Analysis, FLOODsite Report, T04-08-04*.

Hirsch Charles (2007) *Numerical Computation of Internal and External Flows. Volume 1, Fundamentals of Numerical Discretization*. Second Edi. John Wiley & Sons, Ltd.

Hooke, J.M. (1979) 'An analysis of the processes of river bank erosion', *Journal of Hydrology*, 42, pp. 39–62. Available at: [https://doi.org/10.1016/0022-1694\(79\)90005-2](https://doi.org/10.1016/0022-1694(79)90005-2).

Hughes, S.A. *et al.* (2011) *Physical Testing and Hydraulic Simulation of Wave Overtopping of Earthen Levees. SERRI Report 70015-009*. Oak Ridge, Tennessee.

Hughes, S.A. and Nadal, N.C. (2009) 'Laboratory study of combined wave overtopping and storm surge overflow of a levee', *Coastal Engineering*, 56(3), pp. 244–259. Available at: <https://doi.org/10.1016/j.coastaleng.2008.09.005>.

Hughes, S.A., Shaw, J.M. and Howard, I.L. (2012) 'Earthen Levee Shear Stress Estimates for Combined Wave Overtopping and Surge Overflow', *Journal of Waterway, Port, Coastal, and Ocean Engineering*, 138(3), pp. 267–273. Available at: [https://doi.org/10.1061/\(ASCE\)WW.1943-5460.0000135](https://doi.org/10.1061/(ASCE)WW.1943-5460.0000135).

Hunt, S.L. *et al.* (2005) 'Breach Widening Observations From Earthen Embankment Tests', *Transactions of the ASAE, American Society of Agricultural Engineers*, 48(3), pp. 1115–1120.

Julian, J.P. and Torres, R. (2006) 'Hydraulic erosion of cohesive riverbanks', *Geomorphology*, 76, pp. 193–206. Available at: <https://doi.org/10.1016/j.geomorph.2005.11.003>.

Kimiaghalam, N., Clark, S.P. and Ahmari, H. (2016) 'An experimental study on the effects of physical, mechanical, and electrochemical properties of natural cohesive soils on critical shear stress and erosion rate', *International Journal of Sediment Research*, 31(1), pp. 1–15. Available at: <https://doi.org/10.1016/j.ijsrc.2015.01.001>.

Knapen A. *et al.* (2007) 'Resistance of soils to concentrated flow erosion: A review', *Earth-Science Reviews*, 80, pp. 75–109. Available at: <https://doi.org/10.1016/j.earscirev.2006.08.001>.

Korchagova, V. (2017) 'How to use free-surface flows. OpenFoam Training Presentation.'

Kreibich, H. *et al.* (2009) 'Is flow velocity a significant parameter in flood damage modelling?', *Natural Hazards and Earth System Science*, 9(5), pp. 1679–1692. Available at: <https://doi.org/10.5194/nhess-9-1679-2009>.

Launder, B.E. and Spalding, D.B. (1974) 'The Numerical Computation of Turbulent Flow', *Computer Methods in Applied Mechanics and Engineering*, 3, pp.

269–289.

LimiteState Ltd (2016) ‘LimitState: GEO Manual’. Sheffield.

Liu, F. (2017) ‘A Thorough Description Of How Wall Functions Are Implemented In OpenFOAM’, in H. Nilsson (ed.) *In Proceedings of CFD with OpenSource Software*, pp. 1–30. Available at: http://www.tfd.chalmers.se/~hani/kurser/OS_CFD_2016.

Lopes, P. (2013) *Free-surface flow interface and air-entrainment modelling using OpenFOAM*. Available at: <https://estudogeral.sib.uc.pt/handle/10316/24534>.

Luo, Y. *et al.* (2014) ‘Breaking mode of cohesive homogeneous earth-rock-fill dam by overtopping flow’, *Natural Hazards*, 74(2), pp. 527–540. Available at: <https://doi.org/10.1007/s11069-014-1202-8>.

Mehta, A.J. (1986) XV. *Characterization of cohesive sediment properties and transport processes in estuaries, Estuarine Cohesive Sediment Dynamics*. Edited by A.J. Mehta. New York, NY: Springer New York (Lecture Notes on Coastal and Estuarine Studies). Available at: <https://doi.org/10.1007/978-1-4612-4936-8>.

Mehta, A.J. *et al.* (1989) ‘Cohesive Sediment Transport. I: Process Description’, *Journal of Hydraulic Engineering*, 115(8), pp. 1076–1093.

Michelazzo, G. (2014) *Breaching of river levees: analytical flow modelling and experimental hydro-morphodynamic investigations*. University of Florence.

Mitchell, C. and Brown, A. (2018) ‘Report on EURCOLD workshop on overflow of dams and levees Aussois’, *Dams and Reservoirs*, 28(4), pp. 137–141. Available at: <https://doi.org/10.1680/jdare.18.00004>.

Mizutani, H. *et al.* (2013) ‘Numerical modelling of river embankment failure due to overtopping flow considering infiltration effects’, *Journal of Hydraulic Research*, 51(6), pp. 681–695. Available at: <https://doi.org/10.1080/00221686.2013.812151>.

Mohamed, M.A.A. *et al.* (2002) ‘Improving the accuracy of prediction of breach formation through embankment dams and flood embankments’, in *Flow 2002 Conference on Fluvial Hydraulics*, pp. 1–10. Available at: http://www.impact-project.net/publications/wp2_pub1.pdf.

Moramarco, T., Saltalippi, C. and Singh, V.P. (2011) ‘Velocity profiles assessment in natural channels during high floods’, *Hydrology Research*, 42(2–3), pp. 162–170. Available at: <https://doi.org/10.2166/nh.2011.064>.

Morris, M. (2005) *Final Technical Report – January 2005. IMPACT, Investigation of Extreme Flood Processes and Uncertainty.*

Morris, M. (2009) *Breach Initiation & Growth: Physical Processes Analysis of IMPACT Project Field Tests, FLOODsite Project Report, T06-08-11.*

Morris, M. *et al.* (2009) *Breaching Processes: A state of the art review, FLOODsite Project Report, T06-06-03.*

Morris, M. *et al.* (2012) *Evaluation and development of physically-based embankment breach models, Comprehensive Flood Risk Management. Denver.* Available at: <https://doi.org/10.1201/b13715-53>.

Morris, Mark, Dyer, M. and Smith, P. (2007) *Management of Flood Embankments.*

Morris, M., Dyer, M. and Smith, P. (2007) *Management of Flood Embankments. A good practice review.*

Morris, M.W. (2011) *Breaching of Earth Embankments and Dams. PhD thesis The Open University.*

Morris, M.W. and Hassan, M. (2002) *Breach Formation through Embankment Dams & Flood Defence Embankments: A State of the Art Review. IMPACT Project Workshop.*

Morris, M.W., Hassan, M. a. a. M. and Vaskinn, K. a. (2007a) 'Breach formation: Field test and laboratory experiments', *Journal of Hydraulic Research*, 45(sup1), pp. 9–17. Available at: <https://doi.org/10.1080/00221686.2007.9521828>.

Morris, M.W., Hassan, M. a. a. M. and Vaskinn, K. a. (2007b) 'Breach formation: Field test and laboratory experiments', *Journal of Hydraulic Research*, 45(sup1), pp. 9–17. Available at: <https://doi.org/10.1080/00221686.2007.9521828>.

Morris, M.W., Hassan, M. and Vaskinn, K.A. (2005) *Conclusions and recommendations from the IMPACT project WP2: Breach formation, IMPACT Project technical reporting.*

Moukalled, F., Mangani, L. and Darwish, M. (2016) *The Finite Volume Method in Computational Fluid Dynamics, Fluid Mechanics and its Applications.* Springer International Publishing (Fluid Mechanics and Its Applications). Available at: <https://doi.org/10.1007/978-3-319-16874-6>.

el Mountassir, G. *et al.* (2011) 'Behaviour of compacted silt used to construct

flood embankment', *Proceedings of the Institution of Civil Engineers - Geotechnical Engineering*, 164(3), pp. 195–210. Available at: <https://doi.org/10.1680/geng.10.00055>.

Murray, E.J. and Sivakumar, V. (2010) *Unsaturated Soils A fundamental interpretation of soil behaviour*. John Wiley & Sons, Ltd.

Nuth, M. and Laloui, L. (2006) 'Effective stress concept in unsaturated soils: Clarification and validation of a unified framework', *International Journal for Numerical and Analytical Methods in Geomechanics*, 30(13), pp. 1303–1336. Available at: <https://doi.org/10.1002/nag>.

Öberg, A. and Sällfors, G. (1997) 'Determination of Shear Strength Parameters of Unsaturated Silts and Sands Based on the Water Retention Curve', *Geotechnical Testing Journal*. Edited by K.R.D. RC Chaney, 20(1), pp. 40–48. Available at: <https://doi.org/10.1520/GTJ11419J>.

Olsen, N.R.B. (2012) 'OpenFOAM - Spillway Tutorial', *Openfoam*. Norwegian University of Science and Technology, Department of Environmental and Hydraulic Engineering, pp. 1–19. Available at: <https://folk.ntnu.no/nilsol/cases/openfoam/>.

Olsen, N.R.B. (2015) 'Four free surface algorithms for the 3D Navier-Stokes equations', *Journal of Hydroinformatics*, 17(6), pp. 845–856. Available at: <https://doi.org/10.2166/hydro.2015.012>.

Pickert, G., Weitbrecht, V. and Bieberstein, A. (2011) 'Breaching of overtopped river embankments controlled by apparent cohesion', *Journal of Hydraulic Research*, 49(2), pp. 143–156. Available at: <https://doi.org/10.1080/00221686.2011.552468>.

'Plaxis 2018, Users Manual' (2018). Delft, The Netherlands: Plaxis bv, p. 43.

Powledge, George R *et al.* (1989) 'Mechanics of Overflow Erosion on Embankments. II: Hydraulic and Design Considerations', *Journal of Hydraulic Engineering-Asce*, 115(8), pp. 1056–1075.

Powledge, George R. *et al.* (1989) 'Mechanics of Overflow Erosion on Embankments. II: Hydraulic and Design Considerations', *Journal of Hydraulic Engineering*, 115(8), pp. 1056–1075. Available at: [https://doi.org/10.1061/\(ASCE\)0733-9429\(1989\)115:8\(1056\)](https://doi.org/10.1061/(ASCE)0733-9429(1989)115:8(1056)).

Regazzoni, P.L. and Marot, D. (2013) 'A comparative analysis of interface erosion tests', *Natural Hazards*, 67(2), pp. 937–950. Available at:

<https://doi.org/10.1007/s11069-013-0620-3>.

Risher, P. and Gibson, S. (2016) ‘Applying Mechanistic Dam Breach Models to Historic Levee Breaches’, in *FloodRisk 2016 - 3rd European Conference on Flood Risk Management*. Available at: <https://doi.org/10.1051/e3sconf/20160703002>.

Ruches, H. (2002) *Computational Fluid Dynamics of Dispersed Two-Phase Flows at High Phase Fractions*, PhD thesis, University of London and Diploma of Imperial College. Imperial College of Science, Technology & Medicine.

Samuels, P.G. *et al.* (2008) ‘Development of the HR BREACH model for predicting breach growth through flood embankments and embankment dams’, in *River Flow 2008*. Izmir, Turkey, pp. 679–688.

Schmocker, L. and Hager, W.H. (2009) ‘Modelling dike breaching due to overtopping’, *Journal of Hydraulic Research*, 47(5), pp. 585–597. Available at: <https://doi.org/10.3826/jhr.2009.3586>.

Shafii, I. *et al.* (2016) ‘Relationship between soil erodibility and engineering properties’, in *Scour and Erosion - Proceedings of the 8th International Conference on Scour and Erosion, ICSE 2016*. Taylor & Francis Group, 6000 Broken Sound Parkway NW, Suite 300, Boca Raton, FL 33487-2742: CRC Press, pp. 1055–1060. Available at: <https://doi.org/10.1201/9781315375045-134>.

Sheng, D., Zhou, A. and Fredlund, D.G. (2011) ‘Shear Strength Criteria for Unsaturated Soils’, *Geotechnical and Geological Engineering*, 29(2), pp. 145–159. Available at: <https://doi.org/10.1007/s10706-009-9276-x>.

Shields, Ing.A. (1936) *Application of Similarity and Turbulence Research to Bed-Load Movement*. Pasadena, California.

Simm, J. *et al.* (2017) ‘Ten years of lessons learned from English levee performance during severe flood events’, in *ICOLD 2017 - 85th Annual Meeting of International Commission on Large Dams*. Prague, Czech Republic.

Smith, C. and Gilbert, M. (2007) ‘Application of discontinuity layout optimization to plane plasticity problems’, *Proceedings of the Royal Society A: Mathematical, Physical and Engineering Sciences*, 463, pp. 2461–2484. Available at: <https://doi.org/10.1098/rspa.2006.1788>.

Stein, O.R. and Julien, P.Y. (1993) ‘Criterion Delineating the Mode of Headcut Migration’, *Journal of Hydraulic Engineering*, 119(1), pp. 37–50. Available at:

[https://doi.org/10.1061/\(ASCE\)0733-9429\(1993\)119:1\(37\)](https://doi.org/10.1061/(ASCE)0733-9429(1993)119:1(37)).

Stephen M. Westenbroek (2006) *Estimates of Shear Stress and Measurements of Water Levels in the Lower Fox River near Green Bay, Wisconsin. Scientific Investigations Report 2006 – 5226*.

Tarantino, A. (2007) ‘A possible critical state framework for unsaturated compacted soils’, *Geotechnique*, 57(4), pp. 385–389. Available at: <https://doi.org/10.1680/geot.2007.57.4.385>.

Tarantino, A. and di Donna, A. (2019) ‘Mechanics of unsaturated soils: Simple approaches for routine engineering practice’, *Rivista Italiana di Geotecnica*, (4), pp. 5–46. Available at: <https://doi.org/10.19199/2019.4.0557-1405.005>.

Tarantino, A. and el Mountassir, G. (2013) ‘Making unsaturated soil mechanics accessible for engineers: Preliminary hydraulic–mechanical characterisation & stability assessment’, *Engineering Geology*, 165, pp. 89–104. Available at: <https://doi.org/10.1016/j.enggeo.2013.05.025>.

Tarantino, A. and Tombolato, S. (2005) ‘Coupling of hydraulic and mechanical behaviour in unsaturated compacted clay’, *Géotechnique*, 55(4), pp. 307–317. Available at: <https://doi.org/10.1680/geot.2005.55.4.307>.

Temple, D.M. *et al.* (2006) ‘WINDAM – Analysis of Overtopped Earth Embankment Dams’, *ASABE Annual International Meeting*, 0300(06), pp. 1–11.

Temple, D.M. and Hanson, G.J. (1994) ‘Headcut development in vegetated earth spillways’, *Applied Engineering in Agriculture*, 10(5), pp. 677–682.

Thoman, R.W. and Niezgodna, S.L. (2008) ‘Determining Erodibility, Critical Shear Stress, and Allowable Discharge Estimates for Cohesive Channels: Case Study in the Powder River Basin of Wyoming’, *Journal of Hydraulic Engineering*, 134(12), pp. 1677–1687. Available at: [https://doi.org/10.1061/\(ASCE\)0733-9429\(2008\)134:12\(1677\)](https://doi.org/10.1061/(ASCE)0733-9429(2008)134:12(1677)).

Thorne, C.R. (1998) ‘River Width Adjustment. I: Process and Mechanisms’, *Journal of Hydraulic Engineering*, 124(9), pp. 903–917. Available at: [https://doi.org/10.1061/\(ASCE\)0733-9429\(1998\)124:9\(903\)](https://doi.org/10.1061/(ASCE)0733-9429(1998)124:9(903)).

Ubbink, O. (1997) *Numerical prediction of two fluid systems with sharp interfaces*. PhD Thesis. Imperial College of Science, Technology & Medicine. Available at:

<http://powerlab.fsb.hr/ped/kturbo/OpenFOAM/docs/OnnoUbbinkPhD.pdf>.

Utley, B.C. and Wynn, T.M. (2008) 'Cohesive Soil Erosion: Theory and Practice', in *World Environmental and Water Resources Congress 2008*. Reston, VA: American Society of Civil Engineers, pp. 1–10. Available at: [https://doi.org/10.1061/40976\(316\)289](https://doi.org/10.1061/40976(316)289).

Vanapalli, S.K. *et al.* (1996) 'Model for the prediction of shear strength with respect to soil suction', *Canadian Geotechnical Journal*, 33(3), pp. 379–392. Available at: <https://doi.org/10.1139/t96-060>.

Vaskinn, K., LØvoll, A. and Höeg, K. (2003) *WP2.1 Breach formation: Large scale embankment failure, Technical Report IMPACT Project Ref. EVG1-CT2001-00037*. Oslo.

Vaskinn, K.A. *et al.* (2004) 'Physical modeling of breach formation: Large scale field tests', in *Proceedings of Dam Safety*. Phoenix, USA, pp. 1–16.

Versteeg, H.K. and Malalasekera, W. (2007) *An Introduction to Computational Fluid Dynamics. The Finite Volume Method*. Second Edi. Harlow, UK: Pearson Education Limited.

Visser, P.J. (1998) *Breach growth in sand-dikes*.

Volz, C. (2013) *Numerical Simulation of Embankment Breaching Due to Overtopping.*, VAW-Mitteilung.

Volz, C. *et al.* (2017) 'Numerical embankment breach modelling including seepage flow effects', *Journal of Hydraulic Research*, 55(4), pp. 480–490. Available at: <https://doi.org/10.1080/00221686.2016.1276104>.

Wahl, T. *et al.* (2017) *Evaluation of Numerical Models for Simulating Embankment Dam Erosion and Breach Processes - DSO - 2017 - 02*.

Wahl, T.L. (1997) *Predicting Embankment Dam Breach Parameters - A Needs Assessment, XXVIIth IAHR Congress San Francisco, California August 10-15, 1997*.

Wahl, T.L. (1998) *Prediction of Embankment Dam Breach Parameters. A Literature Review and Needs Assessment. DSO-98-004, Dam Safety Office. Water Resources Research Laboratory*.

Wahl, T.L. *et al.* (2008) 'Development of next-generation embankment dam breach models', in *28th Annual USSD Conference 'The Sustainability of Experience - Investing in the Human Factor' Portland, Oregon, April 28 - May 2, 2008*, pp. 767–

Wahl, T.L. (2010) 'A COMPARISON OF THE HOLE EROSION TEST AND JET EROSION TEST', in *Joint Federal Interagency Conference on Sedimentation and Hydrologic Modeling*, pp. 1–12.

Walder, J.S. *et al.* (2015) 'Controls on the breach geometry and flood hydrograph during overtopping of noncohesive earthen dams', *Water Resources Research*, 51(8), pp. 6701–6724. Available at: <https://doi.org/10.1002/2014WR016620>.

Walder, J.S. (2015) 'Dimensionless Erosion Laws for Cohesive Sediment', *Journal of Hydraulic Engineering*, 1, p. 04015047. Available at: [https://doi.org/10.1061/\(ASCE\)HY.1943-7900.0001068](https://doi.org/10.1061/(ASCE)HY.1943-7900.0001068).

Wan, C.F. and Fell, R. (2004) 'Investigation of Rate of Erosion of Soils in Embankment Dams', 130(April), pp. 373–380.

Wei, H. *et al.* (2016) 'Overtopping breaching of river levees constructed with cohesive sediments', *Natural Hazards and Earth System Sciences*, 16(7), pp. 1541–1551. Available at: <https://doi.org/10.5194/nhess-16-1541-2016>.

Weller, H.G. *et al.* (1998) 'A tensorial approach to computational continuum mechanics using object-oriented techniques', *Computers in Physics*, 12(6), p. 620. Available at: <https://doi.org/10.1063/1.168744>.

West, M., Morris, M. and Hassan, M. (2018) 'A guide to breach prediction', pp. 1–40. Available at: <http://eprints.hrwallingford.com/id/eprint/1341>.

Wolam, M.G. (1959) 'Factors influencing erosion of cohesive river banks', *American Journal of Science*, 257, pp. 204–216.

Wu, W. (2016) *Technical Report. Introduction to DLBreach – A Simplified Physically-Based Dam/Levee Breach Model*.

Zhang, L. *et al.* (2016) *Dam Failure Mechanisms and Risk Assessment, Dam Failure Mechanisms and Risk Assessment*. Singapore: John Wiley & Sons Singapore Pte. Ltd. Available at: <https://doi.org/10.1002/9781118558522.ch12>.

Zhao, G. (2016) *Breach Growth in Cohesive Embankments due to Overtopping. PhD Thesis*. PhD Thesis. Technische Universiteit Delft.

Zhao, G., Peeters, P. and Visser, P. (2019) 'Hydrodynamic Erosion in Overtopping Breach of Cohesive Embankments', *38th IAHR World Congress - 'Water: Connecting the World'*, 38, pp. 1375–1384. Available at:

<https://doi.org/10.3850/38wc092019-5554>.

Zhao, G., Visser, P. and Peeters, P. (2014) *Large scale embankment breach experiments in flume. Report of Delft University of Technology.*

Zhenzhen, L.I.U. (2015) *Hydro-Mechanical Analysis of Breach Processes Due to Levee Failure. PhD Thesis.* Universite' D'Aix-Marseille.

Zhong, Q. *et al.* (2016) 'Comparison of simplified physically based dam breach models', *Natural Hazards*, 84(2), pp. 1385–1418. Available at: <https://doi.org/10.1007/s11069-016-2492-9>.

Zhu, Y. (2006) *Breach Growth in Clay-Dikes. PhD Thesis.* Delft University of Technology.

Zhu, Y. *et al.* (2011) 'Experimental investigation on breaching of embankments', *Science China Technological Sciences*, 54(1), pp. 148–155. Available at: <https://doi.org/10.1007/s11431-010-4208-9>.

Zhu, Y., Visser, P. and Vrijling, J. (2004) 'Review on embankment dam breach modeling', in *New Developments in Dam Engineering.* Taylor & Francis, pp. 1189–1196. Available at: <https://doi.org/10.1201/9780203020678.ch147>.

Appendix A. CFD Simulation of Turbulent Flow of Two Immiscible Fluids

This Appendix provides an overview of the fundamental concepts required to perform a turbulent flow simulation in CFD of two immiscible fluids.

The derivation of the Navier-Stokes equations, the turbulence modelling and the finite volume method can be extensively found in literature and textbooks. The main sources consulted are “An Introduction to Computational Fluid Dynamics The Finite Volume Method” (Versteeg and Malalasekera, 2007), “Free-surface flow interface and air-entrainment modelling using OpenFOAM” (Lopes, 2013), “The Finite Volume Method in Computational Fluid Dynamics” (Moukalled, Mangani and Darwish, 2016), “Numerical Computation of Internal and External Flows” (Hirsch Charles, 2007), “Computational Fluid Dynamics of Dispersed Two-Phase Flows at High Phase Fractions” (Ruches, 2002).

A.1 Governing Equations of Fluid Flows

Fluid flow processes are mathematically described by the Navier-Stokes equations, which are expression of the conservation laws of mass, linear momentum and energy. These are highly nonlinear second order partial differential equations in four independent variables since flows are unsteady and three dimensional.

The analysis is conducted considering the fluid as a continuum, thus the macroscopic properties (i.e. velocity, pressure, density, temperature) are functions of space coordinates and time. In the overflow problem it is assumed that water is a Newtonian fluid. This means that there is a linear relationship between the shear stress and the fluid velocity through the molecular viscosity μ . The molecular viscosity μ is a measure of the ability of a fluid subjected to a stress to resist deformation, representing the slope of the linear function, as shown in Figure 3-3b. Also, water is considered as an incompressible fluid, which means that density is constant.

A.1.1 Navier-Stokes Equations in the context of the Finite Volume Method

The first step for deriving the Navier-Stokes equations consists of applying the principle of conservation of mass (i.e. the rate of increase of mass in a fluid element is equal to the net rate of flow of mass into a fluid element), which gives:

$$\frac{\partial \rho}{\partial t} + \text{div}(\rho \mathbf{u}) = 0 \quad \text{Equation A - 1}$$

This is the unsteady, three-dimensional continuity equation where the first term represents the rate of change in time of the density and the second term is the convective term describing the net flow of mass across the faces of the fluid element where $\mathbf{u} = (u, v, w)$ is the velocity vector. Because the fluid is incompressible, density is constant, and the continuity equation reduces to:

$$\text{div } \mathbf{u} = 0 \quad \text{Equation A - 2}$$

The principle of conservation of momentum states that the rate of change of momentum of a fluid particle is equal to the sum of the forces on the particle.

The momentum of the fluid particle in the three directions x, y, z is given by:

$$\rho \frac{Du}{Dt} = \frac{\partial(\rho u)}{\partial t} + \text{div}(\rho u \mathbf{u}) \quad \text{Equation A - 3}$$

$$\rho \frac{Dv}{Dt} = \frac{\partial(\rho v)}{\partial t} + \text{div}(\rho v \mathbf{u}) \quad \text{Equation A - 4}$$

$$\rho \frac{Dw}{Dt} = \frac{\partial(\rho w)}{\partial t} + \text{div}(\rho w \mathbf{u}) \quad \text{Equation A - 5}$$

The forces acting on the fluid particle are divided in surface and body forces.

The state of stress of a fluid element is commonly defined in terms of pressure p (i.e. normal stress) and nine viscous stress components τ_{ij} , where i indicates the surface with normal direction i and j is the direction of application of the stress. To write the equation of conservation of momentum the total surface forces per unit volume are given by the sum of the products of the normal and viscous stresses and the area of the faces of the fluid element. The sum of the surface and body forces must be equal to

the momentum, thus:

$$\rho \frac{Du}{Dt} = \frac{\partial(-p + \tau_{xx})}{\partial x} + \frac{\partial\tau_{yx}}{\partial y} + \frac{\partial\tau_{zx}}{\partial z} + S_{Mx} \quad \text{Equation A - 6}$$

$$\rho \frac{Dv}{Dt} = \frac{\partial\tau_{yx}}{\partial x} + \frac{\partial(-p + \tau_{yy})}{\partial y} + \frac{\partial\tau_{zx}}{\partial z} + S_{My} \quad \text{Equation A - 7}$$

$$\rho \frac{Dw}{Dt} = \frac{\partial\tau_{zx}}{\partial x} + \frac{\partial\tau_{zy}}{\partial y} + \frac{\partial(-p + \tau_{zz})}{\partial z} + S_{Mz} \quad \text{Equation A - 8}$$

where the sign – on the pressure component indicates a normal compressive stress. It is worth specifying that surface forces are explicitly considered, while the body forces are grouped in the source term S_M .

For the embankment overflow/overtopping problem no heat transfers are occurring, therefore the third principle of the conservation of energy is not considered and the flow field is fully described by the continuity and the momentum equations.

In this set of equations, the number of unknowns is larger than the number of equations. Constitutive relations are introduced for the viscous stresses, which can be expressed as a function of the local deformation rate. The deformation rate comprises linear and volumetric deformation rate. In the space the linear deformation rate of a fluid element contains nine components, six of which are independent for isotropic fluids: the linear elongating deformation components are provided by:

$$s_{xx} = \frac{\partial u}{\partial x} \quad s_{yy} = \frac{\partial v}{\partial y} \quad s_{zz} = \frac{\partial w}{\partial z} \quad \text{Equation A - 9}$$

while the six shearing linear deformation components are described below

$$s_{xy} = s_{yx} = \frac{1}{2} \left(\frac{\partial u}{\partial y} + \frac{\partial v}{\partial x} \right)$$

$$s_{xz} = s_{zx} = \frac{1}{2} \left(\frac{\partial u}{\partial z} + \frac{\partial w}{\partial x} \right) \quad \text{Equation A - 10}$$

$$s_{yz} = s_{zy} = \frac{1}{2} \left(\frac{\partial v}{\partial z} + \frac{\partial w}{\partial y} \right)$$

and the volumetric deformation rate is given by:

$$\operatorname{div} \mathbf{u} = \frac{\partial u}{\partial x} + \frac{\partial v}{\partial y} + \frac{\partial w}{\partial z} \quad \text{Equation A - 11}$$

For a Newtonian fluid, the viscous stresses are proportional to the rates of deformations through two constants of proportionality: the dynamic viscosity μ which is related to the linear deformations and the second viscosity λ which relates the shear stresses to the volumetric deformation. The nine viscous stresses are expressed as:

$$\tau_{xx} = 2\mu \frac{\partial u}{\partial x} + \lambda \operatorname{div} \mathbf{u}$$

$$\tau_{yy} = 2\mu \frac{\partial v}{\partial y} + \lambda \operatorname{div} \mathbf{u}$$

$$\tau_{zz} = 2\mu \frac{\partial w}{\partial z} + \lambda \operatorname{div} \mathbf{u}$$

$$\text{Equation A - 12}$$

$$\tau_{xy} = \tau_{yx} = \mu \left(\frac{\partial u}{\partial y} + \frac{\partial v}{\partial x} \right)$$

$$\tau_{xy} = \tau_{yx} = \mu \left(\frac{\partial u}{\partial y} + \frac{\partial v}{\partial x} \right)$$

$$\tau_{yz} = \tau_{zy} = \mu \left(\frac{\partial v}{\partial z} + \frac{\partial w}{\partial y} \right)$$

Because the continuity equation for an incompressible fluid is: $\operatorname{div} \mathbf{u} = 0$, the first third terms in Equations A-12 are:

$$\tau_{xx} = 2\mu \frac{\partial u}{\partial x} \quad \tau_{yy} = 2\mu \frac{\partial v}{\partial y} \quad \tau_{zz} = 2\mu \frac{\partial w}{\partial z} \quad \text{Equation A - 13}$$

The Navier-Stokes equations are obtained by substituting these shear stresses in Equation A - 6, Equation A - 7, Equation A - 8. In a concise form useful for the development of the finite volume method, the Navier-Stokes equations are written as:

$$\frac{\partial(\rho \mathbf{u})}{\partial t} + \operatorname{div}(\rho \mathbf{u} \mathbf{u}) = -\frac{\partial p}{\partial x} + \operatorname{div}(\mu \operatorname{grad} \mathbf{u}) + S_{Mx} \quad \text{Equation A - 14}$$

$$\frac{\partial(\rho v)}{\partial t} + \text{div}(\rho v \mathbf{u}) = -\frac{\partial p}{\partial y} + \text{div}(\mu \text{ grad } v) + S_{My} \quad \text{Equation A - 15}$$

$$\frac{\partial(\rho w)}{\partial t} + \text{div}(\rho w \mathbf{u}) = -\frac{\partial p}{\partial z} + \text{div}(\mu \text{ grad } w) + S_{Mz} \quad \text{Equation A - 16}$$

This is a particular form of the transport equation, which for a general scalar quantity ϕ of the fluid flow can be written as:

$$\frac{\partial(\rho \phi)}{\partial t} + \text{div}(\rho \phi \mathbf{u}) = \text{div}(\Gamma \text{ grad } \phi) + S_{\phi} \quad \text{Equation A - 17}$$

This equation implies that the rate of increase of the quantity ϕ plus the net rate of flow of ϕ out of the fluid element (convective term) is equal to the rate of increase of ϕ due to diffusion (with Γ is the diffusion coefficient) and the rate of increase of ϕ due to the presence of sources.

The finite volume element method starts from this equation integrated over the three-dimensional control volume:

$$\begin{aligned} \int \frac{\partial(\rho \phi)}{\partial t} dV + \int \text{div}(\rho \phi \mathbf{u}) dV \\ = \int \text{div}(\Gamma \text{ grad } \phi) dV + \int S_{\phi} dV \end{aligned} \quad \text{Equation A - 18}$$

The convective and diffusion terms are transformed into surface integrals by using the Divergence's Theorem over the bounding surface A with normal vector \mathbf{n}

$$\begin{aligned} \frac{\partial}{\partial t} \left(\int \rho \phi dV \right) + \oint (\rho \phi \mathbf{u}) \cdot \mathbf{n} dA \\ = \oint (\Gamma \text{ grad } \phi) \cdot \mathbf{n} dA + \int S_{\phi} dV \end{aligned} \quad \text{Equation A - 19}$$

The product $(\rho \phi \mathbf{u}) \cdot \mathbf{n}$ expresses the flux component of property ϕ due to fluid flow along the outward normal vector \mathbf{n} and the product $(\Gamma \text{ grad } \phi) \cdot \mathbf{n}$ is associated with a flux into the element due to diffusion.

In time-dependent problems it is also necessary to integrate with respect to time thus the most general integrated form of the transport equation:

$$\int \frac{\partial}{\partial t} \left(\int \rho \phi \, dV \right) dt + \int \oint (\rho \phi u) \cdot n dA \, dt$$

Equation A - 20

$$= \int \oint (\Gamma \text{grad } \phi) \cdot n dA dt + \int \int S_\phi \, dV \, dt$$

The fluid flow problem includes the specification of initial conditions (values of variables given at time $t = 0$) and the boundary conditions (free stream, solid walls and on fluid boundaries inlet/outlet).

A.2 Turbulence Modelling

The Navier-Stokes equations are specifically for laminar flows, characterised by low values of Reynolds number. The Reynolds Number “Re” provides indication of the relative importance of inertia and viscous forces (UL/ν where U and L are characteristic velocity and length scales of the mean flow and ν is the kinematic viscosity). For values below a Re_{critic} , flow is classified as laminar where adjacent fluid layers tend to slide each other smoothly.

However, the vast majority of flows in nature can be described with large values of Re and are known as turbulent flows. These highly chaotic, irregular and unsteady type of motion in which transported quantities fluctuate in time and space. In this case, the velocity flow field (and any other general flow properties ϕ) is described by the Reynolds decomposition which considers a steady mean flow velocity U in addition to its time-dependent fluctuation $u'(t)$. An example of a typical point velocity measurement in turbulent flow is provided in Figure A - 1. Figure A - 1:

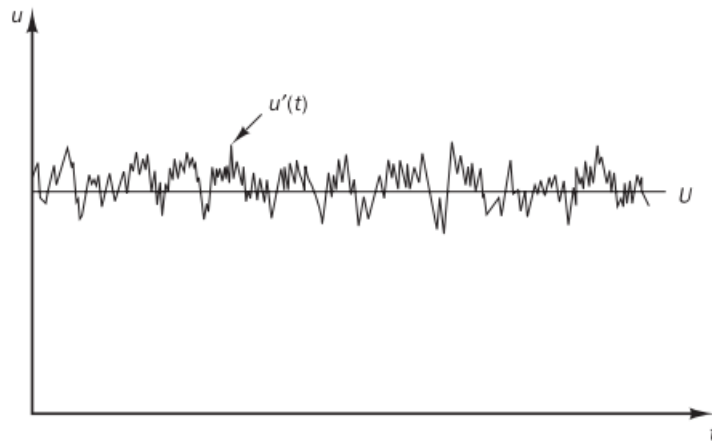


Figure A - 1: typical velocity measurement in turbulent flow made with a hot-wire anemometer after (Versteeg and Malalasekera, 2007)

If ϕ is a flow property, the mean Φ is defined as:

$$\Phi = \frac{1}{\Delta t} \int_0^{\Delta t} \phi(t) dt \quad \text{Equation A - 21}$$

The time average of the fluctuations $\phi'(t)$ is zero by definition.

The Reynolds decomposition provides:

$$\phi = \Phi + \phi' \quad \text{Equation A - 22}$$

Where the fluctuation component expresses statistical characteristic of the turbulent flow.

The variance and root mean square (r.m.s) are used to describe the spread of the fluctuations ϕ' around the mean value:

$$\overline{\phi'^2} = \frac{1}{\Delta t} \int_0^{\Delta t} (\phi')^2 dt \quad \text{Equation A - 23}$$

$$\phi_{\text{rms}} = \sqrt{\overline{\phi'^2}} = \left[\frac{1}{\Delta t} \int_0^{\Delta t} (\phi')^2 dt \right]^{1/2} \quad \text{Equation A - 24}$$

The variance is also called second moment of the fluctuations. The total kinetic energy per unit mass k can be expressed as:

$$k = \frac{1}{2} (\overline{u'^2} + \overline{v'^2} + \overline{w'^2}) \quad \text{Equation A - 25}$$

The turbulence intensity T_i is defined as the average r.m.s and it is related to the kinetic energy by a reference mean flow velocity U_{ref}

$$T_i = \frac{\sqrt{\frac{2}{3} k}}{U_{\text{ref}}} \quad \text{Equation A - 26}$$

The second moment of the fluctuations of two flow properties ϕ and ψ is defined as:

$$\overline{\varphi'\psi'} = \frac{1}{\Delta t} \int_0^{\Delta t} \varphi'\psi' dt \quad \text{Equation A - 27}$$

which provides the second moments of the velocity components $\overline{u'v'}$, $\overline{u'w'}$, $\overline{v'w'}$. They represent turbulent momentum fluxes that are closely linked with the additional shear stresses experienced by fluid elements in turbulent flows. Pressure–velocity moments $\overline{p'u'}$, $\overline{p'v'}$, etc. play a role in the diffusion of turbulent energy.

The structure of the fluctuations is described with relationships between the fluctuations at different times and spaces through auto-correlation functions $R_{\varphi'\varphi'}(\tau)$ and $R_{\varphi'\varphi'}(\xi)$, which are defined as:

$$R_{\varphi'\varphi'}(\tau) = \overline{\varphi'(t)\varphi'(t+\tau)} = \frac{1}{\Delta t} \int_0^{\Delta t} \varphi'(t)\varphi'(t+\tau) dt \quad \text{Equation A - 28}$$

$$\begin{aligned} R_{\varphi'\varphi'}(\xi) &= \overline{\varphi'(x,t)\varphi'(x+\xi,t)} \\ &= \frac{1}{\Delta t} \int_t^{t+\Delta t} \varphi'(x,t')\varphi'(x+\xi,t') dt' \end{aligned} \quad \text{Equation A - 29}$$

When time shift τ (or displacement ξ) is zero the value of the autocorrelation function corresponds to the variance $\overline{\varphi'^2}$ and will be the largest possible value, because the two contributions are perfectly correlated. Since the behaviour of the fluctuations ϕ' is chaotic in a turbulent flow, the fluctuations tend to be decorrelated as $\tau \rightarrow \infty$ (or $|\xi| \rightarrow \infty$). It is also possible to define cross-correlation functions with respect to time shift τ or between pairs of different fluctuations.

The introduction of the Reynolds decomposition in the Navier-Stokes equation leads to the Reynolds-Averaged Navier-Stokes equations.

Under a qualitative point of view, turbulent flow contains a wide range of vortical eddies of different scales which are responsible for a strong mixing of fluid elements with transport of momentum and energy. The largest turbulent eddies interact with and extract energy from the mean flow by a process called vortex stretching. These are dominated by inertia effects. Smaller eddies are stretched strongly by larger eddies with the mean flow. In this way the kinetic energy is handed down from large eddies to progressively smaller and smaller eddies in what is termed the energy cascade. At

the scale of the smallest eddies, viscous effects are not negligible and induce energy dissipation into internal thermal energy.

The momentum exchange due to convective transport by the eddies is such that fluid layers experience additional turbulent shear stresses, which are known as the Reynolds stresses.

Mathematically this means that there is an effect of the fluctuations on the mean flow which can be captured by substituting the flow variables $\mathbf{u}, \mathbf{v}, \mathbf{w}, \mathbf{p}$ with $\mathbf{u} = \mathbf{U} + \mathbf{u}', \mathbf{v} = \mathbf{V} + \mathbf{v}', \mathbf{w} = \mathbf{W} + \mathbf{w}', \mathbf{p} = \mathbf{P} + \mathbf{p}'$, etc.

Under the assumption of incompressible flow, because: $\text{div } \mathbf{a} = \text{div } \mathbf{A}$, where $\mathbf{A} = \mathbf{a} + \mathbf{A}'$ the continuity equation for the mean flow is given by:

$$\text{div } \mathbf{U} = 0 \quad \text{Equation A - 30}$$

To write the conservation of momentum in the x direction, the following relationships need to be considered:

$$\overline{\frac{\partial u}{\partial t}} = \frac{\partial U}{\partial t}$$

$$\overline{\text{div}(\mathbf{u}\mathbf{u})} = \text{div}(\mathbf{U}\mathbf{U}) + \text{div}(\overline{\mathbf{u}'\mathbf{u}'})$$

$$\overline{-\frac{1}{\rho} \frac{\partial p}{\partial x}} = -\frac{1}{\rho} \frac{\partial P}{\partial x}$$

$$\overline{\mathbf{v} \text{div}(\text{grad}(\mathbf{u}))} = \mathbf{v} \text{div}(\text{grad}(\mathbf{U}))$$

$$\text{Equation A - 31}$$

The conservation of momentum in x, y and z direction with these notations becomes:

$$\begin{aligned}
\frac{\partial U}{\partial t} + \text{div}(UU) &= -\frac{1}{\rho} \frac{\partial P}{\partial x} + \nu \text{div}(\text{grad}(U)) \\
&+ \frac{1}{\rho} \left(\frac{\partial(-\rho \overline{u'^2})}{\partial x} + \frac{\partial(-\rho \overline{u'v'})}{\partial y} \right. \\
&\left. + \frac{\partial(-\rho \overline{u'w'})}{\partial z} \right)
\end{aligned}$$

Equation A - 32

$$\begin{aligned}
\frac{\partial V}{\partial t} + \text{div}(VU) &= -\frac{1}{\rho} \frac{\partial P}{\partial y} + \nu \text{div}(\text{grad}(V)) \\
&+ \frac{1}{\rho} \left(\frac{\partial(-\rho \overline{u'v'})}{\partial x} + \frac{\partial(-\rho \overline{v'^2})}{\partial y} \right. \\
&\left. + \frac{\partial(-\rho \overline{v'w'})}{\partial z} \right)
\end{aligned}$$

Equation A - 33

$$\begin{aligned}
\frac{\partial W}{\partial t} + \text{div}(WU) &= -\frac{1}{\rho} \frac{\partial P}{\partial z} + \nu \text{div}(\text{grad}(W)) \\
&+ \frac{1}{\rho} \left(\frac{\partial(-\rho \overline{u'w'})}{\partial x} + \frac{\partial(-\rho \overline{v'w'})}{\partial y} \right. \\
&\left. + \frac{\partial(-\rho \overline{w'^2})}{\partial z} \right)
\end{aligned}$$

Equation A - 34

These are the Reynolds averaged Navier-Stokes equation for incompressible fluid, which contains the products of fluctuating velocities associated with convective momentum transfer due to turbulent eddies.

The extra turbulent stresses: $\tau_{xx} = -\rho \overline{u'^2}$, $\tau_{yy} = -\rho \overline{v'^2}$, $\tau_{zz} = -\rho \overline{w'^2}$, $\tau_{xy} = \tau_{yx} = -\rho \overline{u'v'}$, $\tau_{xz} = \tau_{yz} = -\rho \overline{u'w'}$, $\tau_{yz} = \tau_{zy} = -\rho \overline{v'w'}$ are called Reynolds stresses and are always non-zero as they contain squared velocity fluctuations.

The methods to solve the Navier-Stokes equations can be grouped in three categories with increasing level of complexity: (1) turbulence models (RAS or RANS methods), (2) large eddy simulation (LES), (3) direct numerical simulation (DNS).

This latter aims to solve the unsteady Navier-Stokes equations for all the spectrum of energy characterising the turbulent flow (i.e. Kolomogorov scales). This requires a sufficiently fine spatial grid and an adequately small time-step to capture the fastest fluctuations. For this reason, the DNS method is computationally expensive, and it is not commonly adopted.

The second method focus the attention on the behaviour of the larger eddies by filtering the Navier–Stokes equation in order to block the smaller eddies. However, also this method results demanding and it is used for particular applications.

Finally, in CFD practice, the RAS or RANS methodologies are yet the most popular approach adopted to solve the Reynolds equations. The starting point is the observation that is sufficient to describe the mean flow and to capture the effects of turbulence on mean flow properties. These are represented by the six additional shear stresses (i.e. the Reynolds stresses) resulting from the time-averaged operation of the Navier-Stokes equations. Turbulence models are introduced to predict these Reynolds stresses and the scalar transport terms thus allowing the closure of the system of the mean flow equations. There are various RANS methods depending on the number of additional transport equations introduced. These are: zero-equation model (mixing-length), one-equation model (Spalart-Allmaras), two-equations model (k- ϵ , k- ω , shear stress transport SST k- ω) and seven-equations (RSM – Reynolds Stress Model). At present, the two-equations models are the most used and validated ones.

For the analysis of the embankment overflow problem, the SST k- ω has been implemented within the interFoam solver in OpenFoam. The k- ϵ , k- ω , etc models are based on the Boussinesq assumption that, in analogy with the definition of Newtonian fluid, the Reynolds stresses are proportional to the mean rates of deformation, through the so-called turbulent or eddy viscosity μ_t (Pa s):

$$\tau_{ij} = -\overline{\rho u_i' u_j'} = \mu_t \left(\frac{\partial U_i}{\partial x_j} + \frac{\partial U_j}{\partial x_i} \right) - \frac{2}{3} \rho k \delta_{ij} \quad \text{Equation A - 35}$$

where $k = \frac{1}{2} (\overline{u'^2} + \overline{v'^2} + \overline{w'^2})$ is the turbulent kinetic energy per unit mass.

A.2.1 The k- ϵ model

The k- ϵ model (Launder and Spalding, 1974) analyses the effects of transport by

convection and diffusion of turbulence properties. Two additional model equations are introduced, one for the turbulent kinetic energy k and one for the rate of dissipation ε (m^3/s^2). This is an important quantity since it describes the destruction of the turbulent kinetic energy caused by the work done by the smallest eddies against viscous stresses.

$$\frac{\partial(\rho k)}{\partial t} + \text{div}(\rho k U) = \text{div} \left[\frac{\mu_t}{\sigma_k} \text{grad } k \right] + 2\mu_t S_{ij} \cdot S_{ij} - \rho \varepsilon \quad \text{Equation A - 36}$$

$$\begin{aligned} \frac{\partial(\rho \varepsilon)}{\partial t} + \text{div}(\rho \varepsilon U) \\ = \text{div} \left[\frac{\mu_t}{\sigma_\varepsilon} \text{grad } \varepsilon \right] + C_{1\varepsilon} \frac{\varepsilon}{k} 2\mu_t S_{ij} \cdot S_{ij} \\ - C_{2\varepsilon} \rho \frac{\varepsilon^2}{k} \end{aligned} \quad \text{Equation A - 37}$$

where the eddy viscosity $\mu_t = \rho C_\mu \frac{k^2}{\varepsilon}$, with C_μ a dimensionless constant equal to 0.09; $\sigma_k = 1.00$, $C_{1\varepsilon} = 1.44$ and $C_{2\varepsilon} = 1.92$, S_{ij} is the mean component of the rate of deformation of the fluid element.

In words these equations mean that the rate of change of k or ε plus the transport of k or ε due to convection, must be equal to the transport of k or ε due to diffusion plus the rate of production of k or ε minus the rate of destruction of k or ε . Production and destruction of turbulent kinetic energy are always closely linked. Dissipation rate ε is large where production of k is large. Finally, the Reynolds stresses are given by the Boussinesq formulation.

The implementation of the $k - \varepsilon$ model requires the following boundary conditions:

Table A - 1: Boundary conditions required for the implementation of the $k - \varepsilon$ model

k or ε distribution	INLET BOUNDARIES
$\frac{\partial k}{\partial n} = 0$ $\frac{\partial \varepsilon}{\partial n} = 0$	OUTLET BOUNDARIES and SYMMETRY AXIS
Reynolds Number	SOLID WALL BOUNDARIES

Since measurements of k and ε are rare, it is common practice in CFD to assume value of k and ε at the boundaries based on typical values presented in literature or by approximations from the turbulence intensity T_i and a characteristic flow length L , such that:

$$k = \frac{2}{3} (U_{\text{ref}} T_i)^2 \quad \varepsilon = C_\mu^{3/4} \frac{k^{3/2}}{l} \quad l = 0.07L$$

The flow behaviour at the solid wall boundary is significantly different from the free flows, therefore specific boundary conditions need to be introduced on the basis of the law of the wall.

A.2.2 Wall laws

The flow near solid walls has been studied using a dimensionless approaches based on the analysis of Reynolds number. If y is the distance from the wall, the Reynolds Number can be written as: $Re_y = \frac{Uy}{\nu}$

It is straightforward that in regions far from the wall y is large, Reynolds Number is high, and the inertia forces are predominant on the viscous effects.

However, Reynolds Number tends to decrease as y is decreased to zero towards the wall. Therefore, there are regions with low Reynolds Number where the flow behaviour is dominated by viscous effects and the mean flow velocity depends on the distance y from the wall, on the fluid density ρ and viscosity μ and on the wall shear stress τ_w .

Dimensional analysis provides the law of the wall defined in **Error! Reference source not found.**

$$u^+ = \frac{U}{u_\tau} = f\left(\frac{\rho u_\tau y}{\mu}\right) = f(y^+) \quad \text{Equation A - 38}$$

where u^+ and y^+ are two dimensionless groups. The velocity $u_\tau = \sqrt{\frac{\tau_w}{\rho}}$ is the friction velocity.

Far from the wall, the velocity field is still affected by the wall shear stress, but the viscous effects become less important, therefore:

$$u^+ = \frac{U}{u_\tau} = g\left(\frac{y}{\delta}\right) \quad \text{Equation A - 39}$$

The presence of the wall shear stress causes a reduction of velocity, which can be considered with the following velocity-defect law:

$$\frac{U_{\max} - U}{u_\tau} = g\left(\frac{y}{\delta}\right) \quad \text{Equation A - 40}$$

where δ is the thickness of the boundary layer.

Based on this description, near a solid wall three typical flow behaviours are identified: (1) the viscous or linear sublayer which is the closest to the wall, (2) the buffer layer or mixture region and (3) and the turbulent sublayer which is the furthest region from the wall. These are schematically shown in Figure A - 2.

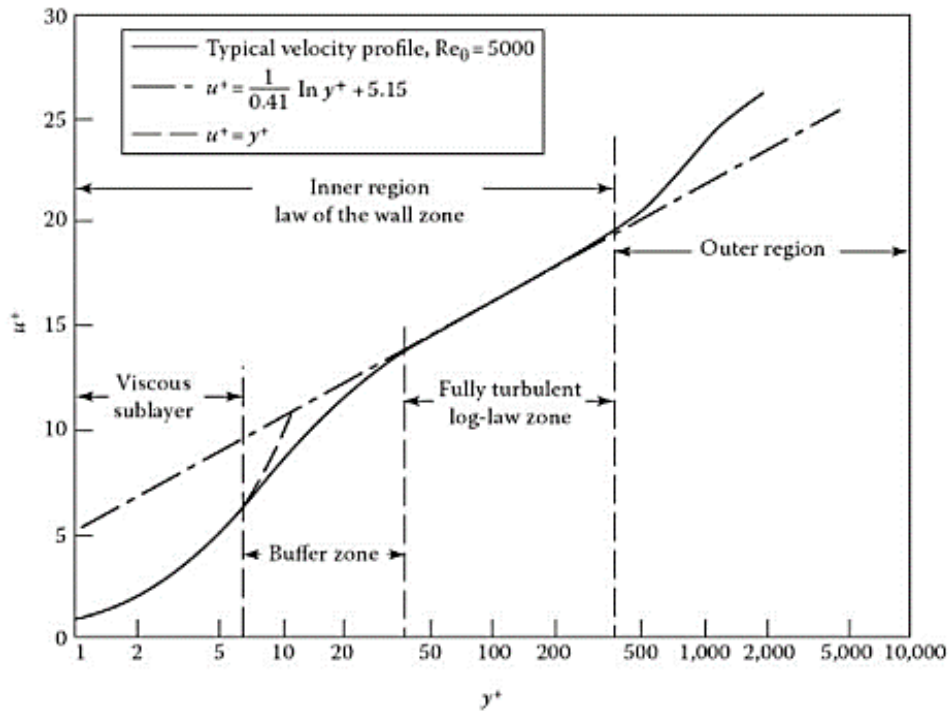


Figure A - 2: Near-wall velocity profile, where $y^+ = \frac{\rho u_\tau y}{\mu}$ is the dimensionless distance from the wall; the dimensionless velocity is $u^+ = \frac{U}{u_\tau}$, with $u_\tau = \sqrt{\frac{\tau_w}{\rho}}$ friction velocity. The viscous sublayer, the buffer zone and the log-law zone are specified.

The viscous sublayer is very thin ($y^+ < 5$) and the shear stress can be considered constant and equal to the wall shear stress τ_w .

$$\tau(y) = \mu \frac{\partial U}{\partial y} \cong \tau_w$$

The integration with respect to y and the application of the boundary condition that $U = 0$ for $y = 0$ leads to $U = \frac{y\tau_w}{\mu}$, which means that in the viscous sublayer: $u^+ = y^+$.

Outside the viscous sublayer, viscous and turbulent effects are both significant and the shear stress varies slowly with the distance from the wall according to a logarithmic law:

$$u^+ = \frac{1}{\kappa} \ln(y^+) + B = \frac{1}{\kappa} \ln(Ey^+)$$

where $\kappa \approx 0.4$ is the von Karman's constant and $B \approx 5.5$ is the value found for smooth walls. This latter term decreases if wall roughness is considered.

For increasing value of y^+ the velocity profile tends towards the velocity defect law.

A.2.3 Implications in turbulence modelling

The standard $k - \varepsilon$ model is known as a high Reynolds number turbulence model valid only for fully turbulent flows which requires additional considerations in regions approaching solid walls. On the contrary, a turbulence model that can be integrated all the way to the wall is denoted in literature by a low Reynolds number turbulence model or a low Reynolds number version (Moukalled, Mangani and Darwish, 2016).

The application of the $k - \varepsilon$ model in the log-law region ($30 < y^+ < 500$), where Reynolds Numbers are typically high, requires the introduction of wall functions which relate the wall shear stress to the mean velocity, turbulence kinetic energy and rate of dissipation.

$$u^+ = \frac{U}{u_\tau} = \frac{1}{\kappa} \ln(Ey^+) \quad k = \frac{u_\tau^2}{\sqrt{C_\mu}} \quad \varepsilon = \frac{u_\tau^3}{\kappa y}$$

$\kappa = 0.41$ is the Von Karman's constant and wall roughness parameter $E = 9.8$ for smooth walls.

However, in the viscous sublayer, where Reynolds Numbers are low, the log-law

is not valid and the application of the $k - \varepsilon$ model requires the introduction of damping function.

This is the reason why CFD research has been focussed on the development of other models to overcome this issue. In this context the $k - \omega$ model is the most popular alternative to the $k - \varepsilon$ model.

A.2.4 The $k - \omega$ model

In the $k - \omega$ model, proposed by Wilcox, the turbulence frequency $\omega = \frac{\varepsilon}{k}$ (measured in 1/s) replaces the rate of dissipation of the kinetic energy ε and the length scale becomes: $l = \frac{\sqrt{k}}{\omega}$. The eddy viscosity is provided by: $\mu_t = \frac{\rho k}{\omega}$.

Like the $k - \varepsilon$ model, two additional transport equations are adopted to close the fluid flow problem.

$$\frac{\partial(\rho k)}{\partial t} + \text{div}(\rho k \mathbf{U}) = \text{div} \left[\left(\mu + \frac{\mu_t}{\sigma_k} \right) \text{grad } k \right] + P_k - \beta^* \rho k \omega \quad \text{Equation A - 41}$$

$$\begin{aligned} \frac{\partial(\rho \omega)}{\partial t} + \text{div}(\rho \omega \mathbf{U}) &= \text{div} \left[\left(\mu + \frac{\mu_t}{\sigma_k} \right) \text{grad } \omega \right] \\ &+ \gamma_1 \left(2\rho S_{ij} \cdot S_{ij} - \frac{2}{3} \rho \omega \frac{\partial U_i}{\partial x_j} \delta_{ij} \right) - \beta_1 \rho \omega^2 \end{aligned} \quad \text{Equation A - 42}$$

where $P_k = 2\mu S_{ij} \cdot S_{ij} - \frac{2}{3} \rho k \frac{\partial U_i}{\partial x_j} \delta_{ij}$, $\sigma_k = 2.0$, $\sigma_\omega = 2.0$, $\gamma_1 = 0.553$, $\beta_1 = 0.075$, $\beta^* = 0.09$

The greatest advantage of replacing the ε -equation by the ω -equation is essentially that this model performs better in the regions near the wall. This is because ω tends to infinity while k tends to zero. It has been demonstrated that near the wall it is sufficient to set ω at a very large value.

At inlet boundaries the values of k and ω must be specified, and at outlet boundaries the usual zero gradient conditions are used. On the other hand, the $k - \omega$ model is very sensitive to the free stream specified values, which leads to strong

dependence of the solution on the arbitrary specification of the free stream ω . This dependence is not present in the $k - \varepsilon$ model.

A.2.5 The SST $k-\omega$ model

The Shear Stress Transport $k - \omega$ model was introduced by Menter who noted that the $k - \varepsilon$ model performs well in the free stream but it is not satisfactory near boundaries. Based on this observation, Menter proposed a hybrid model which implements the $k - \omega$ model in the near-wall regions and the standard $k - \varepsilon$ model in the fully turbulent flow far from the walls. The equations are formally very similar to the standard $k - \omega$ model, but the transport equation for ω contains an additional source term due to the $\omega - \varepsilon$ transformation. Also, blending functions are used to achieve a smooth transition between the two models.

A.2.6 Conclusion on turbulence modelling

This brief overview aimed to discuss the strategy adopted for the study of the embankment overflow problem. The RAS or RANS methodology has been selected among the other options available to model turbulence flows (i.e. the large eddy simulation - LES and the direct numerical simulation - DNS). Furthermore, the SST $k-\omega$ model has been preferred for two main reasons: (1) among the RANS methodologies the two-equations models have been proven to be sufficiently accurate and computationally sustainable at the same time, also these procedures are the most common and the most validated ones in CFD practice; (2) the SST $k-\omega$ model constitutes a good compromise between the $k - \varepsilon$ model and the $k-\omega$ model. The first allows to obtain accurate solution of fully turbulent flows and the second provides better results when the fluid motion interacts with solid surface. Especially this latter problem is the focus of the CFD simulation for the embankment overflow with the final aim of calculating the wall shear stress along the embankment slope.

The solution of the Reynolds-Averaged-Navier-Stokes equations with the SST $k-\omega$ turbulence model for the embankment overflow problem is achievable only with a numerical approach. Thus, the geometrical domain needs to be discretised into a set of non-overlapping elements where the governing equations are transformed into algebraic equations to derive flow properties. The numerical method implemented in

OpenFoam is the finite volume method for which an overview is provided in the section below.

A.3 Finite Volume Method

The solution of partial differential equations by a numerical method involves the calculation of the flow property ϕ in specific points of the space (i.e. grid points or nodes), from which its distribution is constructed over the entire domain of the problem studied.

The finite volume method (FVM) is based on a discretization process (like the finite difference and the finite element methods) which approximates the continuum problem into discrete quantities. The success of the FVM in CFD is due to the strong connection with the physics of the fluid motion is its direct connection to the physical flow properties. Indeed, the basis of the method relies on the direct discretization of the integral form of the conservation law. This process consists of: (1) spatial discretization, (2) temporal discretization (for transient problems), (3) equation discretization.

A.3.1 Spatial Discretization

The original physical space is transformed into a computational domain constituted of non-overlapping cells or control volumes (normally denoted as CV), that completely fill the geometry. This spatial discretization process is referred to as “meshing”.

The fundamental components of the mesh are cells confined by internal or boundary faces defined by vertices. Therefore, a mesh is essentially a list of vertices or points which form convex polyhedral elements bounded by faces which are generally shared by neighbouring elements, except at the boundary. The mesh faces are stored in a list and they can be of two types: interior faces shared by two neighbour cells and boundary faces which are located on the domain boundary.

Two typical cells are shown in Figure A - 3Figure A - 3: : two typical “unstructured” cells in finite volume discretization , where it is highlighted the face f in common. This is an internal face, but there are also boundary faces at the edge of

the computational domain.

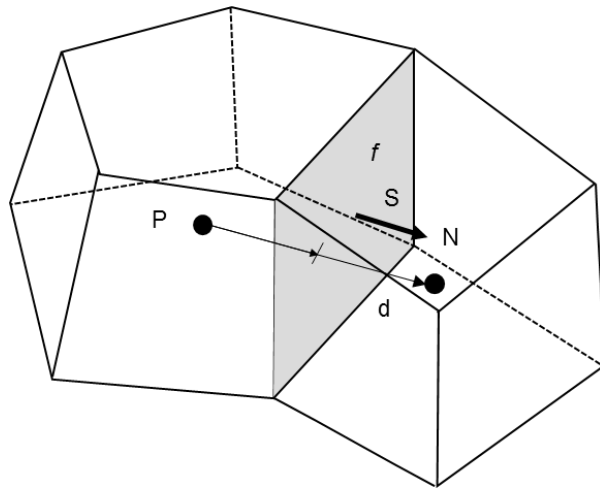


Figure A - 3: : two typical “unstructured” cells in finite volume discretization (Ruches, 2002)

The position vector of the face \mathbf{x}_f is such that:

$$\oint (\mathbf{x} - \mathbf{x}_f) dS = 0$$

and the position vector of the cell centre \mathbf{x}_P is such that:

$$\int (\mathbf{x} - \mathbf{x}_P) dV = 0$$

The face area vector \mathbf{S} is normal to the face, and it points out of the cell of interest P into the neighbouring cell N. The vector $\mathbf{d} = \mathbf{x}_N - \mathbf{x}_P$ denotes the vector between the centre of the cell of interest P. A computational mesh is orthogonal when \mathbf{d} is orthogonal to the face plane.

Among the different mesh characteristics (i.e. structure, orthogonality, blocks, cell shapes and others) mesh topology is critical as it defines the relations between elements (element connectivity), between faces (face connectivity) and between vertices (vertex connectivity). These connections are required to link the local discretized equations at element scale, to the global assembly resulting from the contribution of each element.

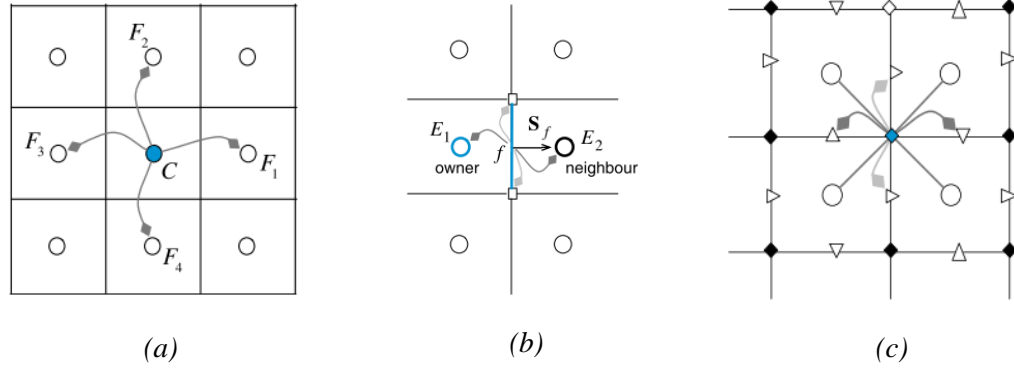


Figure A - 4: Element connectivity (a) relates the local assembly matrix to the global matrix; face connectivity (b) used for the flux terms; vertex connectivity (c) is useful for post-processing and gradient computation (Moukalled, Mangani and Darwish, 2016)

An important aspect of the spatial discretization process is the arrangement and storage of variables. Typically, there are two alternatives: (1) volume field, where the variables are stored at the centre of the cell and; (2) face field, where the variables are stored at the face centres. The obvious choice is to store all dependent variables at the cell centres and to use the same control volumes for all variables; this is called the "collocated" arrangement.

A.3.2 Equation Discretization

The key aspect of the FVM consists of writing the governing partial differential equations as volume integrals over each control volume (i.e. cells) which are successively transformed into algebraic equations.

The procedure is shown with reference to the generic form of the transport equation for a flow property ϕ , provided by:

$$\underbrace{\frac{\partial(\rho\phi)}{\partial t}}_{\text{time derivative}} + \underbrace{\nabla \cdot (\rho\mathbf{U}\phi)}_{\text{convection term}} = \underbrace{\nabla \cdot (\Gamma \nabla \phi)}_{\text{diffusion term}} + \underbrace{S_\phi(\phi)}_{\text{source term}}$$

Equation A - 43

where ρ is the density, \mathbf{U} is the velocity, Γ is the diffusion coefficient and $S_\phi(\phi)$ is the source term. This equation represents the rate of change per unit volume (time

derivative), the efflux by convection (convection term), the rate of transport due to diffusion (diffusion term) and the rate of production/destruction per unit volume (source term).

The first step of the finite volume discretization consists of integrating **Error! Reference source not found.** over the time interval $t, t + \Delta t$ and over the control volume V_P (with P centroid of the cell considered), resulting in:

$$\int_t^{t+\Delta t} \left[\frac{\partial}{\partial t} \int_{V_P} \rho \phi dV + \int_{V_P} \nabla \cdot (\rho U \phi) dV - \int_{V_P} \nabla \cdot (\Gamma \nabla \phi) dV \right] dt$$

$$= \int_t^{t+\Delta t} \left[\int_{V_P} S_\phi(\phi) dV \right] dt$$

Equation A - 44

Face Interpolation

The second fundamental step is the conversion of the volume integrals into surface integrals over the cell faces, thanks to the Gauss theorem (also known as divergence theorem) which states that:

$$\int_V (\nabla \cdot \mathbf{v}) dV = \oint_S \mathbf{v} \cdot \mathbf{n} dS$$

Equation A - 45

The divergence theorem implies that the net flux of a vector field through a closed surface S with outward normal \mathbf{n} , is equal to the total volume of all sources and sinks (i.e., the volume integral of its divergence) over the region inside the surface.

This replacement is applied to the convection and diffusions terms in Equation A - 37.

Error! Reference source not found. can be transformed into a sum of integrals over the faces resulting in:

$$\int_V \nabla \phi dV = \oint_S \phi dS = \sum_f \left(\int_f \phi dS \right) \approx \sum_f A_f \phi_f$$

Equation A - 46

where \mathbf{A} is the outward normal surface area vector of the faces in the control cell

and ϕ_f is the value of the variable in the face. Since the variable ϕ are stored on the cell centre, the respective value on the face needs to be obtained by interpolation. There are many schemes to interpolate the field ϕ , the most common are:

- The Central Differencing (CD) scheme assumes a linear variation of ϕ between P and N:

$$\phi_f = f_x \phi_P + (1 - f_x) \phi_N \quad \text{Equation A - 47}$$

where f_x is an interpolation function, defined as the ratio of the distance \overline{fN} and \overline{PN}

This is second order accurate but can be responsible of unphysical oscillations in the solution due to unsoundness.

- The Upwind Differencing (UP) scheme considered the face value of ϕ determined in the direction of the flow. If the flux F goes from P to N, then $\phi_f = \phi_P$ otherwise is $\phi_f = \phi_N$. The solution in this case is bounded but the accuracy of the discretization is not achieved.
- The Blended Differencing (BD) combines linearly UD and CD in an attempt to find a good compromise between accuracy and boundness of the solution:

$$\phi_f = (1 - \gamma)(\phi_f)_{UD} + \gamma(\phi_f)_{CD} \quad \text{Equation A - 48}$$

Time Derivative

The first term of the transport equation is discretized using a first order accurate scheme in time like the Euler implicit, which assumes a linear variation of ϕ within the stime step Δt :

$$\int_{V_P} \frac{\partial \rho \phi}{\partial t} dV \approx \frac{\rho_P^n \phi_P^n - \rho_P^o \phi_P^o}{\Delta t} \quad \text{Equation A - 49}$$

where $\phi^n \equiv \phi(t + \Delta t)$ is the new value at the time step considered, while $\phi^n \equiv \phi(t)$ is the previous time step.

Convection Term

The application of **Error! Reference source not found.** to the convection term provides:

$$\begin{aligned}\int_{V_P} \nabla \cdot (\rho U \phi) dV &= \int_S dS \cdot (\rho U \phi) \approx \sum_f A_f \cdot (\rho U)_f \phi_f \\ &= \sum_f F_f \cdot \phi_f\end{aligned}\tag{Equation A - 50}$$

where F_f is the mass flux through the face f on a known velocity field and ϕ_f is derived based on one of the interpolations schemes.

Diffusion Term

In a similar way to the convection term, the diffusion term is discretized as:

$$\int_{V_P} \nabla \cdot (\Gamma \nabla \phi) dV = \int_S dS \cdot (\Gamma \nabla \phi) \approx \sum_f \Gamma_f A_f \cdot (\nabla \phi)_f\tag{Equation A - 51}$$

Where the diffusivity Γ_f at the face is calculating with one of the interpolation schemes.

The face normal gradient $(\nabla \phi)_f$ is:

$$\nabla_f \phi = \frac{\phi_N - \phi_P}{|d|}$$

when the vector \mathbf{d} (between the centre of the cell of interest P and N) is parallel to \mathbf{S} the mesh is orthogonal. In case of non-orthogonal mesh a correction term is introduced.

There are numerous possible decompositions to correct the orthogonality. In OpenFOAM, the orthogonal correction is made using an Over-relaxed approach (Ubbink, 1997).

Source Term

The source term is linearised as follows:

$$S_{\phi}(\phi) = S_I + S_E\phi$$

And therefore the volume integral becomes:

$$\int_{V_P} S_{\phi}(\phi)dV = S_I V_P + S_E\phi V_P \quad \text{Equation A - 52}$$

A.3.3 Temporal Discretization

Using the discretized form of the various terms above, the transport equation integrated over the control volume presented in Equation A - 37 becomes:

$$\begin{aligned} \int_t^{t+\Delta t} \left[\int_{V_P} \rho_P \frac{\phi^n - \phi^o}{\Delta t} V_P + \sum_f F_f \cdot \phi_f \right] dt \\ = \int_t^{t+\Delta t} \left[\sum_f \Gamma_f A_f \cdot (\nabla\phi)_f + S_I V_P + S_E \phi_P V_P \right] dt \end{aligned} \quad \text{Equation A - 53}$$

Which is referred to as the “semi-discretised” form of the transport equation.

The next step is the treatment of the time integrals, which is conducted assuming that ϕ_P , the face values and gradients are constant during a time step.

The explicit discretization of the spatial terms considers the old values ϕ^o :

$$\phi_P = \phi_P^o$$

$$\phi_f = \phi_f^o$$

$$A_f \cdot (\nabla\phi)_f = A_f \cdot (\nabla\phi)_f^o = |\Delta|\nabla_f^{\perp}\phi^o + k \cdot (\nabla\phi^o)_f$$

The Courant Number C_o , defined as:

$$C_o = \frac{U_f \cdot S}{d \cdot S} \Delta t \quad \text{Equation A - 54}$$

(where U_f is a characteristic velocity) is calculated to check the stability of the solution (which is satisfied when $C_o < 1$).

The Euler implicit discretization considers the new values ϕ^n

$$\phi_P = \phi_P^n$$

$$\phi_f = \phi_f^o$$

$$A_f \cdot (\nabla\phi)_f = A_f \cdot (\nabla\phi)_f^n = |\Delta|\nabla_f^\perp\phi_f^n + k \cdot (\nabla\phi^o)_f$$

which is unconditionally stable.

If the Euler implicit approach is adopted, the final discrete standard transport equations is:

$$\begin{aligned} \rho_P \frac{\phi^n - \phi^o}{\Delta t} V_P + \sum_f F_f \cdot \phi_f^n \\ = \sum_f \Gamma_f A_f \cdot (\nabla\phi)_f^n + S_I V_P + S_E \phi_P^n V_P \end{aligned} \quad \text{Equation A - 55}$$

This discretization and linearization procedure described lead to a linear algebraic equation which can be written in a general form as:

$$a_P \phi_P^n + \sum_N a_N \phi_N^n = R_P \quad \text{Equation A - 56}$$

the values of ϕ_P^n depends on the value of the neighbouring cells, therefore these equations constitute a system with one equation for each cell. The system can be expressed in a matrix form as:

$$[A][\phi] = [R] \quad \text{Equation A - 57}$$

where $[A]$ is a sparse square matrix with coefficients a_P on the diagonal and a_N off the diagonal, $[\phi]$ is the column vector of the dependent variable and $[R]$ is the source vector.

A.3.4 Boundary and Initial Conditions

The fluid flow problem is completed once that boundary and initial conditions are specified, where initial conditions are required only for transient analysis. In this case initial values of all the flow variables need to be assigned in all-solution points of the flow domain.

Boundary conditions are essentially of two types: (1) Dirichlet conditions, which assign the value of the dependent variable on the boundary, therefore these are known as “fixed value” and, (2) von Neumann conditions also called “fixed gradient” because

prescribe the gradient of the variable normal to the boundary.

Boundary conditions must be specified on all the boundary faces and for each dependent variable.

It is more appropriate to define these conditions for the physical boundaries typically encountered in fluid-flow problems as the one presented in Figure A - 5.

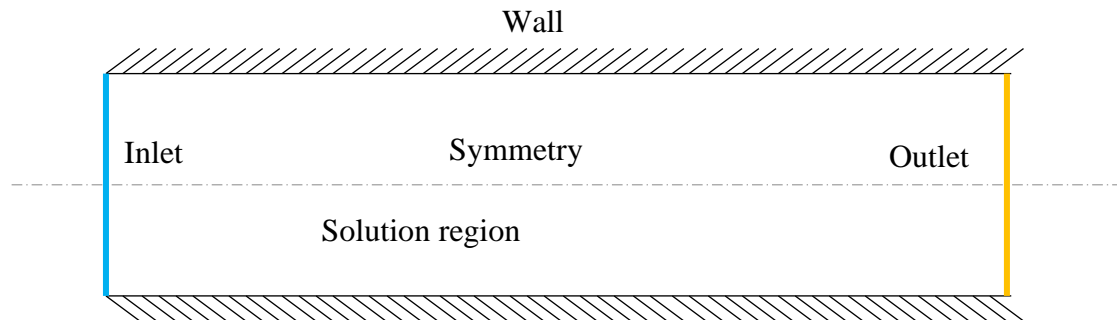


Figure A - 5: Examples of flow boundaries

- The inlet is a boundary where a fluid has a specified velocity distribution. The pressure is unknown, and a boundary value is deduced from the inner part of the solution region. For flow with a moving interface, represented as an indicator function, a fixed value is specified to indicate its position.
- The outlet or open boundaries are located, if possible, where the flow is subjected to small variations. Two common approaches are adopted to guarantee mass continuity: (1) the velocity distribution at the boundary is extrapolated from the first row of cells next to the boundary such that the overall continuity is satisfied; (2) the pressure on the boundary is fixed and a zero gradient condition is applied to the velocities. The position of the interface at the outlet is unknown and assuming that there are no significant variations of the flow, it is common practice to apply a zero-gradient condition.
- Rigid boundaries (walls) are solid surfaces where for the velocity field, the so-called no-slip condition is specified. This means that, at the wall, the fluid takes the velocity of the wall. The values of the indicator function and pressure are unknown at the wall. For the first, it is normally valid to apply the condition of zero-gradient, however if the contact angle is not normal wall adhesion must be introduced. An imposed gradient boundary condition is valid for the pressure

as for fluid at rest, it is valid that $\nabla p = \rho g$.

- Symmetry plane: the normal component of the velocity is zero and the gradient of the tangential components is zero. For all the other scalar properties, zero-gradient conditions hold.
- Initial conditions for transient flow set all the initial variables, particularly velocity and indicator function. The initial pressure field in theory is not required, however in iterative algorithms the previous step is considered and in practice the initial pressure field influences the computational work involved in the first-time step. Thus, it is convenient to adopt an initial pressure consistent with the velocity and density field.

The discretization terms of the transport equation introduced also involve the sum over surfaces or the surface gradient at boundary faces. For example, one of the faces of the element in Figure A - 6: is a boundary face of the computational domain.

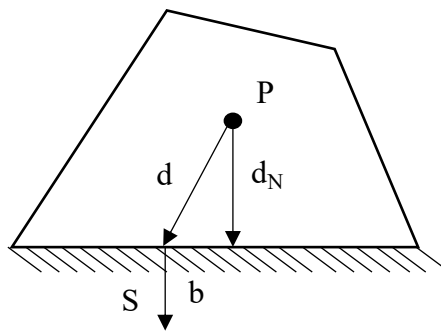


Figure A - 6: example of cell with boundary face

If a fixed value ϕ_B is specified at face b, this is substituted to ϕ_f in the discretised form of the convection term. In the diffusion term, where the face gradient is required, this is calculated as: $S \cdot \nabla_f \phi = |S| \frac{\phi_b - \phi_P}{|d_n|}$

A fixed gradient boundary condition is such that: $g_B = \nabla^\perp_f \phi$ which means that if the discretization require the value ϕ_f this need to be extrapolated as: $\phi_f = \phi_P + d_n \cdot \nabla_f \phi = \phi_P + |d_n| g_B$ or it is g_B itself if the gradient is what is needed in the discretised term.

The zero-gradient boundary condition means that $g_B = 0$.

A.3.5 Modelling Multiphase Flow

The embankment overflow is a bi-phasic flow problem involving two immiscible fluids air and water. This means that the free-surface flow interface, which indicates the water level, must be determined. The accuracy of this assessment is particularly critical for the purpose of calculating the bed shear stresses. If the model predicts water levels too low than reality, this will result in higher velocities hence shear stresses, on the other hand an overestimation of the water levels will produce an underestimation of the shear stress (Olsen, 2015). Two fundamental approaches have been adopted in CFD to predict the free-surface position: (1) surface method (surface fitting) and (2) volume methods (surface capturing).

The latter category includes the particle of fluid method and the volume fraction methods. In the past years several volume fraction methods have been proposed. These are all based on the use of a scalar indicator function, known as the volume fraction, which can assume values between zero and one. A value of zero indicates the presence of one fluid and a value of unity indicates the second fluid. On a computational mesh, volume fraction values between these two limits capture the interface and the values itself indicates the relative proportions occupying the cell volume like in Figure A - 7:

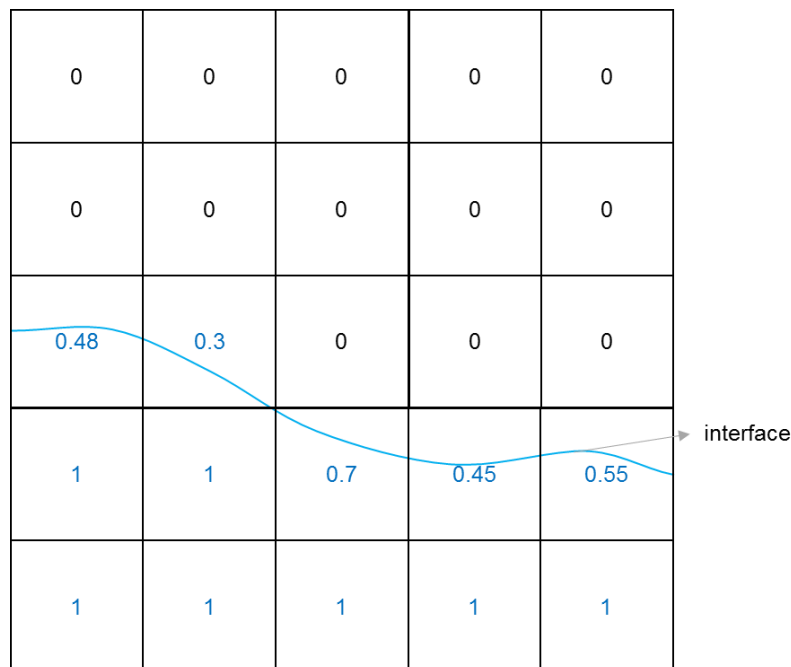


Figure A - 7: the volume fraction method represented on a discrete mesh after Ubbink (Ubbink, 1997)

A review of the different techniques developed in the framework of volume fraction methods can be found in particular in Ubbink (Ubbink, 1997). Among these different approaches (i.e. line techniques, donor-acceptor formulation and higher order differencing scheme), the volume of fluid method (VOF) is the most widely implemented procedure to predict the free-surface in many CFD software, including the interFoam solver of OpenFoam used in this study.

To introduce the use of the VOF in the modelling of multiphase flow, the continuity equation and the conservation of momentum for an incompressible fluid (i.e. $\rho = \text{constant}$) are respectively **Error! Reference source not found.** and **Error! Reference source not found.:**

$$\nabla \cdot \mathbf{u} = 0 \quad \text{Equation A - 58}$$

$$\frac{\partial \rho \mathbf{u}}{\partial t} + \nabla \cdot (\rho \mathbf{u} \mathbf{u}) = -\nabla P + \nabla \tau + \rho \mathbf{g} + \mathbf{F} \quad \text{Equation A - 59}$$

where $P = p \cdot \rho$ is the pressure, τ is the viscosity stress tensor, which can be expressed as:

$$\nabla \tau = \nabla \cdot (\mu \nabla \mathbf{u} + \nabla \mathbf{u}^T) = \nabla \cdot (\mu \nabla \mathbf{u}) + (\nabla \mathbf{u}) \cdot \nabla \mu \quad \text{Equation A - 60}$$

also in OpenFoam the modified pressure p^* (`p_rgh` in OpenFoam code) is adopted such that:

$$\nabla p^* = \nabla P - \nabla(\rho \mathbf{g} \cdot \mathbf{x}) = \nabla P - \rho \mathbf{g} - \mathbf{g} \cdot \mathbf{x} \nabla \rho$$

$\rho \mathbf{g}$ is the force due to gravity and \mathbf{F} is the source of the momentum in regard to the surface tension:

$$\mathbf{F} = \int_{S(t)} \sigma \kappa' \mathbf{n}' \delta(\mathbf{x} - \mathbf{x}') dS \quad \text{Equation A - 61}$$

σ is the surface tension coefficient, κ is the curvature and \mathbf{n} is the normal vector of the interface.

The surface tension is a tensile force tangential to the interface separating the two fluids. Surface tension is due to the fact that at the interface the forces acting on a molecule are unbalanced and there is a resultant force pulling inward. This force tends

to resist to any increase of the area of the interface. The surface tension coefficient is defined as the amount of work to be done to create a unit area of free surface σ and its magnitude is determined by the nature of the fluids. For immiscible fluids the surface tension is always positive.

An important aspect of surface tension is that it creates a pressure jump ∇P across a curved surface. To include this pressure jump into the momentum equations it is necessary to express it as a proper gradient. In the Continuum Surface Force (CSF) model developed by Brackbill et al. after (Ubbink, 1997; Lopes, 2013) the F term is converted into a volume force function of the surface tension. The surface curvature κ is formulated as a function of the phase fraction:

$$\kappa = \nabla \cdot \mathbf{n} = \nabla \cdot \frac{\mathbf{n}}{|\mathbf{n}|} = \nabla \cdot \left(\frac{\nabla \alpha}{|\nabla \alpha|} \right) \quad \text{Equation A - 62}$$

resulting in a volumetric surface tension which is written in terms of the surface tension and therefore it is related to the jump pressure across the interface:

$$F = \sigma \kappa \frac{\rho}{0.5(\rho_1 + \rho_2)} \nabla \alpha \approx \sigma \kappa \nabla \alpha \quad \text{Equation A - 63}$$

On the other hand, the indicator function α (alpha) in OpenFoam is such that:

$$\alpha(x, y, z, t) = \begin{cases} 1 & \text{for } (x, y, z, t) \text{ occupied by fluid 1} \\ (0,1) & \text{for } (x, y, z, t) \text{ at the interface} \\ 0 & \text{for } (x, y, z, t) \text{ occupied by fluid 2} \end{cases}$$

The transport of α in time is expressed by an advection function:

$$\frac{\partial \alpha}{\partial t} + \nabla \cdot (\alpha \bar{\mathbf{u}}) + \nabla \cdot [\mathbf{u}_r \alpha (1 - \alpha)] = 0 \quad \text{Equation A - 64}$$

where $\mathbf{u}_r = \mathbf{u}_1 - \mathbf{u}_2$ is the vector of relative velocity between the two fluids also called compression velocity and $\bar{\mathbf{u}}$ is the mean velocity calculated by a weighted average of the velocity between the two fluids: $\bar{\mathbf{u}} = \alpha \mathbf{u}_1 + (1 - \alpha) \mathbf{u}_2$

The local fluid properties (density and viscosity) are a weight mixture of the physical properties of both fluids:

$$\rho = \alpha \rho_1 + (1 - \alpha) \rho_2 \quad \text{Equation A - 65}$$

$$\mu = \alpha\mu_1 + (1 - \alpha)\mu_2 \quad \text{Equation A - 66}$$

To summarise the final form of the momentum equation using the VOF concept is:

$$\begin{aligned} \frac{\partial \rho u}{\partial t} + \nabla \cdot (\rho uu) - \nabla \cdot (\mu \nabla u) \\ = -\nabla p * + (\nabla u) \cdot \nabla \mu - g \cdot x \nabla \rho + \sigma \kappa \nabla \alpha \end{aligned} \quad \text{Equation A - 67}$$

This **Error! Reference source not found.** together with the continuity **Error! Reference source not found.**, the indicator function **Error! Reference source not found.** and the constitutive equations for density and viscosity **Error! Reference source not found.** and Equation A - 66 respectively, provide the mathematical framework to model the multiphase flow.

The finite volume discretization over the control volume and the time step Δt of the final form of the Phase Fraction Transport Equation is:

$$\begin{aligned} \int_t^{t+\Delta t} \left[\int_V \frac{\partial \alpha}{\partial t} dV \right] dt + \int_t^{t+\Delta t} \left[\int_V \nabla \cdot (\alpha u) dV \right] dt \\ + \int_t^{t+\Delta t} \left[\int_V \nabla \cdot (u_r \alpha (1 - \alpha)) dV \right] dt = 0 \end{aligned} \quad \text{Equation A - 68}$$

Assuming the linear variation of α , the first term can be reduced to:

$$\int_V \frac{\partial \alpha}{\partial t} dV = \frac{\partial \alpha_P}{\partial t} V_P \quad \text{Equation A - 69}$$

The second and third terms of **Error! Reference source not found.** are discretized by applying the Gauss Theorem. The artificial compression term is determined through the gradient of the phase fraction:

$$u_{r,f} = n_f \min \left\{ C_\alpha \frac{|\phi|}{|A_f|}; \max \left(\frac{|\phi|}{|A_f|} \right) \right\} \quad \text{Equation A - 70}$$

where ϕ is the face volume flux and n_f is the face unit normal flux, calculated in the interface region based on the phase fraction gradient at cell faces:

$$n_f = \frac{(\nabla\alpha)_f}{|(\nabla\alpha)_f + \delta_n|} \cdot A_f \quad \text{Equation A - 71}$$

Where $\delta_n = 10^{-5}$, takes into account the non-uniformity of the grid.

A.3.6 Solution Procedure

The solution algorithms available to solve the system described by Equation A - 57 are classified in two categories: (1) direct methods (or simultaneous algorithms), which provide the solution of the system in a finite number of arithmetic operations; and iterative methods (or segregated approach), which start with an initial guess and then continue to improve the current approximation until a pre-defined tolerance is achieved. Iterative methods are often more economical, but they usually impose some requirements on the matrix. On the other hand, direct methods are applicable only if the computational domain is small and the number of equations is not too large.

Pressure-Velocity Solution Procedure

A semi-discretised form of the momentum equation is provided by:

$$a_p u_p = H(u) - \nabla p * - g \cdot x \nabla \rho + \sigma \kappa \nabla \alpha \quad \text{Equation A - 72}$$

$H(u)$ is divided into two parts: (1) the transport part which includes the matrix of coefficients for the neighbouring cells, multiplied by the correspondent velocity, and (2) the second part or source part, composed by the source terms apart from the surface tension and buoyancy terms. From **Error! Reference source not found.** the velocity at the cell centre results as:

$$u_p = [a_p]^{-1} [H(u) - \nabla p * - g \cdot x \nabla \rho + \sigma \kappa \nabla \alpha] \quad \text{Equation A - 73}$$

Interpolating linearly the values at the cell centres using central differencing, the flux predictor and corrector can be achieved using:

$$F = -[a_p]^{-1} A_f \cdot \nabla p_f + [a_p]^{-1} A_f \cdot [H(u) - g \cdot x \nabla \rho + \sigma \kappa \nabla \alpha]_f \quad \text{Equation A - 74}$$

Replacing the velocity Equation A - 73 in the continuity equation:

$$\begin{aligned}
& \nabla \cdot [[a_p]^{-1} \nabla p_f] \\
& = \nabla \cdot [[a_p]^{-1} [H(\mathbf{u}) - \nabla p^* - \mathbf{g} \cdot \mathbf{x} \nabla \rho \\
& + \sigma \kappa \nabla \alpha]_f]
\end{aligned}
\tag{Equation A - 75}$$

Combining the **Error! Reference source not found.** with the Gauss theorem the discretized form of the pressure equation is obtained.

The velocity and pressure have a strongly linear coupling which has been a research topic for several years. In interFoam the PISO (Pressure Implicit with Splitting of Operators) algorithm is implemented, which can be described as follows from Ubbink (Ubbink, 1997):

- **Momentum prediction:** the momentum Equation A - 72 is solved first. But because the exact pressure gradient is an unknown at this step, a guessed pressure field \mathbf{p}^* is assumed from the previous step. The solution of the momentum equation provides the new velocity field \mathbf{u}^* for which the continuity equation is not satisfied.
- **Pressure solution:** the predicted velocity \mathbf{u}^* is used to assemble $\mathbf{H}(\mathbf{u}^*)$, thus the solution of the pressure Equation A - 75 provides the new pressure fields \mathbf{p}^{**} .
- **Explicit velocity correction:** using the new pressure fields, the velocity is corrected through Equation A - 73 The new velocity \mathbf{u}^{**} is now consistent with the new pressure field.

The velocity in a cell is given by Equation A - 73, which means that the velocity not only depends on the pressure gradient but also on $\mathbf{H}(\mathbf{u})$, which includes contribution from the neighbouring cells. The PISO algorithm uses \mathbf{u}^{**} to calculate $\mathbf{H}(\mathbf{u}^{**})$. This gives rise to \mathbf{p}^{***} which is again used to provide \mathbf{u}^{***} . The iterations of these two steps continue until a predefined tolerance is achieved.

Adaptive Time-Step

The adaptive-time step which based on the Courant Number ensures the stability of the solution procedure.

Using values of u_f and Δt from the previous step a maximum local Courant Number Co^0 is determined, and the new time step is assessed at the beginning of the time iteration loop:

$$\Delta t^n = \min \left\{ \frac{Co_{\max}}{Co^0} \Delta t^0; \left(1 + \lambda_1 \frac{Co_{\max}}{Co^0} \right) \Delta t^0; \lambda_2 \Delta t^0; \Delta t_{\max} \right\} \quad \text{Equation A - 76}$$

where Co_{\max} and Δt_{\max} are predefined limits and λ_1, λ_2 are damping factors, assumed equal to 0.1 and 1.2 respectively. However, an intermediate time-step Δt_{int}^* is calculated from an initial very small value Δt_{ini} :

$$\Delta t_{\text{int}}^* = \min \left\{ \frac{Co_{\max}}{Co^0} \Delta t_{\text{ini}}; \Delta t_{\max} \right\} \quad \text{Equation A - 77}$$

therefore, the value Δt^0 is the intermediate time-step.

Sequence of solution

Once that all the equations are discretised and the pressure-velocity coupling is introduced, the solution sequence adopted for the two-phase fluid system is as follows:

1. All the variables are initialised;
2. The Courant Number is calculated, and the time-step is adjusted if necessary;
3. The α Equation A - 68 is solved using the old-time level's volumetric fluxes;
4. The value of α obtained is used in conjunction with the constitutive laws to estimate viscosity, density and face densities;
5. The values above are used to calculate the moment predictor Equation A- 73;
6. The PISO loop is implemented until the pre-defined tolerance for pressure-velocity system is satisfied;
7. If the final time is not reached, the algorithm returns to step 2.

Appendix B. Proof of Concept Via the Infinite Slope Case

B.1 Proof of concept: the infinite slope case

A very simple approach is presented here to estimate the effects of the inward infiltration and the consequent loss of strength of the embankment material in the superficial layers of the downstream slope.

The downstream slope has been idealised as an unsaturated infinite slope to calculate the changes of the factor of safety during infiltration.

This requires the knowledge of the state of effective stresses within the slope, which varies continuously in space and time, according to the distribution of the pore-water pressures driven by the transient water flow.

B.1.1 Water Flow Analysis

The infiltration process related to the overflow is studied by adopting a simplified analysis. The water flow is assumed to take place in vertical direction and described by the following equation:

$$\frac{\partial}{\partial z}(v_z) = -\frac{\partial \theta}{\partial t} \quad \text{Equation B - 1}$$

where v_z (m/s) is the flow velocity in the vertical direction, θ is the volumetric water content (volume of water per total volume), and t is the time (s).

$$\frac{\partial \theta}{\partial t} = n \frac{\partial S_r}{\partial t} + S_r \frac{\partial n}{\partial t} \quad \text{Equation B - 2}$$

$$v_z = -k \frac{\partial h}{\partial z} = -k \frac{\partial}{\partial z} \left(\frac{u_w}{\gamma_w} + z \right) \quad \text{Equation B - 3}$$

where u_w is the pore-water pressure (kN/m²), z is the vertical coordinate (m), γ_w (kN/m³) is the specific weight of water, and k is the hydraulic conductivity (m/s). Combining the above equations:

$$\partial / \partial z \left[k(u_w) \frac{\partial}{\partial z} \left(\frac{u_w}{\gamma_w} + z \right) \right] = n \frac{\partial S_r}{\partial u_w} \frac{\partial u_w}{\partial t} \quad \text{Equation B - 4}$$

Two hypotheses have been adopted to simplify Equation B - 4, (a) the hydraulic conductivity is assumed to be equal to the saturated value k_{sat} (maximum infiltration and hence maximum reduction of suction), and (b) linearization of the soil water retention curve (SWRC) such that

$$n \frac{\partial S_r}{\partial u_w} \sim n \frac{\Delta S_r}{\Delta u_w} = \frac{\Delta \theta}{\Delta u_w} = \text{constant} \quad \text{Equation B - 5}$$

and:

$$\left(\frac{k_{sat}}{\gamma_w \frac{\Delta \theta}{\Delta u_w}} \right) \frac{\partial u^2}{\partial z} = \frac{\partial u_w}{\partial t} \quad \text{Equation B - 6}$$

The term in parentheses is equivalent to the consolidation coefficient in the Terzaghi's consolidation equation for saturated soils:

$$C_{v,unsat} = \frac{k_{sat}}{\gamma_w \frac{\Delta \theta}{\Delta u_w}} \quad \text{Equation B - 7}$$

The final equation is given as:

$$C_{v,unsat} \frac{\partial u^2}{\partial z} = \frac{\partial u_w}{\partial t} \quad \text{Equation B - 8}$$

Equation B - 8 is reduces to the Terzaghi's consolidation 1-D equation that can be solved analytically (Tarantino and el Mountassir, 2013).

B.1.2 Factor of safety of an unsaturated infinite slope

The factor of safety is calculated by considering the equilibrium of a slice of unitary width (Figure B - 1) and because of the shear strength adopted:

$$FS = \frac{\tau_{lim}}{\tau} = \frac{c' + \sigma \tan \varphi' + (-u_w) S_r \tan \varphi'}{\tau} \quad \text{Equation B - 9}$$

$$FS = \frac{c' + z \gamma' \cos \alpha^2 \tan \varphi'}{\tau_w + z \cdot \gamma' \sin \alpha \cos \alpha} + \frac{(-u_w) S_r \tan \varphi'}{\tau_w + z \gamma' \sin \alpha \cos \alpha} \quad \text{Equation B - 10}$$

where γ' (kNm^{-3}) is the submerged unit weight of the soil, z is the vertical coordinate (m), φ' is the soil friction angle (rad), c' is the effective cohesion, u_w is the pore-water pressure (kN/m^2), S_r is the degree of saturation (-), τ_w is the hydraulic shear stress (kN/m^2) associated with the hydrodynamic flow and α (rad) is the inclination of the infinite slope to the horizontal.

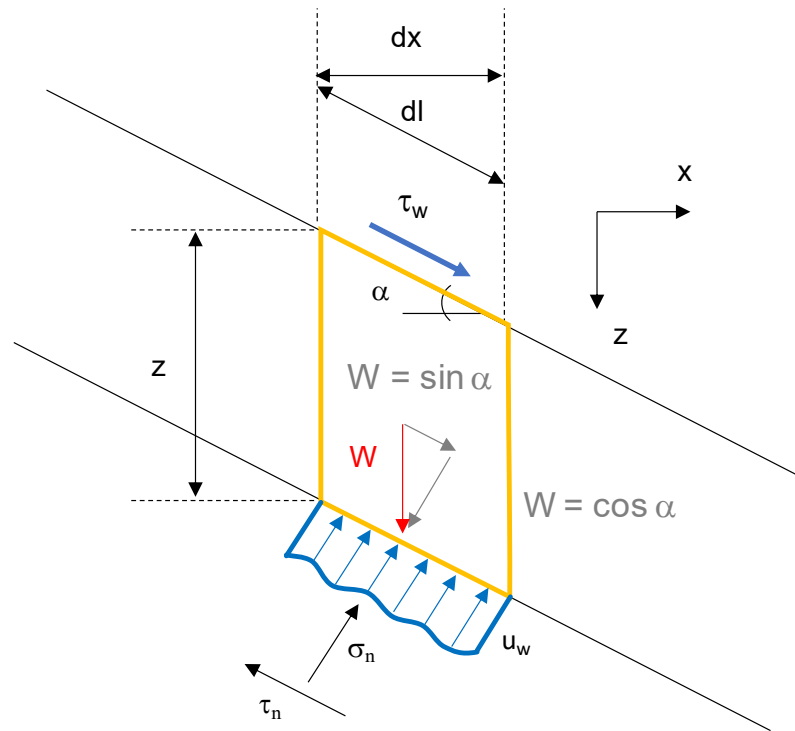


Figure B - 1 Forces acting in an infinite slope.

B.2 Application to an ideal case

With reference to an ideal homogeneous embankment (Figure B - 2), the downstream slope has been divided into three strips P1, P2, P3. The hydraulic shear stresses have been evaluated via computational fluid dynamic (CFD) with the software OpenFoam, simulating an overflow process with a $k-\omega$ turbulence model.

The initial phreatic surface is assumed to horizontal and to pass through the toe of the embankment. The distribution of pore-water pressures with depth is therefore

assumed to be initially hydrostatic.

Table B - 1 Embankment Geometry

Property	P1	P2	P3
Slope (°)	18	18	18
Distance from Water Level (m)	6	4	2
Hydraulic Shear Stress (kN/m ²)	0.125	0.185	0.204

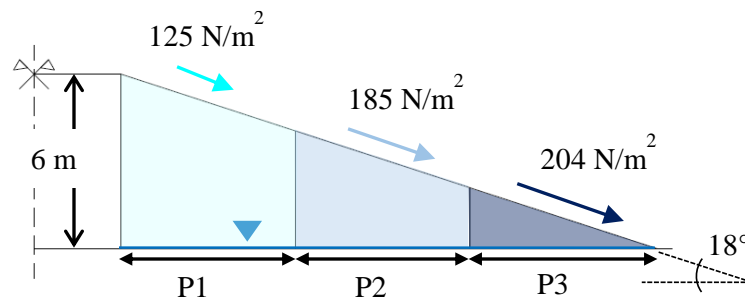


Figure B - 2 Slope geometry and divisions in three strips

For the three strips P1, P2, and P3, the values of suctions at the top of the strip are 60 kN/m², 40 kN/m², and 20 kN/m² respectively. The highest value of suction is 60 kN/m² on the crest of the embankment.

The soil water retention function and the hydraulic conductivity function considered in this exercise are shown in Figure B - 3 and Figure B - 4 respectively. These represent a silty material.

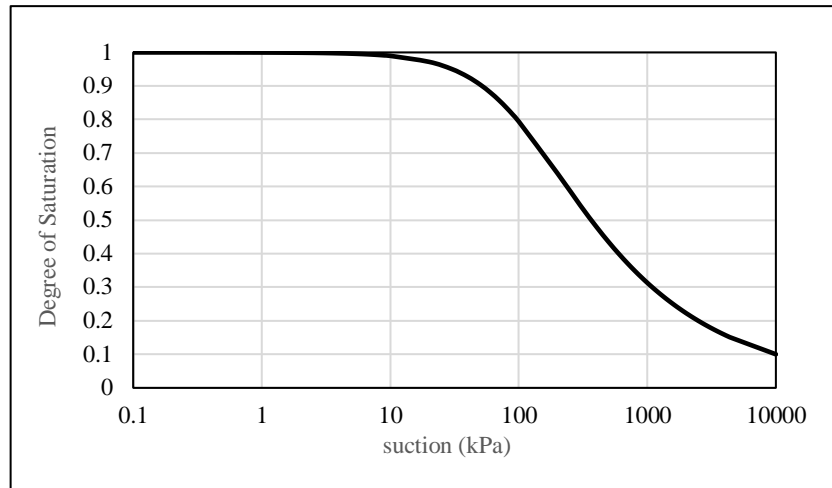


Figure B - 3 Soil Water Retention function

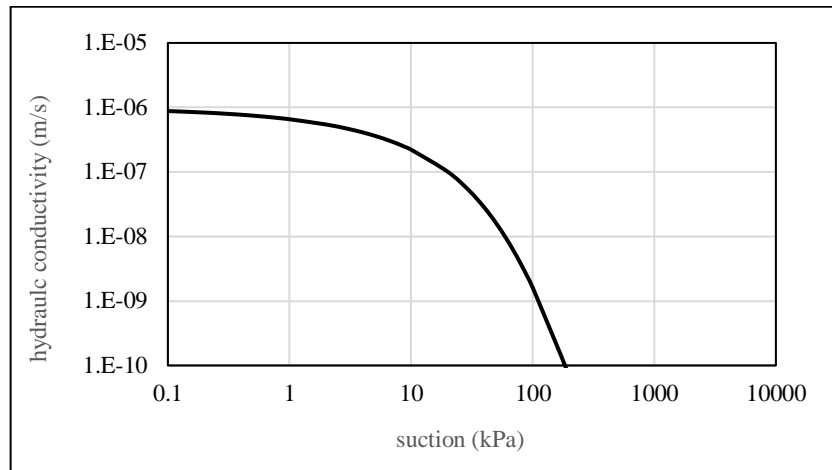


Figure B - 4 Hydraulic Conductivity function

The degree of saturation, the hydraulic conductivity, and the slope of the water retention curve at the top of each strip are determined from Figure B - 3 and Figure B - 4 respectively by considering the values of suction at the top of each strip. The slope $\frac{\Delta\theta}{\Delta u_w}$ is derived by considering the tangent to the water retention function at the value of suction at the top of the strip. The details of the material properties are presented in Table B - 2 for the three segments.

Table B - 2 Material Properties

Property	P1	P2	P3
$\phi'(^{\circ})$	18	18	18
γ (kN/m ³)	19	19	19
$s=-uw$ (kN/m ²)	60	40	20
$ksat$ (m/s)	10 ⁻⁹	10 ⁻⁸	10 ⁻⁷
$\frac{\Delta\theta}{\Delta u_w}$	0.0008	0.0007	0.0005
$C_{v,unsat}$	1.25 E-07	1.43 E-06	2.00 E-05
S_r	0.88	0.93	0.97

B.3 Results

Equation B - 8 was first solved to provide the evolution of pore-water pressure profile with time and Equation B - 10 was then used to calculate the Factor of Safety (FS) based on the pore-water pressure derived previously.

In the following, three different times of exposure to overflow have been considered: 1 hour, 5 hours and 24 hours. In addition, the Factor of Safety has been calculated with and without the presence of the hydrodynamic shear stresses, which develops at the interface soil-water because of the water flow.

The results are plotted Figure B - 5, Figure B - 6 and Figure B - 7 for the strips P1, P2, and P3 respectively. For the strip P1 (Figure B - 5), the FS on the crest is the highest and the effect of the hydraulic shear stress appears to be negligible. Here the hydraulic conductivity is very low due to the relatively high initial suction and FS profiles vary very little over time.

For the strip P2 (Figure B - 6), the FS reduces, more significantly and the effects of the hydrodynamic shear stresses become more important mainly in the first 50 cm and for the overflow time of 1 hour. On the other hand, when the suction drops considerably after 24 hours of overflow, the effects of the hydrodynamic shear stresses tend to reduce.

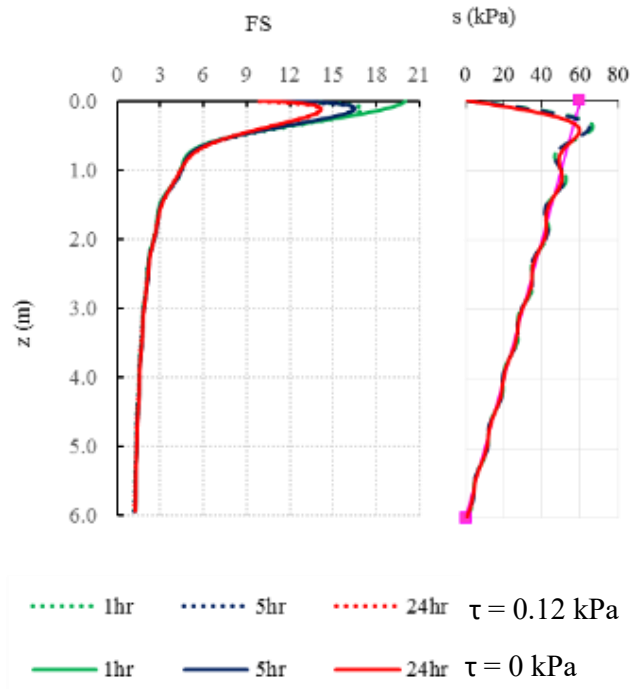


Figure B - 5 Factor of Safety and suction profile for P1 with and without hydraulic shear stresses for time of overflow 1 hr, 5 hr and 24 hr.

The strip P3 (Figure B - 7) shows the lowest value of the FS with FS becoming lower than unity when the presence of the hydrodynamic shear stresses is considered. This occurs at very shallow depth (4 cm for overflow of 1 hr and 5 hrs and 13 cm for overflow of 24 hrs).

The effect of hydraulic shear stresses is again more relevant for an overflow of 1 hr than for overflow of 5 hrs and 24 hrs.

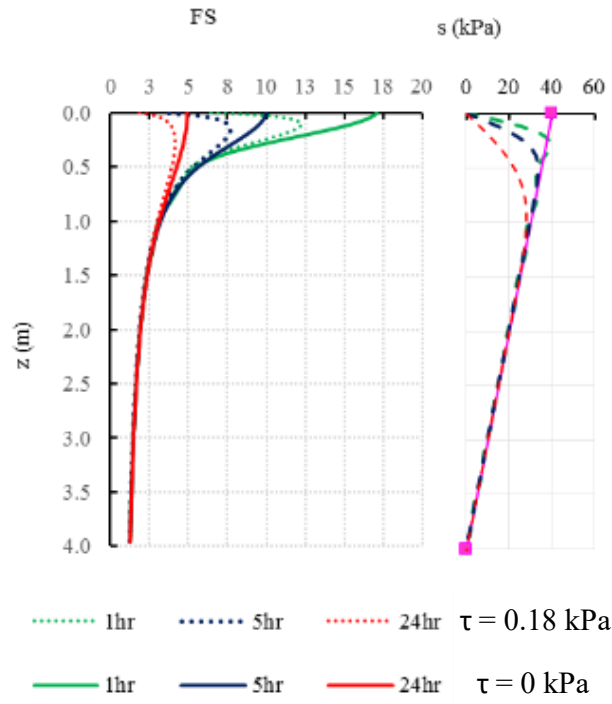


Figure B - 6 Factor of Safety and suction profile for P2 with and without hydraulic shear stresses for time of overflow 1 hr, 5 hr and 24 hr.

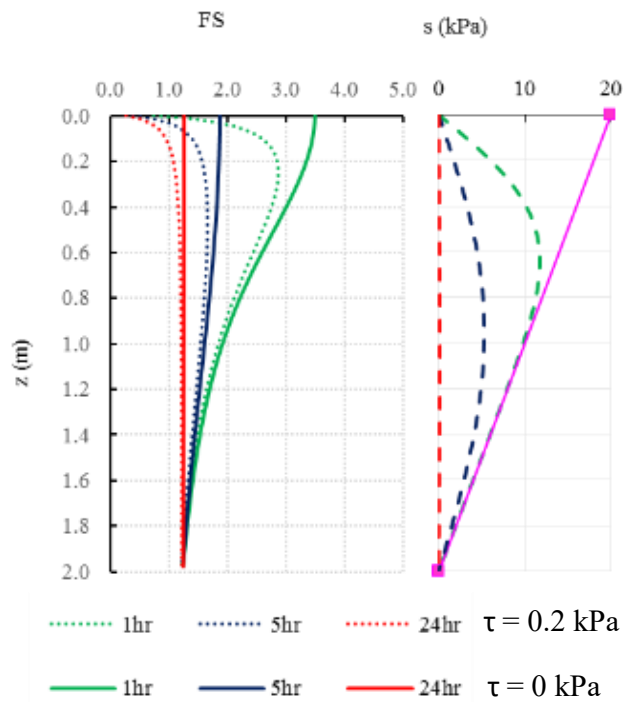


Figure B - 7 Factor of Safety and suction profile for P3 with and without hydraulic shear stresses for time of overflow 1 hr, 5 hr and 24 hr.

B.4 Conclusions

A conceptual model to study the effects of infiltration on the stability of the downstream slope of earth embankment was presented. A simplified approach based on 1-D water flow solution applied to an infinite slope was adopted. The simplified water flow equation was based on the linearization of the water retention curve and a constant value the hydraulic conductivity (equal to the saturated one). The factor of safety of the infinite slope was calculated considering the contribution of suction on soil strength.

The most important outcome is that the hydraulic conductivity of the material seems to govern the process. For very low value (i.e. $k = 10^{-9}$ m/s), which occurs on the highest part of the downstream slope, the FS does not change significantly with time. The high values of FS found here, show that the crest is the most stable part during an overflow, because the hydraulic shear stresses are small and the suction-induced apparent cohesion tends to be maintained.

In this exercise, the upper and middle part of the downstream slope remained stable, whereas the toe became unstable. This was due to the lower initial suction at the toe which generated a relatively high hydraulic conductivity and a more rapid loss in suction during overflow. In this exercise, first 4 cm were “washed away” (FS = 0.72). The destabilizing effects of the hydraulic shear stresses are predominant in the early stage of overflow, but their influence tends to decrease when a longer exposure is considered, which causes an important reduction of strength because the apparent cohesion at the toe reduces quickly and significantly.

Ultimately, this simple approach demonstrated that the hydrodynamic effects related to the overflow are important triggering factors for head-cut formation, but at the same time the loss of strength induced by the infiltration cannot be neglected. At the toe of the embankment, the initial unsaturated hydraulic conductivity is relatively high compared to the upper part of the downstream slope and the loss of suction is faster. The ‘unsaturated’ effects also explain why the breach formation in fine-grained embankment starts from the toe. Further and more rigorous analyses may help to understand the relative importance of these two effects.